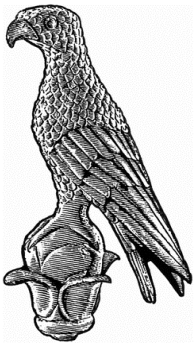

UNIVERSITY OF IOANNINA

SCHOOL OF SCIENCES

DEPARTMENT OF PHYSICS

Ph.D. Thesis

DEVELOPMENT OF HETEROSTRUCTURED CATALYTIC NANO-OXIDES WITH FLAME SPRAY PYROLYSIS TECHNOLOGY

Pavlos Psathas

IOANNINA 2023

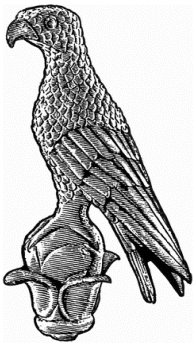

ΠΑΝΕΠΙΣΤΗΜΙΟ ΙΩΑΝΝΙΝΩΝ

ΣΧΟΛΗ ΘΕΤΙΚΩΝ ΕΠΙΣΤΗΜΩΝ

ΤΜΗΜΑ ΦΥΣΙΚΗΣ

ΔΙΔΑΚΤΟΡΙΚΗ ΔΙΑΤΡΙΒΗ

ΑΝΑΠΤΥΞΗ ΕΤΕΡΟΔΟΜΗΜΕΝΩΝ ΚΑΤΑΛΥΤΙΚΩΝ ΝΑΝΟΟΞΕΙΔΙΩΝ ΜΕ ΤΕΧΝΟΛΟΓΙΑ ΨΕΚΑΣΜΟΥ ΠΥΡΟΛΥΣΗΣ ΦΛΟΓΑΣ

ΠΑΥΛΟΣ ΨΑΘΑΣ

ΙΩΑΝΝΙΝΑ 2023

«Η υλοποίηση της διδακτορικής διατριβής συγχρηματοδοτήθηκε από την Ελλάδα και την Ευρωπαϊκή Ένωση (Ευρωπαϊκό Κοινωνικό Ταμείο) μέσω του Επιχειρησιακού Προγράμματος «Ανάπτυξη Ανθρώπινου Δυναμικού, Εκπαίδευση και Δια Βίου Μάθηση», 2014-2020, στο πλαίσιο της Πράξης «Ενίσχυση του ανθρώπινου δυναμικού μέσω της υλοποίησης διδακτορικής έρευνας Υποδράση 2: Πρόγραμμα χορήγησης υποτροφιών ΙΚΥ σε υποψηφίους διδάκτορες των ΑΕΙ της Ελλάδας».

Ευρωπαϊκή Ένωση
Ευρωπαϊκό Κοινωνικό Ταμείο

Επιχειρησιακό Πρόγραμμα
Ανάπτυξη Ανθρώπινου Δυναμικού,
Εκπαίδευση και Διά Βίου Μάθηση
Με τη συγχρηματοδότηση της Ελλάδας και της Ευρωπαϊκής Ένωσης

ΕΣΠΑ 2014-2020
ανάπτυξη - εργασία - αλληλεγγύη

Three-member advisory committee

1. Dissertation supervisor: Yiannis Deligiannakis, Professor, Department of Physics, University of Ioannina, Greece
2. Ioannis Sanakis, Director of Research, Institute of Nanoscience and Nanotechnology NCSR "Demokritos".
3. Athanasios Bourlinos, Associate Professor, Department of Physics, University of Ioannina, Greece

Seven-member assessment committee

1. Dissertation supervisor: Yiannis Deligiannakis, Professor, Department of Physics, University of Ioannina, Greece
2. Ioannis Sanakis, Director of Research, Institute of Nanoscience and Nanotechnology NCSR "Demokritos".
3. Athanasios Bourlinos, Associate Professor, Department of Physics, University of Ioannina, Greece
4. Alexios Douvalis, Professor, Department of Physics, University of Ioannina, Greece
5. Michael Karakassides, Professor, Department of Materials Science and Engineering, University of Ioannina, Greece
6. Maria Louloudi, Professor, Department of Chemistry, University of Ioannina, Greece
7. Anastasios Markou, Assistant Professor, Department of Physics, University of Ioannina,

TABLE OF CONTENTS

ΠΕΡΙΛΗΨΗ

Τα νανοϋλικά περοβσκιτικών οξειδίων [$A_mB_mO_k$] ελκύουν το ενδιαφέρον της ακαδημαϊκής κοινότητας και της βιομηχανίας, εξαιτίας των μοναδικών φυσικών, χημικών και οπτικών ιδιοτήτων τους. Επιπλέον, στο όριο του νανομεγέθους τα περοβσκιτικά οξείδια με κβαντικά φαινόμενα σαν κατηγορία λειτουργικών νανοϋλικών είναι πολλά υποσχόμενη.

Ο στόχος της παρούσας Διδακτορικής Διατριβής ήταν η ανάπτυξη νανοϋλικών περοβσκιτικών οξειδίων με τεχνολογία Ψεκασμού Πυρόλυσης Φλόγας (Flame Spray Pyrolysis, FSP) και την καταλυτική τους αξιολόγηση για τεχνολογίες περιβαλλοντικού ενδιαφέροντος. Ιδιαίτερη έμφαση δόθηκε στη μελέτη και βελτιστοποίηση της φωτοκαταλυτικής απόδοσης των νανοπεροβσκιτών σε αναγωγικές καταλυτικές διεργασίες όπως φωτοκαταλυτική παραγωγή H_2/O_2 από τη διάσπαση του H_2O και στη αναγωγή του CO_2 σε οργανικά καύσιμα (HCOOH, CH_4). Για τη σύνθεση των περοβσκιτικών νανοϋλικών, δημιουργήθηκαν νέα πρωτόκολλα τεχνολογίας FSP, όπου μελετηθήκαν και βελτιστοποιήθηκαν οι σημαντικότερες παράμετροι της διεργασίας. Η τεχνολογία FSP είναι μια ευρέως εφαρμοσμένη τεχνολογία για τη σύνθεση νανοϋλικών, συμπεριλαμβανομένης της παραγωγής νανοσωματιδίων σε βιομηχανική κλίμακα, ωστόσο μέχρι στιγμής, η συστηματική χρήση του FSP στην σύνθεση των περοβσκιτικών οξειδίων είναι ελλιπής. Στόχος μας ήταν να μελετήσουμε το ρόλο των παραμέτρων της διεργασίας FSP στην παραγωγή οξειδίων περοβσκίτη υψηλής καθαρότητας με καταλυτικές ιδιότητες. Ιδιαίτερο επιστημονικό ενδιαφέρον είχε η ανάπτυξη πρωτοκόλλων FSP για την επίτευξη του χαμηλότερου ορίου στο μέγεθος των παραγόμενων περοβσκιτών. Επιπλέον, αναπτύχθηκε και βελτιστοποιήθηκε διεργασία FSP δύο κεφαλών (Double Nozzle FSP) για την παραγωγή ετεροδομών των περοβσκιτών με συνκαταλυτικά νανοσωματίδια, σε ένα βήμα.

Σε αυτό το πλαίσιο οι επιλεγμένες περοβσκιτικές δομές ήταν: $BiFeO_3$, $SrTiO_3$, $LiTaO_3$ και $NaTaO_3$. Για την ολοκληρωμένη αξιολόγησή τους, επιτεύχθηκε επίσης η σύνθεση των σχετικών νανοδομών $Bi_2Fe_4O_9$, $CuBi_2O_4$, $CuFe_2O_4$ και Ta_2O_5. Ως συνκαταλύτες, για να ενισχύσουν τις φωτοκαταλυτικές τους ιδιότητες, μικρές ποσότητες ευγενών μετάλλων Pt,

Pd, Au και Ag εναποτέθηκαν στους περοβσκίτες, σε ένα βήμα από το FSP. Επιπλέον, στην επιφάνεια των περοβσκιτών εναποτέθηκαν συγκαταλυτικά οξείδια CuO και NiO.

Η μελέτη των νανοφάσεων και του μεγέθους των σωματιδίων επιτεύχθηκε μέσω pXRD, TEM και πορομετρίας αζώτου. Ο χαρακτηρισμός της επιφάνειας πραγματοποιήθηκε χρησιμοποιώντας φασματοσκοπίες FT-IR και Raman. Οι ηλεκτρονικές τους ιδιότητες μελετήθηκαν με φασματοσκοπία Diffuse-Reflectance Uv-Vis, καθώς και XPS. Η φασματοσκοπία ηλεκτρονιακού παραμαγνητικού συντονισμού (EPR) χρησιμοποιήθηκε για την ανίχνευση των ριζών OH και φωτοεπαγόμενων οπών/ηλεκτρονίων.

Οι περοβσκιτικοί νανοκαταλύτες αξιολογήθηκαν σε τρεις καταλυτικές εφαρμογές, (i) καταλυτική αναγωγή του βιομηχανικού ρύπου 4-Νιτροφαινόλη σε 4-Αμινοφαινόλη, (ii) τη φωτοκαταλυτική διάσπαση του νερού σε υδρογόνο, καθώς και την επακόλουθη παραγωγή οξυγόνου, και (iii) η φωτοκαταλυτική αναγωγή του διοξειδίου του άνθρακα.

Τα θεμελιώδη ευρήματα της παρούσας διδακτορικής διατριβής περιλαμβάνουν: [i] Θεμελιώδη κατανόηση στη διεργασίας FSP για σχηματισμό καθαρής φάσης νανοσωματιδίων περοβσκίτη σε μικρά μεγέθη. [ii] Θεμελιώδης κατανόηση του ρόλου των νανοπλεγματικών ατελειών, της νανο-διεπαφής και της κάμψης ζωνών των ημιαγωγών στην φωτοπαραγωγή και μεταφορά των οπών/ηλεκτρονίων. [iii] Παραγωγή υψηλής απόδοσης νανοφωτοκαταλυτών για παραγωγή H_2 και αναγωγή του CO_2. [iv] Καθιέρωση πρωτοκόλλων για νέες διεργασίες FSP που επιτρέπουν την παραγωγή νανοϋλικών περοβσκίτη και των ετεροδομών τους σε βιομηχανική κλίμακα με ενισχυμένη φωτοκαταλυτική απόδοση.

ABSTRACT

Perovskite-oxide nanomaterials $A_mB_mO_k$ have gained prominence in the industrial and academic community due to their unique physical, chemical, and optical properties. Moreover, at the low-limit of nanosize perovskite-oxide crystals with quantum-size phenomena constitute a highly promising family of functional nanomaterials.

The aim of the present Ph.D. thesis was the development of perovskite-oxide nanomaterials by Flame Spray Pyrolysis (FSP) technology and their catalytic evaluation. Specific focus was placed on their photocatalytic performance in reductive catalytic processes, photocatalytic H_2/O_2 production from H_2O splitting, and CO_2 reduction to organic-fuels (HCOOH, CH_4). For the synthesis of the perovskite nanomaterials, novel protocols of FSP technology have been studied and optimized. FSP is a widely applied technology for nanomaterials synthesis, including industrial-scale production. However, thus far, systematic application of FSP in the engineering of perovskite-oxides is lacking. Herein, our focus was to study the role of FSP-process parameters towards producing high-purity perovskite-oxides, with catalytic properties. The development of FSP-protocols to achieve the lowest-limit sizes of the produced perovskites was of particular interest. In addition, the FSP-process was optimized to produce heterostructures of the perovskites with cocatalytic nanoparticles in one-step. The deposition method of the cocatalytic nanoparticles for the FSP technology consisted of a Single-Nozzle FSP or a Double-Nozzle FSP process.

In this context, the selected perovskite structures were: $BiFeO_3$, $SrTiO_3$, $LiTaO_3$, and $NaTaO_3$. The synthesis of pertinent nanostructures, e.g., $Bi_2Fe_4O_9$, $CuBi_2O_4$, $CuFe_2O_4$, and Ta_2O_5 nanoparticles was also achieved for their comprehensive evaluation. As cocatalysts, small amounts of noble metals Pt, Pd, Au, and Ag were deposited on the perovskites in one-step by FSP to enhance their photocatalytic properties. In addition, cocatalytic oxides CuO and NiO were deposited on the surface of the perovskites.

The nanophases and particle size was monitored *via* pXRD, TEM, and N_2-porosimetry. Surface characterization was performed using FT-IR and Raman spectroscopies. Their electronic properties were studied by Diffuse-Reflectance Uv-Vis and

XPS spectroscopy. Electron Paramagnetic Resonance (EPR) spectroscopy was used as a state-of-the-art tool to monitor in-situ the photoinduced OH radicals and {hole/electron} pairs.

The so-produced nanocatalysts were evaluated in three catalytic applications: (i) the catalytic reduction of the industrial pollutant 4-Nitrophenol to 4-Aminophenol, (ii) the photocatalytic splitting of water into hydrogen, as well as the consequent production of oxygen, and (iii) the photocatalytic reduction of carbon dioxide.

The key-results of the present Ph.D. thesis include the following:

[i] Fundamental understanding of the FSP-process for pure phase perovskite nanoparticle formation at small sizes.

[ii] Fundamental understanding of the role of nanolattice defects, nano-interfacing, and semiconductor band-bending in the photophysical hole-electron generation and transfer.

[iii] Demonstration of highly efficient nano photocatalysts for H_2 production and CO_2 reduction.

[iv] Establishing protocols for novel FSP-processes that allow industrial-scale production of perovskite nanomaterials and their heterostructures with enhanced photocatalytic efficiency.

ACKNOWLEDGMENTS

I want to express sincere gratitude to the following individuals and organizations for their invaluable contributions and support throughout the research, experiments, and writing of my Ph.D. journey:

I would like to express my deepest appreciation to my supervisor and mentor, Professor **Yiannis Deligiannakis**, Head of the Lab of Physical Chemistry of Materials and Environment. For the duration of 6 years, his door was always open, with a profound willingness to go above and beyond to answer questions, provide constructive feedback, and encourage intellectual curiosity, which has been instrumental in my growth. The contribution to fostering a stimulating academic environment, always organizing our large academic team, distilling the attributes of a great research leader. I am immensely grateful for the opportunities he has provided, including the chance to work on meaningful research projects. Their mentorship will always be pivotal in shaping my academic and professional aspirations.

I would like to extend my appreciation to the other two members of my 3-member advisor committee:

Assoc. Prof. Athanasios Bourlinos, wherever I required, his vast knowledge of chemistry and his insightful feedback were always there to guide me, which many times saved me from weeks of failed experiments. Furthermore, I would like to highlight his unwavering willingness and cheerful disposition throughout the years of my PhD journey, I am truly grateful.

Dr. Ioannis Sanakis, I deeply appreciate his willingness to invest valuable time and provide insightful feedback during the evaluation of my thesis and research.

Special thanks should go to the other examiners of the 7-member committee:

Prof. Maria Louloudi, for her contributions to many research projects in the duration of my Thesis, with her expertise in chemistry provided a much valued perspective on how to complete several challenging tasks.

Prof. Alexios Douvalis and **Assist. Prof. Anastasios Markou**, within our shared workspace laboratories and shared public area, the evident dynamic environment has helped construct many interesting academic subjects.

Prof. Michail Karakasides, is thanked for his generous contribution, professional dedication, and the time devoted to evaluating my work.

I want to thank the many valuable members of our Lab for the superb environment characterized by collaboration, support, and shared dedication to knowledge, which has been instrumental in my accomplishments.

Dr. Yiannis Georgiou, under his guidance, I have understood laboratory etiquette and correct research methodology. He was always supportive, while never hearing a disgruntled comment from his mouth, he was the best researcher I had the privilege of studying under.

Dr. Maria Solakidou, for her contributions to the catalytic methodologies, her involvement in many of my experiments, and her invaluable support in navigating the complexities of university funding policies.

Dr. Constantinos Moularas, we shared our master and Ph.D. journey together, an exceptional office companion, with great academic insight, who provided much needed levity in our difficult careers, a true brother in arms. **Areti Zindrou**, for her incredible professionalism and work ethic, collaborating with her on a project was not only a privilege but also a true joy. **Christos Dimitriou**, for his cheerful workplace demeanor, was always willing to help and share academic knowledge. **Loukas Belles**, for his expertise in machinery and equipment knowledge, which contributed to many fascinating discussions. **Dr. Panagiota Stathi**, for the overall support in the many years of my experiments, contributed at every stage. To our newest lab members**, Christos Sidiropoulos** and **Sokratis Soutzios,** it was exciting to collaborate, and I hope to provided you with assistance in your careers.

Additionally, to our colleagues in the Lab of Biomimetic Catalysis and Hybrid Materials. **Annita Theofanous**, that developed to become my significant other, that helped me through many difficult days, challenges, and tribulations this carrier offers. **Marinos Theodorakopoulos**, on many occasions that demanded cooperation, his merry attitude, and interesting conversation, managed to smooth the challenging laboratory days.

Everyone contributed to make the duration of my Ph.D. academically fulfilling, a joy to research new topics, and truly happy for the experience.

Finally, I want to thank my parents, **Theodosia** and **Panagiotis Psathas.** After many academic years, they have consistently been proud of me and supported me in every possible way. Their unwavering belief in my abilities and their steadfast encouragement allowed me to reach for and achieve my highest dreams, and for this, I will forever be grateful.

Additionally, the IKY Scholarship Program (ΟΠΣ 5113934) for prospective doctoral candidates of Greek Higher Education Institutions for funding my Ph.D. Thesis.

1 Introduction

1.1 Nanomaterials

The application of nanotechnology, the formation of nanomaterials with sizes between 1 and 100nm, has received exceeding growth over the last decades, both in academic research and industrial production. Two attributes constitute nanomaterials appealing i.e. compared to their bulk equivalents [1]. The first attribute is presented when a particle has a size of only a few nanometers, the optical properties fundamentally change as the quantum implications have an exceeding factor on those sizes thus, the radiation absorption of the material changes, and the color of the material, in the case of quantum dots. The second attribute, regarding the transition from bulk to nanosize is that a higher percentage of atoms are positioned on the material's surface, that at small enough particles, half of the overall atoms are found on the surface [2]. To better illustrate the size-surface factor, the [Surface Area: Volume] Ratio compared to the diameter size of a spherical particle is shown in **Table 1-1** and **Figure 1-1**.

Table 1-1: *Correlation between nanoparticle Diameter and Surface Area: Volume Ratio*

Diameter D (nm)	Volume(nm^3)	Surface Area (nm^2)	SA : Vol Ratio (nm^2/nm^3)
100000	523598775598333	31415926536	0.00006
10000	523598775598	314159265	0.0006
1000	523598776	3141593	0.006
100	523599	31416	0.06
10	524	314	0.6
1	0.524	3.14	6

These attributes enable nanotechnology to be appealing for many applications, such as cosmetics, pharmaceuticals, electrocatalysis, and photocatalysis. The sector of nanotechnology, in the case of industrial products that implement nanoparticles or contain nanoparticles for their primary products has made enormous progress over the last decades, showing an increase of 25 times over the course of 2005 to 2015 [3]. The global nanomaterials market size was valued at USD 11.43 billion in 2022, and future projections show that the market will increase to USD 43.1 billion by 2030. The market size derives from Carbon Nanotubes, Titanium Nanoparticles, and Silver Nanoparticles as the three

most industrial applied materials, along with various noble metal and oxide nanomaterials [4].

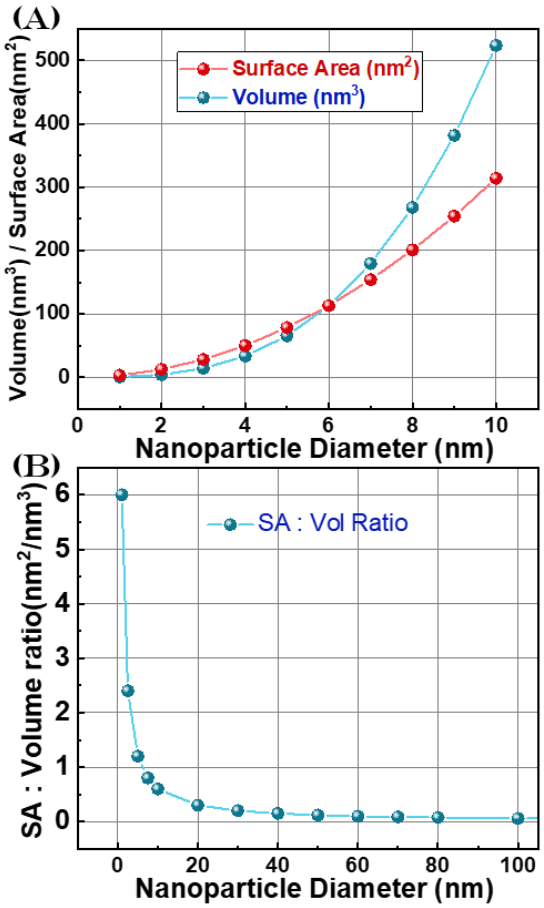

Figure 1-1: *(A) Surface Area and Volume in correlation to the Diameter of a spherical nanoparticle. (B) The Surface Area: Volume Ratio in correlation to the Diameter of a spherical nanoparticle.*

As all catalytic activities occur on the material's surface, an exceedingly high surface area corroborates an exceedingly high catalytic activity. Furthermore, the nanoparticle's shape has an important role that should provide the maximum surface possible and the interfacial conduct with the secondary supporting metal/oxide nanomaterials. These parameters determine the activity and selectivity of the nanoparticles under chemical reactions [5]. For catalytic implementation, the first published paper was published in 1941 for the application of palladium and platinum nanoparticles. Most importantly, the work of Haruta in 1987 measured the catalytic activity compared to the size of gold

nanoparticles for the oxidation of CO with O_2 for the final product of CO_2, showing that nanoparticles smaller than 5 nm have much higher catalytic activities [6].

In the passage of the last three decades, the design and implementation systems for nanomaterials for academic research and industrial establishments have increased, with copious amounts of investment in research for precisely controlled nanoparticles. The complexity of resulting nanomaterials increased from simple oxides or noble metals to precise heterostructures between oxides and noble metals, along with core-shell particles of different oxides for stabilization purposes [7].

In nanomaterials for heterogeneous catalysis, a chemical reaction occurs on the surface of a solid catalyst i.e. oxides/noble metals. A solid catalyst has the role of affecting the activation energy of the chemical reaction, decreasing the energy required in order to increase the reaction rate of the chemical process. Also, a solid catalyst has the fundamental advantage of a much higher lifetime for the operation duration with the limitation of particular changes in the structure. The removal and restoration are more straightforward. Correspondingly a solid catalyst is expected to produce a higher catalytic activity and a selective by-product formation [8].

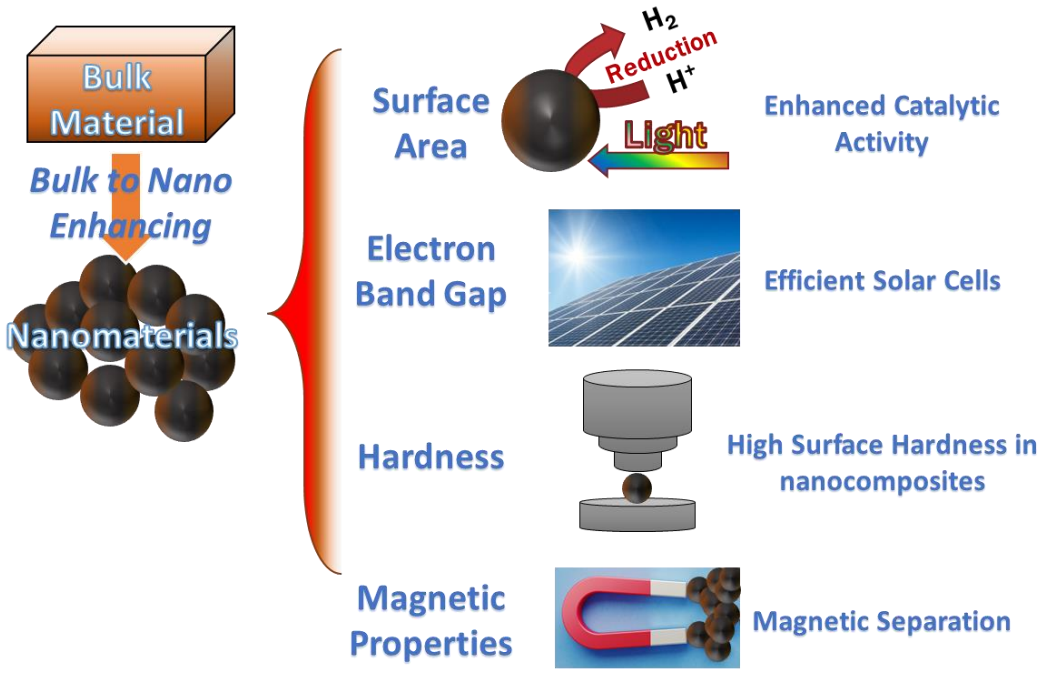

Figure 1-2: *Application of nanomaterials derived from the enhancing properties vs. their Bulk counterparts.*

Nanomaterials can also give selected attributes to other materials. As an example, in the case of polymers that have characteristic lower hardness and low electromagnetic properties, the addition of metals/metal oxides nanomaterials can incorporate the resulting polymer with higher durability and specific properties such as absorption of UV-radiation, optical qualities i.e. color, and magnetic or electrical properties [9], as shown in **Figure 1-2**.

In complex heterostructures that are more common for industrial processes, the two materials consist of a metal particle that acts as the catalyst, while a supporting metal oxide acts as the deposition interface with the properties of high surface area and chemical/ thermal stability [10].

As newfound materials derived from nanotechnology are competing with established materials/processes in industrial markets, the cost constraint for the industrial development of nanotechnology practices creates a bottleneck. Although the total revenue of nanomaterials produced globally is billions, fundamentally, it is still small by global standards of emerging technologies. Fumed silica and carbon black which constitute a high proportion of the market share, at their introduction on the market in the mid-20th century, many of the present industrial applications for these materials didn't exist yet. As the expansion of the nanomaterial sector has increased multitudes of times in academic research, the incorporation of these produced materials will harvest the next generation of industrial applications in the following decades [9].

1.2 Perovskite Structure

1.2.1 History of the Perovskites

The name '*perovskites*' first came from the mineral with the formula $CaTiO_3$, found in 1839 by mineralogist Gustav Rose in an expedition to the Ural Mountains. He gave the newfound compound the name of fellow mineralogist Count Lev Aleksevich von Petrovski [11]. After the discovery, perovskite gave its name to various compounds that created the group of perovskites. The compounds typically have the structure of $\mathbf{ABX_3}$, which will be explained later. Today, hundreds of compounds have been found that hold this structure and exist in the perovskite family [12].

The most common perovskite on earth is the Bridgmanite $FeSiO_3/MgSiO_3$, which constitutes 38% of the earth's interior solid phase structure. Usually, perovskites are not found on Earth's surface ores. Since they require a combination of high temperatures and pressures, typically encountered only in the earth's interior at a depth of thousands of meters [13]. Thus, a key-aim of the present PhD-Thesis deals with using Flame-Spray-Pyrolysis to synthesize perovskites under controlled conditions.

1.2.2 Requirements of perovskite structure

The most common structure of perovskites is **ABX_3**, which consists of three different atoms. Where A is usually a large **cation**, B is a **cation** with a size **smaller** than A, and X is an **anion** that is presented three times in the crystal structure to counter the charge of cations. The different electric charges make perovskites an ionic compound. In order for the structure to form and be stable, a set of requirements must be met [14].

1. **The charge of the compounds:** The overall charge must be neutral to form a stable ionic structure [14]. So, if the charges of each ion are presented as q_A, q_B, and q_X, the charge-neutrality formula should hold, Equation 1-1.

$$\boldsymbol{q_A + q_B = -3q_X} \qquad \text{Equation 1-1}$$

Some examples of combinations of charge ions that can create a perovskite are shown in **Table 1-2**. Where the q_X is the charge of the anion X, as an example of electric charge: (-1) for example Fluorine, (-2) for example oxygen, the perovskite particles of this thesis are oxygen-based since the FSP technology specializes in the formation of oxides. Finally, (-3) for instance Nitrogen.

Table 1-2: *Different charge combinations that form perovskites, with different anion charges of q_X and cation charges (q_A; q_B) depending on the element, for charge neutrality* [14].

q_X= -1	(q_A,q_B) = (1,2), Perovskite $KNiF_3$
q_X= -2	(q_A,q_B) = (1,5), Perovskite $NaNbO_3$
	(q_A,q_B) = (2,4), Perovskite $CaTiO_3$
	(q_A,q_B) = (3,3), Perovskite $LaAlO_3$
q_X= -3	(q_A,q_B) = (4,5), Perovskite $ThTaN_3$

2. **The Goldschmidt tolerance factor**. In 1926, Goldschmidt [15] proposed the *'tolerance factor'* (*t*) expressed *via* Equation 1-2. *The tolerance factor-t represents the probability that a combination of ions produces a stable perovskite structure.* According to Equation 1-2, the tolerance factor t, depends on the ionic size of the ions, r_A is the ionic radius of cation A, r_B is the ionic radius of cation B, and r_X is the ionic radius of anion X [16].

$$t = \frac{(r_A + r_X)}{\sqrt{2}\,(r_B + r_X)} \qquad \text{Equation 1-2}$$

When t=1, the perovskite crystal has the ideal cubic structure. Many functional perovskites have more complex crystal structures [17]. The ideal structure is exemplified as the perovskite $SrTiO_3$ having that idealized cubic structure [14], as presented in **Figure 1-3**.

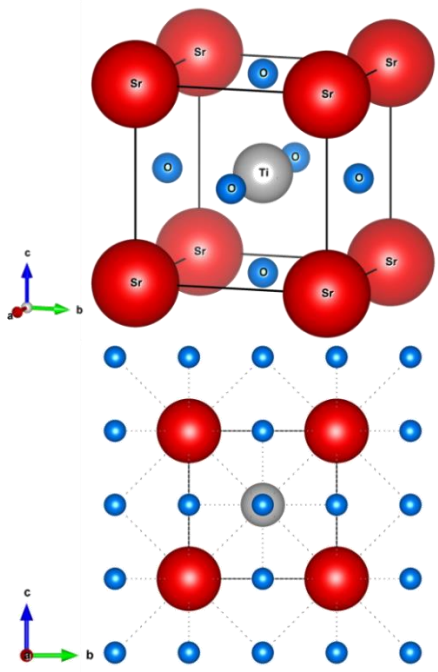

Figure 1-3: *Crystal structure of the ideal Cubic structure as shown in $SrTiO_3$, with the Titanium atom at the center of the structure, the Strontium atom at the edges, and six atoms of Oxygen surrounding the Titanium atom*.

With **t > 1**, the size of A cation is too big and forbids the formation of a perovskite. Perovskite can be formed empirically within the 0.8 < t < 1 range**.** For **t >0.9**, then cubic structures are probable. For **t <0.9**, more complicated structures than cubic are preferred, i.e., tetragonal, orthorhombic, or rhombohedral structures. In the particular case of **t < 0.8**, the cation A is too small in comparison to the B. Thus, other non-perovskite structures are formed [18].

The stability limits are based on the **geometry** parameters of the unit cell rather than *chemical* properties, so as a rule, it is taken to work as a good practical rule for most elements [19].

3. **The octahedral factor μ**. The factor μ is defined **as an index the stability of the octahedra BX_6.** To clarify the Octahedral factor, the example of $SrTiO_3$ perovskite structure is shown fragmented in **Figure 1-4**, with the octahedral in the example of $SrTiO_3$ as the formation TiO_6, the two values of importance for the factor μ comprises of **the ionic radius of the B cation (r_B) and the radius of X anion (r_X)**, calculated from the Equation 1-3.

$$\boldsymbol{\mu = \frac{r_B}{r_X}} \qquad \text{Equation 1-3}$$

The structure of Perovskite is mainly empirically observed to be stable when μ is between the values **0.442 < μ < 0.895**. That is because of the limitation of the B cation derived from the ionic size of the X_6 octahedron [20].

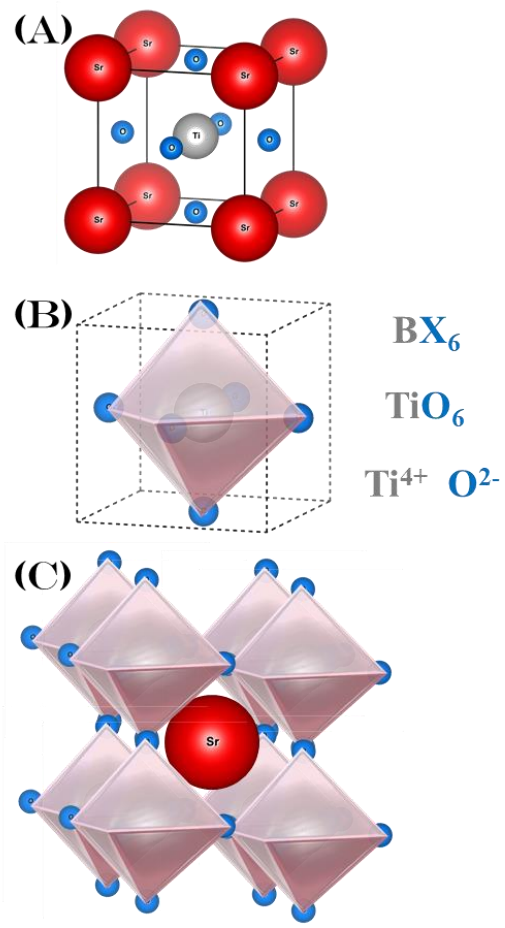

Figure 1-4: *The ideal cubic Perovskite structure of $SrTiO_3$. (A) The cubic structure with the Ti^{+4} at the cell center. (B) The octahedral polyhedron structure TiO_6. (C) Sr^{+2} at the cubic center with the octahedral structure surrounding the Strontium.*

To determine the more complex perovskite crystal structures [12], the ideal structure of cubic perovskite $SrTiO_3$ is shown again as an example, which holds the octahedral polyhedron TiO_6, that consists of the small cation B at the center and the anion X at the edges. The more complex perovskite structures can be thought of as the slight tilt of the angle that joins the two octahedral from the 180 degrees of the cubic structure from the three Cartesian axes, **Figure 1-5**. If the angle tilts in just one of the three Cartesian coordinates, in this example $\Theta 1$, then from a cubic perovskites structure morphs to a tetragonal structure. The structure is orthorhombic if the angle tilts in all Cartesian coordinates ($\Theta 1, \Theta 2, \Theta 3$) [21].

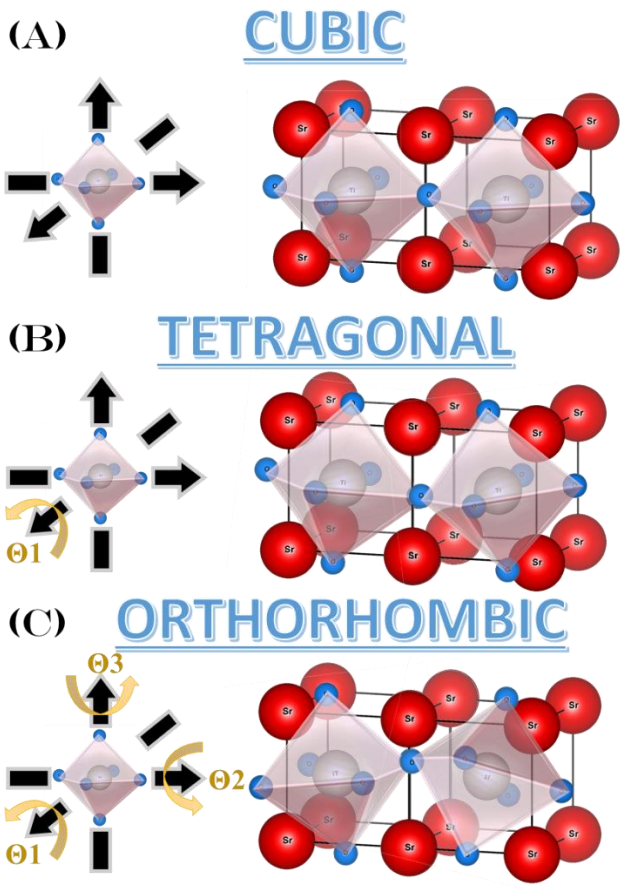

Figure 1-5: *The different perovskite structures, (A) the ideal cubic perovskite with the example of $SrTiO_3$, the axis X, Y, Z of the Octahedral BX_6 have a 180 degrees separation. (B) The Tetragonal perovskite structure, the octahedral BX_6 tilted in only one of the three axes at an angle Θ1. (C) The Orthorhombic structure, the octahedral is titled in all three of the axis, in accordance with the angles Θ1, Θ2, and Θ3.*

The perovskite parameters for the materials in this Thesis ($BiFeO_3$, $SrTiO_3$, and $NaTaO_3$) are shown in **Table 1-3**. For each of the structures, the cation charge is different with $BiFeO_3$ at Bi(+3)/Fe(+3), $SrTiO_3$ at Sr(+2)/Ti(+4), and $NaTaO_3$ at Na(+1)/Ta(+5), although the overall charge is always equal to the charge of O_3(-6). From the ionic radius of the cations and anion of the structures [22], we derive the t and μ factors. As mentioned above, the $SrTiO_3$ has a cubic structure based on the calculated t=0.91, which is higher than 0.9. While the $BiFeO_3$ and $NaTaO_3$ possess values between 0.9>t>0.8, resulting in more

complicated structures, the usually derived phases being rhombohedral for $BiFeO_3$ and orthorhombic for $NaTaO_3$. For the octahedral factor, the three materials in the range **$0.442 < \mu < 0.895$,** thus it is possible for stable Perovskite structures to form.

Table 1-3: *List of the charge, t, and μ parameters for the perovskite materials developed in the present Ph.D. Thesis.*

Perovskite	Charge	*tolerance factor (τ)*	The octahedral factor (μ)
$SrTiO_3$	Sr(+2), Ti(+4)	0.91	0.59
$BiFeO_3$	Bi(+3), Fe(+3)	0.85	0.51
$NaTaO_3$	Na(+1), Ta(+5)	0.84	0.62

1.2.3 Perovskite properties

The perovskite crystal structure allows significant flexibility i.e. via cationic substitutions, since an extensive variability of atoms can be employed. The perovskite can utilize some combination of almost all the metal ions, creating a stable perovskite structure. On the other hand, selective slightly-cationic substitutions can create **designed defects** for the crystal structure in an ordered method, thus encompassing a wide variety of physical properties and applications [23].

The aforementioned **BX_6 octahedra** are the source of many properties, influencing the perovskite's physical and electromagnetic capabilities and changing how the perovskite reacts under external magnetic or electric external fields. *The BX_6 is the core change of the properties due to the electron configurations of the B cations, which are altered by the surrounding six anions, in our case, the oxygen atoms*. While the A cations contribute to the perovskite's characteristics, in most cases, they aren't manipulated to the same degree due to the closed-shell ions with a fixed valence. *Thus, most of the alteration efforts should be placed in the BX_6 octahedral for the metallic cation of the structure but also for the shape and distortion that will be placed on the perovskite crystal structure* [14].

A fundamental property of the perovskite group is the flexibility of the structure, which can allow most atoms for facile replacement of the structure, modifying the physical and chemical properties of the structure in a controlled way. The structure can show a microdomain structure formed from several cation and anion atoms, these domains provide additional structural complexity to the anion matrix [24].

Perovskites with Nanodimensions (**Nano-Perovskites**) have shown much promise as catalysts and cocatalysts. Especially for the oxygen reduction and hydrogen evolution reactions, i.e. the applications of choice in the present Ph.D. Thesis. Perovskites have been found to be efficient at electrocatalytic activity i.e. due to lower activation energy and high electron transfer kinetics, at the same time, possessing the appropriate abilities for an efficient photocatalyst, such as unique long-term stability, excellent reproducibility, and selectivity of catalytic performance [25].

Two major groups of perovskites interest the Research community: the **halide Perovskites and the Perovskite oxides**. Organometallic halide perovskites in the past decade have drawn outstanding interest due to their highly effective properties for photovoltaic solar cells, with good stability and high efficiency [25]. Perovskite solar cells have been demonstrated to be an economically and environmentally viable option for renewable energy compared to traditional solar cell technologies [26].

Inorganic perovskite-type oxides are fascinating nanomaterials that have many essential qualities, such as excellent physical and chemical properties for broad applications in catalysis and can act as photocatalysts under light irradiation for environmental and energy-related applications, where the perovskite oxides have higher catalytic abilities than that of the transition metals compounds [27]. The **$XTiO_3$** group perovskites, where X a variety of cations (Sr, Ba, Ca, Pb, etc.) [28], have been efficient towards environmental remediation and energy conversion due to the unique structure that provides optical, physiochemical, electrical, and thermal unique characteristics. Other interesting properties that derive from the structure, for $XTiO_3$ perovskites, via the "bending" of their conduction and valence bands, can induce piezo-catalytic reactions,

resulting from the separated charge carriers, under ultrasonic vibration or heating [28]. This phenomenon is thoroughly analyzed in section 4.5 of the present Thesis.

Many different synthesis methods exist for perovskite formation, including sol-gel, coprecipitation, hydrothermal, solid-state, etc. [29–31]. These methods affect the perovskite structure, the fundamental reason is the very different application of temperature as well as pressure, which can have a tremendous change in the structural characteristics of the perovskite. Size limitation for the High-temperature synthesis techniques, or impurities of simple oxides, such as TiO_2 in the case of $SrTiO_3$ for the Low-temperature methods, all of which can have a profound significance for the perovskite's physical and chemical properties [32].

1.3 Perovskite materials

1.3.1 Bismuth-Iron Perovskites

The phase diagram of the perovskite $BiFeO_3$ and mullite type $Bi_2Fe_4O_9$ is shown in **Figure 1-6**. According to the definition of a phase-diagram [33], the lines showcase the boundaries of the crystal-phase equilibrium, and phase transitions occur via the crossing of the corresponding lines. The phase diagram in **Figure 1-6** for the components Bi_2O_3 and Fe_2O_3 has been studied extensively by J. F. Scott et al. [34] and produced via pulsed laser deposition.

In this approach, it is assumed that the BiFeO phases can be formed via the incorporation of B_2O_3 and Fe_2O_3 structural units into a stable crystal structure at the appropriate temperature. In this context, as suggested in [34], the amount of B_2O_3 and Fe_2O_3 structural units can be expressed in "moles" just to keep-track of the quantification ratio.

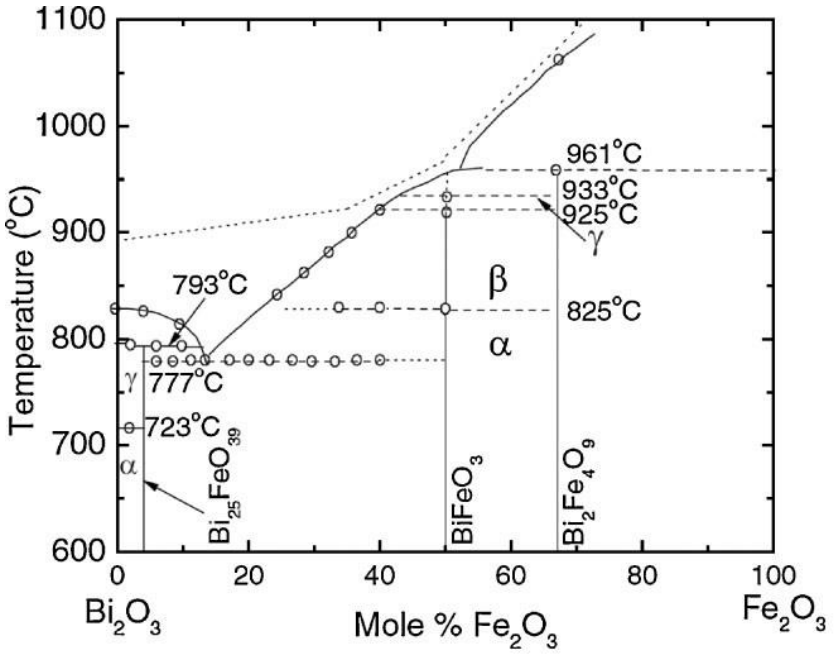

Figure 1-6: *Phase diagram of Fe_2O_3 and Bi_2O_3, showcasing the mole ratio for $BiFeO_3$ and $Bi_2Fe_4O_9$, derived from* [34].

The phase diagram in **Figure 1-6** shows that the $BiFeO_3$ perovskite is most commonly synthesized from the equimolar amount of Bi_2O_3 and Fe_2O_3 units, Equation 1-4, for temperatures above 600 ^{0}C.

$$\mathbf{Fe_2O_3 + Bi_2O_3 \rightarrow 2\ BiFeO_3} \qquad \text{Equation 1-4}$$

Interestingly, this phase diagram entails that if temperatures exceed 950^{0}C, the crystals will start to decompose into the initial oxides. This phenomenon was verified in the present Thesis, as we discuss in the Results section.

In an alternative model, the mullite-type $Bi_2Fe_4O_9$ is predicted from Mukherjee [35] to originate from the $BiFeO_3$, as shown in Equation 1-5a.

$$\mathbf{2\ BiFeO_3 + Fe_2O_3 \rightarrow Bi_2Fe_4O_9} \qquad \text{Equation 1-5a}$$

According to phase-diagram in **Figure 1-6**, when expressed in mol% of Bi_2O_3 and Fe_2O_3 units, Equation 1-5a can be rewritten as Equation 1-6b.

$$\mathbf{3Fe_2O_3 + Bi_2O_3 \rightarrow Bi_2Fe_4O_9} \qquad \text{Equation 1-6b}$$

According to phase-diagram in **Figure 1-6**, the activation energy for $Bi_2Fe_4O_9$ crystallization is higher than that of $BiFeO_3$, corresponding to higher temperatures of formation. As indicated by Equation 1-4 and Equation 1-5a, the $BiFeO_3$ phase must first be crystallized. Thus, in the formation of $Bi_2Fe_4O_9$ the overall process is slower. Notice that due to the narrow window for $BiFeO_3$ formation in the phase diagram, achieving 100% pure $BiFeO_3$ phase i.e. without impurities of the other phases, is a challenging task requiring diligent control of the preparation conditions. This issue was addressed in detail in the present Ph.D. Thesis.

The perovskite crystal $BiFeO_3$ can exist in three different crystal structures, depending on the formation temperature, as depicted by the letters α, β, and γ in the phase diagram in **Figure 1-6**. The $BiFeO_3$ as (α-$BiFeO_3$) has rhombohedral (R3c) crystal structure at low temperatures, **Figure 1-7**. As the temperature increases, the structure changes to **tetragonal (P4mm)** (β-$BiFeO_3$) and to **monoclinic (Bb)** (γ-$BiFeO_3$) [36].

The $Bi_2Fe_4O_9$ phase crystallizes to an **orthorhombic space group (Pbam)**. As seen in **Figure 1-7**, the main characteristic of mullite-type $Bi_2Fe_4O_9$, has edge-sharing with iron ions in the lattice being evenly distributed in two formula units [37], as FeO_6 octahedra running parallel to the c-axis and the FeO_4 tetrahedral in the corners, where the bismuth ions are surrounded in both cases by eight oxygen atoms [38].

So far, the perovskite phase $BiFeO_3$ has been synthesized with various techniques, including liquid chemistry, most notably by sol-gel [39], co-precipitation [40], and hydrothermal synthesis [41]. Wet-synthesis methods pose particular challenges in achieving phase purity because the formation of $BiFeO_3$ occurs in a very narrow region in the thermodynamic phase diagram [42]. Thus, high-purity phases cannot be obtained since a percentage of particles usually crystallize to the following structures present in the phase diagram i.e. $Bi_{25}FeO_{39}$, $Bi_2Fe_4O_9$, and Bi_2O_3 [40]. For the sol-gel synthesis method, the Bi_2O_3 structure can be minimized/removed from the particles by utilizing diluted nitric acid, although it is an additional harsh chemical step [43]. For Solid-state, with the application of added sintering, the particle can be obtained accurately, although due to volatilization of

bismuth at high temperatures, a fraction will be lost. Additionally, high temperatures produce, in general, much larger nanoparticles [44]. Synthesis by Flame Spray Pyrolysis(FSP) technique has produced highly crystalline, high-purity structures of bismuth oxide Bi_2O_3[45] and iron oxide Fe_2O_3 [46,47]. However, the synthesis of neither $BiFeO_3$ nor $Bi_2Fe_4O_9$ has been reported. During the present Ph.D. Thesis: We were the first to establish FSP engineering of pure $BiFeO_3$ and $Bi_2Fe_4O_9$ phases as well as heterostructures at controlled phase percentages.

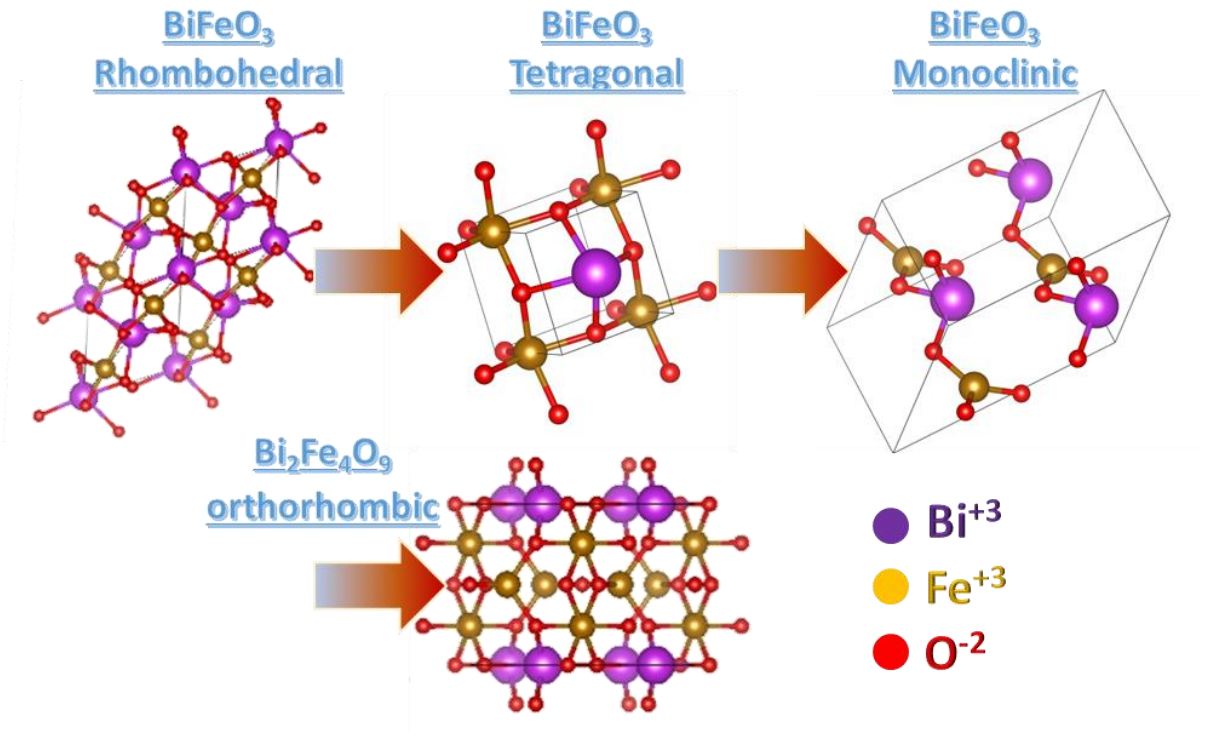

Figure 1-7: *The phase transition* of $BiFeO_3$ crystal phase, from α-$BiFeO_3$ with rhombohedral (R3c), to β-$BiFeO_3$ as tetragonal, and γ-$BiFeO_3$ as monoclinic (Bb). Additionally, the mullite-type $Bi_2Fe_4O_9$ as orthorhombic.

1.3.2 Some Properties of $BiFeO_3$ and $BiFe_4O_9$ materials

Iron is the most common element on Earth, with the fourth most common element in the Earth's crust, thus, iron-based materials belong to the Earth-abundant group along with cobalt and copper. These elements have attracted attention for decades as nanoparticles

and their implementations due to the fundament characteristics of low-cost, high availability in all countries, stable structures and sustainability, and generally low toxicity.

***Perovskite $BiFeO_3$*:** So far, the multiferroic properties of the perovskite phase $BiFeO_3$ are the most significant [48]. Multiferroic is a material that possesses two or more of the following Ferroic properties: ferromagnetism, ferro elasticity, and ferroelectricity, as is schematically depicted in **Figure 1-8**. Ferroelectric materials possess spontaneous electric polarization, by applying an external electric field, the electric polarization can be reversed. Ferroelectric materials have the application of ferroelectric random access memories (FeRAM), the stored information is the remnant polarization of the ferroelectric property [49].

However, so far, Iron oxides have many shortcomings in the application of photocatalysis due to the very high recombination rate of the hole/electron pair [50]. In the present Ph.D. thesis, we focus on these unexplored potentials of $BiFeO_3$ and $Bi_2Fe_4O_9$ as photocatalysts. In the next paragraph –for completeness- we briefly review the multiferroic as well as other pertinent technological properties **of the BiFeO materials**.

Materials that have multiferroic properties are very scarce. In this context, $BiFeO_3$ is particularly interesting showing magnetic and ferroelectric properties [51] at room-temperature conditions $BiFeO_3$ as ferroelectric, has a very high Curie temperature of T_C = 1143 K. The Curie temperature is defined as ferroelectricity ceases to exist with higher temperatures than T_c. The ferromagnetic property has a spontaneous magnetization that changes the polarization with the external magnetic field, while the anti-ferromagnetic property has a Nel temperature of T_N = 643 K [52].

The secondary property of the multiferroic $BiFeO_3$ material has applications for magnetic sensors and data storage. As a multiferroic, both memory applications can be applied, and it can be beneficial for many other secondary applications [53] [54].

The multiferroic properties derive from distortions of structural electrons, and Ferroelectricity derives from off-centered electron distortions of the d^0 position. Magnetic properties require local spin electrons with the electron positions d^j with j being different from zero. The contradiction between the two properties limits the materials that can have

these distorted electrons in their structure [55]. For the multiferroic $BiFeO_3$, the electric polarization derives from the bismuth element, as the Bi^{+3} has a pair of electrons at s^2 orbitals. In contrast, the magnetization derives from the iron element from the state Fe^{+3} [51].

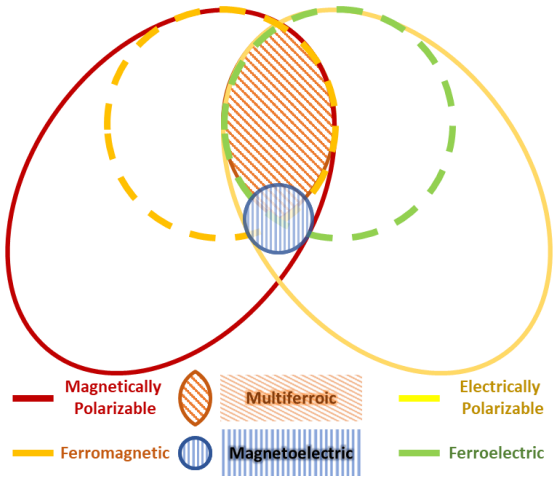

Figure 1-8: *Schematic Summary of all the Ferroic properties, as conceptualized via the "properties-overlap "scheme* [53].

***Mullite-type $Bi_2Fe_4O_9$*:** The $Bi_2Fe_4O_9$ phase has near zero paramagnetic properties at room temperature, whereas if the temperature drops at T_N=264K, it demonstrates antiferromagnetic properties [38]. The structure has magnetic interaction in different directions due to the Fe^{3+} positions at the edge-sharing Fe octahedra and the corner-sharing Fe tetrahedral, which each has a different magnetic field [56].

So far, important applications for $Bi_2Fe_4O_9$ include gas sensors [57], and catalytic oxidation of ammonia to NO, which require noble metals such as Platinum and Rhodium that are very expensive [58]. In [59,60], the materials were employed for two different catalytic applications. (A) Removal of organic pollutant 4-Nitrophenol. (B) Photocatalytic water splitting to H_2 and O_2. The Oxygen Evolution Reaction (OER) procedure will be explored in more detail in section 4.4 of the Ph.D.

$BiFeO_3$:$Bi_2Fe_4O_9$ have been reported to be very stable with unchanged crystal structures and constant catalytic activities under hours of the catalytic processes [61]. $BiFeO_3$ and

$Bi_2Fe_4O_9$ materials have been published to be efficient for catalytic degradation of organic pollutants such as methylene blue (MB), Rhodamine Blue (RhB) [62,63], and Bisphenol-A [64]. A heterostructure of the two materials $BiFeO_3/Bi_2Fe_4O_9$ has also been shown to have an enhanced photodegradation of RhB [65].

Photocatalytic Applications of Bi-Fe-O Nanomaterials: One of the crucial parameters for the application of photocatalysis is the band gap, E_g, of the materials or the photonic energy required to excite one electron from the valence band to the conduction band. The perovskite $BiFeO_3$ has a relatively small bandgap in the range of 2.1-2.8 eV, depending on the morphology of the structure from the synthesis method [66], while $Bi_2Fe_4O_9$ has a bandgap in a similar range of 2.1-2.3 eV, although demonstrating a secondary band gap approximately at 1.6 eV [67]. The low band gap constitutes both materials as visible-light photocatalysts, thus able to absorb a much higher percentage of the Sun radiation [68,69].

So far, nanoparticles with Bismuth-based materials or perovskites have been shown to be efficient photocatalysts, OER specifically the $BiVO_4$ [70,71] and Bi_2WO_6 [72], while the $BiFeO_3$ had some promising publications for OER [68,69]. $BiFeO_3$ has been shown to combine efficiently with other materials to apply visible light photocatalytic properties, such as $BiFeO_3/TiO_2$ nanohybrid that enhanced H_2 production from water [73]. Heterostructure $BiFeO_3/Bi_2Fe_4O_9$ has been found to align the conduction and valence band of the two phases, separating the electron/hole pair and increasing the photocatalytic activity [74]. However, Mullite-type $Bi_2Fe_4O_9$ hasn't been assessed for photocatalytic O_2 production from H_2O.

In the present Ph.D. thesis, we focus on the catalytic/photocatalytic evaluation and optimization of $BiFeO_3$ and $Bi_2Fe_4O_9$ nanoparticles synthesized by FSP technology. A complete, detailed study of the catalytic and photocatalytic properties of $BiFeO_3$ and $BiFe_4O_9$ is presented in Section 4.3 and Section 4.4 of the Thesis.

1.3.3 Spinels $CuFe_2O_4$ and $CuBi_2O_4$

The structural characteristics of spinels remained largely unknown until 1915. Bragg and Nishikawa later verified that spinels typically consist of a configuration composed of A–O tetrahedra and B–O octahedra [75]. In spinels, which are frequently

represented by the composition AB_2O_4 (where A and B denote metal ions), metal A is situated at the centers of positions with tetrahedral coordination, metal B is located at the centers of positions with octahedral coordination, and anion (such as O^{2-}) resides at the vertices of the polyhedra (for conventional spinels) [76]. Generally, the tetrahedral vertices are smaller in size compared to the octahedral vertices. As a result, cations with smaller radii show a preference for occupying the A sites, while larger cations are inclined to occupy the B sites [76]. In order for the spinel to be stable, the overall charge must be neutral, as denoted by Equation 1-7.

$$q_A + 2q_B = 4q_X \qquad \text{Equation 1-7}$$

Within the realm of oxide groups, the CuM_2O_4 spinels, where M typically represents a 3d metal, have not garnered significant focus as photocatalysts. This is despite the fact that they exhibit many favorable traits, such as their very low cost, a band gap attributing to d–d photo transitions, and boast comparatively substantial absorption coefficients [77].

***$CuFe_2O_4$*:** Copper ferrite ($CuFe_2O_4$) has been widely investigated as a magnetic material, given its remarkable magnetic characteristics, high electronic conductivity, prominent thermal stability, and low toxicity [78]. Moreover, its exceedingly affordable nature, due to the presence of constituent elements, copper (Cu) and iron (Fe), renders it highly appealing [78].

As for photocatalytic applications, an additional advantageous aspect of $CuFe_2O_4$ pertains to its chemical stability and direct band gap, strategically positioned in close proximity to the optimal range of the solar spectrum, direct requirements for practical applications on Earth [77]. $CuFe_2O_4$ has a band gap measuring 1.43 eV, with a high Conduction band of -1 eV and a Valence band of +0.4eV [79]. Nonetheless, it suffers from the limitation of a low quantum yield attributed to its restricted electron/hole mobility. Consequently, in catalytic applications, it is being found by creating a heterostructure with an additional semiconductor. Notably, combinations like $CuFe_2O_4/TiO_2$ [78] [80] and $CuFe_2O_4/\alpha\text{-}Fe_2O_3$ [81] have been successfully employed for generating hydrogen from water using visible light irradiation, leading to a significant enhancement in efficiency.

The phase diagram for $CuFe_2O_4$ based on *$CuFe_2O_4$/ ($CuFe_2O_4$/ Fe_3O_4), is shown in* **Figure 1-9(A).** Traces of $CuFe_2O_4$ can be obtained at temperatures over 400 ^oC, although for most synthesis techniques to obtain a 100% $CuFe_2O_4$ phase, temperatures 1000 ^oC are required.

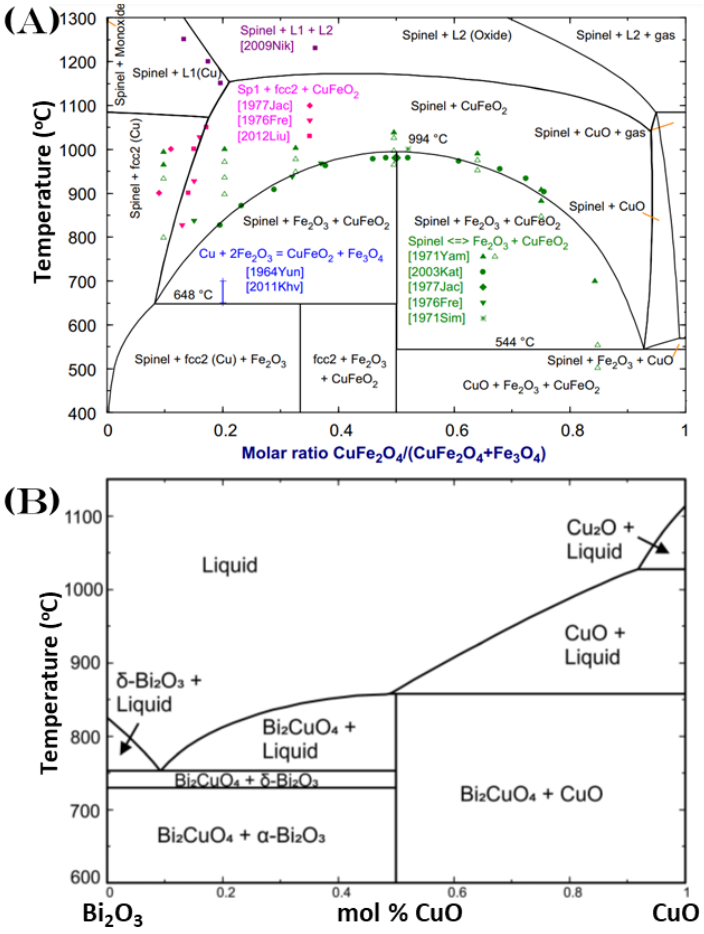

Figure 1-9: *(A) The phase diagram of $CuFe_2O_4$/ ($CuFe_2O_4$/ Fe_3O_4) for the formation of $CuFe_2O_4$ from [82], The phase diagram of Bi_2O_3/ CuO for the formation of $CuBi_2O_4$ from [83].*

***$CuBi_2O_4$*:** Numerous metal oxides based on copper exhibit inherent p-type conductivity, including the archetypal Cu_2O. However, the operational stability of Cu_2O has been attributed due to the presence of Cu 3d character within the conduction band (CB). This characteristic results in a self-reduction induced by photoelectrons, as the reduction potential of Cu_2O/Cu resides within the band gap [84]. To counteract this issue, a prevalent approach involves alloying Cu_2O with another metal oxide to generate a ternary alloy, such

as $CuBi_2O_4$ or $CuFeO_2$. This alloying enables targeted modification of the CB, effectively steering photogenerated electrons toward redox stable metal orbitals rather than the Cu 3d orbitals [84].

$CuBi_2O_4$ possesses several attractive features as a p-type semiconductor, with 1.5–1.8 eV optical band gap [85] appropriate for the solar spectrum and with high Conduction band of -0.66 eV and Valence band of +1.14eV [86]. For these attributes, $CuBi_2O_4$ has been explored extensively as a photocathode for solar water splitting [87] [88]. However, reports are scarce on $CuBi_2O_4$ with high-purity that exhibits a high surface area and small size [87]. These characteristics are important as $CuBi_2O_4$ has low charge mobility, consequently constrains the diffusion length of photocarriers to a range of 10 to 52 nanometers [85].

The phase diagram for $CuFe_2O_4$ based on *Bi_2O_3/CuO, is shown in* **Figure 1-9(B).** $CuFe_2O_4$ has a generally Low melting point around T = 851 °C. For pure phase $CuFe_2O_4$, the precise 1: 1 molar ratio of Bi_2O_3 and CuO, the temperature profile consists of 750 °C/24 h calcination. In contrast, additional Bi or Cu content results in Bi_2O_3 or CuO particles [83] [89].

1.3.4 Tantalum-Oxide-based Perovskites

Tantalum oxides Ta_2O_5 and their perovskites ($NaTaO_3$ and $LiTaO_3$) have been demonstrated to be among the most successful photocatalysts for water splitting and hydrogen production [90–92], determined primarily by the *d*-orbitals of Tantalum and the effect of alkaline atoms [93–96] forming perovskite structure, as shown in **Figure 1-10**.

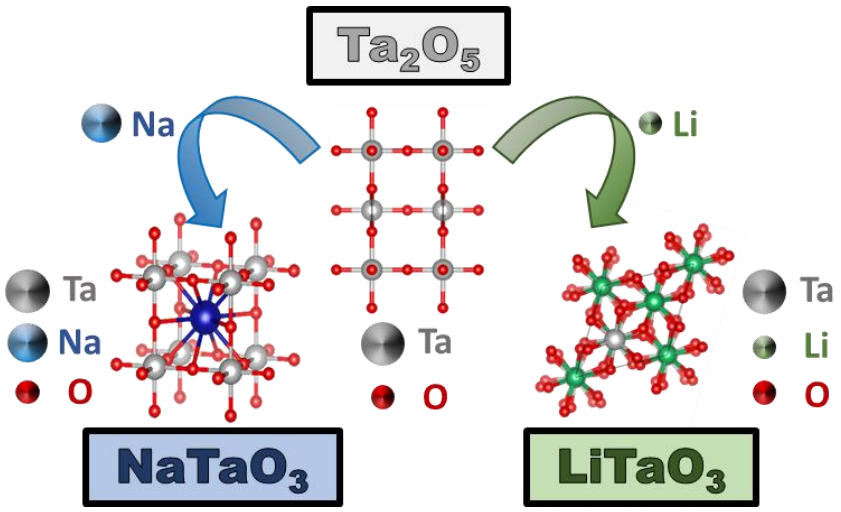

Figure 1-10: *The crystal structures of Ta_2O_5, $NaTaO_3$, and $LiTaO_3$.*

On the Phase-Diagram of Ta-Oxide and its Alkaline (Li, Na, K) Perovskites (Ta_2O_5, $LiTaO_3$, $NaTaO_3$, $KTaO_3$)

Phase Evolution of Ta_2O_5: The phase-diagram for the Ta-Oxygen system, based on the Bulk dimension of Ta_2O_5 material, is presented in **Figure 1-11**(A). Stable Ta_2O_5 can be formed at an oxygen concentration over 70% per mol of Tantalum and Temperatures over 600°C. This shows that the stabilization of solid Ta_2O_5 particles requires diligent control of the O-content and Temperature. In this context, in the present Ph.D. Thesis, we have systematically screened these parameters i.e. Ta:O ratio and Temperature in the FSP process. These results are discussed in section 4.7.2.

Ta_2O_5 exists in two polymorphic configurations, namely αTa_2O_5 and βTa_2O_5 (also denoted as the high-temperature form HTa_2O_5 and the low-temperature form LTa_2O_5, respectively). The initial formation of αTa_2O_5 takes place around 600°C, undergoing a transition to βTa_2O_5 at a temperature documented around 1320°C, which varies based on the stoichiometry of Tantalum and oxygen [97]. The melting point for the βTa_2O_5 phase occurs at 1785°C, while the αTa_2O_5 phase melts at 1872°C [98]. The prevailing symmetry of the low-temperature form is characterized mainly as orthorhombic, whereas the high-temperature form is primarily identified as tetragonal. However, depending on the synthesis methodology, it has also been documented as hexagonal and monoclinic [97].

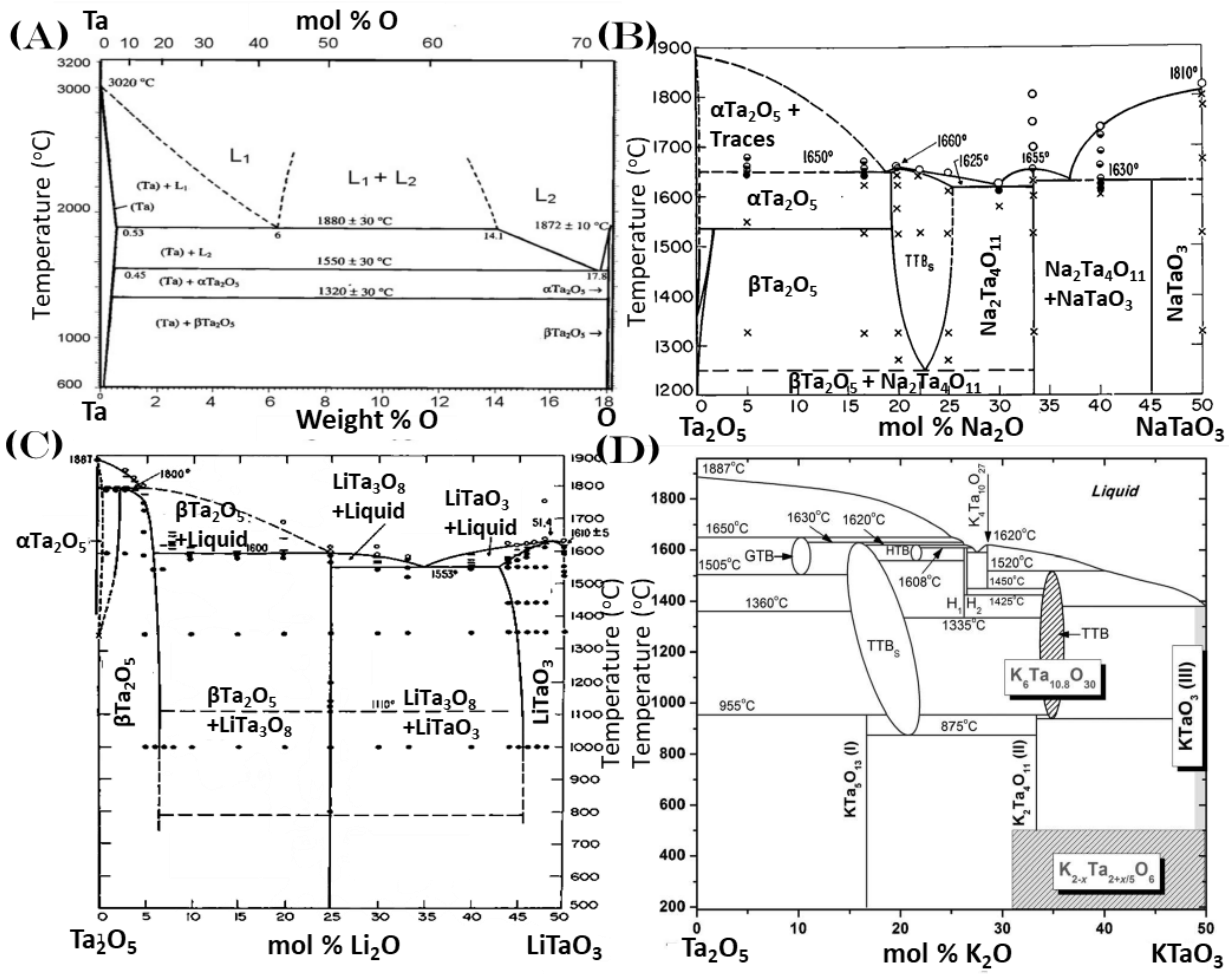

Figure 1-11: *(A) The phase diagram of Ta/Oxygen for the formation of Ta_2O_5 from* [97]*. (B) The phase diagram of Ta_2O_5/ Na_2O for the formation of $NaTaO_3$ from* [99]*. (C) The phase diagram of Ta_2O_5/ Li_2O for the formation of $LiTaO_3$* [99]*. (D) The phase diagram of Ta_2O_5/ K_2O for the formation of $KTaO_3$ from* [100]*.*

Phase Evolution of $NaTaO_3$: In **Figure 1-11**(B), we present the phase-diagram for Na, Ta-Oxygen system [99]. This shows that in Bulk materials, the required temperature is 1200°C, resulting in the highest temperature formation of Ta-oxides perovskites presented. With the Ta_2O_5:$NaTaO_3$ mol ratio of 22% and below, the majority of the crystal phase will result in the βTa_2O_5. With higher Ta_2O_5:$NaTaO_3$ ratios, the phase $Na_2Ta_4O_{11}$ is presented. To even

have a trace of the desirable $NaTaO_3$, a percentage of over 34% is required, with the pure phase obtained only in the limiting range of 45% to 50% Ta_2O_5:$NaTaO_3$ [99]. The $NaTaO_3$ material results in Liquid at temperatures of over 1750°C. For completeness, TTB represents a nonstoichiometric solid solution that exhibits an orthorhombic distortion of tetragonal tungsten bronze-type lattice with superstructure indicating a tripled cell [99].

It is important to note that the phase formation of $NaTaO_3$ differs enormously in the nanomaterials produced with the FSP method. Materials that were not fully crystallized in the FSP synthesis i.e. the initial experiments before the appropriate method was implemented, only required a calcination temperature of 700°C for 1 hour to obtain a fully formed $NaTaO_3$ nanomaterial. This observation correlates with the results from the formation of Bi-Fe-O materials. Additionally, in the present Ph.D. Thesis, we have systematically screened the precursor Na:Ta ratio and the temperature profile of the FSP process. The results are discussed in section 4.7.2.

Phase Evolution of $LiTa0_3$: In **Figure 1-11**(C), we present the phase-diagram for Li, Ta-Oxygen system [99]. In Bulk materials, the stable $LiTaO_3$ perovskite phase can be formed at a narrow region of intermixing of Ta_2O_5 : $LiTaO_3$ ratio of 45-50%, with T>600^oC. At the 25-45% Ta_2O_5 : $LiTaO_3$, the obtained material is a combination of $LiTaO_3$ and $LiTa_3O_8$. At lower ratios of 5-25%, the resulting combination is $LiTa_3O_8$ and βTa_2O_5. At higher temperatures of T>1600 ^oC, the $LiTaO_3$ reaches its melting point [101]. This shows that stabilization of the solid $LiTaO_3$ particles requires diligent control of the O-content, Temperature as well as Li:Ta ratio.

Phase Evolution of $KTa0_3$: In the present Thesis, we did not study the production of $KTaO_3$. However, for completeness, we include the phase diagram for $KTaO_3$ as a homologous material to $LiTaO_3$ and $NaTaO_3$. **Figure 1-11** (D) presents the phase-diagram for the Ta_2O_5/ K_2O system [100]. As the other Ta-perovskites, the pure phase of $KTaO_3$ is achieved at a very narrow Ta_2O_5:$KTaO_3$ mol ratio, for over 48% and a temperature of over 550^oC, similar to $LiTaO_3$. At lower ratios, the phase $K_2Ta_4O_{11}$ is formed similarly to $Na_2Ta_4O_{11}$, although an additional phase KTa_5O_{13} is obtained at a mol ratio below 16% [100].

On the Photocatalytic Properties of Ta-Oxide Perovskites

The selected perovskites have a very high conduction-band edge i.e. E_{CB}= -1.06 *vs.* NHE for $NaTaO_3$ and -2.1 eV *vs.* NHE for $LiTaO_3$ [102–104], that enables photogenerated electrons and holes to be very efficient for photocatalysis. Noticeably, the conduction band is negative enough to reduce the -otherwise very stable- CO_2 whose one-electron reduction potential is -1.9V *vs.* NHE for $CO_2^{\bullet-}/CO_2$, and -0.61V *vs.* NHE for $HCOOH/CO_2$ [105]. In general, photocatalytic materials that can accomplish CO_2 reduction are limited since many nano oxide-semiconductors have E_{CB} near zero NHE or lower [106] e.g. TiO_2 E_{CB}=-0.2V *vs.* NHE [107]. Recently, photocatalytic CO_2 reduction by $NaTaO_3$ has been reported [108].

The Ta_2O_5 material is currently used in several technological applications due to some very unique properties [109–111], such as high refractive index (~2.125) for optoelectronic applications, and teeth-filler [112,113], low-loss coating materials [114] microelectronics such as high-*k* gate insulator [109,115]. Tantalum oxide materials have good thermal, mechanical, and chemical stability, which enables them for consistent photocatalytic efficiency without alteration in the crystal phase [110,116]. Tantalum oxide-based nanoparticles are determined as safe contrast agents and are considered very promising for computed tomography in cancer diagnostics. The properties that enable this function are excellent biocompatibility and modifiable particle surface. At the same time, it is competitive with the alternative particles(Au, Pt, Lu), considering the difference in cost effectiveness [117]. The perovskite $LiTaO_3$ material has been widely used in the fields of acoustics and optics due to excellent electro-optic, non-linear optical [118], with a very narrow phase diagram, as shown in **Figure 1-11**(C) [101].

The Challenge of Nano-Sized $NaTaO_3$: So far, the successful synthesis of nanocrystalline Ta_2O_5 and $NaTaO_3$ phases have been established using various methods, including sol-gel [119,120], hydrothermal [29–31], and solid-state [121,122]. These methods frequently require lengthy pre- and post-synthesis steps, i.e. such as drying and calcination, increasing the synthesis time and energy consumption considerably. In **Figure 1-12**, a comparison is shown for the very drastic time requirements for the most applied

synthesis methods of nano-$NaTaO_3$, including the FSP method of this work. The calcination of very high temperature is primarily a very limiting step that is required by most synthesis methods, which severely increases the $NaTaO_3$ size in order for the stabilization of metal-oxide $NaTaO_3$ perovskite phases, with a necessary 900^0C temperature [123].

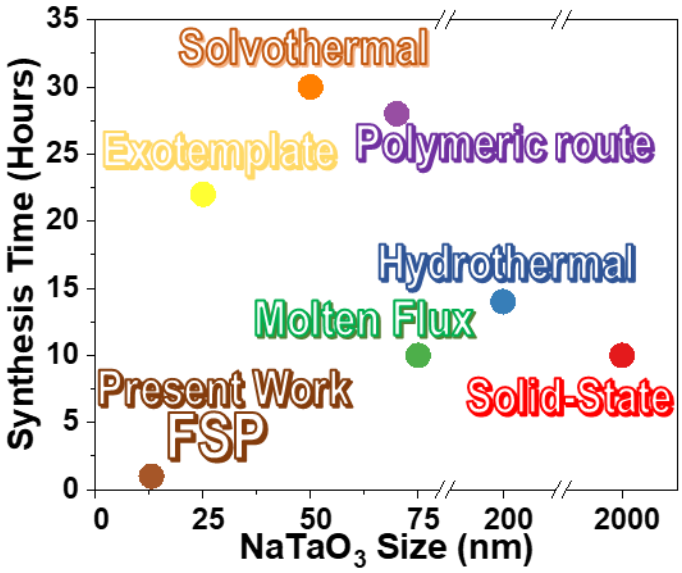

Figure 1-12: *Graph for the nanosize and the total synthesis time for produced $NaTaO_3$ from various synthesis methods.*

Thus, a critical challenge that remains to be addressed is the synthesis of very small-size $NaTaO_3$ nanoparticles in the range below 50nm. In comparison, simple metal-oxides such as TiO_2 sizes of 20nm and below can easily be synthesized with various methods [109]. The reported data on $NaTaO_3$ indicate that the synthesis of micrometric-size $NaTaO_3$ was well established by 2000 onwards, thanks to the pioneering works of Kudo [124] and Domen [125]. However, decreasing the size of the $NaTaO_3$ phase remains challenging for below 100nm. The best method found in the literature, provided by Meyer *et al.,* reported 25nm $NaTaO_3$ using an exotemplate method, although it still requires multiple steps and 22 hours for the final product [126]. The second smallest $NaTaO_3$ is provided by Ahmad et al. with a size of 50nm utilizing a solvothermal synthetic method, with an even longer

timeframe of 30 total hours [127]. In this context, current literature data for synthesizing the smallest $NaTaO_3$ nanoparticles report sizes in the range of over 50nm [127,128].

As for the synthesis of Ta_2O_5, the size barrier is much lower as it is a simple oxide. Although most methods have difficulty with sizes below 10nm [105], either the method isn't applicable to produce these sizes, or the resulting particle is mainly 10nm and below but has high amounts of impurities and amorphous materials[129]. These two factors, nanosize and crystallinity, are well known to be minimal requirements for highly active photocatalysts [130].

In **Table 1-4**, the nano sizes of the $NaTaO_3$ and Ta_2O_5 of the most prevalent and correlated works are showcased, combined with the synthesis method and the total synthesis period of the experiments, including the secondary steps, such as drying. The size in all cases derives from the TEM measurements of the nanoparticles, the size derived from the XRD and BET are omitted. The reason for this stems from the fact that most publications of $NaTaO_3$ have large sizes, so TEM measurement is the most appropriate. For this reason, on our own results, the d_{TEM} is the measurement that has the more considerable importance.

As for the synthesis by the FSP technique, Pratsinis *et al.*[131,132] has already established the capacity of FSP to produce Ta_2O_5 of high purity and crystallinity used for optical applications or in dental fillings. However, the desired perovskite $NaTaO_3$ phase or the perovskite $LiTaO_3$ has yet to be successfully synthesized by FSP.

Table 1-4: *Literature comparison of Size and SSA for Ta_2O_5 and $NaTaO_3$ particles synthesized by different synthesis methods.*

Photocatalyst	Synthesis method	Synthesis period (hours)	Crystallite size(nm)	SSA (m^2g^{-1})	*Ref.*
TDL (Ta_2O_5: 0.5%NiO)	FSP	0.5	9.6 ±0.2(d_{TEM})	34.0	*Our work*
NTDL ($NaTaO_3$: 0.5%NiO)	FSP	0.75	12.3 ±0.3(d_{TEM})	37.3	*Our work*
$NaTaO_3$	exotemplate method	22	25(d_{TEM})	22.4	[126]
$NaTaO_3$	solvothermal synthetic method	24 synthesis + 6 dried/centrifuged	50(d_{TEM})	77.3	[127]

$NaTaO_3$	polymeric citrate precursor route	28	70(d_{TEM})	46.2	[128]
$NaTaO_3$: Sr doping	molten flux	10	75(d_{TEM})	-	[123]
$NaTaO_3$: S doping	hydrothermal process	12 synthesis + 2 dried/centrifuged	200-500nm(d_{TEM})	-	[133]
$NaTaO_3$	solid-state reactions	10	2000(d_{SEM})	0.5	[134]
Ta_2O_5	FSP	0.5	14.4(d_{BET})	51	[132]
Ta_2O_5	Hydrothermal	24	30(d_{TEM})	-	[135]

A further aim of the present research included the one-step deposition of ultrafine cocatalytic nanoparticles on the surface of the Ta_2O_5/$NaTaO_3$/$LiTaO_3$ nanoparticles. These ultrafine nanoparticles, comprised of the noble metals Platinum(Pt) and Palladium(Pd), which have been established as efficient electron acceptors for photocatalysis. Most notably, in our work, we have studied NiO as a non-noble metal electron acceptor with a substantially lower cost. Our hypothesis is that NiO would be effective due to the proper alignment of band edges with those of $NaTaO_3$. This issue of Band-edge alignment and the ensuing band-bending is discussed in section 4.7.6. {$NaTaO_3$/NiO} heterojunction possesses great premise as photocatalysts [90]. In wet-chemistry methods, in general, the NiO deposition as a cocatalyst on the material's surface is accomplished by the introduction of additional synthesis steps, i.e. such as wet impregnation and calcination with the supporting particle, in which the temperature can increase the particle size of tantalates, limiting once again the small size [91]. A specific aim of the present Ph.D. Thesis work was to establish a one-step FSP method to deposit the cocatalyst at the surface of ultrasmall Ta_2O_5 / $NaTaO_3$ / $LiTaO_3$ with high crystallinity at nano sizes of below 15nm.

1.3.5 Strontium Titanate Perovskite

Strontium Titanate ($SrTiO_3$) has the quintessential classical ABO_3 perovskite ideal cubic structure [136]. $SrTiO_3$ was believed to be produced only by artificial methods, but in 1982, it was discovered in Siberia under natural conditions and given the name Tausonite. Although, it continues to be extremely rare in nature and only occurs as tiny crystals. The $SrTiO_3$ perovskite was used for photocatalytic applications in the present thesis, as it has

received enormous attention as a photocatalyst. The advantage of $SrTiO_3$, compared with the Tantalum perovskites, for example, comes from the lower price of the Strontium and Titanium precursors [137]. $SrTiO_3$ The perovskite has the standard properties required for photocatalysis, such as chemical stability, excellent thermal stability e.g. melting point as high as 2080°C, a tolerance for carbon and sulfur, with the structure itself being highly adaptable and modifiable for its oxidative properties [138].

In the BULK, the SrO–TiO_2 equilibrium phase diagram is shown in **Figure 1-13** [139]. The perovskite $SrTiO_3$ is formed when the molar ratio of SrO and TiO_2 each is at 50% under ambient conditions at high temperatures. Various secondary phases can be formed by specific crystal or layer growth during the synthesis method, this can occur from temperature inefficiency or lack of sufficient oxygen, causing the formation of Oxygen vacancies that can result in converting the high symmetry cubic perovskite structure to another symmetry [140].

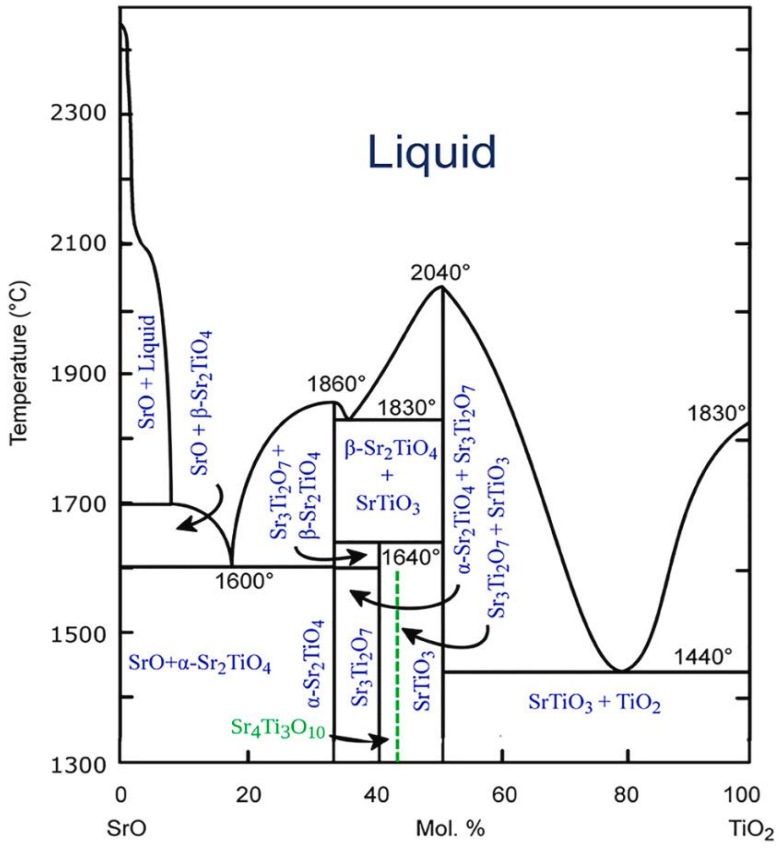

Figure 1-13: *Equilibrium phase diagram of the SrO and TiO_2 phases, derived from* [139].

Some Photophysical properties of $SrTiO_3$

$SrTiO_3$ has a highly reducing conduction-band-edge energy position (E_{CB}) of -1.2eV vs. NHE [141,142], which makes it a highly efficient photocatalyst for hydrogen production from H_2O [143]. Although $SrTiO_3$ has the disadvantage of a broad band gap Eg=3.2eV, though lower than the Eg=4.2 eV of $NaTaO_3$, the photonic absorption can only be permitted for the UV range, thus there are two standard practices to negate this drawback, as shown in **Figure 1-14**. The first is to incorporate appropriate **dopants**, altering the perovskite structure, which can add additional energy states inside the bandgap of the perovskite, i.e. decreasing the bandgap and increasing the lifetime of the photoproduced e^-/h^+ pair. The second practice is to attach another semiconductor on the **surface** of the perovskite, creating a **heterojunction.** The secondary semiconductor has a lower bandgap, this –under appropriate band-edge positioning– can promote photoinduced electron/hole pair generation [144].

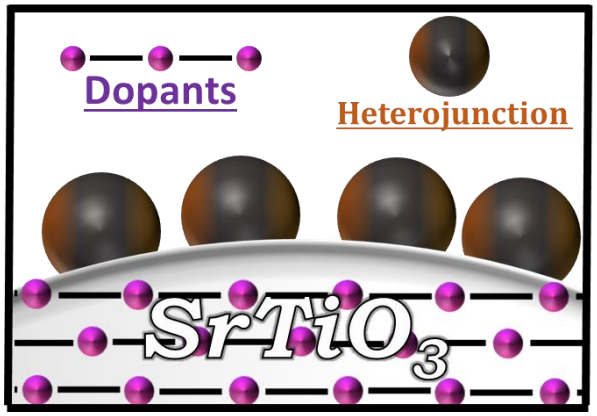

Figure 1-14: *The two practices for the modification of the perovskite nanomaterial, Dopants: adding additional atoms in the crystal structure, Heterojunction:* attaching another semiconductor on the surface of the perovskite *$SrTiO_3$.*

So far, synthesis of nanocrystalline $SrTiO_3$ has been achieved with various methods, each having distinct advantages/disadvantages [136,145] e.g., preparing the perovskite by solid phase [146] has the benefits of relatively low cost, that is simple and can be mass-produced. However, the disadvantage is that due to the high temperature of over 1000 ^{0}C,

the resulting particles have rather large sizes, furthermore, the phase has impurities. The sol-gel method [145] has the advantage of very high phase purity and small nanoparticles, but the drawback is a much higher cost and added difficulty of the raw materials. The hydrothermal method [137] has the advantage of producing nanoparticles of controllable sizes under low temperatures but requires long synthesis times and advanced equipment, resulting in particles that can have impurities. Moreover, a doping synthesis method of $SrTiO_3$ with an appropriate dopant-cation at very low and precise concentrations, or the formation of heterojunctions between only the surface of $SrTiO_3$ and the selected co-catalytic nanoparticles, pose additional difficulties, complexity, and cost of the synthesis process [147], that many of the synthesis methods can only achieve it, by introducing additional steps, that elongate substantially the required time.

In this context, it is of great importance to develop synthesis technologies for high-quality $SrTiO_3$ that in one-step can facilitate doping of $SrTiO_3$ and heterojunction $SrTiO_3/MO_x$ formation, at the same time allowing scale-up production for later commercial applications.

Herein, for the inter-atomic doping of the perovskite $SrTiO_3$, the Lanthanum (La) atom was chosen since it has already been shown to increase the electrochemical properties of the perovskite [148,149]. Furthermore, Lanthanum can act as an efficient co-dopant with other atoms or nanomaterials to create an effective synergy for photocatalysis [150,151]. In this context, the foremost scientists Domen [152,153] and Kudo [154,155] have demonstrated that $SrTiO_3$ co-doped with La and Ruthenium (Ru), exhibits high solar-to-hydrogen energy conversion efficiency for the photocatalytic application of water splitting to H_2. Moreover, selected cations e.g. La^{3+}, Ce^{3+}, or Nitrogen [142,156], change the properties of structural, electronic, and photochemical properties of doped-$SrTiO_3$, controlling and enhancing the photocatalytic efficiency[157,158]. Thus, in this framework, $SrTiO_3$ can act as a versatile template that can be optimized toward specific technologies via doping engineering.

As for Heterojunctions, the controllable Surficial heterojunctions of $SrTiO_3$ with pertinent metal oxides allow control of the selectivity of surface reactions. More

specifically, Cu-atoms and their particles (CuO, Cu_2O, Cu^0) are particularly attractive in photocatalytic processes. Studies show that CuO clusters on the TiO_2 surface can serve as an efficient co-catalyst to enhance H_2 production [159,160]. Also, the Cu_2O on TiO_2 was reported to be more suitable for H_2 production, which was attributed to the better energy band alignment between TiO_2 and Cu_2O, which facilitates charge separation [161,162]. More importantly for our research focus, the nanoparticles CuO, Cu_2O, and Cu^0 have been shown to control selectivity towards specific products i.e., Cu_2O exhibits selectivity towards CH_3OH production and Cu^0 towards hydrocarbons and C_2 products [163,164], as the results in our work show.

In the present work, our advanced working hypothesis was that the *in-tandem* La-doping of $SrTiO_3$, with CuO/ $SrTiO_3$ heterojunctions, can allow the electronic/ photocatalytic properties control of the material in the application of photocatalysis for selective photocatalytic products. This research route has been explored herein using our FSP technology.

1.4 Flame Spray Pyrolysis

1.4.1 Historical Review of Flame Synthesis

Before 25 years ago, there were few publications for nanoparticle synthesis, since then, the drive for accurate and precise nanoparticle synthesis has grown tremendously, with several methods proving to create particles with below micrometric properties, from air-based techniques to liquid-based and top-to-bottom solid technologies. With the development of more and different techniques in the coming years, the technologies that will stay applicable can only possibly be those with key-characteristics [165], such as: for industrial manufacturing, the most fundamental attribute must be a low cost per kilogram of nanomaterial, this is directly correlated to the speed of synthesis since a method that requires a week-long production that requires several steps/ different instruments will have a much higher cost than an hour long production with a single instrument. Moreover, the resulting nanoparticles should have the utmost repeatability, with the attributes of high

purity i.e. zero impurities of secondary phases and amorphous molecules, with precise and controllable nanometric size [165].

The Flame Spray Pyrolysis (FSP) progenitor is the flame spray (FS) technique that applies a **flame** to provide the energy/enthalpy to combine the atoms, with the starting material arriving **as gas or vapor** to create small **particles**. The FS technique originated from prehistoric times without of course clear understanding or application of the chemical process. One of the first recorded nanoparticles was Carbon black, the material consists of 99.5% amorphous carbon with varying atomic sizes and different regions. Carbon black is the oldest aerosol that is still manufactured, which was first created in India and Egypt in prehistoric times, later China created it with the pyrolysis of oils to use it as pigments (1500 BC). Also, it is essential to point out that carbon black was the first commodity to be industrially important because of the wide range of applications that it can be used [166]. Moreover, soot can be flame-made, which had a valuable part in prehistoric life.

The first actual reactor for the technique of flame synthesis was created in the 1940s to develop fumed silica nanoparticles. However, the first principles of the theory behind the process were first published many decades later by G.D. Ulrich in 1971 [167]. At present, the largest quantities produced by FS are Titania TiO_2, where Evonik, one of the biggest chemical companies in the world, produces Aeroxide TiO_2 (P-25). The list of products is shown in **Figure 1-15**. P-25 is an excellent photocatalyst due to selective percentages of rutile/anatase, the two different crystalline structures of TiO_2 [166].

FS comes from two separate types of techniques that use the flame aerosol process. The first is **Flame Vapor Synthesis (FVS),** which uses a flame to transform **vapors** that contain the appropriate atoms with the proper enthalpy that transforms the atoms into nanoparticles. The second is **Flame Spray Pyrolysis (FSP),** which uses a flame to transform **liquid droplets** into nanoparticles [169–171].

Today, FSP is the technology adopted by most industrial and research works. Based on technical advantages, the starting precursor materials are a crucial advantage of the FSP. There aren't many metals in the gas phase at room temperatures, which limits the materials that can be used to FVS or puts extra steps to turn them to their gas phase. In

contrast, the FSP can operate with most of the elements in the periodic table for single or multi-component nanoparticles [172].

Figure 1-15: *Evonik Industries products list produced from industrial Flame Spray Titania* [168].

Overall, today Flame Spray Pyrolysis (FSP) process is well established for industrial-scale production, creating several particles at high production rates of Kg per hour [173,174]. As such, FSP has produced several commonly used metal oxides [175]. FSP utilizes high-temperature combustion in the range of 1000 to 2000K at the center of the flame [176]. A liquid precursor consisting of metal atoms dispersed in an organic solvent, this liquid precursor is then sprayed from a high-pressure oxygen gas to change it to the form of aerosol droplets. Appropriate selection of precursor mixtures and process parameters allows precise control of the crystal phases [175].

1.4.2 FSP Process: Principles of operation

(1) ***Precursor Droplet:*** At the beginning, a Precursor liquid is created from the appropriate atoms and concentrations that are required to synthesize the resulting stable perovskite/Oxides. The overall process is shown in the simplified scheme of **Figure 1-16**.

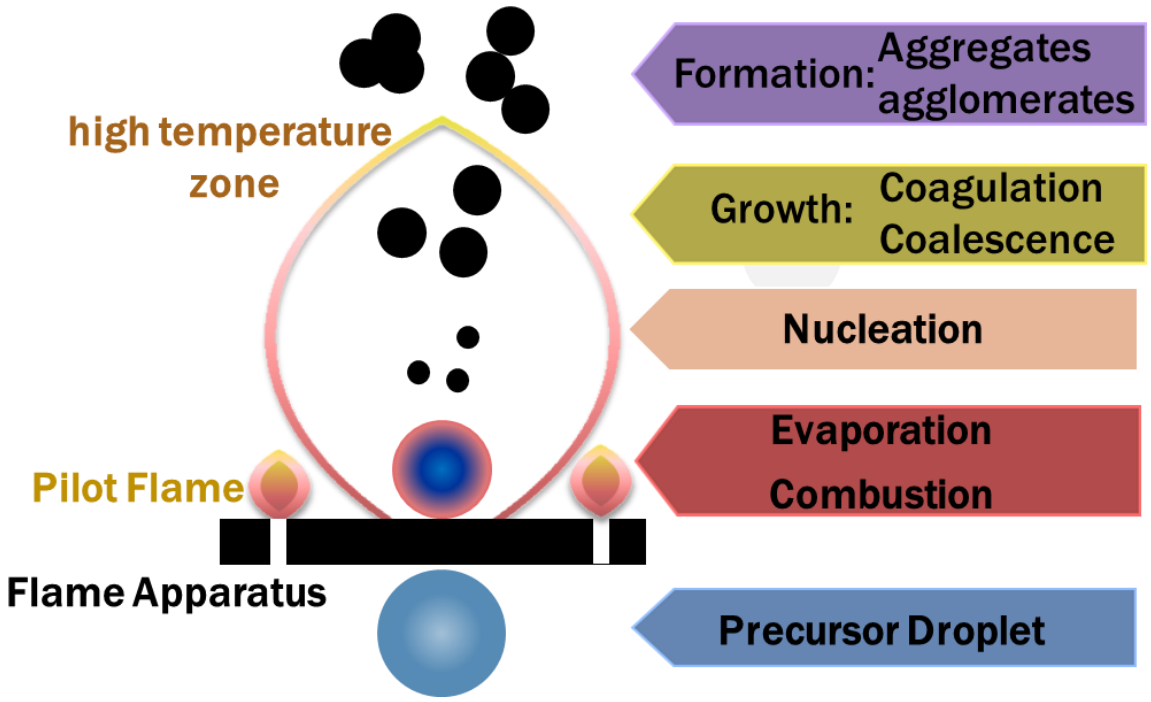

Figure 1-16: *Schematic for the fundamental transition from precursor Droplet to nanoparticle formation mechanisms during flame spray pyrolysis (FSP).*

(2) ***Pilot flame of the FSP nozzle:*** The pilot consists of a mix of oxygen and methane that ignites the liquid precursor. The methane contributes to the total enthalpy of the reaction and for very low enthalpy synthesis, it has a significant role, although the droplet doesn't interact with the pilot flame as such.

(3) ***Evaporation/Combustion:*** The Dispersion Flow rate (usually Oxygen) is inserted to interact with the liquid droplet at a specific oxygen pressure at the tip of the capillary, thus the droplet is dispersed, reducing the volume from a droplet ($0.5cm^3$) to a form of vapor, at that moment it interacts with the pilot flame leading to combustion.

(4) ***Nucleation:*** From the combined sources of enthalpy, pilot flames methane, the carbonate solvent, and the metal powder used. Increasing the temperature to an average of 2000 ^0C at the center of the FSP flame, the vapor starts to create oxides from the surrounding abundant Oxygen. The vapor's oxides begin to interact with itself due to the high temperature, if the supersaturation of oxides reaches a sufficient point, then ultra-fine primary structures begin to form.

(5) ***Coagulation/Coalescence:*** By interacting with the surrounding materials, the primary structures begin to grow into clusters and later into nanoparticles. The growth ensues by coagulation and coalescence to the primary particle size of the nanoparticles [177].

(6) ***Aggregates/Agglomerates:*** When the nanoparticles leave the high-temperature zone (flame residence time). The particles continue to grow, but this time to form aggregates (chemically bonded primary particles) of primary particles or agglomerates (physically bonded) of the primary particle [178].

Agglomerates can be dispersed in liquid matrices, which are found useful in appliances like paints and microelectronics. In contrast, aggregates can be used in porous films and catalysis. While the performance of the nanoparticle usually depends on the primary particle size, the processing will depend on the aggregation that the particle undertook in FSP [179]. The residence time and the temperature of the hot zone impact the size and sintering of the nanoparticles. The particles' size, morphology, and crystallinity can change depending on the variables that consist of the temperature and the height of the flame [178].

Parameters of the FSP process as tools to control the nanoparticles' properties:
The most important FSP-process parameters that were utilized in the present work for the synthesis of nanoparticles, were

(1) Precursor components (metal powder, solvent)

(2) Concentration of precursor

(3) Precursor/dispersion flow rate (P/D ratio)

(4) Dispersion-gas type and pressure

(5) Pilot flame

(6) Enclosure of the flame with a metal or quartz tube

The roles of these parameters can be found in Reviews [172,180,181]. Herein, we detail some pertinent aspects that directly influenced our particles.

Precursor flow rate: Increasing the precursor flow rate (**P**) means increasing the solvent concentration in the flame, which manifests as higher enthalpy content in the flame. As a result, the time for fuel combustion lengthens, producing an increase in the flame's height/volume, with an increase in the **High-Temperature-Residence-Time (HTRT).** This has two immediate consequences: first, an increase in **crystallinity and crystal size**, and second, an increase in the particle-particle sintering rate, corresponding to **larger particles** and larger **agglomerates** being produced [182].

Dispersion gas flow rate: The changes in the dispersion gas flow rate (**D**) impact several attributes of the flame that change the nanoparticle attributes. In our set up, the dispersion gas was always oxygen. Increasing the D flow rate promotes more diffuse flame which decreases the flame height/volume. This results in a lower HTRT, which means less sintering and smaller particle sizes (with **smaller particle sizes and bigger SSA**). Also, increasing D decreases the precursor-droplet concentration in the flame (since there is more D=oxygen), so the number of particles that react with each other decreases, which results again in smaller particle sizes. Finally, with an increased D, the flame has a higher maximum temperature at the center of the flame. Although the temperature drops rapidly at the radial direction, the temperature gradient becomes way steeper, it can result in **transient crystal phase**s.

This brief analysis makes clear that the **High-Temperature-Residence-Time (**HTRT) is among the most important parameters that one should control in FSP to control phase composition and particle size [180]. Thus, in section 4.1.3, we discuss in the HTRT of our FSP set ups.

Enclosing the Flame with a Metallic-Quartz tube: The tubes surround the FSP flame with the aim of stopping the ambient-atmospheric air from interfering with the flame spray jet. The separation of atmospheric air prevents the uncontrolled temperature drop i.e. that would result due to the lower atmospheric-air temperature. Caution should be paid to the fact that in conventional FSP reactors, the flame cannot be fully enclosed since ambient O_2 can provide the necessary supplementary-O_2 (in addition to dispersion O_2) to sustain combustion. Previous experimental and theoretical works [183] show that a very-small gap

of 0.3cm at the tube-base is more than efficient in order for the airflow that enters to fuel the flame and create an upward push for the nanoparticles [183].

In the present work, we have diligently explored the role of enclosing tubes and the gap to achieve optimal formation of the desired perovskite nanostructures. This, together with the systematic study of the HTRT and the precursor's composition, allowed us to establish novel FSP-protocols that allow the production of high-quality perovskites.

Thus, the addition of enclosing tubes in the FSP system can increase the high-temperature residence time [184]. Conversely, if there isn't a gap, we can calculate the exact number of oxygen atoms inserted in the synthesis. To increase this technique's effectiveness further, additional gas is applied externally surrounding the pilot flame, codenamed sheath gas. The sheath gas, in most cases nitrogen gas, decreases the number of oxygen interactions. With this procedure, the anoxic synthesis parameters can result in suboxide nanoparticles such as $SrTiO_{3-X}$. A flame enclosed by a tube typically produces substantially bigger particles because of the increased residence time and the overall increase in temperature above the hot zone, compared with a flame with the same parameters. The tube enclosure can better control the flame combustion and the surrounding atmosphere. In our experimental set-up, the metallic tube has a 20 or 40cm height that is held just 1cm above the flame apparatus or with zero gap (nogap). The tube is held by a clamp fitted in a metallic base.

1.4.3 Combustion Enthalpy Density, Combustion Stoıchiometry Ratio (Φ), and High Temperature Residence Time

***Combustion Enthalpy Density Calculation*:** For an ideal combustion process with final products CO_2 and H_2O in gas form with the resulting nanomaterials e.g. $NaTaO_3$, $SrTiO_3$, the combustion enthalpy density [185], can be calculated by Equation 1-8.

$$\Delta_c h = \frac{\sum_{i=0}^{n} \hat{x}_i \times \Delta_c \hat{h}_i}{\sum_{i=0}^{n} \hat{x}_i \times \hat{m}_i} \qquad \text{Equation 1-8}$$

The overall combustion enthalpy density $\Delta_c h$ per unit (kJ g^{-1}) is determined by the specific combustion enthalpy $\Delta_c h_i$ of each reactant-i, according to m_i the specific mass of each reactant, with x_i being the volume fraction of each reactant in the precursor solution. The index i refers to all compounds participating in the combustion [185], the two gases(O_2/CH_4), and every solvent present in the precursor mixture e.g. ethanol, xylene, and others. The metal precursors can carry a high amount of carbons that assist in the combustion. On the other hand, the precursor of Tantalum i.e. $TaCl_5$ employed for the synthesis of $NaTaO_3$, doesn't contribute to the combustion enthalpy. Finally, the enthalpy $\Delta_c H$ (kJ mol g^{-1}) is calculated per mol of Na and Ta atoms present at any given moment in the combustion process.

Φ Ratio: The combustion stoichiometry ratio (Φ) that in our system expresses the [Fuel–air] equivalence ratio is defined as the Φ=ratio **[fuel-to-oxidizer ratio]/ [stoichiometric fuel-to-oxidizer ratio] taking into account all FSP process parameters, that incorporate all gas and liquid flows provided to the FSP burner**.

To calculate the Φ ratio, Equation 1-9 is used, where

$\mathbf{m_{fuel}}$ represents the mass of **all** the components that **produce enthalpy** in the flame i.e. methane, ethanol, xylene, and others.

$\mathbf{m_{oxidant}}$ is the mass of **all oxygen O_2 molecules** of the system i.e. oxygen from the pilot flame, Dispersion oxygen, oxygen species in the solvents, etc.

The subscript *Stoichiometric* stands for the stoichiometric conditions of the combustion, producing H_2O, CO_2, and the resulting nanoparticles [186].

$$\boldsymbol{\Phi} = \frac{\left(\boldsymbol{m_{fuel}}/\boldsymbol{m_{oxidant}}\right)_{\boldsymbol{Real(fed\ into\ the\ system)}}}{\left(\boldsymbol{m_{fuel}}/\boldsymbol{m_{oxidant}}\right)_{\boldsymbol{Stoichiometric}}} \qquad \text{Equation 1-9}$$

The Φ-rules in FSP:

RULE-I: When in an FSP process **Φ >1**, that signifies that there is **more fuel** in the overall combustion that is required for complete combustion i.e. some **carbon species**

won't be consumed. Otherwise stated **Φ >1 signifies lack of O_2, thus the FSP process can be considered as "oxygen-lean" or "anoxic FSP".**

RULE-II: When in an FSP process **Φ <1**, that signifies that there is **more O_2** in the overall combustion that is required for complete combustion i.e. all **carbon species will be consumed**. Otherwise stated **Φ <1 signifies excess of O_2, thus the FSP process can be considered as "oxygen-rich".**

RULE-III: When **Φ =1**, that signifies that there is **exactly the necessary O_2** that is required for complete combustion i.e. all **carbon species will be consumed**. This **FSP process can be considered as "stoichiometric".**

However, it is important to note that this Φ ratio does **not** include **the atmospheric air** in the event of the open flame FSP set-up, i.e. without an enclosing tube surrounding the flame. Thus, enclosing tubes allows a more precise control of process engineering in FSP.

High-Temperature Residence Time: The combusted droplets produce primary crystallites inside the flame's hot field that grow to form the final particles *via* sintering at the endpoint of the flame [169–171]. Thus, the final particle size is thermodynamically controlled by the flame-temperature profile and the *high-temperature residence time* (HTRT) [169–171]. Hotter temperature flames and longer HTRT tend to increase the probability a nanomaterial will result in a **higher energy-demanding** phase structure i.e. the **perovskite** structure in comparison to the **separate oxides**, with the inherent drawback of producing larger nanosized particles [175]. *Thus, the HTRT should be controlled and calculated to be high enough to produce the desirable phase, but HTRT shouldn't be too high, prohibiting the synthesis of very large particles.*

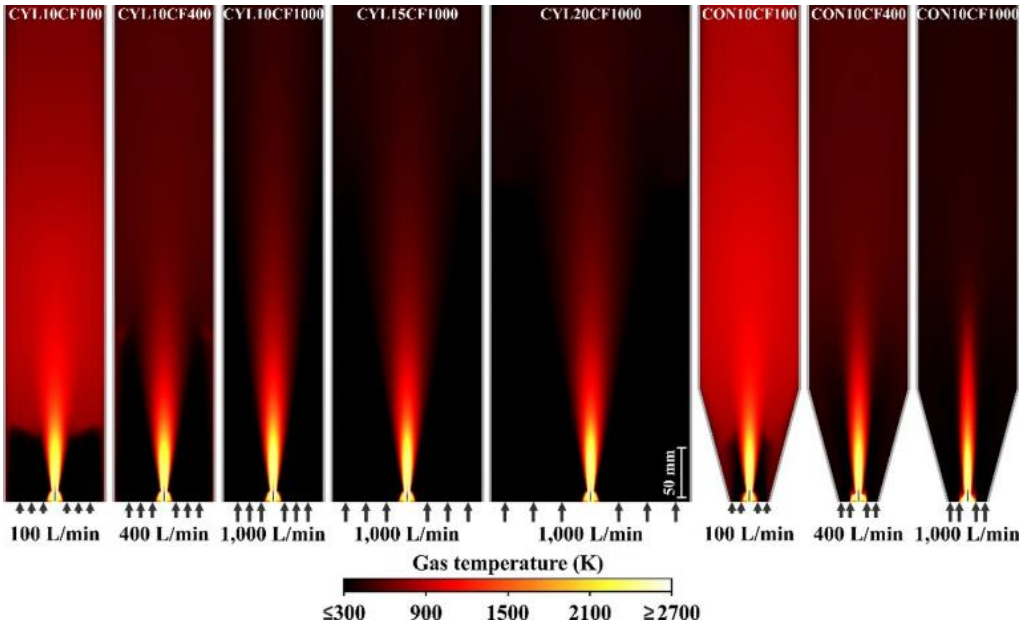

Figure 1-17: *The change in temperature profile for FSP process from different Tube geometries* [183]. *Narrower tubes (left) produce more extended HTRT-profiles i.e. hotter-flame, spread over longer (vertical and radial) distances. A conical-cylindrical tube (right) further enhances the high-T profile near the start of the flame.*

In this context, enclosing the flame with a tube that separates the atmospheric air from interfering with the FSP process and fortifies the generated temperature of the flame, enhances the HTRT. The tube should be a material capable of withstanding temperatures of 1000 ^{0}C. For this purpose, the tube consisted of metal Tubes or Quartz Tubes in the preset work. Examples of the role of the diameter and height of the encircling tube in the HTRT, as shown in the different tube morphology and *geometries* in **Figure 1-17**, derived from [183]. Another important factor for the HTRT consists of the metal precursor concentration in the precursor. Our results will later demonstrate that the concentration can result in the appropriate perovskite phase and impact the particle size [187].

1.4.4 Double Nozzle FSP (DN-FSP)

Herein, we have used a Double-Nozzle FSP (DN-FSP) process i.e. using two FSP-nozzles operating *in tandem* [188], which can produce two types of nanocrystals

controlling each one's properties independently and form a tightly interfaced heterojunction, in one step [189], as shown in **Figure 1-18**.

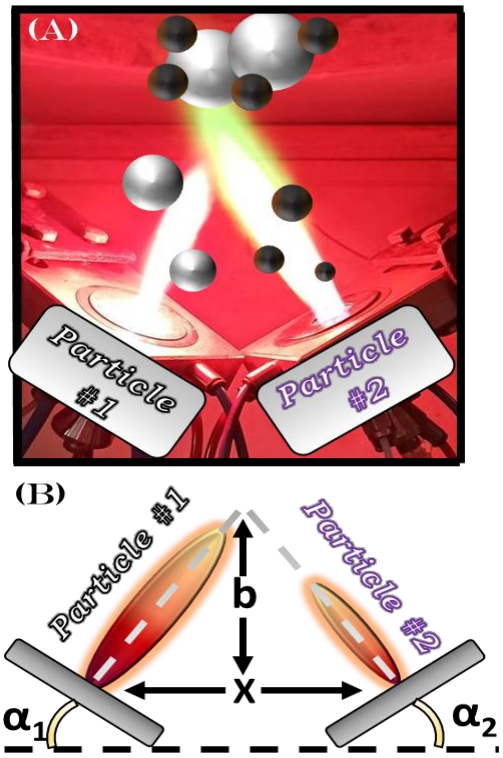

Figure 1-18: *(A) The Double Nozzle FSP (DN-FSP) makes two different nanoparticles simultaneously. (B) The main adjustable geometry parameters (a_1, a_2, b, x) for the two nozzles in DN-FSP.*

The DN-FSP synthesis technique has only recently been investigated to develop nano-heterojunctions for photocatalytic applications [190]. Recently, our team has shown that DN-FSP allows fine-dispersion of <2nm noble metals (Ag, Au, Pd, Pt) cocatalysts on TiO_2 in a single step, promoting the superior photocatalytic H_2 production from H_2O [190]. Herein, we have used DN-FSP to finely disperse/deposit NiO (mean size 2 nm) on the Ta-nanoparticles and nanoparticles CuO at the surface of $SrTiO_3$ nanoparticles.

The Double Nozzle provides the synthesis method with several new possibilities for the final particles [191]. (i) The main advantage is the precision of the deposition. Since the flames are separated, the particles have already crystallized, and the particle size has

almost stabilized when the $NaTaO_3$ and NiO interact with each other. For this reason, the NiO can only be attached on the $NaTaO_3$ particle's surface, i.e. not intermixing of the particles [192].

(ii) The secondary attributes of the secondary particles can easily be controlled by changing the dispersion flow and precursor flow rate separately, thus the resulting NiO size changes. While the size distribution will be lower in comparison with the SN-FSP due to the interaction with the primary atom particles, the resulting NiO will have a resulting broad size.

(iii) Additional synthesis degrees of freedom can be enabled by the geometric parameters (α_1, α_2, b, x) [193], as shown in **Figure 1-18**. From the distance of Nozzles(x) and the height where the flames will join (b), we can determine the size of the nanoparticles when they interact with each other. Furthermore, by changing the distance between them to be high enough, the oxidation state of the particles can be controlled.

1.4.5 Advantages of FSP Technology

The main attributes that facilitate the success of flame spray pyrolysis(FSP) can be assigned to the below three factors, **Figure 1-19**.

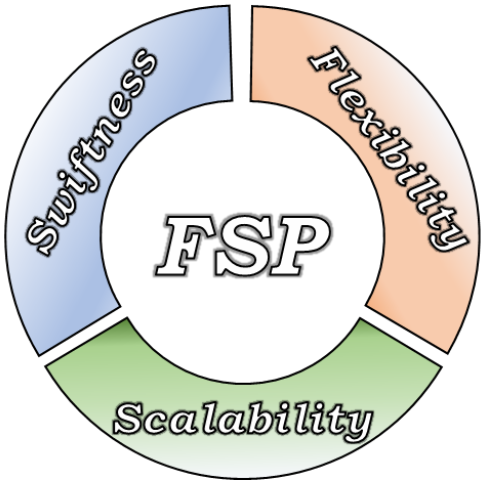

Figure 1-19: *The three fundamental attributes of FSP synthesis.*

1. *Synthesis swiftness:* The swiftness corresponds to the liquid that is inserted into the flame. The total synthesis transition of combustion to nucleation and aggregation only lasts a couple of seconds. Thus, it is one of the fastest synthesis methods that exist for nanoparticle/perovskite synthesis. In comparison, a chemical reaction in the case of wet-chemistry for the main synthesis will require at least one hour for nucleation and the final desirable perovskite. Most importantly, thanks to the very high temperatures, the whole process is accomplished in a single step inside the flame, resulting in high-purity particles. Since every secondary molecule used for the synthesis was transformed into carbon dioxide and water, instant calcination inside the flame is extremely time and cost-efficient. Alternatively, wet chemistry has several steps, consisting of: nucleation, removing irrelevant molecules (filtration, washing, drying), calcination for purity, and the appropriate phase transaction. Moreover, inserting cocatalytic particles on the surface must be a secondary step corresponding to hours or days of additional synthesis time. From start to finish, a typical synthesis can last a week, compared with a total of half an hour for FSP [184]. These different synthesis steps are shown in **Figure 1-20**.
2. *System's flexibility:* The FSP technology is exceptionally versatile, from altering fundamental parameters like the concentration of the precursor, along with precursor and oxygen flow rate, the oxygen pressure, total enthalpy of the flame by changing the solvent, methane flow rate, all of these factors can fundamentally shift the nanoparticle size and specific surface area (SSA), more importantly, the crystal phases can alter depending on the flames enthalpy and the concentration of the different precursor atoms [182,194]. All of these parameters are very easily altered in the equipment, with no unique methods.

   For advanced methods such as double nozzle FSP for the application of synthesis of the heterostructure, anoxic condition of application of a tube that supplies high nitrogen content for the creation of particles with lower oxygen in the molecular structure (TiO_{2-x}). All of these methods can easily be inserted into the methodology, requiring a one-hour set-up at most, providing a whole other range of nanoparticles that can be created.

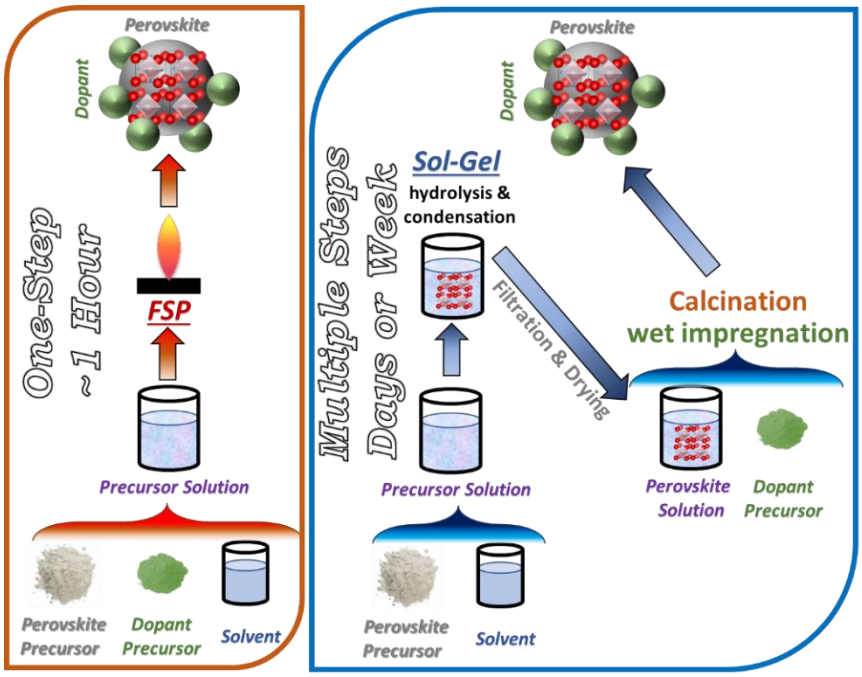

Figure 1-20: *The basic steps of flame spray pyrolysis, powder precursor to precursor solution to nanomaterials. The necessary steps of a wet preparation method include the deposition of a dopant on the surface of the nanomaterial.*

3. *Scalability:* The synthesis process is continuous by fueling the flame with constant amounts of precursor solution for as long as necessary. The precursor flow rate must change from a conventional 5 ml min^{-1} to 30 ml min^{-1} and above. These methods have proved to create successful simple oxide nanoparticles, reaching the industrial manufacture of nanoparticles can reach the order of 1 kg per hour for SiO_2 [178]. For wet synthesis methods, in order to potentially reach large quantities, there must be huge amounts of liquid solution that must remain for hours or days.

Important Secondary benefits compared with wet-preparation methods. The FSP doesn't create liquid byproducts that often require expensive cleaning methods. Also, due to the rapid heating and quenching of FSP-made nanoparticles, there is the possibility of creating metastable phases that can't be produced with wet-chemistry methods[165].

FSP has been shown to produce perovskite-type/ simple oxides producing ultra-fine crystallines with primary particles of 5 nm diameter and below, with a large specific surface area i.e. 100 $m^2 g^{-1}$. In contrast to other conventional synthesis routes, such as solid-state synthesis that requires calcination at very high temperatures and synthesis time in order to obtain the resulting nanoparticles, limiting the produced nanoparticles that will have particles below 100 $m^2 g^{-1}$ [194].

Disadvantages of the FSP technology: Some of the precursors can be very expensive, in the case of Tantalum butoxide, while a limitation derived specifically for perovskites that require multiple atoms, corresponding to multiple precursors, creating the possibility that the combination of precursors/solvents react, resulting in heterogenous solutions or creating precipitates in the solution, translating to incomplete combustion in the FSP [184]. Also, the nanomaterial of FSP commonly has geometries of spherical agglomerations, with different geometries like tetragonal proving to be simply impossible for most particles [179].

1.4.6 FSP as an Industrial Production Technology

Several methods used for nanoparticle synthesis aren't scalable i.e. to transcend laboratory production towards industrial scale for large-volume production. These facts are against the actual implementation of real-life applications, hindering the connection of lab-research to market-level production. When more complex nanoparticles require time-consuming synthesis protocols with complex processes, these factors lead to very high prices per kilo of particles [181].

A majority of researchers occupy themselves with liquid-phase synthesis to create nanomaterials. While gas-phase synthesis has already shown much premise for the industrial production of nanoparticles, so far, single-metal nanomaterials are produced through gas-phase processes [195]. Gas-phase synthesis includes many essential commodity products that have been widely produced for many years, with some of the most widespread nanomaterials for the industry, such as carbon black by the company Cabot [196] as a reinforcing agent, P25 (TiO_2) by Evonik Industries [168], renowned for its

photocatalytic properties, pigmentary titania by the companies DuPont, Cristal, and Ishihara, fumed silica (SiO_2) by Cabot and Evonik, as well as ceramic based nanoparticles with the application of flame aerosol processes. Overall, the production of flame-made nanoparticles generates millions of tons with a valuation reaching $15 billion/year [197].

The successful utilization of aerosol-made nanomaterials in the market indicates the industrial-scale manufacturing of gas-phase will expand further with future applications, using more complex particles and multicomponent particles that can't be easily produced at industrial-scale with other methods [198]. Utilizing the advantages of FSP, several Start-up companies have grown to produce various particles with controlled characteristics to fill the demand for niche markets [199]. Such start-up companies include Turbobeads AG [200], which creates amine-functionalized cobalt carbon-coated nanoparticles. Hemotune AG [201] produces polymer-decorated iron nanoparticles with carbon encapsulation for the purpose of blood purification. Anavo Medical, for bioactive hybrid metal oxides, Avantama AG, with the production of several metal oxides [199]. HeiQ Inc [202], which recently had an IPO with a valuation of 127M £, produces nanosilver by FSP, which is the third most market demanded, following carbon black and fumed oxides [203].

FSP synthesis can be implemented by laboratory FSP with production of 10g h^{-1} to establish the synthesis optimization protocol and the initial exploration for complex particles, and industrial scale FSP with production rates at Kg h^{-1} [204]. With lab-scale FSP, many particles reach 10g h^{-1}. Examples include HfO (5nm, 89 SSA) at 15g h^{-1} [205] and CeO_2(8nm, 101 SSA) at 10g h^{-1} [206]. Pratsinis et al. synthesized particles of Silica/titania with a production rate of 200g h^{-1} [207,208], showing very different results with the change of the fuel flow rate and the oxygen flow rate parameters. In this context, many simple oxides have been synthesized with FSP, such as WO_3/TiO_2 [209], or more complex nanoparticles, such as $La_{0.6}Sr_{0.4}Co_{0.2}Fe_{0.8}O_{3-\delta}$ with production rates as high as 400 g h^{-1} [210].

Table 1-5: *Industrial production of nanoparticles by FSP, parameters, production rate, size, and SSA.*

Nano Particle	Production Rate (Kg h^{-1})	Scale Up Parameters			Size(nm)	SSA ($m^2 g^{-1}$)	*Ref.*
		Molarity	Precursor flow rate(mL/min)	Oxygen flow rate(L/min)			
SiO_2	1.1	4.7	33.3	50	26	108	[211]
ZrO_2	0.6	1	81	50	30	33	[212]
ZrO_2	0.5	1	64	80	25	42	[213]
Y_2O_3/ZrO_2	0.35	0.5	81	50	31	32	[214]
$FePO_4$	0.27	-	20	40	129	108	[204]
ZnO	3	3.3	200	120	30	26.2	[215]
Bellite	0.03	1,1	30	30	54	34	[216]

So far, for the industrial-scale FSP, only a handful of particles were able to be synthesized, see **Table 1-5**. The first industrial-scale FSP production was demonstrated for SiO_2, by Pratsinis et al., producing uniform 25nm particles at 1.1 kg h^{-1} [211]. The next particle achieved was ZrO_2 with a production rate of 0.6Kg/h with an average size of 30nm [212], after Wegner et al. produced ZrO_2 at 0.5 Kg/h [213] with increased technological expertise showing the fundamentals of the High-Temperature Residence Time for the Scale Up synthesis of nanomaterials. In this context, Madler et al. explored CFD-PBM modeling of ZrO_2 FSP synthesis [217] at high productions to discover the attributes of the resulting nanoparticles. Later on, yttria-stabilized zirconia (Y_2O_3/ZrO_2) was produced with the same parameters, with only the molarity dropped by half, decreasing the production rate at 0.35 Kg h^{-1} [214]. Wegner et al. produced $FePO_4$ nanoparticles with 0.27 Kg h^{-1} with a mean size of 129nm [204]. Wegner et. Al manufactured ZnO nanorods with the highest production rate so far, at 3 Kg h^{-1}. The resulting nanorods had a length of 30nm and a mean aspect ratio of the rods at 2.3 [215]. Recently, the production of Belite has been achieved in Scale-Up conditions with a production of 0.03 Kg h^{-1}, the low production is due to the formation of amorphous and other derivatives such as alite, $CaCO_3$, etc. [216].

1.4.7 Perovskite Syntesis by FSP

FSP has been established to successfully produce a wide range of single-metal oxides [175]. However, establishing FSP process parameters for producing ABO3 perovskite nanomaterials is typically more challenging, e.g., avoiding the formation of the separate oxides AO_n and BO_m. The relative importance of process parameters will be exemplified in the duration of this thesis and the publications derived from it. Besides the research conducted in this thesis, there are less than ten overall perovskites FSP synthesis publications by Kudo and Amal for $BiVO_4$ [218] and W and Zr-Doped $BiVO_4$ from our team [219], works on the multiple perovskites based on Lanthanum for $LaMO_3$ (M = Mn, Fe, Co) [220], finally, some Titanium-based perovskites with $BaTiO_3$ [221], as well as Abe and Laine for $La_2Ti_2O_7$ [222].

The First publication for FSP-engineering of $Bi_2Fe_4O_9$ mullite-type and $BiFeO_3$ perovskite [223,224], the second perovskite synthesized $NaTaO_3$ [225], and the $LiTaO_3$ that has yet to be published, to underline in all these perovskite materials, our laboratory team was the first to synthesize them via FSP in the literature, with the exemption of $SrTiO_3$ that while at the first successful production of FSP-made $SrTiO_3$ in our laboratory there wasn't any publication yet submitted. Still, our publication wasn't the first as C. Zhao et al. published the two following works [226,227] that showcased their use for catalytic combustion of CO and CH_4, however with no reference to photocatalytic evaluation or optimization, unlike our publication [228].

1.5 Photocatalysis

1.5.1 Hydrogen as a renewable energy source

A necessity for alternative energy sources: With the projected increased population of the Earth and the increased energy demand from the average human daily life, the generation and the energy source required are of crucial importance in the upcoming years. Currently, the overall global energy production with more than 80% based on fossil fuels such as petroleum, natural gas, and coal. The excessive dependence on fossil fuels from all major economic countries has become a critical global challenge in today's

economy [229]. As the fossil fuel sources are declining steadily every year, with the speculated current fossil fuel reserves resulting in global energy support a maximum of 40 years for petroleum, 60 years for natural gas, and 156 years for coal [230].

Furthermore, fossil fuels severely impact the environment, with hazardous air contamination in major megacities emanating chronic health issues, with the most important effect being the production of greenhouse gases that are a major contributor to planet warming. The overall trajectory shows that global warming will exceed two °C above the pre-industrialized levels, resulting in a devastating change in the world's landscape and sea levels that will drastically deteriorate the global economy [231].

For these reasons, an alternative sustainable energy source should have: (1) Abundant energy supply. (2) Reduction of global carbon emissions. (3) Zero or minimal impact on the environment. (4) Industrial and technological energy base providing the energy source [230].

Solar Radiation: There are three major applications for the formation of renewable energy from a clean and plentiful source: solar radiation, geothermal heat, and the spinning of the earth that results in tidal waves. In this work, the renewable source used was solar radiation, also being easier to apply, with higher amounts of accessible energy. The radiation of the Sun that reaches the Earth amounts to 173.000 TW [232], which is divided into the interactions with the Earth’s atmosphere, with 30% of the radiation getting reflected back to space, 23% gets absorbed in the atmosphere gasses, and 47% of the energy reaches the Earth's surface. From these divisions, the alternative sources are divided that can subsequently generate electricity. The 45% in direct beam radiation is the main attributed source for the employment of photovoltaic or other solar-driven devices, 22% in hydro energy employed in hydroelectric dams, finally minor contributions to wind energy at 2%, and less attributes at 0.02% to photosynthesis [232]. From the direct beam radiation, by estimation of a device with an energy conversion of 20% efficiency that is already achievable, the estimated energy is 15 PW, where the global energy usage at

0.015PW, thus a fraction of the planet surface to be covered with devices such as these, the world will have clean and sufficient energy for the global needs of the future.

Hydrogen as an energy source: The model for employing hydrogen as an energy carrier was theorized over two centuries ago, although the driving forces were recent, with the global energy crisis of the 1970s that increased the price of fossil fuels and the technological advances in the 1980s [233]. As of 2020, most of the hydrogen production, as much as ~95% is produced from fossil fuels, with the main application of steam reforming of the fossil fuel source of natural gas, with secondary application of light hydrocarbons, partial oxidation of heavier hydrocarbons, and coal gasification. Due to this fact, the global output for hydrogen production emits 830 million tons of carbon dioxide to produce merely 74 million tons of hydrogen [234]. Nevertheless, the global hydrogen generation market size was valued at USD 155.35 billion in 2022, with further expected expansion at a compound annual growth rate (CAGR) of 9.3% from 2023 to 2030 [235].

The exploitation of direct beam radiation photons for photocatalysis applications is an established green technology approach [236]. Thus, the current thesis will focus on water splitting with the energy source to be provided with photonic radiation. From the photocatalytic water splitting, two products are obtained oxygen and the desired hydrogen gas. The focus of hydrogen as an energy carrier is examined from the list of fundamental advantages, although the fundamental disadvantages will also be mentioned [237].

Advantages of hydrogen energy:

(1) Hydrogen has a very high specific energy output per mass (142MJ/Kg), as shown in **Table 1-6**, with almost triple specific energy per mass output compared to gasoline.

(2) The source is abundant since the main component is water.

(3) Under hydrogen combustion, the reaction produces non-toxic exhaust emissions, apart from very high temperatures that can result in NOx as a byproduct.

(4) Hydrogen is essential as a component for other chemical syntheses in an industrialized society, i.e. oil refining, production of ammonia, etc.

Table 1-6: *Comparison of some selected fuels compared to energy content and carbon emission [238].*

Fuel Type	Energy per unit mass (MJ Kg^{-1})	Energy per Unit Volume (MJ m^{-3})	Specific Carbon Emission (C per Fuel, Kg^{-1})
Liquid Hydrogen	141.9	10.1	0
Gaseous Hydrogen	141.9	0.013	0
Fuel Oil	45.5	38.65	0.84
Gasoline	47.4	34.85	0.86
Natural Gas	50	0.04	0.46
Charcoal	30	-	0.5
Methanol	22.3	18.1	0.5
Ethanol	29.9	23.6	0.5

As for the disadvantages of hydrogen, in the event hydrogen is in contact with the atmospheric air, unsecured combustion will lead to a safety hazard and the probable subsequent destruction of the devices. Hydrogen liquefies at very low temperatures, thus storage as a compressed gas or low-temperature liquid has additional energy costs. Hydrogen gas transportation needs high-pressurization. However, in-situ production and use can alleviate this drawback.

In conclusion, hydrogen derived from an appropriate green-technology is environmentally clean and the sources required are plentiful. Nevertheless, the global hydrogen supply will steadily increase, which is expected to have a crucial role in the locomotive industry as long as the batteries for electric cars remain costly and based on rare materials [239].

Additionally, in water splitting, the Oxygen evolution reaction(OER), or water oxidation, attracts consideration from the research community, as the OER is more challenging than the equivalent HER [59,60].

1.5.2 Semiconductors for photocatalytic reactions

Semiconductors, metals, and insulators are three types of materials that differ in their ability to transfer charge carriers, as seen in **Figure 1-21**.

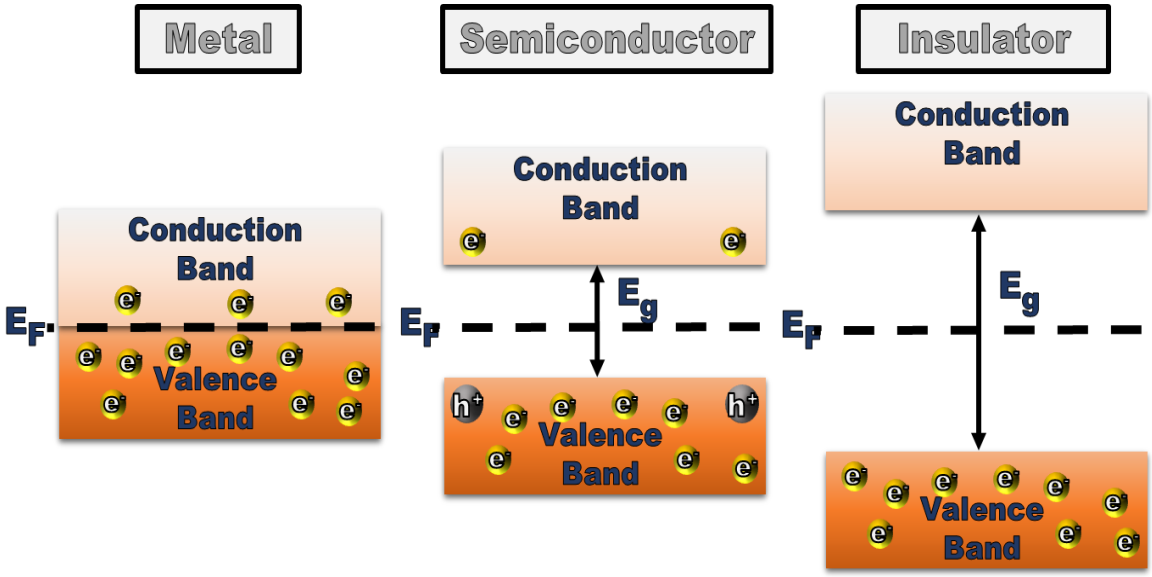

Figure 1-21: *The positions of the Valence Band, Conduction Band, and Fermi level for the three different material classes of Metal, Semiconductor, and Insulator.*

Semiconductors: Semiconductors are materials that have electrical conductivity between that of metals and insulators. They have a relatively small band gap, which is the energy gap between the valence band (the highest occupied energy band) and the conduction band (the lowest unoccupied energy band). This means they can conduct electricity under certain conditions, such as when exposed to light or heat. Semiconductors are commonly used in electronic devices, such as transistors and solar cells [240]. Metals are materials that have high electrical conductivity and nonexistent or very low band gap, with the Valence Band (VB) having less than 0.1 eV potential difference than the next energy lever of the Conduction Band (CB). Insulators are materials that have a very high resistance to the flow of electrical current. They have a huge band gap, which means that they do not conduct electricity efficiently [241].

Fermi level: The Fermi level is a concept in solid-state physics that describes the energy level at which the probability of finding an electron is equal to 0.5 (i.e., there is a

50% chance of finding an electron at or below the Fermi level). In a solid, electrons are restricted to certain energy levels called energy bands. The Fermi level separates the energy bands that are completely filled with electrons from those that are partially filled or empty. At absolute zero temperature, all electrons are in their lowest energy state and occupy the available energy levels up to the Fermi level.

The position of the Fermi level also determines the availability of states for electron transport and affects the behavior of the solid under different conditions, such as temperature and doping. The Fermi level is a fundamental parameter in understanding the electronic properties of metals, semiconductors, and insulators. In semiconductors, for example, the Fermi level lies within the bandgap, in which no electrons exist for this energy range [242].

Direct-Indirect transitions: The bandgap transition exponent can have four different values depending on the transition of the electron [243].

Direct allowed: p=1/2

Direct forbidden: p= 3/2

Indirect allowed: p=2

Indirect forbidden: p=3

The transition can be either direct or indirect, also it can be allowed or forbidden. In a direct transition with the energy of the photon, an electron immediately transfers to the lower part of the conduction band. In an indirect transition, the excited electron must first lose energy in the form of phonons in order to transfer to the lower part of the conduction band. The allowed or forbidden transitions are categorized if the transition-matrix element is equal to non-zero or zero, respectively [243]. In most common cases, p=1/2 is used i.e. assuming direct-allowed. A great example to better understand the Direct-Indirect transitions is the example of $Bi_2Fe_4O_9$, as shown in **Figure 1-22**, since it possesses two band gaps, with the main 2.1eV band gap being an indirect transition, while the secondary band gap of 1.6eV is designated as direct allowed [244], this is further analyzed on the computational results in section 4.4.5.

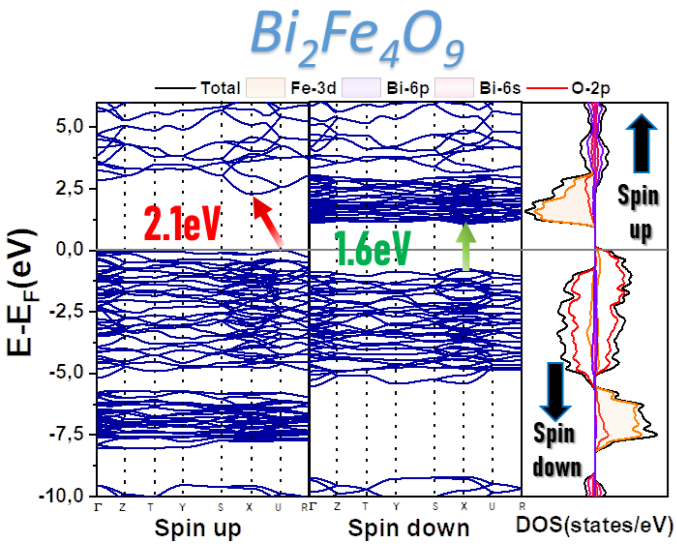

Figure 1-22: Theoretical energy band-structure and DOS of ferromagnetic $Bi_2Fe_4O_9$.

Defects: A defect in a semiconductor is an impurity or an imperfection in the material's crystal structure. Defects can be intentional, such as dopants added to create a p-type or n-type material, or unintentional, such as lattice vacancies or interstitial atoms [245]. Defects can affect the electronic properties of the semiconductor, this can have both negative or positive results in photocatalysis. *The negative results*, when the defect creates a "deep" energy well-localized state in the energy bandgap, codenamed as a "trap." A trap can collect the photoexcited electrons or holes, reduce the lifetime of the charge carriers or act as recombination centers, producing a non-radiative recombination and reducing the efficiency of the semiconductor [245].

Positive results, inserting a small concentration of Cation or anion dopants in the crystal structure [246] or with the removal of oxygen species in the structure [247] i.e. AO_{2-X} , introduces occupied or unoccupied states within the bandgap. Oxygen vacancies(V_O) create a series of transition levels as electrons could be excited from the V_O states into the bulk CB [248], resulting in two-photon electron photoexcitation via VB → Vo, and Vo → CB. Thus, this separate two-photoexcitation can result in a switch from a semiconductor absorbing only Uv radiation to absorbing visible light [249]. This also corresponds to a change in the color of the sample. Furthermore, the overall efficiency of the photocatalysis can increase substantially [249].

Semiconductor photocatalysis: When a semiconductor receives a photon from the sun or another radiating source that possesses energy bigger than the Band Gap. Then an electron (e^-) that originated in the Valence Band is excited to the Conduction Band, from the previous electron energy state, the absence of the electron in the valence band is called a hole (h^+) and is considered a positive charge. The whole process creates an electron-hole pair, but this pair is metastable, meaning that it has a limited lifespan before the system reaches equilibrium again. If nothing interacts with the electron/hole pair, then the electron descends from the Conduction Band to the Valence Band, this process is called recombination. Different semiconductors have very different recombination lifetimes, where materials with a very small band usually recombine much faster than materials with a much larger band gap.

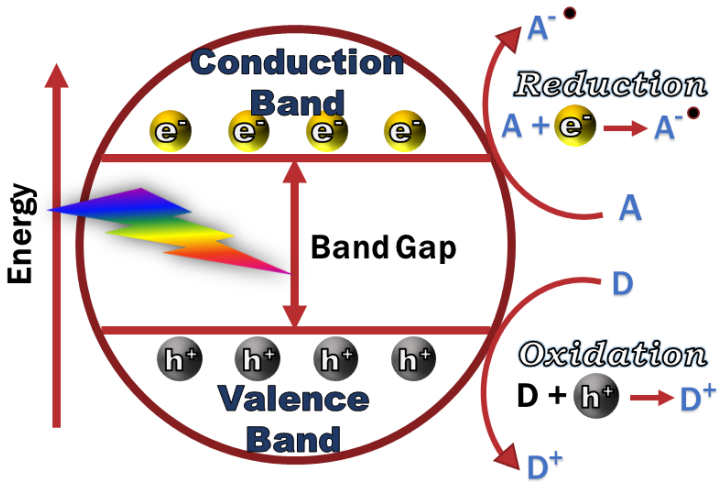

Figure 1-23: *Photocatalysis by application of the separation of the electron/hole pair in a semiconductor, the basic mechanism of oxidation, and reduction of the electron/hole pair.*

The electron-hole pair as an energy source can be utilized for photochemical reactions, as seen in **Figure 1-23**. Suppose the electron in the Conduction Band makes contact with a chemical compound A. In that case, Reduction will occur, where the excess electron of our material will transfer to the new chemical compound producing $A^{-\bullet}$. The second part of the reaction occurs with the hole in the Valence Band. The reaction now is

an Oxidation of the chemical compound D, which means that an electron from the compound D will transfer to the material, altering the chemical compound to D^+. As one of the electron/hole pair contributes to the oxidation/reduction of a compound, then fundamentally, there is no possibility for recombination [250].

The interaction between the elector-hole pair of the semiconductor and a chemical compound in order to occur has some strict criteria. First, the energy position of the material and the chemical compound must have the proper band edges for the redox reaction. For every chemical reaction to occur, the energy supplied by the pair must be more or equal to the energy required for the transition from A to $A^{-\bullet}$ or D to D^+. To graphically make this transition coherent, the Y axis is considered to be the energy level. At the bottom are the chemical reactions that have less energy and are therefore, more stable. In the X axis, the semiconductor's energy levels and the chemical compound's redox band edges are shown. As a general rule, the electron can only go in a lower band edge energy, and a hole can only go higher in a band edge energy [251]. There are four possibilities for the interaction of two compounds, as demonstrated in **Figure 1-24**.

1. **Reduction:** For reduction to happen, the electron of the semiconductor CB must be higher than the reduction band edge of the chemical compound.
2. **Oxidation:** For oxidation to happen, the hole of the semiconductor VB must be lower than the oxidation band edge of the chemical compound.
3. **No reaction:** If the CB is lower than the redox level and the VB is higher than the redox level, neither reduction nor oxidation happens.
4. **Redox reaction:** If the CB is higher than the redox level and the VB is lower than the redox level, then both reduction and oxidation occur.

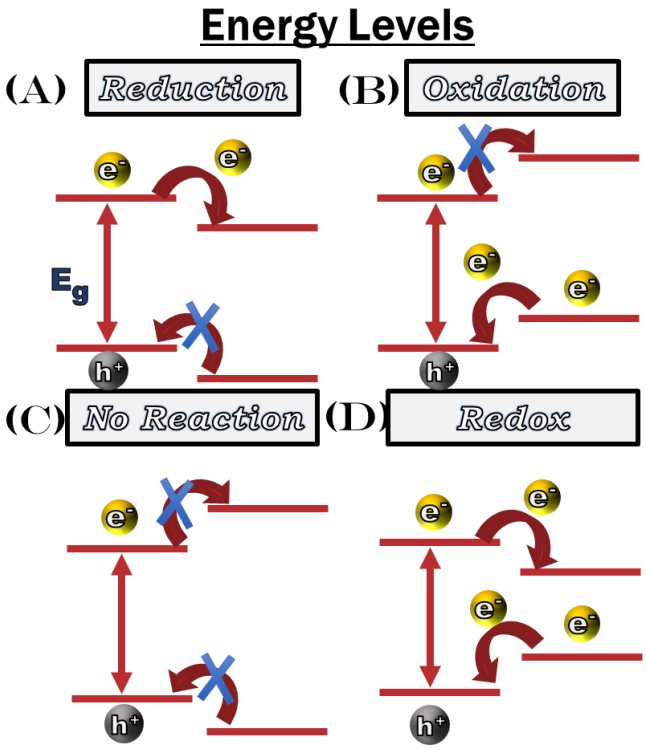

Figure 1-24: *The energy positions of the semiconductor at electron/hole pair (Left) and the energy levels of a chemical reaction(Right) of the four possibilities of the electron-hole pair, (A) reduction, (B) oxidation, (C) no reaction and (D) redox reaction.*

1.5.3 The Electrochemical Energy scale, Standard or Normal Hydrogen Electrode(SHE, NHE)

In solid-state physics, we consider the **Absolute Energy Scale**, on which zero is defined as an electron's energy at rest in a vacuum, as shown in **Figure 1-24** [251]. The vacuum level is expressed as the energy required for an electron to transfer to a position infinitely far from any charges, the position of a free stationary electron without the feeling of charge is considered (E = 0 eV). The formula for converting the material's band edges from NHE to a vacuum level is shown in Equation 1-10 [251]. The arbitrary standard Hydrogen electrode (SHE) OR Normal Hydrogen Electrode (NHE), potential scale used by electrochemists is shifted by −4.5 eV with respect to the vacuum energy. Most major

applications of photocatalysis are depicted with the NHE scale, where the arbitrary 0 V correlates to the energy where water reduction occurs to produce hydrogen.

$$E_{redox} = -4.5\text{eV} - e\,U_{redox} \qquad \text{Equation 1-10}$$

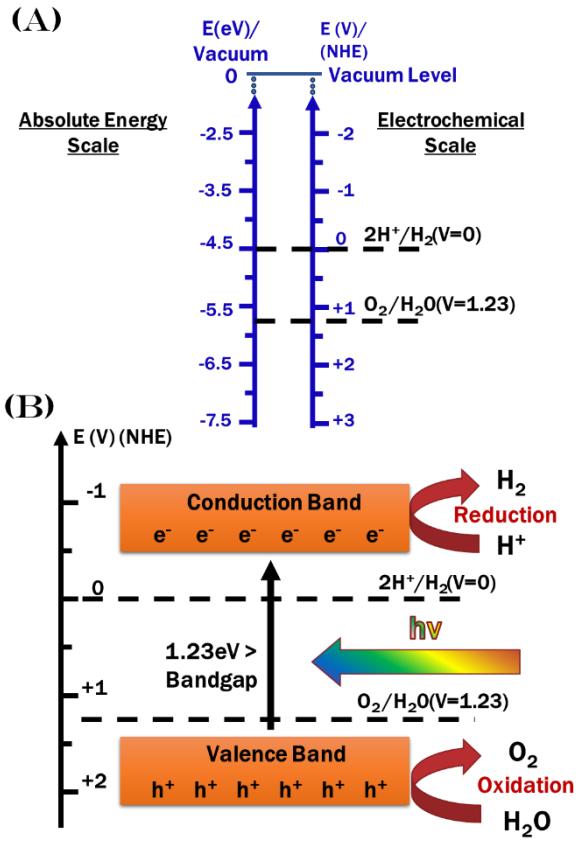

Figure 1-25: *(A) The positions of Vacuum energy compared with the NHE at pH=0, (B) The mechanics of photocatalytic water splitting, with the OER forming from the oxidation and the HER forming from the reduction.*

The main differences between the two scales are

1. In the electrochemical scale, the units are in **Volts** (Voltage), while in the absolute energy scale are in **eV (**energy).

2. In the electrochemical scale**,** the potential (voltage) has the opposite "polarity" to the electron energy, e.g., an increase in potential corresponds to a decrease in energy.

$$E_{VB}(\text{or } E_{CB}) = -\text{constant} - 0.059\,\text{pH}\ (\text{V, NHE}) \qquad \text{Equation 1-11}$$

Figure 1-25(A) graphically shows the comparison of the two energy levels and the two energy levels for the water spitting (redox reaction), which will be expanded upon later. The energy band edges are very dependent on the total pH of the solution. By changing the pH by a factor of one, the band edges shift by 0.059 mV. This result has been calculated theoretically by Nerst et al. [252], as shown in Equation 1-11. Thus, the band edges can be tuned by shifting the Ph values in order for our desired chemical reaction to occur.

In **Figure 1-26**, we present the positions of Vacuum energy compared with the NHE with the altered Redox potentials at pH=7. Noticeably, a shift of almost 0.41V is altered with the pH shift. Additionally, the prominent Redox potential of CO_2 reduction is shown [106].

Electron acceptors/Hole scavengers: To avoid recombination between electrons in the conduction band and holes in the valence band, **Figure 1-26**. Additional substances can be included in the photocatalytic process, that collect one of the charge carriers, inhibiting the recombination rate, thus increasing meaningfully the reduction or oxidation reaction [253]. An electron acceptor draws the CB electrons from the semiconductor, the most common electron acceptors are metals due to their excellent electrical conductivity. The work functions are presented with Pt^0 : φ=5.6 Ev, Au^0 :φ=5.1eV [254], and Ag^0 : φ=4.2eV [255]. The metals collect the electrons from the semiconductor and subsequently reduce the appropriate substrate i.e. water to H_2. Furthermore, electron acceptors such as $Na_2S_2O_8$ [256], reduce themselves to substrates that remain neutral in the photocatalytic reaction, increasing the effectiveness of the semiconductor holes for oxidation.

Hole scavengers include methanol, ethanol, isopropanol, ethylene glycol, glycerol, and many others. These substrates have high potentials i.e. methanol at +0.2 V vs NHE [257], that have fast reactions with the semiconductor holes [258], generating stable species that do not interfere with the reaction, thereby eliminating the effect of recombination of the e^-/h^+ pair [253].

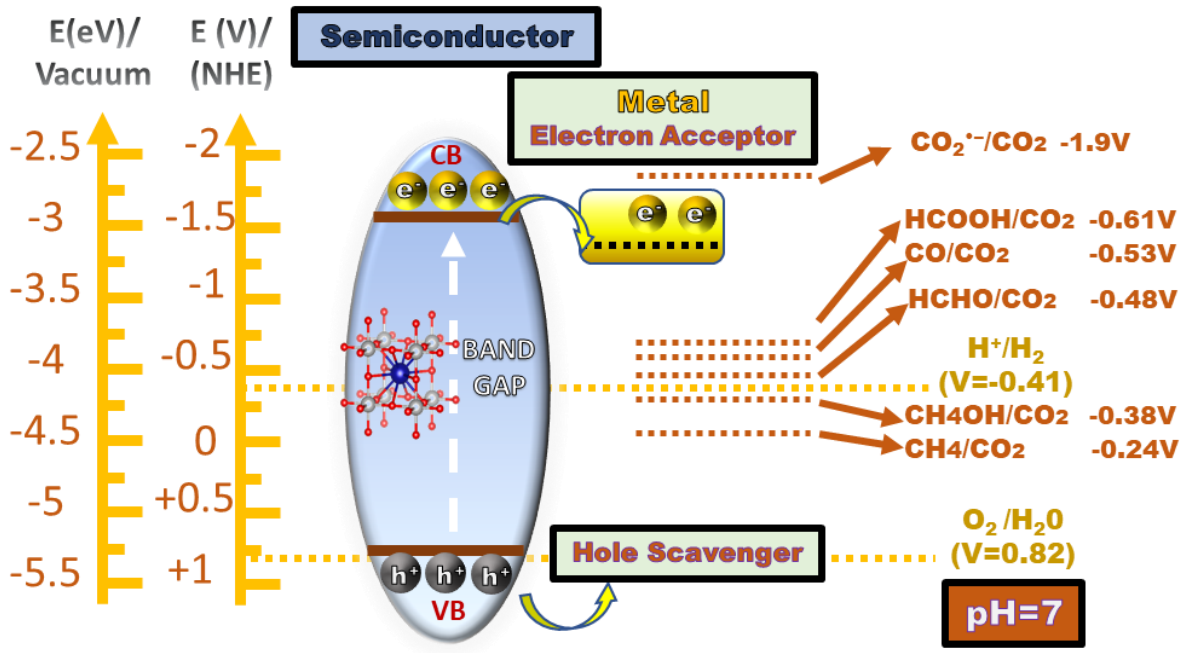

Figure 1-26: *The positions of Vacuum energy compared with the NHE at pH=7. The mechanics of photocatalytic mechanisms that employ Electron acceptor and Hole scavenger, with the Redox potentials for water splitting and CO_2 Reduction.*

1.5.4 Band Bending in Semiconductors and Metals Particles

Band bending refers to the phenomenon wherein the electronic band structure in a material curve upward or downward in the vicinity of a junction or interface. It's important to note that this term does not imply any form of physical bending or deformation. In situations where the electrochemical potential of the free charge carriers differs around a semiconductor's interface, there is a migration of charge carriers between the two substances. This process continues until an equilibrium state is attained, with the elimination of the potential difference [259].

The Band-Bending between a Metal-Semiconductor is first considered, as shown in **Figure 1-29**. In the region where the metal and semiconductor are in contact, the charge carriers will begin to shift according to the E_F of each material [260]. For a metal, the $E_{F,M}$ is at the bottom of its CB [260], while in the event of an intrinsic semiconductor, the $E_{F,S}$ will

be at the center of the E_g. There are two possible cases for the work functions, with $\Phi_m > \Phi_S$ and $\Phi_m < \Phi_S$ (in association with the E_{VAC}).

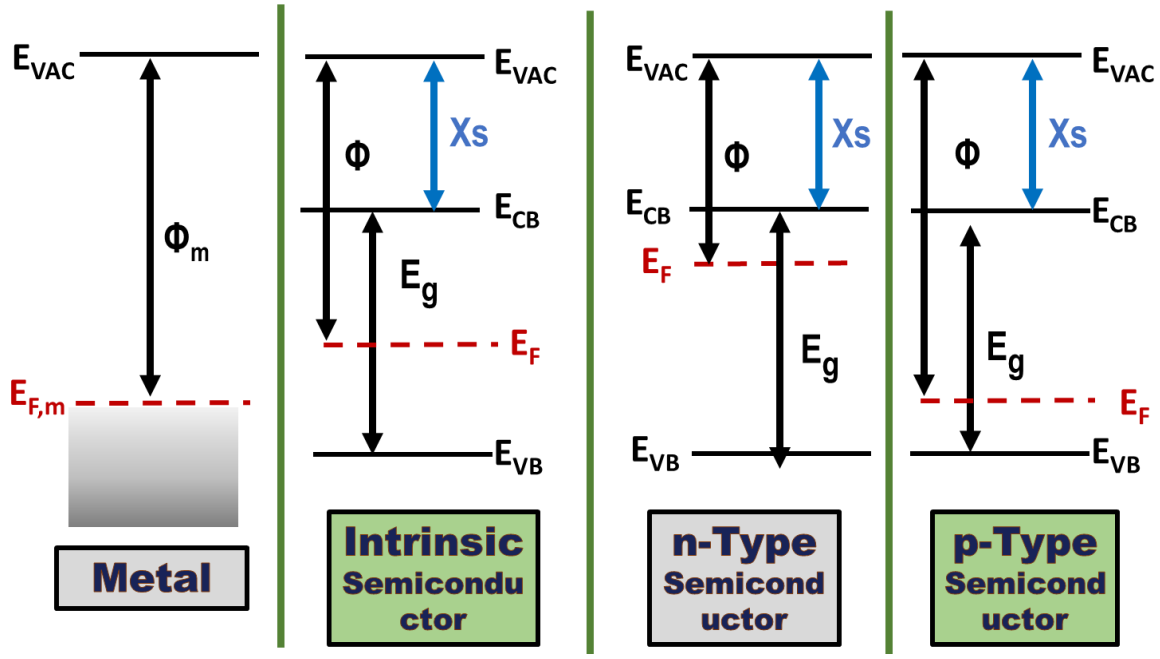

Figure 1-27: *The parameters band gap E_g, Fermi level E_F, electron affinity X_S, and work function Φ, based on the metal and Semiconductor (Intrinsic, n-Type, p-Type).*

The fundamental parameters to understand the band bending phenomenon at the interface of two materials, see **Figure 1-27**,

- The band gap E_g

- The Vacuum energy E_{VAC}

- The Fermi level E_F

- X_S is the electron affinity of the semiconductor

In the case of a metal, the $E_{F,m}$ is determined as the lowest occupied state which is typically taken to mean the bottom of the conduction band.

- the work function of the metal Φm and the work function of the semiconductor Φ_S, the work function is determined as the energy from the E_F to the E_{VAC}.

-The work function of the semiconductor Φ_S. This can be classified in three configurations of the semiconductors i.e. intrinsic, p-type, n-type. An intrinsic semiconductor has the E_F at the center of CB and the VB, meaning that in an intrinsic semiconductor, the work function Φ_S is acceptable to be determined as the X_S in addition to the half of the band gap E_g. The other two states are defined as n-type and p-type semiconductors, where the semiconductor, due to the crystal structure or different atomic dopings in the crystal structure, has a different balance of charge carriers, for the n-type semiconductor that n derives from the negative charge since the electrons are the majority carriers, and holes are the minority carriers, in this case, the E_F is greater than that of the intrinsic semiconductor and lies closer to the CB than the VB. In the case of p-type semiconductors, the p derives from positive charge since the holes are the majority carriers, shifting the E_F below the intrinsic semiconductor being closer to the VB [261].

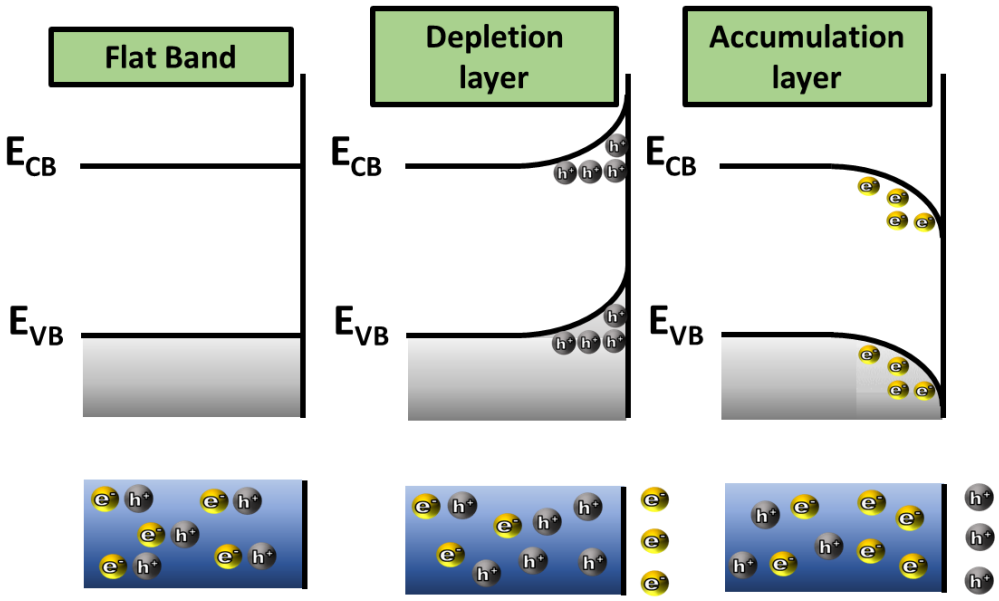

Figure 1-28: *Schematic diagrams showing the Flat Band, Depletion layer, and Accumulation layer.*

Metal-Semiconductor Interface

There are two possible cases for the work functions, with $\Phi_m > \Phi_S$ and $\Phi_m < \Phi_S$ (vs the E_{VAC}).

In CASE $\Phi_m > \Phi_S$, under contact and equilibrium, the free electrons will be transferred between metal and semiconductor, see **Figure 1-29**, Electrons will flow **from** the semiconductor **to** the metal until the Fermi levels of $E_{F,m}$, and $E_{F,S}$ are aligned. As a result, **– at the interface-** the metal will become **negatively charged** and the semiconductor **positively charged** i.e. due to the low concentration of electrons **(=excess of positive holes**) in the semiconductor. The space charge region of the semiconductor, due to the excess positive charge, is named the **depletion layer (Figure 1-28)**.

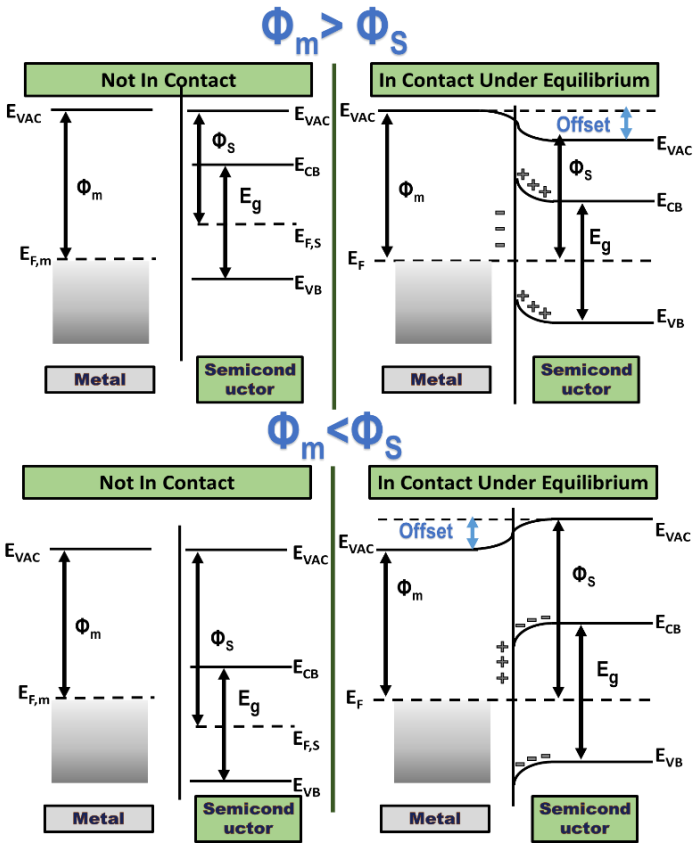

Figure 1-29: *Energy band diagrams (in the Absolute Energy Scale) of a metal and an intrinsic semiconductor, (left panels) not in contact. (right panels) in contact after equilibrium (Schottky Junction). The two different cases of $\Phi_m > \Phi_S$ and $\Phi_m < \Phi_S$.*

In CASE $\Phi_m<\Phi_S$, the electrons transfer from the metal to the semiconductor, with the semiconductor accumulating excess **negative** charge. In this case, the space charge region is called the **accumulation layer** (**Figure 1-28**). For simplicity, if $E_{F,M}$ is below $E_{F,S}$, a transfer of electrons will occur from the metal to the semiconductor until the two Fermi levels are equal.

Thus, in both **$\Phi_m<\Phi_S$** or **$\Phi_m<\Phi_S$**, the band-edge position is **shifted** at the interface. This is the band-bending phenomenon.

-The **depletion layer** has an **upward** band bending, see **Figure 1-28** with the positive charges existing at the semiconductor surface and negative charges accumulate near the surface i.e. the metal in this event.

-The **accumulation layer** has a **downward** band bending, see **Figure 1-28** due to the increase of free electron carriers and the decrease of hole carriers [259].

The *degree of band bending* depends on the relative Fermi levels and carrier concentrations of the materials forming the junction. This can be theoretically calculated from the work function difference between Φ_m and Φ_S, resulting in the band offset, as calculated by Equation 1-12. When $\Phi_m > \Phi_S$, usually derived from an N-type semiconductor, a Schottky barrier (Φ_{SB}) is formed at the interface of the two materials from the difference between the Φ_m and the semiconductor electron affinity X_S, Equation 1-13. No Schottky barrier exists at $\Phi_m < \Phi_S$ in an n-type semiconductor, and the metal–semiconductor contact is ohmic [262].

$$\boldsymbol{band\ offset} = |\boldsymbol{\Phi_1} - \boldsymbol{\Phi_2}| \qquad \text{Equation 1-12}$$

$$\boldsymbol{\Phi_{SB}} = |\boldsymbol{\Phi_m} - \boldsymbol{X_S}| \qquad \text{Equation 1-13}$$

Semiconductor-Semiconductor Interface

For the interface of two different Semiconductors, the same rules apply as in the Metal–Semiconductor interface, as shown in **Figure 1-30**, where we discuss the interface between a n-Type semiconductor and a p-type semiconductor.

When in contact and in equilibrium, the Fermi level of the two semiconductors are aligned. Thus, based on the band offset, the appropriate band bendings are formed, with a **depletion** layer for the **n-type** semiconductor and an **accumulation** layer for the **p-type** semiconductor [262].

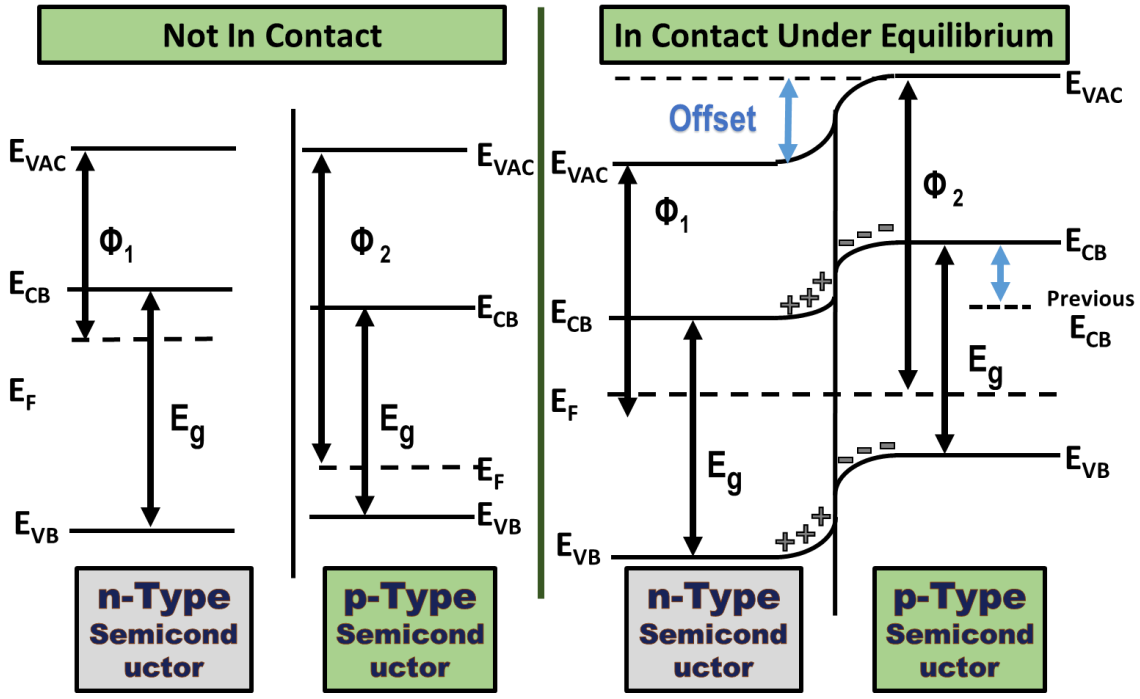

Figure 1-30: *Energy band diagrams of n-Type semiconductor and p-Type semiconductor, in the event of not in contact and in contact under equilibrium.*

The Heterojunctions

For a successful redox reaction, as shown in **Figure 1-24**, there are two cases for successful and efficient electron-hole transfer processes between two interfaced-semiconductors.

We can classify two types of heterojunctions:

- a **Type-II heterojunction**, as shown in **Figure 1-24**(A), where the first Semiconductor (SC1) has a higher VB and CB, thus

$$E_F(SC1) > E_F(SC2)$$

SC1 will transfer the electrons to the second Semiconductor (SC2), while from the VB of SC2, the holes will be transferred to the VB of SC1. Thus, the SCI acts as a hole sink and SCII as an electron sink, separating the electron/hole pair and significantly increasing the half-life of the charges [263].

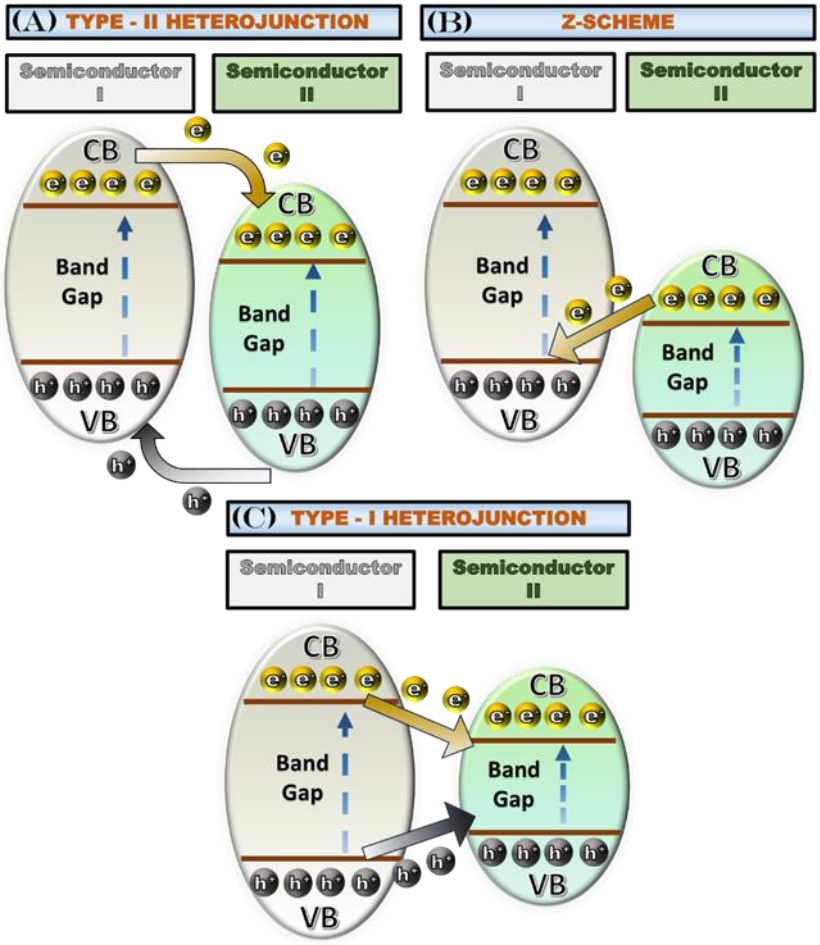

Figure 1-31: *The energy band schematics between two semiconductors: (A) Type-II Heterojunction, (B) Z-Scheme, (C) Type-I Heterojunction.*

-**Z-scheme**, as shown in **Figure 1-24**(B), a particular case of Type-II heterojunction. There is a single charge transfer-event, where the electrons from the lower CB in SC2, are transferred to the VB of SC1, recombining with the holes of SC1. In this case, the electrons remain in the higher CB energy and the holes in the lowest VB energy, which allows a

higher activity of Redox reactions [263]. Furthermore, the electron/hole pair is spatially separated, inhibiting the recombination rate.

-Additionally, **Type-I heterojunctions**, as shown in **Figure 1-24**(C), the bandgap of one semiconductor is completely contained in the bandgap of the other one, thus

$$E_{CB}(SC1) < E_{CB}(SC2) \text{ and } E_{VB}(SC1) > ECV(SC2)$$

This heterojunction is deemed inefficient for photocatalytic applications, as all charge carriers accumulate in the second semiconductor, leading to higher recombination rates. Furthermore, as both charge carriers result in a lower energy potential, the catalytic application becomes fewer and with lower efficiency.

1.5.5 Photocatalytic Water Splitting

For the **Photocatalytic** water splitting, the electrons and holes are generated via excitation of the semiconductor by light-photos. The total procedure, as shown in **Figure 1-25**(B), all interactions and procedures are as follows: photons are absorbed by the semiconductor, producing numerous pairs of electron/holes, and the semiconductor need to have band edges according to the reduction of H^+ to H_2 (0 eV NHE) and H_2O to O_2(-1.23 eV NHE). First, the hydrogen evolution reaction (HER) is the reduction of water from the electrons of the semiconductor Conduction Band. Secondly, the oxygen evolution reaction (OER) is water oxidation from the hole of the semiconductor's Valence Band. The thermodynamically negative reaction requires a minimum total energy for the redox reaction of +1.23 eV. Thus, the band gap of the semiconductor must be at least 1.23 eV and the photon that excites the electron/hole pair of 1.23 eV and above [264].

$$\mathbf{2\,H_2O + 2h^+ \rightarrow 2\,OH^- + 2H^+} \qquad \text{Equation 1-14}$$

$$\mathbf{2\,OH^- + 2h^+ \rightarrow O_2 + 2H^+},\ \mathbf{E_{Oxidation} = -1.23V} \qquad \text{Equation 1-15}$$

$$\mathbf{2H^+ + 2e^- \rightarrow H_2},\ \mathbf{E_{Reduction} = 0.00V} \qquad \text{Equation 1-16}$$

$$\mathbf{Overall\ \ 2H_2O + 4h^+ + 4e^- \rightarrow O_2 + 2H_2} \qquad \text{Equation 1-17}$$

The numerous photogenerated electron/hole pairs simultaneously either recombine or migrate to the surface of the semiconductor and interact with surrounding electron-

acceptors or hole-acceptors, the compound of interest in this example being water. Holes oxidize water to split into O_2 and H^+, Equation 1-15. This is the HER, which needs **two electrons** to create one molecule of Hydrogen. Forming the molecule of oxygen requires an exchange of **four holes** to occur, Equation 1-14 and Equation 1-15. These factors make the OER process kinetically slow and more difficult to achieve than HER. So, the OER is the rate-limiting step to water splitting [265].

1.5.6 Short overview of the Ph.D. Thesis Semiconductors used as photocatalysts

In principle, eligible semiconductors for high-performance photocatalysis must possess specific properties to function and be effective for photocatalysis.

(1) *Band gap*: In the example of water spiting for the simultaneous application of OER and HER, a minimal $E_g > 1.23$ V is needed. On the other hand, a very large band gap is detrimental, as it will absorb much less radiation from the sun.

(2) *Stability:* The semiconductor interacting with the solvent (in this case, water) or the subsequent products of the photocatalysis shouldn't change the original crystal structure of the semiconductor. For example, if the perovskite $BiFeO_3$ is altered through interaction with other chemical components to the separate oxides of BiO_2 and Fe_2O_3, then the photocatalysis will stop entirely after some time.

(3) *Band edges*: The conduction band must be above the redox potential of (H^+ to H_2), and the valence band must be below the redox potential of (H_2O to O_2).

(4) *Resistant to photo corrosion*: Photo-corrosion is the event that the semiconductor itself is oxidized by the holes that were generated through the photons, instead of the water, semiconductors like SiC, ZnO, and CdS that have appropriate band edges for water splitting but can't function because of photo corrosion.

(5) *Visible light absorption*: Most semiconductors that have suitable band edges for photocatalytic application can only absorb ultraviolet light, which is 5% of the total direct sun radiation (this is the case for $NaTaO_3$). So, they can be truly effective only with other

light-sources sources, e.g. from ultraviolet lamps or LEDs, but direct irradiation from the sun yields low efficiency [266].

Furthermore, a semiconductor must have additional attributes to maximize the efficiency of photocatalysis. The semiconductor nanomaterials must have *high crystallinity*, which increases the speed of charge transfer and minimizes the charge traps of defect sites. A ***small particle size*** is desirable since the electron/hole pair can travel a small distance before the pair's half-life is forced to recombine. In that small distance, the pair must reach the particle's surface area in order for the redox of water to occur. *High particle surface area*, this factor is similar to the limitation of size. With a higher SSA, more electron/hole pairs will be able to interact with an increasing volume of reactant compounds [265].

As an example of a proper photocatalyst, the TiO_2 semiconductor will be briefly examined since, at this time, TiO_2 is the world's most successful photocatalyst. Fujishima and Honda were the first to show that TiO_2 could operate as a photo-anode with UV light-assisted photocatalysis, they also were the first to propose the application of Photocatalytic water splitting [267]. Titanium oxide has many advantageous properties that all aforementioned nanoparticles should have. (1) proper band gap and band edges for water splitting, (2) chemically stable under photocatalysis and doesn't exhibit photo-corrosion. (3) It isn't toxic, biologically and chemically inert, everything is combined into an environmentally clean nanomaterial. (4) Relatively abundant in the world and low cost [268]. However, there are three significant disadvantages of TiO_2. (1) Wide band gap of approximately 3.2eV, thus very limited solar spectrum absorption. (2) Short lifetime of the electron-hole pair due to the fast kinetics of the charges. (3) The Conduction Band has only -0.2 eV (NHE). Thus, applications of CO_2 reduction will be limited [269].

According to the photocatalytic application that is pursued herein, for enhanced OER, HER, or CO_2 reduction, several supporting metals and semiconductors were applied to enhance the photocatalytic activity of the nanoparticles. These can be grouped into

[i] **co-catalytic metals (Pt^0, Au^0, and Ag^0)**: Metals have excellent electrical conductivity, while the selected metals have a different work function. Pt^0 has a work

function of φ=5.6 Ev, Au^0 at φ=5.1eV [254]. Ag^0 has a less favorable positioning work function at φ=4.2eV [255], as shown in **Figure 1-32**.

[ii] **Cocatalytic metal oxides**: Oxide semiconductors CuO and NiO were utilized. CuO has a band gap in the range of 1.3-1.7 eV depending on the morphology and size, while the Conduction Band is found approximately to be at -0.5 eV *vs.* NHE and the Valence band at 1 eV [270]. NiO semiconductor is observed in the literature at Eg 3.6eV [271,272]. Accordingly, NiO band edges are positioned approximately at the Conduction Band -0.96 eV and Valence Band +2.64 eV [271,272]. NiO is one of the few *p*-type semiconductors [273,274] that is used in contrast with $NaTaO_3$, which is a *n*-type semiconductor [272].

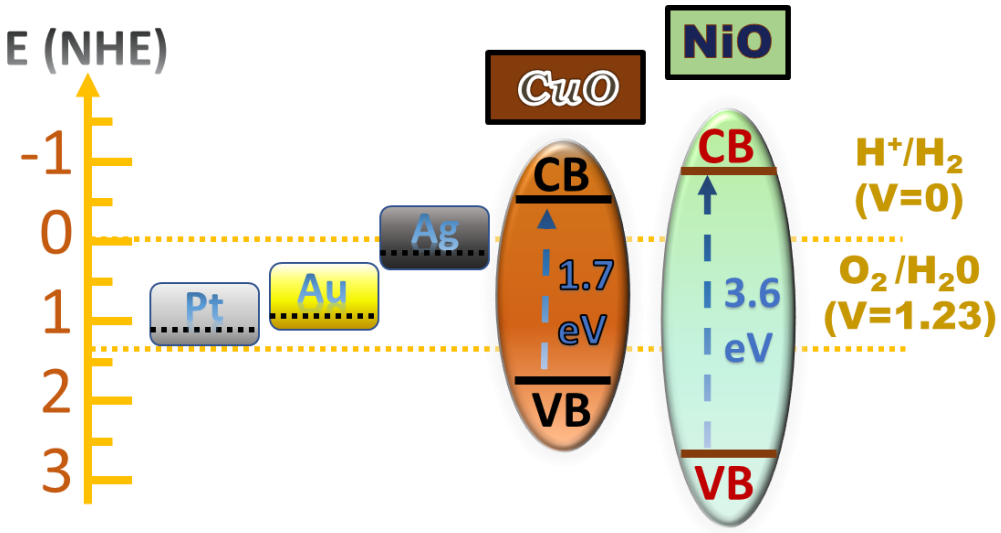

Figure 1-32: *The positions of band edges for the supporting metals Pt^0, Au^0, and Ag^0. The supporting oxide semiconductors CuO and NiO.*

Overview of the band gaps and the band edges of our materials

Bi-Fe-Oxide Perovskites: Starting with the perovskite phase $BiFeO_3$, a direct bandgap in the range of 2.1-2.8 eV [275] has been reported. For the mullite-type $Bi_2Fe_4O_9$, a band gap in the range of 2.1 to 2.3eV is reported [276], also a secondary smaller band gap is observed for the $Bi_2Fe_4O_9$ of 1.6 eV [277]. The Conduction Band-edge energy of $BiFeO_3$ is reported at +0.51 eV *vs.* NHE, and the Valence Band (VB)-edge position at 2.61 eV.

Similarly, $Bi_2Fe_4O_9$ has a CB-edge at +0.5 eV and a VB-edge at 2.55 eV. These are in agreement with CB-edge +0.51 eV for $BiFeO_3$ and CB-edge +0.5 eV for $Bi_2Fe_4O_9$ [278,279], as shown in **Figure 1-33**.

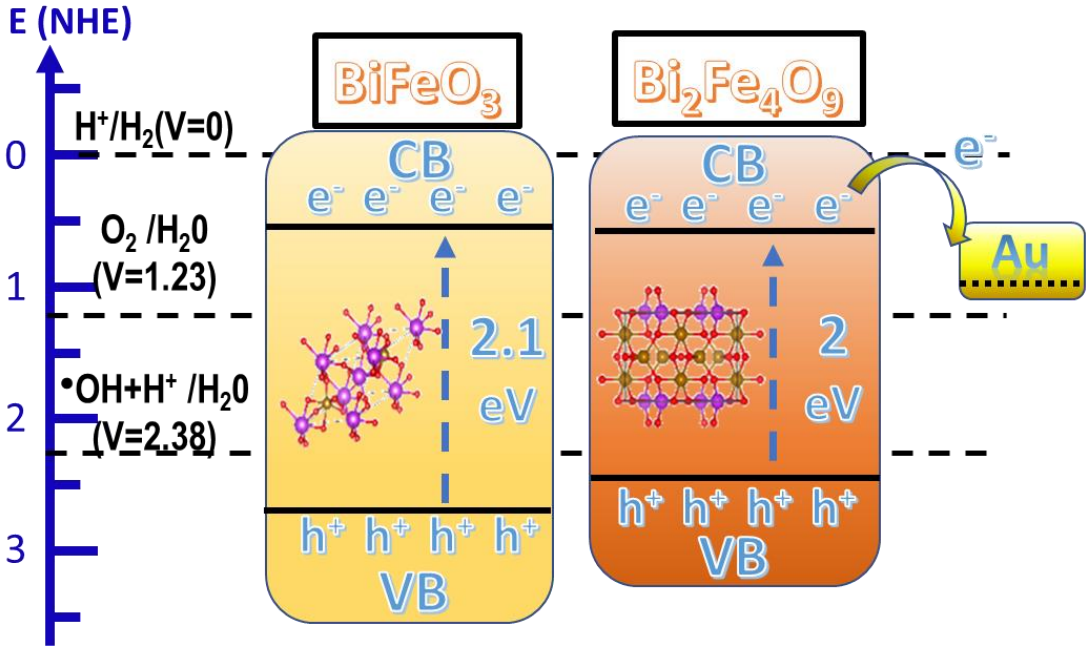

Figure 1-33: *The band edges and band gap positions for the perovskite $BiFeO_3$ and mullite-type $Bi_2Fe_4O_9$.*

Ta-Oxide-Perovskites: literature shows that the Ta_2O_5 particle has E_g~ 4.15eV [280]. $NaTaO_3$ has E_g~ 4.2eV, typical for Ta-particles as originally reported by Kudo's group [124,281]. For $LiTaO_3$, the band gap is found at 4.7eV [282]. $NaTaO_3$ has its valence-band edge, E_{VB}, situated at +3eV *vs.* NHE [272,283] and a conduction-band edge to E_{VB} = -1.2 eV, the E_{VB} and E_{CB} for Ta_2O_5 are positioned at +3.43 eV and -0.72 eV respectively [284,285]. The E_{VB} and E_{CB} for $LiTaO_3$ are positioned at +2.6 eV and -2.1 eV [282], respectively, as shown in **Figure 1-34**.

$SrTiO_3$ has E_g~3.2eV bandgap that is similar to that of the simple oxide TiO_2, but it has a more reducing conduction-band edge energy position E_{CB} of -1.2eV vs. NHE, and consequently, the valence-band edge E_{VB} of 2eV [141,142], as shown in **Figure 1-35**.

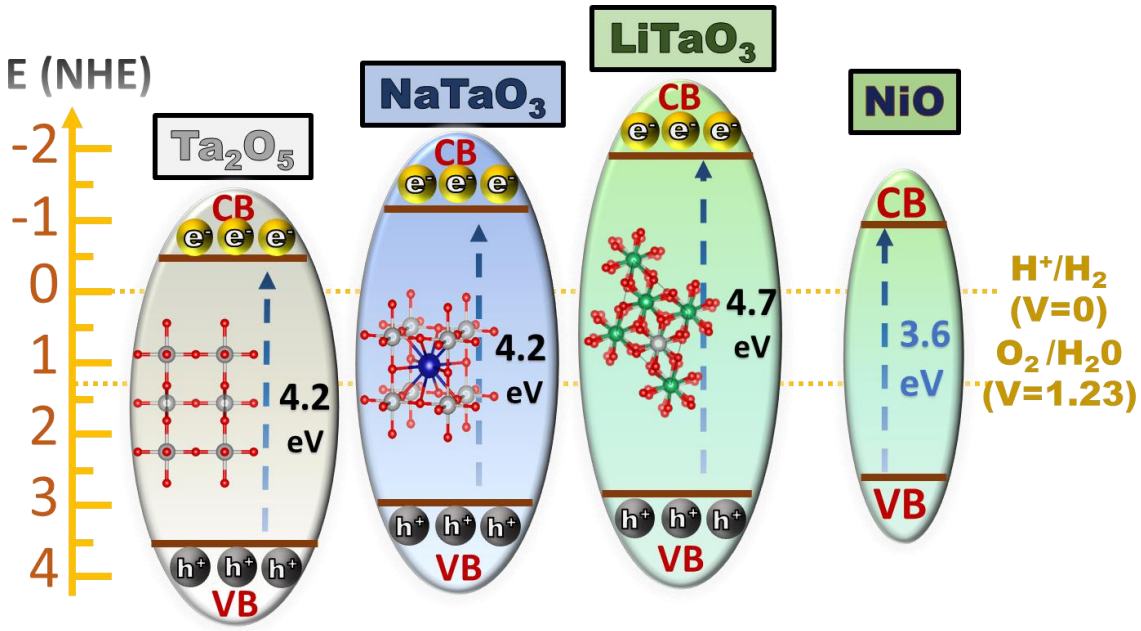

Figure 1-34: *The band edges and band gap positions for the oxide Ta_2O_5, the perovskites $NaTaO_3$ and $LiTaO_3$.*

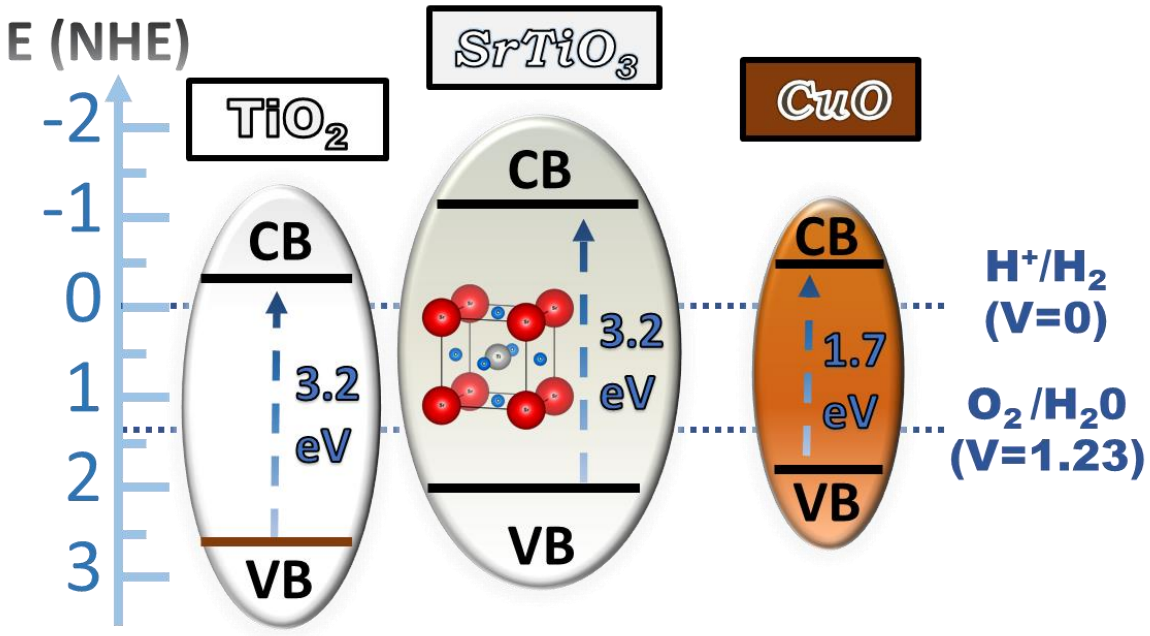

Figure 1-35: *The band edges and band gap positions for the oxide TiO_2 and the perovskite $SrTiO_3$.*

2 SCOPE OF THESIS

The broad scope of the present Ph.D. Thesis was [i] to develop novel Flame-Spray-Pyrolysis protocols that allow controlled production of pure-phase perovskite oxides and their heterostructures. [ii] To optimize the so-produced nanocatalytic materials for catalytic reduction, the photocatalytic H_2/O_2 production from H_2O splitting.

In this context, specific scopes of the present Ph.D. Thesis were:

[1] *Study of the perovskite nanoparticle formation in the FSP-process*. Our strategy was based on the FSP technology (Single-Nozzle and Double-Nozzle) for the synthesis of 100%. Specific aims were: (i) Synthesis of $BiFeO_3$ and $Bi_2Fe_4O_9$ particles and their heterostructure $BiFeO_3$ /$Bi_2Fe_4O_9$ with cocatalytic noble metals Au, Pt, and Ag. (ii) Use of advanced Double-Nozzle FSP for La-doping in the material of $SrTiO_3$ and *in-tandem* $CuO/SrTiO_3$ heterostructure production in one step, resulting in an advanced heterostructure $La:SrTiO_3/CuO$. (iii) The synthesis of the smallest-possible $NaTaO_3$ particle size, and their heterostructures with NiO, Pt, and Pd employing the SN-FSP and DN-FSP methods.

[2] *Study and fundamental understanding of the role of nanolattice defects, nano-interfacing, and semiconductor band-bending in the photophysical hole-electron generation and transfer*. To do this, detailed post-FSP thermal-calcination protocols were screened in combination with XRD, Raman, XPS, and EPR data.

[3] *Demonstration of the nanomaterials for highly-efficient catalytic applications*. (i) $BiFeO_3$ and $Bi_2Fe_4O_9$ were evaluated for reduction of 4-Nitrophenol and physical-chemical study of the activation energy for this process. The Bi-Fe-O materials were also employed for the photocatalytic oxidation of H_2O to O_2, demonstrating that $Bi_2Fe_4O_9$ is an –so far unanticipated- efficient OER photocatalyst. (ii) The perovskite heterostructure $La:SrTiO_3/CuO$, was utilized for photocatalytic production of H_2 or CH_4 from H_2O/CH_3OH. (iii) The high conduction band semiconductors Ta_2O_5, $NaTaO_3$, and $LiTaO_3$ were validated for photocatalytic H_2 production from H_2O. The photoinduced electrons and holes in $NaTaO_3$ were detected for the first time by EPR.

[4] *Establishing protocols for novel FSP-processes that allow industrial-scale production of perovskite nanomaterials and their heterostructures with enhanced photocatalytic efficiency.*

3 Experimental Methods

3.1 Flame Spray Pyrolysis

3.1.1 Single Nozzle FSP (SN-FSP)

The Flame Spray Pyrolysis reactor set-up and basic-principles of operation for the production of nanoparticles will be explained hereafter.

(i) *Preparing the Precursor*: A powder or liquid that contains a high concentration of the specific metal-element is required for the nanoparticle oxide as a final product. Those are obtained from STREM or Sigma Aldrich. The precursor molecule, apart from the metal ion, has to have ligands with high concentrations of carbon and oxygen, i.e. to produce high-enthalpy in the combustion process. Typical precursors for high-enthalpy comprise of Metal-acetylacetonate, Metal-naphthenate. In contrast, Metal-nitrates are poorer as combustible precursors in case the desired particle is able to form in low-enthalpy conditions, they are preferable due to significantly lower cost.

(ii) *Solvent:* In order to have a liquid mixture, a *solvent* is required. The eligible solvents in FSP have to contain high carbon concentration to increase the combustion enthalpy of the flame. In addition, this ensures complete combustion with no carbon-leftovers. An important note for the flame-enthalpy is that at least 50% is fueled by the liquid precursor i.e. the rest can come from the combusted gases. Thus, proper solvent selection is crucial, since the effective temperature of the flame can drastically change [286] [287]. In this thesis, the solvents were most often xylene and 2-Ethylhexanoic acid for high enthalpy synthesis, or ethanol for low enthalpy synthesis.

In order for the precursor mixture to be inserted in the FSP apparatus, it must be devoid of precipitates so that the flow rate of the precursor remains constant without blocking the tubes. For the formation of perovskites that require *two different elements* (two different precursor solvents etc.), the precursor needed to be homogeneous. Thus, great effort was placed on the two solvents to be compatible (miscible) to avoid precipitate formation.

The FSP synthesis apparatus requires three additional pieces of equipment, as shown in **Figure 3-1**. The Gas-Flowmeter, which controls the exact flow rate of O_2/CH_4 for the assist pilot flame, the flow rate for the oxygen dispersion flow rate, the syringe that contains the liquid precursor solution with controlled the precursor flow rates, and the pressure gauge that indicates the dispersion oxygen pressure-drop.

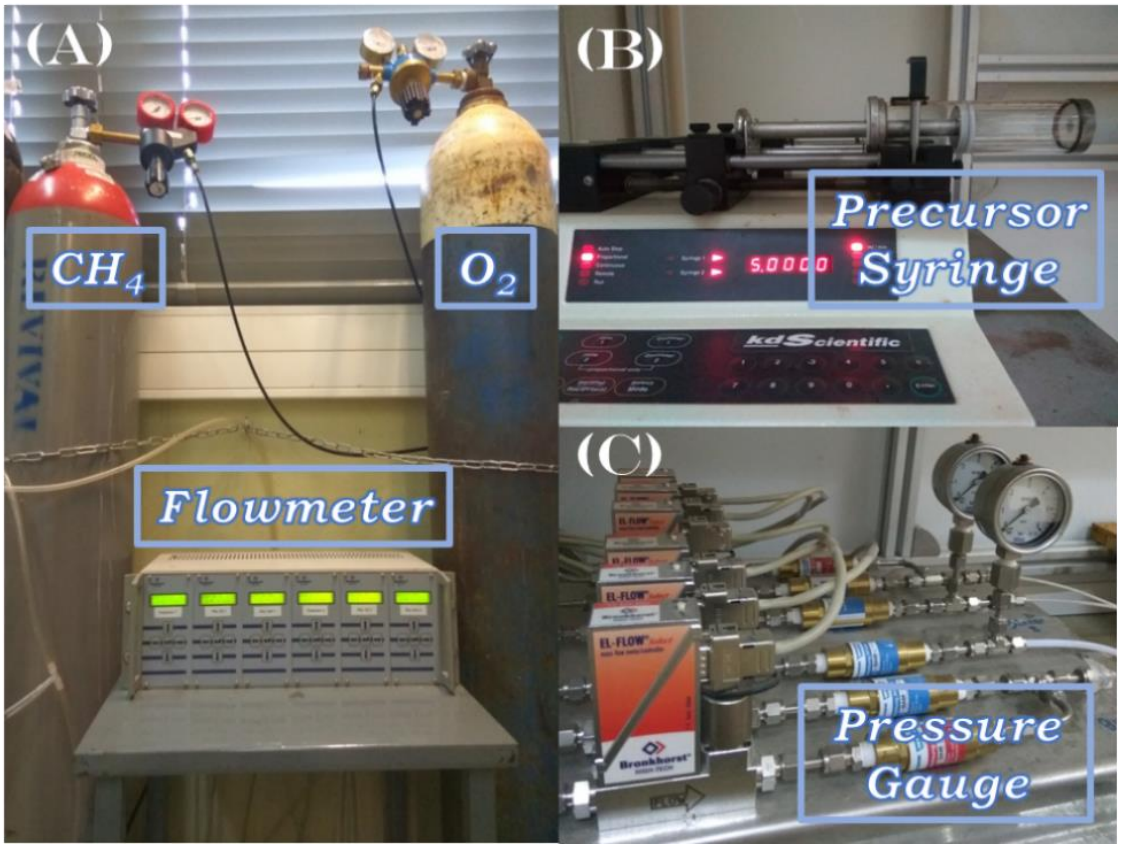

Figure 3-1: *(A) The flow controller of the four gases, with the two metallic tanks of O_2 and CH_4. (B) The specialized syringe pump applies a constant flow of precursor droplets. (C) The valves of the O_2/CH_4 gases measure the dispersion pressure of the FSP apparatus.*

The flame "nozzle" itself consists of four different parts, as shown in **Figure 3-2**. In the first part, a pilot flame is needed for the initial ignition and to sustain the spray combustion of the high-enthalpy organic solution. The standard experiment consists of a mix of oxygen (O_2) and Methane (CH_4) gases, pre-mixed in the valves before arriving in the FSP-nozzle. In the center of the nozzle, the **liquid-droplets of the precursor** are inserted,

with the typical precursor flow rate (**P**) of 5mL per minute, next to the precursor entry point, a gas with a dispersion flow rate (**D**) is inserted, forcing the droplets to disperse inside the flame. The pressure-drop, measured by a gauge, dictates the speed of the spray dispersion. The spray droplets then undergo the combustion procedure to form nanoparticles. There is an option to insert in the outer circle of the FSP-nozzle a sheath gas that surrounds the flame, shielding it from the surrounding atmospheric air.

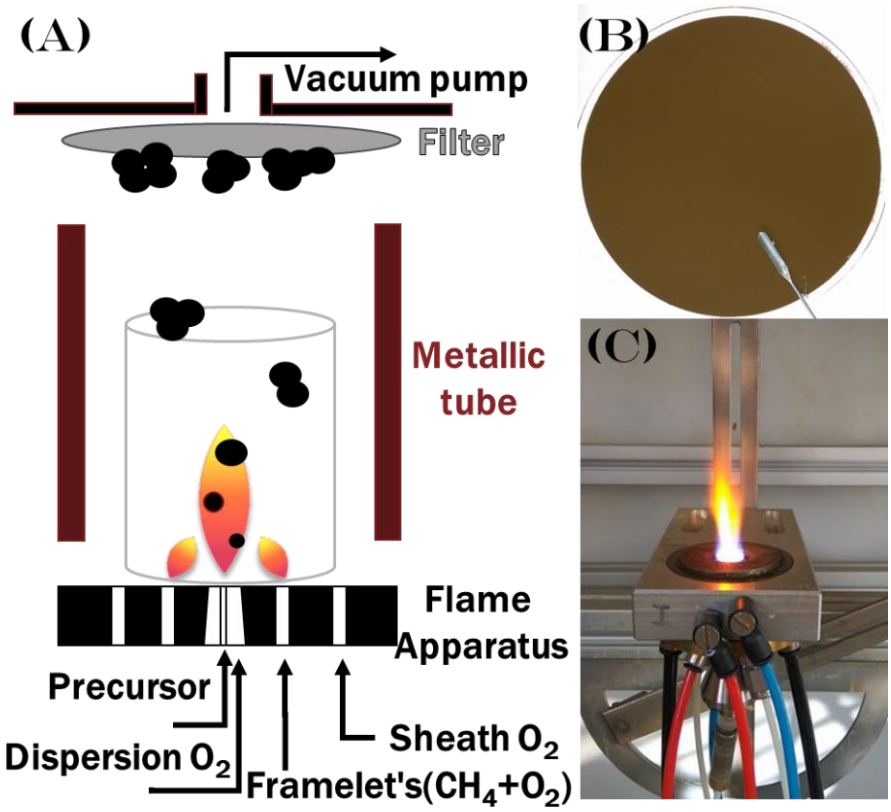

Figure 3-2: *The FSP-reactor scheme (A) depicting the Flame-Nozzle with the insertion of the metal Precursor, the applied gasses (O_2, CH_4), with the collection method of the FSP consisting of a filter and the vacuum pump. (B) The glass-fiber filter filled with the particles, after the particle-production. (C) FSP-nozzle and the flame in operation (the precursor and gas flows are inserted from the tubes beneath the nozzle and are ignited continuously by the pilot flame).*

The nanoparticles are lifted upwards by the gas-convection field and the overhead pumping, to enter the enclosing tube (either a metallic or a quartz tube) that increase

drastically the High-Temperature-Residence-Time. In our work, for many perovskite nanoparticles, the inclusion of an enclosed tube was found to be mandatory, otherwise, the two separate oxide nanoparticles were obtained, **Figure 3-2**. Afterward, the nanoparticles reach a glass-fiber filter. When the required amount of precursor is spent in the syringe, the filter is removed. The particle powder can be collected by scraping with a spatula or used as–it–is in the form of film.

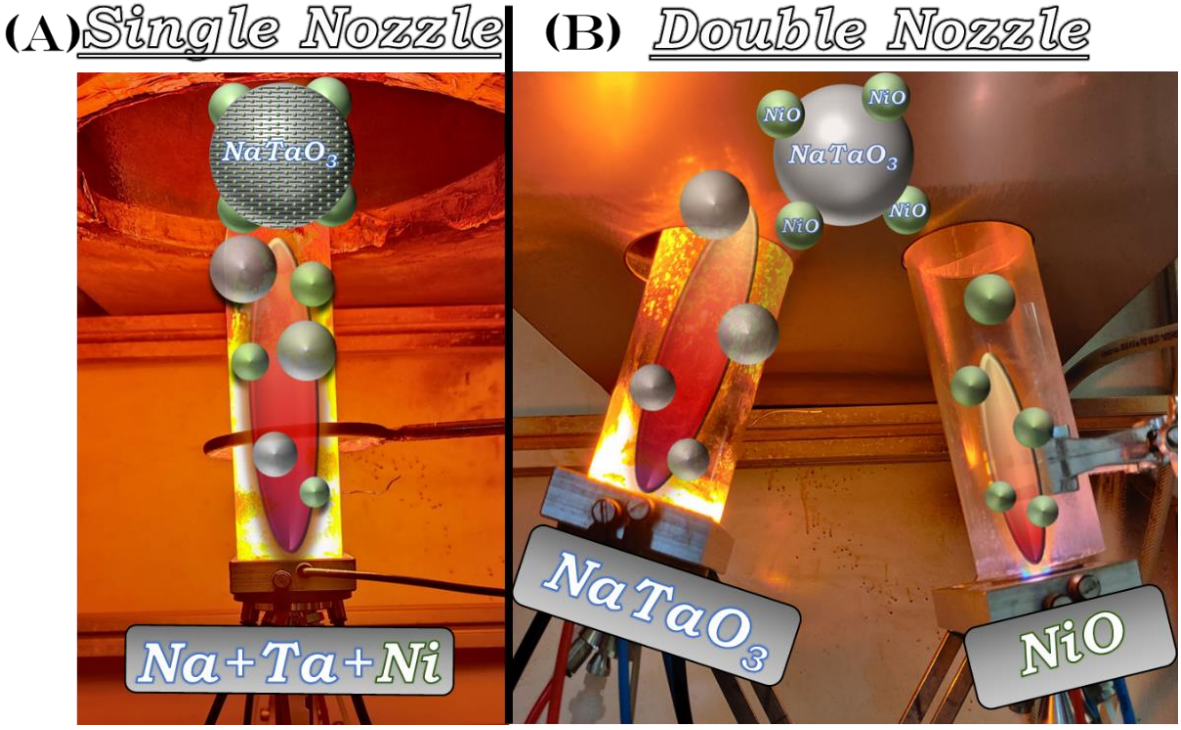

Figure 3-3: *The FSP set-up applied for the synthesis of nanomaterials: (A) Schematics of Single-Nozzle FSP (SN-FSP) reactor, (B) Schematics of Double-Nozzle FSP (DN-FSP) reactor.*

3.1.2 Double Nozzle FSP (DN-FSP)

The Double Nozzle FSP(DN-FSP) set-up in our work is shown in **Figure 3-3**(B). For comparison, the configuration of the two different set-ups, Single-Nozzle and Double-Nozzle are presented side-by-side. The difference of the resulting particle from the two configurations is demonstrated with the example of $NaTaO_3$ and the deposition of NiO, for the application to act as cocatalysts. As the name suggests, in Double Nozzle FSP(DN-FSP), two FSP nozzles are employed. The first nozzle has the precursor for the standard particle

synthesis, in this instance $NaTaO_3$, while the second nozzle has the precursor of the secondary element. The same configuration was employed for the deposition of CuO atoms on the surface of $SrTiO_3$.

The DN-Nozzle configuration ensures that both particles will be formed independently, each one in a separate flame, and their interfacing will occur after the flames are in contact. In contrast, in the case of SN-FSP, both particles are formed *in-tandem*. This means that -in principle- the two metal-atoms can be intermixed in the same particle, or a random mix of two types of particles can occur, see **Figure 3-4**.

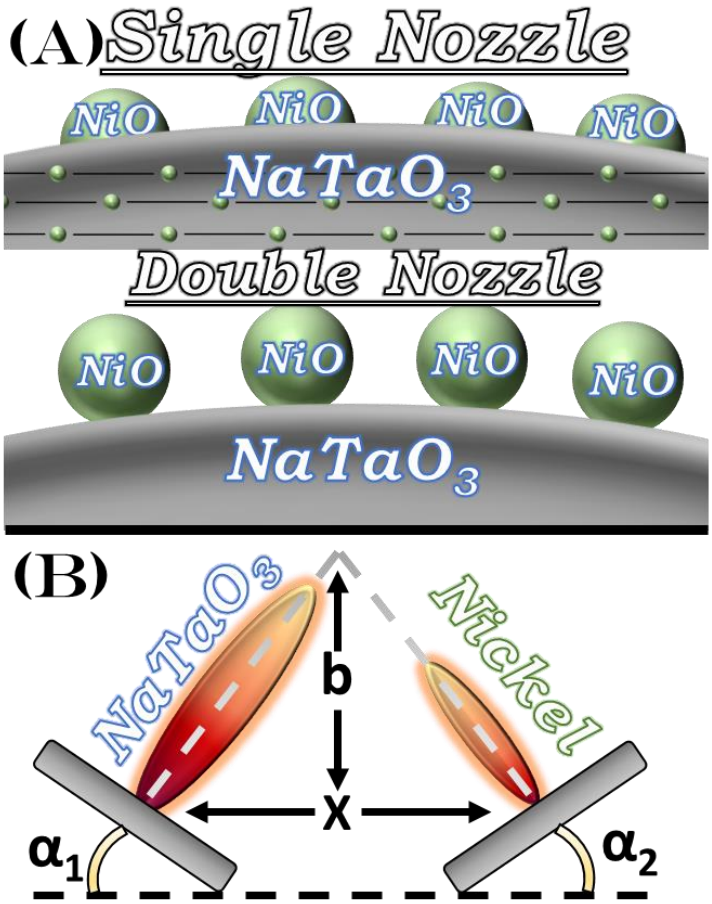

Figure 3-4: *(A) Theoretical Schematic for the deposition process of the two methods SN-FSP/DN-FSP: upper part depicts the SN-FSP, NiO may be incorporated inside the $NaTaO_3$ aggregates as well as on the surface, lower part shows the DN-FSP were NiO is deposited mainly on the surface of $NaTaO_3$, eliminating the probability of NiO to be located inside the*

crystal structure core of the $NaTaO_3$ nanoparticle. (B) The main adjustable geometry parameters (a_1, a_2, b, x) for the two nozzles in DN-FSP.

Thus, DN-FSP is a superior technology for the formation of nano-heterostructures. By adjusting the geometrical parameters of the two flames (a1, a2, b, x), see **Figure 3-4**(B), the process-parameters alter resulting in different particle sizes, interfacial-sintering, location of deposition and so on.

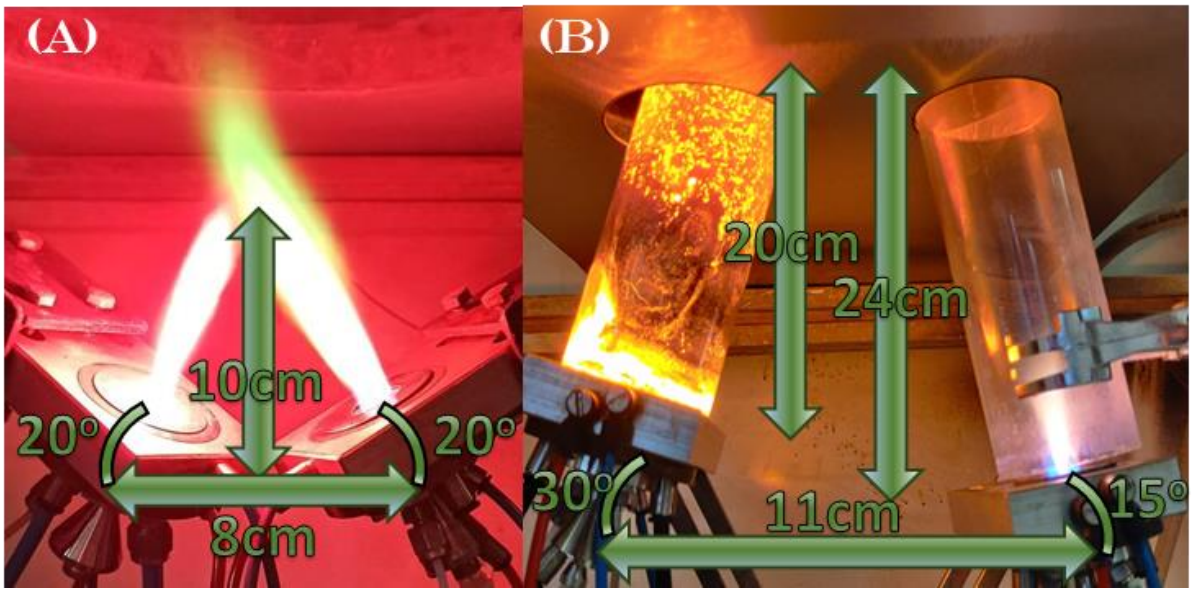

Figure 3-5: *The different adjustable geometry parameters for the formation of stable heterostructures, (A) for $SrTiO_3$/CuO, (B) for $NaTaO_3$/NiO.*

Since different nanomaterials reach the desirable phase at different times in the High-Temperature zone, this entails that this corresponds to different heights of the flame, thus it is imperative to control the geometry parameter b, see **Figure 3-5**. A failure to adjust the appropriate flame-cross point will result in the secondary particle being incorporated into the crystal structure and more importantly, might inhibit the desirable phase formation. An important demonstration derives from the different perovskites of this thesis, as $SrTiO_3$ can be synthesized under open flame conditions i.e. without the inclusion of quartz or metallic tubes to increase the high-temperature residence time, thus the adjustable geometry parameters can be kept at a minimum of b=10cm, as shown in **Figure 3-5**(A).

Equivalently, the perovskite structure $NaTaO_3$, which has a much higher energy-demanding process to form i.e. requiring a quartz tube of 20cm, results in a much more complex Double Nozzle geometry. For the cocatalytic particle NiO/ $NaTaO_3$, the FSP synthesis use of a quartz tube was necessary. For example, with no-tube in the NiO nozzle. The NiO particles were dispersed randomly in the reactor chamber, and only a fraction of NiO particles were deposited on $NaTaO_3$, forming a Heterostructure. With two-enclosing tubes, see **Figure 3-5**, the resulting interaction point of b_{NiO}=24cm produced superfine NiO of 2nm was deposited on $NaTaO_3$.

3.2 Catalytic Experiments

3.2.1 Photocatalytic Experiment Set-Up: Irradiation Reactor

For all the photocatalytic experiments, various Gas-Products (H_2, CO_2, CO, CH_4, O_2) were obtained depending on the targeted applications: O_2 for $BiFeO_3$, H_2 for $NaTaO_3$, H_2/CH_4 for La:$SrTiO_3$/CuO. The gas products were all measured with a Gas-Chromatography System combined with a Thermal-Conductivity-Detector (TCD), TCD-Shimadzu GC-2014, as seen in **Figure 3-6**, with a Carboxen 1000 column. The carrier gas for all cases was an Argon,i.e. He carrier gas interferes with the measurement of H_2 gas.

The Photocatalytic experiments were performed in a double-walled photochemical reactor (Toption Instrument Co. Ltd.), with a total reaction volume of 340 ml. The temperature was held steady for the duration of the experiments, at a temperature of 25±2 ^{0}C, by a recirculation chiller cooling system (Chiller T-300W), as shown in **Figure 3-6**, with a TOPT-II type black box, for UV-shielding.

Standard curves: For accurate measurements of produced gasses, routinely pure gasses of Hydrogen, Oxygen, and CH_4 with various volumes were inserted by a syringe in the Carboxen column, creating a standard curve as shown in **Figure 3-7**.

Figure 3-6: *(A) The Gas chromatography system of the experiments, a TCD- Shimadzu GC-2014, with a Carboxen 1000 column. (B) The Chiller T-300W and TOPT-II photo reactor container. (C) The double-walled photoreactor. (D) The same Reactor under the illumination of the 300W Mercury Lamp.*

Irradiation Sources: The UV-Visible radiation was supplied mainly from three different lamps: a 250W Mercury lamp provided by Philips, a 300W UV lamp, and a 300W xenon lamp, with radiation-equivalence to 3 suns. The radiation source was positioned at the geometrical center of the photoreactor, inside the quartz-immersion well. The quartz-immersion well received the input of the coolant water, reducing the temperature, while quartz as a material absorbs very little of the produced radiation.

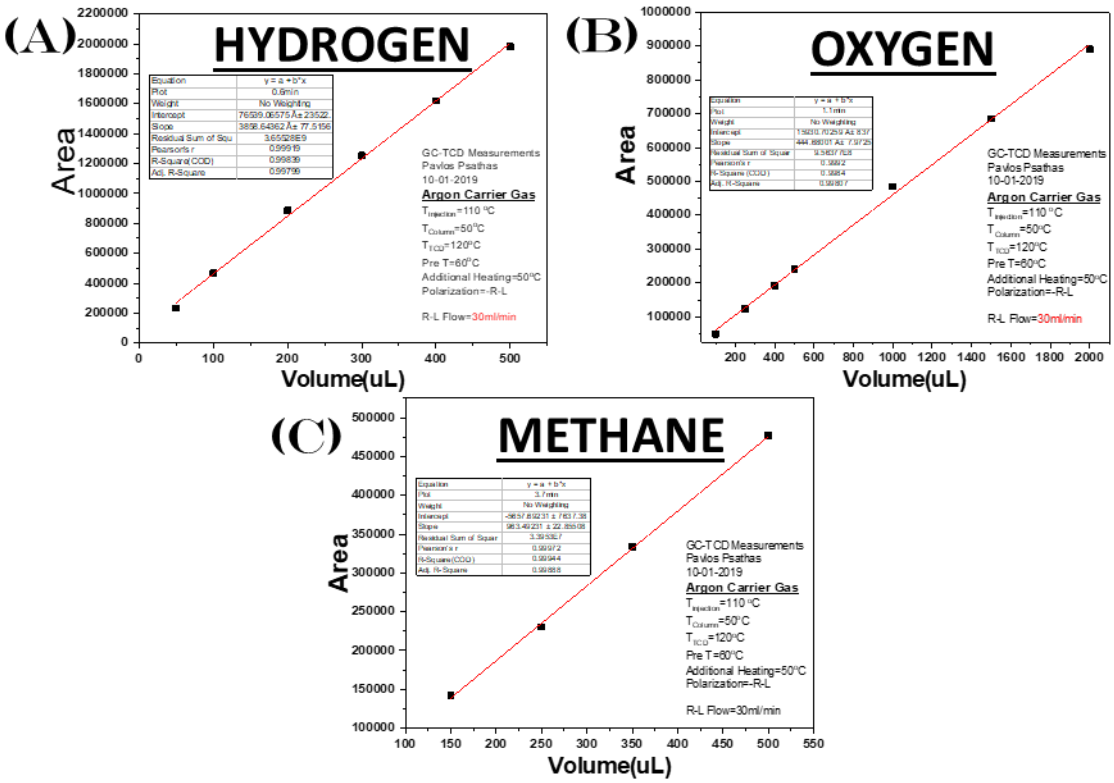

Figure 3-7: *The standard curves for the gasses of:(A) Hydrogen, (B) Oxygen, and (C) Methane.*

Irradiation Power Calibration: The irradiation power of the three lamps was measured by a power meter (Newport model, 1918-C). The Lamps were measured at two different distances: 3cm, which is the mean distance the light travels inside a smaller photocatalytic reactor, and 6cm, which is the mean distance of the 340mL reactor. As seen in **Figure 3-8**, the radiation power riches the peak after at least 5 minutes of operation, with the Xenon 300W having the largest radiation at 0.78 Wcm^{-2}, although as shown later, most of the radiation is in the visible and infrared range. The irradiation power is decreased to about a third by changing the measurement from 3cm to 6cm, although the original irradiation is naturally the same.

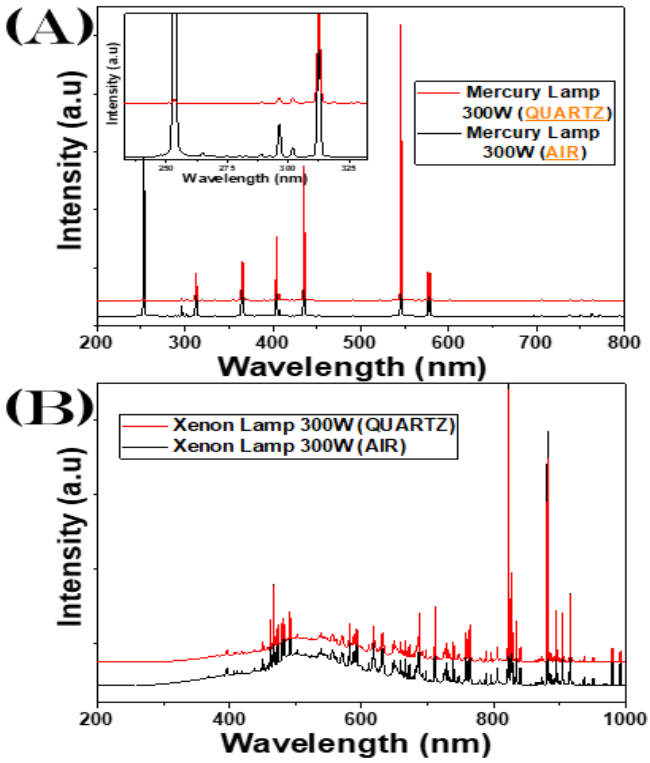

Figure 3-8: *Radiation Spectra for the (A) Mercury Lamp in the atmosphere and with the Quartz* quartz-immersion well*. Inset: Zoom at the wavelength range of 240 to 330nm. (B) Xenon Lamp at the atmosphere and with the Quartz disturbance.*

The radiation spectra in **Figure 3-8** of the Mercury and Xenon lamps show the more intense peaks for each lamp. The mercury lamp has very distinct irradiation peaks, with a very high content of UV light. The highest energy peak was at 250nm, although the Quartz-well of the photoreactor, absorbed most of the 250nm photons, as shown in **Figure 3-8** (A). Thus, most of the 250nm photons were absorbed, while at λ>300nm the rest of the irradiation peaks retained most of their power, with only a slight absorbance by the Quartz. For this reason, in photocatalysis, it is of critical importance to consider the role material between the lamp and the solution. For example, the commonly used Pyrex glass will absorb most of the UV radiation provided by a Mercury lamp.

The Xenon lamp, **Figure 3-8** (B), shows a wide spectral profile i.e. rather than distinct peaks, with most of the irradiation power provided in the range of 400-1000nm, with a small portion of the irradiation power being in the UV range. For this reason, the Xenon lamp can be compared with the irradiation of the Sun, in this instance, the radiation is approximately about three times AM1.5 Suns.

3.2.2 Photocatalytic Experiment: Hydrogen Production

In photocatalytic H_2-production experiments, we have used: (i) Deionized water, the main photocatalytic component, to produce hydrogen from the water splitting. (ii) A Mercury or Xenon lamp that produces UV and visible radiation. (iii) Photocatalytic Nanomaterials.

In all cases, two supplementary agents were added to maximize photocatalytic production. (i) Methanol as a hole-scavenger [288]. (ii) Cocatalytic electron-accepting particles. These serve the purpose of accumulating the photogenerated electrons from the nanomaterial surface and transferring the electrons to the ultimate electron acceptor i.e. H^+ in the case of H_2-production or HCO_3 in the case of CO_2 reduction.

After numerous screening tests, the optimized protocols for hydrogen production were as follows: [Deionized water]: [methanol] ratio = 20% per volume, with a total volume of 250 to 275 mL, i.e. 200mL Deionized water and 50mL methanol to result in the total volume 250mL. The catalytic nanomaterials used in the range of 50mg and 69mg. The pH values with the particles inserted in the mixture were between 4.6 and 6.2. The temperature was set to 25±3 ^oC controlled by tap-water cooling, or in the case of more demanding applications, the T-300W Chiller was used.

The irradiation was provided from two setups. The aforementioned 300W Xenon irradiation flux corresponded to the artificial illumination of 3 times AM1.5 Suns, or for a higher UV radiation, the 300W Mercury lamp (0.34 W cm^{-2}), for the best-performing material. When the cocatalyst wasn't provided in-situ from the FSP synthesis, a photo-deposition of Pt-cocatalyst was implemented to increase the photocatalytic production, using hydrogen hexachloroplatinate (IV) hydrate, ($H_2Pt_4Cl_6 \bullet H_2O$, 99.9 %, Alfa Aesar).

3.2.3 Photocatalytic Experiment: Oxygen Production

For these photocatalytic O_2-production experiments, a Pyrex-glass reactor was used, in order to filter the radiation to λ>380nm, i.e. since the $BiFeO_3$ and $Bi_2Fe_4O_9$ materials are visible light semiconductors. By conducting several screening tests, the optimal parameters were: 50 mg of nanomaterials suspended in 150 mL Deionized water (final concentration of catalyst 0.33 g/L), which contained 0.1M NaOH, pH value of 12.8 in accordance with the literature [289]. Additionally, 0.02 M $Na_2S_2O_8$ was used as an electron acceptor [289], since in these experiments, the charge carriers that drive the photocatalysis are the photogenerated holes.

Several cocatalysts were implemented i.e. with photo deposition of Pt^0, Au^0, or Ag^0. The metal-complexes used were Pt: hydrogen hexachloroplatinate (IV) hydrate, ($H_2Pt_4Cl_6 \bullet H_2O$, 99.9 %, Alfa Aesar), Au: hydrogen tetrachloro-aurate (III) trihydrate ($HAuCl_4 \bullet 3H_2O$, 99.9 %, Alfa Aesar), and Ag: Silver nitrate (I) ($AgNO_3$, 99.9 %, Sigma Aldrich). In all experiments, after the addition of all compounds in the reactor, an irradiation period of 15 min was necessary to achieve the *in-situ* reduction of the Pt, Au, or Ag cations for the corresponding metal particles [290].

The light source was a medium-pressure mercury lamp (Model Oriel 3010, 125 W, total light flux $7x10^{18}$ photons /sec) for all the experiments. Before each catalytic run, the suspension was purged with Ar gas (99.9997%) for at least one hour to remove the atmospheric gases.

3.2.4 Catalytic 4-NP Reduction in the Presence of $NaBH_4$

For the catalytic study of the reduction kinetics of 4-nitrophenol (4-NP) to 4-aminophenol (4-AP) with the addition of $NaBH_4$ as a reducing agent. The components for the experiment were inserted in a quartz-Uv-Vis cuvette containing 2775 μL double-distilled water, 0.123mM 4-NP solution (Alfa Aesar 99%), the reducing agent $NaBH_4$(Merck) at 108 mM, and the $BiFeO_3$/$Bi_2Fe_4O_9$ nanomaterials.

To disperse the $BiFeO_3$/$Bi_2Fe_4O_9$ nanomaterials by adding 2.5 mg in 5ml distilled water, a high-intensity cup-horn sonicator (Sonic-VCX-500), was used at a power of 100 W

for 25 seconds in cycles of 1-sec power on-1sec power off (overall 0.5 kJ for the 5mL). From the homogenous nanomaterial solution, a 75 μL was inserted in the cuvette (14 mg L^{-1}). The catalytic mixture in the 3 ml quartz cuvette was under magnetic stirring in the dark. The final pH of the mixture was measured to be 9.5.

The spectral changes related to the evolution of 4-NP were monitored by recording the spectrum in the UV-visible range using a Hitachi spectrophotometer equipped with a Unisoku cryostat for low-temperature experiments [291]. Rapid scans are recorded in the 250–550 nm wavelength range that is completed every 50 seconds. The characteristic peak of 4-NP at 400nm was used to calibrate the 4-NP concentration [292].

A Unisoku cryostat was inserted inside the UV–Vis spectrophotometer beam chamber to allow the digital control of sample temperature in the range of +100 °C to -100 °C with an error of ±0.1°C. Sample cooling was achieved by a controlled-flow of cold N_2 gas derived from liquid-N_2 heating. Herein, for the Arrhenius analysis, the catalytic 4-NP to 4-AP conversion kinetics were recorded at different temperatures of 5, 15, 25, and 35 °C, respectively, and the obtained kinetic data were used to calculate the activation energy E_a values.

4-NP Adsorption Isotherms: Additionally, we measured the adsorption isotherms for the 4-NP and the nanomaterial. Adsorption Isotherms were recorded for BFO1 to BFO4 at pH 7.5 in the presence of 4-NP at different concentrations 0.01mM-0.2mM, interacting with 4 mg of the materials suspended in 10 mL double distilled water solution in polypropylene tubes. After 4-NP addition, the suspension was allowed to equilibrate for 6 hours at room temperature (RT) while agitated by a magnetic stirrer. After completion of equilibration, the suspension was centrifuged at 9000 rpm in a Centurion centrifuge for 20 min, and the supernatant solution was analyzed by the Uv-Vis spectrum of 4-NP using the peak at 400nm. The amount of 4-NP adsorbed at different concentrations (μmol 4-NP g^{-1}), was calculated from the mass balance between the initial concentration and the concentration determined after the adsorption of 4-NP onto the solid adsorbents [293,294]. The centrifuged particles, where the 4-NP was adsorbed, were collected and analyzed by FT-IR.

3.3 Electron Paramagnetic Resonance (EPR) Spectroscopy

3.3.1 Fundamentals of EPR Spectroscopy

Electron Paramagnetic Resonance or EPR spectroscopy is a state-of-the-art spectroscopy for detecting paramagnetic centers or free radicals [295]. EPR is based on the Zeeman effect, as shown in **Figure 3-9**, with the two essential factors being an external magnetic field (B) and the electron spin (S). The energy states generated for the two ms states with values of +1/2 and -1/2 are given by Equation 3-1. The resulting ΔE is in the range of microwaves [296], the resonance phenomenon is generated using 9-10GHz irradiation (X-Band).

$$E = m_S \, g_e \, \mu_B \, B \quad , m_S = \pm \frac{1}{2} \qquad \text{Equation 3-1}$$

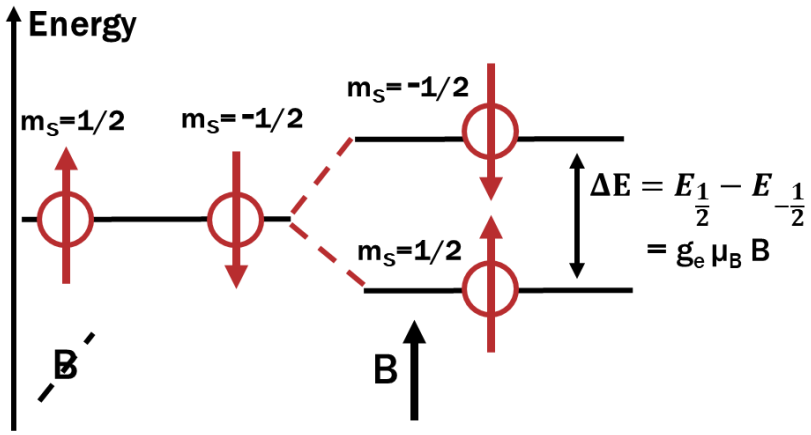

Figure 3-9: *The Zeeman effect on the energy levels of a spin ½ system with ΔE the difference of energy levels due to the external magnetic field B.*

The last two variables are the g_e, a constant for the free electron of value 2.0023, and Bohr magneton (μ_B) [297]. **Figure 3-10** shows a graphic representation of the splitting of the two energy levels by applying an external magnetic field. By changing the magnetic field, the lower energy level (m_s = -1/2), as well as the higher energy level (ms = +1/2) changes. As the frequency remains constant, only when the energy difference is the same as the energy of the photons (**$E_{photons}$ = hv**) will there be "**resonance**" i.e. the absorption of the photons by the sample. The instrument records the absorption and exhibits it as a 1st Derivative to increase the resolution of the spectral response **Figure 3-10**.

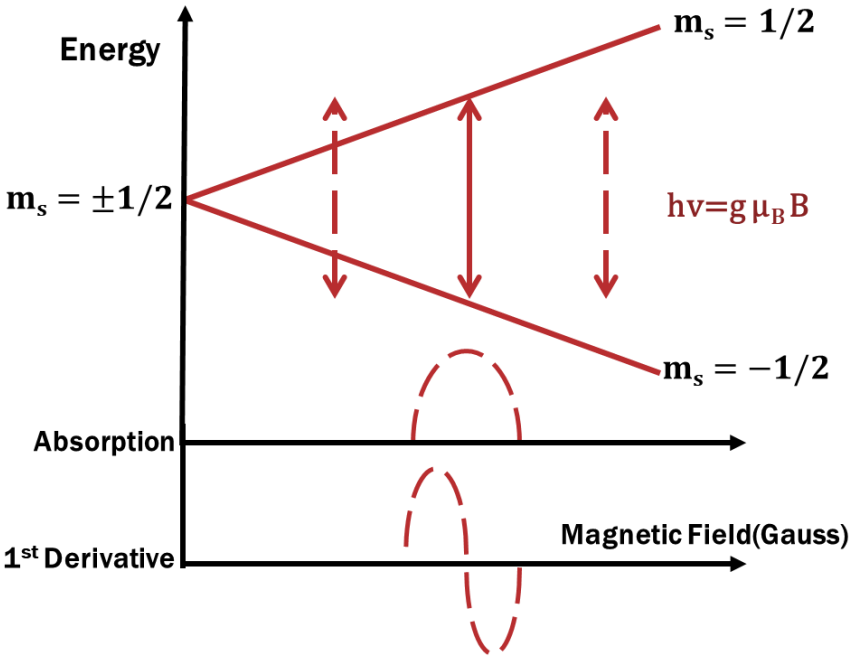

Figure 3-10: *The Zeeman effect for a spin 1/2, with the absorption as detected from an EPR of constant frequency, after the hv is the same as the ΔE the absorption is measured, with the instrument showing the 1st Derivative for increased precision.*

Only paramagnetic materials (such as paramagnetic metal centers or free radicals) that have unpaired electrons are able to be studied by EPR spectroscopy. The Zeeman further splits the energy levels for a system with S >1/2, creating 2S+1 states. These states can absorb frequencies at different values of the external magnetic field B, with the limitation that the difference of the energy levels should be $\Delta M_S = \pm 1$, Equation 3-2 [298].

$$\Delta E = E_{+\frac{1}{2}} - E_{-\frac{1}{2}} = g_e\,\mu_B\,B = h\,\nu \qquad \text{Equation 3-2}$$

In this work, EPR has been utilized to detect the photocatalytically generated paramagnetic centers by the nanoparticles under illumination. These paramagnetic centers were

[i] holes or electrons detected *in-situ* in the solid matrix of the particle [299].

[ii] photogenerated •OH Radicals, originating from the oxidation of H_2O from the holes [59].

3.3.2 Spin Trapping of OH Radicals

The OH-radicals are well known to have short half-lives of the order of 10^{-9} sec at room temperature [300]. Thus, a spin-trap method has been applied [301] in order to form stable radical adducts detectable by EPR.

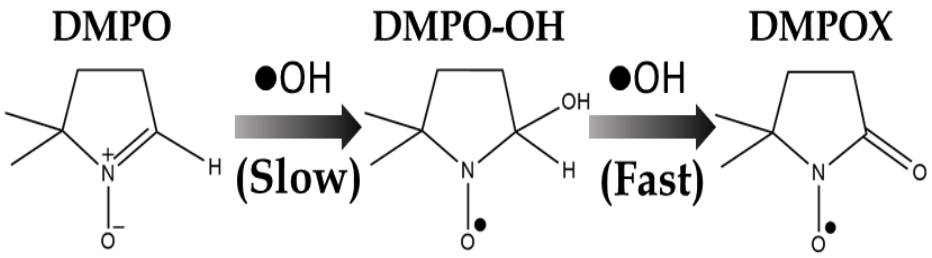

Figure 3-11: *Schematic of Radical •OH transition for slow production and fast production of radicals with DMPO as Spin Trap.*

Among the many spin trap molecules, 5,5-dimethyl-1-pyrroline N-oxide (DMPO), is commonly used, while a-phenyl-butyl-nitrone (PBN) [302], 5-methoxycarbonyl-5-methyl-1-pyrroline N-oxide (EMPO) are available [303]. Herein, we have used DMPO, see **Figure 3-11**, for the OH-trapping chemistry. The reaction of photocatalytic reaction via EPR has been studied extensively, including the most used photocatalyst TiO_2, with a variety of spin traps and solvents that include hole scavengers, obtaining the fundamental Hyperfine Coupling constants for the different resulting radicals [304]. The •OH-DMPO has a characteristic four peaks with intensity ratios of [1:2:2:1] [305], as shown in **Figure 3-12.**

A characteristic 7-line pattern with intensity ratio [1:2:1:2:1:2:1] is the characteristic of two •OH trapped/per/DMPO [306]. The so-formed molecule has the codename DMPOX [307]. The reaction pathway is shown in **Figure 3-12** [308]. The formation of DMPOX reveals that a high local concentration of •OH occurs during the photoexcitation, with each molecule creation requiring double the amount of radicals than the DMPO-OH [309].

In complex systems •OH-DMPO and DMPOX can coexist. Thus, computer simulation is required to analyze the EPR spectra. Herein we have used the EasySpin simulation package with Matlab [310], to simulate all the experimental EPR spectra.

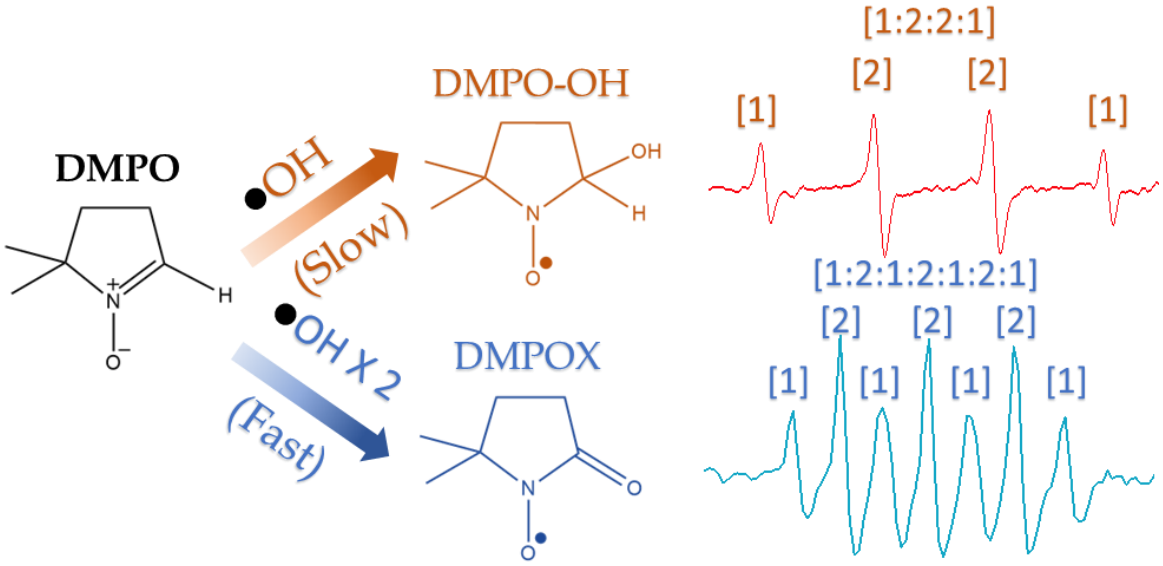

Figure 3-12: *Characteristics peaks of [1:2:1:2:1:2:1] DMPOX and [1:2:2:1] OH-DMPO.*

3.3.3 EPR Photo-induced Electron/Hole Pairs

Alkali tantalates, particularly $NaTaO_3$, are promising photocatalytic perovskites under UV excitation, with a major research focus on their photocatalytic abilities. Despite this fact, there is a lack of knowledge of key aspects of the photo-induced electron/hole pairs [93–96]. As the photo-induced Electron/Hole pairs have a very–short half-life, their detection can be achieved only by *in situ* EPR, under the illumination of the photocatalysts, at low-Temperature (77K).

EPR has already granted valuable knowledge for direct *in situ* detection of e^-/h^+ pairs in TiO_2 as the most widely used semiconductor for photocatalysis, providing an understanding of the relationship of the electrons and holes in the structure of the particles, works revolving around nano-TiO_2 with emphasis on P25-TiO_2 [311–313], and colloidal TiO_2[314,315]. Furthermore, detailed EPR study of e^-/h^+ pairs in Anatase/Rutile

TiO_2 [316], the drastic change in the EPR signal compared to the structure is exhibited in **Figure 3-13**, derived from [317]. Additional important works include Nakaoka et al., which has shown that hole-related EPR signals originate from $\{Ti^{4+}\text{-}O^{\cdot}\text{-}Ti^{4+}\text{-}O(H)\}$ units in TiO_2 [299]. Giamello's group work of photoactive species in N-doped TiO_2 [318] further refined our comprehension of carrier dynamics in TiO_2 semiconductors.

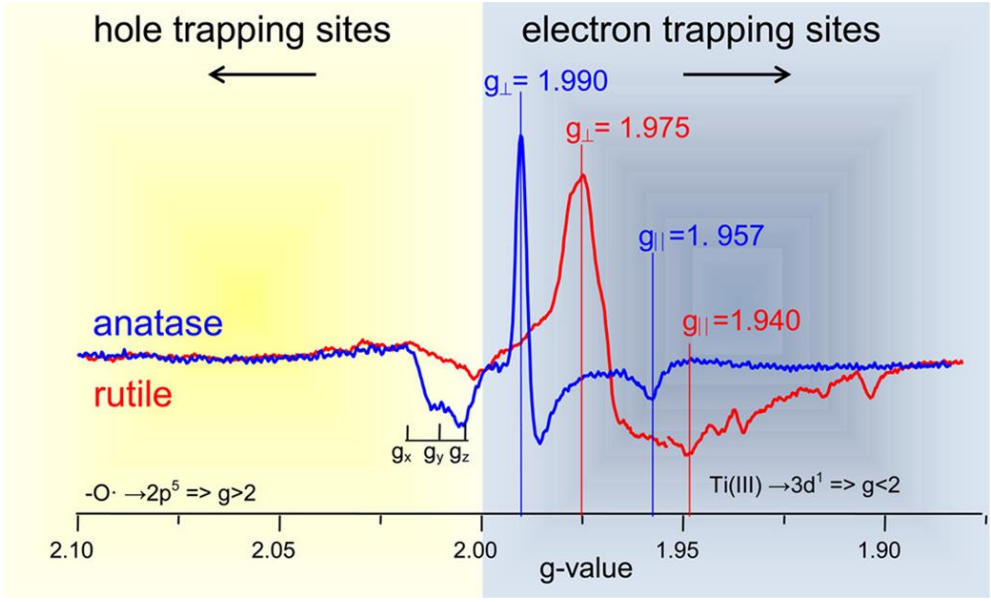

Figure 3-13: The EPR spectra of anatase and rutile nanoparticles obtained under illumination. The generated e^-/h^+ pair is observed as holes are trapped at the surface of nanoparticles as oxygen-centered radicals$^+$, while electrons are trapped at lattice sites as Ti^3, derived from [317].

Thus far, only a few EPR studies exist on photoactive $NaTaO_3$. However, none on photoinduced e^-/h^+ pairs.

These works include, Wang et al. that reported a single derivative EPR signal at g~2 detected in self-dopped $NaTaO_3$, attributed to reduced Ta^{4+} centers [319], although there isn't any mention compared to structure, kinetics, and relation to hydrogen production. Meyer et al. detected photo-induced EPR signals of surface-anchored oxygen species in reasonably small $NaTaO_3$ (25nm), but no direct detection of trapped photo-induced electrons was verified [320].

3.3.4 EPR Spectrometer

The measurements were conducted in an X-band Bruker ER200D spectrometer equipped with an Agilent 5310A frequency counter. Klystron-source was used as microwave radiation source in the 9-10 GHz range. A rectangular (102) metallic waveguide was used to carry the signal to the cavity that houses the sample, as shown in **Figure 3-14**. For all measurements, the EPR tubes of quartz-Willmad glass, were inserted in a quartz-Dewar filled with liqud-N_2.

An adequate signal-to-noise ratio was obtained after 10 to 50 scans with a standard modulation frequency = +50.00 kHz, microwave phase = +30.00 deg, and modulation amplitude = 10 Gauss peak-to-peak. Finally, the magnet spectrometer and the frequency were running under custom-made software based on LabView [321] that was developed in our group. The program also obtains and stores the data of the experiment.

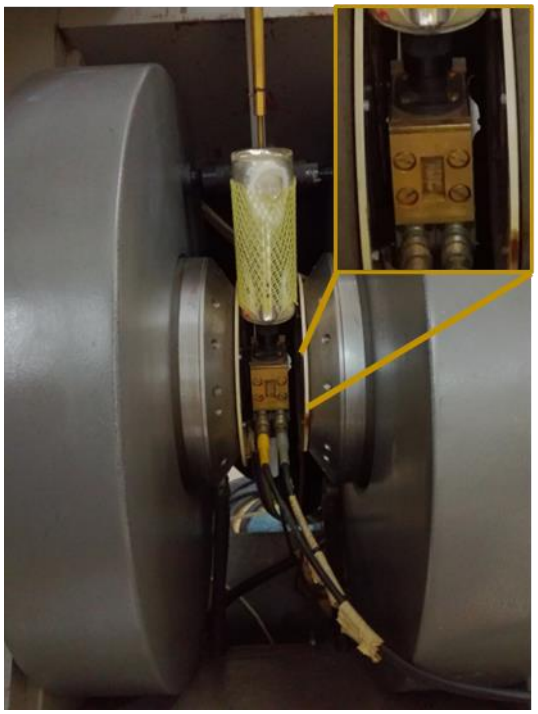

Figure 3-14: *The EPR spectrometer cavity and 77K-dewar rectangular window at the cavity center (marked by the arrows) were used to irradiate the in-situ photocatalysts.*

In situ Irradiation Set-up in EPR: Irradiation of the nanoparticle mixture was performed *in situ* in the EPR cavity through the appropriate window, **Figure 3-14**, using an Arc Xenon Lamp (model: Oriel 6293, 1000 W) operating at a power of 450W to 700W, as shown in **Figure 3-15.** The spectral profile of this light-source is shown in **Figure 3-15(B)**. It covers a wide range of visible and a small percentage of UV, thus this Arc-Xenon lamp can be considered a "sun-light simulator". To eliminate IR photons that cause heating effects -, a water filter was inserted before the focusing lens.

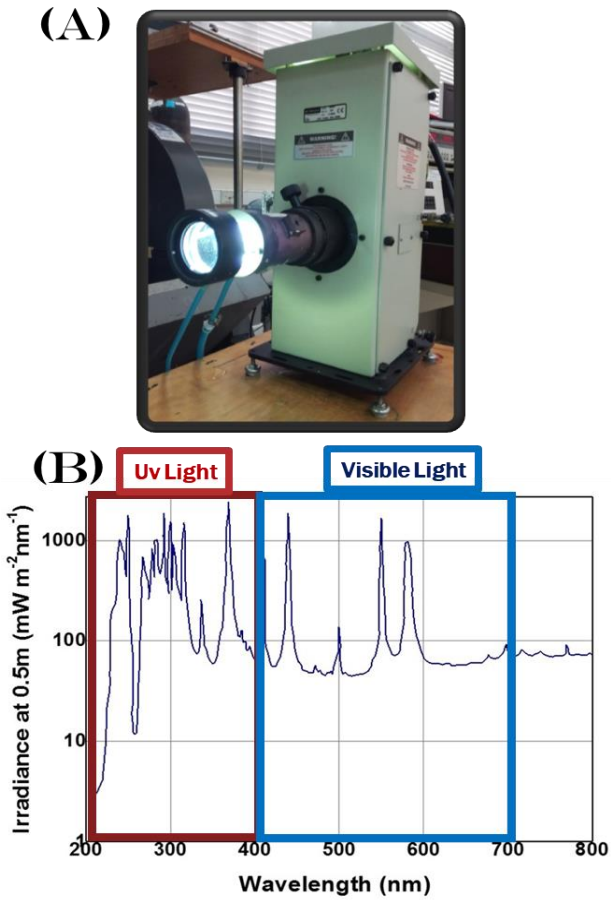

Figure 3-15: *(A) The arc xenon Lamp 1000W under operation, (B) The spectral-profile of radiation of the Xenon Lamp, with the UV and Visible range.*

3.3.5 Quantitative Monitoring of •OH Radicals and photoexcited e^-/h^+ by EPR

Quantitative analysis of OH-Radicals: Each reaction mixture was prepared using 1 mL of ultrapure Milli-Q water (Millipore). Nanomaterial masses used were in the range from 0.4 to 1 mg, dispersed utilizing a 20 W bath sonication. The spin trap DMPO (5,5-dimethylpyrroline-(2)-oxyl, Aldrich) was added at different concentrations depending on the experiment. From this stock suspension, 20 or 30 µL were inserted in two glass-capillaries (Vitrex) and illuminated *in-situ* in the EPR cavity comprising of a quartz tube (25cm x 5mm) diameter. The whole procedure is shown comprehensively in **Figure 3-16**. Irradiation was carried out at room temperature *in-situ* at the EPR cavity for periods from 30 seconds to 10 min.

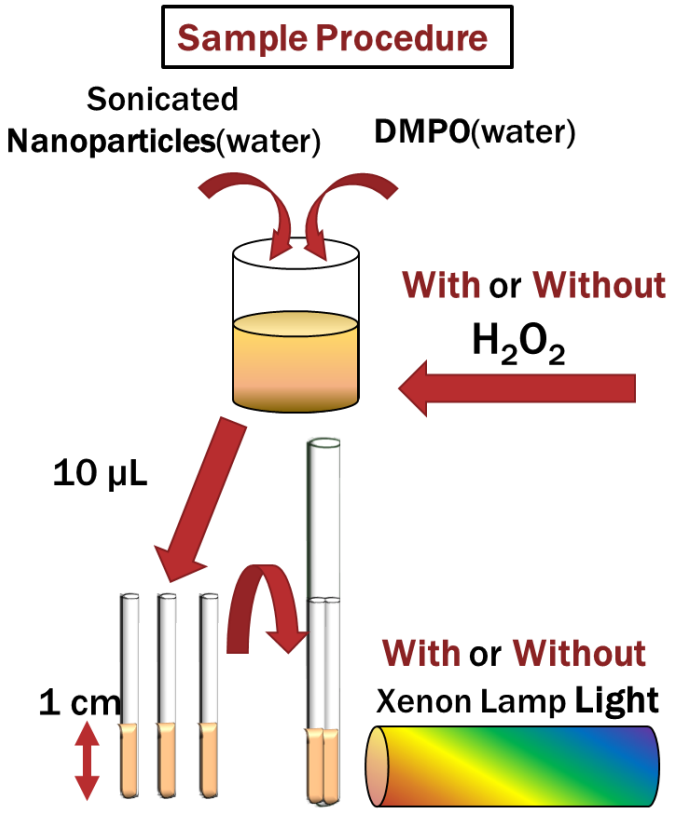

Figure 3-16: *Sample preparation procedure for OH monitoring at room temperature under Xenon Irradiation.*

Quantitative analysis for the •OH is accomplished with the spin standard DPPH (1,1-Diphenyl-2-Picrylhydrazyl, Alfa Aesar) [322]. The spin standard was measured each time with the same EPR conditions as those used to measure the unknown sample. A calibration curve was generated using the double integral of the EPR signals [323].

Photoinduced Electron/hole pair from $NaTaO_3$: The nanoparticles $NaTaO_3$ powder of 15mg is placed in a 5mm EPR tube and then frozen at 77K in the quartz-Dewar filled with liquid Nitrogen. EPR spectra were recorded as follows

[1] Dark-Spectra

[2] Spectra under Illumination

[3] To observe the photo-excited carrier stability and decay-kinetics, after step-2, then the tube is thawed for periods 1 to 5 seconds at RT and frozen instantly. Once the measurement is done, this process is repeated in various time intervals.

3.4 Characterization of Nanomaterials

3.4.1 Powder X-ray Diffraction

X-Ray Diffractograms were obtained using a D8 Advance Bruker diffractometer, as shown in **Figure 3-17**, with a Cu source (Kα, λ=1,5418 Å), with operation parameters 40 KV generator voltage and 40 mA current.

Using Braggs law [324], Equation 3-1, the spacing of each Miller-planes family was identified (λ stands for the wavelength of the incident X-ray beam, while n is an integer).

$$n\,\lambda = 2\,d\,Sin\Theta \qquad \text{Equation 3-3}$$

The crystal phases were analyzed *via* Rietveld analysis employing the Profex software [325], using the corresponding CIF files of the different crystal phases.

By using the diffraction pattern, from the intensities of the photons collected from the XRD, the mean size of the nanocrystals in the powder can be measured with the Scherrer method [326], Equation 3-4, from the peak broadening (FWHM). This method is valid for nanocrystals that in the range of 1 to 200nm.

$$d_{XRD} = \frac{K\,\lambda}{(FWHM) \times cos\Theta}$$ Equation 3-4

d_{XRD} is the mean size of the ordered domains inside the crystalline powder, K is a dimensionless shape factor that depends on the structure shape that is usually close to unity(in our case, it is 0.91), λ is the X-ray wavelength of the instrument with our instrument is set at 1,5418Å, and FWHM is the full-width at half-maximum of the XRD peaks, measured in radians.

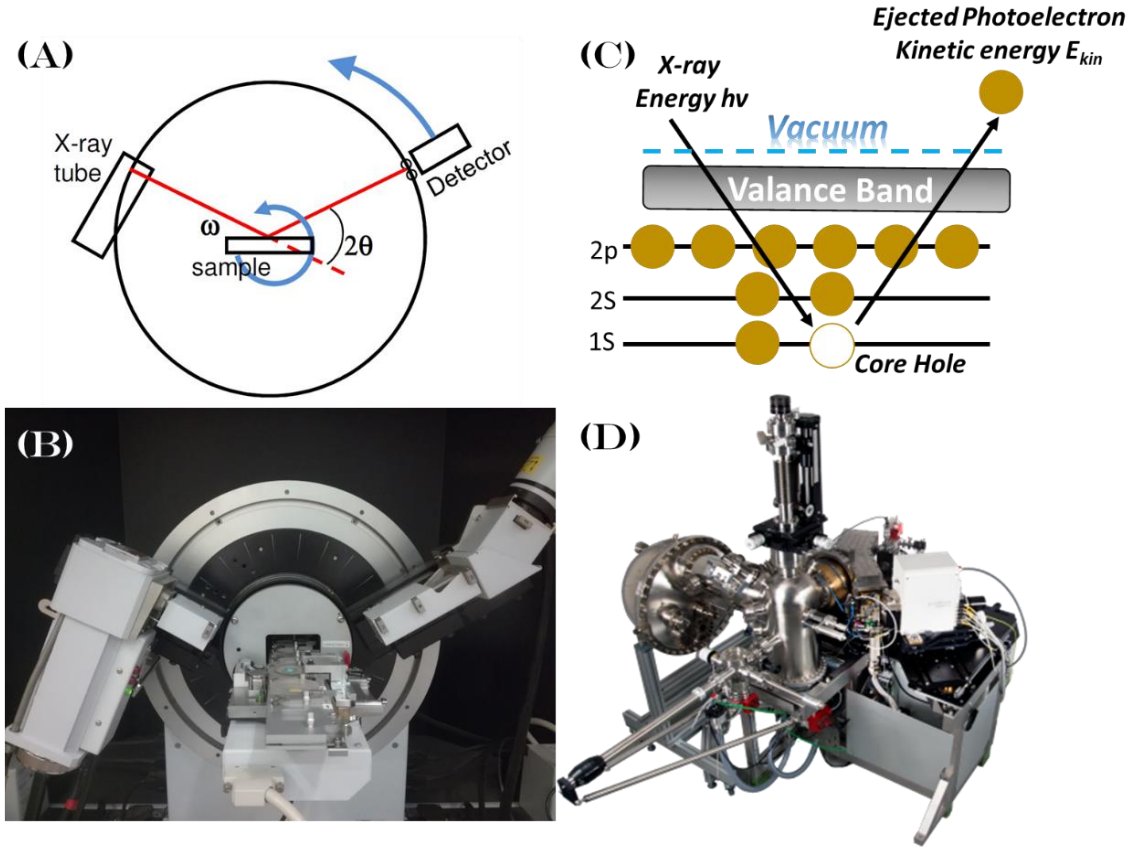

Figure 3-17: *(A) Schematic diagram of the XRD process. (B) Our D8 Advance Bruker diffractometer. (C) Outline of the XPS method. (D) The HSA-Phoibos 100 instrument was used for the particle XPS measurements.*

3.4.2 X-ray photoelectron spectroscopy (XPS)

XPS spectra were recorded using a SPECS spectrometer equipped with a twin Al-Mg anode X-ray source and a multi-channel hemispherical sector electron analyzer (HSA-Phoibos 100), as shown in **Figure 3-17**. The base pressure was 2-5 × 10−9 mbar. A monochromatized Mg Kα line at 1253.6 eV and analyzer pass energy of 20 eV were used in all XPS measurements. The binding energies were calculated concerning the energy of C1s carbon peak at 284.5 eV. The peak deconvolution was carried out using a Shirley background and peak deconvolution employing mixed Gaussian–Lorentzian functions in the least-squares curve-fitting program (WinSpec) developed at the Laboratoire Interdisciplinaire de Spectroscopie Electronique, University of Namur, Belgium.

3.4.3 Diffuse-Reflectance UV-Vis Spectroscopy

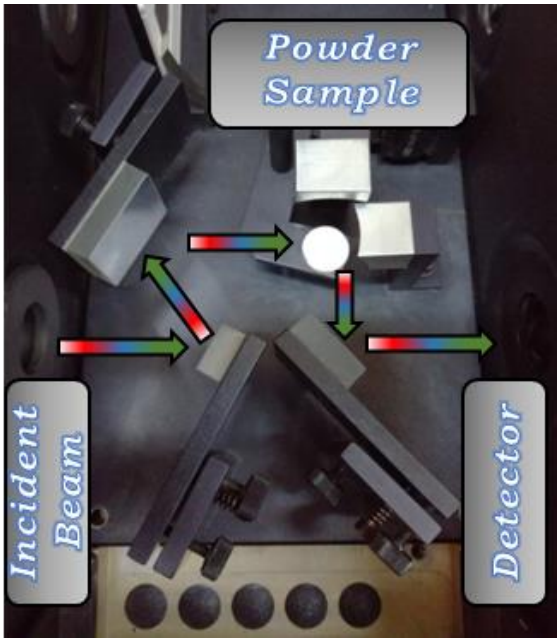

Figure 3-18: *The micro-DRS module (Perkin-Elmer Lambda) for powder analysis.*

Diffuse-Reflectance UV-Vis absorption spectra were recorded with a Perkin Elmer Lambda-35 spectrometer equipped with a micro-DRS module, as shown in **Figure 3-18**. A

white disk of $BaSO_4$ is used as the background standard, and the data were collected at room temperature for the wavelength range of 200–800 nm.

The Band-Gap energy (E_g) was calculated using the Kubelka–Munk method [327]. This is accomplished by plotting the first component of Equation 3-5 in the Y axis and the energy of the photon in the X axis.

$$\frac{\boldsymbol{a\,c\,h}}{\boldsymbol{\lambda}} = \boldsymbol{K}\left(\frac{\boldsymbol{c\,h}}{\boldsymbol{\lambda}} - \boldsymbol{E_{Bandgap}}\right)^{\boldsymbol{p}} \qquad \text{Equation 3-5}$$

The complete parameters of Equation 3-5 are as follows: α is signal intensity, K is a constant, c * h/λ=1240/λ is the photon energy in eV units (when λ is in nanometers), c is the speed of light, h the Planck constant, and λ the wavelength of light. $E_{Bandgap}$ is the band gap energy of the semiconductor particle. The parameter p in Equation 3-5 is the bandgap transition exponent and can have four different values [243], see section 1.5.2. In the example of the perovskites $BiFeO_3$ and $Bi_2Fe_4O_9$, the research community some present it as indirect allowed, while the majority has concluded that the transition is direct allowed [244].

Estimation of the Band-Gap (Eg) from the Tauc-Plot: The bandgap energy can be found from the tangent of the so called Tauc plot, see **Figure 3-19**. In an **ideal crystal** structure with sharp energy states i.e. **no broadening**, when the photon energy exceeds the E_g of the semiconductor, then the photon is absorbed. This results in the formation of an electron/hole pair. In typical UV-Vis DRS spectra, this will mean a zero absorption for all λ values right below the bandgap energy ($E(\lambda)<E_g$), and -ideally- maximum absorption at ($E(\lambda)>E_g$). In this ideal case- the absorption spectrum will have a step-function shape. In the Kubelka-Munk, the interception of the vertical-step line with the X-axis (the photon energy in Ev) would give the exact band gap, as shown in **Figure 3-19**(A).

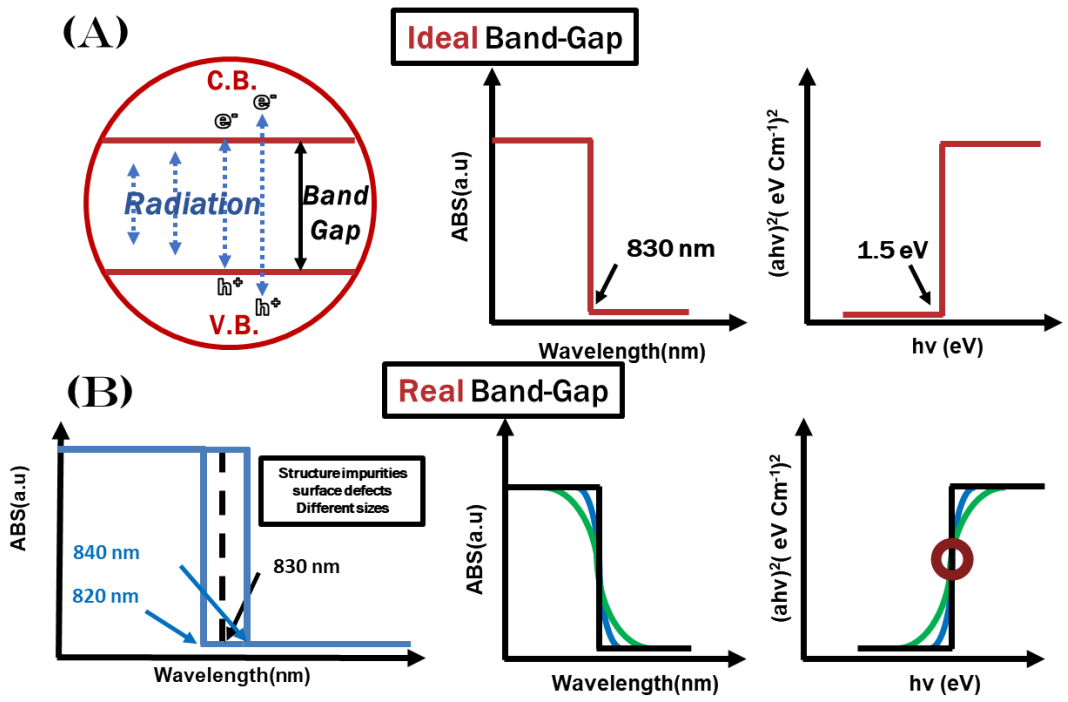

Figure 3-19: D*ifference in band gaps by impurities of the materials, A sift from the ideal straight line, including the contribution of different band gaps.*

In real systems, **broadenings** of the energy levels occur i.e., due to impurities, surface defects, and variance in size, all these factors result in a slight change in the band gap of each infinitesimal region. Combining all these slight energy-level changes from each region i.e. assuming to forts approximation of a Gaussian distribution, creates a "smother" structure of the energy-edges from, as shown in **Figure 3-19**(B). In this –realistic- case, αn approximation of an average value band gap i.e. within the Gaussian distribution can be estimated, by using the vertical tangent from the middle of the absorption in the Tauc-plot.

In liquid UV-Vis measurement, two radiation beam is set to pass through the reference sample (800nm to 200nm wavelength), as shown in **Figure 3-20**. The color of the liquid material is a simple indicator of the absorbed wavelengths. Based on the Beer-Lambert law [328], as shown in Equation 3-6, where ε is the absorptivity of the liquid material, $\boldsymbol{l}$ is the optical path length, and c is the concentration of the liquid material.

$$log\left(\frac{I_0}{I}\right) = \varepsilon\, l\, c$$ Equation 3-6

Shows that the concentration of the absorbing material in the solution is proportional to the number of photons that will be absorbed as the light passes a certain distance inside of it.

Herein, we reiterate the –well-known- principle of liquid UV-Vis spectrophotometry along with the DRS-UV-Vis to alleviate some misunderstandings i.e. the band-gap of semiconductor materials *vs.* the color of simple molecules. The **bandgap** represents a **limiting value** of a **multitude** of absorbances, while the single-molecule absorbable corresponds to an **exact absorbance** between the molecular-orbital levels of the absorbent molecule.

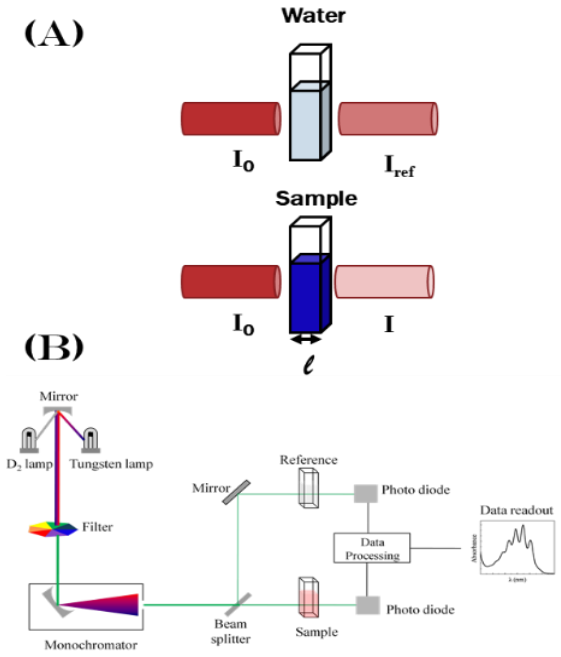

Figure 3-20: *UV-Vis spectroscopy in liquid samples, (A) quartz-glass cuvettes with water-solvent, and the sample under study provide the absorbance signal. (B) schematic of a double beam UV-Visible spectrophotometer, with one beam passing through the reference and the other beam the sample under examination.*

3.4.4 Fourier-Transform Infrared(FT-Ir) and Raman Spectroscopy

FT-IR spectra were recorded using an IR Nicolet IS5 spectrometer with the OMNIC software package, as shown in **Figure 3-21**(A). The materials were dispersed in KBr pellets, measured usually in the wavenumber range 400-4000 cm^{-1}.

Raman spectra were recorded with a HORIBA-Xplora Plus instrument coupled to an Olympus BX41 microscope equipped with a 785nm diode laser as an excitation source focused with the microscope, as shown in **Figure 3-21**(B). The powder samples were placed on a glass plate in softly pressed pellets. Screening experiments showed that a low laser intensity of 15mW was optimal, i.e., to avoid in situ crystal phase changes by the high laser intensity. The spectra were recorded for 30 to 180 seconds for total accumulations of 5 to 30 in order to obtain a sufficient signal-to-noise ratio.

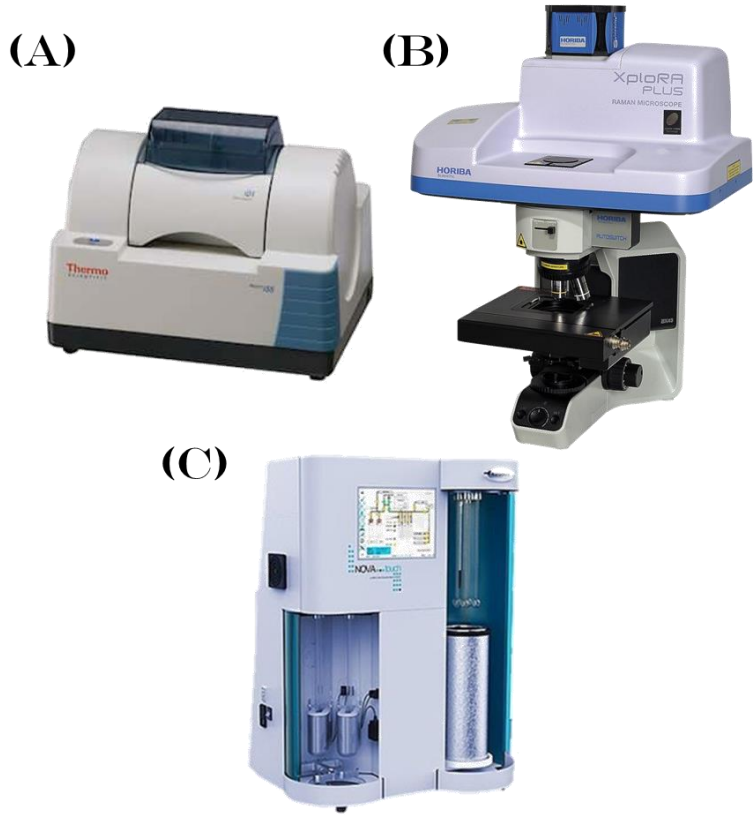

Figure 3-21: *(A) IR Nicolet IS5 spectrometer used for FT-Ir measurements, (B) HORIBA-Xplora Plus with an Olympus BX41 microscope used for Raman measurements, (C)* Quantachrome NOVAtouch LX^2 used for BET measurements.

3.4.5 N_2 adsorption-desorption Brunauer-Emmett-Teller (BET)

The N_2 adsorption-desorption isotherms were measured at 77 K on a Quantachrome NOVAtouch LX², as shown in **Figure 3-21**(C). The samples were outgassed at 150 °C for 16 hours under vacuum before the measurements. Specific surface area (SBET) was determined using adsorption data points in the relative pressure P/P_o range of 0.1–0.3. The BJH method was used for the pore radius using the absorption data points from 0.35-0.99 P/P_o, and the total pore volume was obtained at the 0.99 P/P_o point.

The SSA-equivalent diameter of the particles d_{BET} was calculated with Equation 3-7. Derived from the obtained SSA of each particle [329]. The second factor is p the density of the particles, according to the corresponding crystal structure.

$$\boldsymbol{d_{BET} = \frac{6000}{SSA \times \rho_{NaTaO_3/Ta_2O_5}}} \qquad \text{Equation 3-7}$$

For example, in this thesis for the resulting materials, the following values were used: ρ_{BiFeO3}= *8.4* g/cm³, $\rho_{Bi2Fe4O9}$= *6.48* g/cm³, ρ_{SrTiO3}= 4.81 g/cm³, ρ_{NaTaO3}= 7.129 g/cm³, and ρ_{Ta2O5}= 8.2 g/cm³.

4 Results

4.1 Combustion Enthalpy, Φ, HTRT

According to the phase diagrams in **Figure 1-11**, the reaction temperature i.e. available heat-energy, plays a key-role i.e. it is the determinant parameter for the perovskite phase formation. Notice that the phase-diagrams in **Figure 1-11** assume thermal **equilibrium** i.e. all reactants have enough time to acquire the average temperature of the reaction. In our case,

[1] In FSP, thermal energy is provided by the **combustion** process. Thus, the **combustible substances** (CH_4, solvent, precursors, in addition to O_2) are the sources of heat-energy that determine the phase-formation.

[2] The FSP process is fast i.e. **milliseconds**. Thus -in FSP- the process is largely **out of equilibrium**.

[3] In the FSP process, **the temperature profile is highly heterogeneous.** At the center of the flame, T may approach 2000-3000K however, it drops rapidly **outwards,** see for example, theoretical CFD calculations in **Figure 4-1** [284]. On an average FSP process, a large part of the flame and the reactor can be near 500-600^{0}C**.** Thus, we introduce the concept **of High-Temperature-Residence-Time (HTRT),** which signifies the time each particle spends at regions where T is above the average flame temperature.

In this context, the most important parameters for our FSP parameters are the total contribution of the Combustion Enthalpy Density, the Φ ratio, and the high-temperature residence time (HTRT).

4.1.1 Optimization of Combustion Enthalpy

As shown in **Table 4-1**, at least 50% of the total enthalpy was derived from the Solvent. For the synthesis of the ABO3 perovskites, we found that high-combustion enthalpy was required i.e. to promote interpenetration of A-lattice into B-lattice. For this reason, high enthalpy solvents are employed: Xylene and 2-Ethylhexanoic acid for $BiFeO_3$/$Bi_2Fe_4O_9$, reaching over -4500 kJ mol^{-1} of combustion enthalpy. In the event that

the FSP perovskite formation required a smaller amount of Combustion Enthalpy Density, the solvent was replaced in order for the resulting nanoparticles to have the minimum formation allowed size, i.e. for the Ta_2O_5 /$NaTaO_3$ particles, the solvent used was Ethanol with only -1368 kJ mol^{-1} and for the $SrTiO_3$ the solvent of choice was Acetic Acid.

Table 4-1: *The Combustion Enthalpy of combustibles (solvents and CH_4) used herein for the FSP synthesis of perovskites* [330].

COMBUSTIBLE	Combustion Enthalpy (kJ mol^{-1})
Methane (CH_4)	-891.20
Solvents	
Ethanol (C_2H_6O)	-1368.00
2-Ethylhexanoic acid ($C_8H_{16}O_2$)	-4797.9
Xylene (C_8H_{10})	-4553.00
Acetic Acid ($C_2H_4O_2$)	–876.1

Table 4-2 to **Table 4-7** lists the key parameters under the optimal FSP protocols used for our materials. Notice also that the optimal P/D ratios could vary greatly depending on the targeted material.

For Bi-Fe-O, the appropriate Combustion Enthalpy Density in comparison to the P/D ratio of 7/3, 5/5, and 3/7 is shown in **Table 4-2**, the total concentration of 0.2M of iron acetylacetonate and Bismuth acetate, as metal-precursors, e provides only a fraction of the total enthalpy. Thus, the precursor ratio of 0.1M Bi and 0.1M Fe for the formation of $BiFeO_3$ and the precursor ratio of 0.067M Bi and 0.133M Fe for the $Bi_2Fe_4O_9$ only slightly changed the Combustion Enthalpy Density. The overall Combustion Enthalpy Density for the larger P/D= 7/3 flames has approximately 17.9 kJ gr^{-1}, while the P/D= 3/7 provides much less total energy 13.6 kJ gr^{-1}.

Table 4-2: *The Combustion Enthalpy Density for the FSP synthesis of $BiFeO_3$ and $Bi_2Fe_4O_9$.*

Material	*Combustion Enthalpy Density* P/D=7/3	*Combustion Enthalpy Density* P/D=5/5	*Combustion Enthalpy Density* P/D=3/7
$BiFeO_3$	-17.85	-13.56	-9.60
$Bi_2Fe_4O_9$	-17.88	-13.58	-9.62

The synthesis for $SrTiO_3$, with use of titanium isopropoxide (TTIP) and Sr acetate as solvents, produced the combustion Enthalpy Density at different P/D ratios, as shown in **Table 4-3**. The precursor total concentrations of 0.4M, with 0.2M derived from TTIP and 0.2M from Sr acetate, in combination with xylene and Acetic Acid produced for the selected materials at P/D 5/5 only -11.49 kJ gr^{-1}, since the objective was the production of smaller particles, as the phase was pure regardless of the three P/D parameters.

For comparison, we refer that when reference/ordinary TiO_2 particles were produced in our FSP set up, the Combustion Enthalpy Density was much higher due to the application of pure xylene as the solvent. Thus, Acetic acid further decreases the overall temperature for smaller sized materials.

Table 4-3: *The Combustion Enthalpy Density for the FSP synthesis of $SrTiO_3$ and TiO_2.*

Material	*Combustion Enthalpy Density* P/D=7/3	*Combustion Enthalpy Density* P/D=5/5	*Combustion Enthalpy Density* P/D=3/7
$SrTiO_3$	-14.99	-11.49	-8.2
TiO_2	-19.3	-14.43	-9.9

The synthesis of Ta_2O_5 and $NaTaO_3$ was explored with the different precursors since Pratsinis et al. [132] achieved the synthesis of Ta_2O_5 with the precursor of Ta n-Butoxide. Ta n-Butoxide is much more expensive than our chosen precursor of $TaCl_5$ i.e. as will be demonstrated in a later chapter. Furthermore, the Combustion Enthalpy Density is highly increased which will produce much larger particles. **Table 4-4** shows that calculated

Combustion Enthalpy Density (**CED**), for $NaTaO_3$ different P/D reveal that for 0.6M total metal concentration. For example, we see that for P/D=7/3 with Ta n-Butoxide we had CED=18.14 kJ gr^{-1}, and for $TaCl_5$ CED=-16.03 kJ gr^{-1}. The inclusion of Sodium 2-ethylhexanoate for the production of $NaTaO_3$ increases only marginally the Combustion Enthalpy, as the P/D=5/5 has -11.38 for $NaTaO_3$ and -11.04 for Ta_2O_5, at lower enthalpy in the event of P/D=3/7, the enthalpy fails to produce the desired $NaTaO_3$ phase, as will later be shown.

Table 4-4: *The Combustion Enthalpy Density for the FSP synthesis of $NaTaO_3$ and Ta_2O_5 with the different Ta-precursors, i.e. $TaCl_5$ and Ta n-Butoxide.*

Material	*Combustion Enthalpy Density* P/D=7/3	*Combustion Enthalpy Density* P/D=5/5	*Combustion Enthalpy Density* P/D=3/7
$NaTaO_3$ ($TaCl_5$)	-16.03	-11.38	-7.34
$NaTaO_3$ (Ta n-Butoxide)	-18.14	-12.78	-8.13
Ta_2O_5 ($TaCl_5$)	-15.62	-11.04	-7.11
Ta_2O_5 (Ta n-Butoxide)	-17.78	-12.46	-7.91

4.1.2 Optimization of combustion Stoichiometry Ratio(Φ)

It is important to note that while the overall temperature produced is higher, the ultimate result is the formation of the oxide perovskite particles. Thus, the overall Φ ratio should be Φ<1, to prevent the formation of defects in the structure. In the case of $BiFeO_3$ and $Bi_2Fe_4O_9$, the P/D comparison to the Φ Ratio is shown in **Table 4-5**. The P/D = 7/3 has a value of approximately Φ=1.55 corresponding to a fuel-rich flame, inhibiting the formation of the oxide perovskite due to the lack of available oxygen at the HTRT zone. In comparison, the preferred FSP synthesis employed in our work with P/D=3/7 has Φ=0.54, appropriate for oxide formations.

The Φ ratio for the $SrTiO_3$ /TiO_2 materials is shown in **Table 4-6**. Xylene produces a highly fuel-rich synthesis condition, with $SrTiO_3$ synthesis at P/D =5/5 produces a Φ= 1.04, which is quasi-stoichiometric, i.e. just enough for the appropriate production of oxide perovskites. While under the conditions for the TiO_2 synthesis at P/D =5/5 produces a Φ= 1.12, that will result in non-combustible carbon without implementation of secondary oxygen sources i.e. open flame, oxygen sheath gas.

For the Φ ratio of Ta_2O_5/$NaTaO_3$ with the precursor $TaCl_5$ shown in **Table 4-7,** at every P/D ratio, the overall process is Oxygen-rich, resulting in highly crystalline $NaTaO_3$ particles unrelatedly of P/D ratio for high precursor concentrations, regardless of the prevention of atmospheric air from an enclosing tube.

Table 4-5: *Φ Ratio for different Precursor and Dispersion Flow rates for the FSP synthesis of $BiFeO_3$ and $Bi_2Fe_4O_9$.*

Material	*Φ Ratio* P/D=7/3	*Φ Ratio* P/D=5/5	*Φ Ratio* P/D =3/7
$BiFeO_3$	1.55	0.92	0.52
$Bi_2Fe_4O_9$	1.64	0.97	0.54

Table 4-6: *Φ Ratio for different Precursor and Dispersion Flow rates for the FSP synthesis of $SrTiO_3$ and TiO_2.*

Material	*Φ Ratio* P/D=7/3	*Φ Ratio* P/D=5/5	*Φ Ratio* P/D=3/7
$SrTiO_3$	1.77	1.04	0.58
TiO_2	2.02	1.12	0.67

Table 4-7: *Φ Ratio for different Precursor and Dispersion Flow rates for the FSP synthesis of $NaTaO_3$ and Ta_2O_5.*

Material	*Φ Ratio* P/D=7/3	*Φ Ratio* P/D=5/5	*Φ Ratio* P/D=3/7
(0.6M) $NaTaO_3$	0.95	0.51	0.26
(0.1M) $NaTaO_3$	0.91	0.48	0.25
(0.3M) Ta_2O_5	0.50	0.27	0.14
(0.05M) Ta_2O_5	0.49	0.26	0.13

4.1.3 Optimization of High-Temperature Residence Time(HTRT)

The HTRT: In order for the perovskite phases to form, an appropriate time to alter from atoms/simple oxides to the perovskite phase is required. For this reason, the HTRT in many experiments was enhanced with the application of enclosing-tubes that enclose the flames and stabilize the internal temperature. From Computational-Fluid-Dynamics (CFD-ANSYS) analysis conducted for our FSP set-up, with a metal tube of 40cm, the temperature gradient is shown in **Figure 4-1**, without the precursor flowing (Left) and a precursor flow rate of 5 ml min^{-1} (Right).

As observed, the temperature gradient is kept quasi-constant in presence of the enclosing tube, while in the event of an open flame FSP set-up, the temperature would decrease sharply. Thus, the enclosing tube is mandatory for ensuring HTRT control. This configuration allows the formation of the more challenging perovskite structures i.e. such as $NaTaO_3$, permitting enough time in high-temperature conditions to crystalize, while in the open flame-FSP, the result was always the oxide Ta_2O_5.

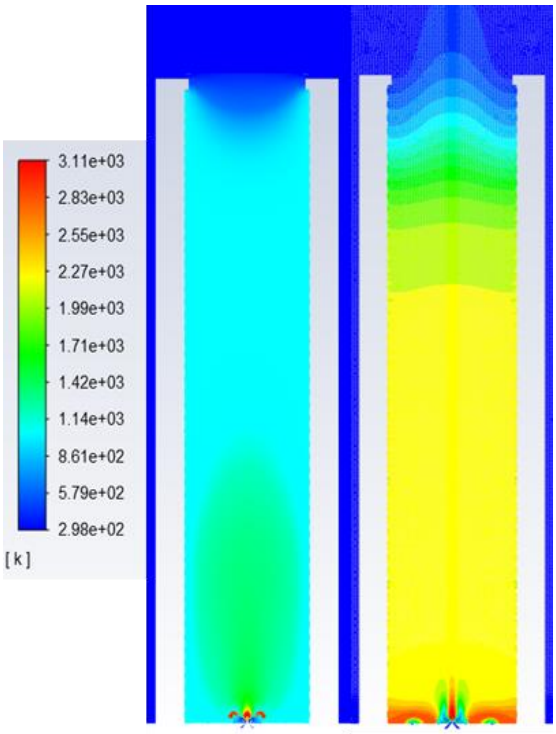

Figure 4-1: Theoretical Computational-Fluid-Dynamics (CFD) calculated with ASNYS for the temperature profile of our FSP Set-up, (left) without solvent, (Right) Precursor flow rate of 5 ml min^{-1} [331].

4.2 Synthesis process for $CuBi_2O_4$ – $CuFe_2O_4$ – $LiTaO_3$

In addition to the key-aimed $BiFeO_3$, $SrTiO_3$, and $NaTaO_3$ nanocatalysts, we have explored the FSP process for the synthesis of $CuBi_2O_4$, $CuFe_2O_4$, and $LiTaO_3$. To our knowledge, so-far, none of these materials has been successfully synthesized with the SP technology, indicating that the synthesis by itself is highly complex and noteworthy for academic purposes. For this reason, the FSP methodology is briefly introduced for the three materials.

4.2.1 FSP Synthesis of $CuBi_2O_4$

The first FSP synthesis was for the development of the visible semiconductor $CuBi_2O_4$ spinel-type structure. The most important parameter for a successful FSP synthesis is the uniform precursor solution containing the two powders of the selected elements, in this case, the elements Copper and Bismuth. The Bismuth acetate was used for all the

experiments, since all bismuth powders have a low solubility limit, the solvent was 2-ethyl hexanoic acid which sufficiently disperses the Bismuth acetate. With 2-ethyl hexanoic acid as the solvent, the Copper powders selected were Copper Naphthenate and Copper acetylacetonate. In each case, the final solution was well dispersed and homogenous.

The most prevalent XRD peaks of the tetragonal $CuBi_2O_4$ phase showed at 2θ = 20.84, 27.00, 29.68, 30.76, 37.42, 46.68, attributed to the Miller planes the (200), (211), (220), (002), (202), (411). The results for the different copper precursors under typical FSP conditions i.e. P/D = 5/5, pilot flame 2/1 (O_2/CH_4), shown in **Figure 4-2**, the appropriate $CuBi_2O_4$ XRD peaks shown in the bottom of the XRD Graph. The results don't possess the characteristic XRD peaks of the $CuBi_2O_4$, with the resulting peaks being assigned to Bismuth and copper oxides. As an easy visual indicator, the peaks at 29.68 and 30.76 clearly define the $CuBi_2O_4$ phase in comparison to the Bismuth and Copper oxides. The material conducted with Copper Naphthenate clearly exhibited higher crystallinity. For this reason, the subsequent experiments will be done with Copper Naphthenate.

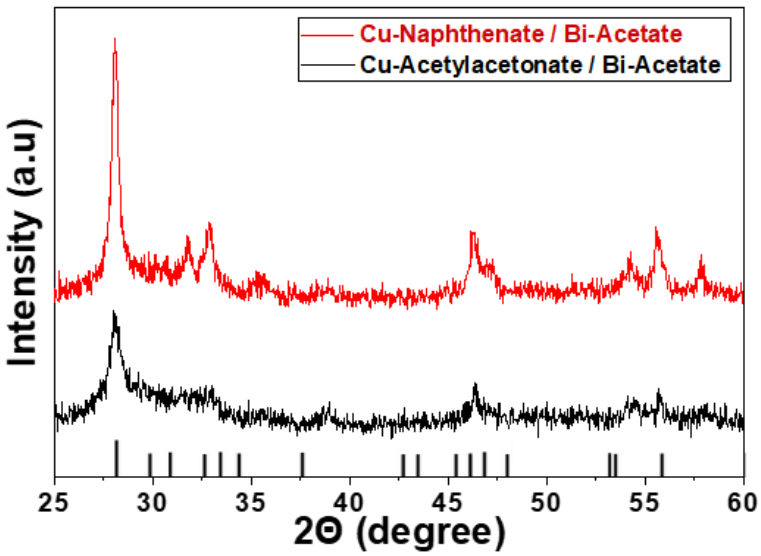

Figure 4-2: XRD graph for $CuBi_2O_4$ FSP synthesis: experiments based on the powder precursors Copper Naphthenate, Copper Acetylacetonate, and Bismuth Acetate. Graph bottom: The characteristic peaks of tetragonal $CuBi_2O_4$

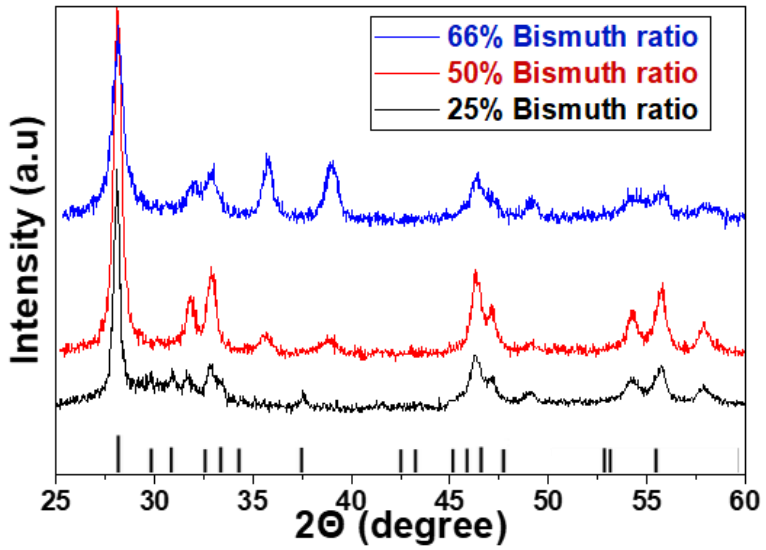

Figure 4-3: *XRD graph for $CuBi_2O_4$ FSP synthesis: experiments based on the Bismuth to Iron ratio of the precursors, with a total Bismuth ratio of 25%, 50%, and 66%.*

The results in **Figure 4-2** were conducted under a precursor ratio of Bismuth and Iron at 50% and 50%. In **Figure 4-3**, the FSP synthesis was conducted under different Bismuth precursor ratios of 25%, 50%, and 66%, since the appropriate ratio for the $CuBi_2O_4$ should be 66%. Additionally, the pilot flame was changed to 4/2 (O_2/CH_4), the increased methane flow rate, increases the overall enthalpy and temperature of the flame. Due to the higher enthalpy, the material has higher crystallinity, although the phase remains that of Bismuth and Copper oxides.

Finally, the FSP parameters of the Precursor flow rate(P) and the Dispersion flow rate(D) were explored. Under the Bismuth ratio of 50% and 66%, the P/D of 7/3 and 5/7 were employed in producing the materials shown in **Figure 4-4**. Since the materials 7/3 produced lower crystallinity particles, the P/D of 5/7 was altered to contain a higher concentration of Methane, thus the overall Dispersion of 7 L min^{-1} was split to 4 L min^{-1} of oxygen and 3 L min^{-1} of Methane. It is important to note that higher methane concentration immediately takes out the flame, ending the combustion. For the material 66% Bi, P/D 5/7 (with methane at 3 L min^{-1}), a percentage of $CuBi_2O_4$ phase was finally detected.

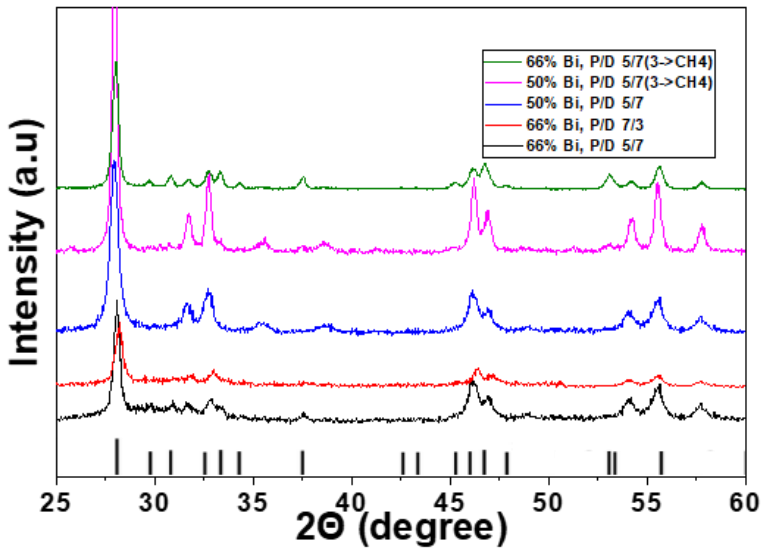

Figure 4-4: *XRD graph for $CuBi_2O_4$ FSP synthesis: experiments based on P/D of 7/3, 5/7, and 5/7 were the 7 Dispersion Flow Rate consists of 4 L min^{-1} of oxygen and 3 L min^{-1} of Methane.*

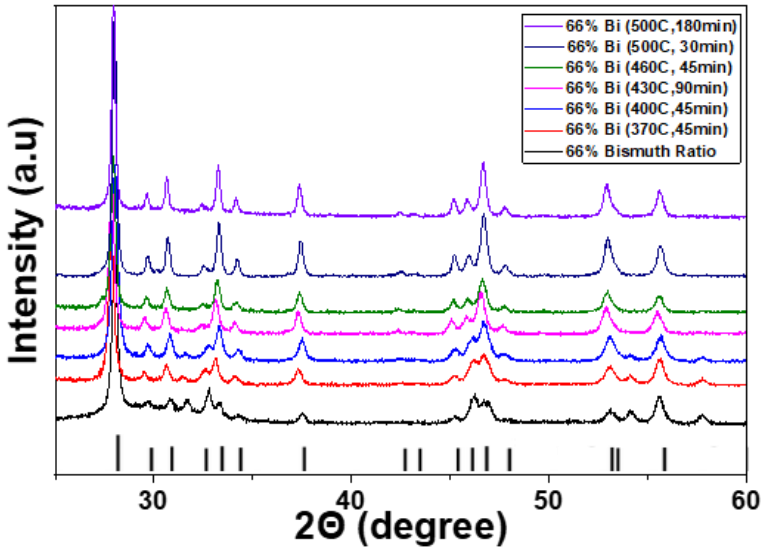

Figure 4-5: *XRD graph for $CuBi_2O_4$ FSP synthesis: post-FSP calcination at temperatures ranging from 370 ^0C to 500 ^0C, and calcination time from 30 min to 180 min.*

Since the advanced method of adding methane in the Dispersion produced -partially- $CuBi_2O_4$, but the pure phase remains elusive, a post-FSP calcination treatment was

conducted. As shown in **Figure 4-5**, the pure phase of $CuBi_2O_4$ can be produced with minimal temperature and calcination time of 370^0C and 45 min. The calcination requirements are much less than indicated by the phase diagram, this finding will be later observed again for the formation of $BiFeO_3$, this is attributed to the FSP materials having a range in the nanometers, in comparison to the Bulk materials used for the phase diagram development.

Overall, the partial synthesis of $CuBi_2O_4$ was achieved for the first time with the FSP technology, while with very minimal calcination conditions, the pure phase of $CuBi_2O_4$ is obtained.

4.2.2 FSP Synthesis of $CuFe_2O_4$

The same methodology with the $CuBi_2O_4$ was conducted for the FSP synthesis of the $CuFe_2O_4$ crystal phase. The most prevalent XRD peaks of the $CuFe_2O_4$ phase showed at 2θ = 30.4, 33.2, 35.8, 43.6, 54, 57.6, 63.2, attributed to the Miller planes the (200), (103), (211), (220), (312), (321), (400). The selection of the appropriate powder for the Iron and Copper was conducted, accordingly to a solvent that will allow homogenous dispersion. The selected precursors for Iron were Iron Acetylacetonate and Iron Naphthenate, neither of which can be dispersed with 2-ethyl hexanoic acid. Xylene was selected as the solvent that has a high enthalpy required for the formation of $CuFe_2O_4$, although for the Copper precursor only Copper Naphthenate is able to disperse in xylene.

The resulting particles under typical FSP conditions i.e. P/D = 5/5, pilot flame 2/1 (O_2/CH_4), are shown in **Figure 4-6** with the appropriate $CuFe_2O_4$ XRD peaks shown in the bottom of the XRD Graph. The results don't possess the characteristic XRD peaks of the $CuFe_2O_4$, with the resulting peaks being assigned mainly to Iron oxides, with some small intensity peaks belonging to copper oxides. This time, the visual indicator for the $CuFe_2O_4$ phase is the peak at 33.2 since almost every other high-intensity peaks are the same as the Iron oxides. The FSP material containing Iron acetylacetonate produced higher crystallinity, but due to the lower solubility limit, the subsequent experiments will be performed with Iron Naphthenate.

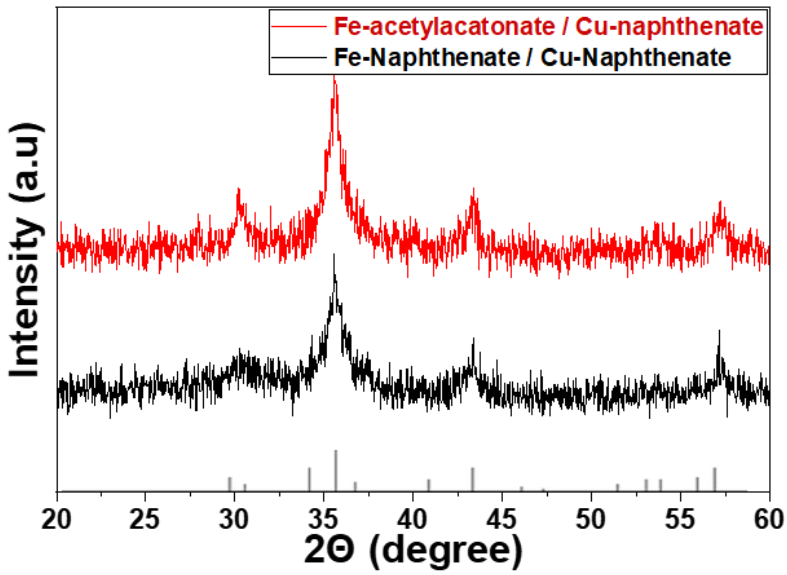

Figure 4-6: *XRD graph for $CuFe_2O_4$ FSP synthesis: experiments based on the powder precursors Fe Naphthenate, Fe Acetylacetonate, and Cu Naphthenate.*

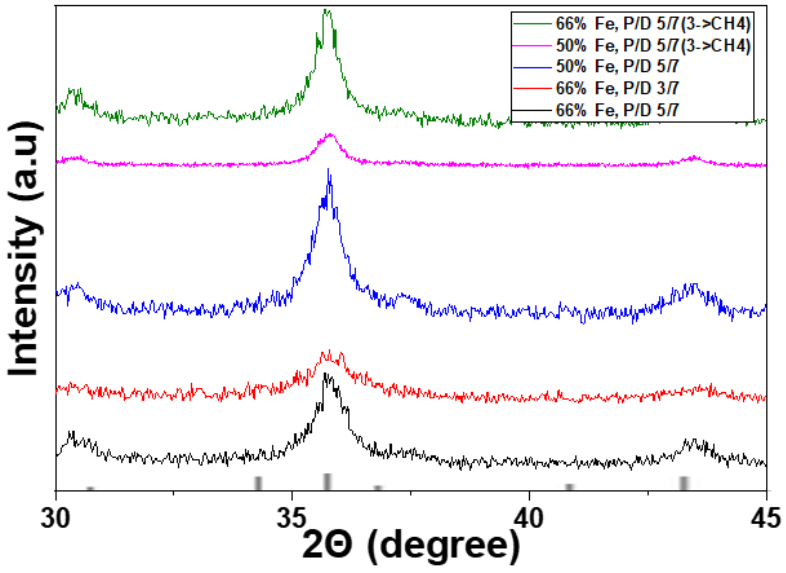

Figure 4-7: *XRD graph for $CuFe_2O_4$ FSP synthesis: experiments based on P/D of 3/7, 5/7, and 5/7 were the 7 Dispersion Flow Rate consists of 4 L min^{-1} of oxygen and 3 L min^{-1} of Methane.*

As for the FSP parameters of the Precursor flow rate(P) and the Dispersion flow rate(D) for the formation of $CuFe_2O_4$. Under the Iron ratio of 50% and 66%, with a change from the previous $CuBi_2O_4$ methodology, the P/D was 5/7 and 3/7 due to the properties of FSP Iron synthesis observed in our laboratory, the materials are shown in **Figure 4-7**. Unfortunately, the P/D of 3/7 still produced lower crystallinity particles. As before, the P/D of 5/7 was altered to contain a higher concentration of Methane, with a combination of 4 L min^{-1} Oxygen and 3 L min^{-1} of Methane. The additional enthalpy from the Methane failed to produce the desired phase of $CuFe_2O_4$.

As the phase $CuFe_2O_4$ wasn't able to be produced with the FSP synthesis, a highly detailed post-FSP calcination treatment was conducted with temperatures ranging from 460 ^{0}C to 900 ^{0}C and calcination times of 30 to 180 minutes, as shown in **Figure 4-8**. With the calcination treatment, a phase transition was detected, unfortunately, the phase of $CuFe_2O_4$ wasn't detected in any of the aforementioned calcination conditions.

Overall, the experiments didn't have much success, requiring more advanced FSP methodology and altering of the fundamental parameters.

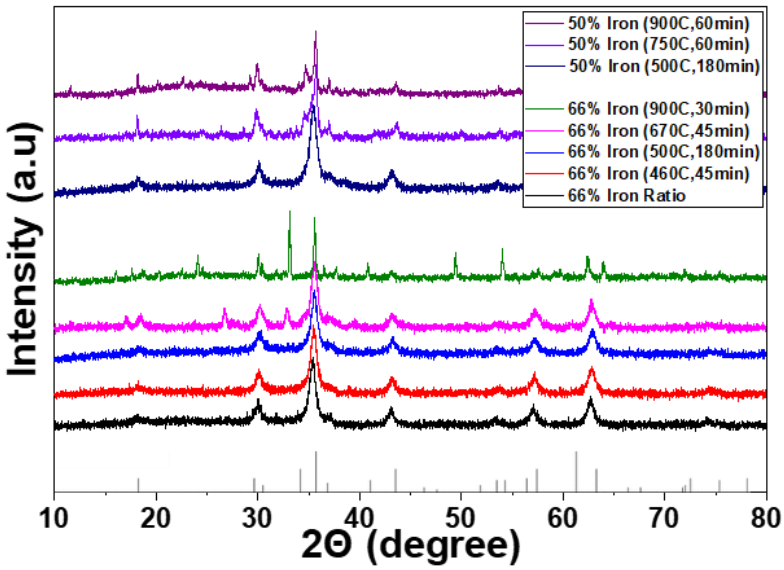

Figure 4-8: *XRD graph for $CuFe_2O_4$ FSP synthesis: post-FSP calcination at temperatures ranging from 460 ^{0}C to 900 ^{0}C, and calcination time from 30 min to 180 min.*

4.2.3 FSP Synthesis of $LiTaO_3$

The selection of the appropriate selectivity for the powder for the Lithium and Tantalum was conducted. The selected precursors for Tantalum were $TaCl_5$ and Ta N-Butoxide. The experiments in the later chapter for the FSP synthesis of Ta_2O_5 and $NaTaO_3$ showed that $TaCl_5$ is an effective precursor for Ta-based nanoparticles and much more cost-efficient. For this reason, the first attempts for $LiTaO_3$ FSP synthesis were based on $TaCl_5$. As for Lithium, the selected precursors were powder Li Butoxide and Li Nitrate. In these experiments, the selected solvent was Ethanol, which enables a homogenous mixture and is efficient for the later nanoparticle formation of Ta_2O_5 and $NaTaO_3$.

The most prevalent XRD peaks of the perovskite $LiTaO_3$ rhombohedral phase showed at 2θ = 23.7, 32.7, 34.8, 42.5, 48.6, 53.4, attributed to the Miller planes of (012), (104), (110), (202), (024), (116). The results for the different Lithium precursors under typical FSP conditions i.e. P/D = 5/5, pilot flame 2/1 (O_2/CH_4), are shown in **Figure 4-9**. The results are clearly the XRD peak pattern of Ta_2O_5, without any XRD signs of Lithium, under calcination conditions of 600 ^{0}C for 1 hour, which is sufficient according to the phase diagram [101], while the crystal phase altered from Ta_2O_5 proving that Lithium was incorporated in the structure, the phase wasn't the desired perovskite $LiTaO_3$.

It is of fundamental importance to note that the resulting material in the event of Butoxide had a green color compared to the appropriate white color for $LiTaO_3$. Even more detrimental, the particles from the Lithium Nitrate had a black color and partial fusion with the silicon filter, making the extraction much harder. These findings are attributed to the inefficient combustion of carbon content. In this Ph.D. research, the results of the effect of carbon content were only evident in the formation of $LiTaO_3$, while every other material based on Fe-Bi-Ta-Ti particles had a complete combustion as expected from the Φ ratio. Resulting in the FSP synthesis of $LiTaO_3$ being one of the most complex in this work.

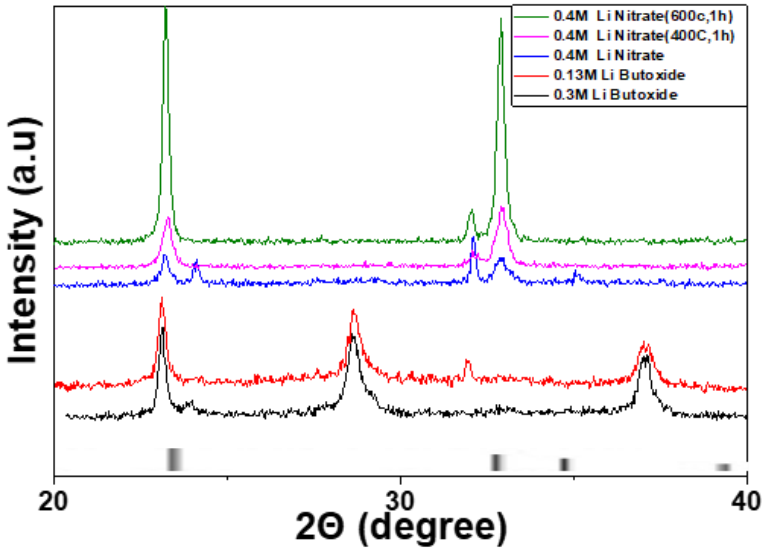

Figure 4-9: *XRD graph for $LiTaO_3$ FSP synthesis: experiments based on Lithium Butoxide, Lithium Nitrate powder precursors. Phase change compared to concentration and Calcination parameters.*

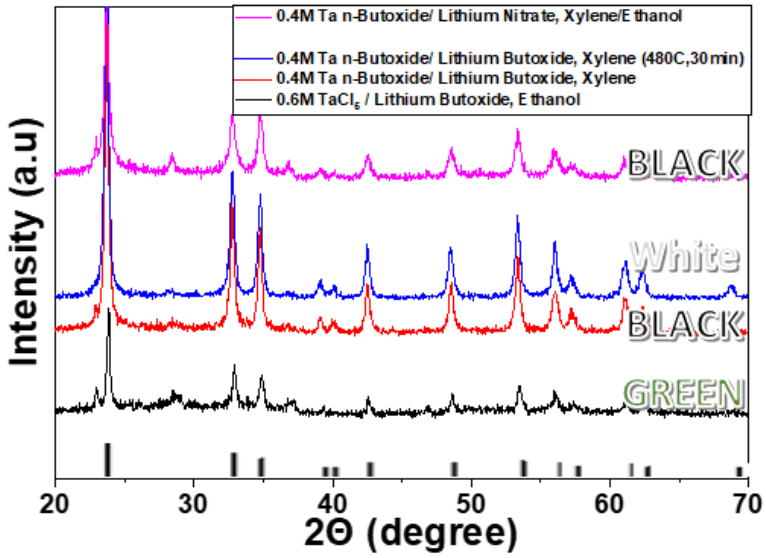

Figure 4-10: *XRD graph for $LiTaO_3$ FSP synthesis: experiments based on the precursor's Lithium Butoxide solution, Tantalum Chloride, and Tantalum N-Butoxide. Phase change compared Calcination parameters.*

As the Lithium Nitrate produced problems in the combustion, we focused on the Lithium Butoxide, where the powder of Lithium Butoxide was first turned into a solution with mineral spirits. The effect on the Lithium precursor change based on $TaCl_5$ and Ta n-Butoxide is shown in **Figure 4-10**. The resulting materials based on $TaCl_5$ still produced a green color, although the perovskite phase $LiTaO_3$ was produced, along with other secondary phases. The formation according to Ta n-Butoxide, with the solvent changed to Xylene for increased combustion enthalpy, for an additional Lithium Nitrate experiment, the solvent consisting of partial Xylene/Ethanol (8:1). In each experiment, the Ta n-Butoxide produced a higher crystallinity and higher phase purity in comparison to $TaCl_5$. Moreover, every particle had incomplete combustion, resulting in a Black or Green color. Short calcination of 480^0C and 30 minutes efficiently removed the carbon content, resulting in the white color of $LiTaO_3$.

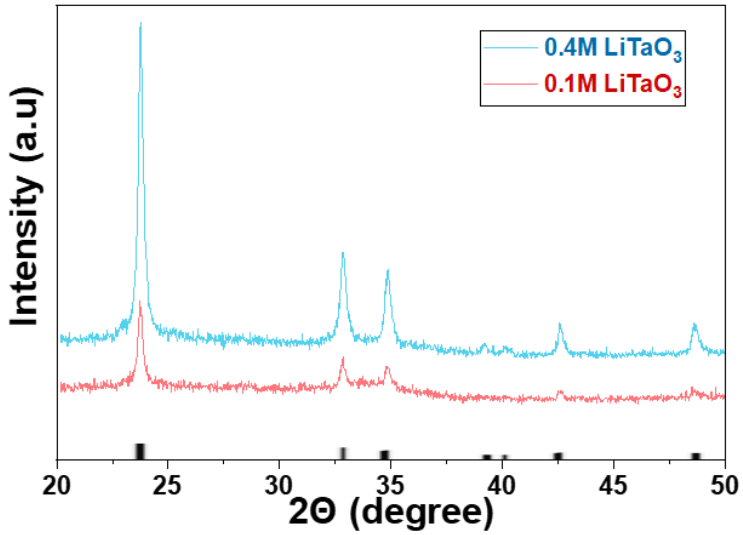

Figure 4-11: *XRD graph for $LiTaO_3$ FSP synthesis: selected pure phase $LiTaO_3$ with different FSP precursor concentrations of 0.1M and 0.4M.*

By changing several FSP parameters altering the combustion enthalpy and the High-Temperature Residence Time, the materials produced had a 100% pure phase $LiTaO_3$, without the previous carbon content **Figure 4-11**. The resulting materials produced had

sizes between 39 and 30 nm d_{XRD}. Preliminary experiments for photocatalytic production of Hydrogen, compared to Ta_2O_5 and $NaTaO_3$, are shown in **Figure 4-12**. Detailed photocatalysis of Ta_2O_5 and $NaTaO_3$ will be shown in later chapters. The overall trend is that $LiTaO_3$ has reduced photocatalytic efficiency, this is in correlation with other studies since it has a much larger band bap of 4.7eV in comparison to 4.1eV for Ta_2O_5 and $NaTaO_3$, although the Conduction band is much higher from the other structures enabling it to achieve more challenging catalytic processes such as photocatalytic reduction of CO_2.

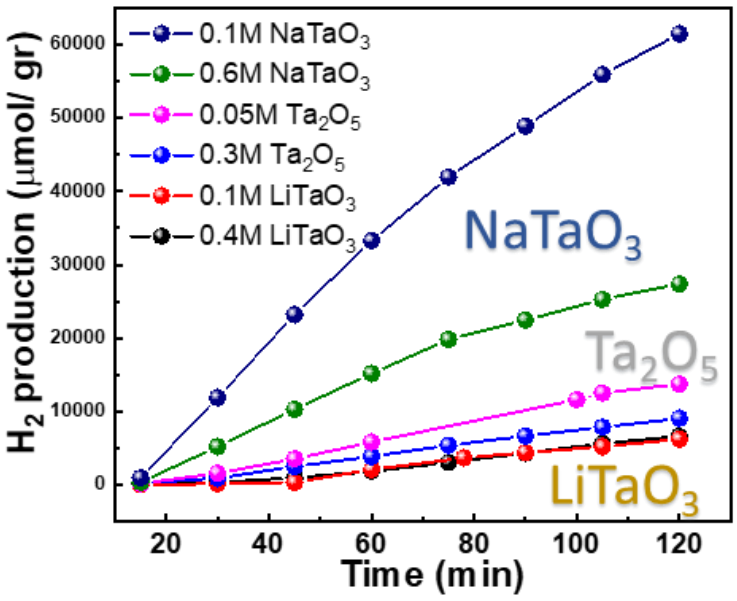

Figure 4-12: *Photocatalytic comparison for Hydrogen production, comparison of the phases Ta_2O_5, $NaTaO_3$, and $LiTaO_3$. Comparison of FSP precursor concentration, changing particle size.*

Overall, the synthesis of 100% pure $LiTaO_3$ was achieved for the first time with the FSP technology, with sizes in the range of 60nm to 30nm, and photocatalytic production of hydrogen was verified.

4.3 $BiFeO_3/Bi_2Fe_4O_9$ particles for 4-Nitrophenol Reduction

4.3.1 aims for $BiFeO_3/Bi_2Fe_4O_9$ as catalyst for pollutants

4-nitrophenol and its derivatives are broadly applied in the manufacturing processes of drying agents and anti-corrosion lubricants, also being essential for pharmaceutical industries in the production of analgesic, antipyretic, and other drugs [332], also resulting from by-products produced from pesticides, herbicides, and synthetic dyes [333]. The molecule 4-Nitrophenol has been well studied to inflict damage to numerous organs, such as the liver and kidneys, and the central nervous system. Thus, the removal from the substantial by-products of industrial production should be processed and environmentally removed [334].

The 4-Nitrophenol reduction has been exemplified as a model to discover if the materials are appropriate for catalytic reactions. This reaction has been thoroughly studied by various research laboratories. The reduction reaction involves a transfer of six electrons from the sodium borohydride that acts as a reductant. The process is under ambient conditions (20 degrees Celsius and atmospheric pressure), with the only product consisting of only 4-aminophenol without any side product [332]. The process removes environmentally hazardous nitrophenol, while the yielded aniline products are industrially applicable for polymers and pharmaceuticals, and it is also the final intermediate for the industrial synthesis of paracetamol [335].

The majority of works show that efficient catalytic reduction for 4-Nitrophen to 4-Aminophenol by $NaBH_4$ can be achieved only by the catalytic assistance of noble metal nanocatalysts, with the majority belonging to Gold(Au), followed by Palladium(Pd) and Platinum(Pt) [336] [337], various compositions of bimetals [338], and reports of nano-oxides supported on graphitic matrix [339]. For metal catalysts, the activation energies that are an indicator of the catalytic activity have a range of 30-50 kJ mol^{-1} [340] [341]. As for non-noble metal materials, there are scarcely shown in scientific literature as valuable and efficient catalysts for the 4-Nitrophenol reduction.

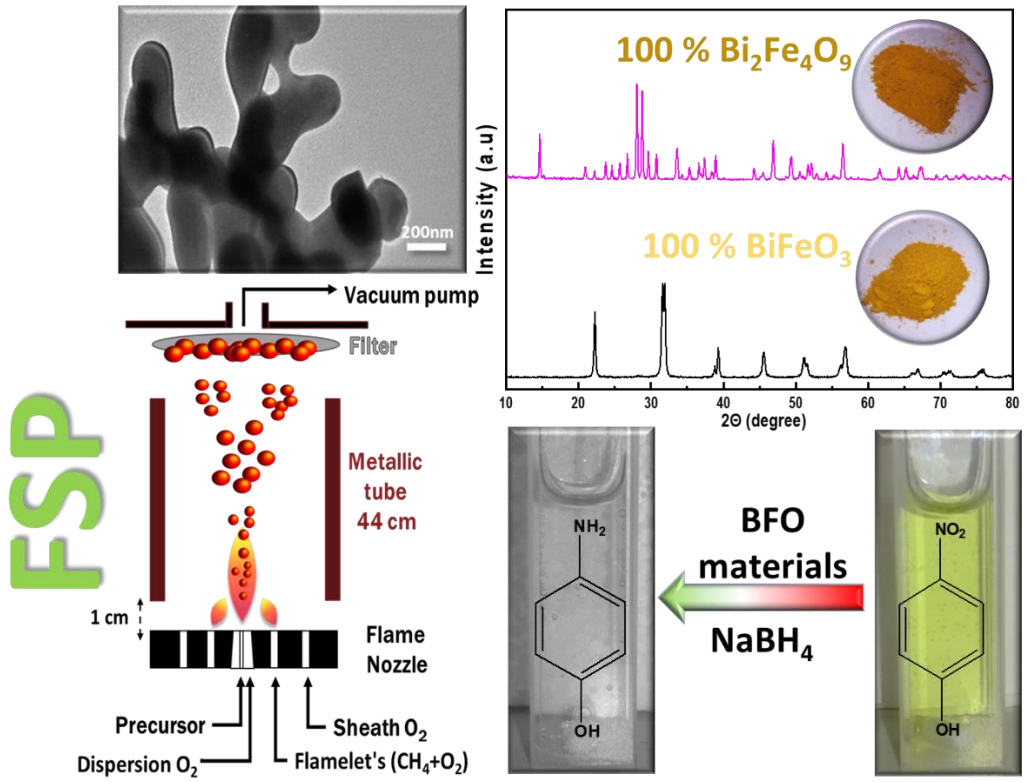

Figure 4-13: *The graphical abstract of $BiFeO_3$ vs. $Bi_2Fe_4O_9$ for the 4-Nitrothenol reduction*

Subsequent scientific works showed that $BiFeO_3$ had been realized to be an efficient catalyst for the 4-Nitrophenol redaction to 4-Aminophenol [336] [342]. Although previous to our submitted work, the mullite type phase $Bi_2Fe_4O_9$ or heterostructures with different concentrations of the two phases $BiFeO_3/Bi_2Fe_4O_9$ weren't explored for the catalytic activity towards 4-Nitrophenol redaction. While the catalytic activity has been investigated, a thorough thermodynamic comprehension was lacking from the previous publication, in accordance with the catalytic activity, energy barrier, and molecular steps for these non-noble metal oxide nanoparticles. For these reasons, the following experiments for the synthesis of pure phase materials of $BiFeO_3$, $Bi_2Fe_4O_9$, and their heterostructure mixed phase $BiFeO_3/Bi_2Fe_4O_9$ materials were characterized and thoroughly explored for the kinetic and thermodynamic-Arrhenius for the 4-Nitrophenon reduction to 4-Aminophenol. The derived activation energy is compared with other $BiFeO_3$ based materials and noble metal-based materials, showing a significantly lower activation energy. Finally, by

employing FTIR spectroscopy and the adsorption isotherms, the results demonstrate an inversely correlation between the adsorption strength of 4-Nitrophenol on the particles and the activation energy.

The experimental results for the $BiFeO_3$ *vs.* $Bi_2Fe_4O_9$ for the 4-Nitrothenol reduction have been published in our work for the Journal of Powder Technology [224], with the graphical abstract shown in **Figure 4-13**.

4.3.2 FSP Synthesis of perovskite $BiFeO_3$ and mullite-type $Bi_2Fe_4O_9$

For the FSP synthesis of the perovskite $BiFeO_3$ and the mullite-type $Bi_2Fe_4O_9$, a workable precursor solvent must be mixed. For these reasons, a combination of different Fe/Bi precursors were employed and different solvents. Two precursors for the Fe Element were screened: (1) Iron(iii) acetylacetonate and (2) Iron(iii) nitrate nonahydrate. Two precursors for the Bi element were screened: (1) the Bismuth(iii) nitrate pentahydrate, and (2) Bismuth(iii) acetate. As powder form for Iron(iii) acetylacetonate and Bismuth(iii) acetate, solid form of crystals for Iron(iii) nitrate nonahydrate and Bismuth(iii) nitrate pentahydrate.

The solvent produces a high amount of enthalpy, with four different solvents considered: Xylene, Acetonitrile, Ethanol, and THF. After stirring for 5 minutes with a small portion of the Bi/Fe precursor, the results are shown in **Table 4-8**, with some producing a small amount of precipitates that disturb the FSP synthesis heavily.

Table 4-8: *The combinations of precursors and solvents for soluble or portion of precipitates in the final solution.*

	Iron(III) nitrate nonahydrate	Iron(III) acetylacetonate	Bismuth(III) acetate	Bismuth(III) nitrate
Xylene	-	Soluble	Soluble	precipitate
Acetonitrile	-	Soluble	precipitate	precipitate
Ethanol	soluble	Soluble	Soluble	Soluble
THF	-	Soluble	precipitate	Soluble

As observed, the workable precursors that can be produced contain Bismuth acetate as a standard, Iron Nitrate or Iron acetylacetonate, and the Iron solvent Ethanol or xylene. Ethanol has much lower combustion enthalpy, reducing the overall temperature in the flame hot. To decrease the possibility of small precipitates, the total concentration of the solvent was 0.2M, where a critical step is to prepare the Fe and Bi precursors separately instead of adding both in the same solvent, Fe- Xylene, and Bi- 2-Ethylhexanoic acid. Second, a sonic bath (5min) was implemented for both solvents, and the stirrer temperature was set at 50 ^{0}C for 5min. The solutions did not have any precipitates while stirred, with the resulting particles shown in **Figure 4-14**. As measured, the materials were amorphous with a hump around 30 degrees and a range approximating 10 degrees.

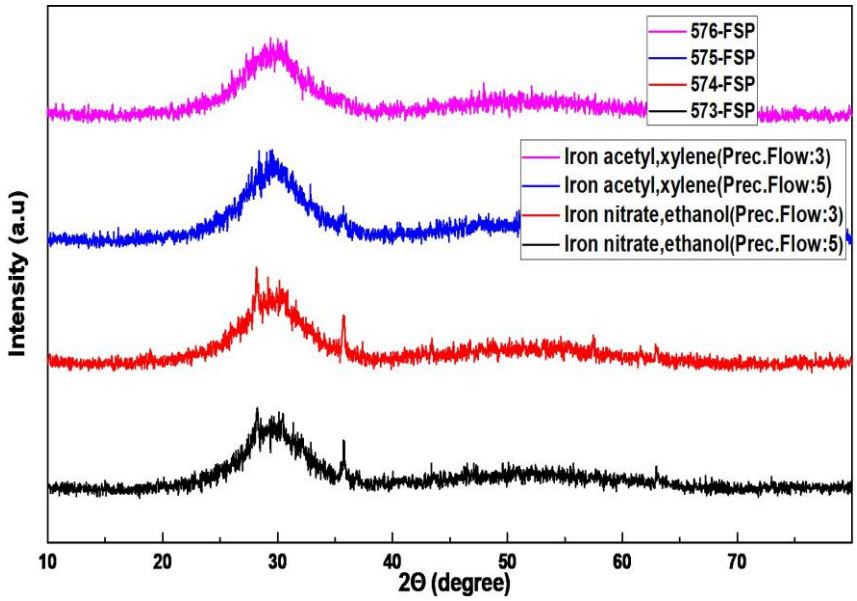

Figure 4-14: *XRD graph with different Iron precursors and solvents for $BiFeO_3$ FSP synthesis.*

By changing the ratio between Fe and Bi, many phase changes occur. A set of experiments were contributed based on the 9.1% to 65% Iron ratio changes. At low concentrations of iron, the crystal phase of Bi_2O_3 is observed, whereas the iron content increases and the amorphous hump at 30 degrees is observed in **Figure 4-15**.

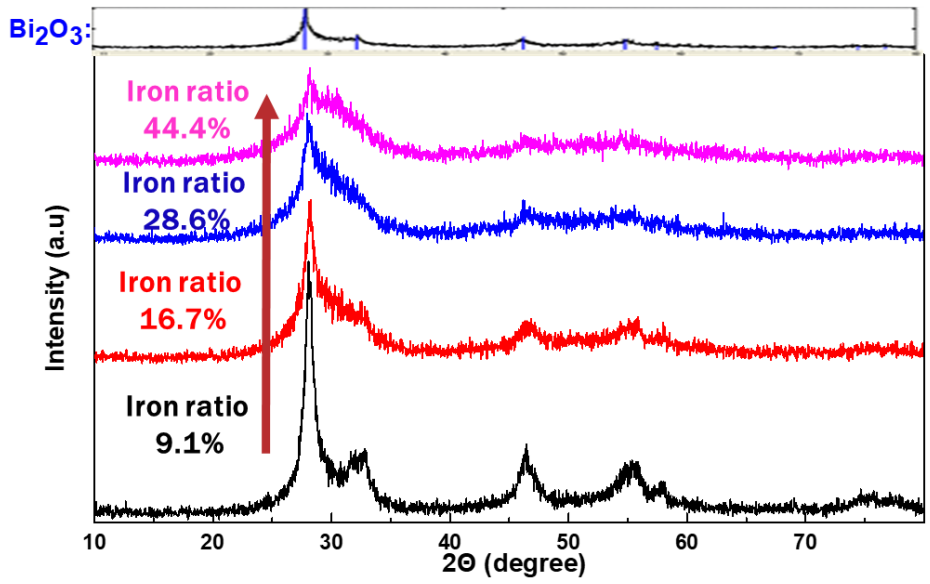

Figure 4-15: *XRD graph with different Iron ratio and Bismuth ratios.*

A different set of parameters were explored, based on the sheath gas, the water cooling the filter (20 or 5 L min^{-1}) and the precursor volume of solvent spent in a continuous synthesis, the last two are focused on changing the temperature in the filter, since in the $BiVO_4$ FSP synthesis, the particles can crystallize while they are on the filter, before the filter sintering as with the $BiFeO_3$ the particles are amorphous. The only change in the crystallinity is shown with the increased precursor volume of 95mL, as shown in **Figure 4-16**(A), although none of the brag peaks are attributed to the $BiFeO_3$ or $Bi_2Fe_4O_9$ crystal structure.

Many more experiments were conducted with high sophistication and techniques, although the direct synthesis of $BiFeO_3$ or $Bi_2Fe_4O_9$ eludes us. For this reason, a post-FSP step is introduced, with calcination under atmospheric conditions to obtain the final crystal structures. The FSP parameters are directly linked to the final particle as obtained after calcination, as shown in **Figure 4-16**(B), with the 95mL precursor volume producing a higher crystallinity of iron and bismuth oxides, finally shows that the result in $BiFeO_3$ particles have a higher crystallinity under the same calcination conditions, i.e. the XRD intensity is much higher.

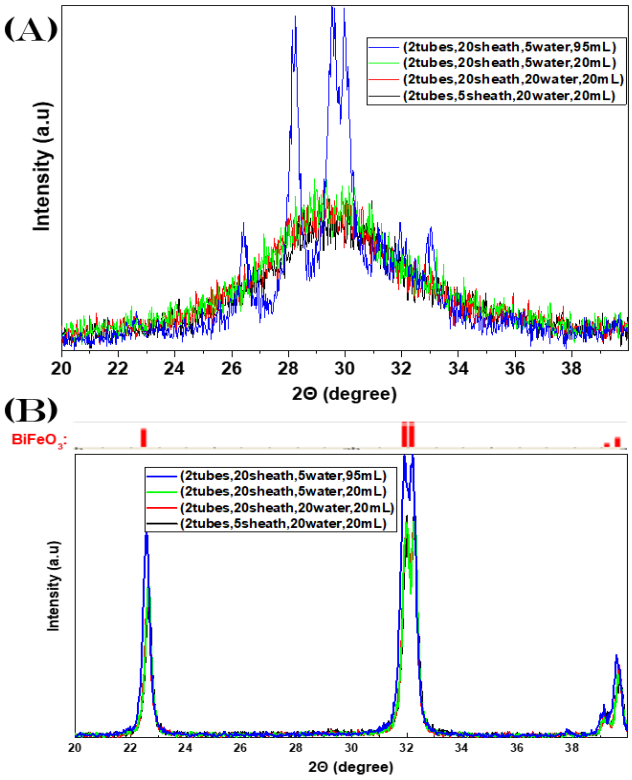

Figure 4-16: *XRD graph for the effect on sheath gas, the cooling water of the filter, and the precursor volume spent in a single experiment, (A) the FSP-obtained particles, (B) after calcination at 550 ^{0}C.*

To further understand the accuracy of FSP $BiFeO_3$ synthesis, a set of experiments at different Iron ratios were conducted at 50%, 44.4%, and 55%, the FSP-as produced still had the same amorphous hump. Calcination of 550^{0}C for 1 hour produces the materials shown in **Figure 4-17**(A). For 50%, only the $BiFeO_3$ structure is observed. The 44.4% iron ratio has the better definition of the two close peaks of $BiFeO_3$, but not only the $Bi_2Fe_4O_9$ structure is observed, but also a small portion of Bi_6O_7. The 55% iron ratio has the peaks of the $Bi_2Fe_4O_9$ structure. To further clarify, all the FSP materials with more than 55% Iron ratio show the $Bi_2Fe_4O_9$ peaks in smaller temperatures. Instead of an amorphous phase before the calcination, the $BiFeO_3$ crystallizes faster in materials with small crystallinity of iron and bismuth oxide.

For the FSP synthesis of the mullite type $Bi_2Fe_4O_9$, higher Iron ratios were tested with 60%, 65%, and 70% since the phase itself requires a 1:2 Bi: Fe ratio instead of the 1:1 Bi: Fe of $BiFeO_3$. The post-FSP calcination was conducted for one hour at 700 ^{0}C, the produced particles are shown in the XRD graph in **Figure 4-17**(B). The results are apparent, where the 60% Iron ratio shows minimal intensity, with more than half in comparison to the others. It is evident that the formation of mullite type $Bi_2Fe_4O_9$ is inefficient at a lower iron ratio. Interestingly enough, the material at 60% had a coarse grain morphology like hard sand, while at the appropriate iron ratios, the results were still powder, the coarse grain had very low dispersibility in water or ethanol, reducing the photocatalytic applications of the material.

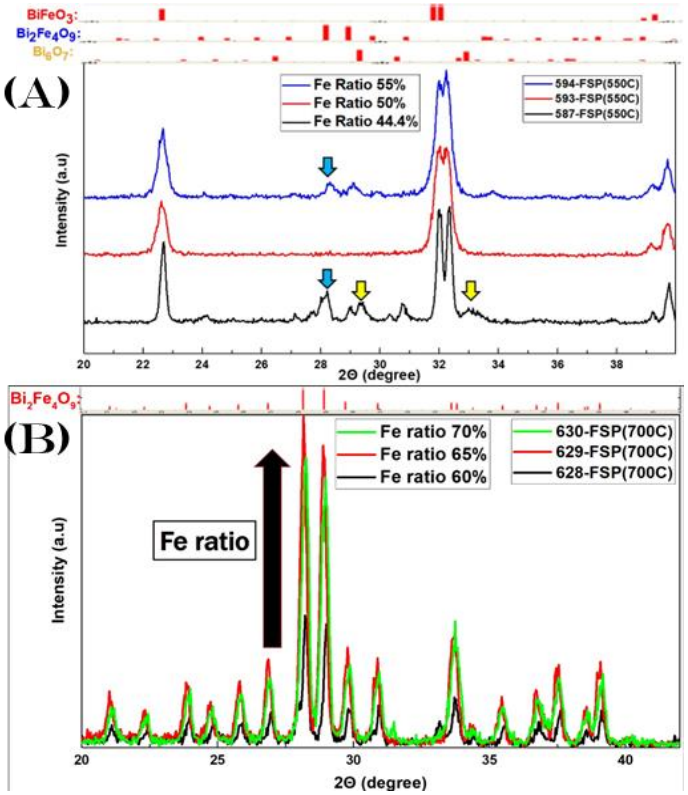

Figure 4-17: *XRD graph of different Iron ratios of FSP powders after calcination. (A) 44.4%, 50%, and 55% iron ration with 550 ^{0}C calcination, producing $BiFeO_3$. (B) 60 %, 65%, and 70% iron ration with 700 ^{0}C calcination, producing $Bi_2Fe_4O_9$.*

The Final selected iron ratio was 65%, this was derived from screening in the temperatures of 550^{0}C to 700^{0}C, and the overall results showed that the phase transition of

$BiFeO_3$ to $Bi_2Fe_4O_9$ was easier accomplished with the 65%, requiring less time and temperature.

Finally, secondary FSP parameters were employed to finetune the resulting FSP material in order for the post-calcination to require less time and temperature to derive the appropriate crystal phases of $BiFeO_3$ and $Bi_2Fe_4O_9$.

No gap tube: Instead of a 2cm gap between the FSP apparatus and the metal tube, the tube made contact with the apparatus, sealing the flame and the particle synthesis from the atmospheric air. This means that there wasn't any oxygen from the atmosphere in contact with the flame, which reduces the temperature and the synthesis at the Hot Residence Time of the flame. The result is a decrease in crystallinity, **Figure 4-18**(A), this is attributed to the much lower mobility of the particles, resulting in much less deposition material in the filter, with an estimated half of the total yield from the 2cm gap experiments.

Burner to Filter Distance (BFD): The distance between the FSP burner and the filter collecting the particles was set at 61 and 66cm. The reduced distance results in higher temperatures on the filter. Since the metal tubes have 44cm in height, the temperature increases by 50 degrees more for the 5cm difference, resulting in a small peak of iron oxide instead of the amorphous data generally received. Overall, the crystallinity decreases as shown in **Figure 4-18**(B).

Precursor flow rate: As the precursor flow rate is a critical parameter for the overall combustion enthalpy for the creation of particles, experiments were conducted for 3, 5, and 7 mL per min. The results shown in **Figure 4-18**(C) find the precursor flow of 3 mL per min to provide superior results, with other studies corroborating that a lower precursor flow rate and small Hot residence times can synthesize elusive crystal phases. The low precursor flow rate provides the additional benefit of not damaging the filter due to the high temperature provided by the additional combustion enthalpy. A severely damaged filter fuses with the nanomaterials, thus constituting material extraction impossible.

Sintering on the filter: After the conclusion of FSP synthesis, the collected filter that had an average of 300mg of material was placed on top of the flame apparatus. The FSP

burned only with the pilot gases. The filter remained for 2 min atop the flame, with the purpose of an in-situ FSP calcination, although the material remained amorphous, and the material had reduced crystallinity **Figure 4-18**(D).

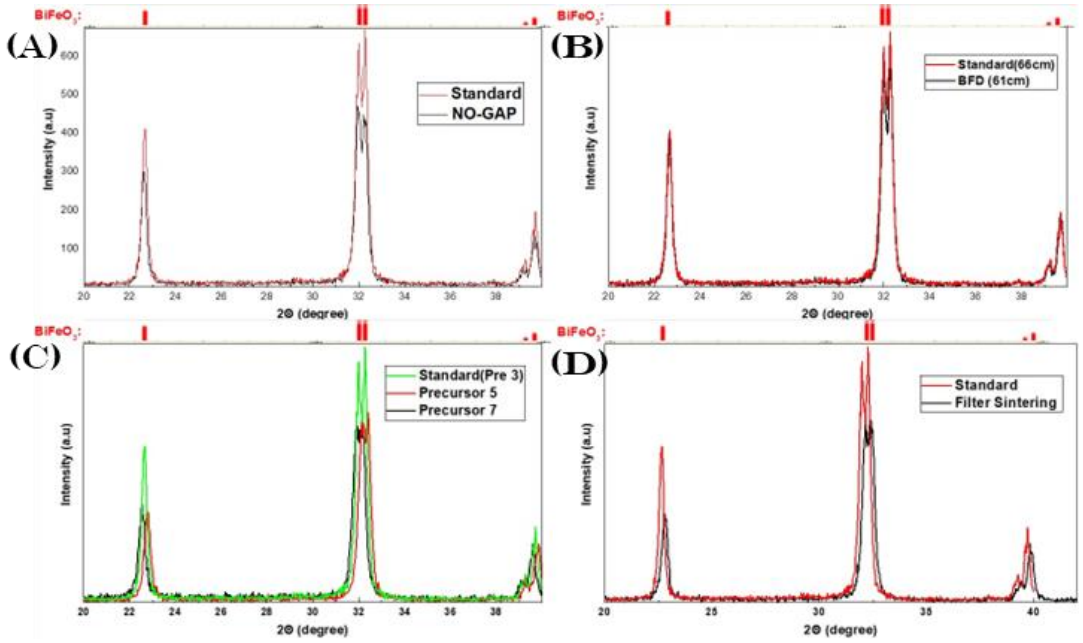

Figure 4-18: *FSP parameters for the $BiFeO_3$ synthesis, (A) No-GAP and 2cm gap of FSP apparatus and the metal tube. (B) Burner to Filter Distance of 66cm and 61cm. (C) Precursor flow rate of 3, 5, and 7 mL per minute. (D) Sintering on the filter with the FSP pilot flame.*

4.3.3 FSP synthesis for the Selected materials for the 4-Nitrophenol Reduction

The selected particles were created with the previous methodology for FSP synthesis, with Iron (III) acetylacetonate (97% Aldrich) dissolved in xylene and Bismuth (III) acetate (99.99% Aldrich) dissolved in 2-Ethylhexanoic acid. For the material BFO1, a 1: 1 volume ratio for the two precursors with a total concentration of 0.2M, which was derived from 0.1M from the Iron (III) acetylacetonate, and 0.1M from Bismuth (III) acetate. As for the materials BFO2 through BFO4, the materials had an excess of Iron at 0.132M, while Bismuth was at 0.066M, in order for the higher iron concentration phase to be obtained ($Bi_2Fe_4O_9$), the parameters are shown in **Table 4-9**. The Bi: Fe stoichiometry's percentages for the materials correspond to the chemical stoichiometry of the metal atoms used in our FSP protocol, as a stoichiometry of 1:1 / Bi: Fe for the material BFO1 that designated to

become $BiFeO_3$, while a stoichiometry of 1:2 / Bi: Fe for the material BFO4 designated to become $Bi_2Fe_4O_9$). The solutions were under stirring for 10 minutes at 40°C, resulting in a transparent final solution free of any precipitates.

The FSP parameters were as mentioned before for a Single Nozzle FSP reactor, with the precursor flow rate at 3 mL min^{-1}, a dispersion oxygen flow rate of 7 L min^{-1} with a nozzle pressure drop of 2 bar. The supporting combustion flame had oxygen/methane flow rates of 5/2.5 L min^{-1}, respectively. An oxygen sheath gas of flow rate 5 L min^{-1}, while the flame was enclosed with metallic tubes, with dimensions of 4.2cm inner diameter and 44 cm height, the reason for the enclosure was an increase in the High-temperature residence time, resulting in higher crystallinity.

Table 4-9: BFO Samples used for 4-Nitrophenol reduction, as characterized by XRD, TEM, BET, and DRS.

Material	precursor ratio Bi/Fe(M)	Calcination Temperature (°C)	%Crystalline volume fraction		crystallite size (nm)		SSA (m^2 gr^{-1})	Total pore volume (cm^3 g^{-1})	Band gap E_g (eV)
			$BiFeO_3$	$Bi_2Fe_4O_9$	d_{BET}	d_{TEM}			
BFO1	0.1/0.1	550	100	0	80	64	8.9	$2.4x10^{-2}$	2.2
BFO2	0.066/0.132	650	57	43	116	-	6.9	$1.6 x10^{-2}$	2.1
BFO3	0.066/0.132	675	19	81	188	150	4.6	$1.1 x10^{-2}$	2.1
BFO4	0.066/0.132	700	0	100	327	230	2.8	$0.8 x10^{-2}$	2.1/1.6

Post-FSP calcination, in order for the selected phases to be produced, by utilizing a Thermawatt furnace, all resulting FSP powder was exposed to atmospheric air. The calcination time was set for the four selected materials at 60 minutes. The temperature for BFO1 was 550 °C, BFO2 at 650 °C, BFO3 at 675 °C, and finally, BFO4 at 700°C in order to have the appropriate phases as shown in **Table 4-9**. As mentioned previously, for these materials an extensive screening was employed with varying temperatures as well as calcination times. The selected time and temperature were selected for a very high crystallinity in order to have a complete understanding of the 4-Nitrophenol reduction according to the different phase percentage, while in the following work that focused on

Oxygen Evolution Reaction, some non-crystalline attributes were preferable, such as a percentage of Fe^{2+} atoms.

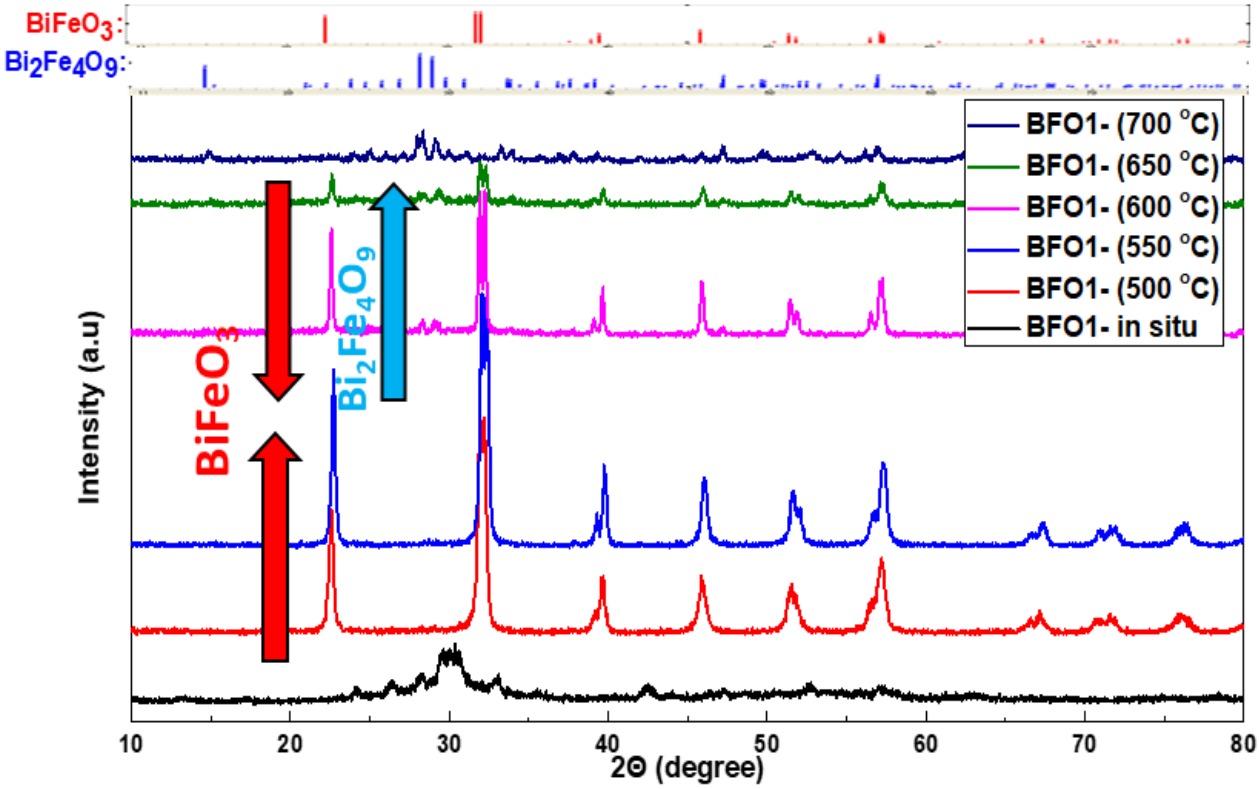

Figure 4-19: *XRD graphs for the BFO1 material as prepared, with calcination temperatures of 500 to 700°C, under atmospheric air and pressure for one hour.*

Additionally, to those experiments, specifically for the material BFO1, temperature control in the range of 500 °C to 700 °C was explored, **Figure 4-19**. Where at 500 °C the $BiFeO_3$ phases are clearly evident, although with decreasing intensity as shown in XRD, while at 600 °C the $BiFeO_3$ starts to shift to the phase $Bi_2Fe_4O_9$, at 700 °C the phase change is complete where only the $Bi_2Fe_4O_9$ is evident. Finally, the addition of tubes was explored for the BFO1 material, where when we used no-tube, the as-prepared FSP particles showed basically no crystallinity in XRD. Increasing the high-temperature residence time by including the metallic tubes resulted in a small improvement of the crystallinity of the as-prepared particles. However, more importantly, the addition of tubes showed a significant enhancement in the intensity of the XRD, meaning more crystalline particles and removal

of small amounts of secondary phases present in the range of 28 degrees, **Figure 4-20**. Our assumption was that the enhanced residence time creates a fraction of ultrafine nanocrystals of sizes below 2nm that are below the detection limit of the XRD, nonetheless, these small particles decrease the time necessary for the crystallization under calcination, forming more efficiently $BiFeO_3$ nanoparticles. Nonetheless, the inclusion of post-FSP calcination treatment was necessary for the high crystallinity materials for the 4-Nitrophenol reduction.

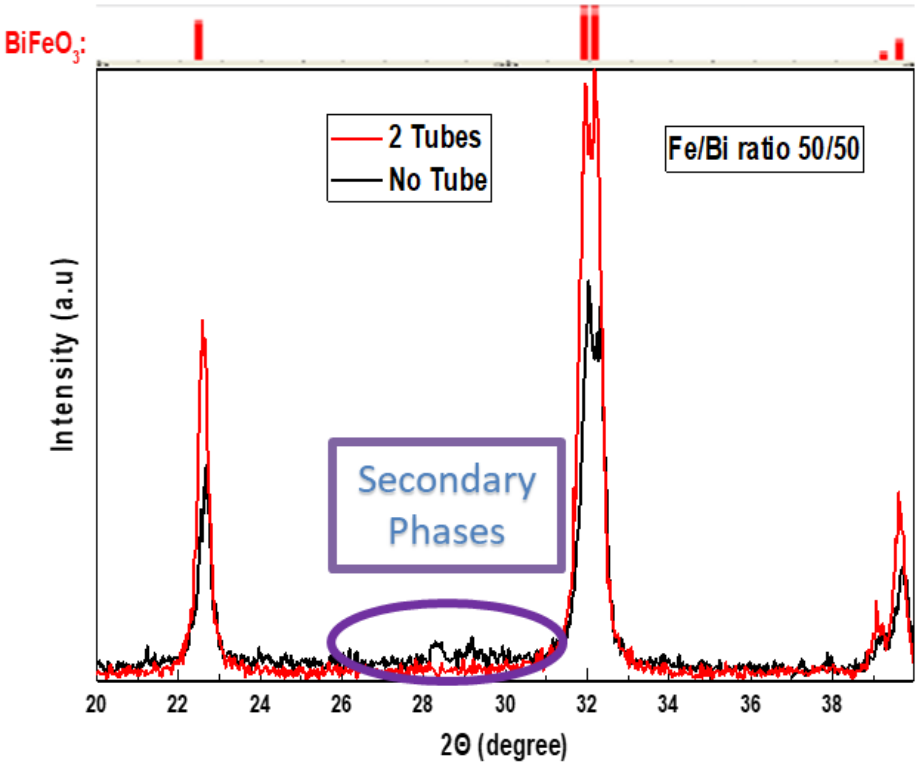

Figure 4-20: *XRD graphs for the BFO1 material, synthesized with no metallic tubes surrounding the flame and with 44cm metal tubes. The calcination conditions were 550^{0}C temperature for 1 hour. The enclosing tubes greatly enhance the crystallinity and eliminate a small fraction of secondary phases.*

The XRD graph of the four selected materials is shown in **Figure 4-21**(A). BFO1 material obtained after calcination at 550°C has the characteristic peaks credited only for the perovskite $BiFeO_3$ space group R*3c* [343]. For the other three materials, by changing

the overall concentration of Iron in the FSP synthesis and increasing the calcination temperature, the $Bi_2Fe_4O_9$ phase emerged. BFO4 material at 700°C calcination temperature shows only the mullite-type $Bi_2Fe_4O_9$ with an orthorhombic structure of P*bam* [344]. In order for the two distinct phases to be understood by the reader, at the top of **Figure 4-21**(A) the distinct peaks of each of the two phases are present, while on the graph, the Miller planes of (012, 104, 110, 006, 024, 116, 214) for the $BiFeO_3$ and the (001, 121, 211, 002, 130, 202, 212, 141) for the $Bi_2Fe_4O_9$ are shown.

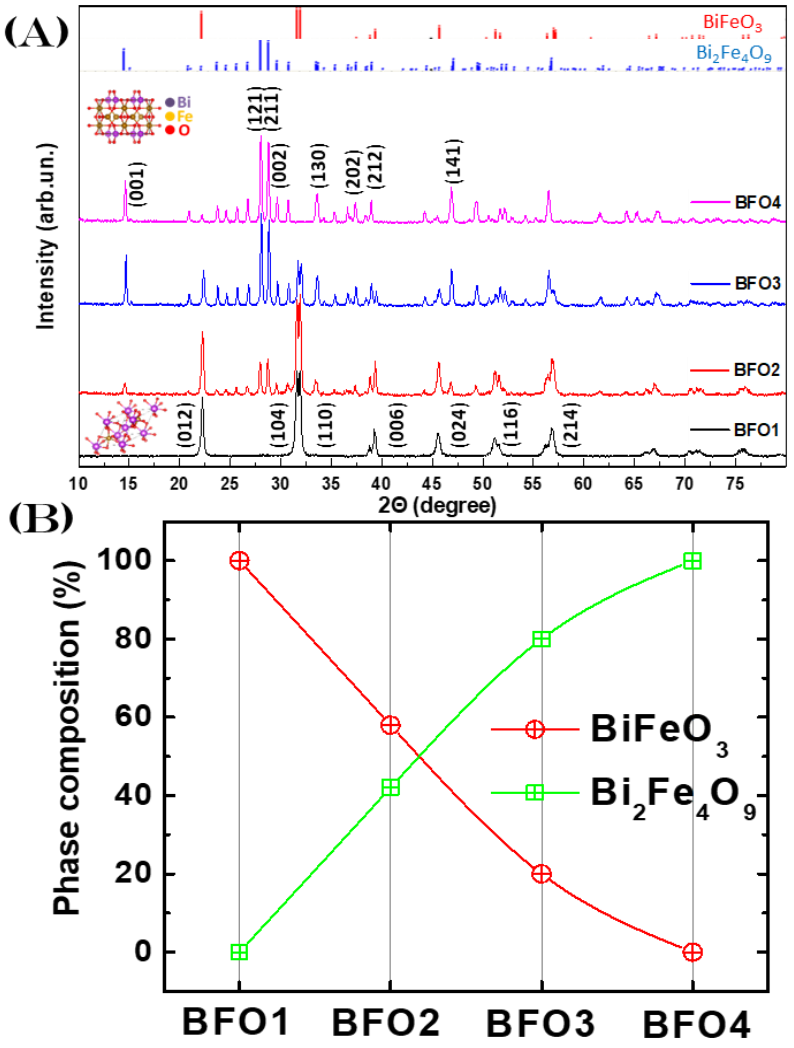

Figure 4-21: *XRD patterns for the BFO1, BFO2, BFO3, and BFO4 materials. The reference Miller-planes reflections for $BiFeO_3$ and $Bi_2Fe_4O_9$ phases are shown at the graph's top. Inset: the percentage of phase composition of each material calculated by Rietveld analysis.*

The crystalline phase composition (%) of the two distinct phases $BiFeO_3$ and $Bi_2Fe_4O_9$ for the four materials was computed through Rietveld analysis using the Maud software by fitting the XRD data of each material, listed in **Table 4-9** and visualized in **Figure 4-21**(B). The results show that BFO1 comprises 100% $BiFeO_3$, while BFO4 has 100% $Bi_2Fe_4O_9$. The BFO2 and BFO3 that were meant to be mixed phase materials had some percentages of each phase, with BFO2 comprised of [57:43] : [$BiFeO_3$:$Bi_2Fe_4O_9$] phase ratio, while BFO3 has a [19:81] : [$BiFeO_3$:$Bi_2Fe_4O_9$] phase ratio. Furthermore, the Riedvielt analysis showed that none of the materials BFO1 through BFO4 possess any secondary phases, i.e., Bi_2O_3, Fe_2O_3, or $Bi_{25}FeO_{40}$, these phases are often in the final resulting nanoparticles for other synthesis methods, such as wet or solid-state synthesis methods [44,345].

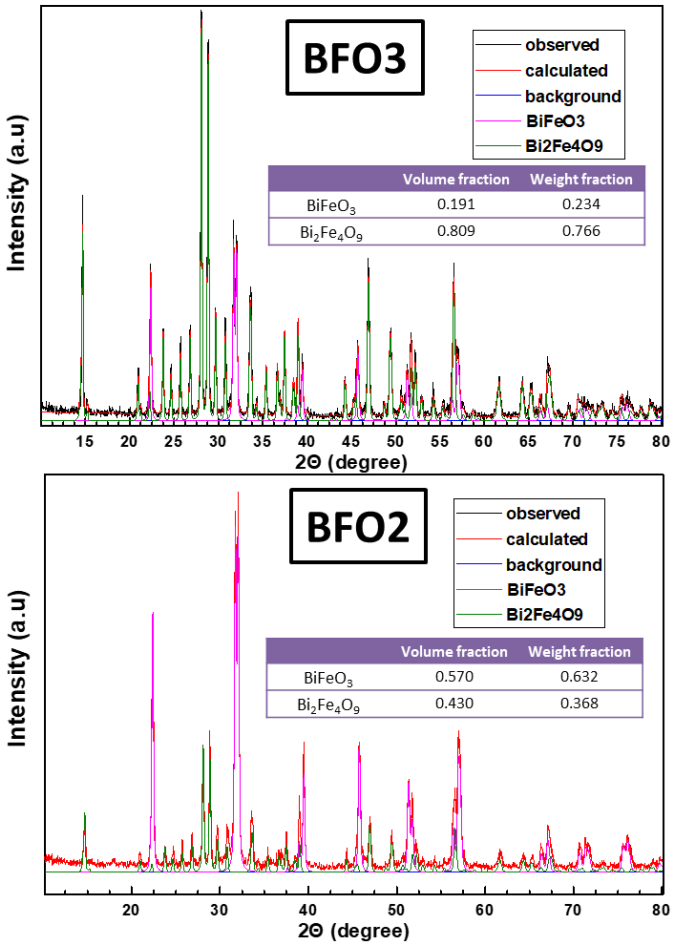

Figure 4-22: *Rietveld analysis of the BFO2 and BFO3 materials, Maud software calculated the percentage of the $BiFeO_3$ and $Bi_2Fe_4O_9$ phases.*

4.3.4 Characterization of the BFO1-4 materials for 4-Nitrophenol

Specific Surface Area (SSA) analysis: The selected materials BFO have the BET-adsorption desorption data shown in **Figure 4-23**, generally have low SSA with the 8.9 m^2 gr^{-1} for BFO1, decreasing steadily with 6.9 m^2 gr^{-1} for BFO2, 4.6 m^2 gr^{-1} for BFO3, and 2.8 m^2 gr^{-1} for BFO4, while the pre-calcinated material as obtained from FSP has 34 m^2 gr^{-1}. From the SSA, we calculated the size of the materials according to the BET measurements d_{BET} [346]. The calculated d_{BET} values of the materials are listed in **Table 4-9**. While the pore radius and the total pore volumes are shown as an inset in **Figure 4-23**, the results mimic those from SSA, with BFO1 Having a total pore volume of 2.4 10^{-2} cm^3 g^{-1} dropping steadily with each material resulting in the BFO4 having almost four times lower pore volume of 0.8 10^{-2} cm^3 g^{-1}.

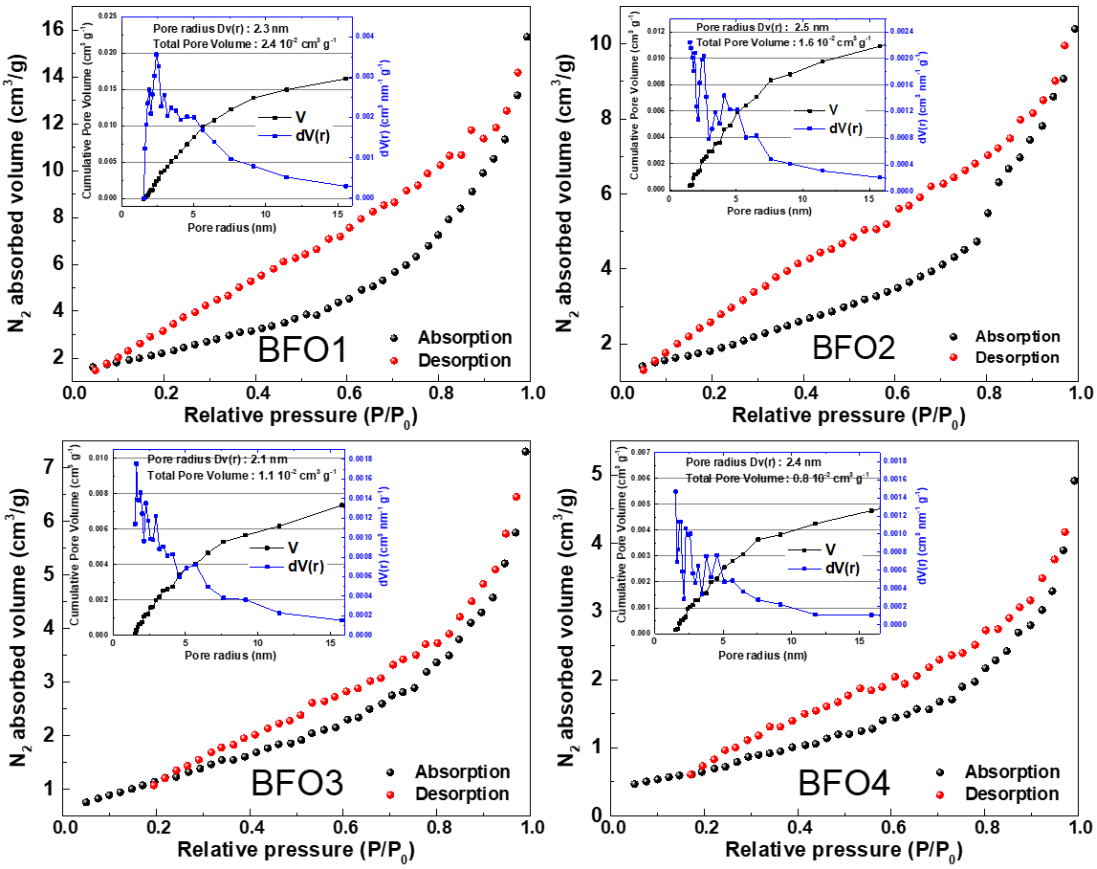

Figure 4-23: *Nitrogen adsorption-desorption isotherms for the BFO materials at 77 K. inset: pore size distribution plot using the BJH method, showing the cumulative pore volume and the volume per pore radius.*

Transmission Electron Microscopy: Transmission Electron Microscopy images for the selected materials BFO1, BFO3, and BFO4 are shown in **Figure 4-24**. The TEM image illustrates neck-sintered nanoparticles forming rod-like morphologies. These morphologies resemble those typically observed by other FSP-made Bi-based materials, such as $BiVO_4$ nanoparticles[347], by Amal et. Al. publication.

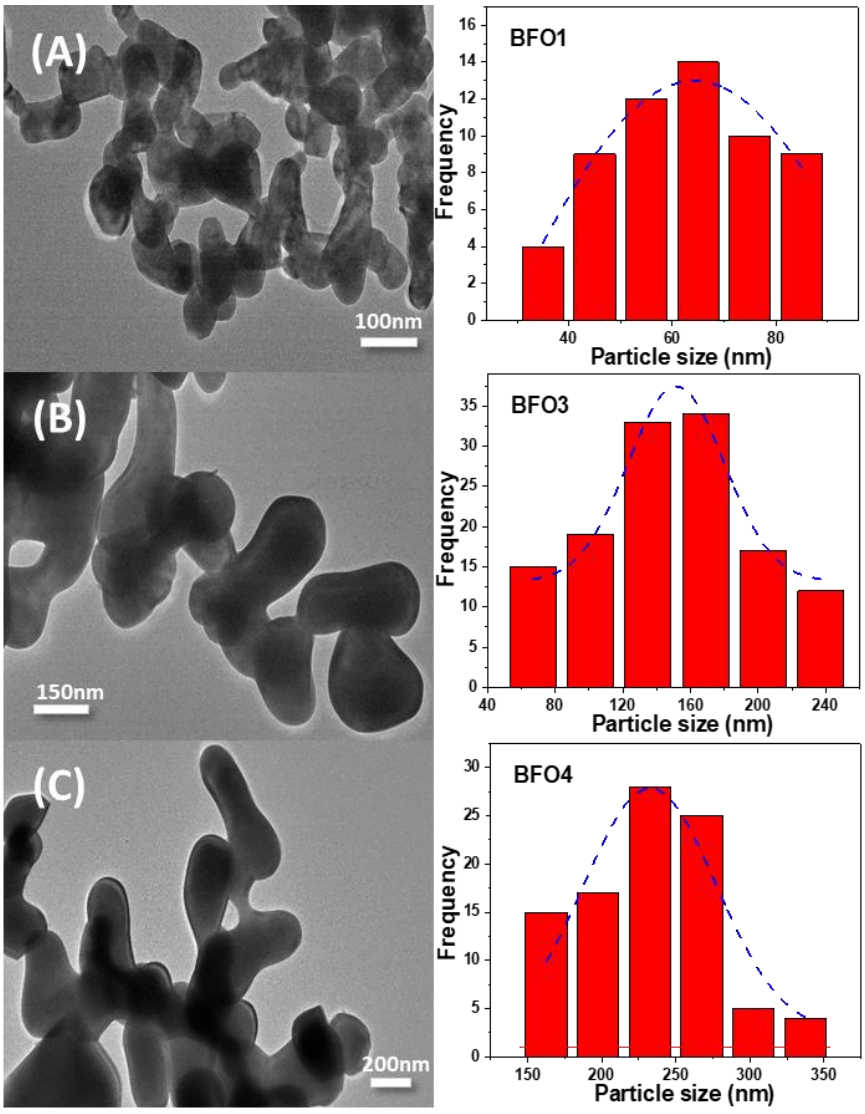

Figure 4-24: *Transmission electron microscopy images for the three calcined materials, showing necked-sintered particles (A) BFO1, (B) BFO3, and (C) BFO4. TEM size distribution.*

The size distribution of the BFO materials, presented in **Figure 4-24**, reveals the average particle size d_{TEM} in the range from 64 to 230 nm. The higher calcination temperatures that promote particle growth via sintering are attributed to the larger sizes of $Bi_2Fe_4O_9$ particles compared to $BiFeO_3$, in accordance with the large particle size as determined by d_{BET}. The consistent trend for the material size as $d_{BET} > d_{TEM}$, this observation is typical for systems with strong particle-particle sintering. The lower SSA due to sintering lowers the overall size obtained by BET, while the primary particle as observed by TEM is lower, especially for the smaller particle BFO1 [348].

FT-IR Spectroscopy: The Fourier transform infrared (FT-IR) spectra of the four selected materials are presented in **Figure 4-25**. The perovskite phase $BiFeO_3$ has two characteristic absorption peaks at 445 and 557 cm^{-1}, originating from Fe-O units stretching and bending vibrations in the octahedral FeO_6 groups stationed in the perovskite structure [349,350]. In comparison, the $Bi_2Fe_4O_9$ phase has several more characteristic bands at 441, 478, 525, 609, 641, and 814 cm^{-1}, as verified from the literature [351]. The $Bi_2Fe_4O_9$ has tetrahedral FeO_4 and octahedral FeO_6 units that compose the crystal structure, from the octahedral group, the Fe cations produce the first bands present 441cm^{-1} and 478cm^{-1}, from the tetrahedral pairs of the bending vibrations O-Fe-O produce the band 525cm^{-1}, while from the tetrahedral the bending vibration Fe-O-Fe create the 609 cm^{-1} band [352]. Finally, the tetrahedral FeO_4 stretching produces the 641cm^{-1} and 814cm^{-1} bands. In the range, this broad signal that is observed in all of the selected materials is attributed to the stretching O-H group from surface nanoparticle absorption from the atmospheric humidity [353].

As BFO2 and BFO3 have two phases at different concentrations, as the concentration of the $Bi_2Fe_4O_9$ phase increases, a progressive shift of the 557 cm^{-1} signal decreases, while the peak at 814 cm^{-1} steadily increases, as shown in **Figure 4-25**.

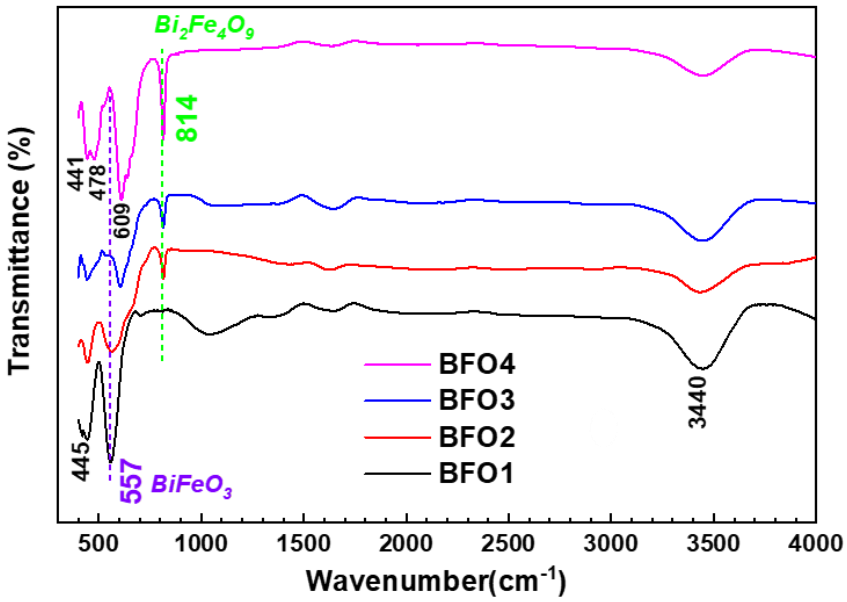

Figure 4-25: *FT-IR data for the four selected BFO materials in the range from 400 to 4000 cm^{-1}. $BiFeO_3$ phase is characterized by the 445 and 557 cm^{-1} peaks, while the $Bi_2Fe_4O_9$ phase is characterized by the 441, 478, 525, 609, 641, and more clearly from 814 cm^{-1}.*

Raman Spectroscopy: The Raman spectra of the selected materials are shown in **Figure 4-26**, the characteristic peaks for the $BiFeO_3$ phases are characterized by two definite peaks at 136cm^{-1} and 170cm^{-1} that correspond with that from the literature [354,355], another significant peak is present at 75cm^{-1}, that it has also been reported for the $BiFeO_3$ structure, although some $BiFeO_3$ material don't possess this peak depending on the synthesis method [356,357] accompanied by seven peaks that have small intensities in the range of 260cm^{-1} to 520cm^{-1} [354,355], as shown the BFO1 material only possesses these characteristic peaks. As for the $Bi_2Fe_4O_9$ structure, as with the FT-IR measurement, the structure has several more distinct peaks, including the peaks at 87, 207, 283, 331, 365, 430, and 552 cm^{-1} [358], as shown for the BFO4 material. The change from the two phases for the BFO2 and BFO3 is again evident from the change in the intensity of these characteristic peaks.

From the data derived from FT-IR and Raman, we observe that BFO1 does not possess any characteristic bands from $Bi_2Fe_4O_9$, nor does the BFO4 spectrum contains any characteristic peaks from $BiFeO_3$. In contrast, the BFO2 and BFO3 have an appropriate change from the peak intensity from the $Bi_2Fe_4O_9$ and $BiFeO_3$ phases. Also, none of the materials show any evidence of the frequently observed phase of Bi_2O_3 or Fe_2O_3 or any other carbon-based structure that could be resulted from the combustion process.

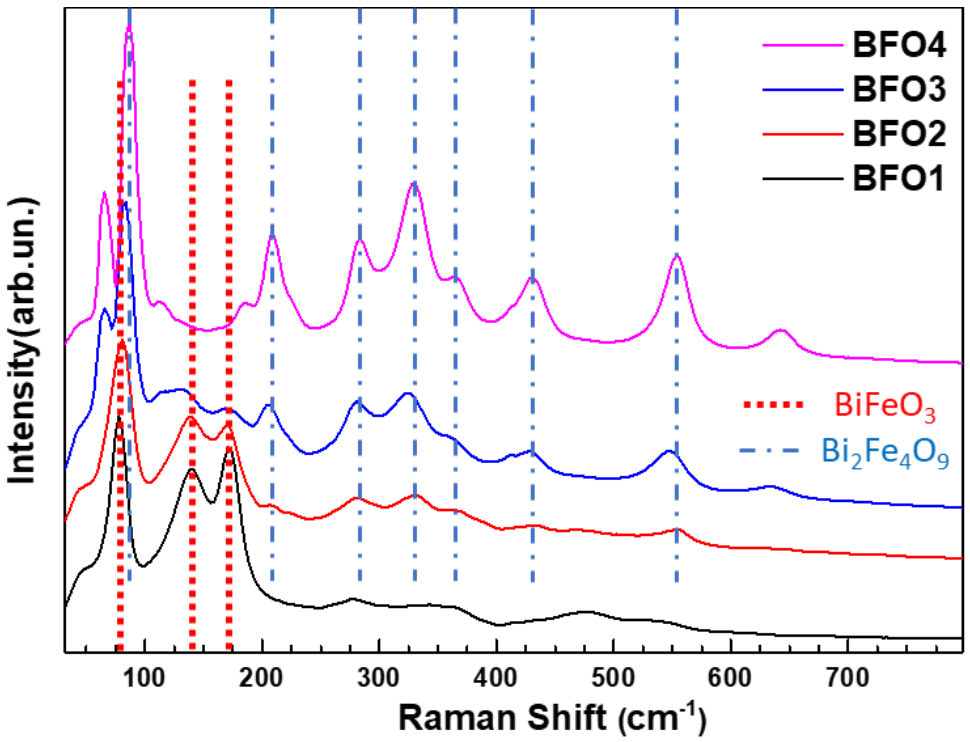

Figure 4-26: *Raman spectra of the four selected BFO materials, with the characteristic peaks of the $BiFeO_3$ and $Bi_2Fe_4O_9$ shown with the corresponding dashed lines.*

UV-Vis DRS: The band gap of each material is not necessary in the case of 4-Nitrophenol reduction. For completeness, these measurements will be shown in **Figure 4-27** and discussed briefly, with the sequential work from this one, it will delve much deeper into the literature. All the materials have a broad absorption from 200 nm to 600 nm, with the highest absorption belonging to the visible range of 400-480 nm, attributing to a color scheme of these particles at dark-brown colors. The bandgap energy E_g is found by the Tauc plot [327], where the perovskite phase $BiFeO_3$ (BFO1) has a direct bandgap of

2.2eV in accordance with the literature [275], while the rest of the materials have a slightly lower primary band gap at 2.1eV. The mullite-type $Bi_2Fe_4O_9$ (BFO4) is expected at 2.1eV [276], furthermore, an additional secondary smaller bandgap is observed at 1.6 eV, evident by the absorbance peak at 700 nm [277], with the transition of the two phases the peak at 700nm is clearly increasing in intensity.

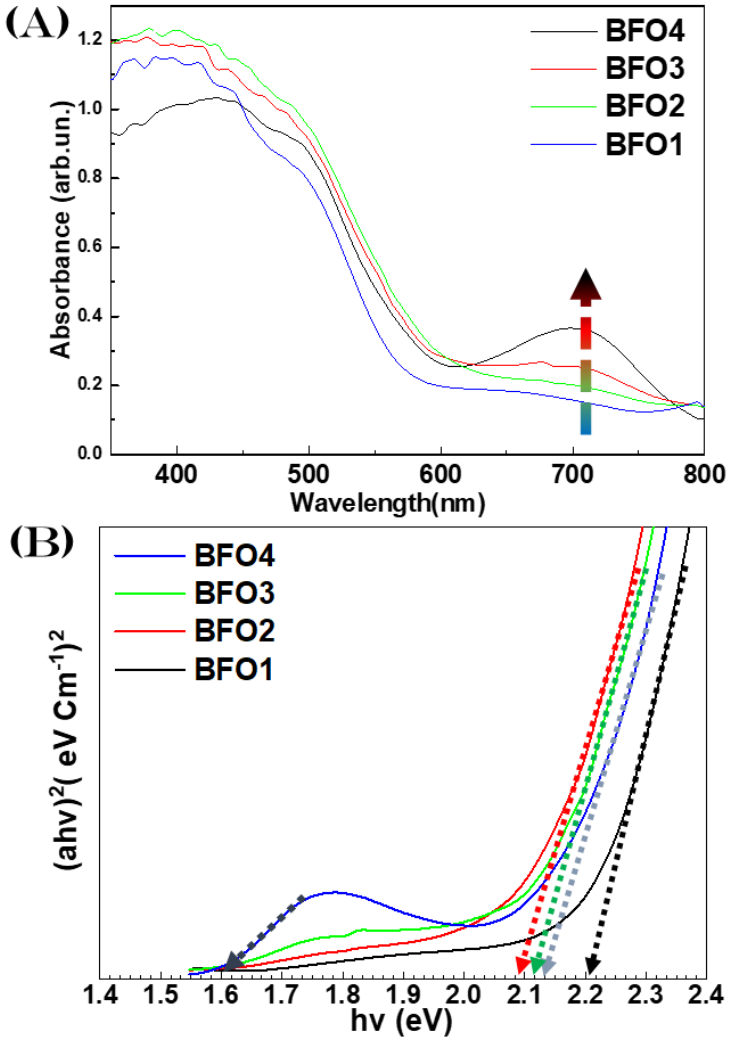

Figure 4-27: *(A) DRS-UV/Vis spectra of the selected materials. (B) The Tauc plot for each material, with the tangential dashed lines marking the estimated band-gap.*

X-ray Photoelectron Spectroscopy: The spectra for the three different atoms that comprise our materials, Iron, Bismuth, and oxygen are explored below.

The XPS spectra for the Fe2p state are presented in **Figure 4-28**. Iron has two oxidation states, $Fe2p_{3/2}$ and $Fe2p_{1/2}$, the fitting for these states must be spin-orbit doublet components, meaning that the two states are linked with an average gap between them of 14 eV. Thus, the first doublet fit has binding energies of Fe $2p_{3/2}$ and Fe $2p_{1/2}$ at 710.3 and 724.6 eV, respectively. The second doublet fit has binding energies of Fe $2p_{3/2}$ and Fe $2p_{1/2}$ at 712.6 and 725 eV, respectively. The location of the $Fe2p_{3/2}$ peaks at 710.3 and 712.6 eV demonstrates that the oxidation state of the Iron is Fe^{3+} [359].

The peak present roughly at 717.5 eV is a satellite that is noticeable without overlapping with the oxidation states of Fe $2p_{3/2}$ or Fe $2p_{1/2}$, supplementary the average gap between the satellite and the $Fe2p_{3/2}$ peak at 7.0 eV and 5.0 eV from 710.3 eV and 712.6 eV respectively, as it is observed in the literature, without the presence of any Fe^{2+} or Fe^{0} impurities [360,361]. Overall, the XPS data indicate that the oxidation state of Fe atoms in the structure is entirely Fe^{3+}.

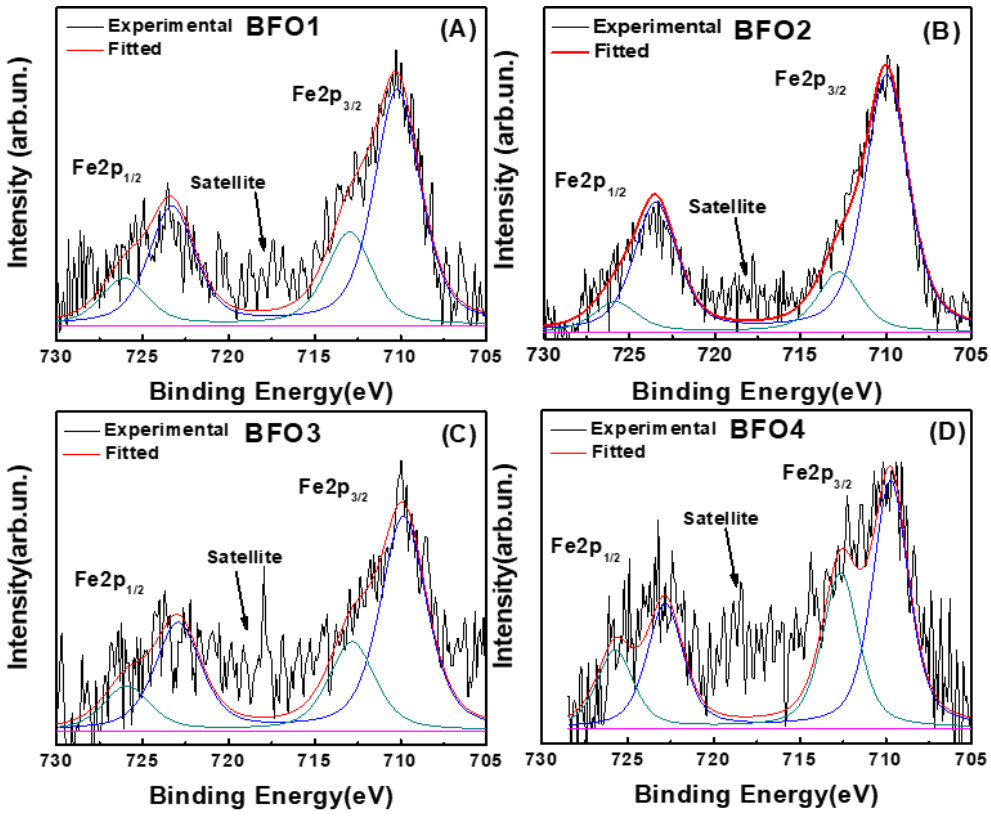

Figure 4-28: *Iron XPS spectra for (A) BFO1, (B) BFO2, (C) BFO3, and (D) BFO4 materials, showing the $Fe2p_{1/2}$ and $Fe2p_{3/2}$ Iron states.*

The XPS spectra for the Bismuth atoms for the selected materials are shown in **Figure 4-29**. The results are straightforward, with the observed characteristic peaks being attributed to the $Bi4f_{5/2}$ and $Bi4f_{7/2}$ spin-orbit splitting states, with bonding energies observed at 158 eV and 164 eV, respectively. Additionally, the 5.3 eV average gap between the two peaks is in accordance with the literature [362].

The Oxygen XPS spectra for the selected materials are shown in **Figure 4-30**, the results requiring four separate oxygen states. The two major O1s peaks found in all our particles are attributed to the Fe-O bond, the ferroelectric nanomaterial properties for these materials are correlated to the Fe-O bond in the unit cell. There are two different Fe-O bond lengths, classified as short-bonded and long-bonded. The short-bonded Fe-O requires additional photonic energy to separate the O1s photoelectron from the long-bonded Fe-O [363]. Thus the binding energy for the short bonded is observed at roughly 531.36eV, while the long bonded is observed at lower binding energies with an average of 529.61 eV [363]. In general, the XPS data are in agreement with the literature data for the phases of $BiFeO_3$ and $Bi_2Fe_4O_9$ [363,364].

The BFO1 with 100% $BiFeO_3$ crystal phase is observed to have a smaller intensity for the short bonded Fe-O peak in comparison to the long bonded Fe-O peak. In contrast, the opposite holds true for the material BFO4 with 100% $Bi_2Fe_4O_9$. These findings can be correlated with the smaller Fe-O bond lengths in the $Bi_2Fe_4O_9$ crystal structure, in comparison to the Fe-O bond lengths in the $BiFeO_3$ crystal structure [343,365]. Thus, the average population for short Fe-O bond will be much higher in the $Bi_2Fe_4O_9$ phase.

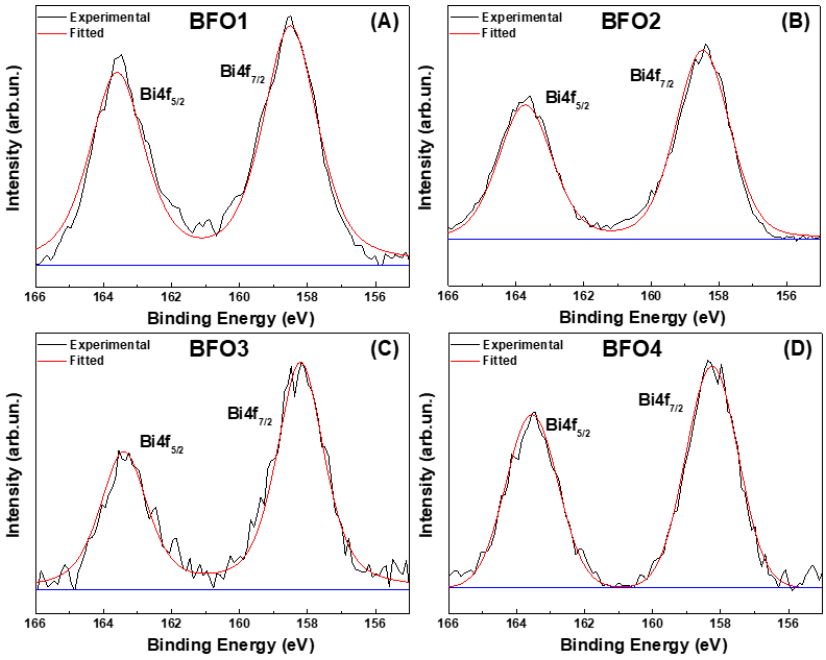

Figure 4-29: *Bismuth XPS spectra for (A) BFO1, (B) BFO2, (C) BFO3, and (D) BFO4 materials, showing the $4f_{5/2}$ and $4f_{7/2}$ Bismuth states.*

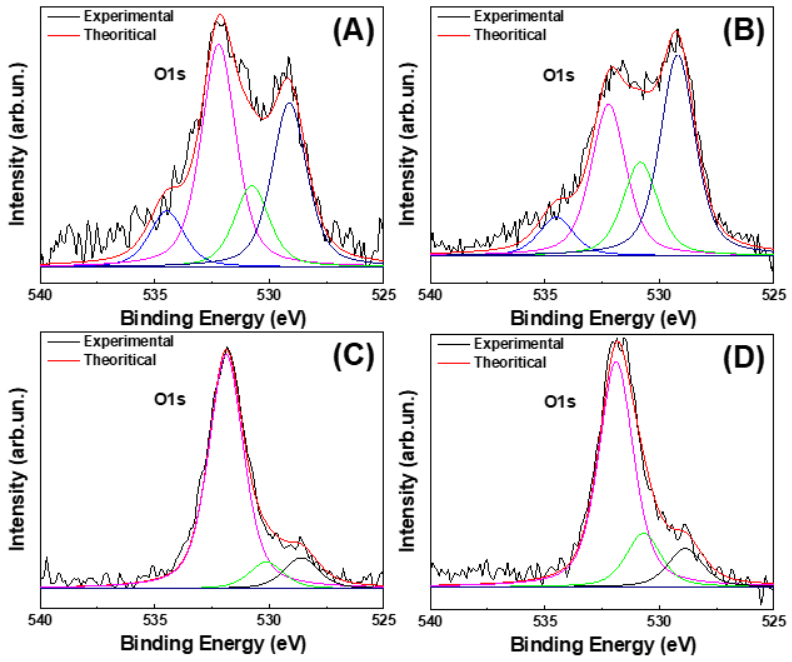

Figure 4-30: *Oxygen XPS spectra for (A) BFO1, (B) BFO2, (C) BFO3, and (D) BFO4 materials, showing the long O-Fe bonds, short O-Fe bonds, hydroxyl groups, and the chemically adsorbed oxygen.*

Additionally, there are two peaks at lower intensity present, although only BFO1 and BFO2 have a peak at 534.5 eV. The low-intensity peak at 532.5 eV corresponds to hydroxyl groups or the adsorbed oxygen on the particle surface [366]. The oxygen peak at 534.5 eV is attributed to the chemically adsorbed oxygen on the surface of the nanoparticles [367]. In both these cases, as the hydroxyl groups and oxygen atoms are only weak bonded on the surface of the materials, it does not correlate to the purity of the particles.

The Overall data from the characterization measurements of XRD, TEM, Raman, FT-IR, and XPS data show several factors for the materials BFO1, BFO2, BFO3, and BFO4. First, the material purity, which was the most crucial factor, was confirmed, unwanted phases such as the separate oxides of Bi_2O_3, Fe_2O_3, or Fe_3O_4 were not detected, while the structure of $Bi_2Fe_4O_9$ was missing from the BFO1 (100% $BiFeO_3$). Secondly, the post-FSP calcination proved that precise calcination temperature and time could produce 100% pure phase of the desired phases without unwanted crystal phases or oxidation states from the present atoms.

4.3.5 4-Nitrophenol Reduction from the materials BFO1-4

The reduction of 4-Nitrophenol (4-NP) to 4-Aminophenol (4-AP) was measured through the UV-Vis spectra, as shown in **Figure 4-31**, as the mixture containing 4-NP has a bright yellow color detectable from a distinct 400nm peak, by adding in the mixture NaBH4 and the BFO materials under constant temperature, from the passage of time the 4-NP is reduced as it is observed the 400nm peak is decreased, with the 300nm peak increases that correspond to the 4-AP [292], thus the color shifts from the bright yellow to a transparent solution at the complete reduction of 4-NP.

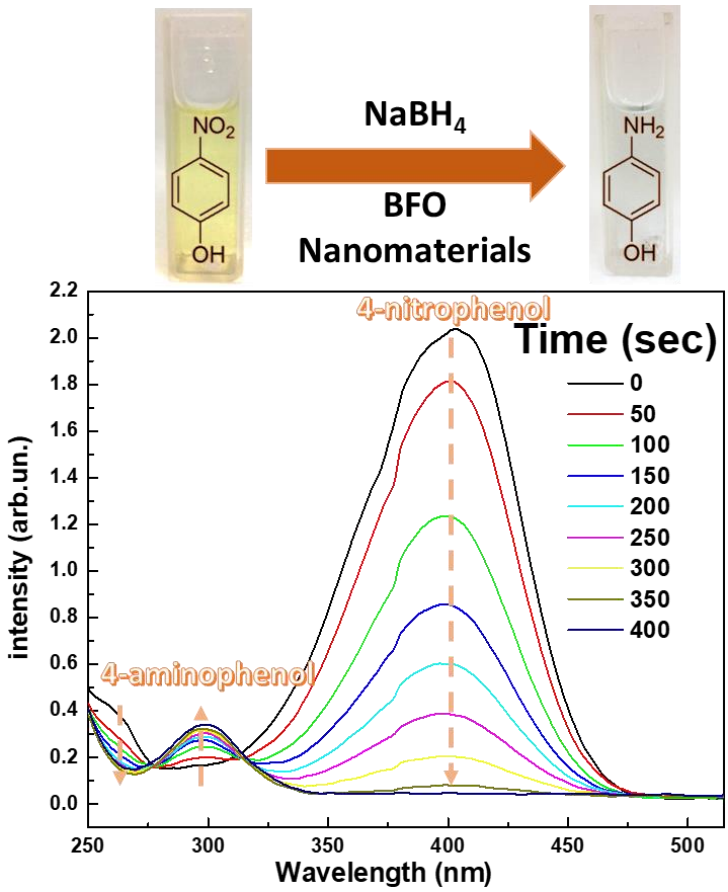

Figure 4-31: *UV-Vis measurement of the reduction of 4-NP to 4-AP at a constant temperature. At the top of the graph is the reaction mixture, with the color changing from yellow to transparent at the end of the reaction.*

The $NaBH_4$ concentration was included in excess as dictated by the catalysis compared to the concentration of 4-NP. For this reason, the reduction of 4-NP by the BFO nanomaterials is considered to be a pseudo-first-order. The first-order rate constants derived from the linear fit from the first reduction data, for each material of the four BFO materials, the reaction took place in four different temperatures 5°C, 15°C, 25°C, and 35 °C. The data are plotted as ln (A_t /A_0) versus time, where A_0 is the initial concentration of 4-NP and A_t after reaction time t from the absorbance intensity of 4-NP at 400 nm from UV-Vis, with the overall data shown in **Figure 4-32**. The calculated rate constants for each material calculated from the linear fit are shown in **Table 4-10**.

Table 4-10: *The rate constant of the four materials for the temperatures 5°C, 15°C, 25°C and 35 °C, including activation energy E_a of the particles.*

Material	Rate constant (10^{-3} s^{-1})				E_a (kJ mol^{-1})
	5 °C	15 °C	25 °C	35 °C	
BFO1	7.5 ±0.4	9.2 ±0.5	15 ±2	19 ±2	22 ±3
BFO2	5 ±0.2	8.5 ±0.7	14 ±2	17 ±3	30 ±3
BFO3	1.9 ±0.1	3.8 ±0.2	4.9 ±0.3	7.7 ±0.3	31 ±4
BFO4	0.8 ±0.02	1.5 ±0.06	2.3 ±0.09	3.6 ±0.2	36 ±2

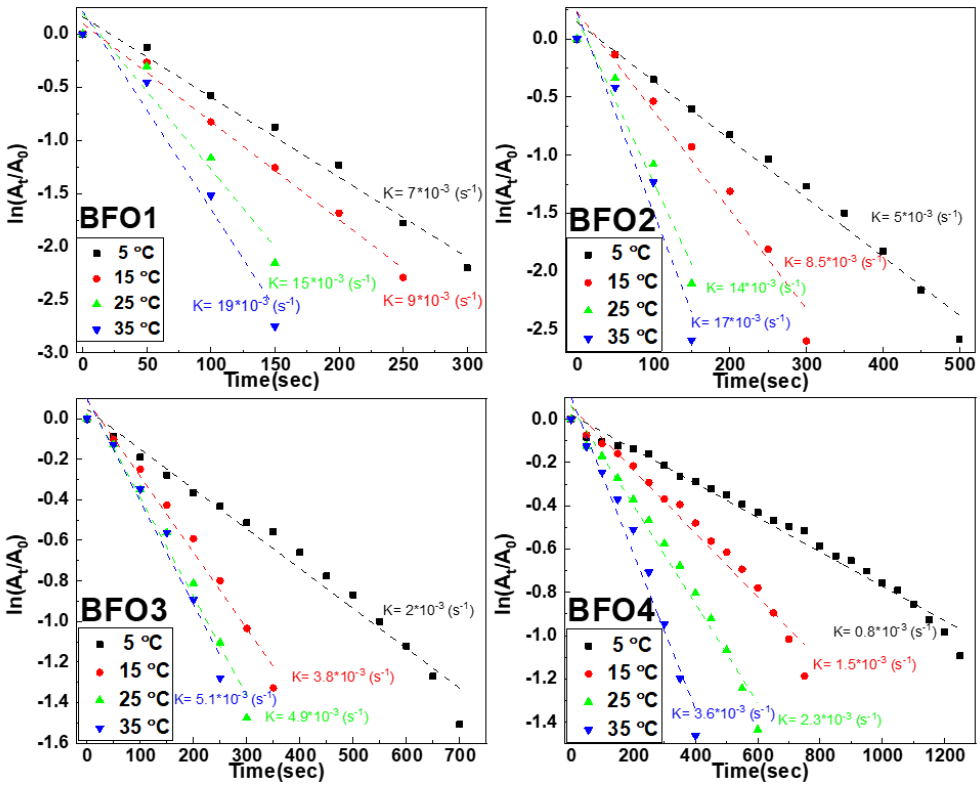

Figure 4-32: *The kinetic data of the four BFO materials for the reduction of 4-NP, with $NaBH_4$ as the reducing agent, by four different temperatures 5, 15, 25, and 35 °C.*

The results of the Rate constants show a direct correlation with the phase percentages of $BiFeO_3$ and $Bi_2Fe_4O_9$. As the $BiFeO_3$ changes to $Bi_2Fe_4O_9$, a sharp decrease in

the reduction rate is observed, with the particle BFO1(100% $BiFeO_3$) requiring only 200 seconds for a complete reduction, while the BFO4(100% $Bi_2Fe_4O_9$) requires at least 900 seconds.

To have a precise control experiment, the experiment at the highest temperature 35 °C was conducted without any nanomaterials, **Figure 4-33**. As observed, catalysis without any materials is incredibly inefficient. For this reason, the non-material reduction is considered negligible, thus nanomaterials are the catalyst that drives the reduction of 4-NP.

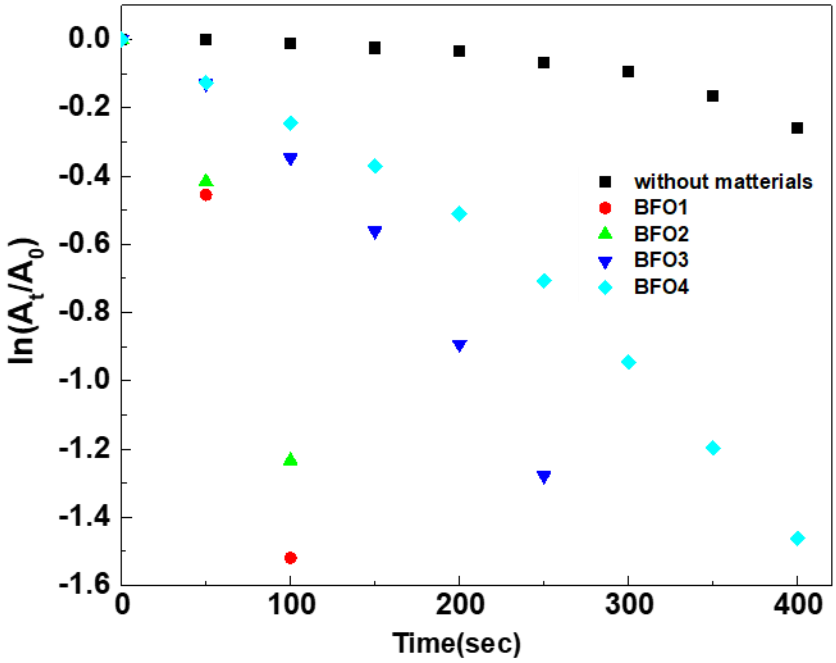

Figure 4-33: *Kinetic data for reduction of 4-NP to 4-AP, without any nanomaterial, with $NaBH_4$ as the reducing agent, at 35 °C temperature.*

Due to the higher calcination temperatures of the BFO4 compared to the BFO1, the SSA has a very high difference of three times. For these reasons, another test experiment was conducted, increasing the concentration of particles three times for the BFO4 material (from 75uL to 225uL volume in the quartz cuvette), while the BFO1 had a decrease in the concentration by three times (from 75uL to 25uL), at temperature 25 °C. As seen in **Figure 4-34**, the expected result of a decrease in catalytic activity occurred for BFO1 almost exactly three times from 15 10^{-3} s^{-1} to 5.1 10^{-3} s^{-1}. At the same time, for the BFO4 the increase was marginal compared to the increase in concentration. With these results, for

comparatively the same surface area, the two particles still have very different catalytic activities, even with an equivalent three times higher surface area (225uL BFO4 in comparison to 75uL BFO1), thus proving that the $BiFeO_3$ phase is more effective than the $Bi_2Fe_4O_9$ phase in 4-NP reduction.

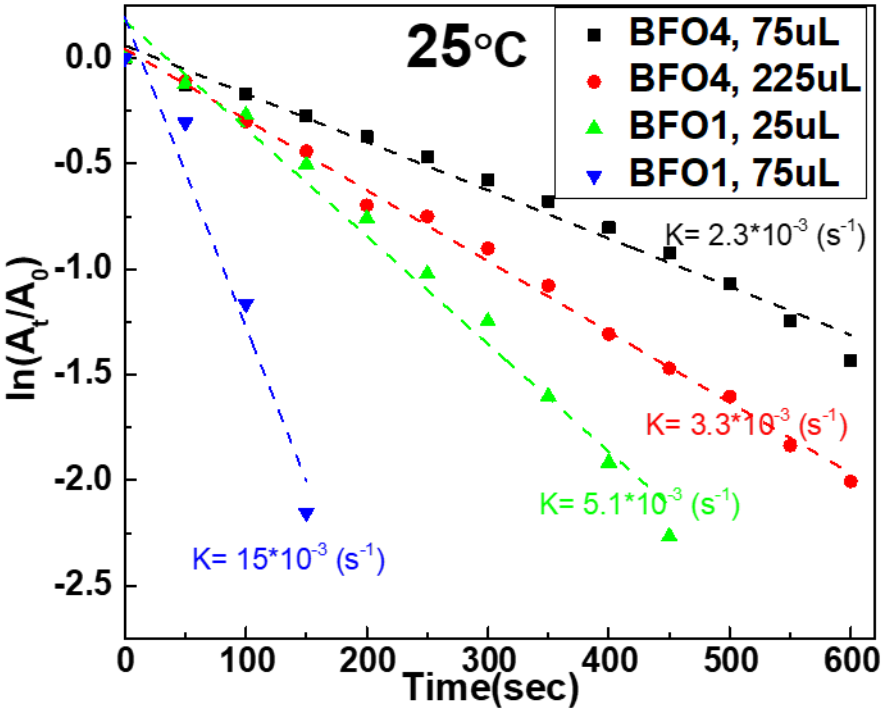

Figure 4-34: *Kinetic data for reduction of 4-NP to 4-AP, with different materials volumes 25, 75, 225uL, meaning different concentrations of the two materials BFO1 and BFO4, in order to compare the SSA influence of the two materials.*

A thermodynamic approach was implemented to better explain the catalytic trends of the materials, with the first-order rate constants K as calculated from the linear fits and already calculated in **Table 4-10**. The rate constant for all materials increases with the increased temperature, as expected for this kind of catalysis that relies on charge transfers. Although most interestingly, the results stay consistent for the four materials, with the highest activity in all temperatures belonging to BFO1, and decreasing with the concentration of $Bi_2Fe_4O_9$, BFO1>BFO2>BFO3>BFO4.

As seen in Equation 4-1 [323], the Arrhenius formula was implemented to calculate the activation energy Ea obtained for the first time in the bibliography for $BiFeO_3$ / $Bi_2Fe_4O_9$. The variables are as follows, R is the ideal gas constant 8.314 J K^{-1} mol^{-1}, and C is a fittable constant. Additional plots were produced with the X axis as 1/T and the Y axis as ln(k) with k as the rate constant for each temperature, as shown in **Figure 4-35**. According to the equation, the slope of the graph produces $-E_a/R$, which is estimated from the linear fit. Thus we derived the activation energy value E_a for each BFO material for the 4-NP reduction. The results are shown in **Figure 4-35** and **Table 4-10**.

$$ln(k) = -\left(\frac{Ea}{R}\right) \times \left(\frac{1}{T}\right) + C \qquad \text{Equation 4-1}$$

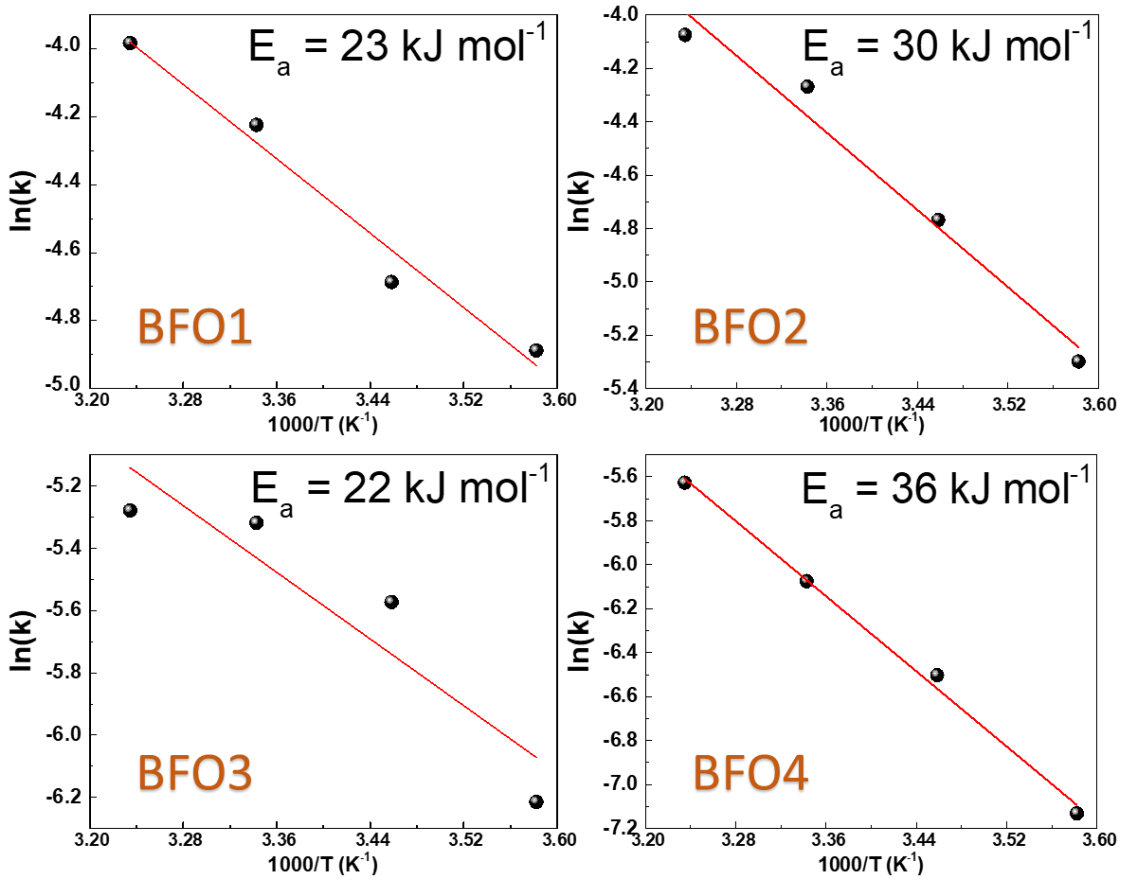

Figure 4-35: *Arrhenius plot, lnk (k: rate constant) versus 1000/T (K^{-1}), with each material's calculated activation energy Ea.*

From the E_a data of the BFO materials, there are three crucial conclusions:

[a] The activation energy E_a for 4-NP reduction is much higher for the $Bi_2Fe_4O_9$ with an E_a= 36 kJ mol^{-1} in comparison to the perovskite phase $BiFeO_3$ with E_a= 22 kJ mol^{-1}.

[b] The activation energy of the materials BFO1 and BFO4 are linked with the rate constants of the reactions, with a lower activation energy producing a much higher rate constant.

[c] The mixed phase materials BFO3, BFO4, with the higher contend $Bi_2Fe_4O_9$ having a much more temperature dependent change E_a=22 kJ mol^{-1}, than the BFO3 with approximately (60% $BiFeO_3$, 40% $Bi_2Fe_4O_9$) at E_a=30 kJ mol^{-1}.

Table 4-11: *Literature comparison for catalytic 4-nitrophenol reduction for the BFO1 with similar $BiFeO_3$ particles and Fe_2O_3 – noble metal assisted materials.*

Catalyst	Initial 4-NP conc. (mmol L^{-1})	Catalyst Conc. (mg mL^{-1})	$NaBH_4$ Conc. (mmol L^{-1})	Rate constant (10^{-2} s^{-1})	E_a (kJ mol^{-1})	*Ref.*
BFO-Materials						
$BiFeO_3$	0.123	0.014	108	1.5	22	*This work*
$Bi_2Fe_4O_9$	0.123	0.014	108	0.23	36	
mesoporous $BiFeO_3$	0.1	1	5	1.8	Not reported	[342]
$BiFeO_3$-RGO	0.051	0.100	25	1.2	Not reported	[369]
NON-BFO (Fe-based materials)						
α-Fe_2O_3	0.087	0.333	54	2.7	Not reported	[370]
Fe_3O_4/graphene/Pd	1.85	1	5	6.1	Not reported	[371]
Fe_2O_3–Au spheres	0.146	x	6	0.84	180	[372]
Fe@Au–ATPGO	0.001	1.4	59	1.4	9.7	[373]

Comparison with Literature: **Table 4-11** has varied data for 4-NP reaction with other materials based on $BiFeO_3$ and other Fe-based materials compared to the FSP-made particles $BiFeO_3$ and $Bi_2Fe_4O_9$. To our knowledge, no studies described the $Bi_2Fe_4O_9$ phase for the reduction of nitrophenol. For the perovskite phase, Papadas *et al.* [368] produced mesoporous $BiFeO_3$ that showed the high reactivity of these materials, as well as Moitra *et al.* [369] produced $BiFeO_3$-RGO materials, as shown they have similar Rate constants, but the particle concentration required is 10 times higher.

At the time of this work's publication, to our knowledge, there wasn't any other publication detailing the activation energy for $BiFeO_3$ and $Bi_2Fe_4O_9$. In order to have a proper comparison of Iron-based particles with noble metals as they are the driving force for these kinds of catalysis [370],[371],[372],[373]. The activation energy can fluctuate from 180 kJ mol^{-1} [372] to 9.7 kJ mol^{-1} [373], in comparison to our materials as well as the rate constants, showing again a much higher concentration for the reduction process.

4.3.6 Insights into the 4-NP catalytic mechanism

To better understand the effect of the rate constants and the activation energies, a study was conducted on the interfacial interaction of the nanomaterial surfaces compared to the 4-NP. The 4-NP interfacial interaction was accomplished first by comparing FTIR measurements for the anchoring of 4-NP on the surface of the two materials and secondly with adsorption isotherms of 4-NP.

FT-IR data for BFO 4-NP adsorption: The FTIR spectra for the 4-NP adsorbed on BFO materials are shown in **Figure 4-36**. Reference 4-NP is first measured, which has at 1346 and 1515 cm^{-1} strong bands of stretching vibrations of anti-symmetric NO_2. The second significant peak is assigned to the phenol aromatic ring's C=C stretching vibrations at 1588 and 1620 cm^{-1} [374]. The peaks are in agreement with the literature and are demonstrated as lines in the FT-IR graph. The BFO materials that had 4-NP adsorbed on their surface showed distinct shifts from these two distinct peaks, with a downshift happening upon adsorption corresponding to the strong or weak interaction between the NO_2 group of 4-NP and the BFO materials surface.

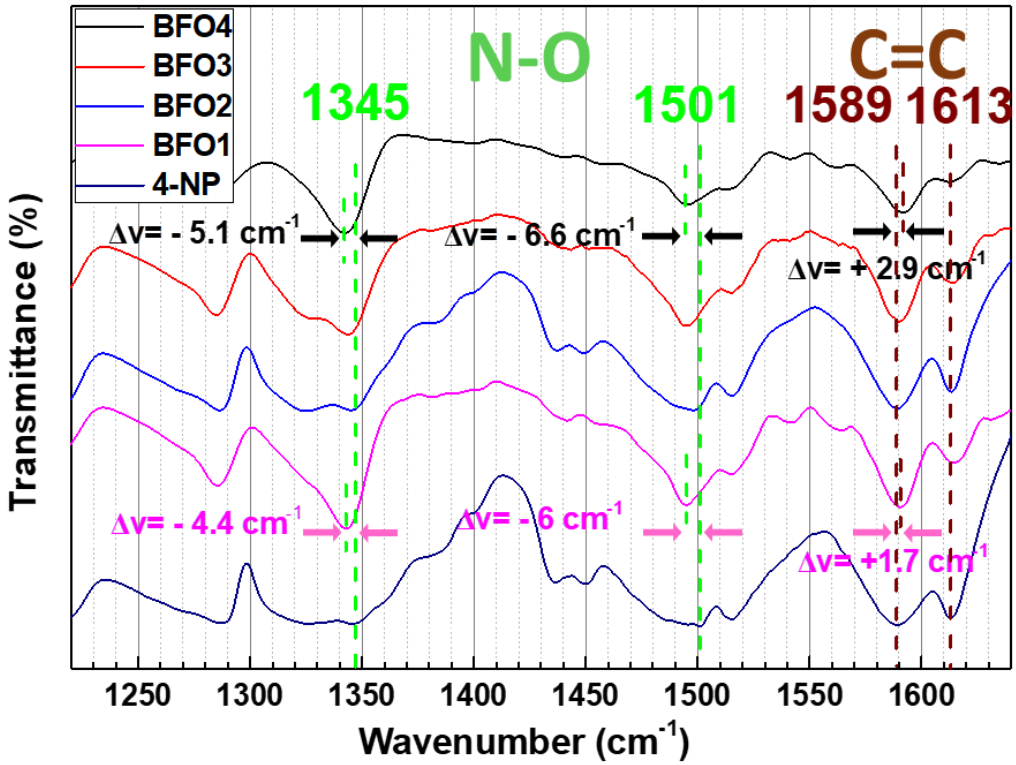

Figure 4-36: *FTIR spectra for the reference 4-NP and BFO materials with 4-NP adsorption. The N-O bond and C=C of 4-NP are depicted with separate lines.*

A clear difference is observed between the various BFO materials for the FT-IR shift from the 4-NP peaks. First, for the interaction with the NO_2 group of 4-NP having a downshift of $\Delta\nu$ = -6 cm^{-1} and $\Delta\nu$ = -6.6 cm^{-1} for $BiFeO_3$ and $Bi_2Fe_4O_9$ respectively, meaning a stronger interaction of the nitro group with the $Bi_2Fe_4O_9$ particles compared to the $BiFeO_3$. Secondly, the interaction between the phenol-ring C=C and the materials shows an upshift of $\Delta\nu$ = 1.7cm^{-1} and $\Delta\nu$ =2.9cm^{-1} for the adsorbed $BiFeO_3$ and $Bi_2Fe_4O_9$, respectively. However, there wasn't any significant shift for the 1613cm^{-1} band, with overall much lower shifts for the phenol-ring C=C compared to the NO_2 group.

The FT-IR data determined three observations. [a] For both phases, $BiFeO_3$ and $Bi_2Fe_4O_9$, the 4-NP has a weak to moderate interaction, determined by the downshifts and upshifts of the NO_2 and p phenol-ring C=C, respectively. [b] While the adsorption from the NO_2 group is much higher in comparison to the phenyl ring. [c] $Bi_2Fe_4O_9$ phase interacts more strongly than the $BiFeO_3$ phase on the surface with 4-NP.

4-NP Adsorption isotherms: 4-NP adsorption isotherms are shown in **Figure 4-37**, for the $Bi_2Fe_4O_9$ and $BiFeO_3$ phases, as found from the BFO1, BFO2, and BFO4 materials. The adsorption isotherms measurement determines that the $Bi_2Fe_4O_9$ phase has a stronger binding capacity of 4-NP than $BiFeO_3$, with the equivalent uptake capacity [293,375] for pH 7.5 at q_m= 24, 26, and 34 μmol g^{-1} for the BFO1, BFO2, and BFO4 respectively. Taking into account the SSA and q_m values, the adsorption-surface density of 4-NPs is calculated to be ~1.4 4-NP per $(nm)^2$ for BFO1 ($BiFeO_3$) in comparison to ~6 4-NP per $(nm)^2$ in $Bi_2Fe_4O_9$.

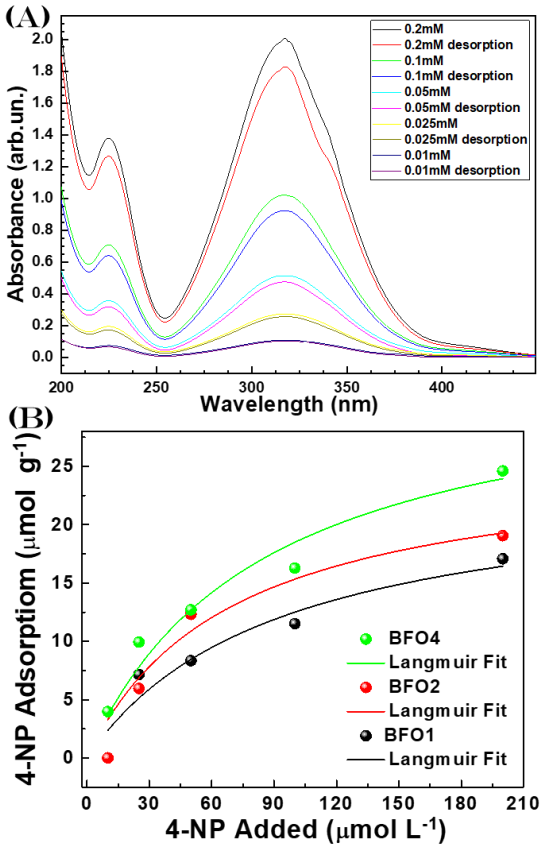

Figure 4-37: *(A) Uv-vis spectra for 4-NP at different concentrations from 0.2M to 0.01M before and after the deposition on BFO1 resulted in adsorption. (B) Isotherm of 4-NP adsorption into (●) BFO1, (●) BFO2, and (●) BFO4 at room temperature: Solid symbols (●/●/●): experimental data. The solid line (—/—/—): theoretical fit.*

The data obtained from the FT-IR measurement and the adsorption data analysis show that 4-NP molecules have a much higher bonded strength on the surface of the $Bi_2Fe_4O_9$ phase than that of $BiFeO_3$. Overall showing that there is an inverse correlation between 4-NP adsorption and the activation energy E_a. As stated by Pozun et al. [376], the interaction between the substrate (4-NP) and the catalyst(BFO materials) should follow a volcano curve, where the bond should be neither too strong nor too weak for the optimal catalytic kinetics/efficiency [376,377]. From the catalytic efficiency, we determine that the optimal bonding strength of the catalyst/substrate is found with the $BiFeO_3$ phase, as found from the smaller E_a compared to the $Bi_2Fe_4O_9$ phase.

4.3.7 Conclusions of 4-NP catalytic by BFO materials

[a] First time synthesis via the scalable Flame-Spray-Pyrolysis method for the 100% pure perovskite $BiFeO_3$, the mullite-type $Bi_2Fe_4O_9$, as well as their mixed-phase heterostructures.

[b] Based on PXRD, FT-IR, Raman, and XPS data, all the produced materials are devoid of secondary Bismuth oxide or Iron oxide phases.

[c] From the catalytic efficiency from the reduction of 4-Nitrophenol to 4-Aminophenol for the four materials, it was determined that the $BiFeO_3$ has a consistently much higher Rate constant than the $Bi_2Fe_4O_9$ in all temperatures and under similar SSA measurements. The Arrhenius analysis determined that the $BiFeO_3$/4-NP system has a much lower activation energy than $Bi_2Fe_4O_9$ i.e. 22 kJ mol^{-1} vs 36 kJ mol^{-1}. The results are comparable to other $BiFeO_3$ and iron-based/noble metals materials with much lower nanomaterial concentrations required.

[d] Through FTIR and adsorption isotherms of the $BiFeO_3$ and $Bi_2Fe_4O_9$, an inverse correlation was found between the Ea values with the interfacial 4-NP adsorption strength.

4.4 *BiFeO$_3$/Bi$_2$Fe$_4$O$_9$ particles for Oxygen Evolution Reaction*

4.4.1 Aims of BiFeO$_3$/Bi$_2$Fe$_4$O$_9$ for Oxygen Evolution Reaction

For the second perovskite Bi-Fe-O-based research, the research involved heavily on the post-FSP synthesis step of annealing, which was only briefly explored in our previous work recent work [224]. However, it profoundly impacts the structural integrity of the phases, as shown in **Figure 4-38**. The materials were employed for the much more challenging catalytic application of Oxygen evolution reaction (OER), the photocatalytic O_2-evolution from H_2O, and the annealing temperature as well as the annealing residence time showed a drastic change in the photocatalytic OER-efficiency of the BFO materials. To understand the underlying mechanisms, we have used a combination of XRD, XPS, Raman, and EPR spectroscopies for a comprehensive study of the OER efficiency *vs.* the lattice and electronic configuration of the perovskite phase $BiFeO_3$ (100%), mullite-type $Bi_2Fe_4O_9$ (100%) and a mixed-phase $BiFeO_3/Bi_2Fe_4O_9$ (50%/50%) material.

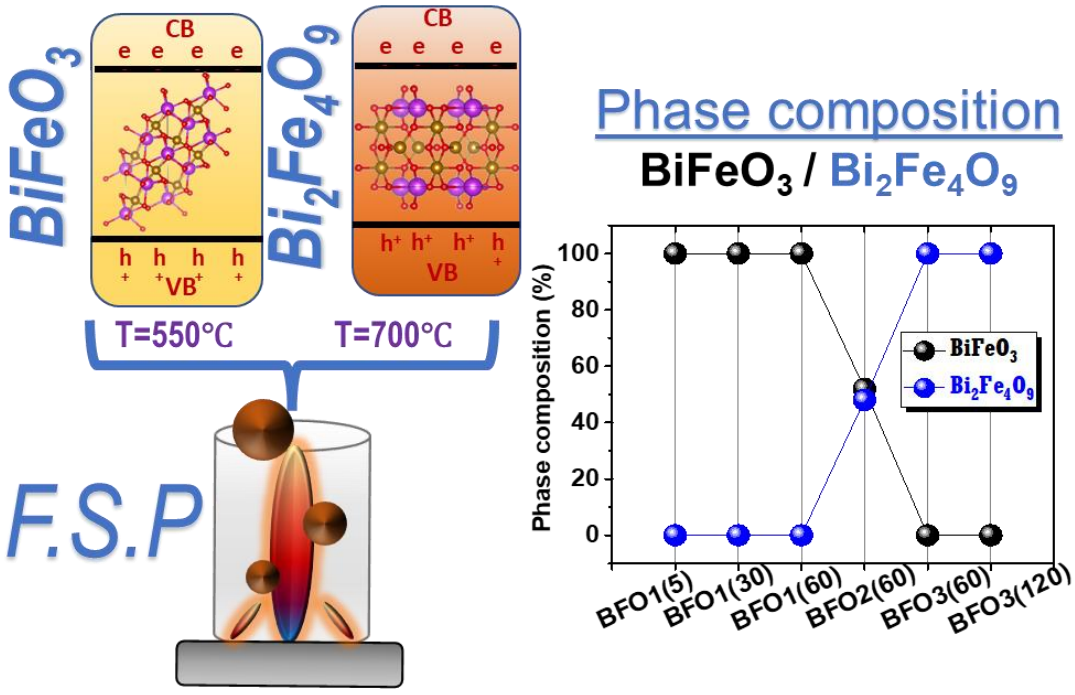

Figure 4-38: *FSP synthesis with different annealing temperatures and times for the production of pure phase BiFeO$_3$, Bi$_2$Fe$_4$O$_9$, and BiFeO$_3$/Bi$_2$Fe$_4$O$_9$ heterostructure.*

The results shown herein, for each BFO nanophase was annealed under O_2-atmosphere for various short or long periods and temperatures with drastic morphological results, even for a very short time such as 5-minutes, impact the photoactivity of the $BiFeO_3$ and $Bi_2Fe_4O_9$ in distinct ways. (1) At the very low annealing period of 5 minutes, the $BiFeO_3$ materials had Fe^{2+}-centers in the crystal structures. These Fe^{2+}-centers can enhance OER efficiency. (2) For the mullite type $Bi_2Fe_4O_9$, the phase is vulnerable to solid-melt formation, which was a limiting factor in its photoactivity, as the efficiency plummeted after 120 minutes of annealing.

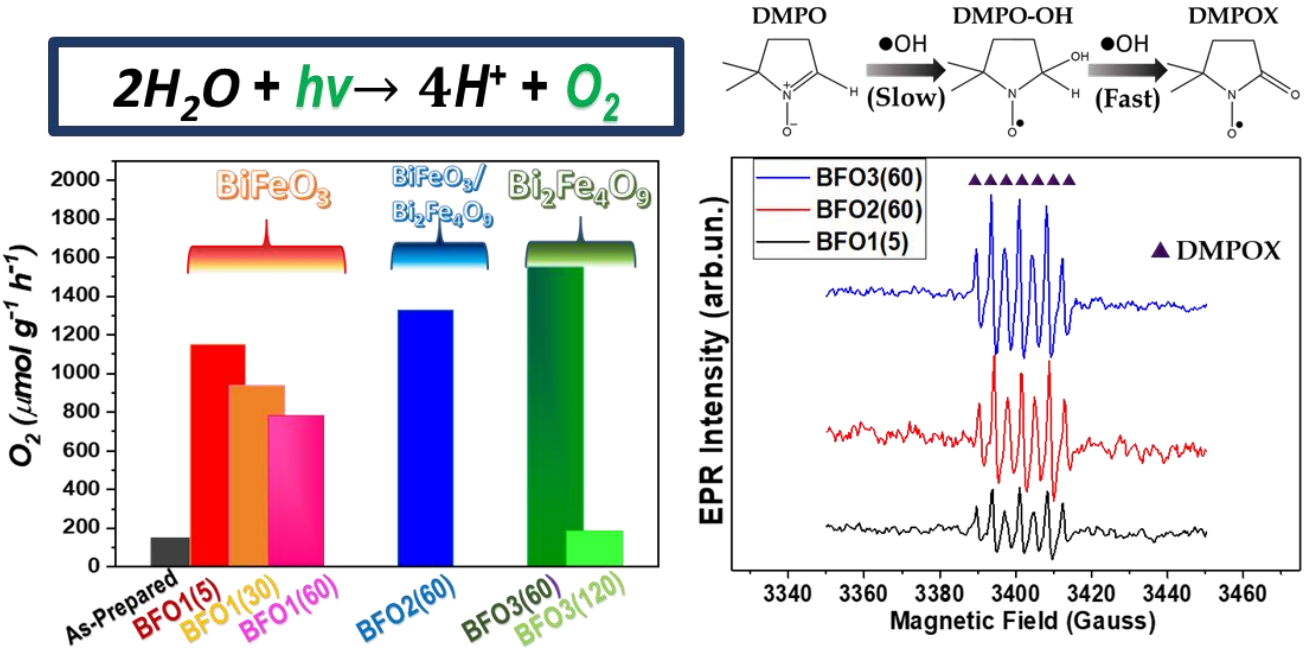

Figure 4-39: *The graphical abstract of $BiFeO_3/Bi_2Fe_4O_9$ particles from FSP synthesis, in accordance with different annealing temperatures and times resulting in drastic changes in the photocatalytic production of oxygen and OH radicals.*

Technology-wise, the present work shows that through the scalable FSP method, with diligent control of the FSP parameters combined with short post-FSP annealing, the resulting BFO nanoparticles can have controlled phase/size and defects to achieve highly efficient O_2 evolving photocatalyst [169,175]. Moreover, the present research data reveal -

for the first time in literature- that the optimized mullite-$Bi_2Fe_4O_9$ phase is a highly efficient OER photocatalyst overperforming the established $BiFeO_3$. Combined with the EPR to detect the kinetics of OH radicals, while through a DFT study for the energy level profile of the BFO phases with Fe^{2+}-centers defects, present a solid underlying mechanism for the efficiency of O_2 production from H_2O.

The experimental results of $BiFeO_3$ *vs.* $Bi_2Fe_4O_9$ for the OER production of oxygen have been published in our work for the Journal of Energies [223], with the graphical abstract shown in **Figure 4-39**.

4.4.2 FSP synthesis of the selected $BiFeO_3$/$Bi_2Fe_4O_9$ for OER

As mentioned in the previous section, the BFO nanomaterials were produced in a single-nozzle FSP reactor [224]. To briefly summarize, the stock solutions contained Fe(III) acetylacetonate (97% Aldrich) dissolved in xylene and Bismuth(III) acetate (99.99% Aldrich) dissolved in 2-Ethylhexanoic acid (EHA). The precursor solution for the production of the $BiFeO_3$ phase had a molar ratio of [50:50] with [Fe]=0.1M and [Bi]=0.1M, while for the production of $Bi_2Fe_4O_9$ phase, the molar ratio of [66:33] [Fe]=0.134M, [Bi] =0.066M. For all the materials, the total concentration was set to [Fe]+[Bi]=0.2M, and the solvents [xylene: EHA] volume ratio was [50: 50]. The FSP parameters comprised of a precursor flow rate of 3 mL min^{-1} and a dispersion oxygen flow rate of 7 L min^{-1} (Linde 99.999%). The flame was enclosed with two metallic tubes with a total of 44 cm in height. The produced nanomaterials were stored in glass vials under an inert Argon atmosphere.

Post-FSP annealing: Post-FSP annealing was performed in a Thermawatt furnace, where a standard mass of 100 mg of nanomaterial was inserted in the tubular compartment under atmospheric O_2. The FSP-prepared BFO material showed poor crystallinity without the expected $BiFeO_3$ or $Bi_2Fe_4O_9$ phases. The short residence time of the particles in our FSP reactor, which is in the order of milliseconds [169,175], does not allow total growth of the desired perovskite crystal structure. Thus, a post-FSP annealing step is necessary for the Bi-based materials to obtain fully crystalline particles [224].

The obtained FSP-produced nanopowder was found to have phase transitions occur at temperatures ~130°C lower [224], i.e. from amorphous to $BiFeO_3$ than in bulk Bi-Fe-O materials [378]. Herein several screening experiments, we have found that post-FSP periods of t_{anneal}=5, 30, 60, and 120 minutes and T_{anneal}=550-700°C values allowed us to span the appropriate phase-transitions in conjunction with the photocatalytic performance. The results found that the lowest annealing periods drastically affected the photocatalytic performance of $BiFeO_3$ and the $Bi_2Fe_4O_9$ phase.

Codenames of the BFO materials for OER: Three materials were focused more heavily on the final results, BFO1 which had a Fe-Bi molar ratio of [50:50] directed for the $BiFeO_3$ phase, BFO2 and BFO3 had a Fe-Bi molar ratio of [66:33] directed for the $Bi_2Fe_4O_9$ phase and the mixed $BiFeO_3/Bi_2Fe_4O_9$, as shown in **Table 4-12**. The second parameters that are intrinsic to the materials are the annealing temperatures(T_{anneal}), with the BFO1 having 550 ^{0}C T_{anneal}, BFO2 having 625 ^{0}C T_{anneal}, and finally, BFO3 having 700 ^{0}C T_{anneal}. The final parameter is the annealing time (t_{anneal}), with each material having the annealing time in the codename i.e. BFO(t_{anneal}). For the BFO1/ $BiFeO_3$ phase having the selected 5, 30, 60 min t_{anneal}, BFO2 with mixed $BiFeO_3/Bi_2Fe_4O_9$ at 60 min t_{anneal}, BFO3/$Bi_2Fe_4O_9$ at 60 and 120min t_{anneal}.

Table 4-12: *Structural Characteristics of the FSP-made BFO materials for OER photocatalysis.*

Photocatalyst	Annealing T/time (°C)/(Min)	%Crystalline phase fraction		crystallite size (nm)		SSA (m^2g^{-1})	Total pore volume ($cm^3\ g^{-1}$)	Band gap E_g (eV)
		$BiFeO_3$	$Bi_2Fe_4O_9$	d_{BET}	d_{TEM}			
BFO1(5)	550/5	100	0	48	55	14.1	4.01×10^{-2}	2.1
BFO1(30)	550/30	100	0	64	-	12.1	2.83×10^{-2}	2.1
BFO1(60)	550/60	100	0	67	-	10.7	2.81×10^{-2}	2.1
BFO2(60)	625/60	52	48	75	130	9.5	2.11×10^{-2}	2.08
BFO3(60)	700/60	0	100	268	240	2.7	0.56×10^{-2}	2.05/1.55
BFO3(120)	700/120	0	100	336	-	2.1	0.46×10^{-2}	2.05/1.55

4.4.3 Phase purity and characterization of selected $BiFeO_3/Bi_2Fe_4O_9$ for OER

In order to gain insight into the relation of the BFO structures *vs.* the photocatalytic performance, we focus on pure phase $BiFeO_3$ & $Bi_2Fe_4O_9$ with varying degrees of crystallinity, quality, and defects. **Table 4-12** provides the complete set of all pertinent structures produced by the controlled [T_{anneal}, t_{anneal}] protocols.

XRD, BET, and TEM for crystal structure and morphology: According to the resulting data from XRD, as shown in **Figure 4-40**, the material BFO1(5) obtained for T_{anneal}=550°C/t_{anneal}=5 min material possesses the characteristic XRD peaks of the perovskite structure of the $BiFeO_3$ with an R3c space group [379], and the most distinct Miller planes {012}, {104}, {110}. The BFO3(60) material obtained at T_{anneal}=700°C/t_{anneal}=60 min exhibits high-quality diffraction peaks of the orthorhombic-$Bi_2Fe_4O_9$ P*bam* structure [380] with prominent peaks at distinct Miller planes {001}, {121}, {211}, {130}. It is underlined that a lower annealing period of 60 min or lower temperatures of 700°C resulted in mixed-phase $Bi_2Fe_4O_9/BiFeO_3$ with increasing concentration of $BiFeO_3$, thus the minimal required to achieve 100% pure $Bi_2Fe_4O_9$ phase was 700°C and 60 min.

The material BFO2(60), which is expected to produce a $BiFeO_3/Bi_2Fe_4O_9$ heterostructure, has been obtained by post-FSP annealing T_{anneal}=625°C/t_{anneal}=60min. To accurately measure the phase percentages, a Rietveld-XRD analysis was employed for the material BFO2(60), as shown in **Figure 4-41**(A), it determines that BFO2(60) consists of 52% $BiFeO_3$/48% $Bi_2Fe_4O_9$ phases. Thus, BFO2(60) represents a ~1:1 heterojunction of $BiFeO_3$: $Bi_2Fe_4O_9$. Thus, with a similar Rietveld-XRD analysis, the *$BiFeO_3/Bi_2Fe_4O_9$* phase composition of the three most important materials is shown in **Figure 4-41**(B).

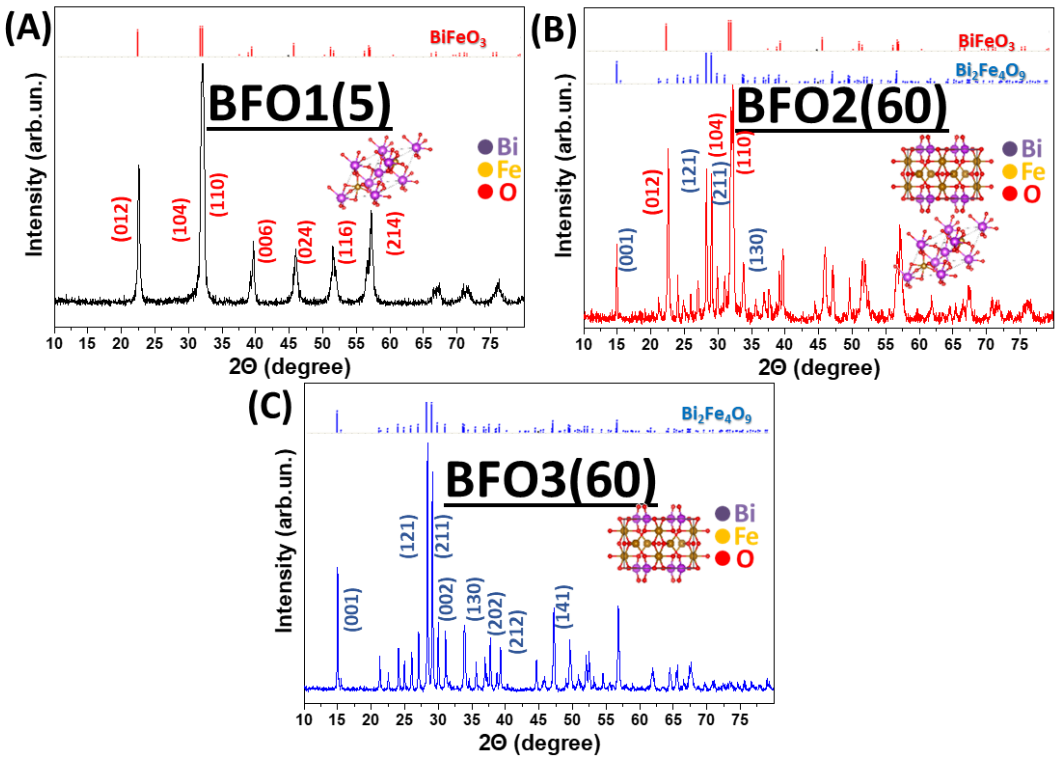

Figure 4-40: *XRD patterns for the (A) BFO1(5), (B) BFO2(60), and (C) BFO3(60) materials. The reference Miller-planes' reflections for $BiFeO_3$ and $Bi_2Fe_4O_9$ phases are shown at the graph's top.*

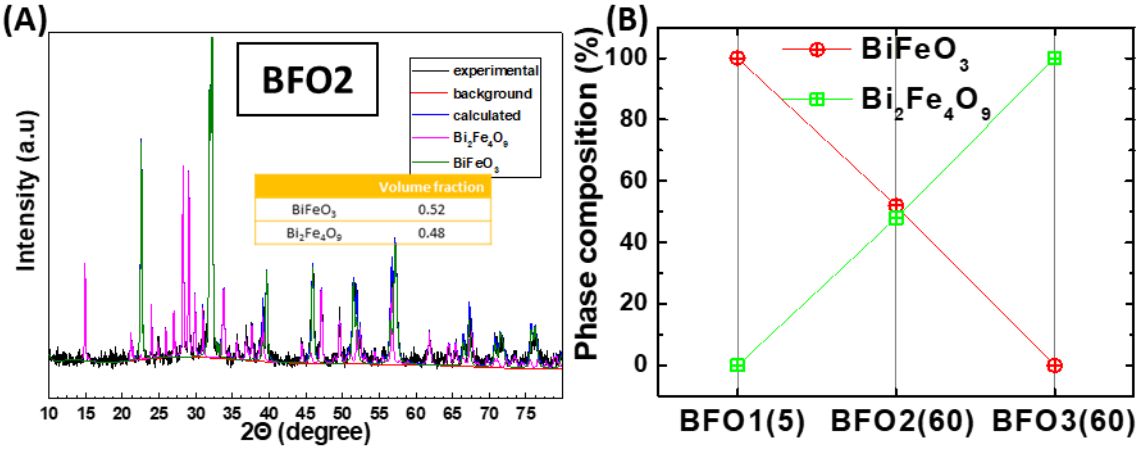

Figure 4-41: *(A) Volume fraction of the mixed-phase BFO2(60) nanocatalyst, calculated by Profex software. (B) $BiFeO_3$/$Bi_2Fe_4O_9$ phase composition of the* three materials *BFO1(5), BFO2(60), and BFO3(60).*

The XRD results at different t_{anneal} are shown in **Figure 4-42**. Overall, the XRD data for BFO reveal that the FSP-made BFO undergoes phase-evolutions from amorphous to $BiFeO_3$, and then to $Bi_2Fe_4O_9$. For the BFO1 Longer t_{anneal} resulted in sharper XRD diffraction peaks, indicating improved crystallinity of the $BiFeO_3$ phase [381]. In BFO1 or BFO2, at a given T_{anneal}, upon prolonged t_{anneal}, the particle crystallinity was increased. In contrast, the pure-$Bi_2Fe_4O_9$ nanophases showed a striking degradation in crystallinity at prolonged t_{anneal}=120 min, where BFO3(120) has much less sharp XRD peaks. The rapid decline of crystal quality was attributed to the formation of solid melt formation [224]. The solid melt formation for BFO3 can be better visualized in TEM measurement following later.

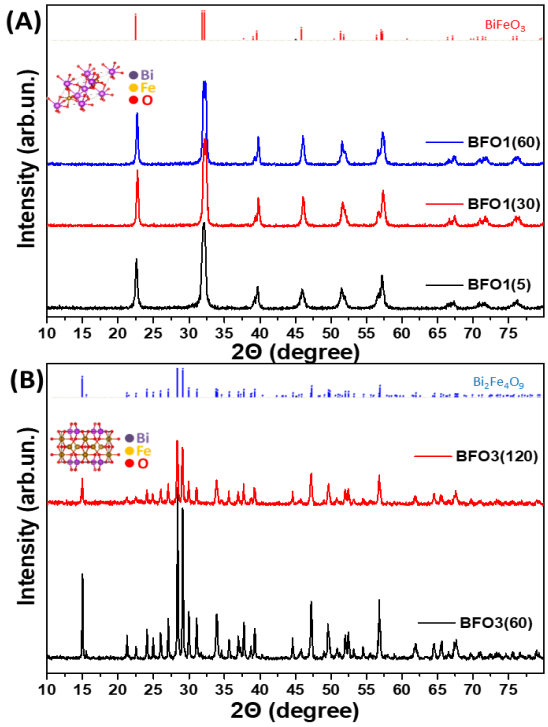

Figure 4-42: *XRD patterns of: (A) BFO1(5), BFO1(30), and BFO1(60) materials, calcinated at 550^{0}C ($BiFeO_3$ phase), (B) BFO3(60) and BFO3(120) calcinated at 700^{0}C ($Bi_2Fe_4O_9$ phase).*

It is underlined that, based on the Rietveld analysis of the XRD data, the particles were found to have only the pure phases of $BiFeO_3$/$Bi_2Fe_4O_9$, without characteristic peaks from

impurities or secondary phases, such as Bismuth-oxides and the more troubling $Bi_{25}FeO_{40}$ or Fe_2O_3 that are usually difficult to eliminate in solid-state or wet synthesis methods [382].

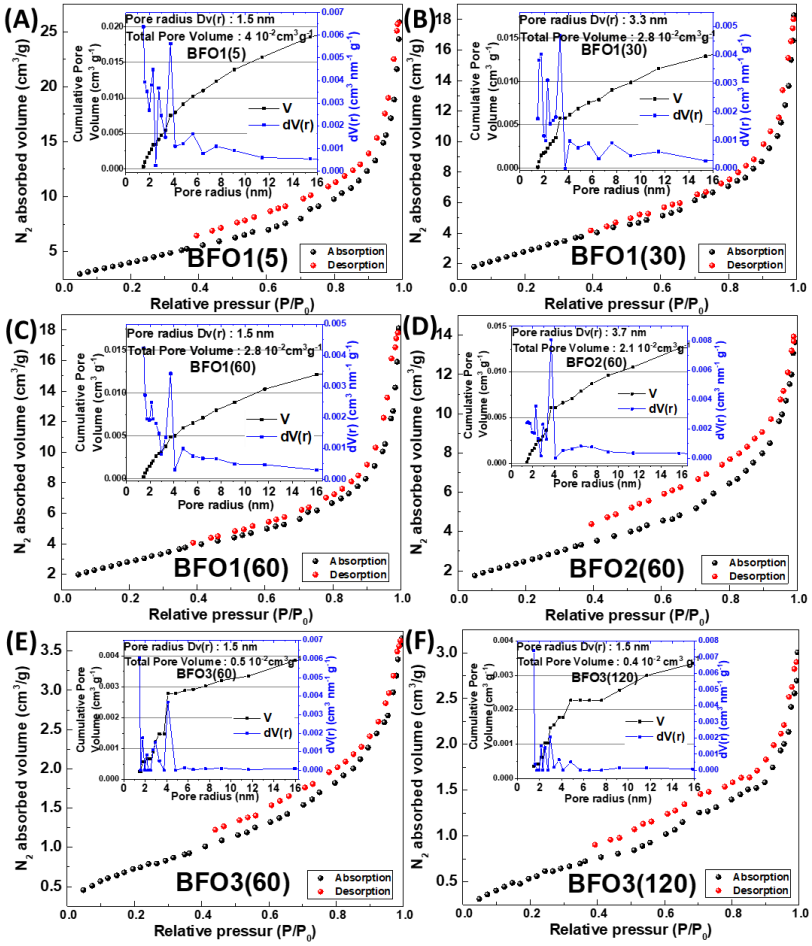

Figure 4-43: *N_2 adsorption-desorption isotherms for the annealing BFO materials: (A) BFO1(5), (B) BFO1(30), (C) BFO1(60), (D) BFO2(60), (E) BFO3(60), and (F) BFO3(120)* ***Inset****: Pore size distribution plot using the BJH method.*

The SSA analysis of the six different BFO materials for OER is shown in **Figure 4-43**(A), while the total pore volume of the materials is shown in **Figure 4-43**(B). The SSA was in direct correlation to the T_{anneal} and t_{anneal}, where the highest SSA was the BFO1(5) at 14.1 $m^2g^{-1,}$ which had the lowest T_{anneal} and t_{anneal}. With a longer annealing time, the SSA is reduced by almost ~30% from the BFO1(5) to BFO1(60) at 10.7 m^2g^{-1}. The requirements of partial solid melt and the high calcination requirements have the BFO3(60)/$Bi_2Fe_4O_9$ had

an SSA of 2.7 m^2g^{-1}, where additional annealing time had again an almost ~30% SSA decrease with BFO3(120) at 2.1 m^2g^{-1}. The total pore volume was in the range of 4.01×10^{-2} to 0.46×10^{-2} cm^3 g^{-1}, where the BFO1(5) has almost ten times higher total pore volume than BFO3(120). The d_{BET} was measured with the empirical equation, showing size results of 48 to 336nm. The phase composition of $BiFeO_3/Bi_2Fe_4O_9$ compared to the annealing parameters and the SSA is shown in **Figure 4-44**.

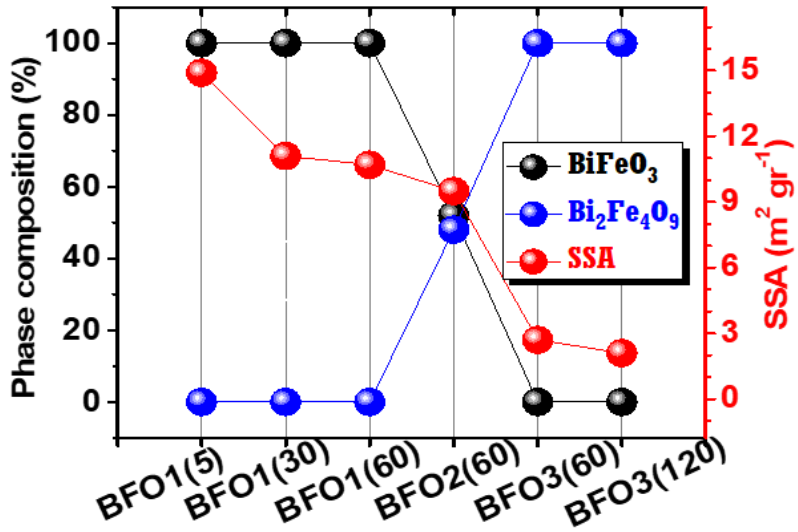

Figure 4-44: *Percentage of crystalline phases and SSA for the various annealing protocols.*

In the HRTEM images of the three pertinent BFO photocatalysts shown in **Figure 4-45**(A-C), the annealed materials appear to possess rod-like morphology with neck-sintering between neighboring particles, as observed previously in our previous work [224]. FSP-made Bi-based perovskites such as $BiVO_4$ nanoparticles [383] possess the same elongated rod-like morphology. The TEM size distribution, **Figure 4-45**(D-F), confirms the increase in particle size, upon the increase of T_{anneal} and t_{anneal}, all materials had a size distribution with a 30% span of the mean d_{TEM} value, with BFO1(5) at 55nm, BFO2(60) at 130nm, and BFO3(60) at 240nm, **Table 4-12**.

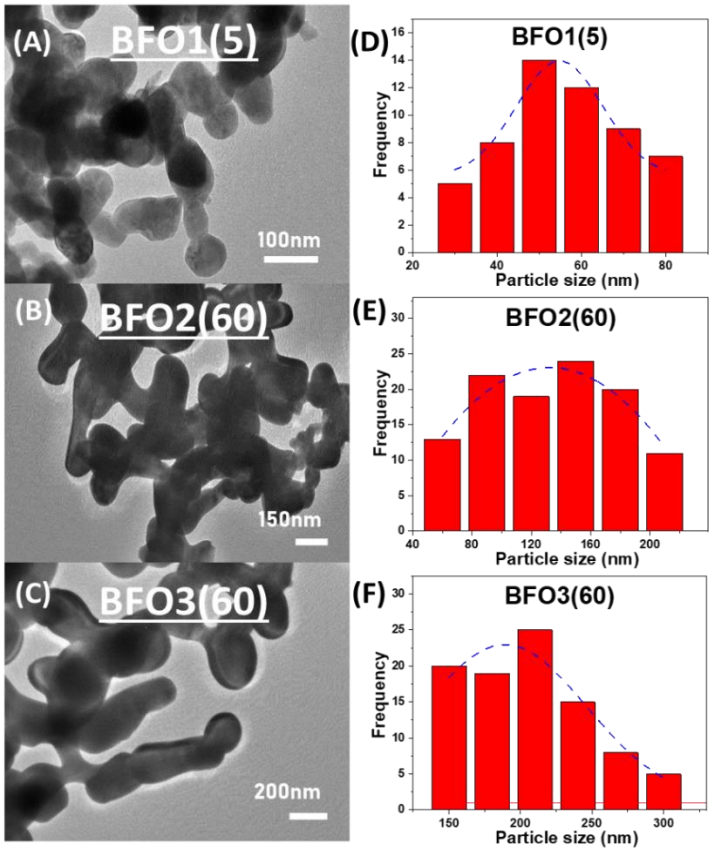

Figure 4-45: *HRTEM images of (A) BFO1(5), (B) BFO2(60), and (C) BFO3(60) and particle size distribution of (D) BFO1(5), (E) BFO2(60), and (F) BFO3(60). All materials show strong neck-sintered structures with elongated architectures, typical for many FSP-made Bi-based metal oxides.*

Diffuse Reflectance Uv-Vis Spectroscopy: All our BFO materials showed characteristic broad absorption from 200 nm to 600 nm, with maximum absorption in the visible wavelengths 400-480 nm, corresponding to their dark-brown colors, inset photo in **Figure 4-46**(A). By employing the Kübelka-Münk transformation, the Tauc plot was derived [327], **Figure 4-46**(B). In addition, a secondary transition was consistently observed for $Bi_2Fe_4O_9$, which is, the band gap of each material is discovered at the dashed arrow intersection. As the *p*-index signifies the direct or indirect band transitions in a semiconductor from the Tauc plot [384], with $p=2$ for indirect-band transition and $p=1/2$

for a direct-band transition, as there is not an explicit agreement in the literature for the phases $BiFeO_3$ and $Bi_2Fe_4O_9$ phases are direct or indirect [275], herein, we proceeded with the assumption of direct transitions for the two phases.

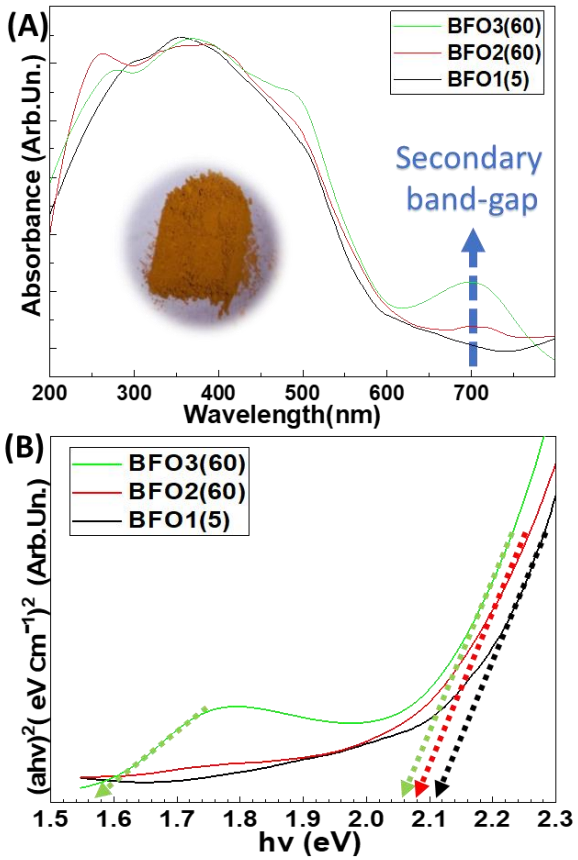

Figure 4-46: *(A) DRS-UV/Vis spectra of the three BFO materials for OER. Inset: the BFO3(60) powder color. (B) The Tauc plot of the three materials, with the dashed lines marking the estimated band gap.*

The direct bandgap of the perovskite phase $BiFeO_3$ has been reported to be in the range of 2.1-2.8 eV [275]. For the mullite-type $Bi_2Fe_4O_9$, E_g is expected in the range of 2.1 to 2.3eV [276]. Also, for the $Bi_2Fe_4O_9$, a secondary smaller bandgap of 1.6 eV [277], evident by the absorbance peak at ~700 nm, usually identified as an indirect transition, suggested to originate from the *d-d* transition of Fe atoms [385]. Our data agree with the literature, with

E_g=2.1 eV for BFO1(5), E_g=2.08 eV for BFO2(60), while the BFO3(60) has E_g=2.05 eV. The secondary bandgap of 1.6 eV is evidenced in the spectrum of BFO3(60).

All other FSP-made catalysts prepared for various t_{anneal} have E_g in the range 2.0-2.1eV, as shown in **Figure 4-47**. In the BFO2(60), this absorbance-hump at 700 nm is lower in accordance with the lower 48% content in $Bi_2Fe_4O_9$. The indirect transitions typically have lower absorbance cross-sections [59,384] since they require a transition of the photoactivated electron between energy states with different lattice-vector *k* [384] between different Brillouin zones. In the context of photocatalysis, an indirect transition can inhibit the recombination of the photoexcited e^-/h^+ pairs [59,384], improving photocatalytic performance.

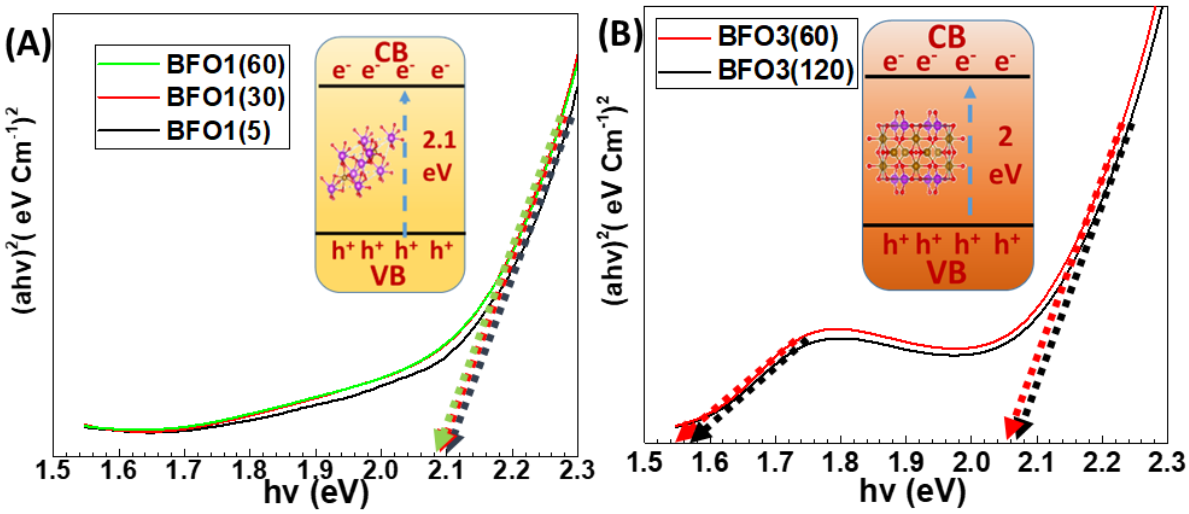

Figure 4-47: *Tauc plots of (A) BFO1(5), BFO1(30), BFO1(60) calcinated at 550°C, and (B) BFO3(60), BFO3(120) calcinated at 700°C.*

FT-IR and Raman Spectroscopy: For the three pertinent BFO materials, the FT-IR measurement is shown in **Figure 4-48**(A). The $BiFeO_3$ phase can be discerned from two characteristic peaks at 445 cm^{-1} and 557 cm^{-1} due to the Fe-O bond stretching and bending vibrations from octahedral FeO_6 groups of $BiFeO_3$ [386,387]. The $Bi_2Fe_4O_9$ phase has a more complex structure and it contains both octahedral FeO_6 and tetrahedral FeO_4 units [388], thus its FT-IR spectrum is characterized by several bands of lower intensity than $BiFeO_3$

[389]. We can identify the $Bi_2Fe_4O_9$ phase by focusing on the bands at 441 cm^{-1}, 609 cm^{-1}, and the more prevalent 814 cm^{-1}. The mixed-phase material BFO2(60) contains the characteristic peaks of both $BiFeO_3$ and $Bi_2Fe_4O_9$ phases, clearly observed from the characteristic peaks of 557 cm^{-1} ($BiFeO_3$) and 814 cm^{-1} ($Bi_2Fe_4O_9$), these findings corroborate the XRD results.

More importantly, the FTIR spectrum of BFO1(5) has additional peaks compared to the rest of the materials, with weak peaks around the 1250-1500 cm-1 range. These peaks are assigned to hydrocarbons in the material, as shown in the zoomed-in region of the FTIR spectra in **Figure 4-48**(B). The existence of hydrocarbons has been known to be due to incomplete combustion in the FSP synthesis [390], with very small quantities of remaining carbon remaining in the material, undetectable from the previous measurement. The calcination temperature is high enough to remove carbon content, although the small t_{anneal} of 5 min still leaves some hydrocarbons in the structure. These findings are significant since, as we will show in the XPS experiments, they can cause a reduction of surrounding Fe-centers in the material forming Fe^{2+} in BFO1(5).

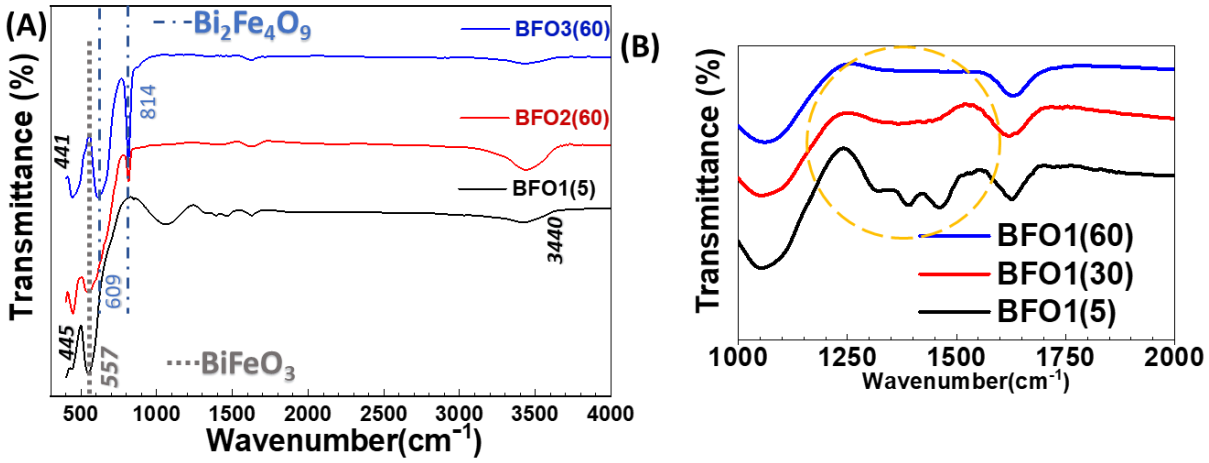

Figure 4-48: *FT-IR spectra of the three BFO materials for OER, (B) in the range 400 to 4000cm-1. (B) zoom into the hydrocarbon region 1000-2000 cm-1. The characteristic peaks that differentiate the two phases $BiFeO_3$ and $Bi_2Fe_4O_9$ are marked with dashed lines.*

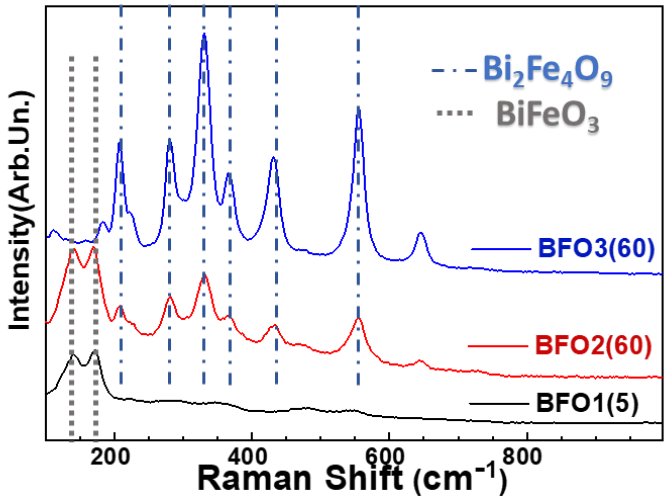

Figure 4-49: *Raman spectra of the three BFO materials for OER. The characteristic peaks that differentiate the two phases $BiFeO_3$ and $Bi_2Fe_4O_9$ are marked with dashed lines.*

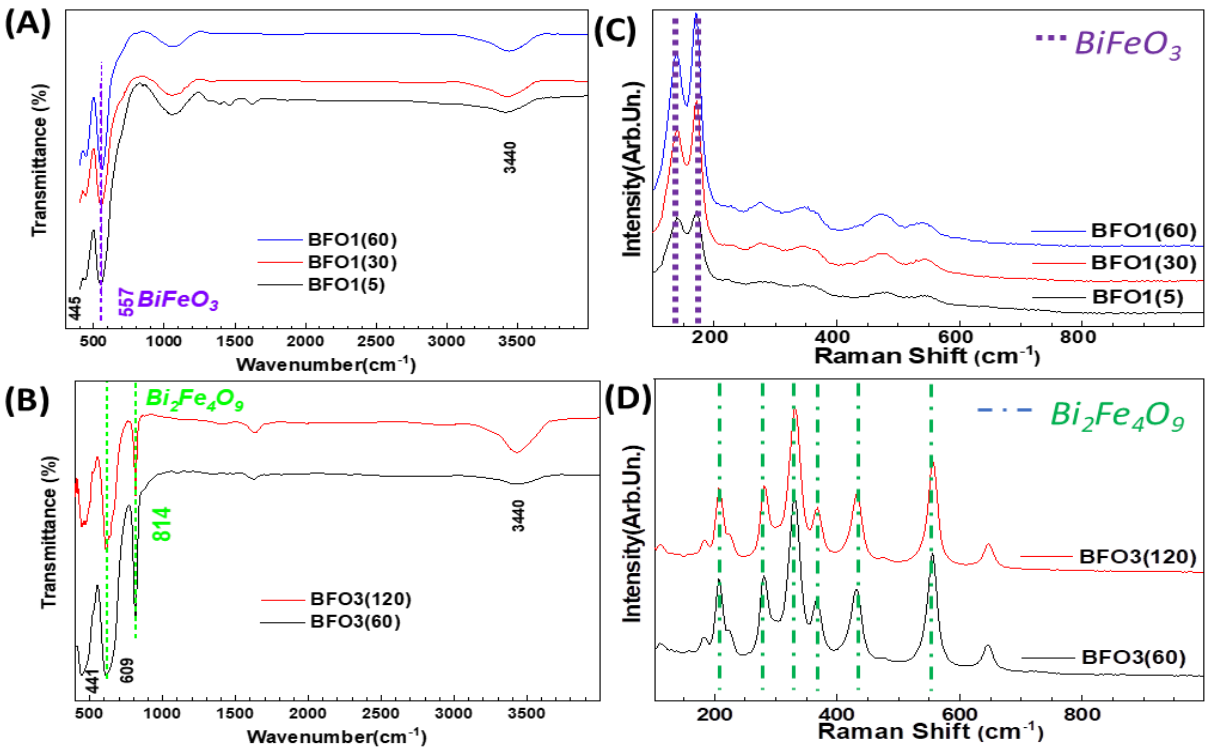

Figure 4-50: *FT-IR spectra of: (A) BFO1(5), BFO1(30), BFO1(60) calcinated at 550 °C, (B) BFO3(60) and BFO3(120) calcinated at 700 °C. Raman spectra of: (C) BFO1(5), BFO1(30), BFO1(60), (D) BFO3(60) and BFO3(120).*

The Raman measurements for the three pertinent BFO materials are shown in **Figure 4-49**. As examined in the previous chapter, the phase $BiFeO_3$ has two characteristic Raman peaks at 136 cm^{-1} and 170 cm^{-1}, accompanied by seven weaker peaks in the range of 260 cm^{-1} to 520 cm^{-1} [391,392]. While the phase $Bi_2Fe_4O_9$ is much more complex, exhibiting multiple bands at 87, 207, 283, 331, 365, 430, and 552 cm^{-1} [393]. To determine the crystal structure of the three materials, the characteristic Raman peaks of the two phases are marked with the corresponding dotted lines. The BFO1(5) exhibits the characteristic peaks of only $BiFeO_3$ without any other detectable secondary molecular bond. While the BFO3(60) has only $Bi_2Fe_4O_9$ peaks detectable, BFO2(60) shows that it has both the characteristic phase peaks with an almost similar intensity ratio.

For completeness, the FTIR and Raman spectra for the remaining BFO materials are shown in **Figure 4-50**. It is important to note that with longer t_{anneal} the hydrocarbon peaks are removed from the sample BFO1, **Figure 4-50**(A). While the peak intensity in Raman with longer t_{anneal} is evidently higher and the peaks at the range 260 cm^{-1} to 520 cm^{-1} are more defined, this is attributed to higher crystalline structure formation and removal of the hydrocarbon content. As for the BFO3 material, we observed no significant alteration in the FTIR or Raman $Bi_2Fe_4O_9$ characteristic peaks.

Thus, from the present FT-IR and Raman data, it is confirmed that BFO1(5) is a 100% $BiFeO_3$, BFO3(60) is a 100% $Bi_2Fe_4O_9$, while BFO2(60) is a mixed phase. Our XRD, FTIR, and Raman data provide clear evidence that the BFO materials are devoid of any secondary crystal phases, i.e., Fe_2O_3, Bi_2O_3, etc.

X-ray Photoelectron Spectroscopy: The XPS spectra for the three pertinent materials and the materials BFO1(60) and BFO3(120) that have the longest t_{anneal} are shown in **Figure 4-51** for the Fe2p energy range.

The Fe2p energy range has two sets of doublets corresponding to Fe^{3+}: the doublet at 710 and 712 eV is attributed to $Fe^{3+}2p3/2$, while the 723.5 and 725.5 eV are attributed to $Fe^{3+}2p1/2$ [394]. The characteristic ΔE= 13.5eV splitting is representative of the spin-orbit

coupling of the $Fe^{3+}2p$ [395]. The weak peak at ~718 eV is the satellite of the $Fe^{3+}2p3/2$ at approximately 6 to 8 eV from the binding energies of the $Fe^{3+}2p1/2$ [394].

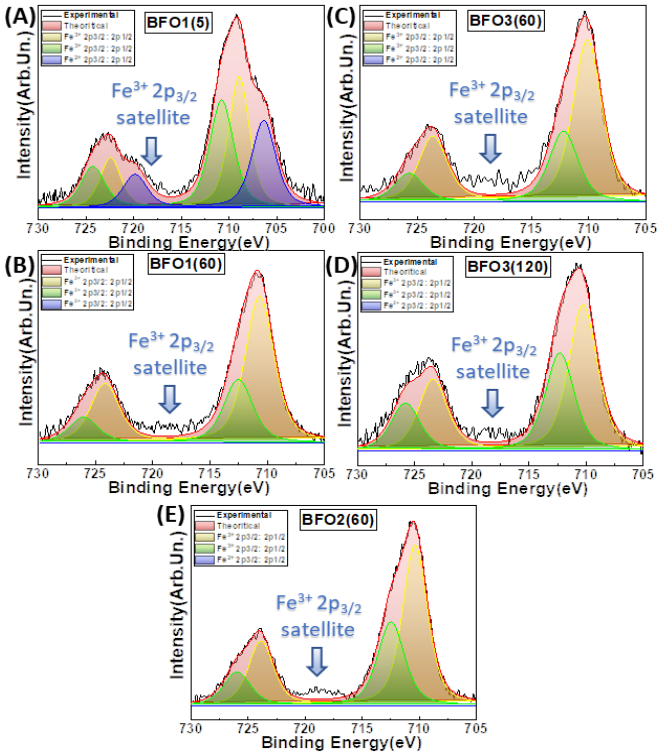

Figure 4-51: Fe-*XPS spectra of: (A) BFO1(5), (B) BFO1(60), (C) BFO3(60), (D) BFO3(120), and (E) BFO2(60) materials, with the corresponding fitted* $Fe^{3+}2p_{3/2}$*:* $2p_{1/2}$*, the* $Fe^{2+}2p_{3/2}$*:* $2p_{1/2}$ *peaks, and satellite peak in the 718eV range.*

In addition to the expected Iron XPS peaks that were shown in the previous chapter as well, the Fe-XPS spectrum of BFO1(5) has peaks of the oxidation state Fe^{2+} specifically the peaks at 706.2eV that correspond to the $Fe^{2+}2p3/2$, and the 719.7eV at $Fe^{2+}2p1/2$ [396]. The resulting concentration of the Fe^{2+} atoms is measured at approximately 10-15% as derived from the XPS areas of the three states. As mentioned in the FT-IR data, we credit this to the reduction of Fe^{3+} centers by traces of small hydrocarbons left over during the FSP process [390]. Notably, the Fe^{2+} atoms were not detected in the XPS spectra in the as-prepared BFO material (shown later in **Figure 4-54**) [224], nor in any other BFO materials prepared at higher T_{anneal} or longer t_{anneal}, meaning that very specific parameters need to be

fulfilled to produce from the FSP synthesis $BiFeO_3$ with the optimal formation of Fe^{2+} centers in the crystal structure, this is accomplished with T_{anneal} at 550 ℃ and t_{anneal} at 5 min.

The XPS spectra for the BFO materials for the Bismuth energy range are shown in **Figure 4-52**. All the materials are found to have uniform peaks at 164.4 eV and 159 eV, where these are attributed to the characteristic two states Bi $4f_{5/2}$ and Bi $4f_{7/2}$, the spin-orbit splitting value ~5.4eV of the two peaks is in accordance with the literature [362] [397].

The XPS spectra for the BFO materials for the Oxygen energy range are shown in **Figure 4-53**. All the materials have two distinct peaks, with the characteristic peak at 532 eV due to oxygen adsorbed on the surface of the material and hydroxyl groups [367], while the peak at 530.1 eV is due to O-Fe units of the crystal structure [398,399]. Although the intensity ratio for the BFO2(60) is very different from the other materials, where the 530.1eV peak has a much higher intensity than the 532 eV peak, possibly the reason is the much different O-Fe units of the crystal structure at the regions where the $BiFeO_3$ and $Bi_2Fe_4O_9$ phases interact.

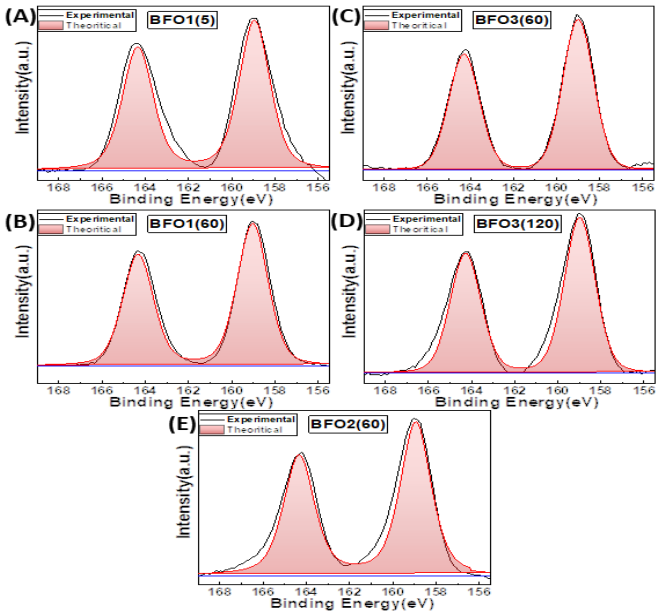

Figure 4-52: *Bi-XPS spectra for: (A) BFO1(5), (B) BFO1(60), (C) BFO3(60), (D) BFO3(120), and (E) BFO2(60) materials. The core level Bi4f5/2 and Bi4f7/2 at 164.4 and 159 eV are depicted.*

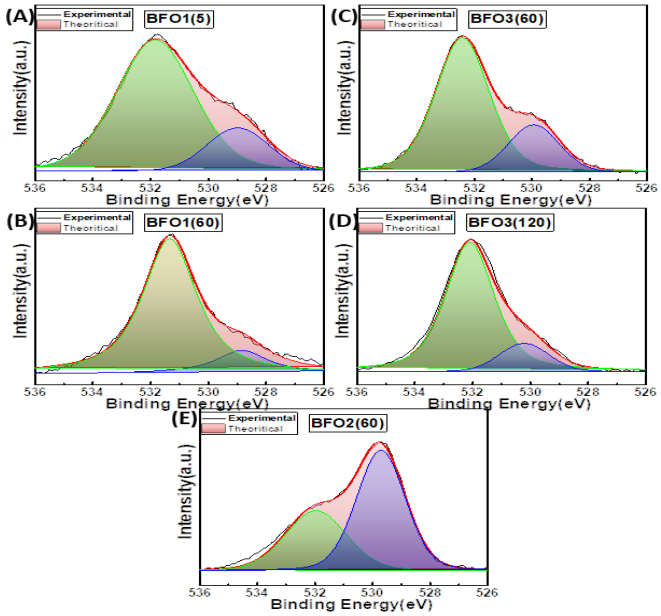

Figure 4-53: *O-XPS spectra for: (A) BFO1(5), (B) BFO1(60), (C) BFO3(60), (D) BFO3(120), and (E) BFO2(60) materials. The strong peak at 532 eV represents surface hydroxyl groups and/or surface-adsorbed oxygen, while the peak at 529.1eV is attributed to the O-Fe bonds.*

To have a complete understanding of the BFO materials, the As-Prepared powder from FSP (i.e. without any calcination treatment) is showcased in **Figure 4-54**. The as-prepared BFO material showed poor crystallinity without any peaks attributed to $BiFeO_3$ or $Bi_2Fe_4O_9$. Furthermore, the XRD revealed the existence of Fe_2O_3, **Figure 4-54**(A). Thus, the short residence time of the particles in our FSP reactor i.e. milliseconds [169,175], does not allow full growth of the BFO crystal structure. Moreover, as mentioned before, the XPS for the Fe2p energy range only possessed the peaks for the oxidation state Fe3+ i.e. the doublets $Fe^{3+}2p3/2$ and $Fe^{3+}2p1/2$ [394], without any corresponding Fe^{2+} peaks i.e. $Fe^{2+}2p3/2$ and $Fe^{2+}2p1/2$ [396]. Thus, the Fe^{2+} centers of BFO1(5) can only be accomplished from partial activation of the hydrocarbons in the material due to a short calcination post-synthesis step.

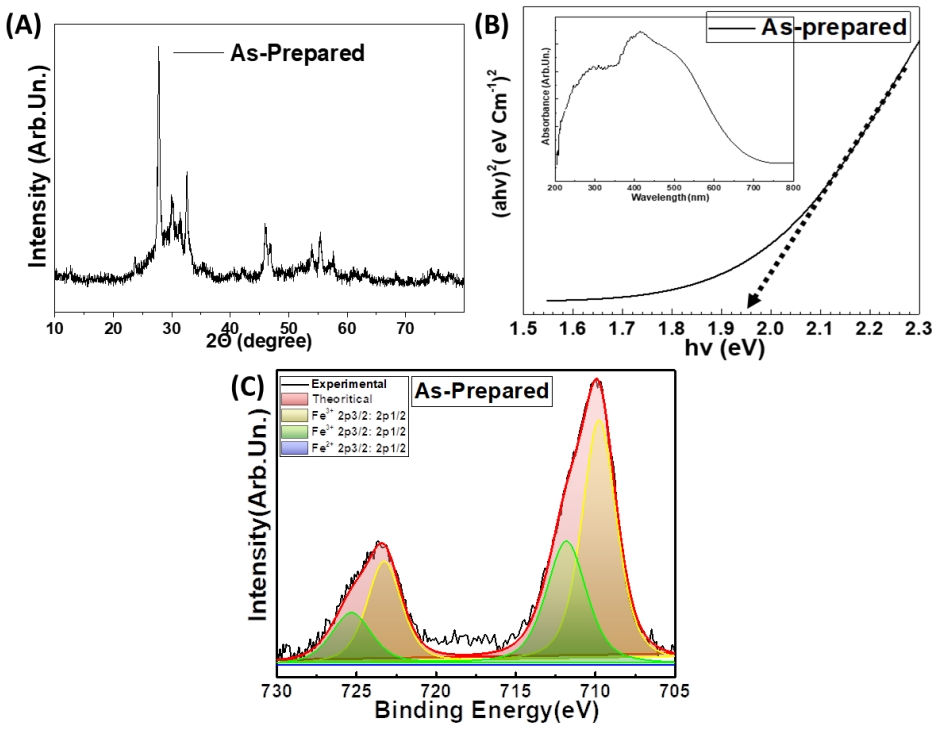

Figure 4-54: *(A) XRD pattern, (B) Tauc plot, Inset: the DRS-UV/Vis spectrum, and (C) XPS spectra of the As-Prepared BFO material. The As-Prepared yellow-brown material had poor crystallinity. Targeted post–FSP calcination protocols allowed the development of high-crystallinity nanomaterials.*

4.4.4 Photocatalytic evaluation of $BiFeO_3$/$Bi_2Fe_4O_9$ for Oxygen Evolution Reaction

photocatalytic Oxygen Evolution Reaction: In order to understand the photocatalytic process for the $BiFeO_3$ and $Bi_2Fe_4O_9$ phases for the Oxygen Evolution Reaction, the Conduction Band (CB) energy position and the Valence Band (VB) energy position of each material are crucial to diagram the reaction scheme.

We can calculate each material's energy positions E_{CB} and E_{VB}, with Equation 4-2 through Equation 4-4. The A_f is the atomic electron affinity, and I_1 is the first ionization potential for each atom in the crystal structure. With the A_f and I_1, we can calculate the individual Mulliken electronegativity X [400]. Finally, the band gaps obtained previously from the Uv-Vis-DRS, the E_{CB} and the E_{VB} are determined.

$$X = \frac{1}{2}(A_f + I_1) \qquad \text{Equation 4-2}$$

$$E_{CB} = X - 4.5 - \frac{1}{2}E_g \qquad \text{Equation 4-3}$$

$$E_{VB} = E_{CB} + E_g \qquad \text{Equation 4-4}$$

The CB of $BiFeO_3$ was found to be at +0.34 eV *vs.* NHE, and the Valence Band (VB) position was at 2.44 eV. Similarly, $Bi_2Fe_4O_9$ has a CB-edge at +0.36 eV and VB-edge at 2.41 eV, as shown in **Table 4-13**. These are in agreement with literature values of a CB-edge of +0.51 eV for $BiFeO_3$ and a CB-edge of +0.5 eV for $Bi_2Fe_4O_9$ [278,279].

Table 4-13: *The X and Eg values of $BiFeO_3$ and $Bi_2Fe_4O_9$ samples obtaining the E_{CB} and E_{VB}.*

Semiconductor	E_{CB}(eV)	E_{VB}(eV)	X(eV)	Eg(eV)
$Bi_2Fe_4O_9$	0.36	2.41	5.895	2.05
$BiFeO_3$	0.34	2.44	5.887	2.1

As the energy level of O_2/H_2O is at +1.23eV *vs.* NHE, both materials are suitable for the oxidation of water, and the holes of the photoproduced electron/hole pair are employed for OER. The electrons as a first step are transferred at the noble metal and secondarily transferred at NaS_2O_8 as an electron scavenger [289]. The overall photocatalytic reaction proceeds according to the reactions in Equation 4-5 and the reaction scheme shown in **Figure 4-55**.

$$\{BFO+hv\} + H_2O + S_2O_8^{2-} -> \{BFO\} + 1/2O_2 + 2H^+ + 2SO_4^{2-} \qquad \text{Equation 4-5}$$

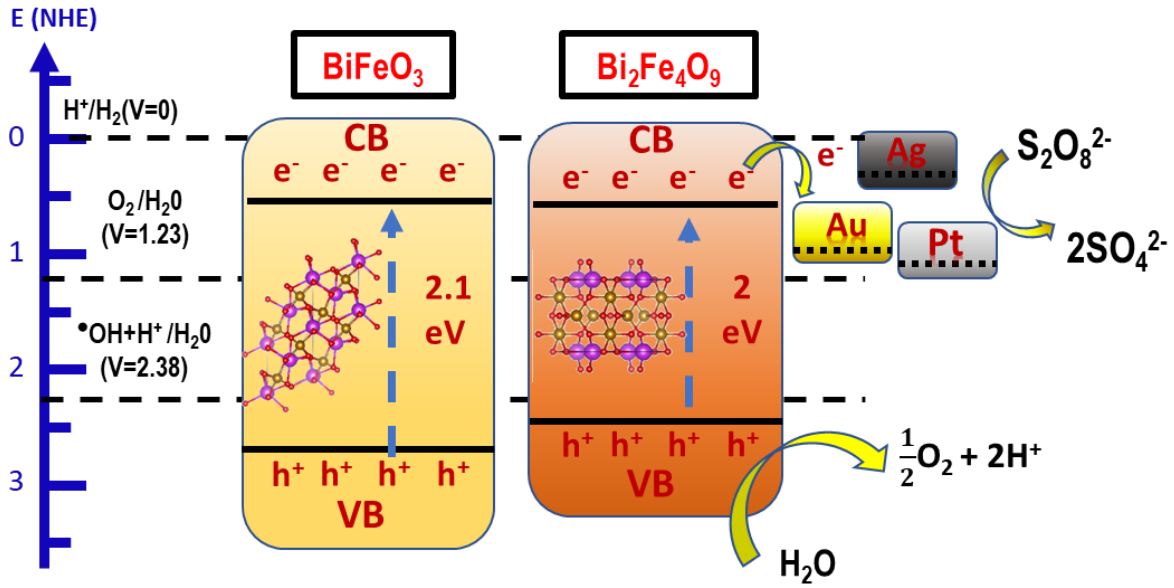

Figure 4-55: *Reaction scheme of the photocatalytic reaction process of $BiFeO_3$ and $Bi_2Fe_4O_9$.*

The photocatalytic O_2 production data for the BFO materials are shown in **Figure 4-56**, where the noble metal employed was Au. The FSP as-prepared BFO material achieved very low O_2 evolution at 151 μmol $g^{-1}h^{-1}$. **$BiFeO_3$:** Annealing at short-time T_{anneal}=550°C, t_{anneal}=5 min, dramatically affected the O_2 generation efficiency, i.e. 1150 μmol $g^{-1}h^{-1}$ for BFO1(5). At prolonged t_{anneal} the O_2-production rates dropped steadily i.e. to 900 μmol $g^{-1}h^{-1}$ for t_{anneal}=30min and 780 μmol $g^{-1}h^{-1}$ for t_{anneal}=60min. The trend in $BiFeO_3$, shown in **Figure 4-56**(B), implies a key-optimization step occurring at short t_{anneal}=5 min.

$BiFeO_3/Bi_2Fe_4O_9$: The mixed-phase BFO2(60), with 52%$BiFeO_3$ and 48%$Bi_2Fe_4O_9$, shows an improved O_2 evolution rate of 1300 μmol $g^{-1}h^{-1}$ that was higher than the performance of the best $BiFeO_3$. **$Bi_2Fe_4O_9$:** the trend for the $Bi_2Fe_4O_9$ phase continued where the pure phase produced an even higher O_2 evolution rate of 1550 μmol $g^{-1}h^{-1}$, which is almost double production from the BFO1(60) that had similar t_{anneal}. Fundamentally noteworthy is that with longer t_{anneal}=120min the O_2 evolution rate dropped at the very low 187 μmol $g^{-1}h^{-1}$, only slightly better than the As-Prepared sample.

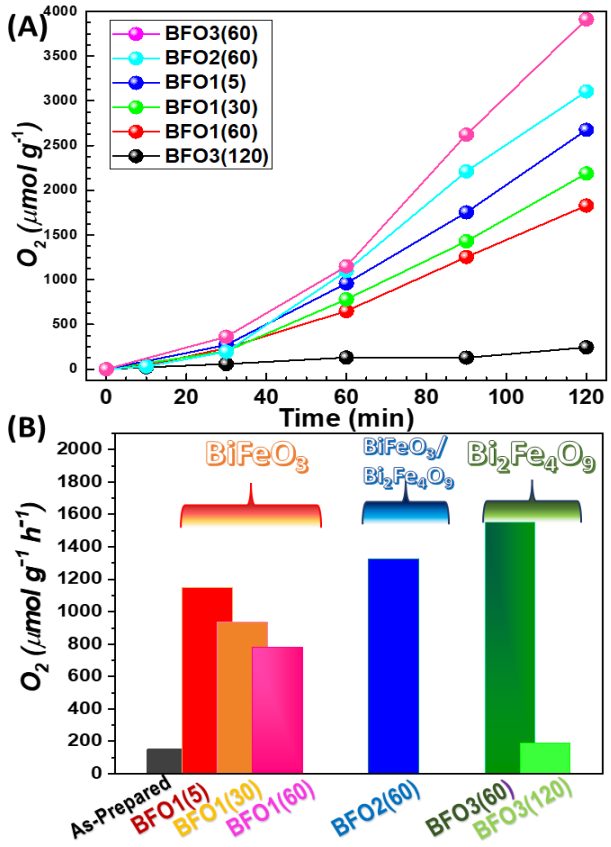

Figure 4-56: *(A) Kinetics of photocatalytic O_2 production by the BFO photocatalysts. (B) The photocatalytic O_2-production per hour for all the studied BFO.*

We have performed a screening of the optimal noble metal loading for the O_2 evolution of the BFO materials. By testing loadings of 0.1, 0.5, 1, 2, and 5 % w/w, concluding that 1% is the most efficient loading ratio, with higher loadings (2% w/w or 5% w/w) inhibited the O_2 production due to coverage of the BFO surface.

To further peer into the band-positioning of the $Bi_2Fe_4O_9$ materials BFO3(60), as it is the best-performing nanoparticle, experiments comparing different electron acceptors were contacted i.e. Pt^0 and Ag^0 in comparison to the previous Au^0 experiments. The exhibited photocatalytic O_2 production efficiency is shown in **Figure 4-57**. The experiments demonstrate that BFO3(60)/Au^0 and BFO3(60)/Pt^0 have almost the same performance, while BFO3(60)/Ag^0 show a lower efficiency by 25%, this can be explained through the energy-level scheme in **Figure 4-55**. The energy levels of the noble metals are derived from the work function of each material, with Pt^0 at φ=5.6 eV *vs.* vacuum, Au^0 at φ=5.1eV [254], and Ag^0 at φ=4.2eV [255]. As the energy level of Ag^0 is in an unfavorable position i.e. higher than $Bi_2Fe_4O_9$ +5eV *vs.* vacuum (+0.5 eV *vs.* NHE) [279], the electron transfer has a much lower kinetic, leading to a higher percentage of electron/ hole pair recombination, leading to the less efficient photocatalysis.

In addition, to ensure the catalytic stability of the BFO3(60) ($Bi_2Fe_4O_9$) catalyst is stable for 4 catalytic cycles with relatively the same photocatalytic production, at the fourth cycle a minor efficiency loss of 5% was observed, as shown in **Figure 4-58**.

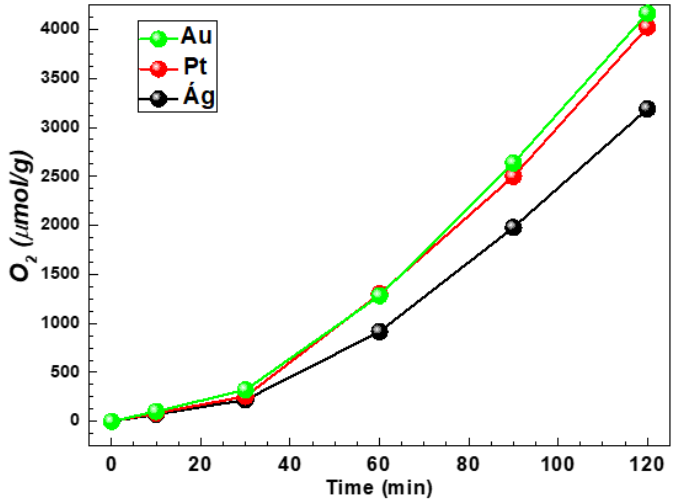

Figure 4-57: *Kinetics of photocatalytic O_2 production by using various cocatalytic noble-metals (Ag^0, Pt^0, or Au^0) for the BFO3(60) nanomaterial.*

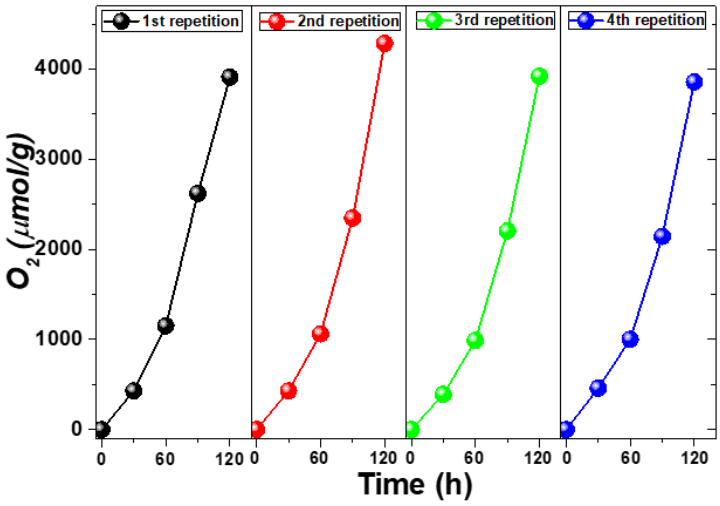

Figure 4-58: *Repetition photocatalytic experiments for the best performing material BFO3(60).*

To ensure the structure and the material properties remain intact, a detailed examination commenced for all the BFO1(5), BFO2(60), and BFO3(60) after their photocatalytic evaluation. The XRD, Tauc plot FT-IR, and XPS for the materials are present in **Figure 4-59**. For all materials, the crystal structure remained intact, proving their structural stability, ensured further from the FT-IR measurements. The XPS measurements didn't show any interesting differences, although the Fe^{2+} XPS signal of BFO1(5) was not detected, it is determined that under photocatalytic conditions the Fe^{2+} centers while beneficial for the photocatalytic efficiency, the Fe^{2+} centers revert to Fe^{3+} due to the rapid change in charge from the photoproduced electron/hole pairs. The absorption properties remained the same with the same observable band gap of 2.1 eV. It is important to note that the photo-deposited gold is not observable due to the low amount deposited and the instruments' inefficiency in detecting them.

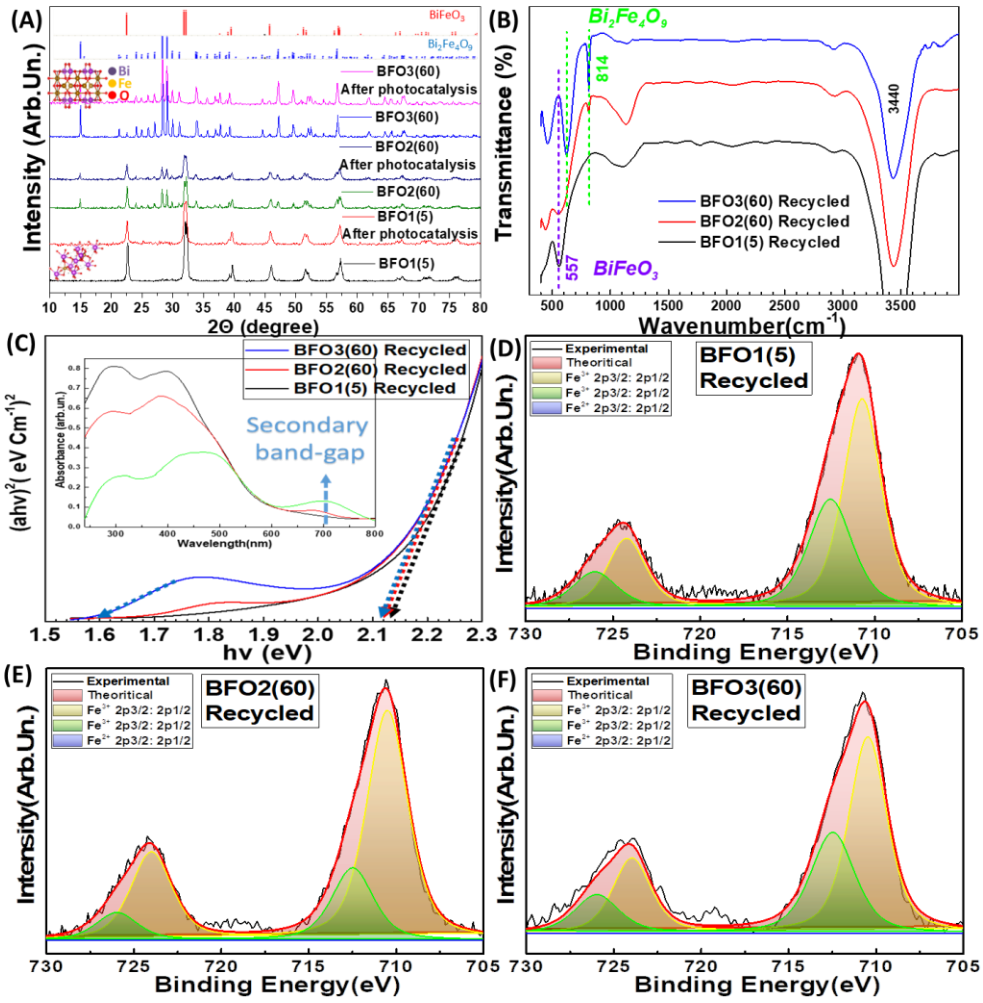

Figure 4-59: *(A) XRD patterns of BFO1(5), BFO2(60), and BFO3(60) before/ and /after photocatalysis, (B) FT-IR spectra of BFO1(5), BFO2(60), and BFO3(60) after photocatalysis, (C) Tauc plot and DRS-UV/Vis plots (inset) of BFO1(5), BFO2(60) and BFO3(60) after photocatalysis. XPS Spectra of Iron for the (D) BFO1(5), (E) BFO2(60), and (F) BFO3(60) after photocatalysis.*

Overall, from the photocatalytic experiments, we can conclude that:

[a] Photocatalytic O_2-evolution is improved significantly when the crystal phase transitions from $BiFeO_3$ towards $Bi_2Fe_4O_9$.

[b] For materials of the same crystal phase, the annealing protocol parameters of T_{anneal} and t_{anneal} allow modulation of the O_2 evolution efficiency. In all cases, longer t_{anneal} is severely detrimental, and synthesis methods should be required to decrease the calcination parameters.

[c] $Bi_2Fe_4O_9$ is sensitive to prolonged t_{anneal}, as determined from XRD the structure deteriorates due to solid melt, this is observed from the particles BFO3(60) and BFO3(120). The solid melt causes severe deterioration of its photocatalytic activity by a factor of ten times. In contrast, $BiFeO_3$ doesn't have solid melt effects, with far less pronounced photocatalytic efficiency upon prolonged annealing.

[d] The XPS data reveal a correlation trend between the Fe^{2+} centers in $BiFeO_3$ and enhanced O_2 production. Theoretical DFT calculations, discussed hereafter, reveal that these Fe^{2+} atoms significantly impact the energy level positioning of the CB and VB edge of $BiFeO_3$.

Table 4-14: *Literature O_2 evolution data of similar photocatalytic systems.*

Photocatalyst	Light Source	Electron acceptor	Activity ($\mu mol\ g^{-1}h^{-1}$)	Ref.
$Au/Bi_2Fe_4O_9$	125 W mercury lamp	$Na_2S_2O_8$	1550	This work
$Au/BiFeO_3$	300 W xenon lamp (optical filter, $\lambda > 380$ nm)	$FeCl_3$	380	[401]
$Au/BiFeO_3$	300 W xenon lamp (optical filter, $\lambda > 380$ nm)	$Na_2S_2O_8$	612	[289]
Au/CeO_2	200 W xenon-doped mercury lamp	$AgNO_3$	233	[402]
Pt/SrTiO$_3$:Rh	300 W xenon lamp	$AgNO_3$	137	[403]
$Pt/MnO_x/BiVO_4$	300 W xenon lamp	$NaIO_3$	650	[404]

As mentioned, the $Bi_2Fe_4O_9$ material has not been evaluated for OER previously, thus to have an accurate comparison with literature data pertinent to Fe, Bi catalysts for photocatalytic OER are presented in **Table 4-14** [289,401–404]. Our FSP-made $BiFeO_3$ i.e. BFO1(5), surpasses the performance of Papadas *et al.* [289], which is comparable to our BFO1(60) catalyst. Among all BFO photocatalysts in **Table 4-14**, the FSP-made $Bi_2Fe_4O_9$ i.e.

BFO3(60), is a superior photocatalyst for O_2 production from H_2O, overperforming all so far known Fe-Bi-O materials.

Photogenerated holes of the Photocatalytic Mechanism through EPR: In OER, an essential step is the oxidation of H_2O by the photogenerated holes *via* the formation of ●OH radicals [59]. To determine the crucial formation of ●OH radicals, EPR spectroscopy is employed to monitor *in-situ* the photogeneration of ●OH through the function of a spin trap DMPO, Quantitative measuring the DMPO-OH and DMPOX formed.

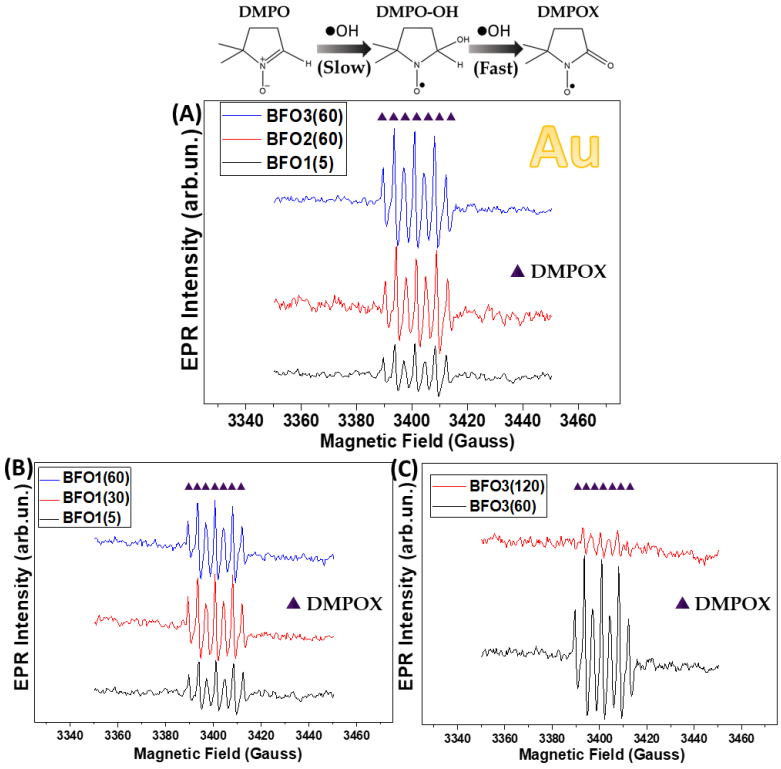

Figure 4-60: EPR spectra of photogenerated OH-radicals for: (A) the three best-performing BFO materials, (B) The BFO1 material with different t_{anneal}, (C) The BFO3 material with different t_{anneal}. The detected EPR signals correspond to DMPOX states, resulting from two ●OH trapped per DMPO molecule.

The EPR data show that all the studied BFO catalysts are very efficient in the photogeneration of ●OH, with the photodeposition of Au as cocatalyst, as shown in **Figure 4-60**. Interestingly, the EPR spectral patterns have a characteristic 7-line pattern with

intensity ratio [1:2:1:2:1:2:1], which is the pattern of two ●OH radicals trapped per DMPO molecule [306], the so-formed structure is codenamed as DMPOX [307]. The reaction path toward ●OH to DMPO-OH and DMPOX is shown on top of **Figure 4-60**. The formation of DMPOX reveals that a high local concentration of ●OH occurs [306] during the photoexcitation of the BFO materials.

The EPR data for the three pertinent BFO materials with the photodeposition of Pt as cocatalyst is shown in **Figure 4-61**. The results are drastically different from the Au as cocatalyst, where the observed intensity ratio is [1:2:2:1], which is the characteristic pattern of DMPO-OH. Moreover, only the most efficient material i.e. BFO3(60) was adequate enough to produce a detectible amount of DMPO-OH. While the photocatalytic for OER is the same for the two cocatalysts, EPR measurements determine that Au-cocatalyst has a localized effect, the charges are kinetically higher than Pt-cocatalyst. The results prove that BFO3(60) is the most efficient photocatalyst, with either Pt or Au as the cocatalyst.

Through the quantification method with calibration of DPPH, the overall produced ●OH radicals were calculated, where DMPOX is measured as two ●OH. The overall ●OH quantification is shown in **Figure 4-62**, and the results provide credit to the O_2 production in **Figure 4-56** following the same trends, (i) BFO3(60) had the highest rate of ●OH at 850 μmol g^{-1}, (ii) a clear trend of BFO3(60)>BFO2(60)>BFO1(5) meaning that the transition of $BiFeO_3$ to $Bi_2Fe_4O_9$ is photocatalytic favorable. For comparison, a reference P25-TiO_2 irradiated under the same conditions and as cocatalyst Au generated 300 μmol g^{-1}, interestingly the EPR signal showed an intensity ratio of [1:2:2:1] describing DMPO-OH, the BFO materials were equal and surpassing the P25 for ●OH photogeneration, where the Au cocatalyst shows very different charge kinetics leading to the formation of DMPOX.

Accordingly, we conclude that the superior photocatalytic efficiency of BFO3(60) and pure $Bi_2Fe_4O_9$ originates from the highly efficient photogeneration of the holes and the superior charge kinetics.

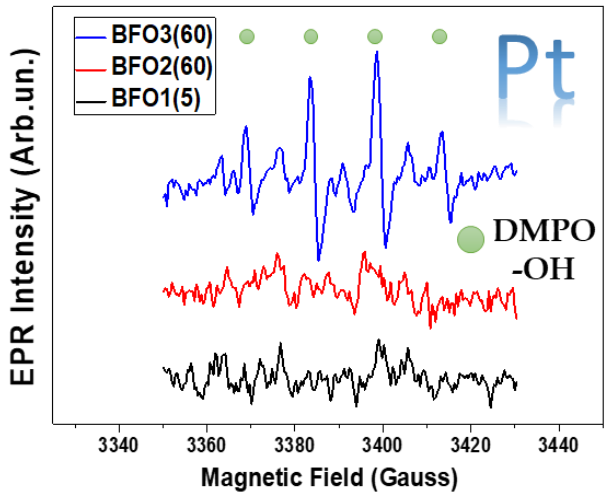

Figure 4-61: *EPR spectra of photogenerated OH-radicals for the three best-performing BFO materials. The detected EPR signals correspond to DMPO-OH states, resulting from one* ●*OH trapped per DMPO molecule.*

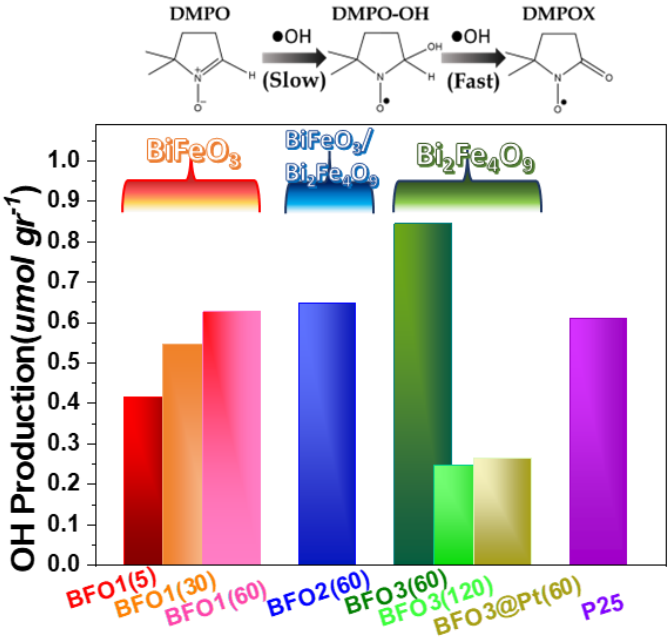

Figure 4-62: *Quantitative* ●*OH-production per gram of photocatalyst for all the materials and P25 for comparison.*

4.4.5 Discussion of $BiFeO_3$/$Bi_2Fe_4O_9$ for OER efficiency mechanism from Theoretical Modeling

Theoretical Modeling (DFT) calculations: The Theoretical calculations were conducted as explained underneath, for the $BiFeO_3$-R3C [405] and $Bi_2Fe_4O_9$-P*bam* structures [406], using DFT as implemented in the Quantum Espresso software [407]. The projector augmented-wave (PAW) method was used to describe the core pseudopotential and the generalized gradient approximation (GGA) as simplified by Perdew, Burke, and Ernzerhof (PBE), and it was used for exchange-correlation effects. Pseudopotentials containing 15 valence electrons were manipulated for Bi ($5d^{10},6s^2,6p^3$), 16 valence electrons for Fe ($3s^2,3p^6,3d^6,4s^2$), and six valence electrons for O ($2s^2,2p^4$). A plane-wave energy cutoff of 70.8 Ry was used for the $BiFeO_3$-R3C and $Bi_2Fe_4O_9$-Pbam structures. Both structures were relaxed until the forces acting on each atom were $<10^{-3}$eV/Å. For geometry optimization and electronic structure calculations, [3x3x3] and [9x9x9] Monkhorst-Pack k-point grids were used, respectively. Considering the strong correlations in transition metal oxides, we used the DFT+U approximation in the approach of Cococcioni and de Gironcoli [408] with a U-value of 4eV applied on both structures.

DFT for $BiFeO_3$: The main reason we conducted DFT calculations was to fundamentally explain the photocatalytic efficiency and the XPS data correlation for the presence of Fe^{2+} atoms in BFO1(5), as it appears to have a vital role in the photocatalysis. Interestingly, the material BFO1(5) i.e. $BiFeO_3$-Fe^{2+} in comparison to the BFO3(60) i.e. pure $BiFeO_3$ did not have any observable difference in the UV-Vis absorbance profile or the band gap value. Thus, the difference is based on the existing band states.

For Fe^{2+} free $BiFeO_3$, the calculated bandgap values are 2.0 eV (indirect, F/Γ→F) and 2.1eV (indirect, F/Γ→Z, and F/Γ→L). In accordance with previous reports regarding $BiFeO_3$ [409], the spin-up and spin-down populations are symmetric due to the antiferromagnetic arrangement of Fe^{3+} magnetic moments. As shown in the DOS plot in **Figure 4-63**(A), the maximum energy of the Valence-band VB_{max} of $BiFeO_3$ is dominated by O-2p states, while the CB_{min} is by Fe-3d states. The VB_{max} of $BiFeO_3$ is located between the F(0.5,0.5,0) and Γ(0,0,0) points and the CB_{min} at the F(0.5,0.5,0) point, in agreement with the previous reports [410]. In **Figure 4-63**(B), one atom of Fe^{2+} has been introduced per unit cell i.e. for

the sake of the discussion, we codename it $\{Fe^{2+}\}BiFeO_3$, comparing with the DOS for $BiFeO_3$ (red *vs.* black lines) reveals that the introduction of Fe^{2+} atoms into the $BiFeO_3$ lattice causes a downshift of *both* CD and VB by 0.9eV, without a change in the band-gap value.

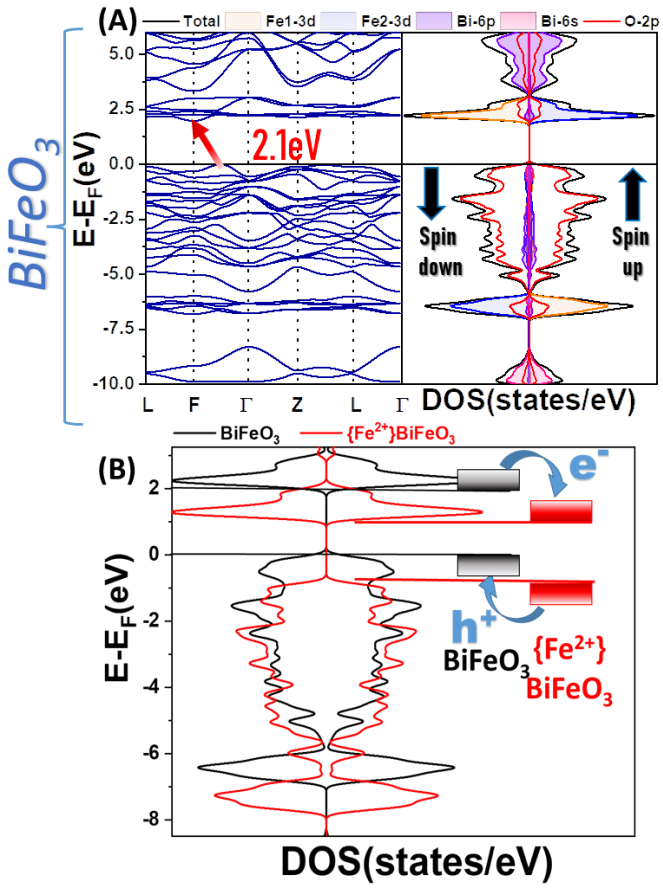

Figure 4-63: *(A) Theoretical energy band-structure and DOS of $BiFeO_3$. (B) DOS for $\{Fe^{2+}\}BiFeO_3$ (red lines) vs. $BiFeO_3$ (black lines).*

The theoretical result is in accordance with the experimental data of photocatalysis, which show that $\{Fe^{2+}\}BiFeO_3$ and $BiFeO_3$ i.e. materials BFO1(5) and BFO1(30, 60) have similar Eg values. [ii] The downshift of CB by +0.9eV i.e. towards more positive potentials, enhances the oxidative capacity of the holes in $\{Fe^{2+}\}BiFeO_3$ *vs.* $BiFeO_3$, which explains the enhanced photoactivity of BFO1(5) than BFO1(30, 60). Thus, the present theoretical analysis indicates that the superior photocatalytic efficiency of BFO1(5) can be attributed

to the more positive potential of the CB induced by the presence of Fe^{2+} atoms in the $BiFeO_3$ lattice.

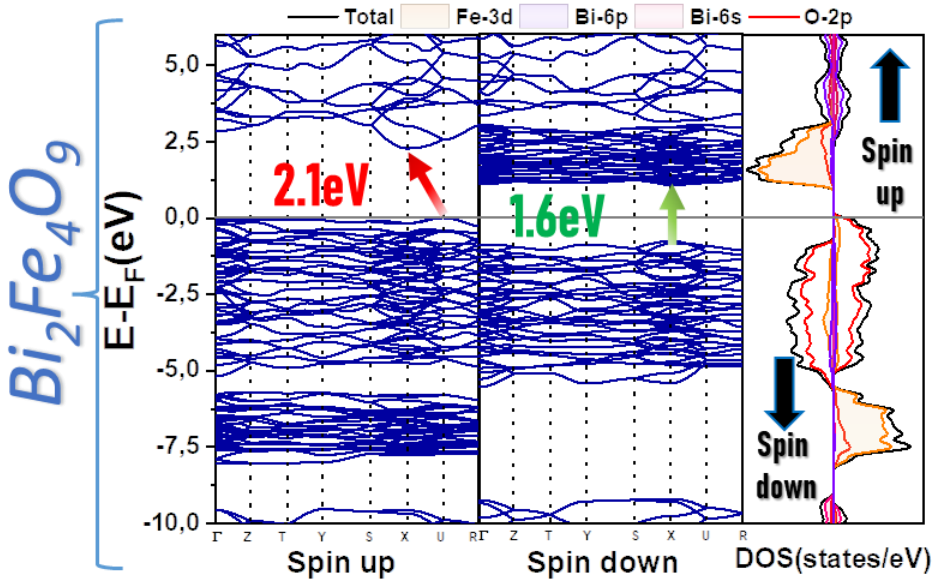

Figure 4-64: *Theoretical energy band structure and DOS of ferromagnetic $Bi_2Fe_4O_9$.*

DFT for $Bi_2Fe_4O_9$: For completeness, we present the energy bands and DOS for $Bi_2Fe_4O_9$, shown in **Figure 4-64**. In $Bi_2Fe_4O_9$ the CB_{min} is mainly populated by Fe-3d states and the VB_{max} by O-2p states, as is the case for $BiFeO_3$. However, in $Bi_2Fe_4O_9$ the DOS profile is fundamentally more complex than $BiFeO_3$ i.e. due to the ferromagnetic character of $Bi_2Fe_4O_9$ [393]. More specifically, various transitions are allowed for the combination of spin-up/spin-down configurations: a transition with energy 2.1eV (indirect, $U^{up} \rightarrow X^{up}$), one with 1.1eV (indirect, $U^{up} \rightarrow X^{down}$) and 1.6eV (direct, $X^{down} \rightarrow X^{down}$). These are in agreement with the DRS-UV/Vis data, where the bands at Eg~2.1eV and ~1.6eV are evidenced in the experimental spectra.

4.4.6 Conclusions of OER photocatalysis from FSP made $BiFeO_3/Bi_2Fe_4O_9$

[a] Synthesis of perovskite $BiFeO_3$, the mullite-type $Bi_2Fe_4O_9$, as well as their mixed-phase heterostructures with Flame-Spray-Pyrolysis including exploration of the post-

annealing step with different temperatures i.e. T_{anneal}: 550, 625, and 700°C, and most importantly for each phase the time i.e. t_{anneal}: 5, 30, 60, and 120min.

[b] Based on PXRD, FT-IR, DRS-UV-Vis, Raman, and XPS data, the produced materials are devoid of secondary Bismuth oxide or Iron oxide phases. Although, the BFO1(5) i.e. the material with the lowest T_{anneal} and t_{anneal} showed signs of hydrocarbons through FT-IR, leading to the existence of Fe^{2+} centers through XPS.

[c] From the Oxygen Evolution Reaction efficiency of the six materials, there are several important results. (i) The as-prepared FSP material has very low activity in comparison even with the lowest annealing materials BFO1(5). (ii) The phase $Bi_2Fe_4O_9$ that is evaluated for the first time in the bibliography is shown to have much higher photocatalytic efficiency than the more studied $BiFeO_3$, with the OER trend revealing to be $BiFeO_3$< $BiFeO_3/Bi_2Fe_4O_9$ <$Bi_2Fe_4O_9$.

[d] The OER in comparison to the annealing parameters for the two phases has the same result of longer t_{anneal} has very detrimental effects on the efficiency, although with very different reasons. (i) For the $BiFeO_3$ phase, the introduction of Fe^{2+} centers in the lowest anneal leads to enhanced efficiency, as demonstrated by DFT. (ii) For the $Bi_2Fe_4O_9$ phase, the solid melt reaction as determined through XRD has a severe reduction of ten times for the OER production. Thus the lower calcination requirements provided by the FSP synthesis for the $Bi_2Fe_4O_9$ materials with higher photocatalytic production in comparison to other synthesis methods.

[e] Through DFT analysis, $\{Fe^{2+}\}BiFeO_3$ i.e. $BiFeO_3$ with Fe^{2+} centers, shows a downshift of CB by +0.9eV i.e. towards more positive potentials, enhances the oxidative capacity of the holes in comparison to pure phase $BiFeO_3$. The theoretical results support the enhanced photoactivity of BFO1(5) compared to BFO1(30, 60).

4.5 La: $SrTiO_3$/CuO particles for the selective production of H_2/CH_4

4.5.1 Aims for $SrTiO_3$ with Lanthanum doping and CuO Heterojunction

Our key research objects for the following publication of the perovskite $SrTiO_3$.

$SrTiO_3$ perovskite as a photocatalyst has a highly reducing conduction-band edge. The most important aspect of $SrTiO_3$ perovskite is that it offers versatile photoactive nano-templates that can be optimized towards specific technologies, either by doping or *via* heterojunction engineering.

[a] To employ a Single-Nozzle FSP (SN-FSP) process for the synthesis of high crystallinity $SrTiO_3$ nanoparticles with controlled La-doping (La:$SrTiO_3$). [b] Double-Nozzle FSP (DN-FSP) creates a heterojunction of CuO finely dispersed on $SrTiO_3$ ($SrTiO_3$/CuO) [411]. [c] *in-tandem* FSP synthesis of Lanthanum doped $SrTiO_3$ with CuO-heterojunction formation (La:$SrTiO_3$/CuO) in one step [412,413]. Technology-wise, this work is among the first to exemplify the application of Double Nozzle FSP for scalable production of complex nanomaterials i.e. La:$SrTiO_3$/CuO, with a diligent control of doping and heterojunction in a single-step synthesis.

[d] Control of the $SrTiO_3$ electronic/photocatalytic properties through the *in-tandem* La-doping of $SrTiO_3$ and heterojunctions with CuO. [e] To study the hydrogen and methane selectivity from the photocatalysis of an H_2O/CH_3OH mixture, the comparison is made toward the effect of La atoms in the $SrTiO_3$ lattice regarding the hydrogen product, while the effect of interfacial CuO has a selectivity towards methane production. CH_3OH is employed as a well-known hole-scavenger [414]. However, most publications do not examine the CH_3OH involvement in the reaction path and the final products e.g. eventually CH_4.

The results from the research have been published in our work with the title "In Tandem Control of La-Doping and CuO-Heterojunction on $SrTiO_3$ Perovskite by Double-Nozzle Flame Spray Pyrolysis: Selective H_2 vs. CH_4 Photocatalytic Production from H_2O/CH_3OH" for the Journal of Nanomaterials [228], with the graphical abstract shown in **Figure 4-65**.

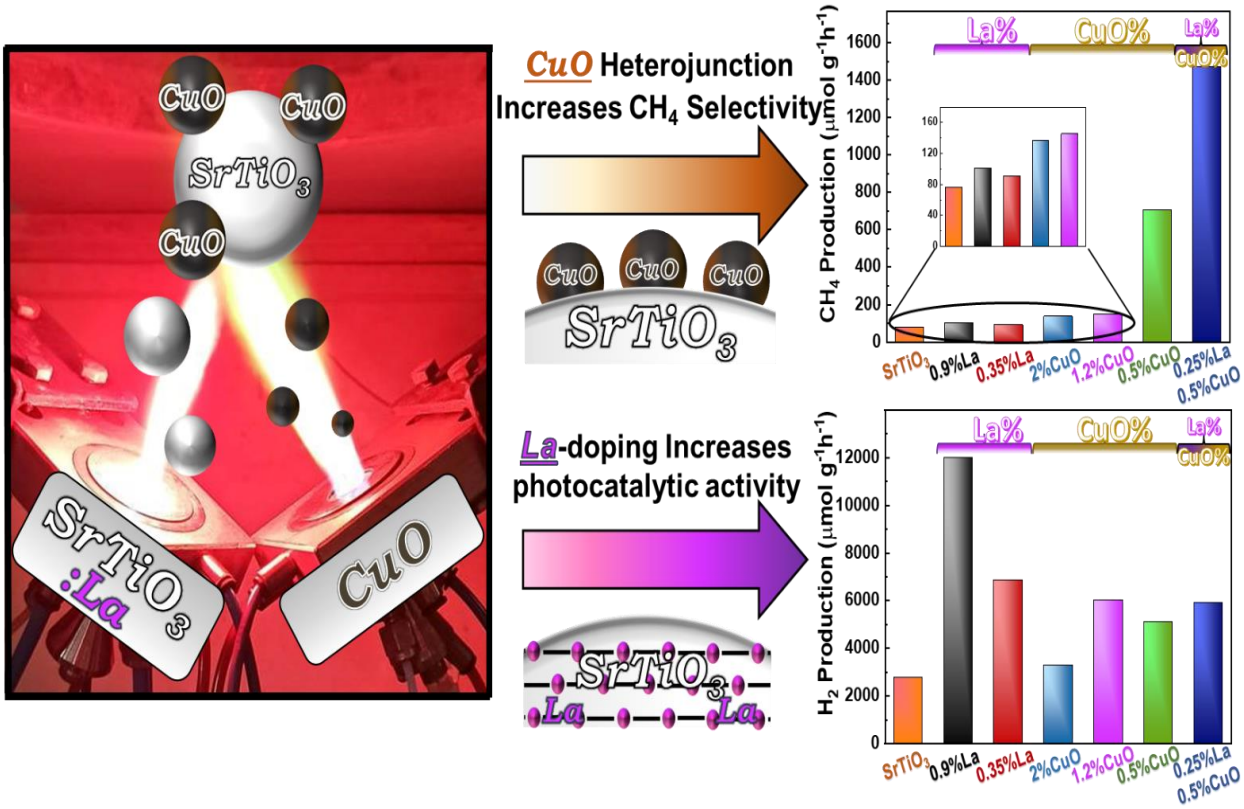

Figure 4-65: *The graphical abstract of Double Nozzle FSP synthesis for Nanosized La:SrTiO3/CuO, resulting in drastic changes in the production of Hydrogen and methane compared to the La doping and the CuO heterojunction.*

4.5.2 DN FSP synthesis of $SrTiO_3$ in tandem Lanthanum doping and CuO heterojunction

The FSP parameters were extensively selected under several experiments, some of which will be presented below, thus we arrived at the FSP parameters of the highly crystalline and pure phase of $SrTiO_3$.

The precursor solution contains 0.2M Strontium acetate (STREM) and 0.2M Titanium(VI) isopropoxide (97%, Aldrich), with a total precursor concentration of 0.4M with the same amount of mols of Srontium and Titanium for the synthesis of perovskite $SrTiO_3$. The Sr and Ti precursors were dispersed in a mixture of Acetic acid and Xylene (1:1 volume ratio). Acetic acid was one of the very few solvents appropriate for FSP that can

efficiently disperse higher molar ratios of Strontium, while xylene was employed for the Ti precursor as it is well documented for FSP synthesis of TiO_2, xylene provides a high percentage of the total combustion enthalpy of the flame.

For the deposition of cocatalytic metals i.e. Lanthanum atoms as lattice-dopant of $SrTiO_3$, the precursor Lanthanum Acetylacetonate (97%, STREM) was used for all the experiments. As the Lanthanum Acetylacetonate cannot be efficiently dispersed with the Acetic acid nor with Xylene, the La precursor was dispersed in a mixture of toluene and 2-EHA (1:1 volume ratio), this extra mixture consisted of approximately 10% of the total volume of the final precursor solution, with the other 90% being Acetic acid and Xylene (1:1 volume ratio). It is essential to note that each precursors were dispersed with their appropriate solvents i.e. Sr acetate with Acetic acid and Ti Isopropoxide with Xylene separately, after the successful dispersion in the solvents, then all solvents combined to the final mixture.

The FSP parameters for the synthesis of the nanoparticles consisted of an oxygen dispersion flow rate D of 5 L min^{-1} (Linde 99.999%) and a precursor flow rate P of 5 mL min^{-1}. The pilot flame was ignited by premixed O_2 and CH_4 (4 L min^{-1}, 2 L min^{-1}). As shown below, the inclusion of a Quartz Tube to enhance the high-temperature residence time wasn't necessary, thus the experiments were contacted in open flame i.e. No-Tube inclusion. The produced particles were deposited on a glass microfiber filter with a binder (Albet Labscience GF_6_257) and collected by scrubbing the nanoparticles from the filter. The nanomaterials were collected in glass vials under an inert Argon atmosphere until use.

The derived FSP parameters were determined from various experiments, some important conditions will be presented shortly. The XRD measurements were employed as a basis for the correct characterization of the $SrTiO_3$ phase and the basic minimum for the purity of the structure i.e. no secondary phases or amorphous content. Pure cubic perovskite $SrTiO_3$ structure (JCPDS74–1296) has the distinct peaks 2θ at 22.71 32.34, 39.91, 46.43, 52.29, 57.74, 67.78, and 77.13 degrees, these diffraction peaks are assigned to Miller indices of the (100), (110), (111), (200), (210), (211), (220), and (310) planes for the cubic perovskite structure (Pm3m).

The Strontium and Titanium molar ratio was screened, with the total concentration always being 400mM, and the Titanium concentration was screened at 67mM, 134mM, 200mM, 266mM, and 333mM, as shown in **Figure 4-66**. As expected, the proper formation of $SrTiO_3$ can be accomplished with a 1 :1 ratio of Ti: Sr, although a small deviation of 10% can still produce the $SrTiO_3$ phase, but there is a chance of small contents of secondary phases.

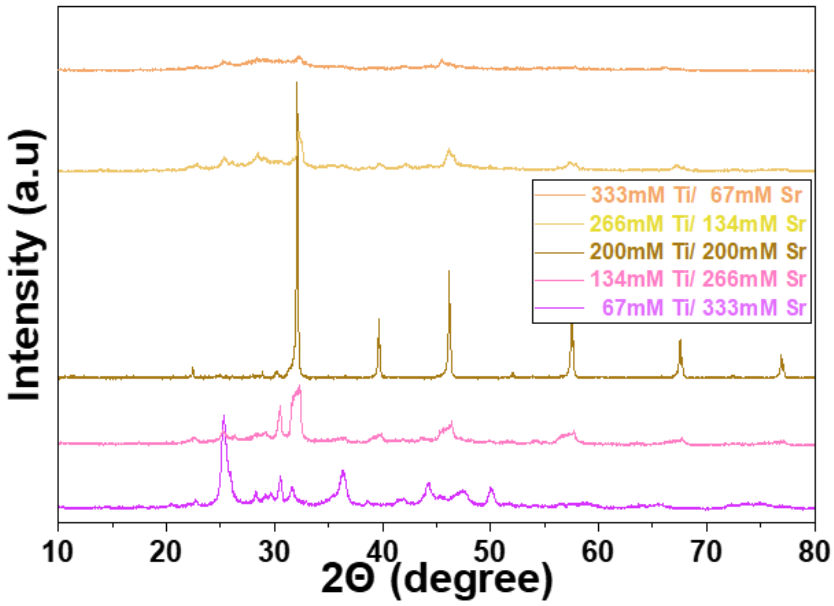

Figure 4-66: *XRD graph showing the effect of different molar ratios of Titanium and Strontium for the formation of $SrTiO_3$.*

Different precursors of Strontium were employed with the aforementioned Sr acetate and Sr nitrate. The Sr nitrate had the major drawback that it doesn't disperse with any solvent favored for FSP synthesis, much worse a high percentage of water was needed, which is heavily detrimental for FSP synthesis creating micro explosions inside the flame, with the final solvent being a mixture of water and Nitric acid at (8.7 : 1 ratio). Even though the solvent was so detrimental to FSP synthesis, a high percentage of $SrTiO_3$ was obtained, as seen in **Figure 4-67**. However, secondary phases were obtained, as shown in the encircled areas, under calcination of 800 ^{0}C for 1 hour under atmospheric air, the material exhibited 100% pure $SrTiO_3$ phase, although this is an additional high energy cost solution.

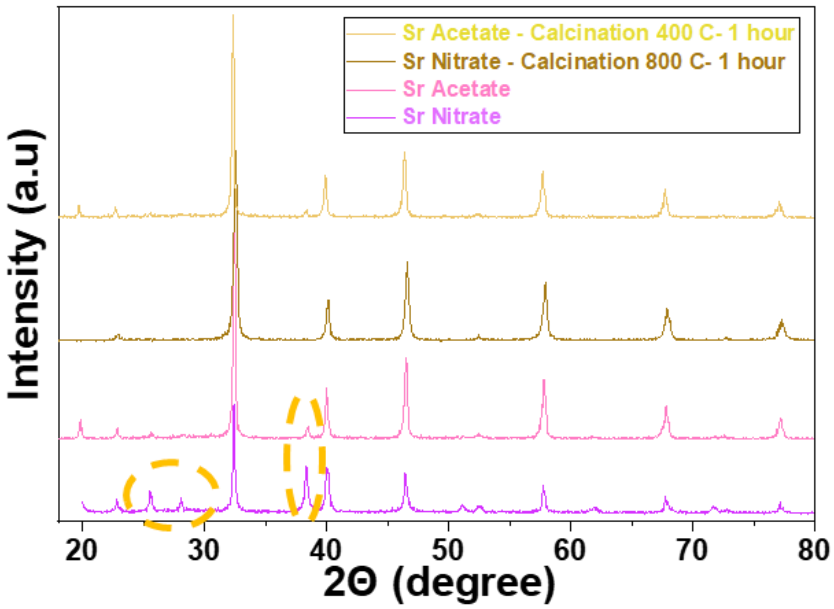

Figure 4-67: *XRD graph showing the effect of different precursors of Strontium Nitrate and Sr acetate for the formation of $SrTiO_3$, encircled areas show secondary phases.*

Another essential factor for the FSP synthesis, which in many particles determines the size of the produced nanomaterials, is the total concentration of the precursor. For this reason, we screened the total concentrations of 0.8M, 0.4M, and 0.1M with the Sr to Ti atoms always being 1: 1. The XRD results, as shown in **Figure 4-68**, present that for each material a very high crystalline $SrTiO_3$ phase was obtained. However, the material produced from 0.1M shows a small percentage of secondary phases (encircled peaks). As the highest crystalline and pure $SrTiO_3$ was observed with 0.4M, all following experiments were conducted with this total concentration. It is important to note that the d_{XRD} size of the materials doesn't alternate from the average 45nm despite the very different FSP parameters, with the lowest obtained size being produced from the 0.1M concentration of d_{XRD} 35nm. This observation will be discussed later.

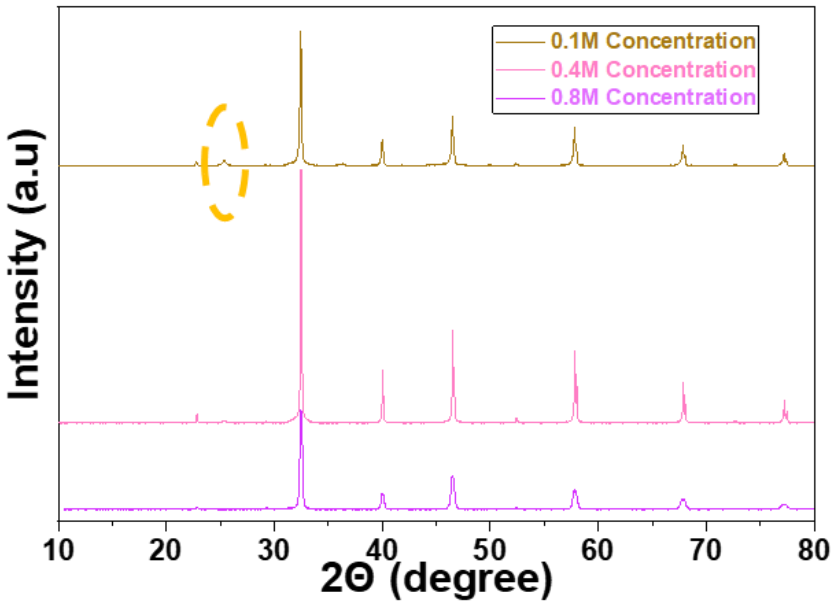

Figure 4-68: *XRD graph showing the effect of different precursor concentrations (0.8M, 0.4M, and 0.1M) encircled areas show secondary phases.*

Finally, the screening of the FSP synthesis high-temperature residence time was conducted by altering the height of the Quartz tube surrounding the flame from 40cm, 20cm, and 0cm i.e. open flame. Additionally, to increase and decrease the size of the flame, the precursor flow rate and the Oxygen dispersion flow rate (P/D) were changed from 3/7, 5/5, and 7/3. The XRD graph is shown in **Figure 4-69**. The crystallinity and the purity of the phase weren't impacted by the lower high-temperature residence time, and neither did the P/D change the resulting particles, with the most interesting finding being that the size of the resulting particles remained more or less the same at 45nm. Although with the 20cm Quartz Tube, the SSA was much lower at 22.9 $cm^3\ g^{-1}$, and the open flame produced an SSA of 32.3 $cm^3\ g^{-1}$. Thus every produced material was produced with the open flame FSP method.

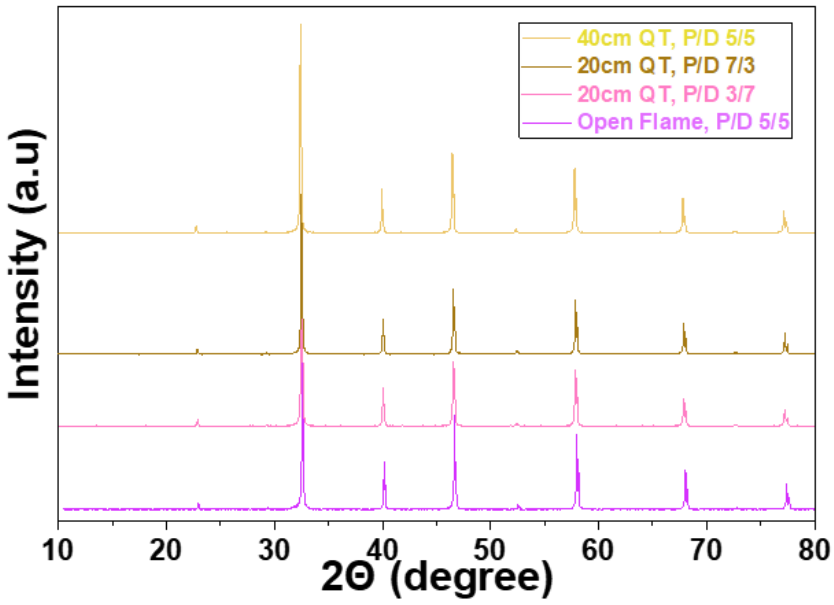

Figure 4-69: *XRD graph showing the effect of Quartz Tube (QT) of different Height (20cm, 40cm) and open flame FSP, secondary observation of different P/D ratios (3/7, 5/5, 7/3).*

4.5.3 Selected materials for DN-FSP synthesis of $SrTiO_3$ in tandem Lanthanum doping and CuO heterojunction

Double-Nozzle FSP: As shown in **Figure 4-70**, two FSP nozzles operate *in-tandem* that are asymmetrically positioned so that the system generates two different kinds of nanomaterials by controlling the properties of each nozzle independently. One nozzle sprays the precursor containing the atoms of Srtronium, Titanium, and small quantities of Lanthanum for inter-lattice dopping, while the second FSP nozzle contains the precursor of Copper the $Cu(NO_3)_2 \bullet 3H_2O$ (Supelco) dispersed in the mixture Acetonitrile: Ethyleglygol at a volume ratio 1:1. The Second FSP nozzle for the Copper particles had D and P rates were 5/5, and the pilot flame gases where 4 / 2 L min^{-1}, the same as the nozzle producing La:$SrTiO_3$.

Screening experiments were conducted to find the preferent geometric parameters: α_1 nozzle angle at 20^o, and $\alpha_2=20^o$. The internozzle distance was placed at x=8cm, and the vertical intersection distance of the two flames was b=10, see **Figure 4-70**(C).

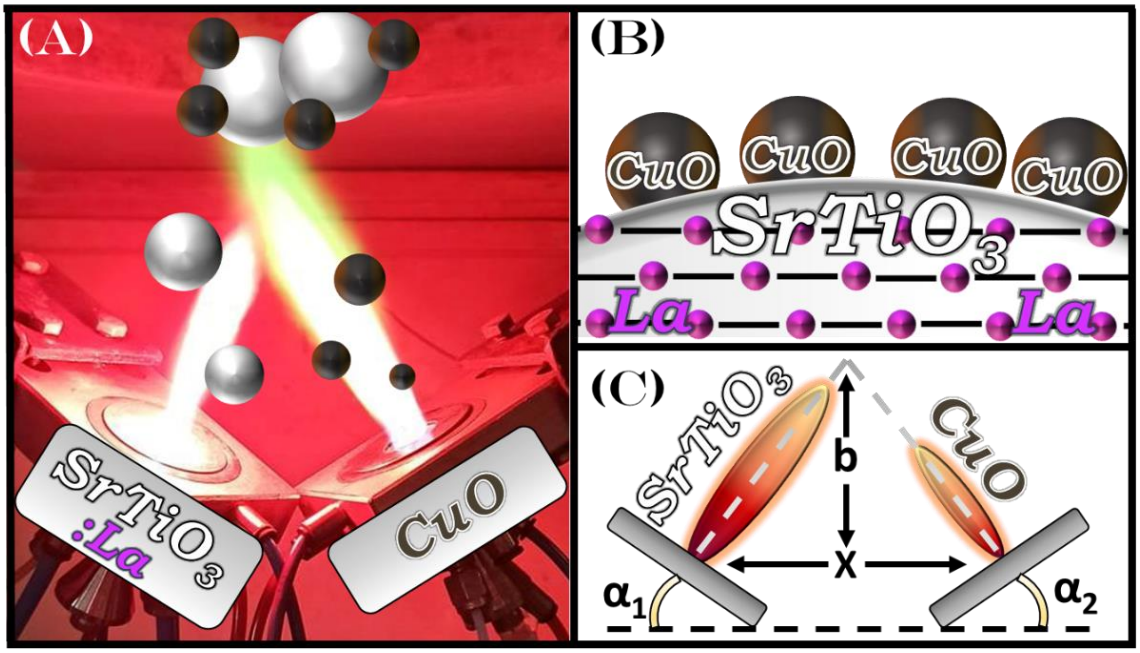

Figure 4-70: *(A) Description of the Double-Nozzle FSP (DN-FSP) set-up, the left-side nozzle produces La:SrTiO₃ nanoparticles, and the right-side nozzle produces the CuO nanoparticle cocatalyst. (B) Schematic depiction of the structure of La:SrTiO₃/CuO particle. (C) The geometric parameters for the two nozzles in DN-FSP (a_1, a_2, b, and x).*

The selected materials for the work of selected photocatalytic production were determined to be seven different particles, including a pristine $SrTiO_3$ that is used as a control particle, as shown in **Table 4-15**. The particles were codenamed as such: X_La:STO/Y_Cu, for the 3 different particle parameters, with the perovskite of $SrTiO_3$ shortened to STO, X the nominal % La-content per weight for $SrTiO_3$ for interatomic doping of Lanthanum, Y= the nominal % Cu-content per weight of $SrTiO_3$ for the heterojunction of $CuO/SrTiO_3$.

In this way, we have prepared with the Single Nozzle FSP the particles of pristine $SrTiO_3$, 0.9La:STO, and 0.35La:STO. For the DN-FSP experiments, we have produced STO/2Cu, STO/1.2Cu, and STO/0.5Cu. Finally, a particle containing Lanthanum doping and CuO heterojunction, the 0.25La:STO/0.5Cu produced by DN-FSP, is codenamed as La:STO/Cu, listed in **Table 4-15**.

To reiterate, the Cubic (Pm3m) perovskite $SrTiO_3$ structure (JCPDS74–1296) has distinct peaks 2θ at 22.71 32.34, 39.91, 46.43, 52.29, 57.74, 67.78 and 77.13 degrees. The XRD data of the six selected materials La:$SrTiO_3$/CuO are shown in **Figure 4-71**. All materials present high crystallinity, with the obtained peaks corresponding precisely to the Cubic (Pm3m) perovskite $SrTiO_3$ structure, with no traces of other crystalline byproducts, such as TiO_2 or Sr-oxide. The d_{XRD} calculated by the Scherrer method [326] indicates dXRD sizes in the 45-55nm range, as shown in **Table 4-15**.

Single-Nozzle FSP La-doped $SrTiO_3$ materials retain their high crystallinity and purity. More importantly, there weren't any additional Lanthanum secondary phases, such as La_2O_3. The materials drastically change photophysical properties with increased La-doping increasing a pink-hue color, in correlation of 0.9La:$SrTiO_3$ *vs.* the white $SrTiO_3$, see photos in **Figure 4-79**. The size of the materials, the La-doping shows an increase in the $SrTiO_3$-particle size, from 45nm d_{XRD} to 55nm d_{XRD}. Strikingly, counterintuitively to the usual correlation between size and surface area, the Specific Surface Area of $SrTiO_3$-particle increases also. This observation is further analyzed in the BET-data analysis, henceforth, **Figure 4-78**.

Double-Nozzle FSP synthesis of $SrTiO_3$/CuO heterojunctions retains once again the high crystallinity of $SrTiO_3$, with an absence of any XRD peaks derived from Cu^0, Cu_2O, or CuO, this fact is attributed to the very low Copper concentration, that the XRD accuracy fails to capture, thus the oxidation state of the copper particles will be determined with other techniques. Although there is a clear correlation between $SrTiO_3$ size and Cu content, with a tendency towards larger particle sizes at increased Cu-content, this observation is in agreement with previous reports [227], where this can be attributed to the increased enthalpy that is added due to the second flame, thus increasing the overall synthesis temperature, and extending the temperature at the stage of agglomeration.

Table 4-15: *Structural Characteristics of La:SrTiO₃, SrTiO₃/CuO, and La:SrTiO₃/CuO nanoparticles.*

Nanomaterial	La-, Cu-content XRF analysis (%wt)	d_{XRD}(nm) (±4)	SSA (m^2g^{-1}) (±0.5)	Total pore volume ($cm^3\ g^{-1}$) ($\pm0.02\times10^{-2}$)	Band gap E_g (eV) (±0.1)
Single-Nozzle FSP					
Pristine SrTiO₃	La:0 /Cu:0	45	32.3	0.14×10^{-2}	3.2
0.9La:STO	La:0.93±0.05 /Cu:0	47	53.1	0.39×10^{-2}	3.2
0.35La:STO	La:0.36±0.05 /Cu:0	55	57.5	0.36×10^{-2}	3.2
Double-Nozzle FSP					
STO/2Cu	La:0.05±0.05 /Cu:2±0.1	53	34.9	0.12×10^{-2}	3.2
STO/1.2Cu	La:0 /Cu:1.2±0.1	49	32.1	0.11×10^{-2}	3.2
STO/0.5Cu	La: 0.05±0.05 /Cu:0.5±0.1	45	32.0	0.11×10^{-2}	3.2
La:STO/Cu	La: 0.26±0.05 /Cu:0.5±0.1	52	37.3	0.16×10^{-2}	3.2

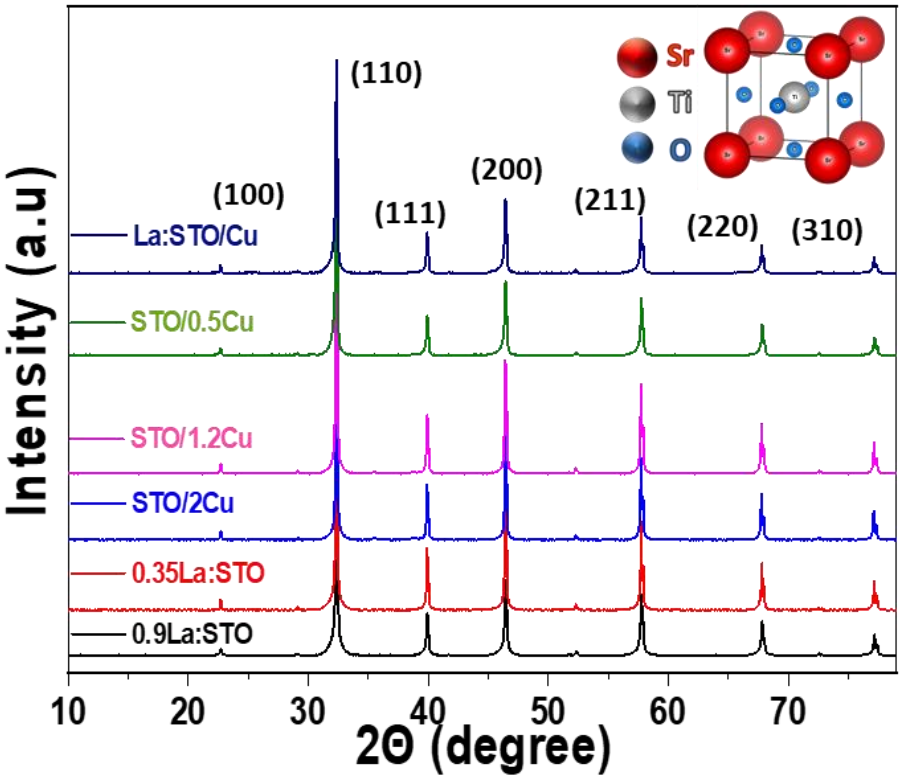

Figure 4-71: *XRD patterns for the selected La:STO/Cu nanomaterials. Inset: The unit-cell structure of the cubic $SrTiO_3$ structure.*

The TEM images of the pristine $SrTiO_3$ are shown in **Figure 4-72**, the other particles aren't shown as the resulting particles will be very similar to the pristine $SrTiO_3$, and the morphology of the nanoparticles are shown to be quasi-spherical with an average wide a distribution of particle sizes, as shown from the other perovskite particles in the Ph.D. the spherical morphology is consistent and with other FSP-made particles [175].

The ensuing particle-size distribution was calculated from multiple TEM images and fitted through a Gaussian fitting, as shown in **Figure 4-72**(B). The FSP-made $SrTiO_3$ includes a few large particles with 40-100nm diameters and many smaller particles with below 20nm diameters, resulting in a mean size of d_{TEM} =17±0.2nm. The comparison of the two different interpretations of nanoparticles size the d_{XRD} and d_{TEM}, exemplifies the well-known effect of large particles to predominate the diffraction peaks in XRD, thus d_{XRD} overestimates the average particle size.

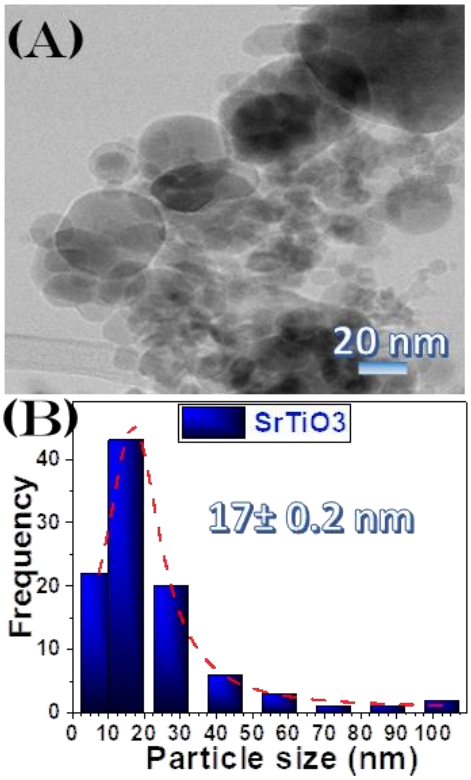

Figure 4-72: *(A) TEM image of the pristine $SrTiO_3$ particle. (B) Size distribution graph obtained from several TEM images.*

The morphology and phase composition of the six particles La:STO/Cu particle was studied using an FEI Talos F200i field-emission (scanning) transmission electron microscope (Thermo Fisher Scientific Inc., Waltham, MA, USA) operating at 200 kV, equipped with a windowless energy-dispersive spectroscopy microanalyzer (6T/100 Bruker, Hamburg, Germany). The resulting percentages of Lanthanum compared to the total weight of Strontium and Titanium for the materials 0.9La:STO, 0.35La:STO, and La:STO/Cu, calculated from **Figure 4-73**(A). While the Copper in comparison to the total height of Strontium and Titanium for the materials STO/2Cu, STO/1.2Cu, STO/0.5Cu, and La:STO/Cu, calculated from **Figure 4-73**(B), the La/Cu percentages are depicted in **Table 4-15**.

It is important to note that the Copper concentration used in the FSP precursor was five times higher than the observed concentration found in the final particles, this is attributed to the open flame methodology resulting in many copper particles being irrevocably lost from the filter. In comparison, the Lanthanum concentration in the precursor was only 30% higher than what is observed in the resulting particles, where the single nozzle forces the particles to bond in the perovskite structure.

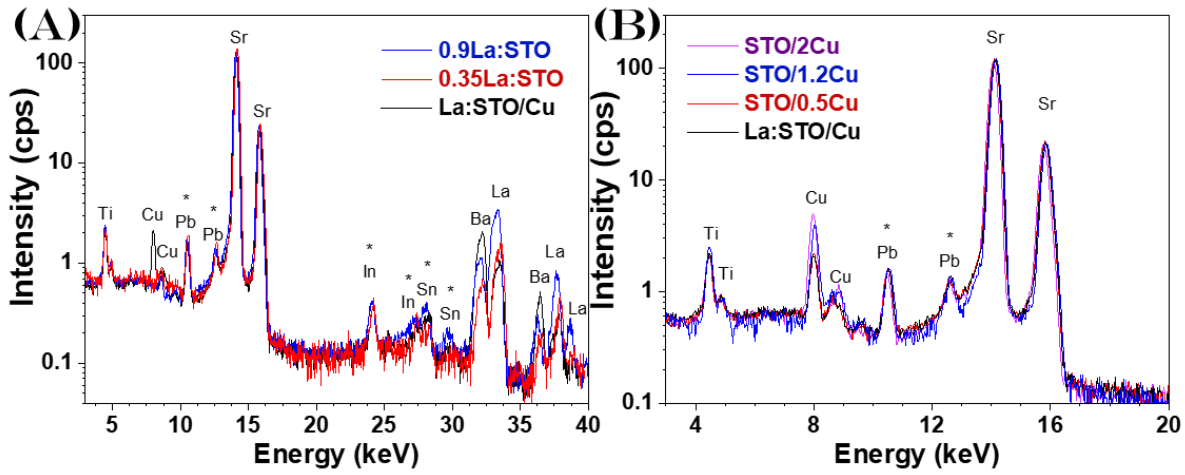

Figure 4-73: *The phase composition of: (A) For the Lanthanum percentage found in the 0.9La:STO, 0.35La:STO, and La:STO/Cu materials. (B) For the Copper percentage found in the STO/2Cu, STO/1.2Cu, STO/0.5Cu, and La:STO/Cu, as obtained from the (scanning) transmission electron microscope.*

In **Figure 4-74,** the Scanning-TEM images for La:STO/Cu are shown as the only material that possesses the La structural doping and the expected heterojunction with small Cu-nanoparticles on the surface. **Figure 4-74**(A to D) shows the atomic mapping of (A) Ti, (B) Sr, (C) La, and (D) Cu of La:STO/Cu. The $SrTiO_3$ perovskite structure is shown to have high Crystallinity and pure phases since the Ti and Sr mapping does not show any holes or excess concentration of either atom, negating the possibility of nano regions of Sr/Ti oxides. The atomic distribution of the Lanthanum atom in the structure is observed to be uniformly distributed, without La-clusters or separate nano regions of Lanthanum particles. For the Copper mapping, caution is drawn to the fact that the faint blue-hue is the enhanced emissions from the Cu-grid atoms employed for the TEM measurements methodology. The blue-hue signals are found due to the close proximity to the Sr-atoms producing secondary signals of Cu-electrons from the Strontium excitations enhancing. Thus, only the signal inside the white circles is an actual Copper signal with a dense structure. Verifying that dense signal is located only on the surface of the $SrTiO_3$ perovskite due to the DN-FSP methodology.

Although the uniformly structural deposition of Lanthanum was verified and Cu-particles are on the surface of $SrTiO_3$, the question of the oxidation state of Copper particles remains. Two separate identification methods were employed, first through XPS, which will be shown below, and second through the HRTEM images for the particle La:STO/Cu, as shown in **Figure 4-75**. The copper nanoparticles show distinct Miller planes of CuO (110), with the distance between the planes calculated to be d=2.75Å [415], verifying that the copper particles have the oxidation state of CuO deposited on the surface of the $SrTiO_3$ perovskite, with an average size of <2nm, therefore, they are not detected in the XRD.

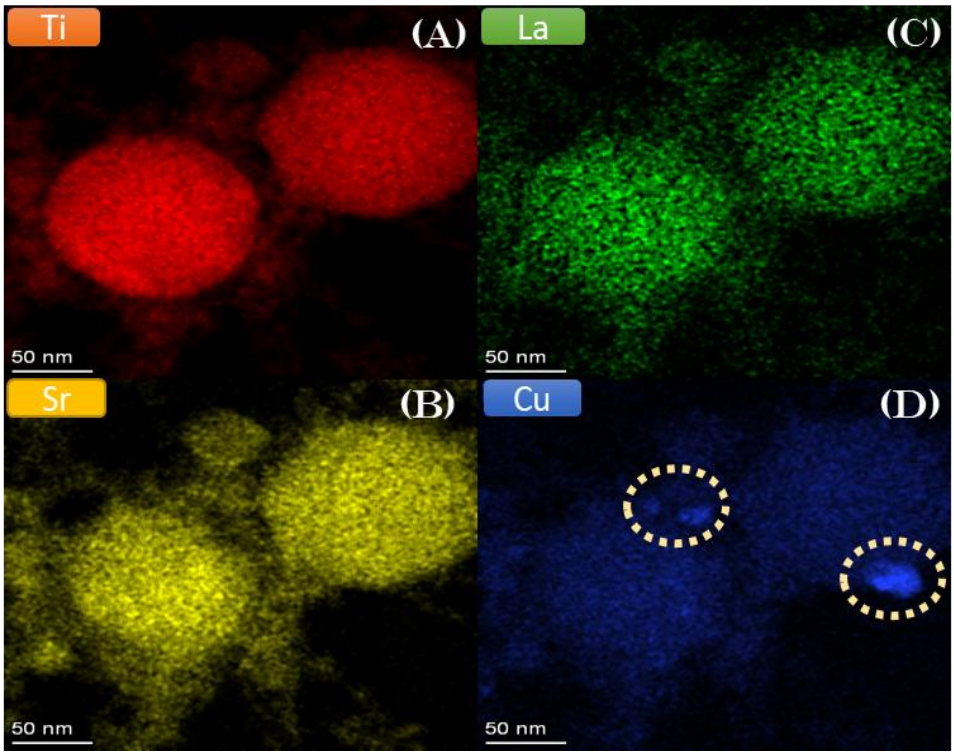

Figure 4-74: *Scanning-TEM images with (A) Titanium, (B) Strontium, (C) Lanthanum, and (D) Copper atom mapping for material La:STO/Cu.*

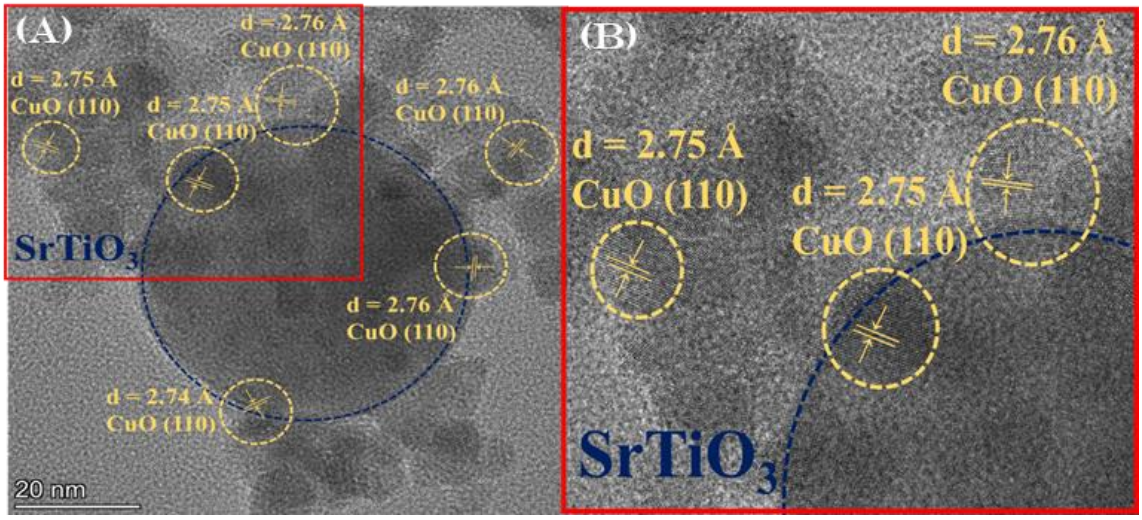

Figure 4-75: *(A) HRTEM images for La:STO/Cu particle, with the distinct Miller planes of CuO (110) deposited on the $SrTiO_3$ surface. (B) The zoomed area of the previous STEM image to distinguish the CuO planes.*

4.5.4 Electronic/photocatalytic property characterization for La:$SrTiO_3$/CuO nanoparticles

The N_2-adsorption isotherms for the seven nanomaterials are presented in **Figure 4-76**. All seven nanomaterials have the characteristic type-IV isotherm. The pore size distribution plot using the BJH method of the seven $SrTiO_3$ particles and the overall pore volume is present in **Figure 4-77.**

To have a clearer understanding of the effect of Lanthanum doping, four selected materials are shown for the N_2-adsorption isotherms in **Figure 4-78**(A). The results show some interesting trends: First, the La-dopped particles show an increase in their SSA values, with almost double the SSA of the pristine $SrTiO_3$ compared to the 0.35La:STO. However, considering the XRD data that reveals the size d_{XRD}, this increased SSA does not concur with the particle size i.e., a bigger SSA should have a smaller size.

Second, another interesting trend is found by examining the pore-size and pore volume trends upon La-doping of the $SrTiO_3$ perovskite, see **Figure 4-78**(B). The typically total pore volume found in the literature for $SrTiO_3$ nanoparticles is reported to possess around 15 $cm^3\ g^{-1}$ [174,416], which is in the same range observed for our pristine $SrTiO_3$ nanomaterial and the CuO heterojunction nanomaterials. Upon La-doping, as mentioned, there is a sharp increase in SSA, but more importantly a 3-fold increase of the pore volume to 39 $cm^3\ g^{-1}$ for 0.9La:STO.

This trend can be attributed to a geometrical effect of aggregation, as depicted in the scheme in **Figure 4-78**. This is a result of the FSP-process, where the La-doping decreases the packing/aggregation of the $SrTiO_3$, even though some $SrTiO_3$ might grow bigger nanoparticle sizes. It is worth mentioning the relatively high surface area and pore volume in our nanomaterials in comparison to other synthesis methods for $SrTiO_3$ that possessed lower SSA, which is in large part attributed to the high calcination temperatures application [137,417] in comparison to the short synthesis time/high temperature of FSP.

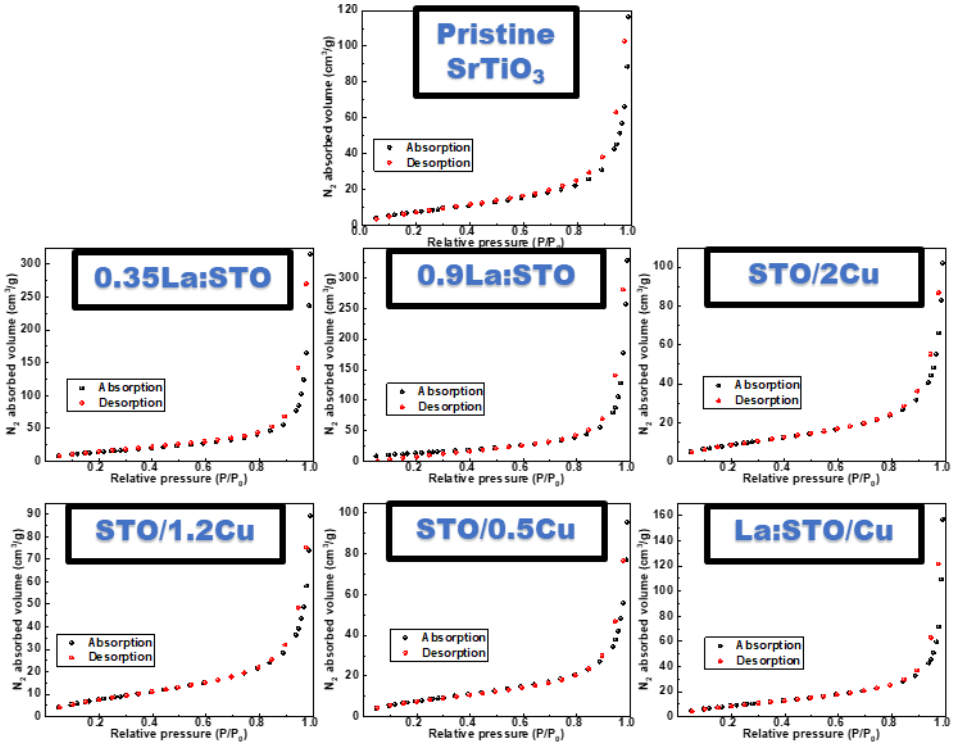

Figure 4-76: *N_2 adsorption-desorption isotherms of the seven $SrTiO_3$ particles.*

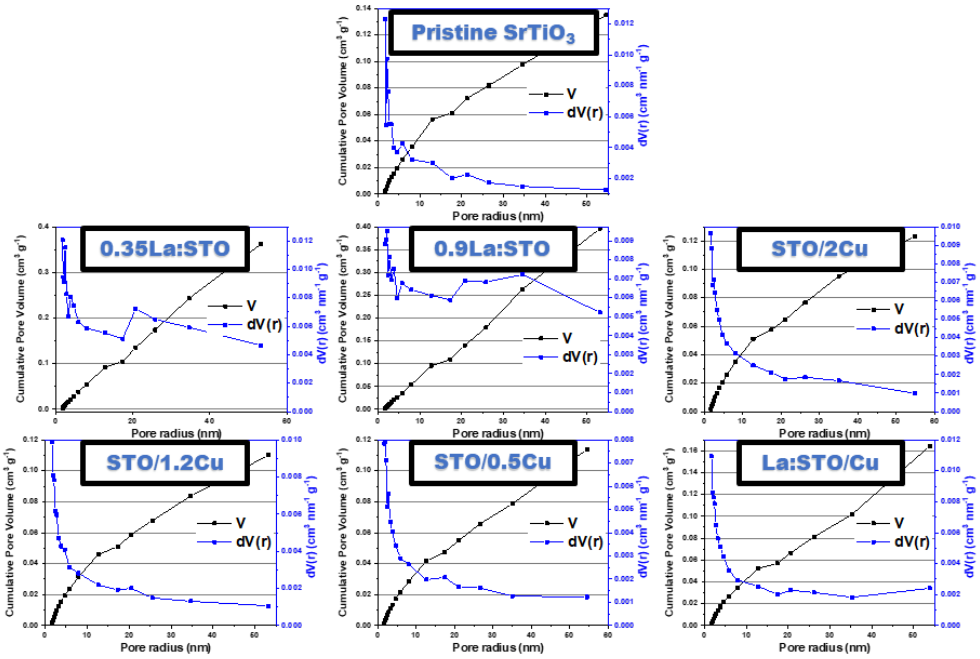

Figure 4-77: *Pore size distribution plot using the BJH method of the seven $SrTiO_3$ particles.*

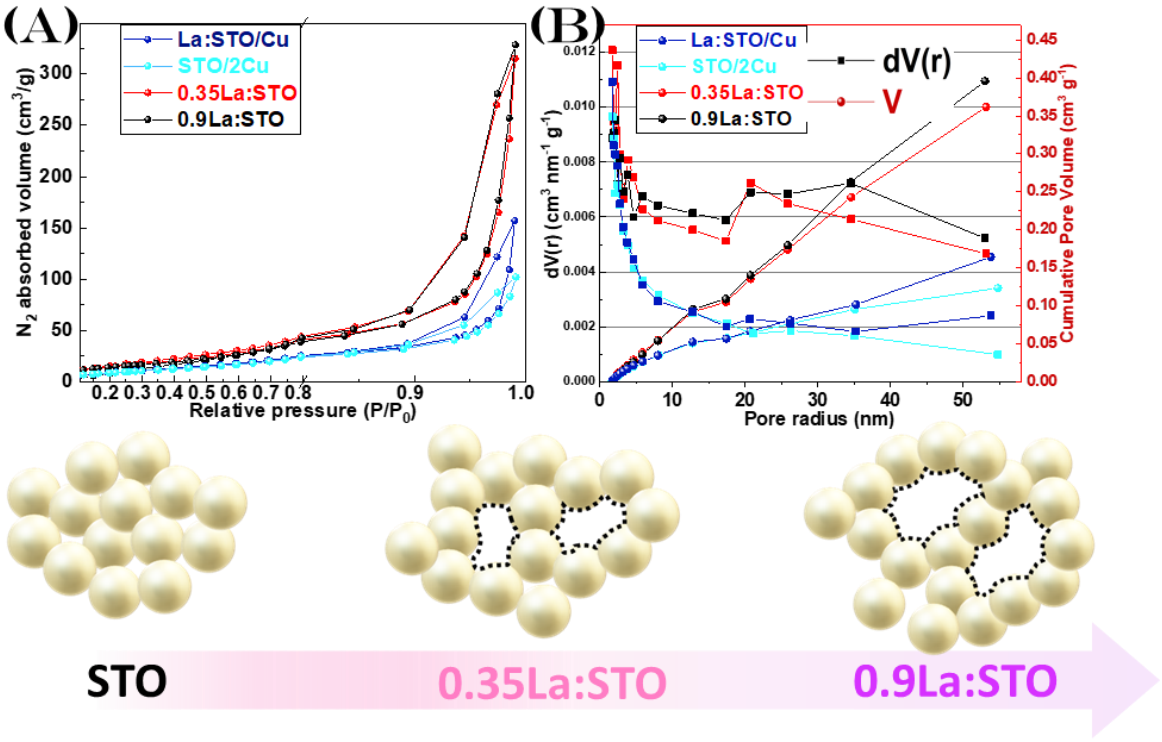

Figure 4-78: *Selected Lanthanum doped $SrTiO_3$ nanoparticles compared to standard non-doped particles (STO/2Cu) for: (A) Nitrogen adsorption isotherms. (B) The corresponding pore-size distribution plot using the BJH method and the Cumulative Pore Volume. Bottom: Schematic nanomaterial visualization of the La-doping effect on the formation aggregation.*

DRS-UV-Vis data for the seven selected $SrTiO_3$ nanoparticles are shown in **Figure 4-79**(A), and the indirect band-gap has been calculated using the Kubelka–Munk method [327], **Figure 4-79**(B). The $SrTiO_3$ perovskite as a semiconductor has been measured to have an indirect bandgap of 3.25 eV and a direct bandgap of 3.75 eV [418]. Furthermore, specific atomic doping such as La or Nb or oxygen vacancies can introduce additional Density of States(DOS) in the band gap [418], with DOS showing below the Conduction Band producing an *n*-type alteration for the structure.

For all the seven materials, the absorption begins at 390nm correlating to a band gap close to 3.2eV [419], listed in **Table 4-15**. Lanthanum doping or Copper heterojunction fundamentally alters the material's color, in comparison to the white color of pristine $SrTiO_3$, as shown in the side-photos of **Figure 4-79**, Lanthanum doping results in a purple

hue, while a deep brown tint was observed for the CuO heterojunctions [227], this is further evident by the extra visible absorption in the 400-580nm range in the DRS Uv-Vis. Overall the changes in the perovskite attributes based on the La-doping and Cu-heterojunction are in accordance with the literature data.

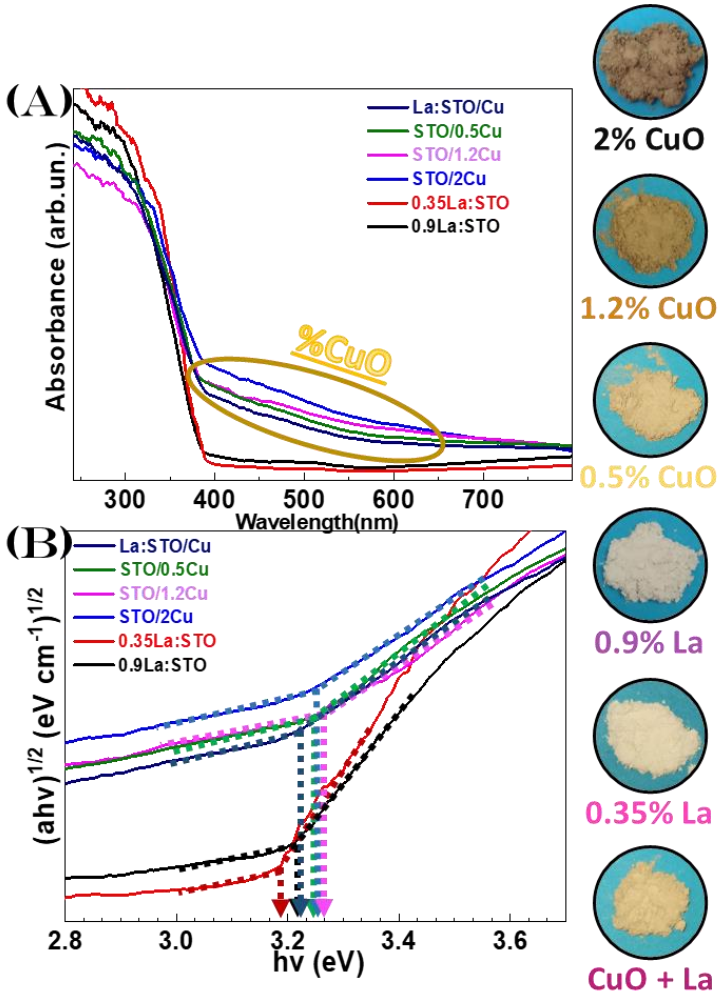

Figure 4-79: *For the seven selected materials $SrTiO_3$:(A) DRS-UV-Vis data, with CuO increasing visible absorption. (B) Tauc-Plots with the dotted arrows show the calculated bandgap. Side-photos: The powder nanoparticles showcase the color shift in comparison to the white color of pristine $SrTiO_3$.*

X-Ray Photoelectron Spectroscopy: XPS data for the oxidation states of Ti - Sr- O- and Cu atoms are presented below. For convenience, the three most remarkable materials are presented, the material with the highest Lanthanum deposition 0.9La:STO, the highest

Copper deposition STO/2C, and the material La:STO/Cu with the deposition of Lanthanum and Copper atoms.

For the Titanium XPS spectra, all materials have peaks located at 457.7eV and 463.4 eV, which are the binding states of Ti $2p_{3/2}$ and Ti $2p_{1/2}$ respectively, corresponding to typical Ti^{4+} states, as shown in **Figure 4-80**(A-C). For the Strontium XPS spectra, the materials exhibited binding energies at 132.2 eV and 134 eV that are identified as the Sr $3d_{5/2}$ and Sr $3d_{3/2}$, corresponding to the oxidation state of Sr^{2+} for the $SrTiO_3$ [420,421], as shown in **Figure 4-80**(D-F). The Titanium and Strontium oxidation states are consistent with the expected for the perovskite structure $SrTiO_3$, thus there aren't any Sr-Ti impurities in the structure.

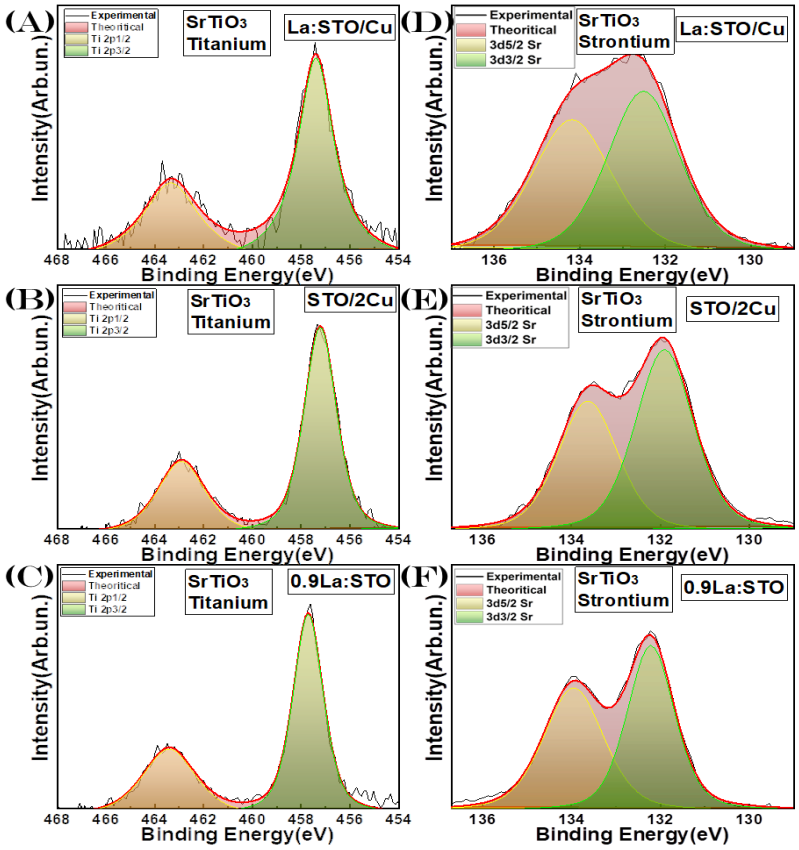

Figure 4-80: *XPS spectra of Titanium for the binding energies of Ti $2p_{3/2}$ and Ti $2p_{1/2}$ for the (A) La:STO/Cu, (B) STO/2Cu, and (C) 0.9La:STO materials. XPS spectra of Strontium for the binding energies of Sr $3d_{5/2}$ and Sr $3d_{3/2}$ XPS spectra for the (D) La:STO/Cu, (E) STO/2Cu, and (F) 0.9La:STO materials.*

The XPS Oxygen data are shown in **Figure 4-81**(A). For all the materials, three peaks were observed, starting with the lowest binding energy at 528.9eV that can be attributed to the lattice oxygen species of the $SrTiO_3$ crystal structure [421,422]. The binding energy at 531.1eV is attributed to chemisorbed oxygen. Finally, the peak at 532.4eV is attributed to adsorbed oxygen from the atmosphere on the particle surface or hydroxyl groups [421,422]. The material La:STO/Cu (0.25%La/0.5%CuO) has a partially different intensity ratio between the lattice peak and the chemisorbed oxygen species. This can be possibly attributed to oxygen vacancies in the crystal structure derived from the lattice bending from the lanthanum doping, this lattice bending can impact the adsorption and efficiency of the oxygen species at the catalyst surface [421,422].

The XPS Copper data are shown in **Figure 4-81**(B). The copper oxidation state is crucial in determining the crystal phase of the copper and secondary impurities. As already seen from the STEM Miller spacing, the particles were found to be CuO, although the XPS can show a much more broad area of the nanoparticles and more accurately determine small copper species. The material STO/2Cu i.e., the material with the higher Cu-loading is measured since it possesses strong Cu-XPS signals to ascertain the Cu-oxidation state precisely.

The binding energies located broadly at 932.8eV and 952.7eV correspond to the Cu $2p_{3/2}$ and Cu $2p_{1/2,}$ respectively [423,424], with the peak for metallic copper distinctively absent, from the XPS there are two other possible oxidation states Cu(II) or Cu(I). The distinction can be determined from the strong satellite signal presence at 941eV and the broader peaks of Cu $2p_{3/2}$ and Cu $2p_{1/2}$ indicate that the Cu atoms are in the Cu(II) oxidation state [423,424]. Thus, XPS results further confirm that the heterostructure is indeed $SrTiO_3$/CuO. This is in agreement with the FSP-methodology that we employ, with the Precursor/Dispersion(O_2) rates of 5/5 and open flame set-up (i.e. the flame wasn't surrounded by Quartz Tube) that produces a highly oxidizing environment [175] that in the case of the copper nanoparticle synthesis promotes the formation of CuO.

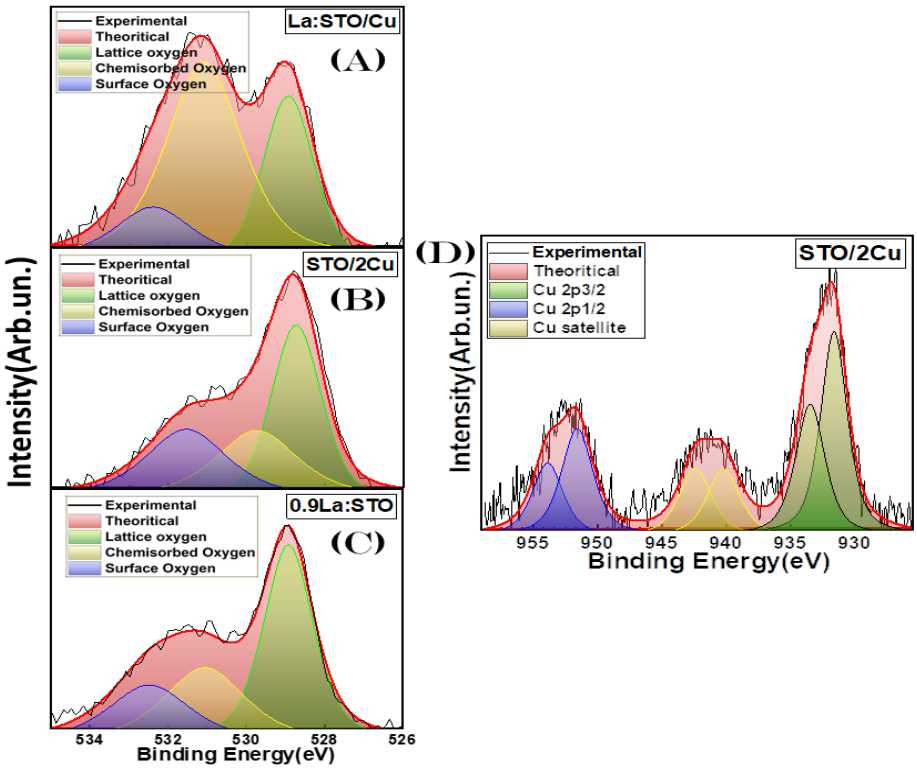

Figure 4-81: *XPS spectra of Oxygen for the binding energies of Lattice, chemisorbed, and surface Oxygen for (A) La:STO/Cu, (B) STO/2Cu, and (C) 0.9La:STO materials. (D) XPS spectra of Copper for the binding energies of Cu $2p_{3/2}$ and Cu $2p_{1/2}$ XPS spectra for the STO/2Cu material.*

Overall, the XPS data for the oxidation states of Ti - Sr- O- and Cu atoms shows the deposition of Lanthanum doping in the structure or the heterojunction of CuO particles in the surface does not alter the $SrTiO_3$ oxidation states, with the typical Ti^{4+} and Sr^{2+} oxidation states, although there are some O-vacancies in all materials. The nanoparticles of Copper are confirmed as CuO from XPS and TEM. La-could not be detected by XPS in any of our materials due to the very low concentration in the materials.

4.5.5 La:$SrTiO_3$/CuO materials for selective photocatalytic production of H_2/CH_4

Photocatalytic results for photocatalytic hydrogen production of the seven $SrTiO_3$ materials were evaluated using a mixture of H_2O/CH_3OH as a catalytic substrate. The catalytic products were observed to be only H_2 and CH_4 for all the particles. Beginning with

the most academically explored product of Hydrogen, the results are shown in **Figure 4-82**(A), with the corresponding rates per hour in **Figure 4-82**(B).

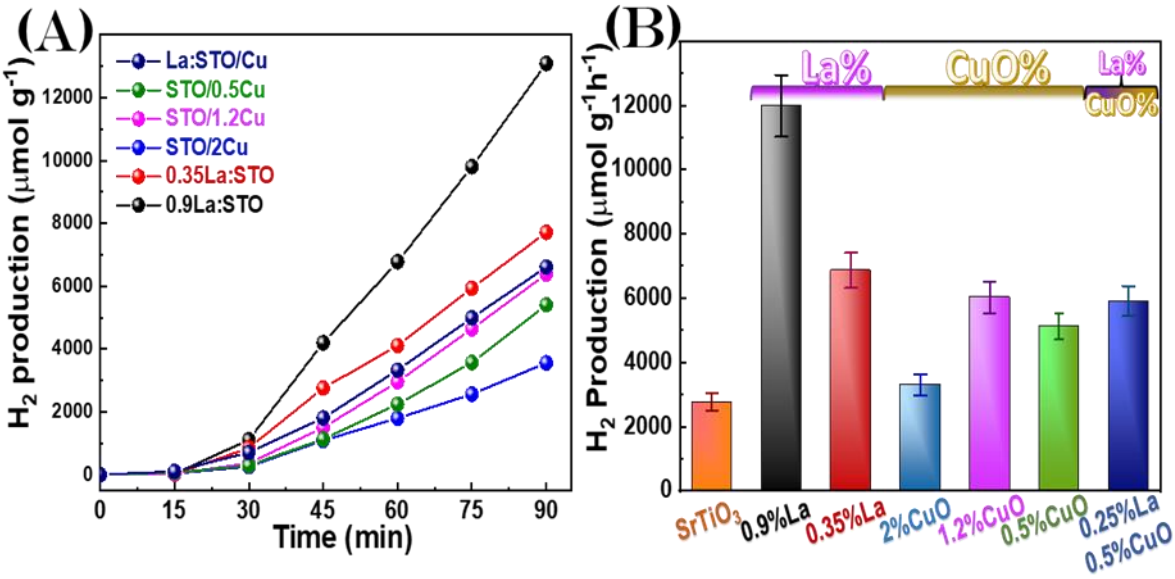

Figure 4-82: *Photocatalytic production by the nanomaterials from an H_2O/CH_3OH mixture. (A) Hydrogen per time. (B) The Hydrogen production rate [umols per gr catalyst per hour].*

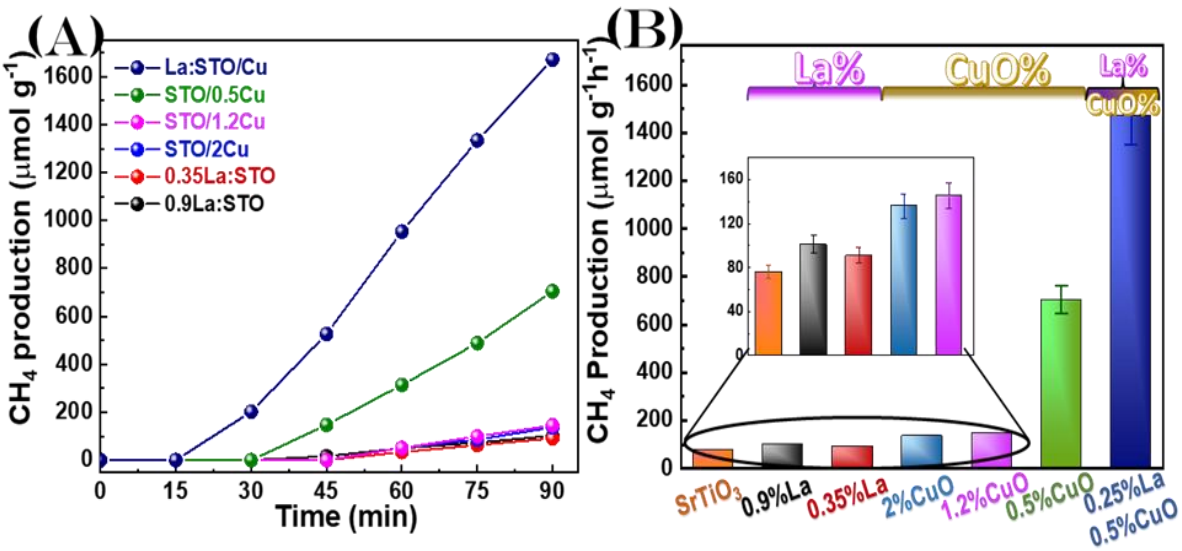

Figure 4-83: *Photocatalytic production by the nanomaterials from an H_2O/CH_3OH mixture. (A) Methane per time. (B) The Methane production rate [umols per gr catalyst per hour].*

The highest H_2-yield was 11980 umol $g^{-1}h^{-1}$, achieved by the 0.9%La: $SrTiO_3$, which is ~500% higher than for pristine $SrTiO_3$ that has H_2-yield of 2760 umol $g^{-1}h^{-1}$. A clear beneficial trend is observed between 0.9La:STO, 0.35La:STO, and pristine $SrTiO_3$, with higher La-doping promoting the photocatalytic efficiency of H_2-production, the photocatalytic beneficial effect of Lanthanum doping trend is in agreement with the literature [150,151]. As hydrogen production has already been explored compared to Lanthanum doping, the most intriguing aspect of the observed materials is the effect on methane production.

The results of the photocatalytic production of methane are shown in **Figure 4-83**(A), with the corresponding rates in **Figure 4-83**(B). From the results, it is evident that in the absence of CuO, the production of CH_4 from the photoreduction of methanol was minimal, while the selectivity towards CH_4 is apparent for all CuO heterojunctions, where the least efficient material $SrTiO_3$/2%CuO has almost the same H_2 production as the pristine $SrTiO_3$. However, there is a sharp increase in the CH_4 (76 to 136 umol $g^{-1}h^{-1}$). Decreasing CuO content to 0.5% CuO resulted in almost double the hydrogen production of 2% CuO, while most importantly, the methane production of $SrTiO_3$/0.5%CuO increased to 704 umol $g^{-1}h^{-1}$, ten times increase from the pristine and 5 times increase from 2% CuO.

The drastic change in the photocatalytic efficiency derives from the Cu-loading of $SrTiO_3$ surface, where a higher percentage of the surface is covered with CuO, which in turn might act as an inhibitor of light-absorbance by the $SrTiO_3$. This 'darkening' effect plays a key role in diminishing the photocatalytic activity. Most interestingly, the material 0.25%La/0.5%Cu combined the effect of La/CuO, where the Lanthanum enhanced the photocatalytic efficiency, with the CuO harnessing this enhanced efficiency towards the selective photocatalytic production of methane, with the CH_4 reaching 1469 umol $g^{-1}h^{-1}$ and H_2 to 5907 umol $g^{-1}h^{-1}$.

Overall, the present data in **Figure 4-82** and **Figure 4-83** demonstrate that: [i] In all instances, La-doping significantly increases the photocatalytic activity, [ii] CuO on $SrTiO_3$ drives the products toward the reduction of CH_3OH to CH_4, controlling the photocatalytic product through selectivity of H_2/CH_4. Where SN or DN FSP can offer a competitive synthesis technique for the production of nano $SrTiO_3$, La:$SrTiO_3$, $SrTiO_3$/CuO, and more complex nanoparticles such as La:$SrTiO_3$/CuO in one step, these materials show significant photocatalytic activity that can be tailored towards either pure H_2 production or CH_4/H_2 production from H_2O/CH_3OH mixture. After the photocatalytic application, the particles fully retained their structure, as evidenced by XRD data, as seen in **Figure 4-84**.

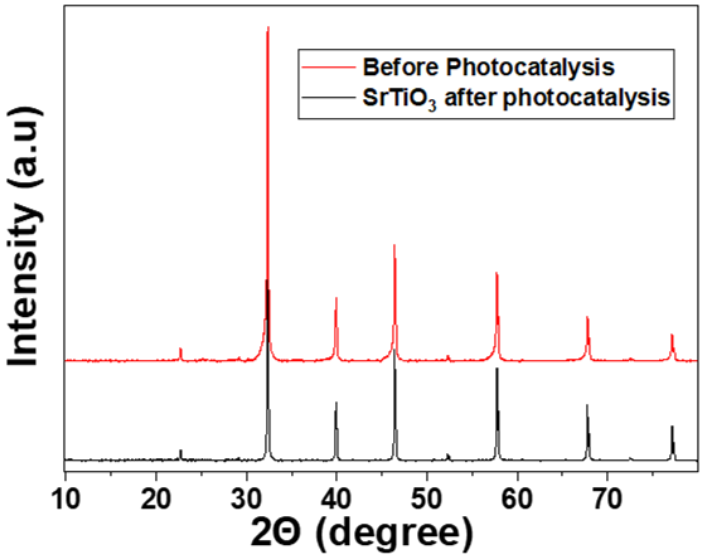

Figure 4-84: *XRD data of $SrTiO_3$ before and after photocatalysis production of H_2/CH_4.*

An analytical comparison of photocatalytic activity for $SrTiO_3$-based nanocatalysts in the literature vs. the present FSP particles is shown in **Table 4-16**. From the literature, there isn't any applicable measurement of CH_4 production, although the application of methanol or ethanol as a sacrificial agent is well established, only the hydrogen production is published. For this reason, the literature comparison is only for Hydrogen production. Most research publications utilize Xenon radiation which is similar to solar radiation, with

the highest yields shown in **Table 4-16**, although there are several works that utilize Mercury lamp radiation that consists of a high percentage of UV-irradiation.

Table 4-16: *Hydrogen production rates and conditions reported for similar particles/methods.*

Photo catalyst	Synthesis method	Cocatalyst (wt%)	Light Source	Reaction solution	H_2 Yield (umol $g^{-1}h^{-1}$)	*Ref.*
0.9%La:$SrTiO_3$	FSP	1% Pt	Hg(250W)	H_2O + 20% CH_3OH	**11978**	*This work*
0.25%La:SrTiO/ 0.5% Cu	FSP	1% Pt	Hg(250W)	H_2O + 20% CH_3OH	5907	*This work*
Ag-STO	Microwave assisted hydrothermal	2% Ag	UV-low pressure Hg	50% H_2O + 50% ethanol	463	[425]
Pt- $SrTiO_3$	Polymerized-Complex	0.32% Pt	Hg (500W)	Pure water+ 40% methanol	3200	[426]
Nanofibers $SrTiO_3$	Electrospinning	-	Hg (450W)	Pure water+ 40% methanol	160	[427]
La: CoO/$SrTiO_3$	Solid state reaction	-	Hg(400W)	Pure water+ Na_2CO_3	2800	[428]
Na:$SrTiO_3$	polymerizable complex	0.3% Rh	Hg(450W)	Pure Water	1600	[429]
Macroporous $SrTiO_3$	emulsion polymerization	0.7% Pt	Xe(300W)	Pure water+ 25% methanol	3599	[430]
g-C_3N_4/Rh-$SrTiO_3$/RGO	Multiple methods	0.58% Rh	Xe(260W)	Pure water+ 10% TEOA	3467	[431]

In the case of $SrTiO_3$, full utilization of the material as a semiconductor requires Uv radiation, since its band-gap is 3.2eV, in order to maximize the photocatalytic production of Hydrogen [425–429], in comparison with the high percentage of visible-light H_2 production [430,431]. In this context, the Single Nozzle FSP-made 0.9%La:$SrTiO_3$ nanocatalyst has the highest yield in comparison to the literature data on pertinent La:$SrTiO_3$ materials, although the irradiation method that was employed of Mercury lamp certainly boosts the photocatalytic production.

Methane photoproduction isn't mentioned in the literature for $SrTiO_3$/CuO heterojunctions. For this reason, other works are showcased to determine the effect of Copper based particles on the photocatalytic effect on hydrogen or methane selectivity. First, for hydrogen production, stabilizing CuO or Cu_2O NPs on metal oxides with lower conduction-band positions is a common strategy to enhance photocatalytic H_2 production

[432,433], with predominant applications of Cu_2O particles coupling with TiO_2 or ZnO leads to efficiency photocatalysts [432,434].

Secondly, for the methane selectivity, Xiong *et al.* demonstrated that on a TiO_2-Pt-Cu_2O nanohybrid, Cu_2O promotes the CH_4 production and at the same time, suppresses the H_2 evolution [435]. Chen *et al.* had shown that the co-existence of Cu^{1+}/Cu^0 species on TiO_2 enhances the photocatalytic efficiency by increasing the lifetime of electrons leading to an enhancement of CO_2 hydrogenation. In the same study, the reduction of CuO to Cu^0 was found to be more efficient for the photocatalytic production of CH_4. The hybrid Cu-Cu_2O/TiO_2 has shown an excellent selectivity for CH_4 which is attributed to the suppression of CO formation from Cu^0 species, while Cu^{1+} species act as the active sites for CH_4 production [436]. All these data pose the possibility that the promotion of CH_4 production by $SrTiO_3$/CuO or La:$SrTiO_3$/CuO heterojunctions might involve the formation of Cu^{1+} or Cu^0 species at the $SrTiO_3$/CuO interface.

4.5.6 Conclusions of FSP made La:$SrTiO_3$/CuO for photocatalytic production of H_2/CH_4

[a] Implementation of Single-Nozzle Flame Spray Pyrolysis technology as a synthesis method to produce controlling Lanthanum-Doping in the crystal structure of $SrTiO_3$, while Double-Nozzle Flame Spray Pyrolysis for *in-tandem* CuO/$SrTiO_3$-heterojunction. The proposed FSP-technology allows controlled production of complex nanoparticles such as La:$SrTiO_3$/CuO with fundamental advantages of one-step production and the potential for scalable production.

[b] The resulting nanomaterials showed distinct structural-electronic properties, with a distinct change in structural property from the La-doping inducing a characteristic increase of SSA *via* the formation of larger pore-voids, sequentially the electronic properties altered with the CuO heterojunction, with the wavelength absorption shifting toward visible light.

[c] Diligent control of the La-doping and $SrTiO_3$/CuO heterostructure allowed selective control of photocatalytic production of H_2 or CH_4 from an H_2O/CH_3OH mixture. La-doping in all cases increased the photocatalytic activity of $SrTiO_3$ nanocatalysts, with the 0.9La:STO

showing a benchmark H_2-production rate of 12 mmol $g^{-1}h^{-1}$, approximately a five times increase from pristine $SrTiO_3$. Incorporation of CuO drastically shifted the selectivity from H_2 toward CH_4, with the $SrTiO_3$/0.5%CuO having CH_4 production of 704 umol $g^{-1}h^{-1}$, a ten times increase in comparison to the pristine $SrTiO_3$. The highest CH_4 production was achieved with *in-tandem* incorporation of La and CuO, for the 0.25%La:$SrTiO_3$/0.5%CuO catalyst, with a CH_4 production rate of 1.5 mmol $g^{-1}h^{-1}$.

Thus, the present work exemplifies FSP as a potential synthesis technology to produce complex nanocatalysts while bringing new insights into photocatalysis for H_2/CH_4 production.

4.6 EPR Study of Photo-induced Hole/Electron Pairs in $NaTaO_3$ Nanoparticles

4.6.1 Aims of $NaTaO_3$ photoactivity from EPR

Alkali tantalates, particularly $NaTaO_3$ are highly efficient photocatalysts under UV excitation [93–96] due to highly-negative conduction band energy, determined primarily by the *d*-orbitals of Tantalum and the effect of alkaline atoms. The photo-induced electron/hole pair facilitates the photocatalytic reduction and oxidation i.e. Hydrogen generation from water or CO_2 reduction, while the h^+/e^- pair are key-step the direct detection of them remains elusive. To detect and understand the h^+/e^- pair, we applied the electron paramagnetic resonance (EPR). There are only a few EPR studies that exist on photoactive $NaTaO_3$, however, none on photoinduced $\{h^+/e^-\}$ pairs.

In order to have a successful detection, we synthesized the Perovskite $NaTaO_3$ for the first time through flame spray pyrolysis (FSP). The FSP technology allowed the formation of the smallest nanoparticle size in the bibliography. Herein, we made the hypothesis that the smallest nano-$NaTaO_3$ particles would expose the elusive photo-induced $\{h^+/e^-\}$ pairs, as the semiconductor particle size is of key importance in correlation to the recombination of $\{h^+/e^-\}$ pairs.

To understand the role of the particle size in $\{h^+/e^-\}$ dynamics, two $NaTaO_3$ sizes (14 and 26nm) were studied. The aim of the present work: [a] Synthesis by FSP

for small perovskite $NaTaO_3$ nanoparticles. [b] *In situ* trapping and detection of photoinduced $\{h^+/e^-\}$ pairs and identification of their lattice *vs.* surface nature by low-temperature CW-EPR (77K). [c] Study of the recombination dynamics of the photogenerated h^+/e^- pairs in comparison with photocatalytic H_2 production performance.

The results from the research have been published in our work with the title "Electron paramagnetic resonance study of photo-induced hole/electron pairs in $NaTaO_3$ nanoparticles" for the Journal of Chemical Physics Letters [225], with the graphical abstract shown in **Figure 4-85**.

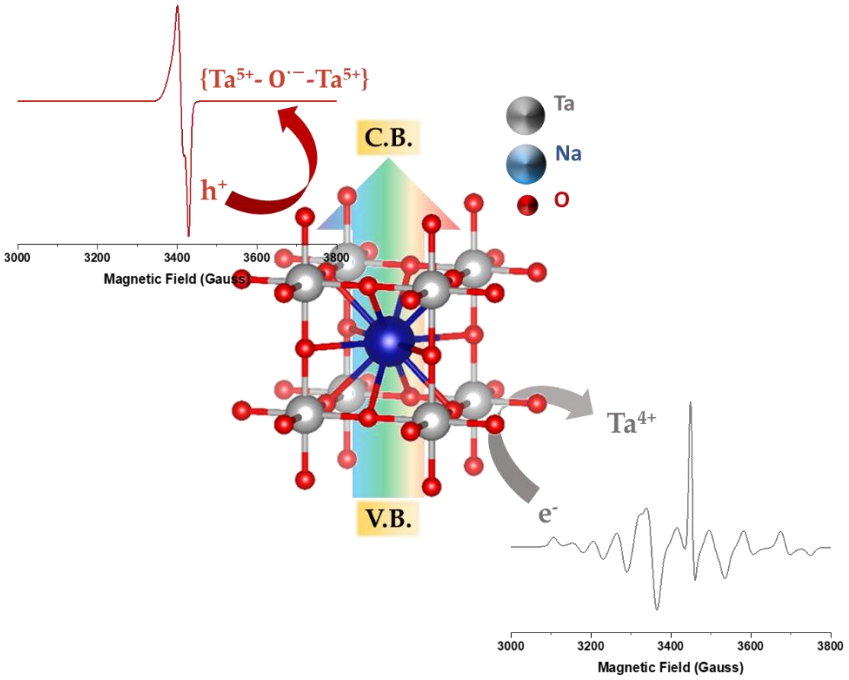

Figure 4-85: *The graphical abstract of Nanosized $NaTaO_3$ for photoinduced h^+/e^- pairs and recombination dynamics.*

4.6.2 Characterization for the $NaTaO_3$ Nanoparticles for photoinduced e^-/h^+:

Flame Spray Pyrolysis Synthesis of $NaTaO_3$*:* The bulk of the experiments for the $NaTaO_3$ formation will be detailed in the next section for easier comprehension and simplicity.

To mention only the fundamental parameters, the two $NaTaO_3$ nanoparticles were produced in a single-nozzle enclosed FSP reactor, the precursor solution had a molar ratio of 1:1 Tantalum(V) chloride (anhydrous 99.9%, STREM) and sodium 2-ethylhexanoate (98%, TCI), dissolved in ethanol. The 14nm-$NaTaO_3$ had a total Na-Ta concentration of 0.1M, while the 26 nm-$NaTaO_3$ had a total Na-Ta concentration of 0.6M. The flame was surrounded by a quartz tube of 20 cm in height, and the FSP parameters comprised a dispersion oxygen flow rate of 5 L min^{-1} (Linde 99.999%) and a precursor flow rate of 5 mL min^{-1}.

Morphology of the two-sized $NaTaO_3$: The two materials are codenamed $14NaTaO_3$ and $26NaTaO_3$ according to their 14nm and 26nm size. The overall size, morphology, and photocatalytic efficiency are shown in **Table 4-17**.

Table 4-17: *Structural characteristics of nano-$NaTaO_3$ for EPR photoinduced e^-/h^+.*

Material	crystallite size (nm)		SSA (m^2g^{-1})	Total pore volume ($cm^3\ g^{-1}$)	Hydrogen (umol $g^{-1}\ h^{-1}$)
	d_{TEM}	d_{BET}			
$14NaTaO_3$	14 ±1	12	60.5	18×10^{-2}	1621
$26NaTaO_3$	26 ±1	27	27.5	7×10^{-2}	645

The XRD data of the two materials are shown in **Figure 4-86**, Fitting of the XRD data shows that their crystal structure is close to either orthorhombic (a = 5.5213Å, b = 7.7952Å, c = 5.4842Å, JCPDS 73-0878) or cubic phase ($a = b = c$ = 3.929Å, JCPDS 74-2488). In contrast, no other secondary phase was detected, most notably the oxide Ta_2O_5. Although the particles are very small in size, the XRD peaks have high intensity/ high crystallinity without any background signal of amorphous content.

The Adsorption/desorption isotherms and total pore volume are shown in **Figure 4-87**. The two materials have drastically different SSA, where $14NaTaO_3$ has 60.5 m^2g^{-1} and the particle $26NaTaO_3$ has 27.5 $m^2\ g^{-1}$, which is less than half of the 14nm particle. The Total pore volume corroborates the same results, $14NaTaO_3$ has 18 10^{-2} $cm^3\ g^{-1}$, and $26NaTaO_3$ has 7 10^{-2} $cm^3\ g^{-1}$. Finally, the particle size as measured by the SSA is obtained, with

14NaTaO$_3$ having 12 nm d_{BET} and 26NaTaO$_3$ having more than double the size at 27 nm d_{BET}. The total precursor concentration change from 0.6M to 0.1M, as observed, has a tremendous change in the SSA and the size of the materials.

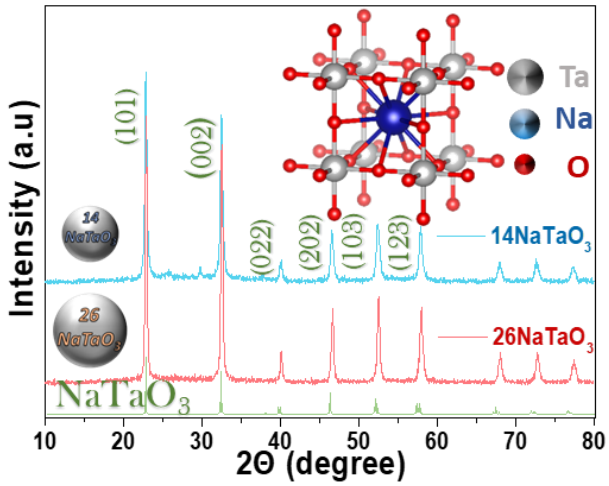

Figure 4-86: *XRD pattern of 14NaTaO$_3$ and 26NaTaO$_3$, inset: the crystal structure of the cubic phase.*

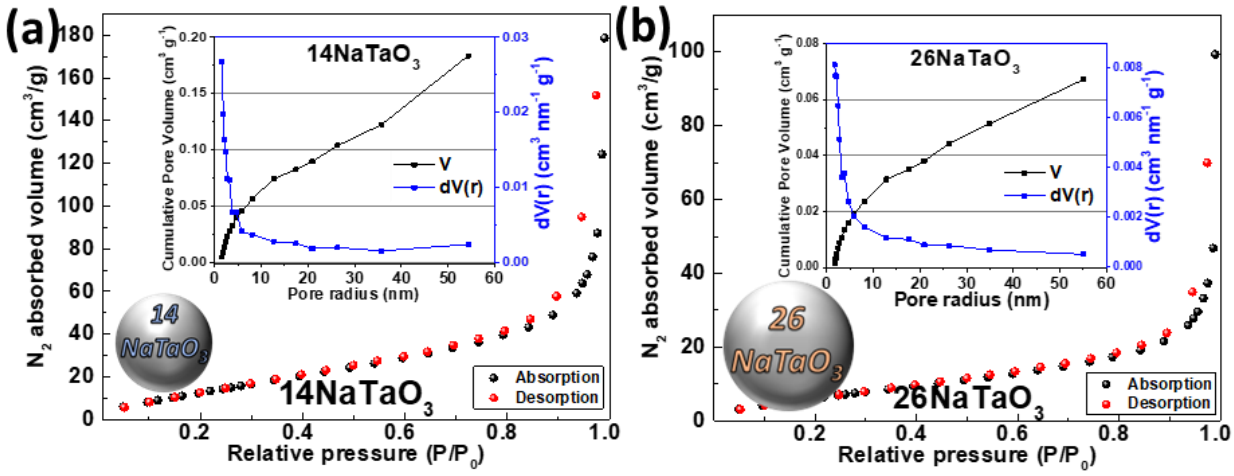

Figure 4-87: *Adsorption/desorption isotherms of (a) 14NaTaO$_3$ and (b) 26NaTaO$_3$. Inset: dV(r) vs pore radius plot.*

The TEM images of the two particles are shown in **Figure 4-88**. The morphology of the FSP-NaTaO$_3$ particles is quasi-spherical, forming soft agglomerates, **Figure 4-88**(a,b). The spherical morphology is a general trend of flame-made materials as it is repeated with

many different particles in this Ph.D. thesis and in general for FSP nanoparticle synthesis. From the resolved TEM fringes for the two FSP-$NaTaO_3$ particles in **Figure 4-88**(bottom), we discern interlattice distance of 3.95Å in $14NaTaO_3$ and 4.05Å in $26NaTaO_3$ in agreement with the spacings of {101} planes for the cubic phase $NaTaO_3$ [319]. Thus it is concluded that the FSP-$NaTaO_3$ particles have a Cubic structure, excluding the orthorhombic structure.

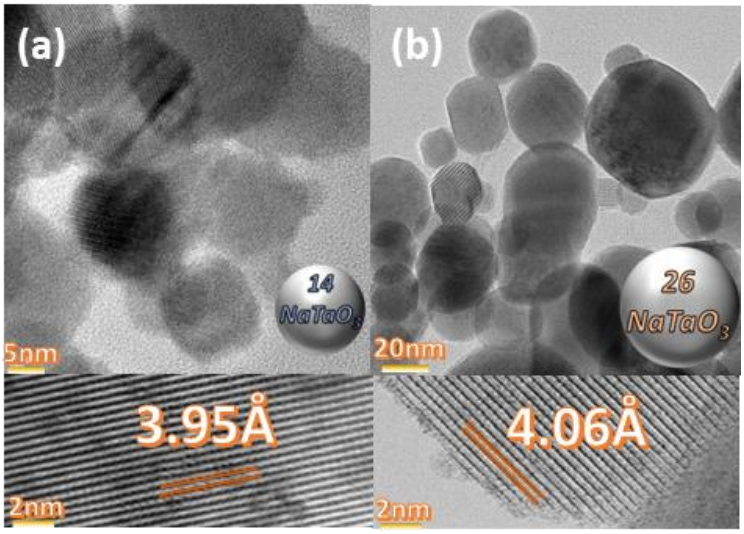

Figure 4-88: *HR-TEM images of (a) $14NaTaO_3$ and (b) $26NaTaO_3$. (bottom) The lattice fringes of each material.*

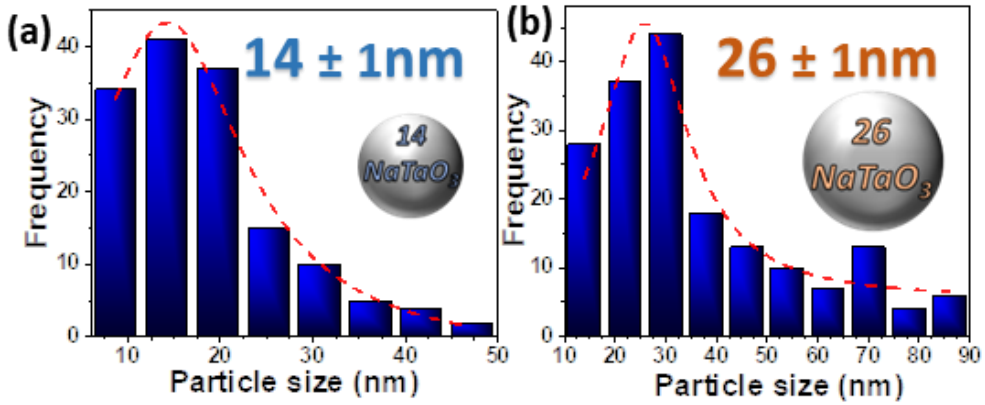

Figure 4-89: *Size distribution of (a) $14NaTaO_3$ and (b) $26NaTaO_3$, obtained by multiple TEM images.*

From multiple TEM images, the Size distribution as predicted by TEM is obtained, **Figure 4-89**. The d_{TEM} for the two FSP-$NaTaO_3$ particles are 14 nm for $14NaTaO_3$ and 26 nm for $26NaTaO_3$, the results have a very high correlation with the calculated d_{BET}.

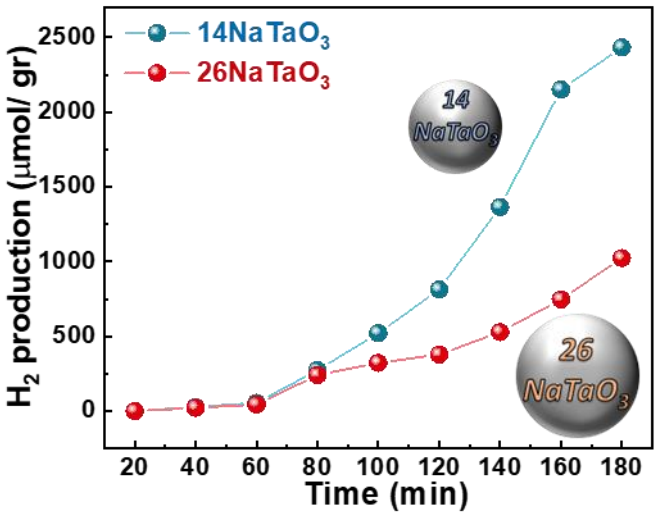

Figure 4-90: *H_2 evolution rates of $14NaTaO_3$ and $26NaTaO_3$ in a time interval of 3 hours, by illumination of 250W Mercury lamp.*

The two FSP-made $NaTaO_3$ particles were employed for the photocatalytic evaluation of H_2 production from H_2O, as shown in **Figure 4-90**. The overall efficiency of the particle is 1620 μmol H_2 $g^{-1}h^{-1}$ for the $14NaTaO_3$ and 645 μmol H_2 $g^{-1}h^{-1}$ for the $26NaTaO_3$. It is important to consider whether the increase of almost 3 times in hydrogen production originates from a difference in SSA. Thus, with an SSA normalization according to the data from **Table 4-17** shows that the H_2 production yield per SSA is 2.52 mmol $g^{-1}h^{-1}$ for $14NaTaO_3$ exceeds by far the H_2 per SSA 1.36 mmol $g^{-1}h^{-1}$ of $26NaTaO_3$. Thus the enhanced photocatalytic performance of $14NaTaO_3$ is not only attributed to simply an increase in surface area.

4.6.3 EPR signals for photoinduced e^-/h^+ by $NaTaO_3$ under N_2

The photo-induced EPR spectrum is obtained by subtracting the EPR signal under illumination from the EPR signal under normal conditions i.e. in the dark. The signal obtained at 77K, under liquid nitrogen conditions for the $14NaTaO_3$, is shown in

Figure 4-91(a). There is a clear signal in the center of 3400 Gauss with many smaller lines, all these signals rapidly perish after switching off the light i.e. returning to dark conditions and room temperature. Upon subsequent illumination under 77K, the EPR signal is fully restored. The kinetics profile is obtained after further illumination cycles and resetting at dark conditions, as shown in **Figure 4-91**(b).

In more detail, these EPR signals are assigned to photo-induced hole/electron $\{h^+/e^-\}$ pairs in the $NaTaO_3$ nanoparticles structure, where the illuminated particles are under N_2 atmosphere, thus their disappearance at RT/dark should be attributed mainly to $\{h^+/e^-\}$ pair recombination, not to catalytic applications with the environment or the structure itself. The experimental EPR spectra can be fully simulated using four subspectra, with two spectra attributed to electron (e1) and (e2), and two spectra attributed to holes (h1) and (h2) as shown in **Figure 4-91**(c), the precise g-tensors for the Spin-Hamiltonian are listed in **Table 4-18**.

The subspectra with the most percentage of the overall signal derive from the (h1), with a calculated g-tensor of g^{h1}=[2.028, 2.0050, 2.0018]. To compare the results with other semiconductors, photoinduced holes for TiO_2[299], $ZrTiO_4$, and ZnO [437] are localized at the oxygen radical anion of the lattice h^+ = {M-$\mathbf{O}^{\cdot-}$-M}, detectable in EPR at the low-field region ($g>g_e$) with a slight g-anisotropy. For this reason, we assign the subspectra (h1) in $NaTaO_3$ to {Ta^{5+}-$\mathbf{O}^{\cdot-}$-Ta^{5+}} and the g-values are determined by the spin-orbit coupling and local environment of the oxygen radical-anion [438]. For crystal structures, the local environment of $\mathbf{O}^{\cdot-}$ is expected to position at $2p_z$ orbital that has higher energy than the $2p_x$, $2p_y$ orbitals, thus the g-values of the holes are determined by the energy difference of $E(2p_z)$ - $E(2p_x,2p_y)$ [439].

The second hole subspectra (h2), observed by the signal shoulder on the (h1) EPR signal, with g^{h2}-tensor [2.010, 2.0199, 2.0398]. The higher g-anisotropy of (h2) may possibly indicate a more distorted local environment, this is attributed to the exposure of surface atoms, while hole (h1) originates in the bulk of the $NaTaO_3$ crystal structure.

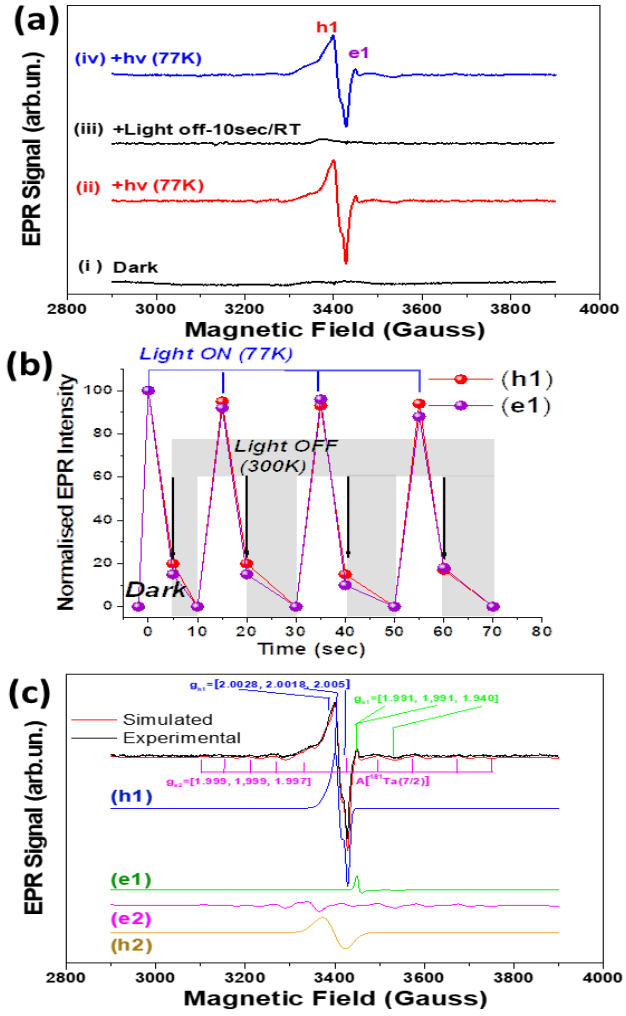

Figure 4-91: *(a) EPR spectra of 14NaTaO3 under N2 atmosphere (i): dark, (ii): under illumination at 77K, (iii): the previous signal of (ii) plus 10sec of dark/RT conditions, (iv): previous signal of (iii) plus illumination at 77K. (b) Kinetics of holes (h1) and electrons (e1) in 14NaTaO3, derived from Illumination - dark/RT cycles. (C) Experimental spectra of 14NaTaO3 under N2 atmosphere (black) and simulated (red) EPR spectra holes=(h1), (h2) & electrons=(e1), (e2).*

Regarding the photo-generated electrons (e1) and (e2), they can be localized on the metal atom, giving rise to ERP fingerprints at the $g<g_e$ region [440]. EPR-detectable paramagnetic centers in the perovskite $NaTaO_3$ structure can derive from Ta^{4+} centers with a $5d^1(S=1/2)$ configuration, as shown in **Figure 4-91**(c). Specifically, the two-electron

subspectra are observed as follows: first, the (e1) has a sharp signal peak defined by an axial g-tensor g^{e1}=[1.991, 1.991, 1.940]. Secondly, the (e2) has a broad riddle-like signal, defined with the g-tensor g^{e2}=[1.997, 1.997, 1.999], **Table 4-18**.

Table 4-18: *Spin Hamiltonian parameters of $14NaTaO_3$ under N_2 or exposed to H_2O.*

$14NaTaO_3$ (under N_2 atmosphere)	g-tensor (±0.002)			$A^{181}Ta$(I=7/2) Hyperfine Tensor (Gauss) (±1)		
	g_1	g_2	g_3	A_1	A_2	A_3
(h1) {Ta^{5+}- $O^{\cdot -}$-Ta^{5+}}	2.005	2.018	2.028	-	-	-
(h2) {Ta^{5+}- O -Ta^{5+}- $O^{\cdot}$ H}	2.010	2.019	2.037	-	-	-
(e1) Ta^{4+} (lattice electron)	1.940	1.991	1.991	-	-	-
(e2) Ta^{4+} (lattice electron)	1.997	1.997	1.999	71	71	214
$14NaTaO_3$ (exposed to H_2O)						
(h1) {Ta^{5+}- $O^{\cdot -}$-Ta^{5+}}	2.005	2.018	2.022	-	-	-
(h2) {Ta^{5+}- O -Ta^{4+}- $O^{\cdot}$ H}	2.013	2.022	2.039	-	-	-
(e1) Ta^{4+} (lattice electron)	1.946	1.993	1.993	-	-	-
(e2) Ta^{4+} (surface electron)	1.933	1.933	1.973	-	-	-
(e3) Ta^{4+} (surface electron)	1.930	1.960	1.960	-	-	-

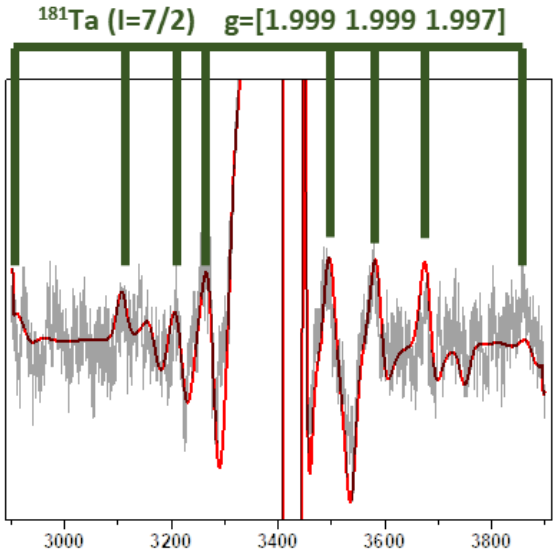

Figure 4-92: *Magnified EPR spectra of $NaTaO_3$ particles under N_2 atmosphere showing the simulated hyperfine splitting due to electron-^{181}Ta coupling.*

The (e2) is assigned to an electron coupled with one ^{181}Ta[I=7/2] nucleus (100% nat. abundance). The **A**(^{181}Ta[I=7/2]) tensor of e2 is strongly anisotropic, thus producing the broad riddle-like signal i.e. distributing the resonance magnetic fields over 2I+1 values for each g-component, **Figure 4-92**. The g-tensor and **A**(^{181}Ta[I=7/2]) for (e2) - (Ta^{4+}) in 14$NaTaO_3$ are in accordance with previously reported values for synthetic (π-C_5H_5), $Ta^{4+}Cl_2$ complexes [441]. In distorted tetrahedral symmetry, Ta^{4+} has a $5d^1$ configuration, with the unpaired electron residing in a [c_1 dx^2-y^2 + c_2 d_z^2] molecular orbital, with mainly dx^2-y^2 character, and small d_z^2 admixture, i.e. c_1>>c_2. The 5s and 6s configurations of Ta^{4+} are expected to be negligible. The Aiso(^{181}Ta[I=7/2])=119 Gauss is attributed mainly to indirect spin-polarization effects by *d*-spins, thus the 119/5359~2% spin on a Ta-atom.

4.6.4 EPR signals for photoinduced e^-/h^+ by $NaTaO_3$ under H_2O

After exposure to H_2O or ambient humidity, the photogenerated EPR signals of perovskite $NaTaO_3$ show altered and additional subspectra.

As it interacts with the H_2O, the nanoparticle produces an additional subspectra of (e3) that will be identified later. To measure the EPR spectra of the $NaTaO_3$-H_2O interaction accurately, a saturation plot must be produced with the implementation of increased microwave power through the decreased dB i.e. from 30 to 6 dB, **Figure 4-93**. From the saturation plot, two significant results emerged. First, that the almost-saturation of the h2 signal indicates that the hole is trapped in an oxygen anion radical near the surface. Second, Localised electrons (e1) and (e2) exhibit more intense spin-lattice interactions compared to, as we will determine later, delocalized surface electrons (e3).

As the appropriate microwave power was determined, the two materials were exposed to H_2O, obtaining the Light-minus-dark EPR spectra and the kinetics of the EPR signals under light/dark-RT cycles, as shown in **Figure 4-94**. Despite the similarity in the kinetics of holes and electrons, the signals assigned to the hole display a slower decrease, indicating that a portion of the photo-excited electrons is scavenged by atmospheric oxygen.

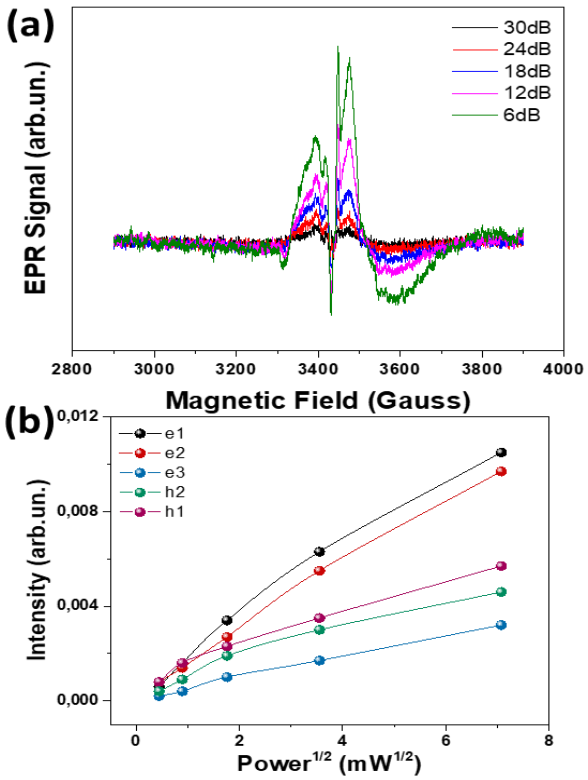

Figure 4-93: *(a) Light-minus-dark EPR spectra of 14NaTaO₃ exposed to H₂O, varying microwave power from 6 to 30 dB. (b) Saturation plot of 14NaTaO₃ for the subspectra (h1), (h2), (e1), (e2), and (e3).*

The spectra are analyzed to 5 different subspectra, with two holes (h1) and (h2), and three different electrons (e1),(e2), and (e3), as shown in **Figure 4-95**. The final resolved g-tensors are listed in **Table 4-18**(exposed to H_2O).

For the (h1) subspectra, the tensors g^{h1} are rather comparable for both cases i.e. under N_2 or H_2O. Althgouht the (h2) tensors exposed to H_2O, g^{h2} for $14NaTaO_3(H_2O)$, shows small, but perceivable alterations compared to (h2) holes of $14NaTaO_3(N_2)$. Considering that g^{h2} is attributed to the $14NaTaO_3$ surface, the differences in the tensors are reflected in the effect of H_2O adsorbed on the surface. The intensity yield of (h2) in **Figure 4-94** is higher than in **Figure 4-91**, thus (h2)-states are promoted by the presence of H_2O, again showing surface-related changes. Altogether, we suggest that these differences between (h2) and (h1) spectra are attributed to (h1) that are trapped inside the lattice, while (h2) are exposed

near the surface. An analogous occurrence happens in TiO_2, where two hole configurations can be resolved by EPR, first the {Ti^{4+}- $\mathbf{O}^{\cdot -}$-Ti^{4+}}, and secondly the {Ti^{4+}- O -Ti^{4+}- $\mathbf{O}^{\cdot}$ H}, depending on the state of surface-occupation by H_2O [299]. By all the experiments findings and the bibliography based on the much better explored TiO_2, we suggest that:

Bulk Holes (h1) = {Ta^{5+}- $\mathbf{O}^{\cdot -}$-Ta^{5+}}

Surface Holes (h2) = {Ta^{5+}- O -Ta^{5+}- $\mathbf{O}^{\cdot}$ H}

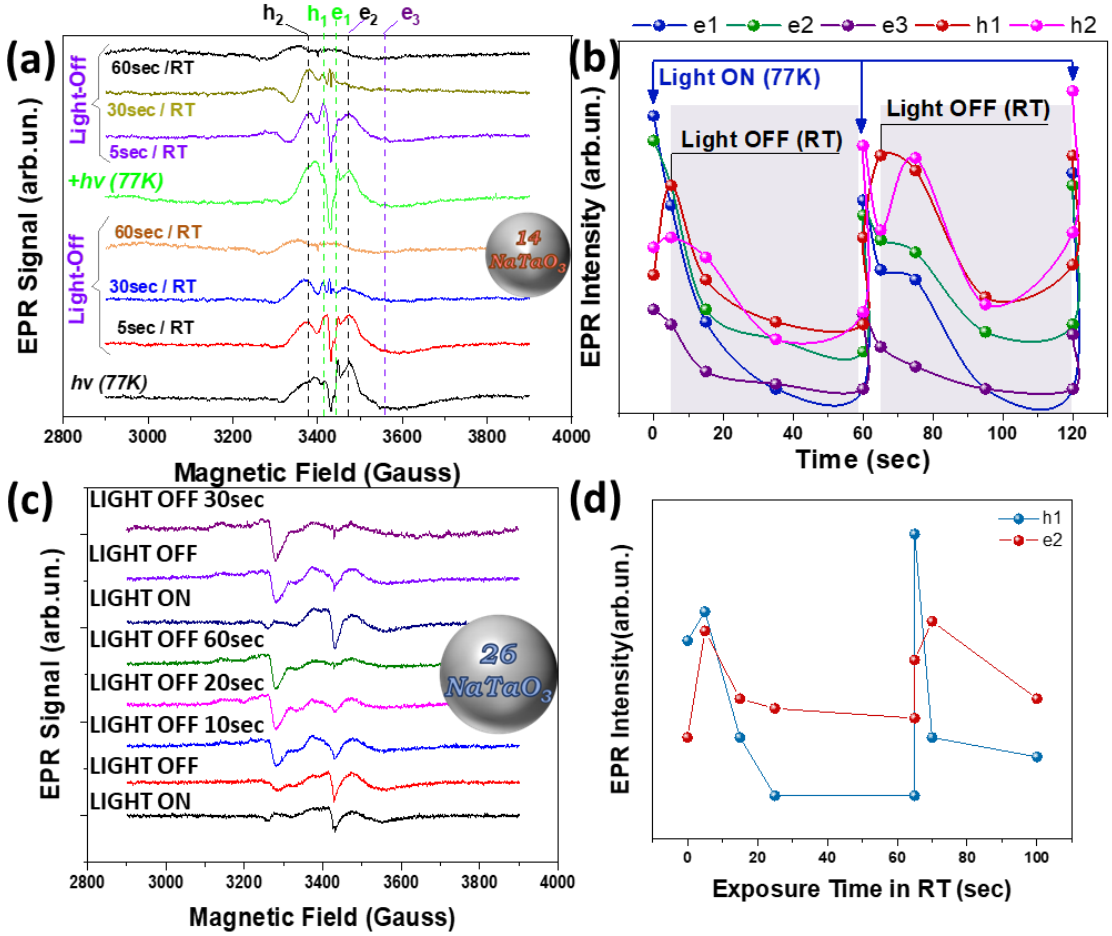

Figure 4-94: *The particle 14$NaTaO_3$ exposed to H_2O: (a) Light-minus-dark EPR spectra, and (b) kinetics of the EPR signals under light/dark-RT cycles. The particle 26$NaTaO_3$ exposed to H_2O: (c) Light-minus-dark EPR spectra varying irradiance conditions, and (d) kinetics of the EPR signals under light/dark-RT cycles.*

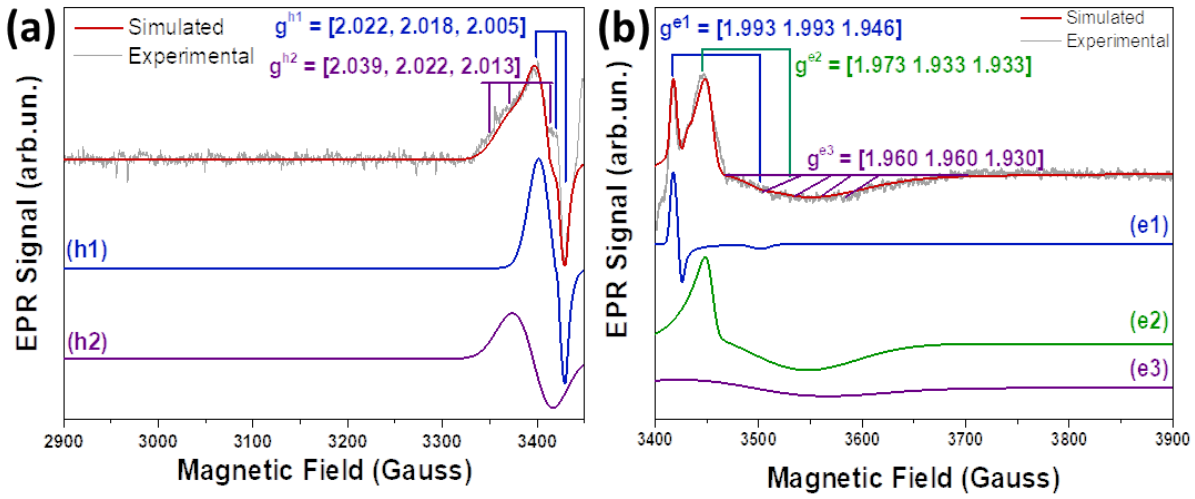

Figure 4-95: *Exposed to H_2O the particle $14NaTaO_3$: (a) (black) Experimental, (red) simulated EPR spectra of holes=(h1), (h2). (b) (black) Experimental, (red) simulated EPR signals of electrons=(e1), (e2), and (e3), under degassed conditions plus 2-propanol as a hole scavenger.*

As further experiments to prove that conclusion, the $14NaTaO_3$ material had an addition of 2-propanol to the H_2O. The 2-propanol can act as a hole scavenger, where it is used to enhance the photocatalytic activities, much like methanol in the present Ph.D. photocatalytic experiment for hydrogen production. The 2-propanol diminishes the (h1) and (h2) subspectra, as shown in **Figure 4-96**. These results further confirm the spectra assignments to photoinduced holes.

As for the electron spectra, In **Figure 4-95**(b), the presence of 2-propanol promotes the intensity of the Ta^{4+}-electron EPR signals. Two types of electrons subspectra are well determined (e1) and (e2), with the tensors mentioned in **Table 4-18**(exposed to H_2O). The sharp signal peaks of (e1) indicate that it is probably localized inside the $14NaTaO_3$ lattice, analogous to lattice Ti^{3+}-electrons in Anatase TiO_2 [314]. As for the subspectra (e2), with axial tensor g^{e2}=[1.933, 1.933, 1,973] along with the broad g-component, dominates the EPR spectrum of $14NaTaO_3(H_2O)$, even with a lack of 2-propanol, **Figure 4-94**. The strong broadening of the g-component indicates significant heterogeneity in the local environment of these (e2) (Ta^{4+}) centers in the material $14NaTaO_3(H_2O)$.

An additional third subspectra was observed, with a broad component (e3), and as well as the subspectra of (e2) and (e3) can be attributed to trapped Ta^{4+} electrons close to the surface of $14NaTaO_3$, in accordance to the well-known surface Ti^{3+} species in TiO_2. Noticeably, strong ^{181}Ta-hyperfine coupling, as resolved in $14NaTaO_3(N_2)$, is not noted in the case of $14NaTaO_3(H_2O)$.

From the electron kinetics in **Figure 4-96**(b), when the illumination stops, the narrow signal (red line) displays a rapid decrease, assigned to an electron localized in the interior of the $NaTaO_3$ crystal. In contrast, the slow decrease of the broader signal (green line) indicates the existence of delocalized electrons in the particle surface.

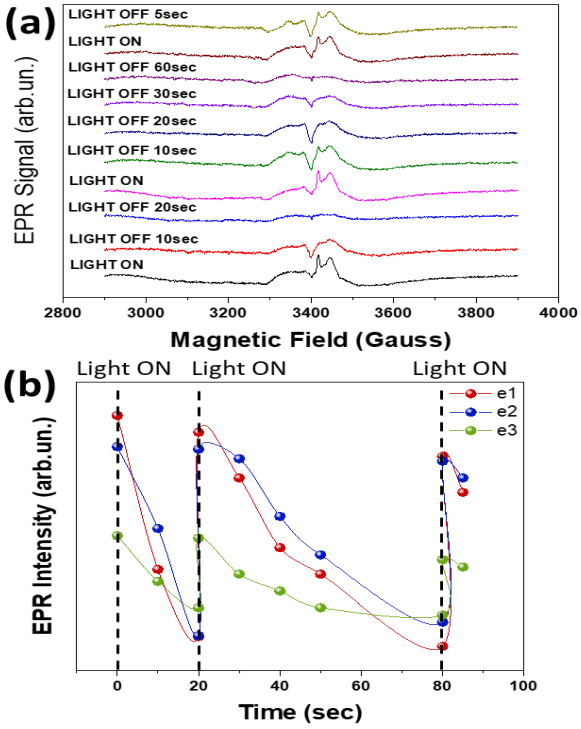

Figure 4-96: *(a) Light-minus-dark EPR spectra of $14NaTaO_3$ exposed to H_2O, with the addition of isopropanol as a hole scavenger varying time in RT after illumination. (b) Correlation plots of electron kinetics derived by the EPR signals.*

4.6.5 $NaTaO_3$ Size effect on EPR signal

Size-effect: When the size of the $NaTaO_3$ particles was increased from 14nm to 26nm, the yield of photoinduced $\{h^+/e^-\}$ EPR spectra at 77K was significantly lower. For the photoinduced electron/hole pairs under H_2O-exposed particles, as shown in

Figure 4-97. In further detail, for the increased size 26nm $NaTaO_3$ particle, the subspectra (e2)-type electrons are resolved, while the (h1) and (h2) holes display much diminished intensity. Overall, decreasing the particle size is an efficient route to mitigate the carrier separation in the perovskite $NaTaO_3$ crystal. By correlating the EPR findings with H_2 production, the decrease in size shows additional enhanced photocatalytic efficiency.

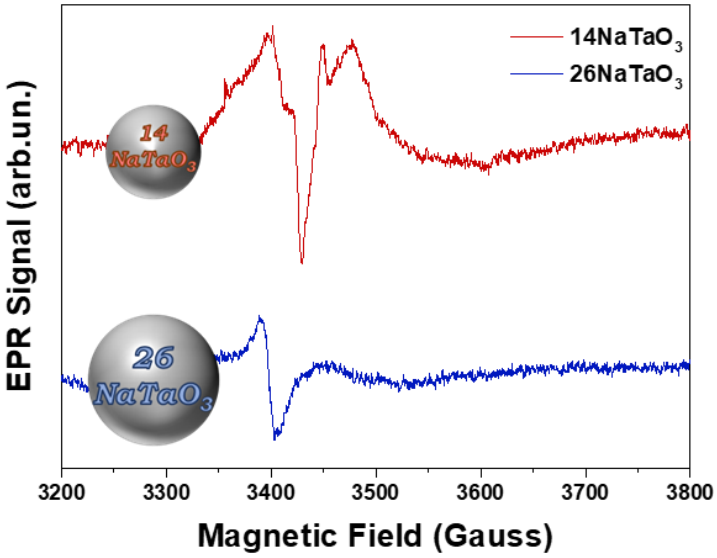

Figure 4-97: Under e*xposed H_2O – particle conditions, the Light-minus-dark EPR spectra for: (i) the $14NaTaO_3$ particle, (ii) the $26NaTaO_3$ particle.*

4.6.6 Conclusions for EPR photoinduced e^-/h^+ by $NaTaO_3$ Size effect

[a] The fundamentally smallest size of 14nm $NaTaO_3$ particles reveals a detailed EPR landscape concerning the electronic configuration and kinetics of photoinduced electron/hole pairs.

[b] The EPR spectra under N_2 conditions and under H_2O conditions were determined with five separate subspectra, two subspectra attributed to holes= (h1) and (h2), two subspectra attributed to electrons=(e1), (e2) and (e3). Detailing the specific tensors of each subspectra.

[c] With the implementation of Isopropanol as a hole scavenger in the H_2O conditions provided further evidence to consider the (h1) and (h2) subspectra as that produced from holes in the bulk of the material and at the surface of the material, respectively.

[d] Increased Perovskite $NaTaO_3$ particle size from 14nm to 26nm diminishes the yield of stable photo-excited {h+/e-} pairs significantly due to rapid recombination events. This claim is further supported by the photocatalytic H_2 production, with an approximately 2.5 times higher production from 14nm compared to 26nm.

The reason that such detailed EPR spectra concerning photoinduced electron/hole subspectra derives from the FSP produced small size of 14nm, thus other studies could not have detection of photoinduced carriers successfully by EPR. Furthermore, the direct detection and comprehension of the photoactive species in $NaTaO_3$ can lead to a fundamental understanding of their promising contribution to challenging photocatalytic reactions. The results are in immediate correlation to the photocatalytic experiments in section 4.7 of the Ph.D.

4.7 Ta$_2$O$_5$ and NaTaO$_3$/NiO Heterojunctions DN-FSP for Solar-to-H$_2$ Conversion

4.7.1 Aims of Ta_2O_5 and $NaTaO_3$/NiO Heterojunctions

Our key research objects for the following publication of the perovskite $NaTaO_3$/NiO Heterojunctions. [a] To exploit flame spray pyrolysis (FSP) technology to establish a methodology for scalable, high crystallinity, controlling the size, and ultimately create the smallest nanoparticles in the bibliography (under 25nm) for the perovskite phase $NaTaO_3$. [b] To understand the thermodynamics/limitations of $NaTaO_3$-nanosize control in flame synthesis. [c] To perform for the materials Ta_2O_5 and $NaTaO_3$ one-step deposition of co-catalysts NiO and Platinum, utilizing the Single and Double Nozzle FSP method, since {$NaTaO_3$/NiO} heterojunctions have shown great promise as photocatalysts [90]. [d] To utilize the nanosize and high crystallinity [130] for highly active hydrogen production from H_2O. [e] Finally, to correlate the hydrogen production with the photoinduced radical generation detectable via EPR spectroscopy.

The results from the research have been published in our work for the Journal of ACS Applied Nanomaterials [442], with the graphical abstract shown in **Figure 4-98**.

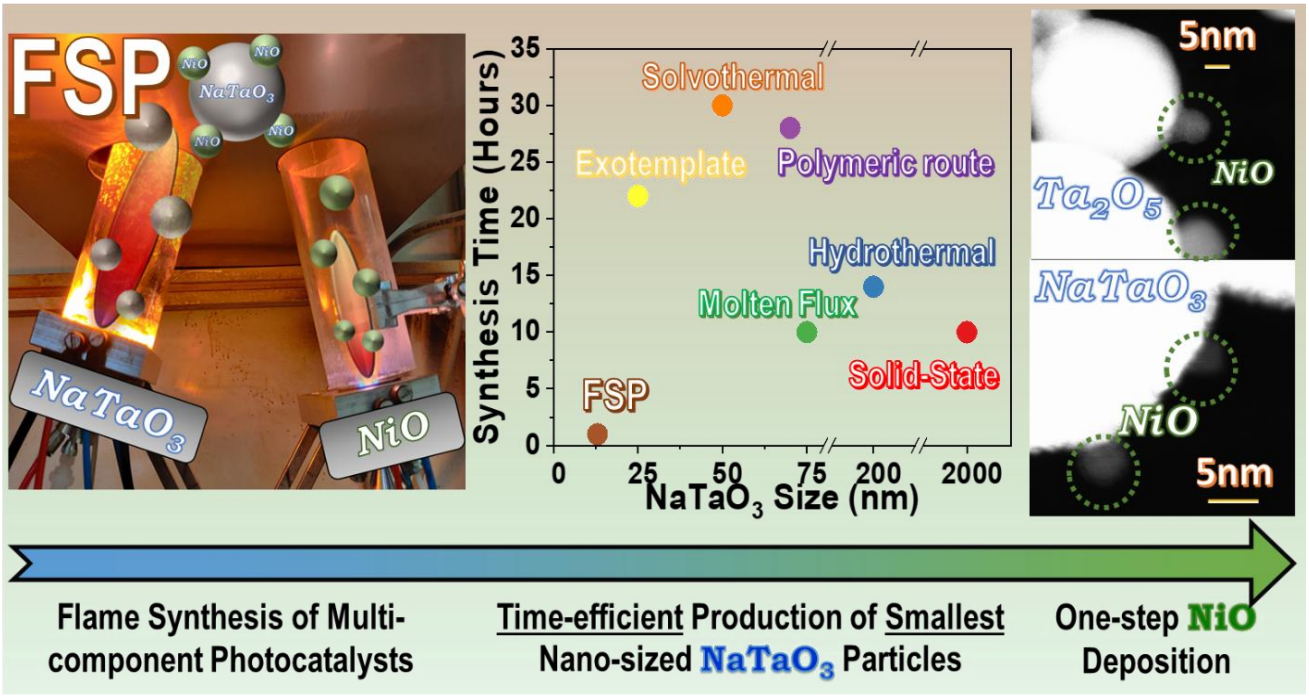

Figure 4-98: *The graphical abstract of Nanosized $NaTaO_3$/NiO heterojunction from Double Nozzle FSP, producing the smallest size compared to the bibliography at the most time-efficient synthesis method.*

4.7.2 FSP synthesis of Ta_2O_5 and $NaTaO_3$ for phase and size control

The Single-Nozzle FSP (SN-FSP) and Double-Nozzle-FSP (DN-FSP) are reminded in correlation to the resulting materials for this research in **Figure 4-99**. The heterostructure of Ta_2O_5/NiO and $NaTaO_3$/NiO was synthesized with both SN-FSP and DN-FSP. In the case of SN-FSP, the precursor of the atoms Na-Ta-Ni was deposited in a single nozzle, while in the case of DN-FSP, one nozzle contained the precursor of the Na-Ta atoms, the second nozzle contained only the Ni atoms. The advantage of the DN-FSP is ensuring that fully grown NiO particles will be deposited on the surface of fully grown Ta_2O_5 or $NaTaO_3$ nanoparticles. In the case of SN-FSP, while a high percentage will be on the surface, there is also a high probability of NiO or Ni atoms being found inside the nanoparticle crystal structure. In both cases of SN-FSP and DN-FSP, the deposition of the cocatalysts is done in one-step.

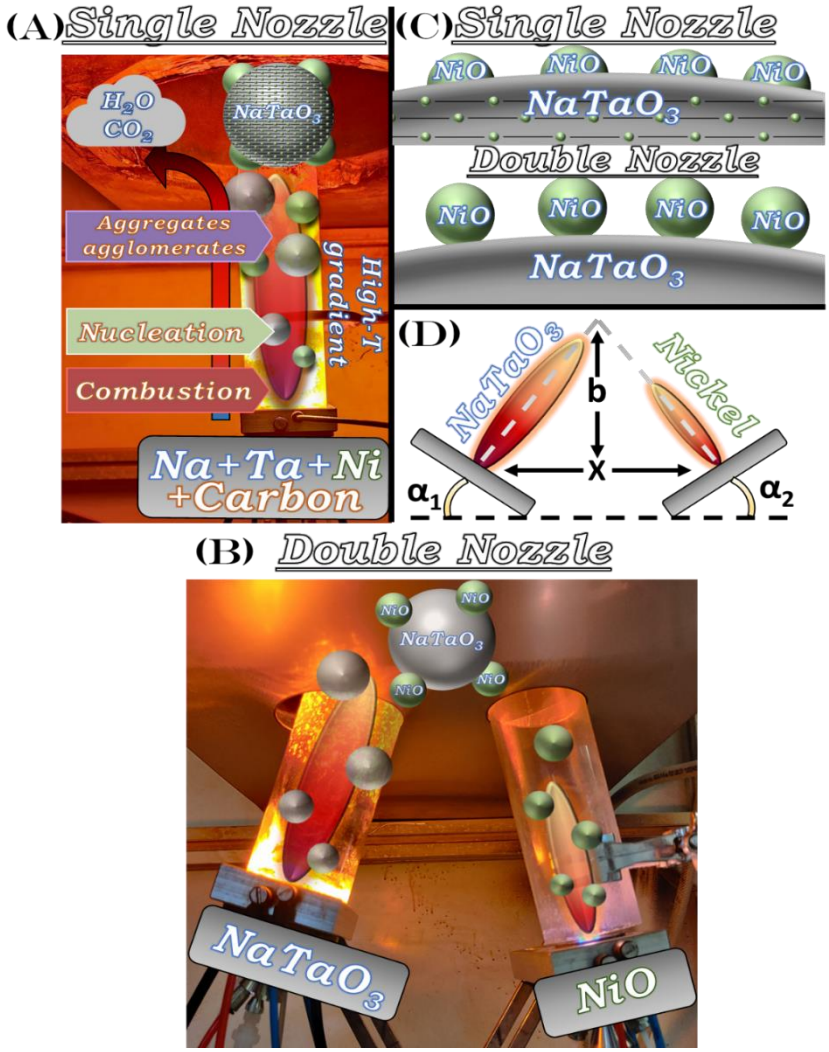

Figure 4-99: *The FSP technology set-up employed for one-step synthesis of heterostructures Ta_2O_5/NiO and $NaTaO_3$/NiO: (A) Single-Nozzle FSP reactor, depicting the formation steps of combustion, nucleation, and agglomeration of the nanoparticles. (B) Double-Nozzle FSP (DN-FSP) reactor, left nozzle for $NaTaO_3$, right nozzle for NiO. (C) Schematics of the deposition process of SN-FSP and DN-FSP. (D) The adjustable geometry parameters for the two nozzles in DN-FSP.*

FSP synthesis Parameters: The stock solutions contained anhydrous Tantalum(V) chloride (99.9%-Ta, STREM) for the Ta_2O_5, while for the $NaTaO_3$ also was added sodium 2-ethylhexanoate (98%, TCI). For the cocatalytic particles, NiO or Pt^0 that were deposited on the tantalum particle surface, Nickel(II) 2-ethylhexanoate (78% in 2-ethyl hexanoic acid, STREM) and Platinum(II) acetylacetonate (98%, STREM) were used. For the Single-Nozzle

FSP synthesis, the stock solution of Tantalum-Sodium was dispersed in ethanol (99%, Emsure), along with the cocatalytic NiO or Pt^0.

After a screening of different precursor flow rates, oxygen dispersion flow rates, and precursor concentrations that will be thoroughly explored afterward, the flow rates for the final particles comprised of a dispersion oxygen flow rate of 5 L min^{-1} (Linde 99.999%) and precursor flow rate of 5 mL min^{-1}. The initial flame was ignited by premixed O_2 and CH_4 (2 L min^{-1}, 1 L min^{-1}). The nanomaterials were stored in glass vials under an inert Argon atmosphere. There were two concentrations applied for the final particles. Two concentrations for Tantalum were implemented, a High and a Low concentration: 0.3M $TaCl_5$ and 1.8M $C_8H_{15}NaO_2$ for high molar concentration, 0.05M $TaCl_5$ and 0.3M $C_8H_{15}NaO_2$ for low molar concentration.

Pratsinis et al. [443] has produced high crystallinity Ta_2O_5 by applying the FSP technology, although employed for Tantalum precursor the Tantalum(V) n-butoxide (99.99%-Ta, STREM), as the following work is based on the industrial production of the smallest $NaTaO_3$, the precursor was changed to Tantalum(V) chloride (99.9%-Ta, STREM) as an economical factor, that decreases the precursor cost seven times, and the overall production cost five times, although the $TaCl_5$ requires a filtration step detailed below. The complete cost of the FSP method is shown in **Table 4-19**. The solvent and Na-Ta precursors are bought on a laboratory scale, thus industrial production will lower the overall cost significantly, as observed the most significant cost is the Tantalum precursor, this is the reason for the five times reduction, with the second highest being the Sodium precursor.

Table 4-19: *The complete cost calculation for the production of 1gr of $NaTaO_3$ particles, including precursor, solvent, and gas costs of the FSP method.*

Raw materials expenses	ethanol for analysis		Tantalum(V) chloride, anhydrous (99.9%-Ta) CAS: 7721-01-9 (STREM)	Sodium 2-Ethylhexanoate(98% Na) CAS:19766-89-3 (TCI)	Tantalum(V) n-butoxide (99.99+%-Ta) PURATREM CAS:51094-78-1 (STREM)		Gas expenses (CH_4 +O_2)
volume(L)	2.5	**gr**	50	250	25	**Volume (L)**	7

Price(€)	50	**Price (€)**	154	67	382	**Price (€)**	0.12
1gr yield $NaTaO_3$ From 0.6M solution	ethanol for analysis		Tantalum chloride 0.3M (gr)	Sodium 1.8M (gr)	Tantalum(V) n-butoxide 0.3M (gr)		Gas expenses (CH_4 +O_2)
Volume (mL)	30	**gr**	3.228	9.159	4.92	**Volume (L)**	42
Price(€)	0.6	**Price (€)**	9.9	2.45	75	**Price (€)**	0.72
			$NaTaO_3$ From Ta chloride	$NaTaO_3$ From Ta n-butoxide	**$NaTaO_3$**		
		price (€)	**14**	**77**	**1 gr**		

Based on systematic screening, we found that an excess of Na-precursor over Ta should be used in the precursor solution. The excess of Sodium atoms interacted with the Chlorine atoms from the tantalum stock solution $TaCl_5$, thus 5 out of 6 sodium atoms were consumed creating NaCl, and the remaining 1 out of 6 sodium atoms had 1: 1 concentration with the Tantalum atoms. We applied centrifugation twice to remove the NaCl, removing the salt each time before the FSP synthesis procedure. NaCl removal is truly a crucial step, as the produced nanoparticles otherwise are drastically different, as seen in **Figure 4-100**. XRD clearly detects the distinct peaks of crystallized NaCl at ~31 and 46 degrees, when the particles were washed with water for the purpose of removing the NaCl, the resulting particles were calcinated for 2 hours under an ambient atmosphere at 600 ^{0}C, normally sufficient for the $NaTaO_3$ phases for FSP-synthesis particles, the resulting material had very low crystallinity and high amounts of amorphous content, in comparison with particles that only underwent filtration of NaCl and FSP synthesis.

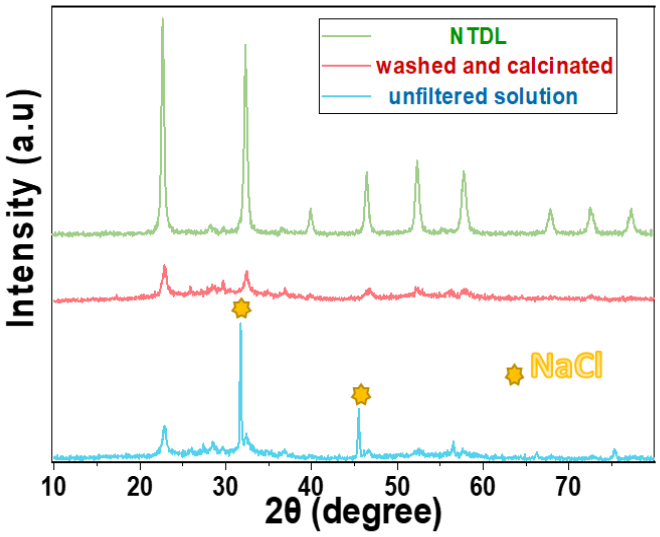

Figure 4-100: *XRD graph for the effect of NaCl filtration step on the $NaTaO_3$ particle composition: non-filtrated Na-precursor indicates the formation of NaCl crystals (blue-line). After post-FSP washing and calcination at 600°C for 2 hours produce, low-crystallinity/mixed phase particles (red line) compared to filtered Na-precursor with pure-phase $NaTaO_3$ (NTDL).*

Analysis of the particle phase-composition from the XRD data, in the following work, only two different phases are observed, Ta_2O_5 orthorhombic phase, a =3.86 Å, b = 3.87 Å, c = 13.39 Å (JCPDS card no. 25-0922), diffraction peaks at 22.8°, 28.3°, 36.7°, 46.7°, and 55.5° that are indexed to the (001), (110), (111), (002), and (021) Miller planes. The perovskite $NaTaO_3$ peaks correspond to its cubic phase, a = b = c = 3.929Å (JCPDS card no. 74-2488), diffraction peaks at 22.6°, 32.4°, 46.4°, 52.3°, 57.7° with (100), (110), (200), (210), and (211) Miller planes.

Properly controlling the particle's phase/crystallinity and particle size requires two parameters of the FSP synthesis. First, it is thermodynamically controlled by the flame-temperature profile and the flame's high-temperature residence time (HTRT) [169–171]. Hotter flames and longer HTRT tend to produce larger nanosized particles [175]. Secondly, the overall combustion enthalpy density $\Delta_c h$ per unit (kJ g^{-1}) is determined by the specific combustion enthalpy $\Delta_c h_i$ of each reactant-i. The index i refers to all compounds participating in the combustion, including the precursors (controlled by the precursor

concentration, solvent, and gases (controlled by the precursor and O_2 dispersion flow rates) [185]. The enthalpy used to better determine the $NaTaO_3$ particle size is attributed to the enthalpy ΔcH (kJ mol g^{-1}) calculated per mol of Na and Ta atoms present at any given moment in the combustion process.

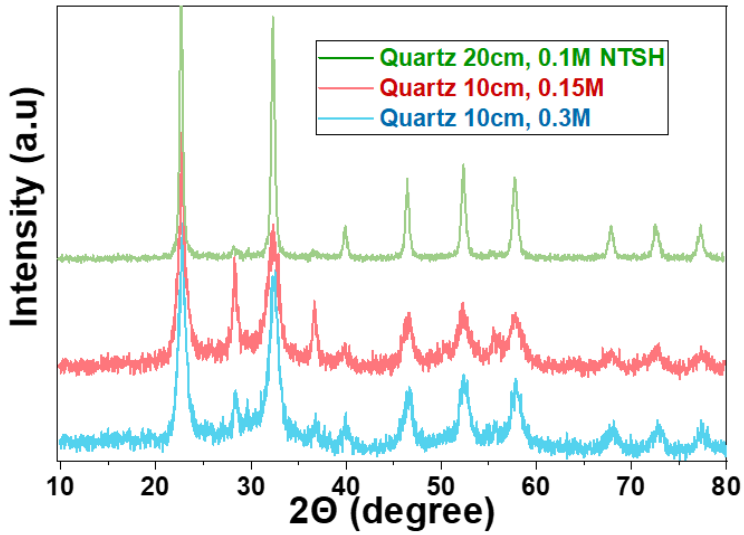

Figure 4-101: *XRD graph showing the effect of the enclosing Quartz tube length on the phase purity of $NaTaO_3$. The longer Q-tube of 20cm allows $NaTaO_3$ particles of high crystallinity and purity to be synthesized.*

Quartz Tube: An enclosing quartz tube encircled the flame is applied to control these parameters. In the FSP process, the enclosing tube retains the flame's high-temperature profile, throughout its cylindrical volume [169–171], with longer tubes allowing longer high-temperature residence times. Furthermore, more extended tube height allows perovskite-phase stabilization. Without any enclosing quartz tube, the HTRT was very low to be able to produce the higher energy-demanding phase of $NaTaO_3$, only producing the phase Ta_2O_5. Additionally, two different quartz tubes were experimented with 10cm and 20cm height, as shown in **Figure 4-101**. In the case of the 10cm enclosing tube, the HTRT was lower than required, although a high percentage was observed to be $NaTaO_3$, resulting in a mixed-phase $NaTaO_3/Ta_2O_5$ particles, while the 20cm tube allowed the total 100% $NaTaO_3$ phase. Thus, longer tubes allow longer high-temperature residence times, as the

$NaTaO_3$ phase requires higher-temperatures, the longer tube favors the perovskite-phase stabilization. From these experiments, all the selected particles from here on out were produced with a quartz tube of 20 cm in height.

In addition, the metal Na-Ta precursor concentration changes the combustion enthalpy as shown briefly from the 10cm tube 0.3M and 0.15M concentration, where lower precursor concentration that changes the Δ_cH, clearly has a much higher phase percentage of Ta_2O_5 in comparison to the desirable $NaTaO_3$. Another way to influence the combustion enthalpy Δ_cH is through the precursor flow rate and the oxygen dispersion rate. As a variable to change the particle size [175].

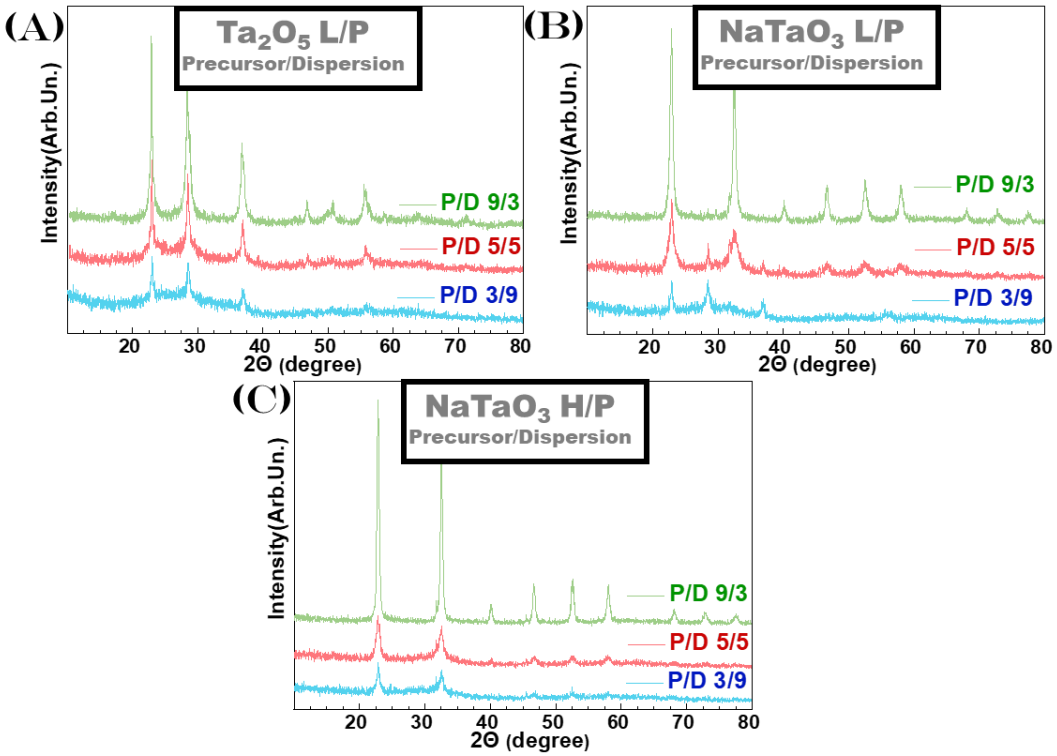

Figure 4-102: *XRD data compiling the effect of P/D-ratio on the particle phase and size. All other FSP parameters were the same as mentioned. (A) Ta_2O_5 phase with Low precursor concentration. (B) $NaTaO_3$ phase with Low precursor concentration. (C) $NaTaO_3$ with High concentration.*

Flow rate (P/D): The flow rate of liquid precursor coded as (P) and the flow rate of dispersion-O_2 gas coded as (D) produce the combined parameters of Flow rate (P/D), which is a crucial parameter determining the nanocrystal formation process [169–171].

Figure 4-102 is a complete exploration of the two parameters, P/D flow rates of 3/9, 5/5, and 9/3, with two different concentrations of Tantalum/Sodium precursor, codenamed: **L** that stands for Low-metal precursor at [Ta]=0.05M, while **H** that stands for High-metal precursor at [Ta]=0.3M, those Low and High concentrations will be applied to the final selected materials.

Materials without Ni atoms: The materials were codenamed as follows: "Na-Ta-O_L/H" where L/H stands for Low/High metal-precursor concentration, respectively.

A total of nine materials were measured with BET, producing the SSA (m^2g^{-1}) and nanoparticle size derived from BET (d_{BET}), as shown in **Figure 4-103**(A). From the data obtained from **Figure 4-102**, the analysis of $Ta_2O_5/NaTaO_3$ Phase percentage was measured in **Figure 4-103**(B) for the P/D ratios 3/9, 5/5, and 9/3 under Low [Ta] concentration for the particle $NaTaO_3$ (Na-Ta-O_L), including the nanoparticle size derived from XRD (d_{XRD}), all the data are presented in **Table 4-20**.

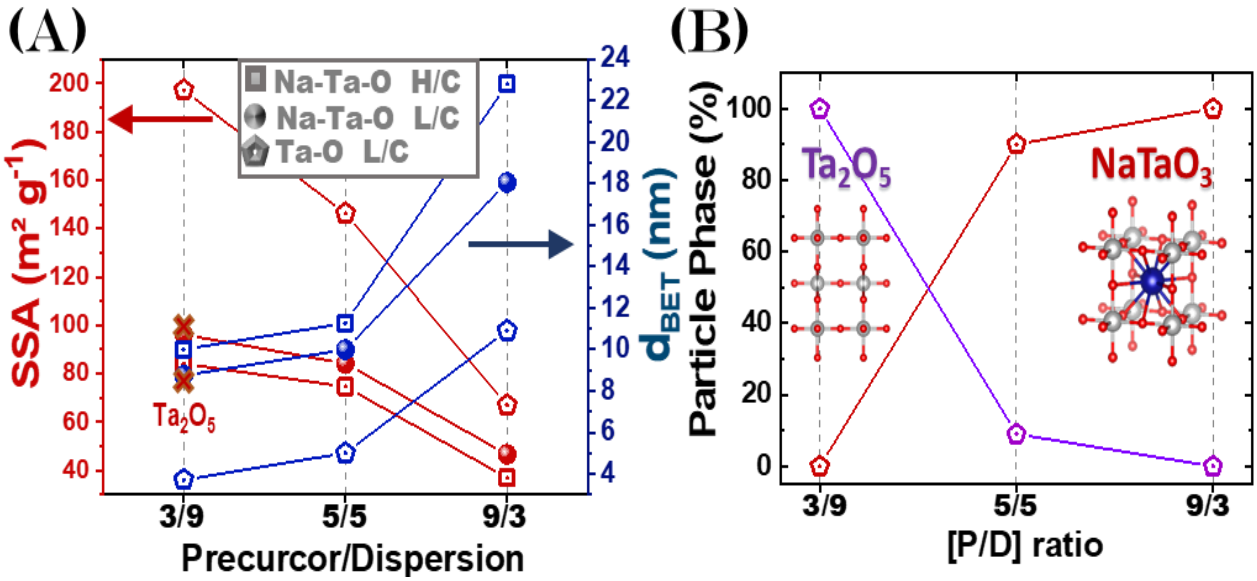

Figure 4-103: *(A) BET and dBET graph for the P/D ratios 3/9, 5/5, and 9/3 under High and Low [Ta] concentrations. (B) The percentage of $NaTaO_3$ phase formed by FSP under P/D ratios 3/9, 5/5, and 9/3 for Low [Ta] concentration (Na-Ta-O_L).*

Table 4-20: *Structural Characteristics of Ta_2O_5 and $NaTaO_3$ nanoparticles, as a function of the P/D ratio from 3/9 to 9/3 and [Ta/Na] concentrations.*

P/D Material	[Ta/Na] Concentration (mM)	% Phase (± 5%)		Crystallite Size (nm) (± 0.5)		SSA (m^2g^{-1}) (± 0.5)
		Ta_2O_5	$NaTaO_3$	d_{BET}	$d_{XRD(max)}$	
3/9 Ta-O_L	50/0	100	0	3.7	15	197.2
5/5 Ta-O_ L	50/0	100	0	5.0	17	146.2
9/3 Ta-O_L	50/0	100	0	10.9	20	67.0
3/9 Na-Ta-O_L	50/50	100	0	8.7	16	96.2
5/5 Na-Ta-O_L	50/50	14	86	10.0	23	84.2
9/3 Na-Ta-O_L	50/50	0	100	18.0	26	46.6
3/9 Na-Ta-O_H	300/300	0	100	10.0	28	84.1
5/5 Na-Ta-O_H	300/300	0	100	11.3	32	74.7
9/3 Na-Ta-O_H	300/300	0	100	22.8	34	36.9

To determine the final effect on P/D over the structures Ta_2O_5 and $NaTaO_3$, and in order to be simpler for the reader, the most important XRD data are shown in **Figure 4-104**. Under Low concentration, Ta-only particles (Ta-O_L), the Ta_2O_5 phase is formed, while in the Na-containing particles {Na-Ta-O_L}, mixtures of Ta_2O_5 and $NaTaO_3$ nanophases are formed. As can be clearly seen, P/D has a profound effect on the phase composition as well as the crystallinity. At P/D=9/3, the $NaTaO_3$ perovskite is formed at 100% and high crystallinity, while at lower P/D=3/9, Na is incorporated in the nanolattice fails since only Ta_2O_5 tends to form. Process-wise, an increase in P involves an increase in solvent feed-flow in the flame, thus increasing combustion enthalpy Δ_cH [185]. Thus, the promotive effect of increased P/D indicates that the high-enthalpy FSP process favors the formation of the perovskite nanophase $NaTaO_3$ due to increased Ethanol-solvent combustion. This issue is discussed quantitatively hereafter.

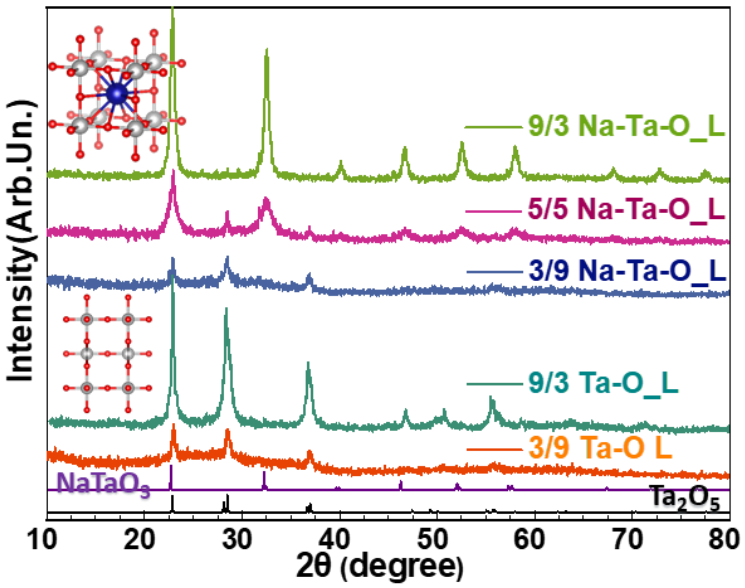

Figure 4-104: *XRD of Ta-based nanomaterials produced by FSP for various P/D ratios 3/9, 5/5, and 9/3. The index "L" stands for low concertation [Ta] of 50mM, Ta-O only has Tantalum precursor, while Na-Ta-O has Tantalum and Sodium Precursors. Insert: unit-cell structures for Ta_2O_5 and $NaTaO_3$ crystals.*

Precursor concentration: In our pursuit of producing small $NaTaO_3$, we have screened a wide range of Ta/Na precursor concentrations under steady P/D=5/5, the XRD data in **Figure 4-105**. The result shows that as observed previously that increased Na/Ta concentrations promote the formation of pure $NaTaO_3$ crystals. Deducing the [Ta] concentration further from 0.05M to 0.025M (total concentration 0.05M) further increases the phase percentage of Ta_2O_5 compared to $NaTaO_3$. While reducing the [Ta] concentration to only 0.067M for the production of Ta_2O_5 only decreases the crystallinity degree but still produces a high degree of purity.

The d_{XRD} and d_{SSA} for the production of the phase $NaTaO_3$ for the total concentration from 1M to 0.05M, while for Ta_2O_5 with concentrations of 1.2M to 0.067M are shown in **Figure 4-106**. As a general trend, d_{BET} and d_{XRD} are well-correlated, although a small but discernible difference indicates that there is a size distribution, not a single particle size. The largest $NaTaO_3$ particles determine the XRD peaks, thus the obtained d_{XRD} value is the upper-size limit of the FSP-produced particles ($d_{XRD}^{(max)}$). On the other hand, smaller

particles contribute to higher SSA and influence the d_{BET}, thus d_{BET} represents the average particle size.

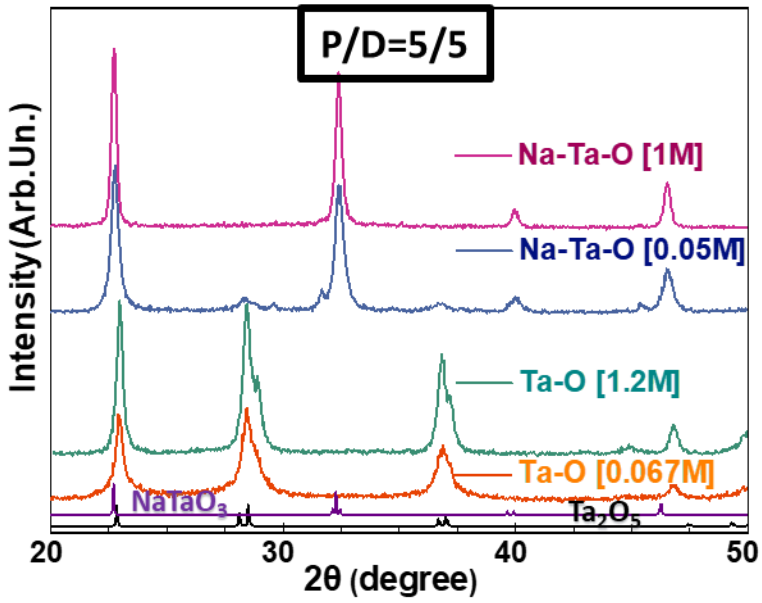

Figure 4-105: *XRD of Ta-based nanomaterials produced by FSP for various Ta/Na-precursor concentrations for the same P/D=5/5.*

$NaTaO_3$ particle size can be decreased only at [Ta/Na] concentrations below 300mM, dropping from an average of 30nm to the least size of around 20nm. At [Ta]>300mM, while the total size increased with higher concentrations, the change is relatively small, with a quasi-steady particle size near 30nm always obtained. In the case of Ta_2O_5, while the maximum size dictated from $d_{XRD}^{(max)}$ does not alternate much from 15nm, the average size dictated by d_{BET} has a tremendous chance in comparison to the concentration dropping from 25nm to only 6nm.

Table 4-20 lists the complete FSP materials synthesized by P/D. Accordingly, the smallest mostly pure $NaTaO_3$ particles obtained by our FSP setup were the {5/5 Na-Ta-O_L}, with FSP parameters of P/D=5/5, [Ta]=50mM, producing a particle with average d_{BET}=10nm, $d_{XRD}^{(max)}$=23nm, and SSA=84.2 m^2/gr. As for the Ta_2O_5, which was not bound by impurity constraints, the smallest particle was {3/9 Ta-O_L}, with average d_{BET}=3.7nm, $d_{XRD}^{(max)}$=15nm, and SSA=197.2 m^2/gr.

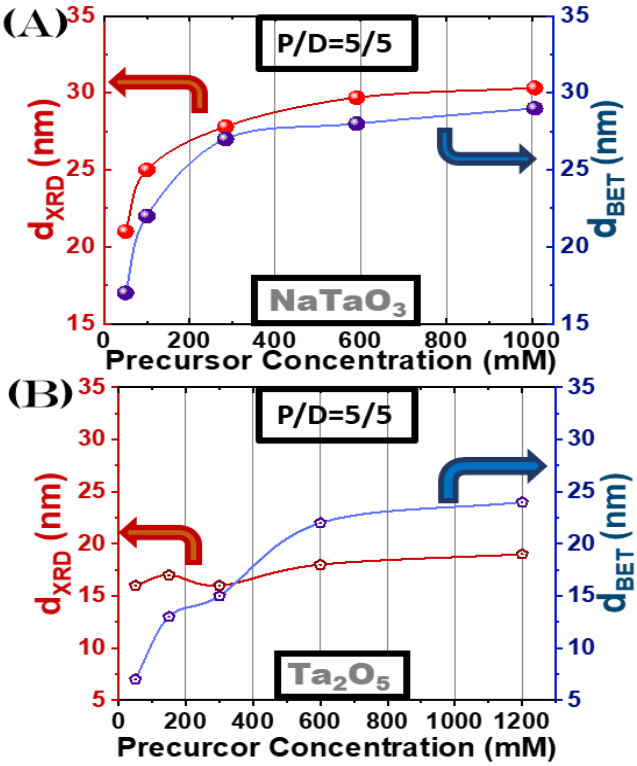

Figure 4-106: *Particle size diameters determined by XRD (left Y-axis) and BET (right Y-axis) for Ta-based nanomaterials produced by FSP for P/D=5/5. (A) For various Ta/Na-precursor concentrations. (B) For various Ta- precursor concentrations.*

From the FSP parameters of Precursor/O_2 dispersion flow rate, and the precursor concentration to control the phase/size of the nanoparticles, we underline that:

[i] The formation of $NaTaO_3$ particles is in competition with the phase Ta_2O_5.

[ii] Achieving high crystallinity requires high combustion enthalpy and long high-temperature residence times.

[iii] This is accomplished from 5/5 P/D to ensure the $NaTaO_3$ phase, while low Ta/Na concentration decreases the size.

Interestingly, an apparent lower $NaTaO_3$-size limit near 10 nm cannot be further decreased, resulting in creating the Ta_2O_5 phase instead. The size limit reveals that in the FSP process, a critical local concentration of Ta and Na is necessary to allow concomitant insertion of the Na and the Ta atoms in the formed oxide lattice.

Finally, through Scanning-TEM data, images presented for 5/5 Na-Ta-O_H material in **Figure 4-107** show the morphology of spherical $NaTaO_3$ particles, with a homogeneous disposition of the Na, Ta, O atoms within the $NaTaO_3$. Thus, the STEM data are in agreement with XRD, verifying the formation of pure $NaTaO_3$ phase, further confirming the lack of 1nm or smaller particles that can't be detected from XRD, showing any secondary heterophase i.e. Ta-oxide or Na-oxide. Overall, we demonstrated that FSP technology could be applied for the synthesis of $NaTaO_3$ perovskite phase of high purity and crystallinity, as the XRD and STEM data show, by correctly controlling the HTRT and $\Delta_c H$ by [i] high [P/D] and [ii] high [Ta/Na] concentrations.

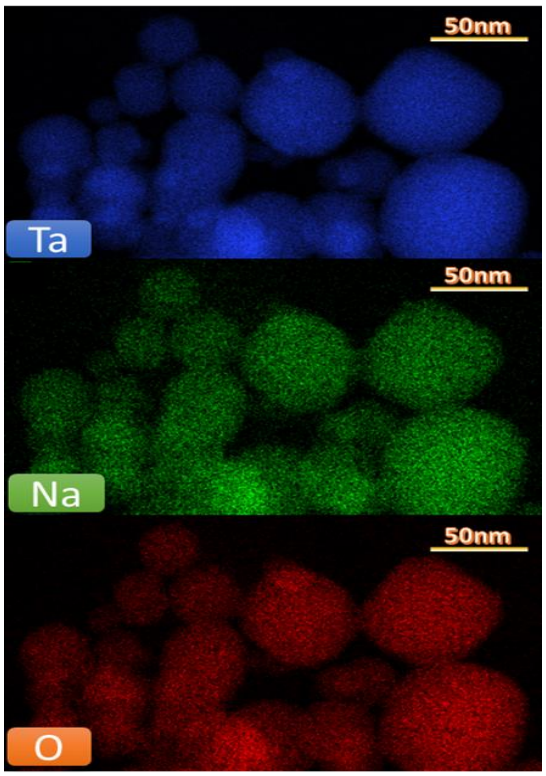

Figure 4-107: *Scanning-TEM images with Na, Ta, O atom mapping for material 5/5 Na-Ta-O_H.*

4.7.3 Double Nozzle FSP for selected Ta_2O_5 and $NaTaO_3$/NiO nanoparticles

Double-Nozzle FSP: In the DN-FSP setup, **Figure 4-99**, two enclosed nozzles were positioned asymmetrically, the first nozzle containing the Na/Ta precursor with ethanol as

solvent, the second nozzle contained Ni-precursor with xylene as solvent. The xylene was applied in order to give a much higher combustion enthalpy in comparison with the ethanol since we required well-formed NiO particles. Both nozzles were set at a precursor flow rate of 5 ml min ^{1}. After several screening experiments, the nozzle angles were adjusted at α_1=30^{o} and α_2=15^{o} respectively, and the internozzle distance was fixed at x=11cm. For the first nozzle (Na-Ta), there was a no-gap between the nozzle and quartz tube, and the second nozzle (Ni) had a gap of 1cm in order to have a higher airflow to combine more smoothly with the $NaTaO_3$ particles. The vertical intersection distance above the nozzle level of the formed $NaTaO_3$ and NiO particles was b=20 and b=24cm, respectively.

To compare the FSP NiO deposition method with more standard deposition methods, an equivalent FSP synthesized $NaTaO_3$ had wet impregnation NiO deposition. The wet impregnation proceeded as thus, Nickel nitrate hexahydrate (Sigma Aldrich >99%) was dissolved in Milli-Q water, and FSP-made low-concentration $NaTaO_3$ particles were added to the solution in proper amounts for the desired 0.5% wt NiO loading. After the wet impregnation, the sample was dried overnight at 100^{o}C, the dried powder was then calcined to 400 ^{0}C at 5 ^{0}C min^{-1} and held for 3 hours under air. The resulting material will be later compared in the photocatalysis section.

Effect of FSP-Combustion Enthalpy on the $NaTaO_3$ perovskite nanophase: From the FSP synthesis of the $NaTaO_3$ section, for the selected materials certain FSP parameters remained constant, [i] the Quartz tube was set at 20cm height, as longer tubes provide longer high-temperature residence times enough for the Ta_2O_5 phase to change to $NaTaO_3$. [ii] Precursor/Dispersion flow rate for 5/5, as lower rates i.e. 3/9 produced Ta_2O_5 particles, and higher rates i.e. 9/3 produced high crystalline $NaTaO_3$, but the particles had much higher size/ lower SSA. [iii] Precursor concentration, from a threshold of Total concentrations 0.05M and below, a percentage of Ta_2O_5 was produced, thus for a low concentration of the final materials the total concentration of 0.1M will be used, as higher concentrations produce much larger sizes of $NaTaO_3$, although in order to compare the size parameter in photocatalysis a high total concentration of 0.6M will be used as well.

All the parameters contribute to the high-temperature-residence-time and the combustion enthalpy and have a determinant effect on the formation of the desired small

$NaTaO_3$ perovskite particles, as the formation of $NaTaO_3$ perovskite nanocrystal is more challenging than e.g. Ta_2O_5, where the particle formation occurs within the HTRT at a short timescale (milliseconds) [175].

Selected Na-Ta particles/ Nio Heterostructures for photocatalysis: As mentioned, two alternative FSP setups were applied for the Heterostructures of NiO particles and $NaTaO_3$ nanoparticles. [i] Single-Nozzle FSP (SN-FSP), where the Ta- and Ni- atoms are introduced in the same flame Nozzle. [ii] Double-Nozzle FSP (DN-FSP), where the Ta- and Ni- atoms are introduced in the separate flame Nozzles.

The NiO-containing Heterojunctions had code names for simplification purposes: "TDL" where T stands for Ta_2O_5, D for Double-Nozzle, and 'L' for low-metal concentration. Additionally, "NTSL" and "NTSH" where NT stands for $NaTaO_3$, "NTDL" where S stands for Single-Nozzle FSP process, and 'H' for high-metal concentration.

We have calculated the combustion enthalpy density [185] for the FSP synthesis for the four selected Ta-materials, TDL(Ta_2O_5) and NTSH, NTSL, NTDL($NaTaO_3$). As the concentration has a fundamental role, the lowest combustion enthalpy belongs to Ta_2O_5, TDL had Δ_cH =-0.52 kJmol g^{-1}. For the $NaTaO_3$ particles, two different combustion enthalpies were found, with the fundamental concentration parameters, as NTSL and NTDL had the same low total concentration of 0.1M the resulted combustion enthalpy had the same estimated enthalpy of Δ_cH =-1.04 kJmol g^{-1}, while the NTSH with high total concentration of 0.6M had Δ_cH=-6.92 kJmol g^{-1}. The significant increase in Δ_cH in NTSH is of key importance for the perovskite-phase $NaTaO_3$ formation and size.

For simplification reasons, the four materials with the fundamental different parameters are shown in **Figure 4-108**, while the full properties of the materials: FSP parameters, phases, sizes, SSA, and band gap are shown in **Table 4-21**.

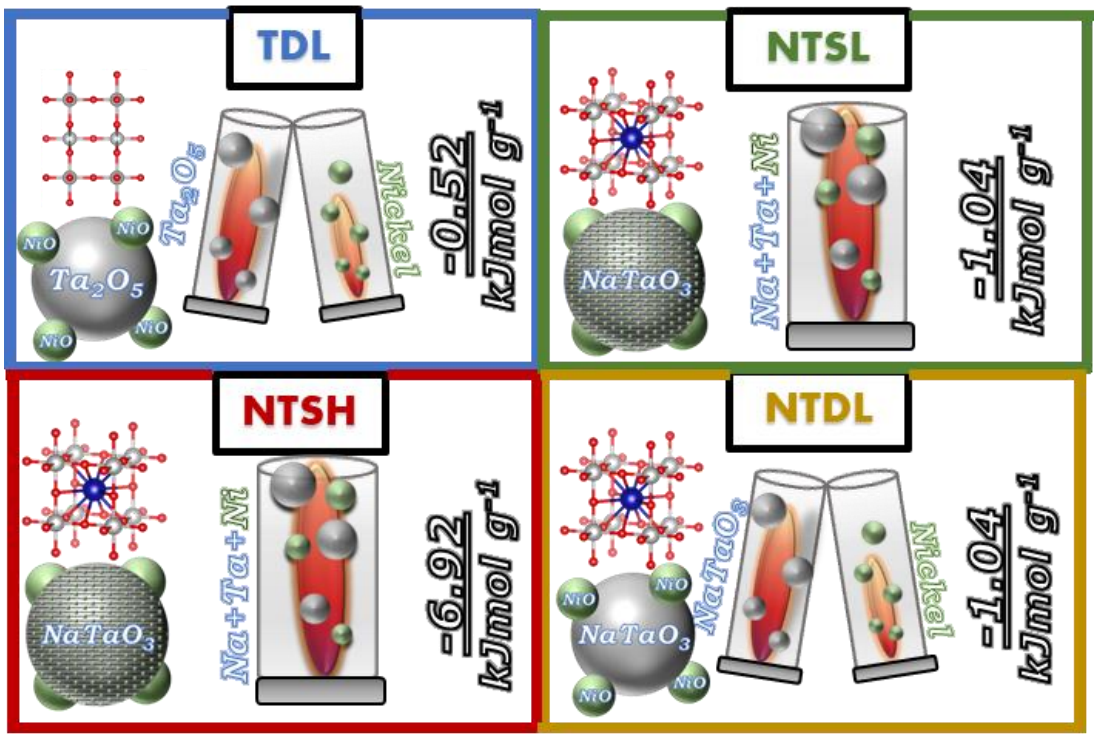

Figure 4-108: *Scheme of FSP set-ups for each nanomaterial. The combustion-enthalpy values ($\Delta_c H$) are shown for each process to emphasize the direct correlation with the $NaTaO_3$ particle size.*

Table 4-21: *Structural Characteristics of FSP-made, NiO-containing, Ta_2O_5, and $NaTaO_3$ particles produced with a P/D=5/5.*

Material	NiO-deposition method	Ta/Na Concentration (mM)	Phase (Ta_2O_5/ $NaTaO_3$)	Crystallite Size (nm)			SSA (m^2g^{-1})	Pore Volume (cm^3g^{-1})	Band gap E_g (eV) (±0.04)
				d_{TEM}	d_{XRD}	d_{BET}			
TDL	Double-Nozzle (0.5% NiO)	50/0	100/0	9.6±0.2	18	22	34.0	8.8 10^{-2}	4.2
NTSH	Single-Nozzle (0.5% NiO)	300/300	0/100	19.1±0.6	33	43	19.4	4.1 10^{-2}	4.28
NTSL	Single-Nozzle (0.5% NiO)	50/50	20/80	14.1±0.6	25	30	28.1	8.9 10^{-2}	4.2
NTDL	Double-Nozzle (0.5% NiO)	50/50	6/94	12.3±0.3	21	23	37.3	11.6$10^{-2}$	4.2

For the FSP synthesized selected for materials TDL (Ta_2O_5), NTSL, NTSH, and NTDL ($NaTaO_3$) the Powder X-ray diffraction (XRD) patterns are shown in **Figure 4-109**. The characteristic peaks of the Ta_2O_5 orthorhombic phase (JCPDS card no. 25-0922) and the perovskite $NaTaO_3$ (JCPDS card no. 74-2488) are shown at the bottom of the graph. For all four selected materials, highly crystalline nanophases were acquired. For TDL, all the diffraction peaks can be indexed as Ta_2O_5 orthorhombic phase, while in NTSH, NTSL, and NTDL correspond mainly to $NaTaO_3$ cubic phase. A small percentage of Ta_2O_5 was observed for NTSL and NTDL due to prioritizing the size and bringing the FSP parameters to the precipice of $NaTaO_3$ formation.

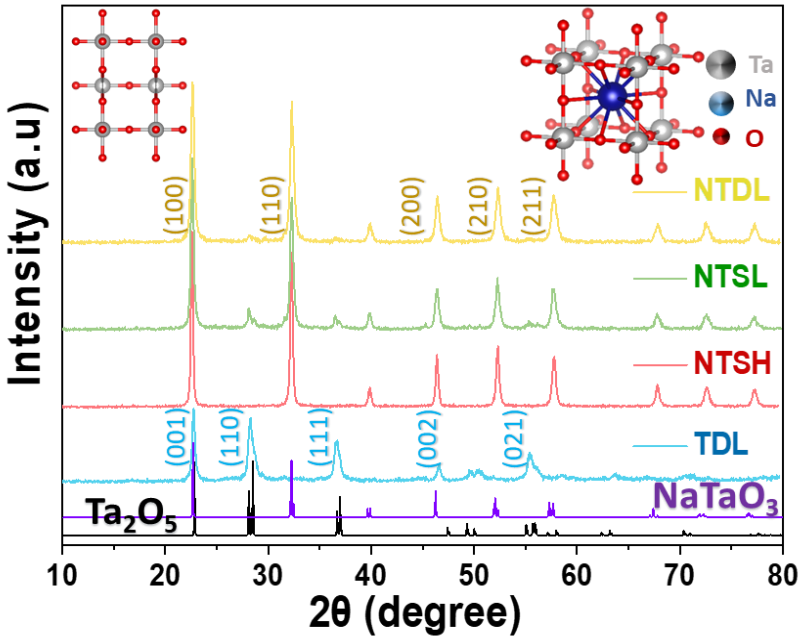

Figure 4-109: *XRD patterns for TDL (Ta_2O_5) and NTSL, NTSH, NTDL ($NaTaO_3$) nanomaterials. The reference XRD peaks of orthorhombic Ta_2O_5 (black) and cubic-$NaTaO_3$ (purple) are displayed at the bottom. Insets: unit-cell structures of the two phases*

To detect the deposition of NiO particles from the SN and DN FSP, HRTEM EDX has been applied, as seen in **Figure 4-110**(A). The NiO particles signal was detected for the small NiO 2-4nm particles as seen in the STEM images, as seen from the green circles on the STEM pictures, **Figure 4-110**(B-E). Overall, all four particles have very clearly sub 5-nm NiO particles on the surface of the nanoparticles. XRD wasn't sufficient in detecting these

small nanoparticles, as the small size and the very low percentage of NiO particles prohibited their detection.

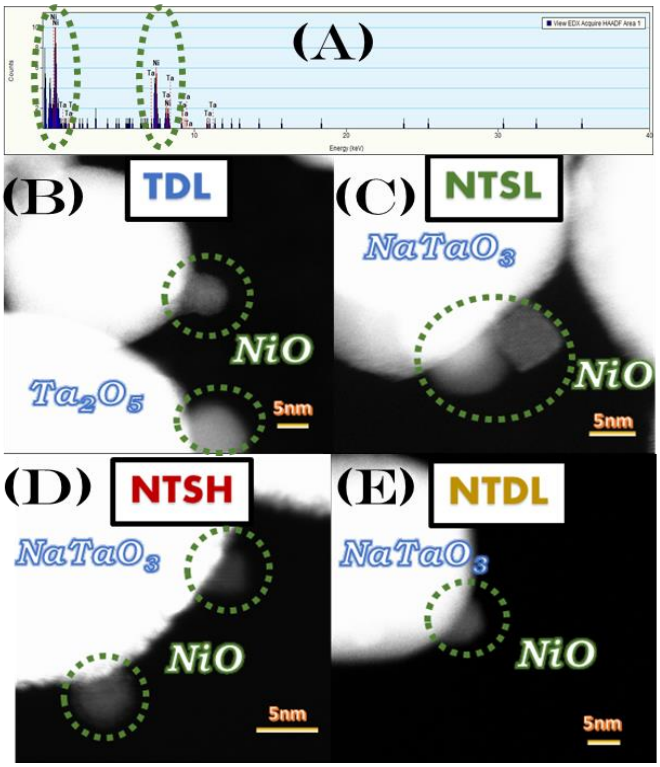

Figure 4-110: *(A) EDX data, focusing on the NiO, the encircled part of the TEM images below. HRTEM analysis for NiO oxide allocation on the particles (B) TDL, (C) NTSL, (D) NTSH, and (E) NTDL. The data verify the fine dispersion of 2-3nm NiO particles.*

From **Figure 4-109**, from the Shcerrer equation, the Crystallite Size d_{XRD} of the four selected materials TDL, NTSH, NTSL, and NTDL was calculated to be 18, 33, 25, and 21 nm, respectively. The N_2 adsorption-desorption isotherms of the four materials produced the SSA 34.0, 19.4, 28.1, and 37.3 (m^2g^{-1}) SSA, respectively, as shown in **Figure 4-111**, calculating the size of the particles through d_{BET} as 22, 43, 30, and 23 nm respectively. From d_{XRD} and d_{BET} a clear correlation exists, with TDL being the smallest, which is expected from the simple oxide, interestingly NTDL is only a few nanometers bigger, and the reduction of total enthalpy through the change of precursor concentration has a significant role, reducing the size by almost a half and doubling the surface area. The same trend is seen in

the pore volume, **Figure 4-112**, for the materials TDL, NTSH, NTSL, and NTDL obtained as 8.8 10^{-2}, 4.1 10^{-2}, 8.9 10^{-2}, 11.6 10^{-2} ($cm^3\ g^{-1}$) Pore Volume, respectively.

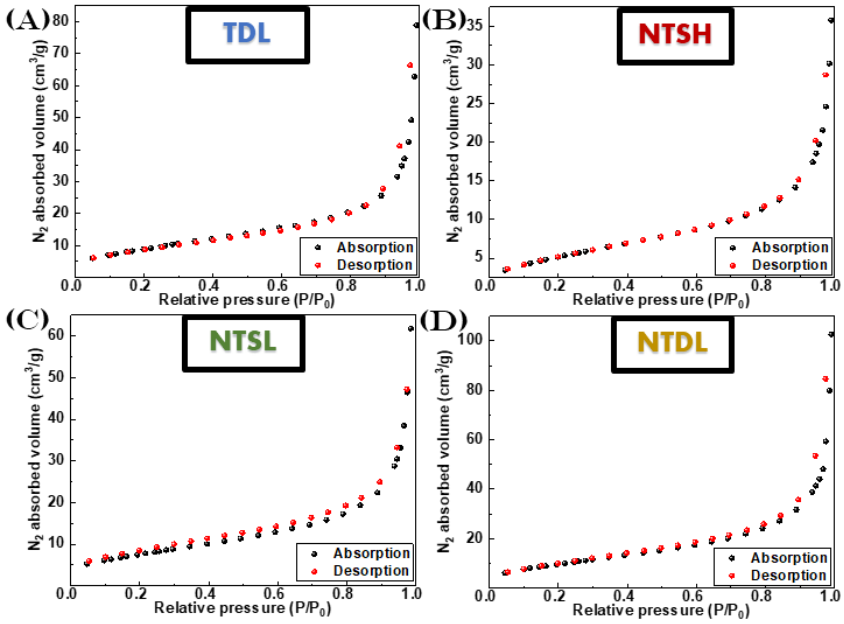

Figure 4-111: *N_2 adsorption-desorption isotherms of (A) TDL, (B) NTSL, (C) NTSH, and (D) NTDL materials.*

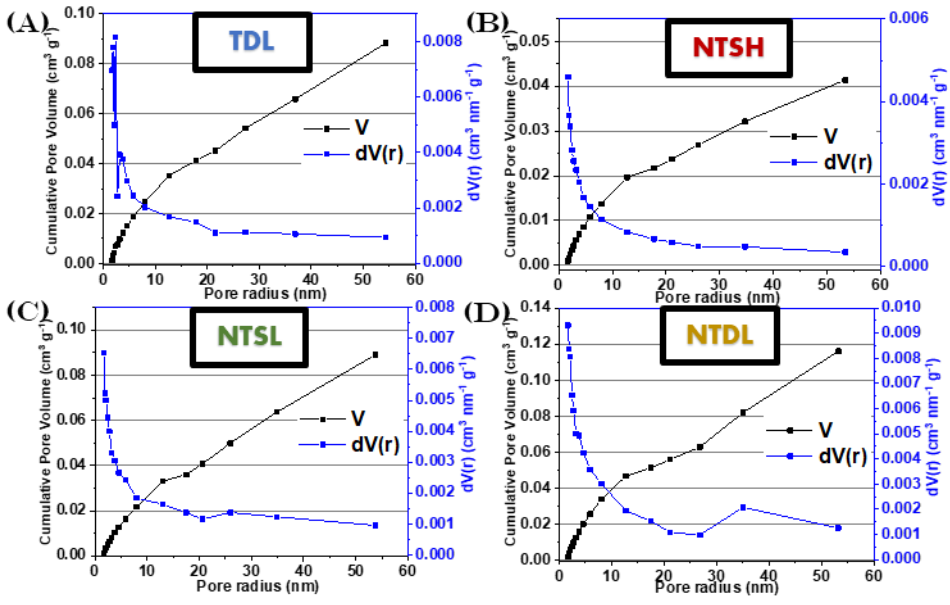

Figure 4-112: *Pore size distribution plot using the BJH method of (A) TDL, (B) NTSL, (C) NTSH, and (D) NTDL materials.*

For further identification of the phases, from the STEM images in **Figure 4-113**, the TDL (Ta_2O_5) material has a lattice spacing of 3.95 Å, this is identified as the (001) plane, corresponding to the 22.8° diffraction peak for orthorhombic Ta_2O_5 [444]. While, the material NTSL ($NaTaO_3$) displays a highly crystalline lattice, with a lattice spacing of 3.75 identified as the (101) plane for the cubic-$NaTaO_3$ phase [127]. All other $NaTaO_3$ (NTSH, NTDL) FSP-produced materials showed similar lattice spacings.

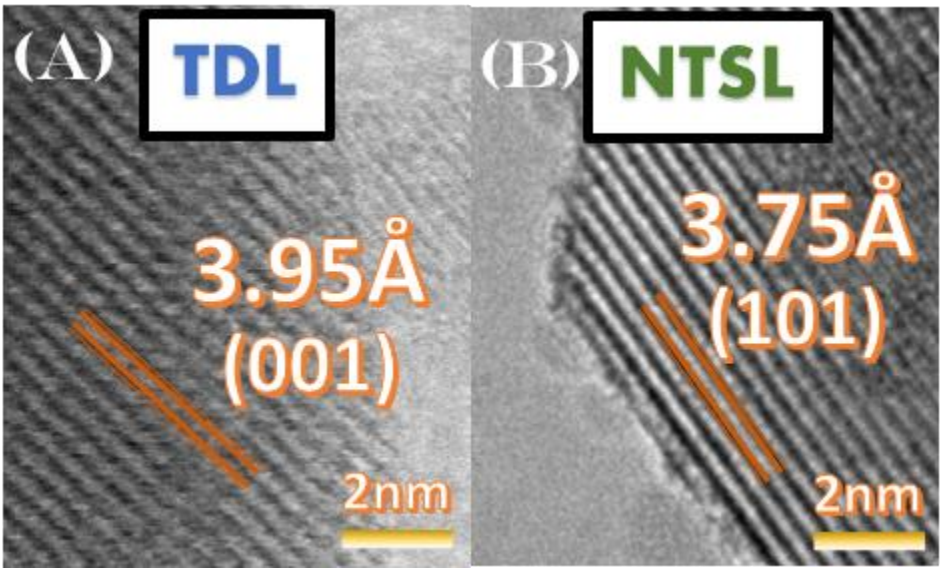

Figure 4-113: *HRTEM images for Miller planes for the materials (A) TDL as the phase Ta_2O_5, (B) NTSL with the perovskite phase $NaTaO_3$.*

The STEM images of the materials TDL, NTSL, NTSH, and NTDL, shown in **Figure 4-114**, show that the Ta_2O_5 and $NaTaO_3$ particles have quasi-spherical morphology, as expected since the majority of FSP-produced oxides have spherical morphologies, while only the NTDL some cube-shapes were also formed, this could be derived from the very small particle size.

The size-distribution statistics calculated from multiple STEM images for each material are shown in **Figure 4-115**. The TDL(Ta_2O_5) has a d_{TEM} size of 9.6 nm, as for the $NaTaO_3$ particles, NTSL, NTSH, and NTDL have a d_{TEM} size of 19.1, 14.1, and 12.3 nm, respectively. All the d_{TEM}, d_{XRD}, d_{BET}, and SSA parameters for these materials show similar trends from smaller to bigger materials.

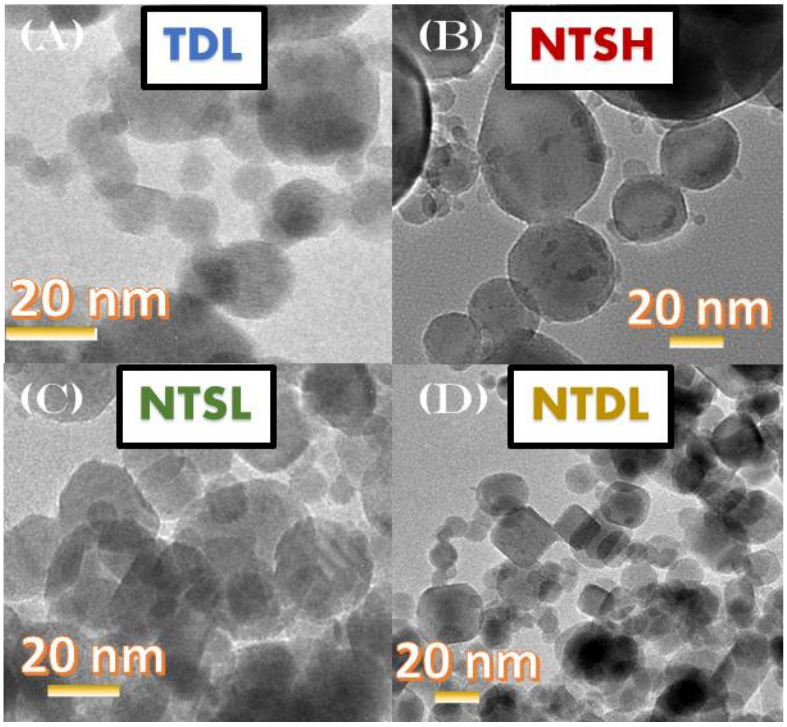

Figure 4-114: *HRTEM images for the particles (A) TDL, (B) NTSL, (C) NTSH, and (D) NTDL.*

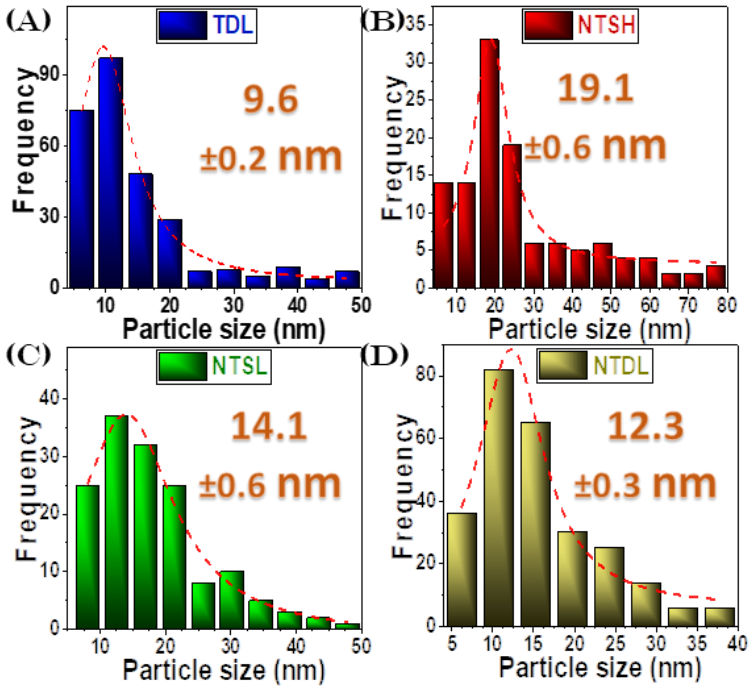

Figure 4-115: *HRTEM size distribution of (A) TDL, (B) NTSL, (C) NTSH, and (D) NTDL.*

According to the size determined with whatever applied method d_{TEM}, d_{XRD}, d_{BET}, the NTDL {$NaTaO_3$/NiO} material has the smallest $NaTaO_3$ size with an average of d_{TEM} 12.3nm, which is the smallest $NaTaO_3$ particle-size so far reported in the literature [123,126–128,131,133,135,271].

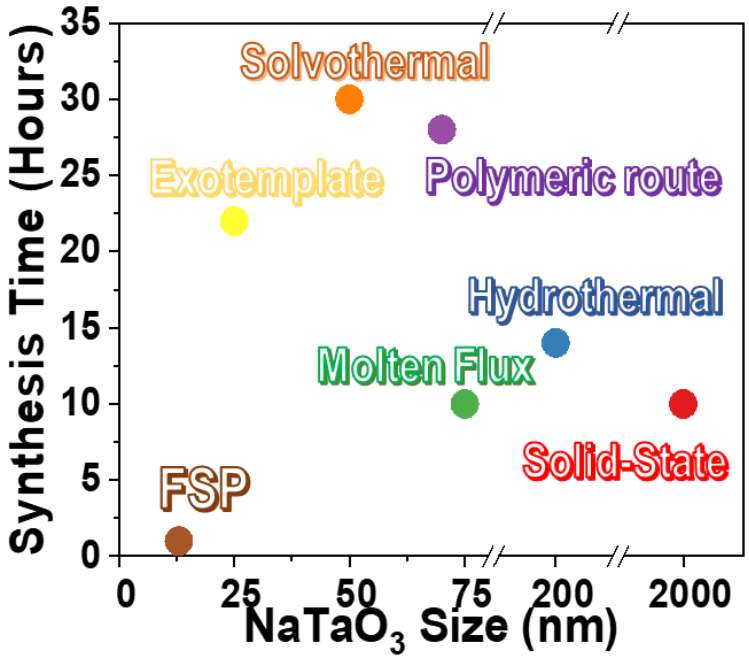

Figure 4-116: *Graph containing the synthesis time and perovskite $NaTaO_3$ size, for the best and most prevalent works, according to the smallest size.*

A detailed comparison of pertinent synthesis methods with the derived $NaTaO_3$ size, SSA, and synthesis time is shown in **Figure 4-116** for a more visual representation and in **Table 4-22** [123,126–128,131,133,135,271]. The FSP technology, further than producing the smallest size for the $NaTaO_3$ perovskite, can have the lowest synthesis time as a critical advantage, where the core synthesis requires only minutes, with the complete procedure needing only 30 minutes, in comparison with other methods of **Table 4-22**, that require multiple hours or even days.

Overall, the derived thermodynamic insight from these experiments shows that in order to obtain small $NaTaO_3$ particles in the FSP process, two conditions need to be fulfilled at least:

[i] Favorable combustion-enthalpy, the Δ_cH should be controlled at the lower acceptable limit, with these experiments observed it as Δ_cH = -1.04 kJmol g^{-1}, with a size-limit of ~12nm, higher Δ_cH results in larger particle sizes.

[ii] Long High-Temperature-Residence-Times, in our set-up this was satisfied using a 20cm enclosing quartz tube.

Table 4-22: *Literature comparison of Size and SSA for $NaTaO_3$ and Ta_2O_5 nanoparticles synthesized by different synthesis methods.*

Photocatalyst	Synthesis method	Synthesis period (hours)	Crystallite size(nm)	SSA (m^2g^{-1})	*Ref.*
TDL (Ta_2O_5: 0.5%NiO)	FSP	0.5	9.6 ±0.2(d_{TEM})	34.0	*This work*
NTDL ($NaTaO_3$: 0.5%NiO)	FSP	0.75	12.3 ±0.3(d_{TEM})	37.3	*This work*
$NaTaO_3$	exotemplate method	22	25(d_{TEM})	22.4	[126]
$NaTaO_3$	solvothermal synthetic	24 synthesis + 6 dried/centrifuged	50(d_{TEM})	77.3	[127]
$NaTaO_3$	polymeric citrate precursor route	28	70(d_{TEM})	46.2	[128]
$NaTaO_3$: Sr doping	molten flux	10	75(d_{TEM})	-	[123]
$NaTaO_3$: S doping	hydrothermal process	12 synthesis + 2 dried/centrifuged	200-500nm(d_{TEM})	-	[133]
$NaTaO_3$	solid-state reactions	10	2000(d_{SEM})	0.5	[134]
Ta_2O_5	FSP	0.5	14.4(d_{BET})	51	[443]
Ta_2O_5	Hydrothermal	24	30(d_{TEM})	-	[135]

4.7.4 Phase purity and characterization for the selected Ta_2O_5 and $NaTaO_3$/NiO nanoparticles

DRS-UV-vis: The pristine FSP-produced Ta_2O_5 and $NaTaO_3$ powders have a crispy-white color. While with the NiO deposition in the selected heterostructures {NiO/$NaTaO_3$} and {NiO/Ta_2O_5} the powders obtained a light-green color. It has been observed that increased Ni deposition from 0.5% to 5% intensified the green color accordingly. The band-

gaps, Eg, of the produced Ta_2O_5 and $NaTaO_3$ semiconductors were determined with the Kubelka–Munk method [327], where *p* was set to 1/2 for direct-band transition. Thus, the Tauc plot of the four Ta-materials is shown in **Figure 4-117**.

All derived band-gap values E_g are listed in **Table 4-21**. The band gap of the materials is as follows: The Ta_2O_5 particle (TDL) had E_g 4.15eV, which is in accordance with literature band gap energies for this phase at 4eV [280]. The $NaTaO_3$ particles had E_g=4.18eV for NTDL and NTSL, while there was a small shift with 4.25eV for NTSH. The literature presents the band gap of the perovskite phase at values in the range of 4.2eV, as initially reported by Kudo's group [124,281].

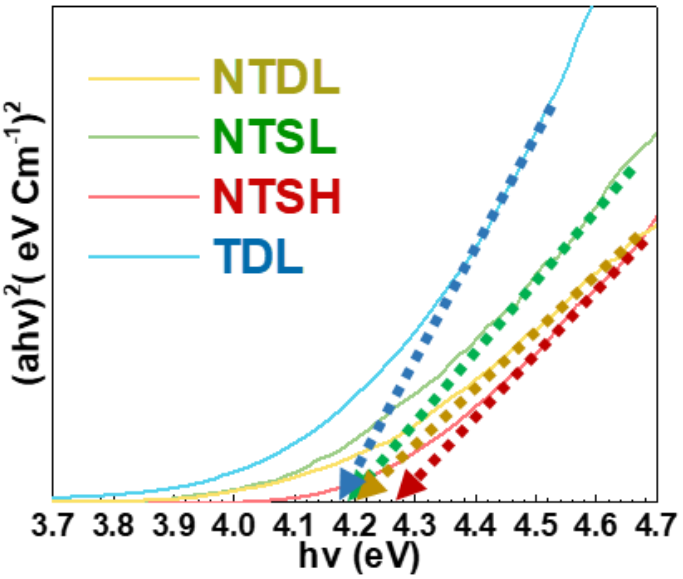

Figure 4-117: *Tauc-Plots derived from DRS-UV-Vis data for TDL, NTSH, NTSL, and NTDL. The dotted arrows show the calculated bandgap.*

FT-IR spectroscopy: **Figure 4-118**(A) shows FTIR spectra of the selected Ta-materials. For the Ta_2O_5 phase (TDL), the Ta–O and Ta–O–Ta stretching vibration modes at 500–700 cm^{-1} are detected, with some additional weaker bands in 700–900 cm^{-1} [445,446]. In perovskite $NaTaO_3$ (NTSH, NTSL, and NTDL), for the main bands at 500–800 cm^{-1}, the responsible vibrations are the Ta–O stretching, and Ta–O–Ta bridge stretching modes, while an asymmetrically centered peak around 700 cm^{-1} being the perovskite phase characteristic feature [133,447]. The IR band at 3440 cm^{-1} corresponds to O–H vibrations

of water adsorbed on the surface. The NiO didn't produce additional vibration modes due to very low concentration.

Raman Spectroscopy*:* The Raman spectra of the four selected Ta-materials are shown in **Figure 4-118**(B). The Ta_2O_5(TDL)-Raman spectra can be divided into three internal modes in the range of 150 to 1000cm^{-1}, the inclusion of each of the three vibration modes ranges is presented at the top of **Figure 4-118**(B) for the readers' convenience. The first range is attributed to O-2Ta or O-3Ta deformation in the range 150-400 cm^{-1}, while separately, the O-2Ta and O-3Ta stretching vibrations are found in the range 400-1000 cm^{-1} [448,449]. The $NaTaO_3$ (NTSH, NTSL, and NTDL)-Raman possesses similar peaks due to the similar Ta-O groups in the perovskite structure, the observed spectra are in accordance with literature data and theoretical calculations [450,451]. Most importantly, the detection of the vibrations in 200 to 250 cm^{-1} ensures that the materials don't have amorphous regions [448,449], providing more evidence for the high crystallinity of the materials.

The lack of Raman phonons in the range 1000-1600cm^{-1} indicates the absence of carbon-induced vibrations [452]. This is highly important, as it shows that the selected four Ta-materials are formed by the high carbon content FSP process as carbon-free materials. Thus under the FSP-combustion process, all carbons atoms from the solvent and the metal-precursor are completely combusted to carbon dioxide due to the sufficient combustion enthalpy and oxygen-rich process used in the present FSP-protocols [169–171].

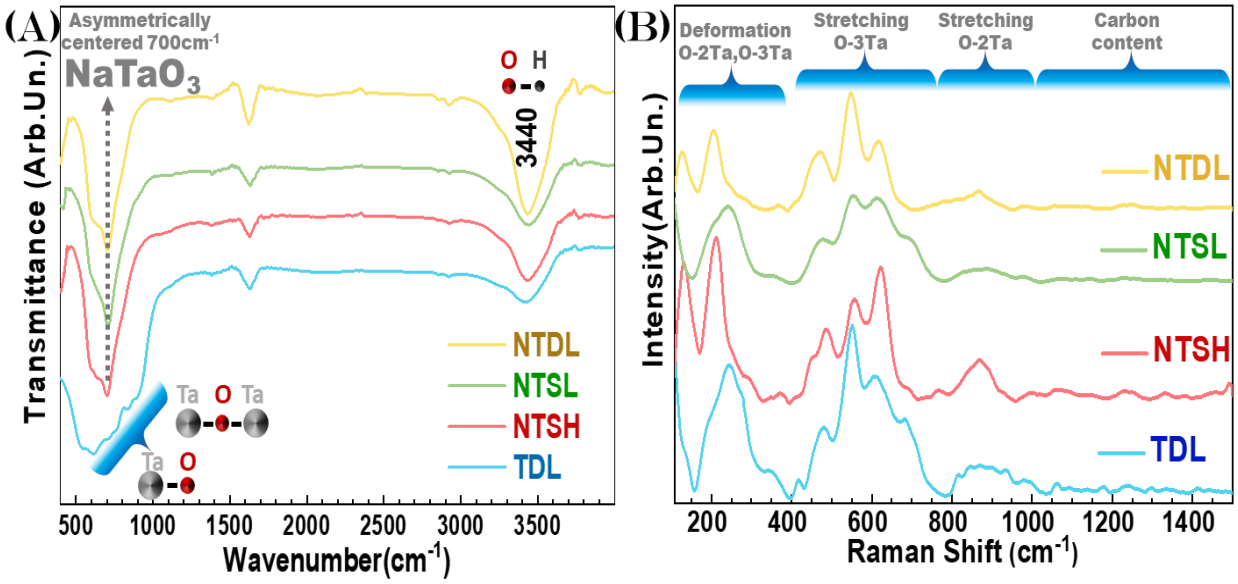

Figure 4-118: *(A) FT-IR spectra of the materials, the main vibrating modes are displayed graphically. (B) Raman spectra of the materials, with the assigned deformation/stretching vibrations modes of O-2Ta and O-3Ta.*

X-Ray Photoelectron Spectroscopy: The Na-XPS spectrum for NTSH $NaTaO_3$ material is shown in **Figure 4-119**. The characteristic Na1s binding energy of 1071 eV confirms Na-atoms' presence in the $NaTaO_3$ material [453]. The same peaks were observed for the other $NaTaO_3$ materials (NTSL, NTDL), the same can be said for the later Tantalum and oxygen spectra, this shows a high uniformity in the crystal structure between the materials, changing only the size/SSA and place deposition of the NiO particles,

The Tantalum XPS spectra for TDL and NTSH are present in **Figure 4-120**. The Ta-XPS spectra show the distinct $Ta^{5+}{}_{5/2}$ and $Ta^{5+}{}_{7/2}$ peaks observed in the binding energies 27.8 and 26 eV, respectively. The Tantalum XPS spectra confirm the lack of secondary reduced Ta-states, such as Ta^{4+}, Ta^{3+}, or Ta^{0}, from small atomic regions not detectably by XRD [454]. Oxygen XPS spectra for TDL and NTSH are present in **Figure 4-121**. The Oxygen-XPS spectra contain characteristic peaks of surface hydroxyl groups at 532 eV and O-Ta bonds of the crystal at 530.1 eV peak [399]. Overall, XPS data confirm that all four of the selected Ta-material are without any small percentages of O-defects or reduced Ta-atoms in the crystal structure.

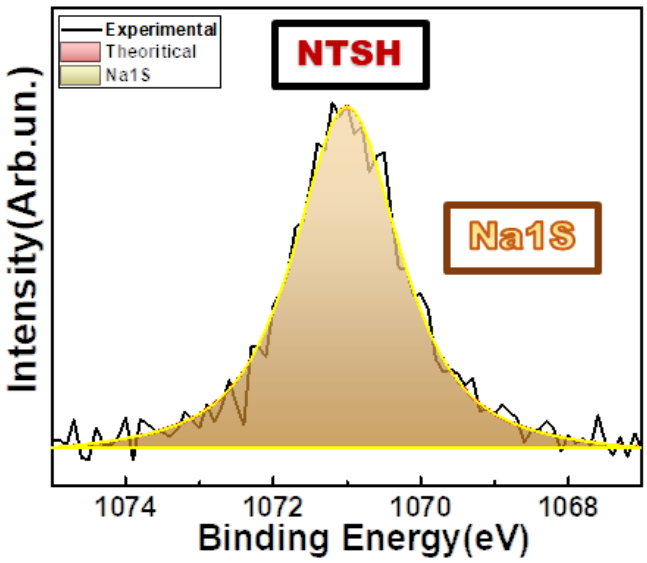

Figure 4-119: *Sodium XPS spectra for NTSH material, showing the fitted Na1s state.*

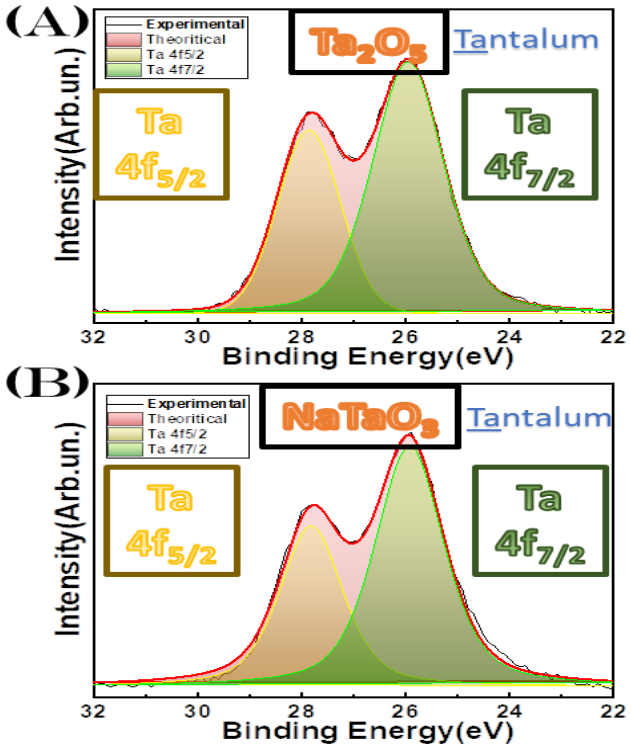

Figure 4-120: *Tantalum XPS spectra for, (A) TDL (Ta_2O_5), (B) NTSH ($NaTaO_3$) nanomaterials, showing the fitted $Ta4f_{5/2}$ and $Ta4f_{7/2}$ states.*

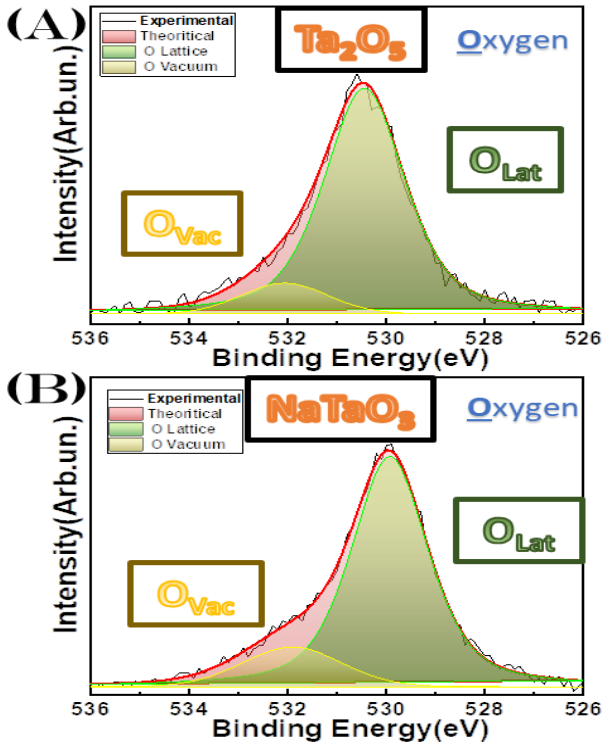

Figure 4-121: *Oxygen XPS spectra for (A) TDL (Ta_2O_5), and (B) NTSH ($NaTaO_3$) nanomaterials, showing the fitted surface O-Ta bonds and hydroxyl group states.*

Overall, the present spectroscopic FTIR, Raman, and XPS data for the FSP-produced Ta-materials ensure that their structures contain only pure phases, free of defects such as Ta^{4+}, Ta^{3+}, or Ta^{0} oxidation states at small percentages, free of amorphous Tantalum regions, and free of carbon deposits. Taking into account the XRD and TEM data, we conclude that the FSP process we developed produces $NaTaO_3$ and Ta_2O_5 with surface-deposited NiO heterostructures of high purity and crystallinity. For completeness, we report that deposition of NiO doesn't appear to have any impact on any of the spectroscopic data due to the low loading i.e. 0.5%.

4.7.5 Ta_2O_5 and $NaTaO_3$/NiO for Photocatalytic H_2-Production from H_2O

The photocatalytic H_2-production data from H_2O of the four selected materials, the heterostructures {$NaTaO_3$/NiO} and {Ta_2O_5/NiO}, are shown in **Figure 4-122**. In these

experiments, we underline that Pt or other noble metals were not included as catalysts, while the photon radiation was achieved from a Solar-light simulating Xenon-lamp. The kinetics show an initial delay of H_2-production in all materials, this is attributed to the electron-storage effect of the cocatalyst, where the majority of the photogenerated electrons at the beginning of photocatalysis are collected/stored by the NiO-cocatalyst in accordance with previous reports [455].

The kinetics of the photocatalytic H_2-production show that the most efficient of the four selected materials is the NTDL 12nm {$NaTaO_3$/NiO} produced by Double-Nozzle FSP by a wide margin, achieving a hydrogen rate of 390 umol $g^{-1}h^{-1}$. This is attributed to three different factors produced from the comparison of the four materials.

[i] **Crystal Structure**: In all cases, the performance of Ta_2O_5 Nanocatalysis was inferior compared to $NaTaO_3$, despite its smaller size of 9.6 nm and higher SSA. As we discuss hereafter, this can be attributed to the lower energy of the conduction-band edge of E_{CB}= -100mV for Ta_2O_5. vs. E_{CB} =-600mV for $NaTaO_3$, and appropriate band alignment of the Ta-material in comparison to the cocatalyst NiO.

[ii] **Material Size**: The profound effect of the $NaTaO_3$-size on photocatalytic H_2-production can be demonstrated by comparing the two materials, 19nm NTSH and 12nm NTSL: the smaller $NaTaO_3$ (NTSL) has a ~330% higher H_2-production efficiency. Normalization per SSA from 28m^2/gr to 19m^2/gr of the two materials, clearly the higher SSA of 12nm NTSL, cannot fully account for the difference in the H_2-production rates.

This phenomenon supports the findings of our previous work, where EPR spectroscopy showed that the {hole/electron} pair lifetime is affected severely and non-linearly by the $NaTaO_3$ particle size [225]. Larger $NaTaO_3$ particles (NTSH) display significantly lower {hole-electron} lifetimes *vs.* the smaller $NaTaO_3$ particles (NTSL). Photoinduced holes and electrons migrate rapidly to the particle surface at smaller $NaTaO_3$ sizes, thus the hole-electron recombination rate is inhibited [225]. As mentioned before, the hole/electron charges that are on the surface are employed for the photocatalytic activities, in this case, the reduction of H^+ to H_2.

[iii] **NiO Deposition method**: The deposition method shows clearly very different hydrogen efficiencies, this is observed by all direct particle comparisons for the deposition method of the two FSP-setups, NTSL that was produced by Single Nozzle-FSP in comparison to the NTDL by Double Nozzle-FSP, where NTDL has a superior H_2-production rate of 380 vs 330umol $gr^{-1}h^{-1}$ of NTSL. Although an even more substantial change is observed at the start of the photocatalysis, where the NTDL photocatalysis shows that NiO particles require less charge storing, resulting in total hydrogen production in three hours of ~1200 vs. 600 umol gr^{-1} of NTDL vs. NTSL.

Overall, the present data shows {12nm$NaTaO_3$/NiO} NTDL material produced by Double-Nozzle FSP technology is the far superior photocatalyst due to the crystal structure, material size, and NiO deposition method. We focused on this photocatalyst to prove the production under UV light, the stability of the photocatalysis, and the solar to hydrogen production.

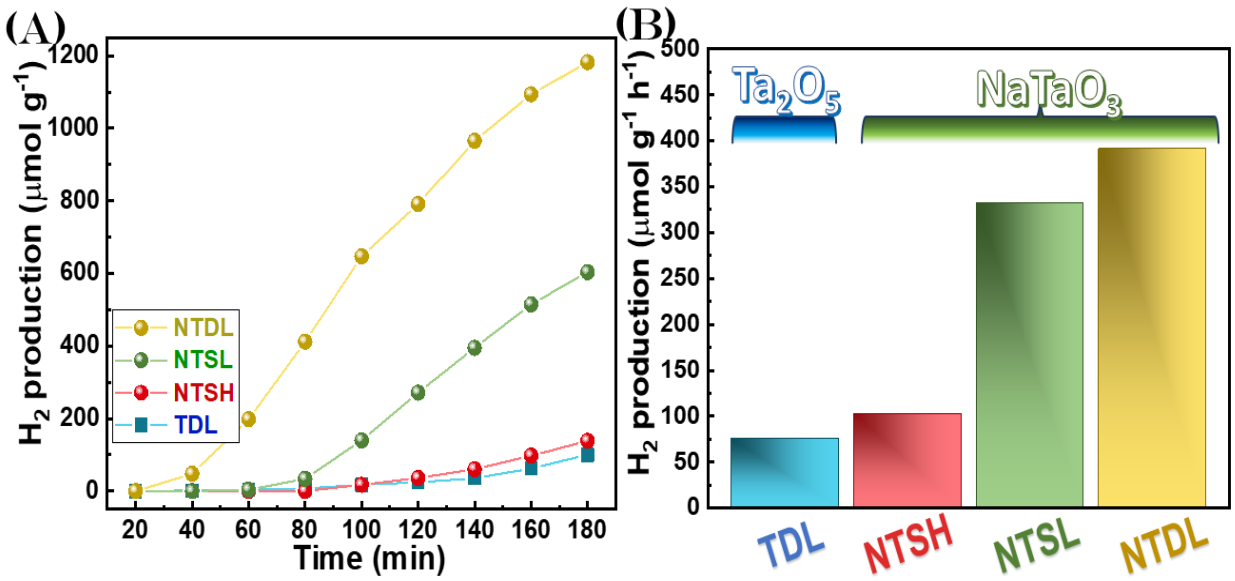

Figure 4-122: *Photocatalytic H_2-production from the four selected Ta-materials under Xenon-radiation. (A) Kinetics of photocatalytic H_2-production. (B) H_2-production yields (μmol g^{-1} h^{-1}) for the four materials.*

Two light-irradiation sources were tested: [i] Solar-light simulating, Xenon-lamp as seen from the previous experiments, most photocatalysis semiconductors are tested under

sun simulating radiation, the solar simulating radiation provides a fair assessment of the solar to hydrogen efficiency, a better correlation between the following EPR experiments as they were conducted with a similar Xenon-lamp. [ii] UV-light, mercury lamp, to better compare the Hydrogen production with other studies, while more efficient due to the larger band-gap.

Figure 4-123 shows the very different radiation profiles of the two lamps, with xenon having continuous radiation spectra with a very high percentage being in the energies of infrared, while the mercury lamp rather than continuous radiation, has radiation peaks, with the majority of the radiation energy being in the UV-range. As the Tantalum materials have a high band gap of 4.1eV that absorbs only UV radiation, the hydrogen production from the 391 μmol $g^{-1}h^{-1}$ with the photocatalyst NTDL under 300W Xenon irradiation increases exponentially under the 300W Hg-irradiation achieving a rate of 10684 μmol g^{-1} h^{-1}.

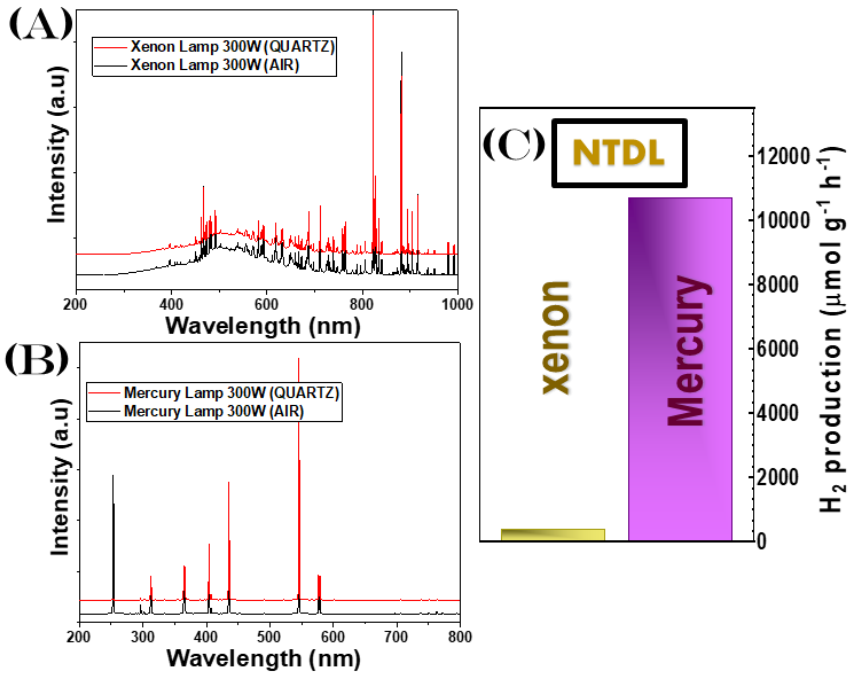

Figure 4-123: *Radiation profile of (A) Xenon Lamp 300W and (B) Mercury Lamp 300W. (C) Comparison of the H_2-production yields for the NTDL {$NaTaO_3$/NiO} photocatalyst under Xenon vs. UV-Mercury lamp irradiation.*

To further verify the structural stability of the materials and the stable production of hydrogen, the XRD profile of all four selected Ta-materials was obtained after the photocatalytic hydrogen production. The obtained data compared with the XRD profiles before the photocatalysis, as shown in **Figure 4-124**(A), have a one-to-one correlation, meaning that the crystal structure of all the materials remained stable, proving high structural stability. In order to prove the stable production of hydrogen, the most efficient catalyst (NTDL) was used for three consecutive reuses, with the H_2-production rates remaining stable and highly efficient, as seen in **Figure 4-124**(B).

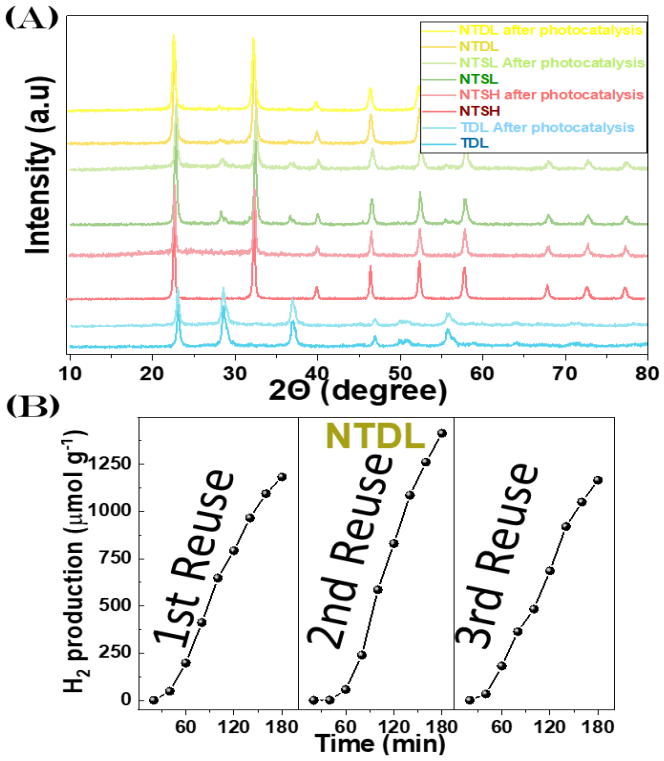

Figure 4-124: *(A) XRD data for the nanomaterials before and after photocatalysis. (B) Reuse experiments for the best-performing material NTDL.*

Solar to Hydrogen (STH) efficiency: To correctly measure the efficiency of the particles, rather than the bibliographic comparison that will follow, since there aren't any two laboratory systems exactly comparable, a gross offender of this fact is the very

different production of photons of 300W Mercury lamps from different companies, a better representation is the Solar to Hydrogen efficiency, that shows the amount of photons used for the reduction of water, producing molecules of Hydrogen. Although at the time of our publication, to our knowledge, the STH of $NaTaO_3$ materials has never been measured, thus the present study will provide a much better comparison and understanding of the photocatalytic efficiency of $NaTaO_3$ materials.

STH efficiency or n_{STH} [456] of the best achieving NTDL material was calculated from Equation 4-6, where Φ_{H2} is the produced hydrogen under the illuminated area (mol $s^{-1}m^{-2}$), the Gibbs free energy $G^0_{f,H2}$ for the formation of hydrogen 237 kJ mol^{-1}, and the energy of incident solar light P_{Light} (0.78 W cm^{-2}, Xe lamp). The resulting n_{STH} for the NTDL was calculated to be 0.89%.

$$n_{STH} = \frac{\Phi_{H2} G^0_{f,H2}}{P_{Light}} \qquad \text{Equation 4-6}$$

As mentioned, to compare with literature data i.e. most reports [90,271,123,457], we utilized Hg-lamps that produce much higher amounts of UV radiation. **Table 4-23** lists pertinent literature data for other well-performing $NaTaO_3$ photocatalysts for H_2-production under xenon [458] and mercury [90,271,123,457] irradiation. This comparison shows that {12nm $NaTaO_3$/NiO} NTDL material has a higher catalytic performance. For completeness, the H_2-photogeneration results of TDL {9nm Ta_2O_5/NiO} are included in **Table 4-23**, which is comparably performing with pertinent literature reports for Ta_2O_5 under xenon-irradiation [92,459].

Table 4-23: *Comparison of H_2 photoproduction data for our FSP-made catalysts vs. pertinent literature systems.*

Photocatalyst	Synthesis method	Cocatalyst(% loading)	Light Source	Reaction solution	H_2 production (μmol $g^{-1}h^{-1}$)	*Ref.*
TDL (Ta_2O_5)	FSP	0.5% NiO	Xe(300W)	Pure water+20% methanol	**76**	*This work*
NTDL ($NaTaO_3$)	FSP	0.5% NiO	Xe(300W)/ Hg(300W)	Pure water+20% methanol	**391/ 10.684**	*This work*
Ta_2O_5	hydrolysis method	2% Pt	Xe(300W)	Pure water+20% methanol	**350**	[92]
Ta_2O_5 Grey nanowires	novel synthetic route	-	Xe(500W)	Pure water+20% methanol	**210**	[459]
$NaTaO_3$	Electrospinning method	-	Xe(300W)	Pure water+20% methanol	**150**	[458]
$NaTaO_3$	molten flux	2% La	Hg(400W)	Pure water	784	[123]
$NaTaO_3$	Solid-State reaction	0.05% NiO	Hg(400W)	Pure water	2.180	[271]
$NaTaO_3$:La	Sol-gel	0.3% NiO	Hg(400W)	Pure water+10% methanol	29.200	[457]

Effect of cocatalyst-type (Ni vs. Pt) and deposition method (FSP vs. wet-method): To compare our FSP-deposition method for NiO on the $NaTaO_3$ materials surface with typical procedure for other synthesis methods of wet impregnation and calcination of Nickel deposition. An FSP- $NaTaO_3$ material with the exact synthesis method of NTDL (except the NiO deposition) was loaded with NiO particles utilizing wet impregnation and calcination. The calcination as expected due to the increased temperature, resulted in a 20% SSA decrease, as the SSA dropped from 38.3 to 30.4 m^2/gr.

The H_2-production rate of this material was 32 μmol $g^{-1}h^{-1}$ which is 1/10 of the {12nm$NaTaO_3$/NiO} NTDL performance, **Figure 4-125**. This overwhelming x10 times higher Hydrogen production of NTDL material can't be attributed to the drop of the SSA but correlates to the superiority of Double-Nozzle FSP as a more efficient deposition method for heterostructures. This can be attributed to several factors, in the liquid method/ wet impregnation and calcination, the size distribution and dispersion of NiO particles cannot be precisely controlled as in Double-nozzle FSP, where the high mobility and sintering of deposited NiO

particles provide a higher dispersion of NiO particles, while the enhanced oxide/oxide interaction and the rapid quenching in the temperature provide a heterostructure with the minimum needed incorporation of the two surfaces of the materials. Thus, NiO/$NaTaO_3$ interface and the overall band edge alignment in the flame-made heterostructure may differ compared to the one prepared by wet impregnation.

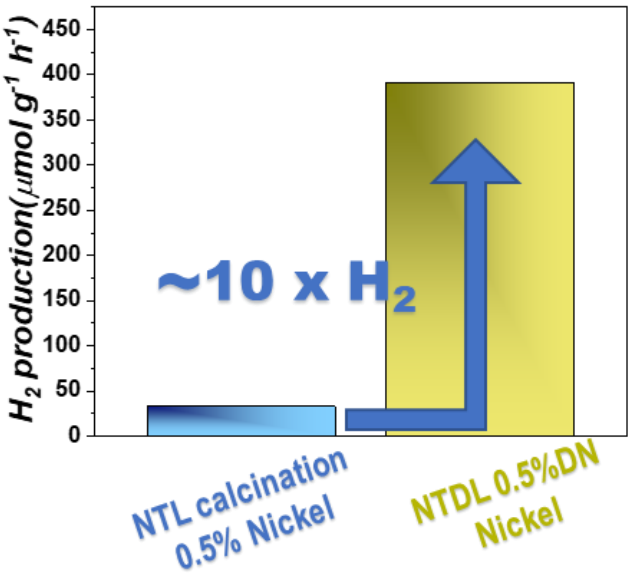

Figure 4-125: *Rate of H_2 evolution (μmol $g^{-1}h^{-1}$) for comparison of the effect of the Ni-deposition method on the H_2-production efficiency. NTL material wet impregnated with 0.5Ni nickel and calcined vs. the Double-Nozzle FSP (NTDL) material.*

A detailed screening of the deposition Nickel loading was conducted with various concentrations from 5%, 2%, 1%, and 0.5% according to the $NaTaO_3$ material. The deposition method was the Double Nozzle FSP, as it was shown to be the most efficient in comparison to hydrogen production. The FSP parameters were the same as mentioned with the four selected materials, at High concentrations (H) of total Na-TA precursor concentrations of 0.6M. The resulting hydrogen productions are shown in **Figure 4-126**. It is observed that lower concentrations provide a much higher H_2 production, with the 0.5% having almost double than 1% and five times higher than 2%, as the higher amount of Nickel can cause the inhibition of the surface, lowering the incident radiation reaching the

$NaTaO_3$ particle, while from the primary FSP synthesis attributes, the resulting NiO particles will have a bigger size resulting in higher recombination of the electron/hole pair.

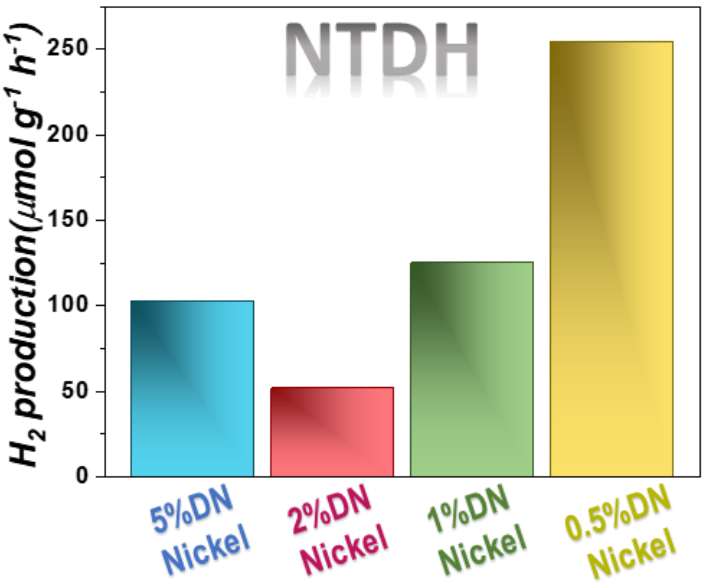

Figure 4-126: *Rate of H_2 evolution (μmol $g^{-1}h^{-1}$), using 5, 2, 1, and 0.5% loading of Nickel as co-catalyst, for the NTDH methodology of FSP-synthesis.*

From the previous measurements for the phase Ta_2O_5, only the TDL was shown, similar experiments were conducted to prove or disprove the effectiveness of the Nickel loading of the surface, lower combustion enthalpy through lower Ta-concentrations, and the deposition method of SN or DN FSP, as shown in **Figure 4-127**. [i] The Nickel loading at 2% produced 10.3 μmol $g^{-1}h^{-1}$, by dropping to the previously most efficient 0.5% the production as with the $NaTaO_3$ had a tremendous increase of 5 times at 25.6 μmol $g^{-1}h^{-1}$. [ii] Ta_2O_5 materials with lower enthalpy and therefore smaller size had an increased efficiency several times, where the production changed from 25.6 to 76.5 μmol $g^{-1}h^{-1}$. [iii] The SN or DN FSP as Nickel deposition, showed once again a similar result with the $NaTaO_3$ materials, as the SN deposition produced 46 μmol $g^{-1}h^{-1}$, in comparison to the much more efficient DN of 76.5 μmol $g^{-1}h^{-1}$.

Overall, the results closely mirror those of the $NaTaO_3$ material, where with the proper FSP parameters, the same material can adjust drastically the photocatalytic efficiency from 10.3 μmol $g^{-1}h^{-1}$ to a seven times increase of 76.5 μmol $g^{-1}h^{-1}$.

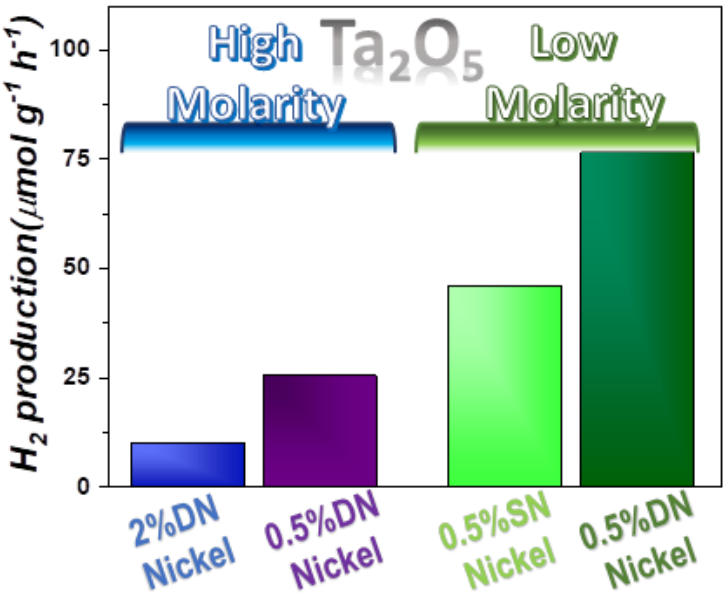

Figure 4-127: *Rate of H_2 evolution ($\mu mol\ g^{-1}h^{-1}$), for Ta_2O_5 materials, screening the precursor concentration, the Ni-loading amount, and the deposition method SN or DN FSP.*

Platinum co-catalyst: To further explore the correlation of the cocatalyst-effect deposition mechanism, we have tested the deposition of 2% and 0.5% of platinum using the Double-Nozzle FSP to produce Ta_2O_5/Pt and $NaTaO_3$/Pt. These particles were compared with 1% platinum deposited through the typical deposition of other synthesis methods, with liquid photo deposition in-situ during the photocatalytic experiment.

STEM images for the DN-FSP $NaTaO_3$/Pt show finely-dispersed platinum on the particle surface with sizes of about 5nm, **Figure 4-128**(A). In both Tantalum phases, the results show similarities with the NiO deposition, where the higher loading proves inefficient, with the 0.5% showing higher H_2-production. **Figure 4-128**(B) shows the H_2-production rate for DN-FSP Ta_2O_5/ (0.5%)Pt is 327 μmol $g^{-1}h^{-1}$, 20% higher than {Ta_2O_5/photo deposited Pt} at 258 μmol $g^{-1}h^{-1}$. **Figure 4-128**(C) shows similar results with DN-FSP $NaTaO_3$/ (0.5%)Pt were 480 μmol $g^{-1}h^{-1}$, that is 29% higher than {$NaTaO_3$/photo deposited Pt} at 342 μmol $g^{-1}h^{-1}$.

Thus, in both cases of wet impregnation of NiO and the photo deposition of Pt, the Double Nozzle FSP method shows much higher efficiency for the deposition of cocatalysts in the surface of materials, creating a highly productive heterostructure for the reduction of water.

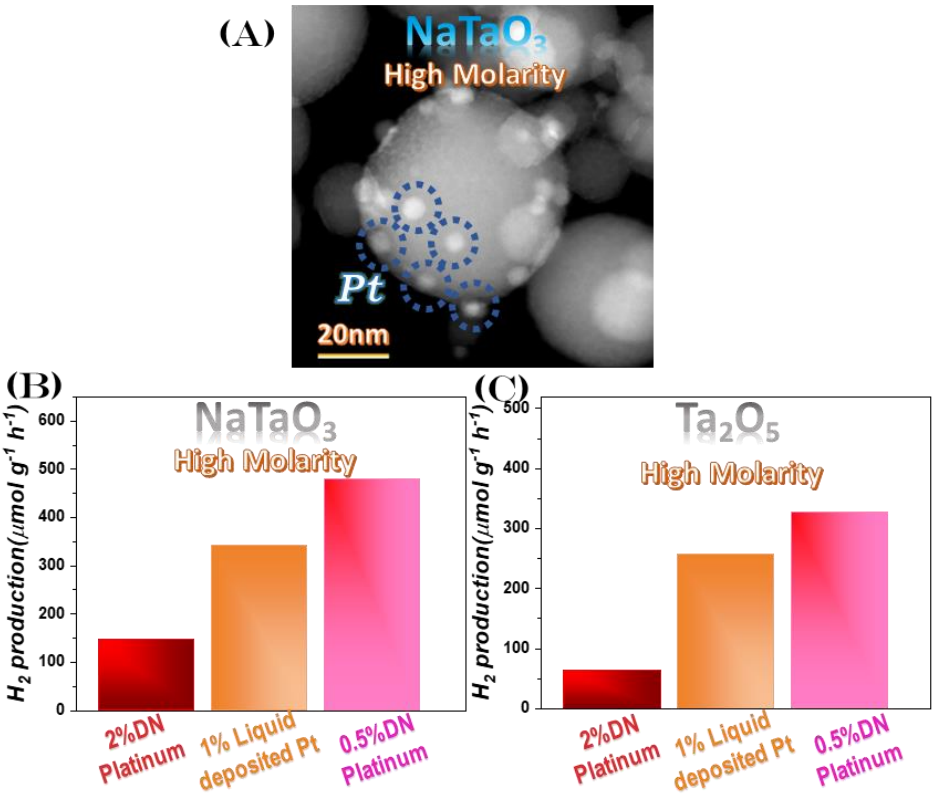

Figure 4-128: *(A) TEM image of DN-FSP made 0.5% Pt-$NaTaO_3$ deposition, showing the fine dispersion of Pt on the surface of the material. Rate of H_2 evolution (μmol $g^{-1}h^{-1}$) of : (B) Effect of Pt-loading on Ta_2O_5, comparison of Double Nozzle-FSP (2%, 0.5%) and liquid photo deposition (1%) of Pt. (C) Effect of Pt-loading on $NaTaO_3$, comparison of Double Nozzle-FSP (2%, 0.5%) and liquid photo deposition (1%) of Pt.*

Overall, the present data confirms that the Double-Nozzle FSP technology enables fine dispersion of the co-catalysts, NiO or Pt, on the Ta-particles. The present data show that a low percentage (0.5%) of co-catalytic particles is always preferable for optimal H_2-production. Compared to other synthesis methods, the present Double Nozzle-FSP is faster, enabling efficient particle size control and superior photocatalytic performance.

4.7.6 Discussion Ta_2O_5 and $NaTaO_3$/ NiO heterostructure photocatalytic mechanism

The heterostructure mechanism needs to have appropriate energy level alignment of the conduction band (CB) and valence band(VB) at the interface of the two materials i.e.

$NaTaO_3$ and NiO [460]. To properly measure the CB and VB, the NiO produced from the FSP should be measured since different morphologies of the same phase can result in different band gaps, thus we produced an FSP-made NiO, with the appropriate Tauc plot shown in **Figure 4-129**, the resulting band gap was approximately E_g=3.6eV, in accordance with the literature [271,272], with other DFT studies for the NiO material has a valence-band edge E_{VB} positioned at +2.64 eV and the conduction-band edge E_{CB} = -0.96 eV [271,272].

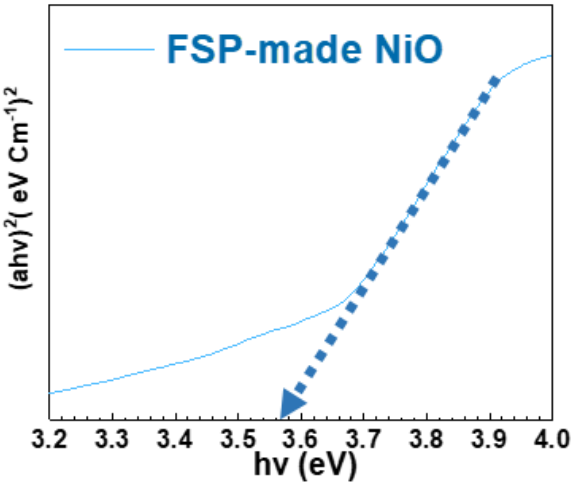

Figure 4-129: *Tauc plot of FSP-made NiO, showing a band gap of Eg=3.57eV.*

The E_{VB} and E_{CB} of the materials Ta_2O_5 and $NaTaO_3$ were found in two different ways, through DFT data, the E_{VB} of $NaTaO_3$ is situated at +3eV *vs.* NHE [272,283]. We have shown that the band gap is mainly 4.2 eV for our materials. From these facts, we estimated that E_{CB} of $NaTaO_3$ is -1.2 eV. The E_{VB} and E_{CB} for Ta_2O_5 are positioned at +3.43 eV and -0.47 eV, respectively [284,285]. The total E_{VB} and E_{CB} of NiO, Ta_2O_5, and $NaTaO_3$ are shown in **Figure 4-130**. These values can also be estimated by taking into account the Mulliken electronegativity **Table 4-24**. The calculations are done as follows: By using the A_f the atomic electron affinity, I_1 the first ionization potential, for each atom in the crystal structure, we arrive at the Mulliken electronegativity X, Equation 4-7. We can arrive at the E_{CB} and the E_{VB} of each material.

$$X = \frac{1}{2}\left(A_f + I_1\right) \quad , \quad E_{CB} = X - 4.5 - \frac{1}{2}E_g \quad , \quad E_{VB} = E_{CB} + E_g \qquad \text{Equation 4-7}$$

Table 4-24: *Reference values for the parameters X, Eg, E_{CB}, and E_{VB} of Ta_2O_5, $NaTaO_3$, and NiO materials.*

Semiconductor	E_{CB}(eV)	E_{VB}(eV)	X(eV)	Eg(eV)
Ta_2O_5	-0.26	3.94	6.337	4.2
$NaTaO_3$	-1.11	3.09	5.494	4.2
NiO	-0.34	2.86	5.760	3.2

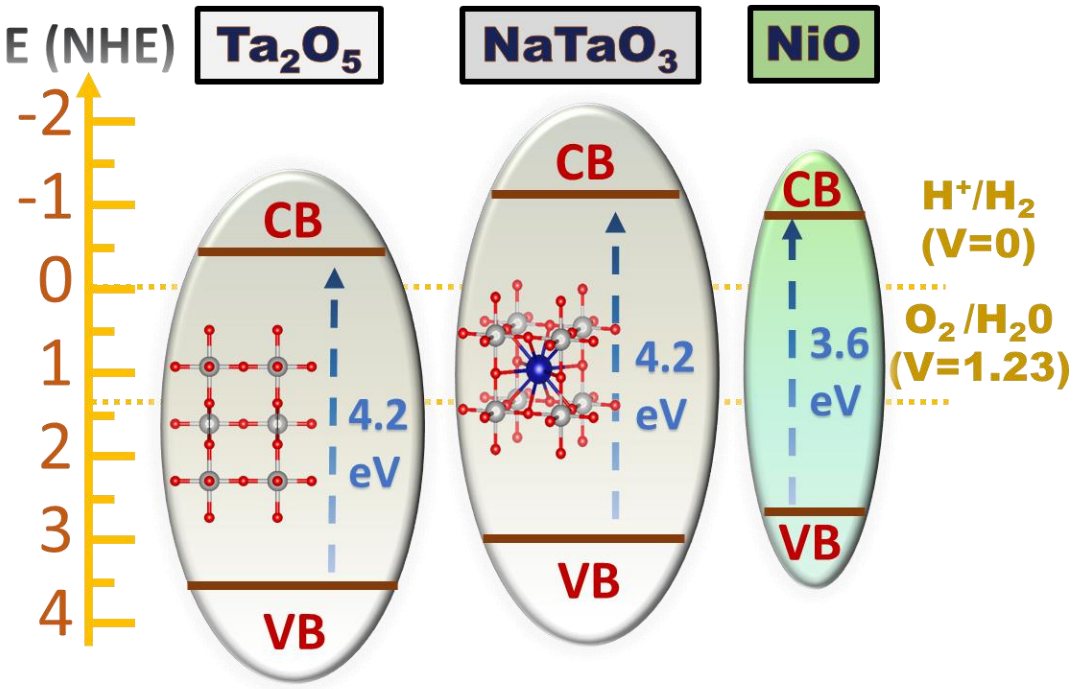

Figure 4-130: *Schematic diagram of the band edge positions vs. NHE for Ta_2O_5, $NaTaO_3$, and NiO by DFT calculations.*

Band Alignment-Band Bending in nano-$NaTaO_3$/NiO Heterojunction: To properly understand the charge dynamics at the interface of the two materials, the ensuing band bending [460] must be measured. While $NaTaO_3$ is an *n*-type semiconductor [272], NiO is the opposite *p*-type semiconductor [273,274]. As shown in **Figure 4-130**(A), before

contact, the Fermi level positionings are $E_{F,NaTaO3}$ > $E_{F,NiO}$ with the work functions positioned at 5.4eV for NiO [273,274] and 4.5eV for $NaTaO_3$ [272] respectively.

In the {$NaTaO_3$/NiO} heterojunction under equilibrium of the Fermi levels, we have band bending of the conduction and valence bands, with the calculated band offset of 0.9eV [460]. **Figure 4-130**(B), after the band offset, at the interface allows the transfer of electrons from CB_{NiO} to CB_{NaTaO3}, thus with the accumulating electrons the CB_{NaTaO3} acts as the hydrogen reduction site, while at the same time, NiO acts as a hole-acceptor as confirmed also in other works [461]. The resulting heterostructure is an efficient type-II heterojunction hindering the electron/hole pair recombination, increasing the photocatalytic efficiency of the $NaTaO_3$ material [462].

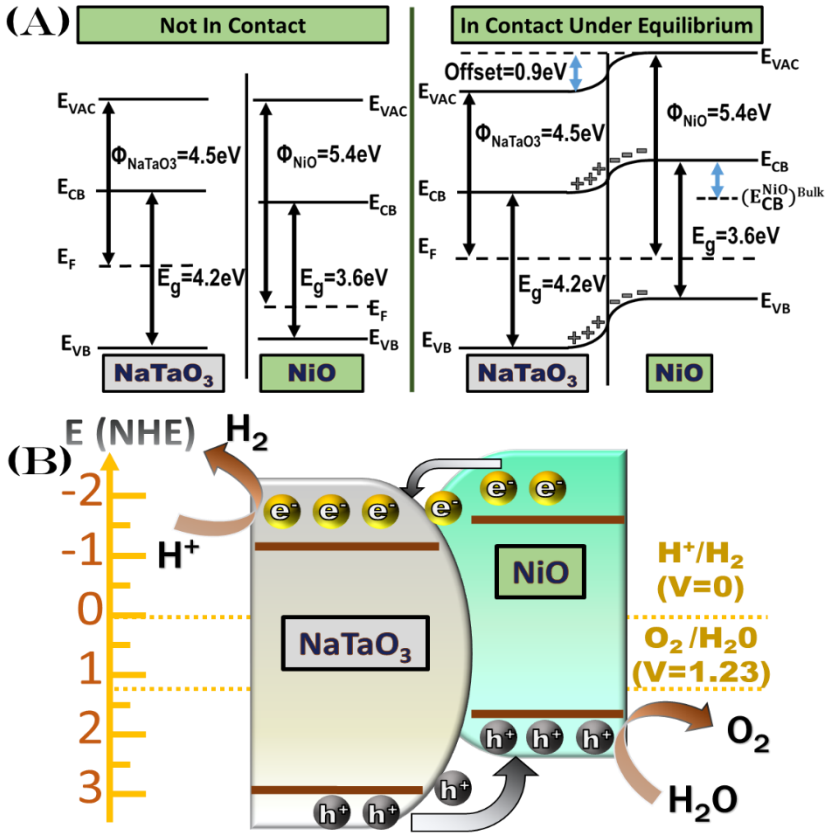

Figure 4-131: *(A) Band alignment in {$NaTaO_3$/NiO} heterojunction interface, before contact and in contact after equilibrium. (B) The implication of type-II heterojunction with energy positioning for optimal water oxidation and hydrogen reduction.*

Direct Monitoring of Photogenerated Holes/Electrons by in-Situ EPR Spectroscopy: Photocatalytic H_2-production entails the formation of electron-hole pairs for the heterostructure surface where electrons are used for the reduction of water to H_2, while the holes are used for the oxidation of water and the sacrificial agents. To further corroborate this mechanistic aspect, herein, we have used EPR spectroscopy to directly measure the photoproduced holes as oxidants that form OH radicals and the electrons for the reduction of Cr^{6+} to the components of Cr^{5+} and Cr^{3+}.

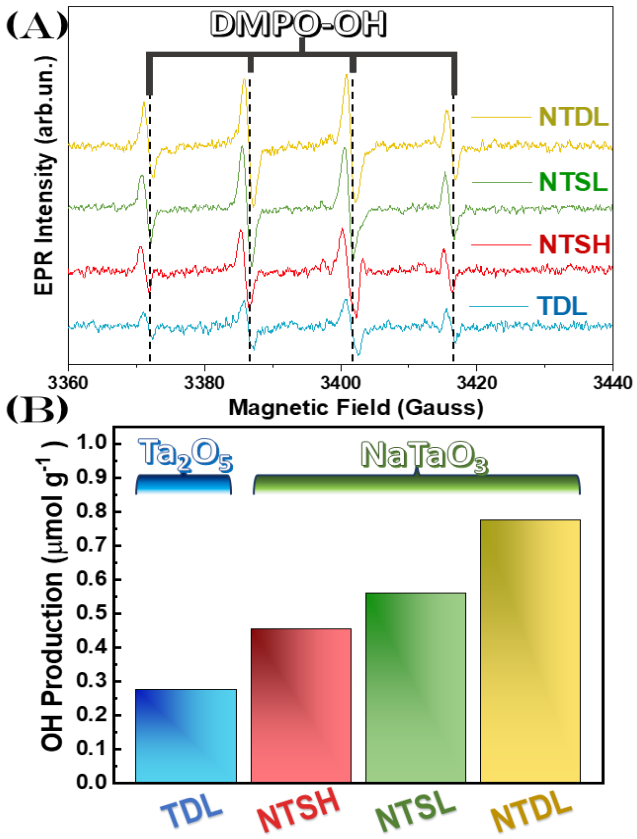

Figure 4-132: *(A) EPR spectra of photogenerated OH-radicals for the four selected Ta-materials. (B) Quantitative ●OH-production per gram of photocatalyst.*

The Ta_2O_5 and $NaTaO_3$ materials were irradiated *in situ* using a Xenon-lamp and the EPR spectra of the photogenerated OH-radicals are shown in **Figure 4-132**. Only a few works exist on ●OH radicals detection for Ta_2O_5 [463] and $NaTaO_3$ [453]. Under dark, no EPR signal was detected. Under illumination, the characteristic quadruple peaks of ●OH-DMPO emerged [305]. These OH-radicals are generated by oxidation from the

photoinduced holes produced by the Ta_2O_5 and $NaTaO_3$ semiconductors. Quantitative analysis applying DPPH allows us to measure the produced holes as μmol g^{-1}. The resulting production of OH-radical correlates completely with the results from H_2-photocatalysis, with the TDL/Ta_2O_5 and NTDL/$NaTaO_3$ demonstrating the lower and the highest photocatalytic activity, respectively.

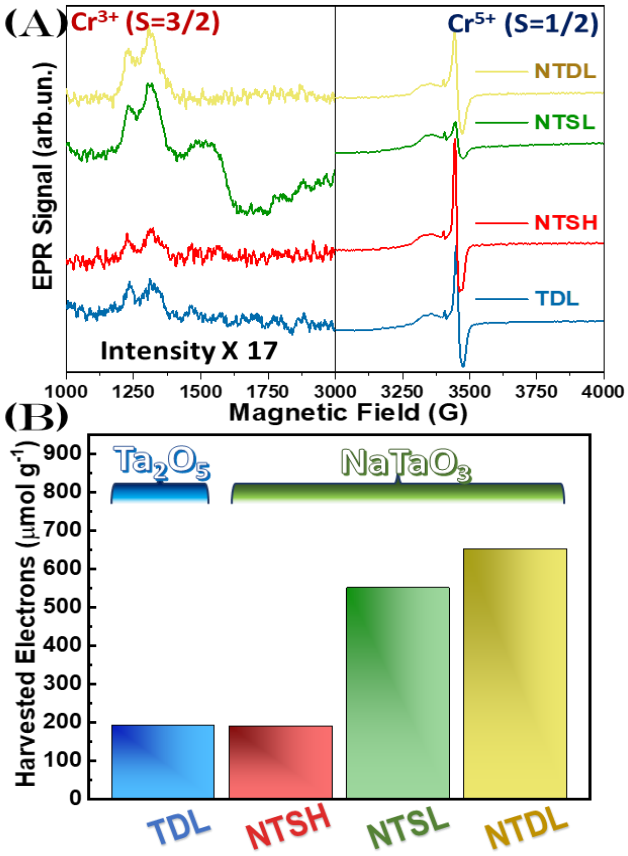

Figure 4-133: *(A) EPR spectra of photogenerated Cr^{+5} and Cr^{+3} for the four selected Ta-materials. (B) Quantitative harvested electrons per gram of photocatalyst.*

As our team showcases, the EPR measurement of Cr^{6+} reduction from photoinduced electrons at the materials conduction band can produce the components of Cr^{5+} and Cr^{3+} [464]. We can determine the total photoinduced electrons from the quantitative analysis of the two components, as shown in **Figure 4-133**. The results mirror not only the OH-radical but the H_2-photocatalysis, which means that all the materials have a distinct electron/hole generation where the total of these pairs has a linear application to hydrogen photoproduction.

4.7.7 Conclusions of Hydrogen production from FSP made Ta_2O_5 and $NaTaO_3$/ NiO heterostructures.

[a] First-time synthesis via the scalable Flame-Spray-Pyrolysis method for the 100% pure perovskite $NaTaO_3$, Control of the FSP-process parameters, with emphasis on the combustion enthalpy and the high-temperature-residence-time, is shown to be prerequisites for the synthesis of very small $NaTaO_3$ <15nm, which is well below the so-far achieved nanosize of $NaTaO_3$ by other conventional synthesis methods.

[b] A library of large/small nano-$NaTaO_3$, and Ta_2O_5 were synthesized, employing different NiO deposition methods. With the application of Single-Nozzle FSP and Double-Nozzle FSP, we produced Ta_2O_5 and $NaTaO_3$ with proper interfacing of ultrasmall NiO in a single step.

[c] Based on XRD, FT-IR, Raman, and XPS data, all the produced materials are devoid of secondary phases or impurities.

[d] The Double-Nozzle FSP {12nm $NaTaO_3$/NiO} achieved benchmark photocatalytic H_2 production >10.000 umol $g^{-1}h^{-1}$ from H_2O, without the application of any noble metal as cocatalyst. The $NaTaO_3$ and NiO band alignment forms an *n-p* heterojunction promoting efficient electron-hole separation. The deposition method of DN-FSP of NiO and Pt was superior in comparison to the typical deposition methods of wet-impregnation and photodeposition.

[e] *In situ* monitoring of the photoinduced holes and electrons using EPR spectroscopy corroborates the efficient photocatalytic H_2-production being linked to the small $NaTaO_3$ nanosize.

The present research exemplifies the DN-Nozzle FSP towards a foreseeing technology of scalable production of nano-perovskites with high photocatalytic efficiency, with one-step production and cocatalytic deposition.

5 Conclusions

In this Ph.D. thesis, FSP synthesis of several perovskite materials with catalytic properties was thoroughly studied and examined, where up to–date, very few perovskite materials had been synthesized from FSP.

(**Chapter 4.1**) The parameters of combustion density enthalpy, Φ ratio, and HTRT were explored for selected perovskite particles of the Thesis. (**Chapter 4.2**) Synthesis of $CuFe_2O_4$ and $CuBi_2O_4$ materials has been explored with various precursors and FSP parameters, although without achieving the one-step synthesis of FSP so-far. The perovskite $LiTaO_3$ was achieved through meticulous combinations of precursors, the effect of combustion density enthalpy, and the enclosure of the FSP reactor.

(**Chapter 4.3**) First-time FSP synthesis of 100% pure phase of $BiFeO_3$ perovskite and the mullite type $Bi_2Fe_4O_9$. The obtained materials $BiFeO_3$, $Bi_2Fe_4O_9$, and their two mixed-phase heterostructures $BiFeO_3/Bi_2Fe_4O_9$ were employed for catalytic reduction of 4-Nitrophenol to 4-Aminophenol. The results clearly demonstrate that the $BiFeO_3$ perovskite phase has a consistently much higher rate constant than $Bi_2Fe_4O_9$. Additionally, an Arrhenius analysis of these materials was studied for the first time, which determined that the $BiFeO_3$/4-NP system has much lower activation energy than $Bi_2Fe_4O_9$ i.e. 22 kJ mol^{-1} vs 36 kJ mol^{-1}. Furthermore, an inverse correlation was observed between the activation energy and the nanomaterial interface with the 4-NP adsorption strength.

(**Chapter 4.4**) Following the FSP synthesis of $BiFeO_3$ and $Bi_2Fe_4O_9$, a post-calcination treatment was explored, producing Fe^{2+}-enriched $BiFeO_3$. The materials $BiFeO_3$, $Bi_2Fe_4O_9$, and $BiFeO_3/Bi_2Fe_4O_9$ were evaluated for visible light Oxygen Evolution Reaction. In all cases, high temperature and long time-post FSP calcination significantly hindered the photocatalytic efficiency, while the $Bi_2Fe_4O_9$, phase had remarkably higher OER efficiency from the well-known $BiFeO_3$. The role of the add-on Fe^{2+} centers was analyzed by DFT, revealing a downshift of CB by +0.9eV, resulting in more positive potentials that enhanced the oxidative capacity of the holes in comparison to pure phase $BiFeO_3$. The observed hindrance from the prolonged calcination effect on the $Bi_2Fe_4O_9$ phase is caused by a solid-melt reaction. This explains why -so far- in other synthesis methods that require high

temperatures and a prolonged calcination time resulted in non-photocatalytic active $Bi_2Fe_4O_9$.

(**Chapter 4.5**) Single-Nozzle FSP technology was successfully employed to produce controlled crystal structure La-Doped $SrTiO_3$, while Double-Nozzle FSP was employed for *in-tandem* CuO/$SrTiO_3$-heterojunction. The complex perovskite nanoparticles La:$SrTiO_3$/CuO, showed distinct structural-electronic properties, with La-doping inducing a significant increase of SSA via the formation of larger pore-voids. Additionally, the CuO nanoparticles at the heterojunction showed an increase in the absorption of visible light. The materials were evaluated for the photocatalytic production of H_2 or CH_4 from an H_2O/CH_3OH mixture. The La-doping in all cases increased the photocatalytic activity of the perovskite $SrTiO_3$, with the 0.9%La:$SrTiO_3$ having a five times hydrogen increase from the pristine perovskite. While the heterostructures $SrTiO_3$/CuO drastically shifted the selectivity from H_2 toward CH_4, with $SrTiO_3$/0.5%CuO having a ten times CH_4 increase in comparison to the pristine $SrTiO_3$. Incorporation of Lanthanum with the material 0.25%La:SrTiO/0.5%CuO, further increased the CH_4 production by two times, reaching a surprising 1.5 mmol $g^{-1}h^{-1}$.

First-time synthesis of pure perovskite $NaTaO_3$ via FSP was achieved. A systematic mapping of the FSP-process parameters [combustion enthalpy and the high-temperature-residence-time, including several other important synthesis parameters] was accomplished. The developed FSP method achieved the smallest so-far reported $NaTaO_3$ size at 12-14nm. (**Chapter 4.6**) EPR spectroscopy allowed for the first time the detection of photogenerated holes and electrons in 14nm $NaTaO_3$ particles. Detailed EPR analysis provided key-insight into the landscape concerning the electronic configuration and kinetics of photoinduced electron/hole pairs. EPR spectra under N_2 and under H_2O conditions were determined with five separate subspectra with their equivalent tensors, two subspectra attributed to holes= (h1) and (h2), two subspectra attributed to electrons= (e1), (e2), and (e3). The implementation of Isopropanol as a hole scavenger in the H_2O conditions provided further evidence to consider the (h1) and (h2) subspectra. The fundamental particle size change from 14nm to 26nm $NaTaO_3$, diminished the yield of stable photo-excited {h+/e-} pairs significantly due to rapid recombination events, thus

other studies couldn't have successfully detected photoinduced carriers by EPR. This claim is further supported by the 2.5 times higher photocatalytic H_2 production and the subsequent experiments. (**Chapter 4.7**) A collection of large/small nano-$NaTaO_3$, and Ta_2O_5 materials were synthesized, employing different deposition methods with the application of Single-Nozzle FSP and Double-Nozzle FSP. In a single step, we produced the Tantalum nanomaterials with proper interfacing of ultrasmall NiO and Pt^0. The Double-Nozzle FSP {12nm $NaTaO_3$/NiO} achieved benchmark photocatalytic H_2 production >10.000 umol $g^{-1}h^{-1}$ from H_2O, without the application of any noble metal as a co-catalyst. The Band alignment was calculated, showing that $NaTaO_3$ and NiO form an n-p heterojunction promoting efficient electron-hole separation. The deposition method of DN-FSP of NiO and Pt^0 was far superior in comparison to the typical deposition methods of wet-impregnation and photodeposition. Furthermore, in situ monitoring of the photoinduced holes and electrons using EPR spectroscopy corroborates the efficient photocatalytic H_2-production being linked to the small size of $NaTaO_3$.

Overall, the present thesis exemplifies a deep-understanding of the solid-state Physics of ABO_3 perovskite nanoparticles, along with innovative FSP-technologies for the production of controlled-size perovskite materials. We exemplify versatile SN-FSP and DN-Nozzle FSP towards a scalable production of nano-perovskites with high photocatalytic efficiency.

Regarding future research perspectives, this thesis established the controlled synthesis of perovskite semiconductors, as the perovskite $NaTaO_3$, $LiTaO_3$, and $SrTiO_3$ have high conduction band sufficient for the photocatalytic reduction of CO_2, the subsequent research will be the screening of size, morphology, and deposition of several cocatalysts, metal (Ag^0, Pt^0, Pd^0) or oxides(CuO, NiO) for the efficient reduction of CO_2. Furthermore, a detailed screening of the FSP parameters based on the formation of FSP synthesis of $LiTaO_3$ is expected to be published. Materials based on FSP atomic deposition of Bismuth atoms and Copper atoms in the surface of $NaTaO_3$ are envisaged to be of interest in future research and technology. The FSP formation of $SrTiO_3$ materials with anoxic conditions resulted in $SrTiO_{3-x}$ materials with several different amounts of oxygen vacancies in the crystal structure, showing changes in their photocatalytic efficiency and EPR spectra.

6 REFERENCES

1. Vollath, D. *Nanomaterials: An Introduction to Synthesis, Properties and Applications*; Second Edition.; Wiley-VCH Verlag GmbH & Co. KGaA: Weinheim, Germany, 2013; ISBN 978-3-527-33379-0.
2. Schimmel, T. Nanotechnology. An Introduction. Von Jeremy J. Ramsden. *Angew. Chem.* **2012**, *124*, 9871–9871, doi:10.1002/ange.201206358.
3. Bundschuh, M.; Filser, J.; Lüderwald, S.; McKee, M.S.; Metreveli, G.; Schaumann, G.E.; Schulz, R.; Wagner, S. Nanoparticles in the Environment: Where Do We Come from, Where Do We Go To? *Environ Sci Eur* **2018**, *30*, 6, doi:10.1186/s12302-018-0132-6.
4. Precedence Research, The Global Nanomaterials Market Size, Https://Www.Precedenceresearch.Com/Nanomaterials-Market, Accessed 29/05/2023.
5. Tao, F. (Feng); Salmeron, M. In Situ Studies of Chemistry and Structure of Materials in Reactive Environments. *Science* **2011**, *331*, 171–174, doi:10.1126/science.1197461.
6. Astruc, D. Introduction: Nanoparticles in Catalysis. *Chem. Rev.* **2020**, *120*, 461–463, doi:10.1021/acs.chemrev.8b00696.
7. *Nanoparticles in Catalysis: Advances in Synthesis and Applications*; Philippot, K., Roucoux, A., Eds.; 1st ed.; Wiley, 2021; ISBN 978-3-527-82176-1.
8. Zhou, Y.; Jin, C.; Li, Y.; Shen, W. Dynamic Behavior of Metal Nanoparticles for Catalysis. *Nano Today* **2018**, *20*, 101–120, doi:10.1016/j.nantod.2018.04.005.
9. Stark, W.J.; Stoessel, P.R.; Wohlleben, W.; Hafner, A. Industrial Applications of Nanoparticles. *Chem. Soc. Rev.* **2015**, *44*, 5793–5805, doi:10.1039/C4CS00362D.
10. Dou, J.; Sun, Z.; Opalade, A.A.; Wang, N.; Fu, W.; Tao, F. (Feng) Operando Chemistry of Catalyst Surfaces during Catalysis. *Chem. Soc. Rev.* **2017**, *46*, 2001–2027, doi:10.1039/C6CS00931J.
11. Crystal Structure of Barium Titanate. *Nature* **1945**, *155*, 484–485, doi:10.1038/155484b0.
12. Wenk, H.-R.; Bulakh, A.G. *Minerals: Their Constitution and Origin*; Cambridge University Press: Cambridge ; New York, 2004; ISBN 978-0-521-82238-1.
13. Murakami, M.; Hirose, K.; Kawamura, K.; Sata, N.; Ohishi, Y. Post-Perovskite Phase Transition in $MgSiO_3$. *Science* **2004**, *304*, 855–858, doi:10.1126/science.1095932.
14. Tilley, R.J.D. *Perovskites: Structure-Property Relationships*; First edition.; Wiley: Chichester, West Sussex, United Kingdom, 2016; ISBN 978-1-118-93566-8.
15. Goldschmidt, V.M. Die Gesetze der Krystallochemie. *Naturwissenschaften* **1926**, *14*, 477–485, doi:10.1007/BF01507527.
16. Shannon, R.D. Revised Effective Ionic Radii and Systematic Studies of Interatomic Distances in Halides and Chalcogenides. *Acta Cryst A* **1976**, *32*, 751–767, doi:10.1107/S0567739476001551.
17. Søndenå, R.; Stølen, S.; Ravindran, P.; Grande, T.; Allan, N.L. Corner- versus Face-Sharing Octahedra in A Mn O 3 Perovskites (A = Ca , Sr, and Ba). *Phys. Rev. B* **2007**, *75*, 184105, doi:10.1103/PhysRevB.75.184105.
18. Travis, W.; Glover, E.N.K.; Bronstein, H.; Scanlon, D.O.; Palgrave, R.G. On the Application of the Tolerance Factor to Inorganic and Hybrid Halide Perovskites: A Revised System. *Chem. Sci.* **2016**, *7*, 4548–4556, doi:10.1039/C5SC04845A.
19. Hoefler, S.F.; Trimmel, G.; Rath, T. Progress on Lead-Free Metal Halide Perovskites for Photovoltaic Applications: A Review. *Monatsh Chem* **2017**, *148*, 795–826, doi:10.1007/s00706-017-1933-9.
20. Li, C.; Lu, X.; Ding, W.; Feng, L.; Gao, Y.; Guo, Z. Formability of ABX_3 (X = F, Cl, Br, I) Halide Perovskites. *Acta Crystallogr B Struct Sci* **2008**, *64*, 702–707, doi:10.1107/S0108768108032734.
21. Meloni, S.; Palermo, G.; Ashari-Astani, N.; Grätzel, M.; Rothlisberger, U. Valence and Conduction Band Tuning in Halide Perovskites for Solar Cell Applications. *J. Mater. Chem. A* **2016**, *4*, 15997–16002, doi:10.1039/C6TA04949D.
22. Shannon, R.D. Revised Effective Ionic Radii and Systematic Studies of Interatomic Distances in Halides and Chalcogenides. *Acta Cryst A* **1976**, *32*, 751–767, doi:10.1107/S0567739476001551.
23. Sun, C.; Alonso, J.A.; Bian, J. Recent Advances in Perovskite-Type Oxides for Energy Conversion and Storage Applications. *Adv. Energy Mater.* **2021**, *11*, 2000459, doi:10.1002/aenm.202000459.
24. Bhalla, A.S.; Guo, R.; Roy, R. The Perovskite Structure—a Review of Its Role in Ceramic Science and Technology. *Materials Research Innovations* **2000**, *4*, 3–26, doi:10.1007/s100190000062.
25. Wang, R.; Mujahid, M.; Duan, Y.; Wang, Z.; Xue, J.; Yang, Y. A Review of Perovskites Solar Cell Stability. *Adv. Funct. Mater.* **2019**, *29*, 1808843, doi:10.1002/adfm.201808843.
26. Yan, J.; Saunders, B.R. Third-Generation Solar Cells: A Review and Comparison of Polymer:Fullerene, Hybrid Polymer and Perovskite Solar Cells. *RSC Adv.* **2014**, *4*, 43286–43314, doi:10.1039/C4RA07064J.
27. Quan, L.N.; Rand, B.P.; Friend, R.H.; Mhaisalkar, S.G.; Lee, T.-W.; Sargent, E.H. Perovskites for Next-Generation Optical Sources. *Chem. Rev.* **2019**, *119*, 7444–7477, doi:10.1021/acs.chemrev.9b00107.
28. Djellabi, R.; Ordonez, M.F.; Conte, F.; Falletta, E.; Bianchi, C.L.; Rossetti, I. A Review of Advances in Multifunctional XTiO3 Perovskite-Type Oxides as Piezo-Photocatalysts for Environmental Remediation and Energy Production. *Journal of Hazardous Materials* **2022**, *421*, 126792, doi:10.1016/j.jhazmat.2021.126792.
29. Duan, J.; Shi, W.; Xu, L.; Mou, G.; Xin, Q.; Guan, J. Hierarchical Nanostructures of Fluorinated and Naked Ta2O5 Single Crystalline Nanorods: Hydrothermal Preparation, Formation Mechanism and Photocatalytic Activity for H2 Production. *Chem. Commun.* **2012**, *48*, 7301, doi:10.1039/c2cc33211f.
30. Liu, J.; Chen, G.; Li, Z.; Zhang, Z. Hydrothermal Synthesis and Photocatalytic Properties of ATaO3ATaO3 and ANbO3ANbO3 (A=NaA=Na and K). *International Journal of Hydrogen Energy* **2007**, *32*, 2269–2272, doi:10.1016/j.ijhydene.2006.10.005.
31. Li, X.; Zang, J. Facile Hydrothermal Synthesis of Sodium Tantalate ($NaTaO_3$) Nanocubes and High Photocatalytic Properties. *J. Phys. Chem. C* **2009**, *113*, 19411–19418, doi:10.1021/jp907334z.
32. Feng, L.M.; Jiang, L.Q.; Zhu, M.; Liu, H.B.; Zhou, X.; Li, C.H. Formability of ABO3 Cubic Perovskites. *Journal of Physics and Chemistry of Solids* **2008**, *69*, 967–974, doi:10.1016/j.jpcs.2007.11.007.
33. Predel, B.; Hoch, M.J.R.; Pool, M. *Phase Diagrams and Heterogeneous Equilibria: A Practical Introduction*; Engineering materials and processes; Springer: Berlin ; New York, 2004; ISBN 978-3-540-14011-5.
34. Palai, R.; Katiyar, R.S.; Schmid, H.; Tissot, P.; Clark, S.J.; Robertson, J.; Redfern, S.A.T.; Catalan, G.; Scott, J.F. β Phase and γ − β Metal-Insulator Transition in Multiferroic Bi Fe O 3. *Phys. Rev. B* **2008**, *77*, 014110, doi:10.1103/PhysRevB.77.014110.

35. Mukherjee, J.L.; Wang, F.F.Y. Kinetics of Solid-State Reaction of Bi_2O_3 and Fe_2O_3. *Journal of the American Ceramic Society* **1971**, *54*, 31–34, doi:10.1111/j.1151-2916.1971.tb12162.x.
36. Wang, J.; Neaton, J.B.; Zheng, H.; Nagarajan, V.; Ogale, S.B.; Liu, B.; Viehland, D.; Vaithyanathan, V.; Schlom, D.G.; Waghmare, U.V.; et al. Epitaxial $BiFeO_3$ Multiferroic Thin Film Heterostructures. *Science* **2003**, *299*, 1719–1722, doi:10.1126/science.1080615.
37. Iliev, M.N.; Litvinchuk, A.P.; Hadjiev, V.G.; Gospodinov, M.M.; Skumryev, V.; Ressouche, E. Phonon and Magnon Scattering of Antiferromagnetic Bi 2 Fe 4 O 9. *Phys. Rev. B* **2010**, *81*, 024302, doi:10.1103/PhysRevB.81.024302.
38. Ressouche, E.; Simonet, V.; Canals, B.; Gospodinov, M.; Skumryev, V. Magnetic Frustration in an Iron-Based Cairo Pentagonal Lattice. *Phys. Rev. Lett.* **2009**, *103*, 267204, doi:10.1103/PhysRevLett.103.267204.
39. Kim, J.K.; Kim, S.S.; Kim, W.-J. Sol–Gel Synthesis and Properties of Multiferroic BiFeO3. *Materials Letters* **2005**, *59*, 4006–4009, doi:10.1016/j.matlet.2005.07.050.
40. Ke, H.; Wang, W.; Wang, Y.; Xu, J.; Jia, D.; Lu, Z.; Zhou, Y. Factors Controlling Pure-Phase Multiferroic BiFeO3 Powders Synthesized by Chemical Co-Precipitation. *Journal of Alloys and Compounds* **2011**, *509*, 2192–2197, doi:10.1016/j.jallcom.2010.09.213.
41. Di, L.J.; Yang, H.; Xian, T.; Li, R.S.; Feng, Y.C.; Feng, W.J. Influence of Precursor Bi3+/Fe3+ Ion Concentration on Hydrothermal Synthesis of BiFeO3 Crystallites. *Ceramics International* **2014**, *40*, 4575–4578, doi:10.1016/j.ceramint.2013.08.134.
42. Palai, R.; Katiyar, R.S.; Schmid, H.; Tissot, P.; Clark, S.J.; Robertson, J.; Redfern, S.A.T.; Catalan, G.; Scott, J.F. β Phase and γ − β Metal-Insulator Transition in Multiferroic Bi Fe O 3. *Physical Review B* **2008**, *77*, doi:10.1103/PhysRevB.77.014110.
43. Xu, J.-H.; Ke, H.; Jia, D.-C.; Wang, W.; Zhou, Y. Low-Temperature Synthesis of BiFeO3 Nanopowders via a Sol–Gel Method. *Journal of Alloys and Compounds* **2009**, *472*, 473–477, doi:10.1016/j.jallcom.2008.04.090.
44. Sowmya, N.S.; Srinivas, A.; Suresh, P.; Shukla, A.; Kamat, S.V. Synthesis and Study of Structural, Magnetic and Microwave Absorption Properties in Multiferroic BiFeO3 Electroceramic. *Journal of Materials Science: Materials in Electronics* **2015**, *26*, 5368–5372, doi:10.1007/s10854-015-3081-5.
45. Mädler, L.; Pratsinis, S.E. Bismuth Oxide Nanoparticles by Flame Spray Pyrolysis. *Journal of the American Ceramic Society* **2004**, *85*, 1713–1718, doi:10.1111/j.1151-2916.2002.tb00340.x.
46. Strobel, R.; Pratsinis, S.E. Direct Synthesis of Maghemite, Magnetite and Wustite Nanoparticles by Flame Spray Pyrolysis. *Advanced Powder Technology* **2009**, *20*, 190–194, doi:10.1016/j.apt.2008.08.002.
47. Knijnenburg, J.T.N.; Seristatidou, E.; Hilty, F.M.; Krumeich, F.; Deligiannakis, Y. Proton-Promoted Iron Dissolution from Nanoparticles and the Influence by the Local Iron Environment. *The Journal of Physical Chemistry C* **2014**, *118*, 24072–24080, doi:10.1021/jp506024g.
48. Wang, J. Epitaxial BiFeO3 Multiferroic Thin Film Heterostructures. *Science* **2003**, *299*, 1719–1722, doi:10.1126/science.1080615.
49. Dawber, M.; Rabe, K.M.; Scott, J.F. Physics of Thin-Film Ferroelectric Oxides. *Rev. Mod. Phys.* **2005**, *77*, 1083–1130, doi:10.1103/RevModPhys.77.1083.
50. Wang, D.; Astruc, D. The Recent Development of Efficient Earth-Abundant Transition-Metal Nanocatalysts. *Chem. Soc. Rev.* **2017**, *46*, 816–854, doi:10.1039/C6CS00629A.
51. Catalan, G.; Scott, J.F. Physics and Applications of Bismuth Ferrite. *Adv. Mater.* **2009**, *21*, 2463–2485, doi:10.1002/adma.200802849.
52. Wang, J. Epitaxial BiFeO3 Multiferroic Thin Film Heterostructures. *Science* **2003**, *299*, 1719–1722, doi:10.1126/science.1080615.
53. Eerenstein, W.; Mathur, N.D.; Scott, J.F. Multiferroic and Magnetoelectric Materials. *Nature* **2006**, *442*, 759–765, doi:10.1038/nature05023.
54. Béa, H.; Gajek, M.; Bibes, M.; Barthélémy, A. Spintronics with Multiferroics. *J. Phys.: Condens. Matter* **2008**, *20*, 434221, doi:10.1088/0953-8984/20/43/434221.
55. Filippetti, A.; Hill, N.A. Coexistence of Magnetism and Ferroelectricity in Perovskites. *Phys. Rev. B* **2002**, *65*, 195120, doi:10.1103/PhysRevB.65.195120.
56. Shamir, N.; Gurewitz, E.; Shaked, H. The Magnetic Structure of $Bi_2Fe_4O_9$ – Analysis of Neutron Diffraction Measurements. *Acta Cryst A* **1978**, *34*, 662–666, doi:10.1107/S0567739478001412.
57. Poghossian, A.S.; Abovian, H.V.; Avakian, P.B.; Mkrtchian, S.H.; Haroutunian, V.M. Bismuth Ferrites: New Materials for Semiconductor Gas Sensors. *Sensors and Actuators B: Chemical* **1991**, *4*, 545–549, doi:10.1016/0925-4005(91)80167-I.
58. Zakharchenko, N.I. Catalytic Properties of the Fe2O3–Bi2O3 System in Ammonia Oxidation to Nitrogen Oxides. *Kinetics and Catalysis* **2002**, *43*, 95–98, doi:10.1023/A:1014209415066.
59. Kubacka, A.; Fernández-García, M.; Colón, G. Advanced Nanoarchitectures for Solar Photocatalytic Applications. *Chem. Rev.* **2012**, *112*, 1555–1614, doi:10.1021/cr100454n.
60. Di, J.; Chen, C.; Yang, S.-Z.; Ji, M.; Yan, C.; Gu, K.; Xia, J.; Li, H.; Li, S.; Liu, Z. Defect Engineering in Atomically-Thin Bismuth Oxychloride towards Photocatalytic Oxygen Evolution. *J. Mater. Chem. A* **2017**, *5*, 14144–14151, doi:10.1039/C7TA03624H.
61. Gao, F.; Chen, X.Y.; Yin, K.B.; Dong, S.; Ren, Z.F.; Yuan, F.; Yu, T.; Zou, Z.G.; Liu, J.-M. Visible-Light Photocatalytic Properties of Weak Magnetic BiFeO3 Nanoparticles. *Adv. Mater.* **2007**, *19*, 2889–2892, doi:10.1002/adma.200602377.
62. Lam, S.-M.; Sin, J.-C.; Mohamed, A.R. A Newly Emerging Visible Light-Responsive BiFeO 3 Perovskite for Photocatalytic Applications: A Mini Review. *Materials Research Bulletin* **2017**, *90*, 15–30, doi:10.1016/j.materresbull.2016.12.052.
63. Zhang, H.; Tong, T.; Chen, J.; Cheng, J. Synthesis and Visible Light Photocatalytic Properties of Bi2Fe4O9 Particles via EDTA-Assisted Sol–Gel Route. *J Sol-Gel Sci Technol* **2016**, *78*, 135–143, doi:10.1007/s10971-015-3931-x.
64. Wang, N.; Zhu, L.; Lei, M.; She, Y.; Cao, M.; Tang, H. Ligand-Induced Drastic Enhancement of Catalytic Activity of Nano-$BiFeO_3$ for Oxidative Degradation of Bisphenol A. *ACS Catal.* **2011**, *1*, 1193–1202, doi:10.1021/cs2002862.
65. Yang, X.; Zhang, Y.; Xu, G.; Wei, X.; Ren, Z.; Shen, G.; Han, G. Phase and Morphology Evolution of Bismuth Ferrites via Hydrothermal Reaction Route. *Materials Research Bulletin* **2013**, *48*, 1694–1699, doi:10.1016/j.materresbull.2013.01.032.
66. Ortiz-Quiñonez, J.L.; Díaz, D.; Zumeta-Dubé, I.; Arriola-Santamaría, H.; Betancourt, I.; Santiago-Jacinto, P.; Nava-Etzana, N. Easy Synthesis of High-Purity $BiFeO_3$ Nanoparticles: New Insights Derived from the Structural, Optical, and Magnetic Characterization. *Inorganic Chemistry* **2013**, *52*, 10306–10317, doi:10.1021/ic400627c.
67. Kirsch, A.; Murshed, M.M.; Schowalter, M.; Rosenauer, A.; Gesing, T.M. Nanoparticle Precursor into Polycrystalline $Bi_2Fe_4O_9$: An Evolutionary Investigation of Structural, Morphological, Optical, and Vibrational Properties. *The Journal of Physical Chemistry C* **2016**, *120*, 18831–18840, doi:10.1021/acs.jpcc.6b04773.
68. Papadas, I.; Christodoulides, J.A.; Kioseoglou, G.; Armatas, G.S. A High Surface Area Ordered Mesoporous $BiFeO_3$ Semiconductor with Efficient Water Oxidation Activity. *J. Mater. Chem. A* **2015**, *3*, 1587–1593, doi:10.1039/C4TA05272B.

69. Li, S.; Zhang, J.; Kibria, M.G.; Mi, Z.; Chaker, M.; Ma, D.; Nechache, R.; Rosei, F. Remarkably Enhanced Photocatalytic Activity of Laser Ablated Au Nanoparticle Decorated BiFeO3 Nanowires under Visible-Light. *Chem. Commun.* **2013**, *49*, 5856, doi:10.1039/c3cc40363g.
70. Kim, T.W.; Choi, K.-S. Nanoporous BiVO4 Photoanodes with Dual-Layer Oxygen Evolution Catalysts for Solar Water Splitting. *Science* **2014**, *343*, 990–994.
71. Yang, J.; Wang, D.; Zhou, X.; Li, C. A Theoretical Study on the Mechanism of Photocatalytic Oxygen Evolution on $BiVO_4$ in Aqueous Solution. *Chem. Eur. J.* **2013**, *19*, 1320–1326, doi:10.1002/chem.201202365.
72. Di, J.; Chen, C.; Zhu, C.; Ji, M.; Xia, J.; Yan, C.; Hao, W.; Li, S.; Li, H.; Liu, Z. Bismuth Vacancy Mediated Single Unit Cell Bi2WO6 Nanosheets for Boosting Photocatalytic Oxygen Evolution. *Applied Catalysis B: Environmental* **2018**, *238*, 119–125, doi:10.1016/j.apcatb.2018.06.066.
73. Humayun, M.; Zada, A.; Li, Z.; Xie, M.; Zhang, X.; Qu, Y.; Raziq, F.; Jing, L. Enhanced Visible-Light Activities of Porous BiFeO3 by Coupling with Nanocrystalline TiO2 and Mechanism. *Applied Catalysis B: Environmental* **2016**, *180*, 219–226, doi:10.1016/j.apcatb.2015.06.035.
74. Zhang, T.; Shen, Y.; Qiu, Y.; Liu, Y.; Xiong, R.; Shi, J.; Wei, J. Facial Synthesis and Photoreaction Mechanism of $BiFeO_3$ /$Bi_2Fe_4O_9$ Heterojunction Nanofibers. *ACS Sustainable Chemistry & Engineering* **2017**, *5*, 4630–4636, doi:10.1021/acssuschemeng.6b03138.
75. Bragg, W.H. The Structure of Magnetite and the Spinels. *Nature* **1915**, *95*, 561–561, doi:10.1038/095561a0.
76. Zhao, Q.; Yan, Z.; Chen, C.; Chen, J. Spinels: Controlled Preparation, Oxygen Reduction/Evolution Reaction Application, and Beyond. *Chem. Rev.* **2017**, *117*, 10121–10211, doi:10.1021/acs.chemrev.7b00051.
77. Gurunathan, K.; Baeg, J.-O.; Lee, S.M.; Subramanian, E.; Moon, S.-J.; Kong, K. Visible Light Active Pristine and Fe 3 + Doped CuGa 2 O 4 Spinel Photocatalysts for Solar Hydrogen Production. *International Journal of Hydrogen Energy* **2008**, *33*, 2646–2652, doi:10.1016/j.ijhydene.2008.03.018.
78. Kezzim, A.; Nasrallah, N.; Abdi, A.; Trari, M. Visible Light Induced Hydrogen on the Novel Hetero-System CuFe2O4/TiO2. *Energy Conversion and Management* **2011**, *52*, 2800–2806, doi:10.1016/j.enconman.2011.02.014.
79. Taffa, D.H.; Dillert, R.; Ulpe, A.C.; Bauerfeind, K.C.L.; Bredow, T.; Bahnemann, D.W.; Wark, M. Photoelectrochemical and Theoretical Investigations of Spinel Type Ferrites ($M_xFe_{3-x}O_4$) for Water Splitting: A Mini-Review. *J. Photon. Energy* **2016**, *7*, 012009, doi:10.1117/1.JPE.7.012009.
80. Yang, H.; Yan, J.; Lu, Z.; Cheng, X.; Tang, Y. Photocatalytic Activity Evaluation of Tetragonal CuFe2O4 Nanoparticles for the H2 Evolution under Visible Light Irradiation. *Journal of Alloys and Compounds* **2009**, *476*, 715–719, doi:10.1016/j.jallcom.2008.09.104.
81. Hussain, S.; Hussain, S.; Waleed, A.; Tavakoli, M.M.; Wang, Z.; Yang, S.; Fan, Z.; Nadeem, M.A. Fabrication of $CuFe_2O_4$ /α-Fe_2O_3 Composite Thin Films on FTO Coated Glass and 3-D Nanospike Structures for Efficient Photoelectrochemical Water Splitting. *ACS Appl. Mater. Interfaces* **2016**, *8*, 35315–35322, doi:10.1021/acsami.6b12460.
82. Shishin, D.; Hidayat, T.; Jak, E.; Decterov, S.A. Critical Assessment and Thermodynamic Modeling of the Cu–Fe–O System. *Calphad* **2013**, *41*, 160–179, doi:10.1016/j.calphad.2013.04.001.
83. Wolff, N.; Klimm, D.; Habicht, K.; Fritsch, K. Crystal Growth and Thermodynamic Investigation of $Bi_2M^{2+}O_4$ (M = Pd, Cu). *CrystEngComm* **2021**, *23*, 3230–3238, doi:10.1039/D1CE00220A.
84. Cooper, J.K.; Zhang, Z.; Roychoudhury, S.; Jiang, C.-M.; Gul, S.; Liu, Y.-S.; Dhall, R.; Ceballos, A.; Yano, J.; Prendergast, D.; et al. $CuBi_2O_4$: Electronic Structure, Optical Properties, and Photoelectrochemical Performance Limitations of the Photocathode. *Chem. Mater.* **2021**, *33*, 934–945, doi:10.1021/acs.chemmater.0c03930.
85. Berglund, S.P.; Abdi, F.F.; Bogdanoff, P.; Chemseddine, A.; Friedrich, D.; Van De Krol, R. Comprehensive Evaluation of $CuBi_2O_4$ as a Photocathode Material for Photoelectrochemical Water Splitting. *Chem. Mater.* **2016**, *28*, 4231–4242, doi:10.1021/acs.chemmater.6b00830.
86. Oropeza, F.E.; Dzade, N.Y.; Pons-Martí, A.; Yang, Z.; Zhang, K.H.L.; De Leeuw, N.H.; Hensen, E.J.M.; Hofmann, J.P. Electronic Structure and Interface Energetics of $CuBi_2O_4$ Photoelectrodes. *J. Phys. Chem. C* **2020**, *124*, 22416–22425, doi:10.1021/acs.jpcc.0c08455.
87. Kang, D.; Hill, J.C.; Park, Y.; Choi, K.-S. Photoelectrochemical Properties and Photostabilities of High Surface Area $CuBi_2O_4$ and Ag-Doped $CuBi_2O_4$ Photocathodes. *Chem. Mater.* **2016**, *28*, 4331–4340, doi:10.1021/acs.chemmater.6b01294.
88. Wang, F.; Septina, W.; Chemseddine, A.; Abdi, F.F.; Friedrich, D.; Bogdanoff, P.; Van De Krol, R.; Tilley, S.D.; Berglund, S.P. Gradient Self-Doped $CuBi_2O_4$ with Highly Improved Charge Separation Efficiency. *J. Am. Chem. Soc.* **2017**, *139*, 15094–15103, doi:10.1021/jacs.7b07847.
89. Tsang, C.-F.; Meen, J.K.; Elthon, D. Phase Equilibria of the Bismuth Oxide-Copper Oxide System in Oxygen at 1 Atm. *J American Ceramic Society* **1994**, *77*, 3119–3124, doi:10.1111/j.1151-2916.1994.tb04558.x.
90. Zhang, P.; Zhang, J.; Gong, J. Tantalum-Based Semiconductors for Solar Water Splitting. *Chem. Soc. Rev.* **2014**, *43*, 4395–4422, doi:10.1039/C3CS60438A.
91. Kato, H.; Asakura, K.; Kudo, A. Highly Efficient Water Splitting into H_2 and O_2 over Lanthanum-Doped $NaTaO_3$ Photocatalysts with High Crystallinity and Surface Nanostructure. *J. Am. Chem. Soc.* **2003**, *125*, 3082–3089, doi:10.1021/ja027751g.
92. Yu, X.; Li, W.; Li, Z.; Liu, J.; Hu, P. Defect Engineered Ta2O5 Nanorod: One-Pot Synthesis, Visible-Light Driven Hydrogen Generation and Mechanism. *Applied Catalysis B: Environmental* **2017**, *217*, 48–56, doi:10.1016/j.apcatb.2017.05.024.
93. Kato, H.; Kudo, A. Photocatalytic Water Splitting into H2 and O2 over Various Tantalate Photocatalysts. *Catalysis Today* **2003**, *78*, 561–569, doi:10.1016/S0920-5861(02)00355-3.
94. Kato, H.; Kudo, A. Water Splitting into H_2 and O_2 on Alkali Tantalate Photocatalysts $ATaO_3$ (A = Li, Na, and K). *J. Phys. Chem. B* **2001**, *105*, 4285–4292, doi:10.1021/jp004386b.
95. Kudo, A.; Kato, H.; Nakagawa, S. Water Splitting into H_2 and O_2 on New $Sr_2M_2O_7$ (M = Nb and Ta) Photocatalysts with Layered Perovskite Structures: Factors Affecting the Photocatalytic Activity. *J. Phys. Chem. B* **2000**, *104*, 571–575, doi:10.1021/jp9919056.
96. Zhang, P.; Zhang, J.; Gong, J. Tantalum-Based Semiconductors for Solar Water Splitting. *Chem. Soc. Rev.* **2014**, *43*, 4395–4422, doi:10.1039/C3CS60438A.
97. Garg, S.P.; Krishnamurthy, N.; Awasthi, A.; Venkatraman, M. The O-Ta (Oxygen-Tantalum) System. *JPE* **1997**, *18*, 407–407, doi:10.1007/s11669-997-0076-9.
98. Reisman, A.; Holtzberg, F.; Berkenblit, M.; Berry, M. Reactions of the Group VB Pentoxides with Alkali Oxides and Carbonates. III. Thermal and X-Ray Phase Diagrams of the System K_2O or K_2CO_3 with Ta_2O_5. *J. Am. Chem. Soc.* **1956**, *78*, 4514–4520, doi:10.1021/ja01599a003.

99. Roth, R. S.; H. S. Parker; W. S. Brower; D. Minor. Alkali Oxide-Tantalum Oxide and Alkali Oxide-Niobium Oxide Ionic Conductors. **1974**, doi:No. NASA-CR-134599.
100. Zlotnik, S.; Sahu, S.K.; Navrotsky, A.; Vilarinho, P.M. Pyrochlore and Perovskite Potassium Tantalate: Enthalpies of Formation and Phase Transformation. *Chem. Eur. J.* **2015**, *21*, 5231–5237, doi:10.1002/chem.201405666.
101. Xiao, X.; Si, J.; Liang, S.; Xu, Q.; Zhang, H.; Ma, L.; Yang, C.; Zhang, X. Preparation, Properties, and Applications of Near Stoichiometric Lithium Tantalate Crystals. *Crystals* **2023**, *13*, 1031, doi:10.3390/cryst13071031.
102. Li, M.; Li, P.; Chang, K.; Wang, T.; Liu, L.; Kang, Q.; Ouyang, S.; Ye, J. Highly Efficient and Stable Photocatalytic Reduction of CO_2 to CH_4 over Ru Loaded $NaTaO_3$. *Chem. Commun.* **2015**, *51*, 7645–7648, doi:10.1039/C5CC01124H.
103. Teramura, K.; Okuoka, S.; Tsuneoka, H.; Shishido, T.; Tanaka, T. Photocatalytic Reduction of CO2 Using H2 as Reductant over ATaO3 Photocatalysts (A=Li, Na, K). *Applied Catalysis B: Environmental* **2010**, *96*, 565–568, doi:10.1016/j.apcatb.2010.03.021.
104. Nakanishi, H.; Iizuka, K.; Takayama, T.; Iwase, A.; Kudo, A. Highly Active $NaTaO_3$ -Based Photocatalysts for CO_2 Reduction to Form CO Using Water as the Electron Donor. *ChemSusChem* **2017**, *10*, 112–118, doi:10.1002/cssc.201601360.
105. Habisreutinger, S.N.; Schmidt-Mende, L.; Stolarczyk, J.K. Photocatalytic Reduction of CO_2 on TiO_2 and Other Semiconductors. *Angew. Chem. Int. Ed.* **2013**, *52*, 7372–7408, doi:10.1002/anie.201207199.
106. Li, K.; Peng, B.; Peng, T. Recent Advances in Heterogeneous Photocatalytic CO_2 Conversion to Solar Fuels. *ACS Catal.* **2016**, *6*, 7485–7527, doi:10.1021/acscatal.6b02089.
107. Ola, O.; Maroto-Valer, M.M. Review of Material Design and Reactor Engineering on TiO2 Photocatalysis for CO2 Reduction. *Journal of Photochemistry and Photobiology C: Photochemistry Reviews* **2015**, *24*, 16–42, doi:10.1016/j.jphotochemrev.2015.06.001.
108. Nakanishi, H.; Iizuka, K.; Takayama, T.; Iwase, A.; Kudo, A. Highly Active $NaTaO_3$ -Based Photocatalysts for CO_2 Reduction to Form CO Using Water as the Electron Donor. *ChemSusChem* **2017**, *10*, 112–118, doi:10.1002/cssc.201601360.
109. Naveenraj, S.; Lee, G.-J.; Anandan, S.; Wu, J.J. Nanosized Tantala Based Materials – Synthesis and Applications. *Materials Research Bulletin* **2015**, *67*, 20–46, doi:10.1016/j.materresbull.2015.02.060.
110. Dezelah; Wiedmann, M.K.; Mizohata, K.; Baird, R.J.; Niinistö, L.; Winter, C.H. A Pyrazolate-Based Metalorganic Tantalum Precursor That Exhibits High Thermal Stability and Its Use in the Atomic Layer Deposition of Ta_2O_5. *J. Am. Chem. Soc.* **2007**, *129*, 12370–12371, doi:10.1021/ja074043s.
111. Devan, R.S.; Gao, S.-Y.; Ho, W.-D.; Lin, J.-H.; Ma, Y.-R.; Patil, P.S.; Liou, Y. Electrochromic Properties of Large-Area and High-Density Arrays of Transparent One-Dimensional β-Ta2O5 Nanorods on Indium-Tin-Oxide Thin-Films. *Appl. Phys. Lett.* **2011**, *98*, 133117, doi:10.1063/1.3568896.
112. Asghar, M.H.; Placido, F.; Naseem, S. Characterization of Ta_2O_5 Thin Films Prepared by Reactive Evaporation. *Eur. Phys. J. Appl. Phys.* **2006**, *36*, 119–124, doi:10.1051/epjap:2006113.
113. Devan, R.S.; Lin, C.-L.; Gao, S.-Y.; Cheng, C.-L.; Liou, Y.; Ma, Y.-R. Enhancement of Green-Light Photoluminescence of Ta2O5 Nanoblock Stacks. *Phys. Chem. Chem. Phys.* **2011**, *13*, 13441, doi:10.1039/c1cp21283d.
114. Rodríguez-de Marcos, L.V.; Larruquert, J.I.; Méndez, J.A.; Aznárez, J.A. Self-Consistent Optical Constants of SiO_2 and Ta_2O_5 Films. *Opt. Mater. Express* **2016**, *6*, 3622, doi:10.1364/OME.6.003622.
115. Cava, R.F.; Peck, W.F.; Krajewski, J.J. Enhancement of the Dielectric Constant of Ta2O5through Substitution with TiO2. *Nature* **1995**, *377*, 215–217, doi:10.1038/377215a0.
116. Chang, J.P.; Steigerwald, M.L.; Fleming, R.M.; Opila, R.L.; Alers, G.B. Thermal Stability of Ta2O5 in Metal–Oxide–Metal Capacitor Structures. *Appl. Phys. Lett.* **1999**, *74*, 3705–3707, doi:10.1063/1.123227.
117. Koshevaya, E.; Krivoshapkina, E.; Krivoshapkin, P. Tantalum Oxide Nanoparticles as an Advanced Platform for Cancer Diagnostics: A Review and Perspective. *J. Mater. Chem. B* **2021**, *9*, 5008–5024, doi:10.1039/D1TB00570G.
118. Hatanaka, T.; Nakamura, K.; Taniuchi, T.; Ito, H.; Furukawa, Y.; Kitamura, K. Quasi-Phase-Matched Optical Parametric Oscillation with Periodically Poled Stoichiometric LiTaO_3. *Opt. Lett.* **2000**, *25*, 651, doi:10.1364/OL.25.000651.
119. Sreethawong, T.; Ngamsinlapasathian, S.; Suzuki, Y.; Yoshikawa, S. Nanocrystalline Mesoporous Ta2O5-Based Photocatalysts Prepared by Surfactant-Assisted Templating Sol–Gel Process for Photocatalytic H2 Evolution. *Journal of Molecular Catalysis A: Chemical* **2005**, *235*, 1–11, doi:10.1016/j.molcata.2005.03.021.
120. Hu, C.-C.; Teng, H. Influence of Structural Features on the Photocatalytic Activity of NaTaO3 Powders from Different Synthesis Methods. *Applied Catalysis A: General* **2007**, *331*, 44–50, doi:10.1016/j.apcata.2007.07.024.
121. An, L.; Kitta, M.; Iwase, A.; Kudo, A.; Ichikuni, N.; Onishi, H. Photoexcited Electrons Driven by Doping Concentration Gradient: Flux-Prepared $NaTaO_3$ Photocatalysts Doped with Strontium Cations. *ACS Catal.* **2018**, *8*, 9334–9341, doi:10.1021/acscatal.8b02437.
122. Xu, J.; Xue, D.; Yan, C. Chemical Synthesis of NaTaO3 Powder at Low-Temperature. *Materials Letters* **2005**, *59*, 2920–2922, doi:10.1016/j.matlet.2005.04.043.
123. An, L.; Kitta, M.; Iwase, A.; Kudo, A.; Ichikuni, N.; Onishi, H. Photoexcited Electrons Driven by Doping Concentration Gradient: Flux-Prepared $NaTaO_3$ Photocatalysts Doped with Strontium Cations. *ACS Catal.* **2018**, *8*, 9334–9341, doi:10.1021/acscatal.8b02437.
124. Kudo, A.; Kato, H. Effect of Lanthanide-Doping into NaTaO3 Photocatalysts for Efficient Water Splitting. *Chemical Physics Letters* **2000**, *331*, 373–377, doi:10.1016/S0009-2614(00)01220-3.
125. Phivilay, S.P.; Puretzky, A.A.; Domen, K.; Wachs, I.E. Nature of Catalytic Active Sites Present on the Surface of Advanced Bulk Tantalum Mixed Oxide Photocatalysts. *ACS Catal.* **2013**, *3*, 2920–2929, doi:10.1021/cs400662m.
126. Meyer, T.; Priebe, J.B.; da Silva, R.O.; Peppel, T.; Junge, H.; Beller, M.; Brückner, A.; Wohlrab, S. Advanced Charge Utilization from $NaTaO_3$ Photocatalysts by Multilayer Reduced Graphene Oxide. *Chem. Mater.* **2014**, *26*, 4705–4711, doi:10.1021/cm500949x.
127. Wang, J.; Su, S.; Liu, B.; Cao, M.; Hu, C. One-Pot, Low-Temperature Synthesis of Self-Doped NaTaO3 Nanoclusters for Visible-Light-Driven Photocatalysis. *Chem. Commun.* **2013**, *49*, 7830, doi:10.1039/c3cc42487a.
128. Farooq, U.; Ahmed, J.; Alshehri, S.M.; Ahmad, T. High-Surface-Area Sodium Tantalate Nanoparticles with Enhanced Photocatalytic and Electrical Properties Prepared through Polymeric Citrate Precursor Route. *ACS Omega* **2019**, *4*, 19408–19419, doi:10.1021/acsomega.9b02830.
129. Wang, Z.; Hou, J.; Yang, C.; Jiao, S.; Huang, K.; Zhu, H. Hierarchical Metastable γ-TaON Hollow Structures for Efficient Visible-Light Water Splitting. *Energy Environ. Sci.* **2013**, *6*, 2134, doi:10.1039/c3ee24370b.
130. Burda, C.; Chen, X.; Narayanan, R.; El-Sayed, M.A. Chemistry and Properties of Nanocrystals of Different Shapes. *Chem. Rev.* **2005**, *105*, 1025–1102, doi:10.1021/cr030063a.

131. Schulz, H.; Schimmoeller, B.; Pratsinis, S.E.; Salz, U.; Bock, T. Radiopaque Dental Adhesives: Dispersion of Flame-Made Ta2O5/SiO2 Nanoparticles in Methacrylic Matrices. *Journal of Dentistry* **2008**, *36*, 579–587, doi:10.1016/j.jdent.2008.04.010.
132. Schulz, H.; Mädler, L.; Pratsinis, S.E.; Burtscher, P.; Moszner, N. Transparent Nanocomposites of Radiopaque, Flame-Made Ta_2O_5/SiO_2 Particles in an Acrylic Matrix. *Adv. Funct. Mater.* **2005**, *15*, 830–837, doi:10.1002/adfm.200400234.
133. Li, F.-F.; Liu, D.-R.; Gao, G.-M.; Xue, B.; Jiang, Y.-S. Improved Visible-Light Photocatalytic Activity of NaTaO3 with Perovskite-like Structure via Sulfur Anion Doping. *Applied Catalysis B: Environmental* **2015**, *166–167*, 104–111, doi:10.1016/j.apcatb.2014.10.049.
134. Kato, H.; Kudo, A. Water Splitting into H_2 and O_2 on Alkali Tantalate Photocatalysts $ATaO_3$ (A = Li, Na, and K). *J. Phys. Chem. B* **2001**, *105*, 4285–4292, doi:10.1021/jp004386b.
135. Lü, X.; Hu, Q.; Yang, W.; Bai, L.; Sheng, H.; Wang, L.; Huang, F.; Wen, J.; Miller, D.J.; Zhao, Y. Pressure-Induced Amorphization in Single-Crystal Ta_2O_5 Nanowires: A Kinetic Mechanism and Improved Electrical Conductivity. *J. Am. Chem. Soc.* **2013**, *135*, 13947–13953, doi:10.1021/ja407108u.
136. Phoon, B.L.; Lai, C.W.; Juan, J.C.; Show, P.; Chen, W. A Review of Synthesis and Morphology of $SrTiO_3$ for Energy and Other Applications. *Int J Energy Res* **2019**, *43*, 5151–5174, doi:10.1002/er.4505.
137. Suárez-Vázquez, S.I.; Gil, S.; García-Vargas, J.M.; Cruz-López, A.; Giroir-Fendler, A. Catalytic Oxidation of Toluene by SrTi1-XBXO3 (B = Cu and Mn) with Dendritic Morphology Synthesized by One Pot Hydrothermal Route. *Applied Catalysis B: Environmental* **2018**, *223*, 201–208, doi:10.1016/j.apcatb.2017.04.042.
138. Moos, R.; Hardtl, K.H. Defect Chemistry of Donor-Doped and Undoped Strontium Titanate Ceramics between 1000° and 1400°C. *Journal of the American Ceramic Society* **2005**, *80*, 2549–2562, doi:10.1111/j.1151-2916.1997.tb03157.x.
139. Ropp, R.C. *Encyclopedia of the Alkaline Earth Compounds*; Amsterdam : Elsevier, 2013; ISBN 978-0-444-59550-8.
140. Stöcker, H.; Hanzig, J.; Zschornak, M.; Mehner, E.; Jachalke, S.; Richter, C.; Hanzig, F.; Meutzner, F.; Leisegang, T.; Meyer, D.C. Strontium Titanate: From Symmetry Changes to Functionality: Strontium Titanate: From Symmetry Changes to Functionality. *Crystal Research and Technology* **2017**, *52*, 1600222, doi:10.1002/crat.201600222.
141. Opoku, F.; Govender, K.K.; van Sittert, C.G.C.E.; Govender, P.P. Enhancing Charge Separation and Photocatalytic Activity of Cubic $SrTiO_3$ with Perovskite-Type Materials $MTaO_3$ (M=Na, K) for Environmental Remediation: A First-Principles Study. *ChemistrySelect* **2017**, *2*, 6304–6316, doi:10.1002/slct.201700886.
142. Zhang, C.; Jiang, N.; Xu, S.; Li, Z.; Liu, X.; Cheng, T.; Han, A.; Lv, H.; Sun, W.; Hou, Y. Towards High Visible Light Photocatalytic Activity in Rare Earth and N Co-Doped $SrTiO_3$: A First Principles Evaluation and Prediction. *RSC Adv.* **2017**, *7*, 16282–16289, doi:10.1039/C6RA27840J.
143. Fan, Y.; Liu, Y.; Cui, H.; Wang, W.; Shang, Q.; Shi, X.; Cui, G.; Tang, B. Photocatalytic Overall Water Splitting by SrTiO3 with Surface Oxygen Vacancies. *Nanomaterials* **2020**, *10*, 2572, doi:10.3390/nano10122572.
144. Chen, H.-C.; Huang, C.-W.; Wu, J.C.S.; Lin, S.-T. Theoretical Investigation of the Metal-Doped $SrTiO_3$ Photocatalysts for Water Splitting. *J. Phys. Chem. C* **2012**, *116*, 7897–7903, doi:10.1021/jp300910e.
145. Ma, Y.; Wu, Z.; Wang, H.; Wang, G.; Zhang, Y.; Hu, P.; Li, Y.; Gao, D.; Pu, H.; Wang, B.; et al. Synthesis of Nanocrystalline Strontium Titanate by a Sol–Gel Assisted Solid Phase Method and Its Formation Mechanism and Photocatalytic Activity. *CrystEngComm* **2019**, *21*, 3982–3992, doi:10.1039/C9CE00495E.
146. Kakihana, M.; Okubo, T.; Arima, M.; Nakamura, Y.; Yashima, M.; Yoshimura, M. Polymerized Complex Route to the Synthesis of Pure SrTiO3 at Reduced Temperatures: Implication for Formation of Sr-Ti Heterometallic Citric Acid Complex. **1998**, 15.
147. Kubacka, A.; Fernández-García, M.; Colón, G. Advanced Nanoarchitectures for Solar Photocatalytic Applications. *Chem. Rev.* **2012**, *112*, 1555–1614, doi:10.1021/cr100454n.
148. Ahmed, A.J.; Hossain, Md.S.A.; Kazi Nazrul Islam, S.M.; Yun, F.; Yang, G.; Hossain, R.; Khan, A.; Na, J.; Eguchi, M.; Yamauchi, Y.; et al. Significant Improvement in Electrical Conductivity and Figure of Merit of Nanoarchitectured Porous $SrTiO_3$ by La Doping Optimization. *ACS Appl. Mater. Interfaces* **2020**, *12*, 28057–28064, doi:10.1021/acsami.0c01869.
149. Lu, Z.; Zhang, H.; Lei, W.; Sinclair, D.C.; Reaney, I.M. High-Figure-of-Merit Thermoelectric La-Doped A-Site-Deficient $SrTiO_3$ Ceramics. *Chem. Mater.* **2016**, *28*, 925–935, doi:10.1021/acs.chemmater.5b04616.
150. Jia, Y.; Shen, S.; Wang, D.; Wang, X.; Shi, J.; Zhang, F.; Han, H.; Li, C. Composite Sr2TiO4/SrTiO3(La,Cr) Heterojunction Based Photocatalyst for Hydrogen Production under Visible Light Irradiation. *J. Mater. Chem. A* **2013**, *1*, 7905, doi:10.1039/c3ta11326d.
151. Abdi, M.; Mahdikhah, V.; Sheibani, S. Visible Light Photocatalytic Performance of La-Fe Co-Doped SrTiO3 Perovskite Powder. *Optical Materials* **2020**, *102*, 109803, doi:10.1016/j.optmat.2020.109803.
152. Wang, Q.; Warnan, J.; Rodríguez-Jiménez, S.; Leung, J.J.; Kalathil, S.; Andrei, V.; Domen, K.; Reisner, E. Molecularly Engineered Photocatalyst Sheet for Scalable Solar Formate Production from Carbon Dioxide and Water. *Nat Energy* **2020**, *5*, 703–710, doi:10.1038/s41560-020-0678-6.
153. Moss, B.; Wang, Q.; Butler, K.T.; Grau-Crespo, R.; Selim, S.; Regoutz, A.; Hisatomi, T.; Godin, R.; Payne, D.J.; Kafizas, A.; et al. Linking in Situ Charge Accumulation to Electronic Structure in Doped SrTiO3 Reveals Design Principles for Hydrogen-Evolving Photocatalysts. *Nat. Mater.* **2021**, *20*, 511–517, doi:10.1038/s41563-020-00868-2.
154. Wang, Q.; Hisatomi, T.; Suzuki, Y.; Pan, Z.; Seo, J.; Katayama, M.; Minegishi, T.; Nishiyama, H.; Takata, T.; Seki, K.; et al. Particulate Photocatalyst Sheets Based on Carbon Conductor Layer for Efficient Z-Scheme Pure-Water Splitting at Ambient Pressure. *J. Am. Chem. Soc.* **2017**, *139*, 1675–1683, doi:10.1021/jacs.6b12164.
155. Iwashina, K.; Kudo, A. Rh-Doped $SrTiO_3$ Photocatalyst Electrode Showing Cathodic Photocurrent for Water Splitting under Visible-Light Irradiation. *J. Am. Chem. Soc.* **2011**, *133*, 13272–13275, doi:10.1021/ja2050315.
156. Tse, J.; Aziz, A.; Flitcroft, J.M.; Skelton, J.M.; Gillie, L.J.; Parker, S.C.; Cooke, D.J.; Molinari, M. Unraveling the Impact of Graphene Addition to Thermoelectric $SrTiO_3$ and La-Doped $SrTiO_3$ Materials: A Density Functional Theory Study. *ACS Appl. Mater. Interfaces* **2021**, *13*, 41303–41314, doi:10.1021/acsami.1c10865.
157. Ura, B.; Trawczyński, J.; Kotarba, A.; Bieniasz, W.; Illán-Gómez, M.J.; Bueno-López, A.; López-Suárez, F.E. Effect of Potassium Addition on Catalytic Activity of SrTiO3 Catalyst for Diesel Soot Combustion. *Applied Catalysis B: Environmental* **2011**, *101*, 169–175, doi:10.1016/j.apcatb.2010.09.018.
158. Niishiro, R.; Tanaka, S.; Kudo, A. Hydrothermal-Synthesized SrTiO3 Photocatalyst Codoped with Rhodium and Antimony with Visible-Light Response for Sacrificial H2 and O2 Evolution and Application to Overall Water Splitting. *Applied Catalysis B: Environmental* **2014**, *150–151*, 187–196, doi:10.1016/j.apcatb.2013.12.015.

159. Chen, W.-T.; Jovic, V.; Sun-Waterhouse, D.; Idriss, H.; Waterhouse, G.I.N. The Role of CuO in Promoting Photocatalytic Hydrogen Production over TiO2. *International Journal of Hydrogen Energy* **2013**, *38*, 15036–15048, doi:10.1016/j.ijhydene.2013.09.101.
160. Yu, J.; Hai, Y.; Jaroniec, M. Photocatalytic Hydrogen Production over CuO-Modified Titania. *Journal of Colloid and Interface Science* **2011**, *357*, 223–228, doi:10.1016/j.jcis.2011.01.101.
161. Lalitha, K.; Sadanandam, G.; Kumari, V.D.; Subrahmanyam, M.; Sreedhar, B.; Hebalkar, N.Y. Highly Stabilized and Finely Dispersed Cu $_2$ O/TiO $_2$: A Promising Visible Sensitive Photocatalyst for Continuous Production of Hydrogen from Glycerol:Water Mixtures. *J. Phys. Chem. C* **2010**, *114*, 22181–22189, doi:10.1021/jp107405u.
162. Chen, J.-L.; Liu, M.-M.; Xie, S.-Y.; Yue, L.-J.; Gong, F.-L.; Chai, K.-M.; Zhang, Y.-H. Cu2O-Loaded TiO2 Heterojunction Composites for Enhanced Photocatalytic H2 Production. *Journal of Molecular Structure* **2022**, *1247*, 131294, doi:10.1016/j.molstruc.2021.131294.
163. Ali, S.; Razzaq, A.; Kim, H.; In, S.-I. Activity, Selectivity, and Stability of Earth-Abundant CuO/Cu2O/Cu0-Based Photocatalysts toward CO2 Reduction. *Chemical Engineering Journal* **2022**, *429*, 131579, doi:10.1016/j.cej.2021.131579.
164. Wang, Y.; Chen, E.; Tang, J. Insight on Reaction Pathways of Photocatalytic CO $_2$ Conversion. *ACS Catal.* **2022**, *12*, 7300–7316, doi:10.1021/acscatal.2c01012.
165. Trommer, R.M.; Bergmann, C.P. *Flame Spray Technology: Method for Production of Nanopowders*; Topics in Mining, Metallurgy and Materials Engineering; Springer Berlin Heidelberg: Berlin, Heidelberg, 2015; ISBN 978-3-662-47161-6.
166. *Aerosol Science and Technology: History and Reviews*; RTI International, Ensor, D., Eds.; 1st ed.; RTI Press, 2011; ISBN 978-1-934831-01-4.
167. Ulrich, G.D. Theory of Particle Formation and Growth in Oxide Synthesis Flames. *Combustion Science and Technology* **1971**, *4*, 47–57, doi:10.1080/00102207108952471.
168. Https://Corporate.Evonik.Com/En/Products-and-Solutions/Markets 2023.
169. Madler, L.; Kammler, H.K.; Mueller, R.; Pratsinis, S.E. Controlled Synthesis of Nanostructured Particles by Ame Spray Pyrolysis. *Aerosol Science* **2002**, 21.
170. Mädler, L.; Stark, W.J.; Pratsinis, S.E. Flame-Made Ceria Nanoparticles. *J. Mater. Res.* **2002**, *17*, 1356–1362, doi:10.1557/JMR.2002.0202.
171. Mueller, R.; Mädler, L.; Pratsinis, S.E. Nanoparticle Synthesis at High Production Rates by Flame Spray Pyrolysis. *Chemical Engineering Science* **2003**, *58*, 1969–1976, doi:10.1016/S0009-2509(03)00022-8.
172. Strobel, R.; Baiker, A.; Pratsinis, S.E. Aerosol Flame Synthesis of Catalysts. *Advanced Powder Technology* **2006**, *17*, 457–480, doi:10.1163/156855206778440525.
173. Shih, S.-J.; Tzeng, W.-L. Manipulation of Morphology of Strontium Titanate Particles by Spray Pyrolysis. *Powder Technology* **2014**, *264*, 291–297, doi:10.1016/j.powtec.2014.05.056.
174. Kang, H.W.; Park, S.B. Doping of Fluorine into SrTiO3 by Spray Pyrolysis for H2 Evolution under Visible Light Irradiation. *Chemical Engineering Science* **2013**, *100*, 384–391, doi:10.1016/j.ces.2012.11.012.
175. Teoh, W.Y.; Amal, R.; Mädler, L. Flame Spray Pyrolysis: An Enabling Technology for Nanoparticles Design and Fabrication. *Nanoscale* **2010**, *2*, 1324, doi:10.1039/c0nr00017e.
176. Gröhn, A.J.; Pratsinis, S.E.; Sánchez-Ferrer, A.; Mezzenga, R.; Wegner, K. Scale-up of Nanoparticle Synthesis by Flame Spray Pyrolysis: The High-Temperature Particle Residence Time. *Ind. Eng. Chem. Res.* **2014**, *53*, 10734–10742, doi:10.1021/ie501709s.
177. Okuyama, K.; Kousaka, Y.; Tohge, N.; Yamamoto, S.; Wu, J.J.; Flagan, R.C.; Seinfeld, J.H. Production of Ultrafine Metal Oxide Aerosol Particles by Thermal Decomposition of Metal Alkoxide Vapors. *AIChE J.* **1986**, *32*, 2010–2019, doi:10.1002/aic.690321211.
178. Pratsinis, S.E. Flame Aerosol Synthesis of Ceramic Powders. *Progress in Energy and Combustion Science* **1998**, *24*, 197–219, doi:10.1016/S0360-1285(97)00028-2.
179. Strobel, R.; Pratsinis, S.E. Flame Aerosol Synthesis of Smart Nanostructured Materials. *J. Mater. Chem.* **2007**, *17*, 4743, doi:10.1039/b711652g.
180. Mädler, L.; Kammler, H.K.; Mueller, R.; Pratsinis, S.E. Controlled Synthesis of Nanostructured Particles by Flame Spray Pyrolysis. *Journal of Aerosol Science* **2002**, *33*, 369–389, doi:10.1016/S0021-8502(01)00159-8.
181. Salameh, S.; Gómez-Hernández, J.; Goulas, A.; Van Bui, H.; van Ommen, J.R. Advances in Scalable Gas-Phase Manufacturing and Processing of Nanostructured Solids: A Review. *Particuology* **2017**, *30*, 15–39, doi:10.1016/j.partic.2016.07.003.
182. Mueller, R.; Mädler, L.; Pratsinis, S.E. Nanoparticle Synthesis at High Production Rates by Flame Spray Pyrolysis. *Chemical Engineering Science* **2003**, *58*, 1969–1976, doi:10.1016/S0009-2509(03)00022-8.
183. Buss, L.; Noriler, D.; Fritsching, U. Impact of Reaction Chamber Geometry on the Particle-Residence-Time in Flame Spray Process. *Flow Turbulence Combust* **2020**, *105*, 1055–1086, doi:10.1007/s10494-020-00187-1.
184. Koirala, R.; Pratsinis, S.E.; Baiker, A. Synthesis of Catalytic Materials in Flames: Opportunities and Challenges. *Chem. Soc. Rev.* **2016**, *45*, 3053–3068, doi:10.1039/C5CS00011D.
185. Spyrogianni, A.; Herrmann, I.K.; Keevend, K.; Pratsinis, S.E.; Wegner, K. The Silanol Content and in Vitro Cytolytic Activity of Flame-Made Silica. *Journal of Colloid and Interface Science* **2017**, *507*, 95–106, doi:10.1016/j.jcis.2017.07.096.
186. Trivanovic, U.; Kelesidis, G.A.; Pratsinis, S.E. High-Throughput Generation of Aircraft-like Soot. *Aerosol Science and Technology* **2022**, *56*, 732–743, doi:10.1080/02786826.2022.2070055.
187. Gröhn, A.J.; Pratsinis, S.E.; Sánchez-Ferrer, A.; Mezzenga, R.; Wegner, K. Scale-up of Nanoparticle Synthesis by Flame Spray Pyrolysis: The High-Temperature Particle Residence Time. *Ind. Eng. Chem. Res.* **2014**, *53*, 10734–10742, doi:10.1021/ie501709s.
188. Strobel, R.; Mädler, L.; Piacentini, M.; Maciejewski, M.; Baiker, A.; Pratsinis, S.E. Two-Nozzle Flame Synthesis of Pt/Ba/Al $_2$ O $_3$ for NO $_x$ Storage. *Chem. Mater.* **2006**, *18*, 2532–2537, doi:10.1021/cm0600529.
189. Horlyck, J.; Pokhrel, S.; Lovell, E.; Bedford, N.M.; Mädler, L.; Amal, R.; Scott, J. Unifying Double Flame Spray Pyrolysis with Lanthanum Doping to Restrict Cobalt–Aluminate Formation in Co/Al $_2$ O $_3$ Catalysts for the Dry Reforming of Methane. *Catal. Sci. Technol.* **2019**, *9*, 4970–4980, doi:10.1039/C9CY01293A.
190. Solakidou, M.; Georgiou, Y.; Deligiannakis, Y. Double-Nozzle Flame Spray Pyrolysis as a Potent Technology to Engineer Noble Metal-TiO2 Nanophotocatalysts for Efficient H2 Production. *Energies* **2021**, *14*, 817, doi:10.3390/en14040817.
191. Lovell, E.C.; Großman, H.; Horlyck, J.; Scott, J.; Mädler, L.; Amal, R. Asymmetrical Double Flame Spray Pyrolysis-Designed SiO $_2$ /Ce $_{0.7}$ Zr $_{0.3}$ O $_2$ for the Dry Reforming of Methane. *ACS Appl. Mater. Interfaces* **2019**, *11*, 25766–25777, doi:10.1021/acsami.9b02572.
192. Tada, S.; Larmier, K.; Büchel, R.; Copéret, C. Methanol Synthesis *via* CO $_2$ Hydrogenation over CuO–ZrO $_2$ Prepared by Two-Nozzle Flame Spray Pyrolysis. *Catal. Sci. Technol.* **2018**, *8*, 2056–2060, doi:10.1039/C8CY00250A.

193. Strobel, R.; Mädler, L.; Piacentini, M.; Maciejewski, M.; Baiker, A.; Pratsinis, S.E. Two-Nozzle Flame Synthesis of Pt/Ba/Al $_2$ O $_3$ for NO $_x$ Storage. *Chem. Mater.* **2006**, *18*, 2532–2537, doi:10.1021/cm0600529.
194. Ferri, D.; Heel, A.; Burnat, D. Aerosol Spray Synthesis of Powder Perovskite-Type Oxides. In *Perovskites and Related Mixed Oxides*; Granger, P., Parvulescu, V.I., Parvulescu, V.I., Prellier, W., Eds.; Wiley-VCH Verlag GmbH & Co. KGaA: Weinheim, Germany, 2015; pp. 69–90 ISBN 978-3-527-68660-5.
195. Teoh, W. A Perspective on the Flame Spray Synthesis of Photocatalyst Nanoparticles. *Materials* **2013**, *6*, 3194–3212, doi:10.3390/ma6083194.
196. Https://Www.Cabotcorp.Com/Solutions#products-Plus 2023.
197. Li, S.; Ren, Y.; Biswas, P.; Tse, S.D. Flame Aerosol Synthesis of Nanostructured Materials and Functional Devices: Processing, Modeling, and Diagnostics. *Progress in Energy and Combustion Science* **2016**, *55*, 1–59, doi:10.1016/j.pecs.2016.04.002.
198. Meierhofer, F.; Fritsching, U. Synthesis of Metal Oxide Nanoparticles in Flame Sprays: Review on Process Technology, Modeling, and Diagnostics. *Energy Fuels* **2021**, *35*, 5495–5537, doi:10.1021/acs.energyfuels.0c04054.
199. Kelesidis, G.A.; Pratsinis, S.E. A Perspective on Gas-Phase Synthesis of Nanomaterials: Process Design, Impact and Outlook. *Chemical Engineering Journal* **2021**, *421*, 129884, doi:10.1016/j.cej.2021.129884.
200. Https://Www.Turbobeads.Com 2023.
201. Https://Www.Hemotune.Ch/Technology 2023.
202. Https://Www.Heiq.Com/Products/ 2023.
203. Sotiris E. Pratsinis; Height M Antimicrobial and Antifungal Powders Made by Flame Spray Pyrolysis, U.S. Patent Application 11/884,039, 2009.
204. Wegner, K.; Schimmöller, B.; Thiebaut, B.; Fernandez, C.; Rao, T.N. Pilot Plants for Industrial Nanoparticle Production by Flame Spray Pyrolysis. *KONA* **2011**, *29*, 251–265, doi:10.14356/kona.2011025.
205. Gerken, L.R.H.; Neuer, A.L.; Gschwend, P.M.; Keevend, K.; Gogos, A.; Anthis, A.H.C.; Aengenheister, L.; Pratsinis, S.E.; Plasswilm, L.; Herrmann, I.K. Scalable Synthesis of Ultrasmall Metal Oxide Radio-Enhancers Outperforming Gold. *Chem. Mater.* **2021**, *33*, 3098–3112, doi:10.1021/acs.chemmater.0c04565.
206. Mädler, L.; Stark, W.J.; Pratsinis, S.E. Flame-Made Ceria Nanoparticles. *J. Mater. Res.* **2002**, *17*, 1356–1362, doi:10.1557/JMR.2002.0202.
207. Wegner, K.; Pratsinis, S.E. Gas-Phase Synthesis of Nanoparticles: Scale-up and Design of Flame Reactors. *Powder Technology* **2005**, *150*, 117–122, doi:10.1016/j.powtec.2004.11.022.
208. Wegner, K.; Pratsinis, S.E. Scale-up of Nanoparticle Synthesis in Diffusion Flame Reactors. *Chemical Engineering Science* **2003**, *58*, 4581–4589, doi:10.1016/j.ces.2003.07.010.
209. Akurati, K.K.; Vital, A.; Dellemann, J.-P.; Michalow, K.; Graule, T.; Ferri, D.; Baiker, A. Flame-Made WO3/TiO2 Nanoparticles: Relation between Surface Acidity, Structure and Photocatalytic Activity. *Applied Catalysis B: Environmental* **2008**, *79*, 53–62, doi:10.1016/j.apcatb.2007.09.036.
210. Heel, A.; Holtappels, P.; Hug, P.; Graule, T. Flame Spray Synthesis of Nanoscale La0.6Sr0.4Co0.2Fe0.8O3-δ and Ba0.5Sr0.5Co0.8Fe0.2O3-δ as Cathode Materials for Intermediate Temperature Solid Oxide Fuel Cells. *Fuel Cells* **2010**, *10*, 419–432, doi:10.1002/fuce.200900093.
211. Mueller, R.; Mädler, L.; Pratsinis, S.E. Nanoparticle Synthesis at High Production Rates by Flame Spray Pyrolysis. *Chemical Engineering Science* **2003**, *58*, 1969–1976, doi:10.1016/S0009-2509(03)00022-8.
212. Mueller, R.; Jossen, R.; Pratsinis, S.E.; Watson, M.; Akhtar, M.K. Zirconia Nanoparticles Made in Spray Flames at High Production Rates. *Journal of the American Ceramic Society* **2004**, *87*, 197–202, doi:10.1111/j.1551-2916.2004.00197.x.
213. Gröhn, A.J.; Pratsinis, S.E.; Sánchez-Ferrer, A.; Mezzenga, R.; Wegner, K. Scale-up of Nanoparticle Synthesis by Flame Spray Pyrolysis: The High-Temperature Particle Residence Time. *Ind. Eng. Chem. Res.* **2014**, *53*, 10734–10742, doi:10.1021/ie501709s.
214. Jossen, R.; Mueller, R.; Pratsinis, S.E.; Watson, M.; Akhtar, M.K. Morphology and Composition of Spray-Flame-Made Yttria-Stabilized Zirconia Nanoparticles. *Nanotechnology* **2005**, *16*, S609–S617, doi:10.1088/0957-4484/16/7/039.
215. Hembram, K.; Sivaprakasam, D.; Rao, T.N.; Wegner, K. Large-Scale Manufacture of ZnO Nanorods by Flame Spray Pyrolysis. *J Nanopart Res* **2013**, *15*, 1461, doi:10.1007/s11051-013-1461-4.
216. Betancur-Granados, N.; Pöllmann, H.; Restrepo-Baena, O.J.; Tobón, J.I. Nanosized Belite Phases Obtained by Flame Spray Pyrolysis: Assessment of Process Conditions on the Mineralogy and Reactivity. *Cement and Concrete Research* **2023**, *164*, 107062, doi:10.1016/j.cemconres.2022.107062.
217. Meierhofer, F.; Mädler, L.; Fritsching, U. Nanoparticle Evolution in Flame Spray Pyrolysis—Process Design via Experimental and Computational Analysis. *AIChE J* **2020**, *66*, doi:10.1002/aic.16885.
218. Kho, Y.K.; Teoh, W.Y.; Iwase, A.; Mädler, L.; Kudo, A.; Amal, R. Flame Preparation of Visible-Light-Responsive BiVO $_4$ Oxygen Evolution Photocatalysts with Subsequent Activation via Aqueous Route. *ACS Appl. Mater. Interfaces* **2011**, *3*, 1997–2004, doi:10.1021/am200247y.
219. Stathi, P.; Solakidou, M.; Deligiannakis, Y. Lattice Defects Engineering in W-, Zr-Doped BiVO4 by Flame Spray Pyrolysis: Enhancing Photocatalytic O2 Evolution. *Nanomaterials* **2021**, *11*, 501, doi:10.3390/nano11020501.
220. Angel, S.; Schneider, F.; Apazeller, S.; Kaziur-Cegla, W.; Schmidt, T.C.; Schulz, C.; Wiggers, H. Spray-Flame Synthesis of LaMO3 (M = Mn, Fe, Co) Perovskite Nanomaterials: Effect of Spray Droplet Size and Esterification on Particle Size Distribution. *Proceedings of the Combustion Institute* **2021**, *38*, 1279–1287, doi:10.1016/j.proci.2020.07.116.
221. Patil, L.A.; Suryawanshi, D.N.; Pathan, I.G.; Patil, Dhanashri.G. Effect of Firing Temperature on Gas Sensing Properties of Nanocrystalline Perovskite BaTiO3 Thin Films Prepared by Spray Pyrolysis Techniques. *Sensors and Actuators B: Chemical* **2014**, *195*, 643–650, doi:10.1016/j.snb.2013.12.048.
222. Abe, Y.; Laine, R.M. Photocatalytic Plate-like La $_2$ Ti $_2$ O $_7$ Nanoparticles Synthesized via Liquid-feed Flame Spray Pyrolysis (LF-FSP) of Metallo-organic Precursors. *J Am Ceram Soc* **2020**, *103*, 4832–4839, doi:10.1111/jace.17196.
223. Psathas, P.; Solakidou, M.; Mantzanis, A.; Deligiannakis, Y. Flame Spray Pyrolysis Engineering of Nanosized Mullite-Bi2Fe4O9 and Perovskite-BiFeO3 as Highly Efficient Photocatalysts for O2 Production from H2O Splitting. *Energies* **2021**, *14*, doi:10.3390/en14175235.

224. Psathas, P.; Georgiou, Y.; Moularas, C.; Armatas, G.S.; Deligiannakis, Y. Controlled-Phase Synthesis of Bi2Fe4O9 & BiFeO3 by Flame Spray Pyrolysis and Their Evaluation as Non-Noble Metal Catalysts for Efficient Reduction of 4-Nitrophenol. *Powder Technology* **2020**, *368*, 268–277, doi:10.1016/j.powtec.2020.04.059.
225. Moularas, C.; Psathas, P.; Deligiannakis, Y. Electron Paramagnetic Resonance Study of Photo-Induced Hole/Electron Pairs in NaTaO3 Nanoparticles. *Chemical Physics Letters* **2021**, *782*, 139031, doi:10.1016/j.cplett.2021.139031.
226. Yuan, X.; Meng, L.; Zheng, C.; Zhao, H. Deep Insight into the Mechanism of Catalytic Combustion of CO and CH_4 over $SrTi_{1-x}B_xO_3$ (B = Co, Fe, Mn, Ni, and Cu) Perovskite via Flame Spray Pyrolysis. *ACS Appl. Mater. Interfaces* **2021**, *13*, 52571–52587, doi:10.1021/acsami.1c14055.
227. Yuan, X.; Meng, L.; Xu, Z.; Zheng, C.; Zhao, H. CuO Quantum Dots Supported by $SrTiO_3$ Perovskite Using the Flame Spray Pyrolysis Method: Enhanced Activity and Excellent Thermal Resistance for Catalytic Combustion of CO and CH_4. *Environ. Sci. Technol.* **2021**, *55*, 14080–14086, doi:10.1021/acs.est.1c03639.
228. Psathas, P.; Zindrou, A.; Papachristodoulou, C.; Boukos, N.; Deligiannakis, Y. In Tandem Control of La-Doping and CuO-Heterojunction on SrTiO3 Perovskite by Double-Nozzle Flame Spray Pyrolysis: Selective H2 vs. CH4 Photocatalytic Production from H2O/CH3OH. *Nanomaterials* **2023**, *13*, 482, doi:10.3390/nano13030482.
229. Veziroğlu, T.N.; Şahi˙n, S. 21st Century's Energy: Hydrogen Energy System. *Energy Conversion and Management* **2008**, *49*, 1820–1831, doi:10.1016/j.enconman.2007.08.015.
230. Abe, J.O.; Popoola, A.P.I.; Ajenifuja, E.; Popoola, O.M. Hydrogen Energy, Economy and Storage: Review and Recommendation. *International Journal of Hydrogen Energy* **2019**, *44*, 15072–15086, doi:10.1016/j.ijhydene.2019.04.068.
231. Zheng, X.; Streimikiene, D.; Balezentis, T.; Mardani, A.; Cavallaro, F.; Liao, H. A Review of Greenhouse Gas Emission Profiles, Dynamics, and Climate Change Mitigation Efforts across the Key Climate Change Players. *Journal of Cleaner Production* **2019**, *234*, 1113–1133, doi:10.1016/j.jclepro.2019.06.140.
232. Da Rosa, A.V.; Ordóñez, J.C. *Fundamentals of Renewable Energy Processes*; Fourth edition.; Academic Press: London [England] ; San Diego, CA, 2022; ISBN 978-0-12-816036-7.
233. Niaz, S.; Manzoor, T.; Pandith, A.H. Hydrogen Storage: Materials, Methods and Perspectives. *Renewable and Sustainable Energy Reviews* **2015**, *50*, 457–469, doi:10.1016/j.rser.2015.05.011.
234. Megía, P.J.; Vizcaíno, A.J.; Calles, J.A.; Carrero, A. Hydrogen Production Technologies: From Fossil Fuels toward Renewable Sources. A Mini Review. *Energy Fuels* **2021**, *35*, 16403–16415, doi:10.1021/acs.energyfuels.1c02501.
235. Hydrogen Generation Market Size, Share & Trends Analysis Report By System (Merchant, Captive), By Technology (Steam Methane Reforming, Coal Gasification), By Application, By Source, By Region, And Segment Forecasts, 2023 - 2030.
236. Zou, Z.; Ye, J.; Sayama, K.; Arakawa, H. Direct Splitting of Water under Visible Light Irradiation with an Oxide Semiconductor Photocatalyst. *Nature* **2001**, *414*, 625–627, doi:10.1038/414625a.
237. Midilli, A.; Ay, M.; Dincer, I.; Rosen, M.A. On Hydrogen and Hydrogen Energy Strategies. *Renewable and Sustainable Energy Reviews* **2005**, *9*, 255–271, doi:10.1016/j.rser.2004.05.003.
238. Https://H2tools.Org/Hyarc/Calculator-Tools/Lower-Andhigher-Heating-Values-Fuels.
239. Jafari, T.; Moharreri, E.; Amin, A.; Miao, R.; Song, W.; Suib, S. Photocatalytic Water Splitting—The Untamed Dream: A Review of Recent Advances. *Molecules* **2016**, *21*, 900, doi:10.3390/molecules21070900.
240. Shewchun, J.; Singh, R.; Green, M.A. Theory of Metal-insulator-semiconductor Solar Cells. *Journal of Applied Physics* **1977**, *48*, 765–770, doi:10.1063/1.323667.
241. Kittel, C. *Introduction to Solid State Physics*; 7th ed.; Wiley: New York, 1996; ISBN 978-0-471-11181-8.
242. Kahn, A. Fermi Level, Work Function and Vacuum Level. *Mater. Horiz.* **2016**, *3*, 7–10, doi:10.1039/C5MH00160A.
243. Rosencher, E.; Vinter, B. *Optoelectronics*; Cambridge University Press: Cambridge, UK ; New York, NY, 2002; ISBN 978-0-521-77129-0.
244. Zhang, Y.; Guo, Y.; Duan, H.; Li, H.; Yang, L.; Wang, P.; Sun, C.; Xu, B.; Liu, H. Photoelectrochemical Response and Electronic Structure Analysis of Mono-Dispersed Cuboid-Shaped $Bi_2Fe_4O_9$ Crystals with near-Infrared Absorption. *RSC Adv.* **2014**, *4*, 28209–28218, doi:10.1039/C4RA01727G.
245. Berger, O. Understanding the Fundamentals of TiO_2 Surfaces. Part I. The Influence of Defect States on the Correlation between Crystallographic Structure, Electronic Structure and Physical Properties of Single-Crystal Surfaces. *Surface Engineering* **2022**, *38*, 91–149, doi:10.1080/02670844.2022.2063482.
246. Li, W.; Long, R.; Tang, J.; Prezhdo, O.V. Influence of Defects on Excited-State Dynamics in Lead Halide Perovskites: Time-Domain Ab Initio Studies. *J. Phys. Chem. Lett.* **2019**, *10*, 3788–3804, doi:10.1021/acs.jpclett.9b00641.
247. Xu, J.; Teng, Y.; Teng, F. Effect of Surface Defect States on Valence Band and Charge Separation and Transfer Efficiency. *Sci Rep* **2016**, *6*, 32457, doi:10.1038/srep32457.
248. Gionco, C.; Paganini, M.C.; Giamello, E.; Burgess, R.; Di Valentin, C.; Pacchioni, G. Paramagnetic Defects in Polycrystalline Zirconia: An EPR and DFT Study. *Chem. Mater.* **2013**, *25*, 2243–2253, doi:10.1021/cm400728j.
249. Deligiannakis, Y.; Mantzanis, A.; Zindrou, A.; Smykala, S.; Solakidou, M. Control of Monomeric Vo's versus Vo Clusters in ZrO2−x for Solar-Light H2 Production from H2O at High-Yield (Millimoles Gr−1 H−1). *Sci Rep* **2022**, *12*, 15132, doi:10.1038/s41598-022-19382-3.
250. Ameta, R.; Ameta, S.C. *Photocatalysis*; 0 ed.; CRC Press, 2016; ISBN 978-1-4822-5494-5.
251. Hennig, H. **Semiconductor Photocatalysis: Principles and Applications** . By Horst Kisch. *Angew. Chem. Int. Ed.* **2015**, *54*, 4429–4429, doi:10.1002/anie.201501876.
252. Tahir, M.; Pan, L.; Idrees, F.; Zhang, X.; Wang, L.; Zou, J.-J.; Wang, Z.L. Electrocatalytic Oxygen Evolution Reaction for Energy Conversion and Storage: A Comprehensive Review. *Nano Energy* **2017**, *37*, 136–157, doi:10.1016/j.nanoen.2017.05.022.
253. Schneider, J.T.; Firak, D.S.; Ribeiro, R.R.; Peralta-Zamora, P. Use of Scavenger Agents in Heterogeneous Photocatalysis: Truths, Half-Truths, and Misinterpretations. *Phys. Chem. Chem. Phys.* **2020**, *22*, 15723–15733, doi:10.1039/D0CP02411B.
254. Hölzl, J.; Schulte, F.K. Work Function of Metals. In *Solid Surface Physics*; Hölzl, J., Schulte, F.K., Wagner, H., Eds.; Springer Tracts in Modern Physics; Springer: Berlin, Heidelberg, 1979; pp. 1–150 ISBN 978-3-540-35253-2.
255. Kaur, J.; Singh, R.; Pal, B. Influence of Coinage and Platinum Group Metal Co-Catalysis for the Photocatalytic Reduction of m-Dinitrobenzene by P25 and Rutile TiO2. *Journal of Molecular Catalysis A: Chemical* **2015**, *397*, 99–105, doi:10.1016/j.molcata.2014.11.007.

256. Zheng, J.; Li, J.; Bai, J.; Tan, X.; Zeng, Q.; Li, L.; Zhou, B. Efficient Degradation of Refractory Organics Using Sulfate Radicals Generated Directly from WO3 Photoelectrode and the Catalytic Reaction of Sulfate. *Catalysts* **2017**, *7*, 346, doi:10.3390/catal7110346.
257. Berr, M.J.; Wagner, P.; Fischbach, S.; Vaneski, A.; Schneider, J.; Susha, A.S.; Rogach, A.L.; Jäckel, F.; Feldmann, J. Hole Scavenger Redox Potentials Determine Quantum Efficiency and Stability of Pt-Decorated CdS Nanorods for Photocatalytic Hydrogen Generation. *Applied Physics Letters* **2012**, *100*, 223903, doi:10.1063/1.4723575.
258. Kumaravel, V.; Imam, M.; Badreldin, A.; Chava, R.; Do, J.; Kang, M.; Abdel-Wahab, A. Photocatalytic Hydrogen Production: Role of Sacrificial Reagents on the Activity of Oxide, Carbon, and Sulfide Catalysts. *Catalysts* **2019**, *9*, 276, doi:10.3390/catal9030276.
259. Zhang, Z.; Yates, J.T. Band Bending in Semiconductors: Chemical and Physical Consequences at Surfaces and Interfaces. *Chem. Rev.* **2012**, *112*, 5520–5551, doi:10.1021/cr3000626.
260. Jiao, Y.; Hellman, A.; Fang, Y.; Gao, S.; Käll, M. Schottky Barrier Formation and Band Bending Revealed by First- Principles Calculations. *Sci Rep* **2015**, *5*, 11374, doi:10.1038/srep11374.
261. Neamen, D.A. *Semiconductor Physics and Devices: Basic Principles*; 3rd ed.; McGraw-Hill: Boston, 2003; ISBN 978-0-07-232107-4.
262. Jeffries, W.R.; Fagan, A.M.; Schaak, R.E.; Knappenberger, K.L. Influence of Band Alignment on Electronic Relaxation in Plasmonic Metal–Semiconductor Hybrid Nanoparticles. *J. Phys. Chem. C* **2022**, *126*, 8384–8392, doi:10.1021/acs.jpcc.2c01378.
263. San Martín, S.; Rivero, M.J.; Ortiz, I. Unravelling the Mechanisms That Drive the Performance of Photocatalytic Hydrogen Production. *Catalysts* **2020**, *10*, 901, doi:10.3390/catal10080901.
264. Yang, X.; Wang, D. Photocatalysis: From Fundamental Principles to Materials and Applications. *ACS Appl. Energy Mater.* **2018**, *1*, 6657–6693, doi:10.1021/acsaem.8b01345.
265. Jafari, T.; Moharreri, E.; Amin, A.; Miao, R.; Song, W.; Suib, S. Photocatalytic Water Splitting—The Untamed Dream: A Review of Recent Advances. *Molecules* **2016**, *21*, 900, doi:10.3390/molecules21070900.
266. Midilli, A.; Ay, M.; Dincer, I.; Rosen, M.A. On Hydrogen and Hydrogen Energy Strategies. *Renewable and Sustainable Energy Reviews* **2005**, *9*, 255–271, doi:10.1016/j.rser.2004.05.003.
267. Fujishima, A.; Honda, K. Electrochemical Photolysis of Water at a Semiconductor Electrode. *Nature* **1972**, *238*, 37–38, doi:10.1038/238037a0.
268. *Biofuels - Economy, Environment and Sustainability*; Fang, Z., Ed.; InTech, 2013; ISBN 978-953-51-0950-1.
269. Pelaez, M.; Nolan, N.T.; Pillai, S.C.; Seery, M.K.; Falaras, P.; Kontos, A.G.; Dunlop, P.S.M.; Hamilton, J.W.J.; Byrne, J.A.; O'Shea, K.; et al. A Review on the Visible Light Active Titanium Dioxide Photocatalysts for Environmental Applications. *Applied Catalysis B: Environmental* **2012**, *125*, 331–349, doi:10.1016/j.apcatb.2012.05.036.
270. Nakaoka, K.; Ueyama, J.; Ogura, K. Photoelectrochemical Behavior of Electrodeposited CuO and Cu[Sub 2]O Thin Films on Conducting Substrates. *J. Electrochem. Soc.* **2004**, *151*, C661, doi:10.1149/1.1789155.
271. Kato, H.; Kudo, A. Water Splitting into H_2 and O_2 on Alkali Tantalate Photocatalysts $ATaO_3$ (A = Li, Na, and K). *J. Phys. Chem. B* **2001**, *105*, 4285–4292, doi:10.1021/jp004386b.
272. Wang, M.; Ma, Y.; Fo, Y.; Lyu, Y.; Zhou, X. Theoretical Insights into the Origin of Highly Efficient Photocatalyst NiO/NaTaO3 for Overall Water Splitting. *International Journal of Hydrogen Energy* **2020**, *45*, 19357–19369, doi:10.1016/j.ijhydene.2020.05.131.
273. Uddin, Md.T.; Nicolas, Y.; Olivier, C.; Jaegermann, W.; Rockstroh, N.; Junge, H.; Toupance, T. Band Alignment Investigations of Heterostructure NiO/TiO_2 Nanomaterials Used as Efficient Heterojunction Earth-Abundant Metal Oxide Photocatalysts for Hydrogen Production. *Phys. Chem. Chem. Phys.* **2017**, *19*, 19279–19288, doi:10.1039/C7CP01300K.
274. Greiner, M.T.; Helander, M.G.; Wang, Z.-B.; Tang, W.-M.; Lu, Z.-H. Effects of Processing Conditions on the Work Function and Energy-Level Alignment of NiO Thin Films. *J. Phys. Chem. C* **2010**, *114*, 19777–19781, doi:10.1021/jp108281m.
275. Ortiz-Quiñonez, J.L.; Díaz, D.; Zumeta-Dubé, I.; Arriola-Santamaría, H.; Betancourt, I.; Santiago-Jacinto, P.; Nava-Etzana, N. Easy Synthesis of High-Purity $BiFeO_3$ Nanoparticles: New Insights Derived from the Structural, Optical, and Magnetic Characterization. *Inorganic Chemistry* **2013**, *52*, 10306–10317, doi:10.1021/ic400627c.
276. Kirsch, A.; Murshed, M.M.; Schowalter, M.; Rosenauer, A.; Gesing, T.M. Nanoparticle Precursor into Polycrystalline $Bi_2Fe_4O_9$: An Evolutionary Investigation of Structural, Morphological, Optical, and Vibrational Properties. *The Journal of Physical Chemistry C* **2016**, *120*, 18831–18840, doi:10.1021/acs.jpcc.6b04773.
277. Zhang, Q.; Gong, W.; Wang, J.; Ning, X.; Wang, Z.; Zhao, X.; Ren, W.; Zhang, Z. Size-Dependent Magnetic, Photoabsorbing, and Photocatalytic Properties of Single-Crystalline $Bi_2Fe_4O_9$ Semiconductor Nanocrystals. *The Journal of Physical Chemistry C* **2011**, *115*, 25241–25246, doi:10.1021/jp208750n.
278. He, J. Characterization and Visible Light Photocatalytic Mechanism of Size-Controlled BiFeO3 Nanoparticles. *Materials Research Bulletin* **2013**, 8.
279. Wang, X.; Zhang, M.; Tian, P.; Chin, W.S.; Zhang, C.M. A Facile Approach to Pure-Phase Bi2Fe4O9 Nanoparticles Sensitive to Visible Light. *Applied Surface Science* **2014**, *321*, 144–149, doi:10.1016/j.apsusc.2014.09.166.
280. Knausenberger, H. Selected Properties of Pyrolytic Ta 05 Films. *Journal of The Electrochemical Society* **1973**, *120*, 5.
281. He, Y.; Zhu, Y.; Wu, N. Synthesis of Nanosized NaTaO3 in Low Temperature and Its Photocatalytic Performance. *Journal of Solid State Chemistry* **2004**, *177*, 3868–3872, doi:10.1016/j.jssc.2004.07.011.
282. Edalati, K.; Fujiwara, K.; Takechi, S.; Wang, Q.; Arita, M.; Watanabe, M.; Sauvage, X.; Ishihara, T.; Horita, Z. Improved Photocatalytic Hydrogen Evolution on Tantalate Perovskites $CsTaO_3$ and $LiTaO_3$ by Strain-Induced Vacancies. *ACS Appl. Energy Mater.* **2020**, *3*, 1710–1718, doi:10.1021/acsaem.9b02197.
283. Modak, B.; Srinivasu, K.; Ghosh, S.K. Band Gap Engineering of $NaTaO_3$ Using Density Functional Theory: A Charge Compensated Codoping Strategy. *Phys. Chem. Chem. Phys.* **2014**, *16*, 17116, doi:10.1039/C4CP01578A.
284. Chun, W.-J.; Ishikawa, A.; Fujisawa, H.; Takata, T.; Kondo, J.N.; Hara, M.; Kawai, M.; Matsumoto, Y.; Domen, K. Conduction and Valence Band Positions of Ta_2O_5, TaON, and Ta_3N_5 by UPS and Electrochemical Methods. *J. Phys. Chem. B* **2003**, *107*, 1798–1803, doi:10.1021/jp027593f.
285. Liu, Q.-L.; Zhao, Z.-Y.; Yi, J.-H. Effects of Crystal Structure and Composition on the Photocatalytic Performance of Ta–O–N Functional Materials. *Phys. Chem. Chem. Phys.* **2018**, *20*, 12005–12015, doi:10.1039/C8CP00432C.
286. Teoh, W.Y.; Amal, R.; Mädler, L. Flame Spray Pyrolysis: An Enabling Technology for Nanoparticles Design and Fabrication. *Nanoscale* **2010**, *2*, 1324, doi:10.1039/c0nr00017e.

287. Deligiannakis, Y.; Tsikourkitoudi, V.; Stathi, P.; Wegner, K.; Papavasiliou, J.; Louloudi, M. PdO/Pd ^{0} /TiO $_{2}$ Nanocatalysts Engineered by Flame Spray Pyrolysis: Study of the Synergy of PdO/Pd ^{0} on H $_{2}$ Production by HCOOH Dehydrogenation and the Deactivation Mechanism. *Energy Fuels* **2020**, *34*, 15026–15038, doi:10.1021/acs.energyfuels.0c02399.
288. Kumaravel, V.; Imam, M.; Badreldin, A.; Chava, R.; Do, J.; Kang, M.; Abdel-Wahab, A. Photocatalytic Hydrogen Production: Role of Sacrificial Reagents on the Activity of Oxide, Carbon, and Sulfide Catalysts. *Catalysts* **2019**, *9*, 276, doi:10.3390/catal9030276.
289. Papadas, I.; Christodoulides, J.A.; Kioseoglou, G.; Armatas, G.S. A High Surface Area Ordered Mesoporous BiFeO $_{3}$ Semiconductor with Efficient Water Oxidation Activity. *J. Mater. Chem. A* **2015**, *3*, 1587–1593, doi:10.1039/C4TA05272B.
290. Solakidou, M.; Georgiou, Y.; Deligiannakis, Y. Double-Nozzle Flame Spray Pyrolysis as a Potent Technology to Engineer Noble Metal-TiO2 Nanophotocatalysts for Efficient H2 Production. *Energies* **2021**, *14*, doi:10.3390/en14040817.
291. Bletsa, E.; Stathi, P.; Dimos, K.; Louloudi, M.; Deligiannakis, Y. Interfacial Hydrogen Atom Transfer by Nanohybrids Based on Humic Acid Like Polycondensates. *Journal of Colloid and Interface Science* **2015**, *455*, 163–171, doi:10.1016/j.jcis.2015.05.039.
292. Pradhan, N.; Pal, A.; Pal, T. Catalytic Reduction of Aromatic Nitro Compounds by Coinage Metal Nanoparticles. *Langmuir* **2001**, *17*, 1800–1802, doi:10.1021/la000862d.
293. Georgiou, Y.; Mouzourakis, E.; Bourlinos, A.B.; Zboril, R.; Karakassides, M.A.; Douvalis, A.P.; Bakas, Th.; Deligiannakis, Y. Surface Decoration of Amine-Rich Carbon Nitride with Iron Nanoparticles for Arsenite (AsIII) Uptake: The Evolution of the Fe-Phases under Ambient Conditions. *Journal of Hazardous Materials* **2016**, *312*, 243–253, doi:10.1016/j.jhazmat.2016.03.066.
294. Mouzourakis, E.; Georgiou, Y.; Louloudi, M.; Konstantinou, I.; Deligiannakis, Y. Recycled-Tire Pyrolytic Carbon Made Functional: A High-Arsenite [As(III)] Uptake Material PyrC350®. *Journal of Hazardous Materials* **2017**, *326*, 177–186, doi:10.1016/j.jhazmat.2016.12.027.
295. *EPR Spectroscopy: Fundamentals and Methods*; Goldfarb, D., Stoll, S., Eds.; Wiley/Blackwell: Hoboken, N.J, 2018; ISBN 978-1-119-16297-1.
296. Wertz, J.E.; Bolton, J.R. *Electron Spin Resonance: Elementary Theory and Practical Applications*; Chapman and Hall: New York, 1986; ISBN 978-0-412-01181-8.
297. O'Handley, R.C. *Modern Magnetic Materials: Principles and Applications*; Wiley: New York, 2000; ISBN 978-0-471-15566-9.
298. Eaton, G.R.; Eaton, S.S.; Barr, D.P.; Weber, R.T. *Quantitative EPR*; Springer Vienna: Vienna, 2010; ISBN 978-3-211-92947-6.
299. Nakaoka, Y.; Nosaka, Y. ESR Investigation into the Effects of Heat Treatment and Crystal Structure on Radicals Produced over Irradiated TiO2 Powder. *Journal of Photochemistry and Photobiology A: Chemistry* **1997**, *110*, 299–305, doi:10.1016/S1010-6030(97)00208-6.
300. Pryor, W.A. Oxy-Radicals and Related Species: Their Formation, Lifetimes, and Reactions. *Annu. Rev. Physiol.* **1986**, *48*, 657–667, doi:10.1146/annurev.ph.48.030186.003301.
301. Keszler, A.; Kalyanaraman, B.; Hogg, N. Comparative Investigation of Superoxide Trapping by Cyclic Nitrone Spin Traps: The Use of Singular Value Decomposition and Multiple Linear Regression Analysis. *Free Radical Biology and Medicine* **2003**, *35*, 1149–1157, doi:10.1016/S0891-5849(03)00497-0.
302. Kanigaridou, Y.; Petala, A.; Frontistis, Z.; Antonopoulou, M.; Solakidou, M.; Konstantinou, I.; Deligiannakis, Y.; Mantzavinos, D.; Kondarides, D.I. Solar Photocatalytic Degradation of Bisphenol A with CuO x /BiVO 4 : Insights into the Unexpectedly Favorable Effect of Bicarbonates. *Chemical Engineering Journal* **2017**, *318*, 39–49, doi:10.1016/j.cej.2016.04.145.
303. Zhao, H.; Joseph, J.; Zhang, H.; Karoui, H.; Kalyanaraman, B. Synthesis and Biochemical Applications of a Solid Cyclic Nitrone Spin Trap: A Relatively Superior Trap for Detecting Superoxide Anions and Glutathiyl Radicals. *Free Radical Biology and Medicine* **2001**, *31*, 599–606, doi:10.1016/S0891-5849(01)00619-0.
304. Dvoranová, D.; Barbieriková, Z.; Brezová, V. Radical Intermediates in Photoinduced Reactions on TiO2 (An EPR Spin Trapping Study). *Molecules* **2014**, *19*, 17279–17304, doi:10.3390/molecules191117279.
305. Dikalov, S.; Jiang, J.; Mason, R.P. Characterization of the High-Resolution ESR Spectra of Superoxide Radical Adducts of 5-(Diethoxyphosphoryl)-5-Methyl-1-Pyrroline *N* -Oxide (DEPMPO) and 5,5-Dimethyl-1-Pyrroline *N* -Oxide (DMPO). Analysis of Conformational Exchange. *Free Radical Research* **2005**, *39*, 825–836, doi:10.1080/10715760500155688.
306. Brezová, V.; Dvoranová, D.; Staško, A. Characterization of Titanium Dioxide Photoactivity Following the Formation of Radicals by EPR Spectroscopy. *Res. Chem. Intermed.* **2007**, *33*, 251–268, doi:10.1163/156856707779238630.
307. ROSEN, G.M.; RAUCKMAN, E.J. Spin Trapping of the Primary Radical Involved in the Activation of the Carcinogen N-Hydroxy-2-Acetylaminofluorene by Cumene Hydroperoxide-Hematin. *Molecular pharmacology* **1980**, *17*, 233–238.
308. Chen, C.; Li, F.; Chen, H.-L.; Kong, M.G. Interaction between Air Plasma-Produced Aqueous ^{1} O $_{2}$ and the Spin Trap DMPO in Electron Spin Resonance. *Physics of Plasmas* **2017**, *24*, 103501, doi:10.1063/1.4986008.
309. Nosaka, Y.; Nosaka, A.Y. Generation and Detection of Reactive Oxygen Species in Photocatalysis. *Chem. Rev.* **2017**, *117*, 11302–11336, doi:10.1021/acs.chemrev.7b00161.
310. Stoll, S.; Schweiger, A. EasySpin, a Comprehensive Software Package for Spectral Simulation and Analysis in EPR. *Journal of Magnetic Resonance* **2006**, *178*, 42–55, doi:10.1016/j.jmr.2005.08.013.
311. Micic, O.I.; Zhang, Y.; Cromack, K.R.; Trifunac, A.D.; Thurnauer, M.C. Trapped Holes on Titania Colloids Studied by Electron Paramagnetic Resonance. *J. Phys. Chem.* **1993**, *97*, 7277–7283, doi:10.1021/j100130a026.
312. Micic, O.; Zhang, Y.; Cromack, K.R.; Trifunac, A.; Thurnauer, M. Photoinduced Hole Transfer from Titanium Dioxide to Methanol Molecules in Aqueous Solution Studied by Electron Paramagnetic Resonance. *J. Phys. Chem.* **1993**, *97*, 13284–13288, doi:10.1021/j100152a036.
313. Hurum, D.C.; Agrios, A.G.; Gray, K.A.; Rajh, T.; Thurnauer, M.C. Explaining the Enhanced Photocatalytic Activity of Degussa P25 Mixed-Phase TiO $_{2}$ Using EPR. *J. Phys. Chem. B* **2003**, *107*, 4545–4549, doi:10.1021/jp0273934.
314. Howe, R.F.; Gratzel, M. EPR Observation of Trapped Electrons in Colloidal Titanium Dioxide. *J. Phys. Chem.* **1985**, *89*, 4495–4499, doi:10.1021/j100267a018.
315. Howe, R.F.; Gratzel, Michael. EPR Study of Hydrated Anatase under UV Irradiation. *J. Phys. Chem.* **1987**, *91*, 3906–3909, doi:10.1021/j100298a035.
316. Kumar, C.P.; Gopal, N.O.; Wang, T.C.; Wong, M.-S.; Ke, S.C. EPR Investigation of TiO $_{2}$ Nanoparticles with Temperature-Dependent Properties. *J. Phys. Chem. B* **2006**, *110*, 5223–5229, doi:10.1021/jp057053t.
317. Rajh, T.; Dimitrijevic, N.M.; Bissonnette, M.; Koritarov, T.; Konda, V. Titanium Dioxide in the Service of the Biomedical Revolution. *Chem. Rev.* **2014**, *114*, 10177–10216, doi:10.1021/cr500029g.

318. Livraghi, S.; Paganini, M.C.; Giamello, E.; Selloni, A.; Di Valentin, C.; Pacchioni, G. Origin of Photoactivity of Nitrogen-Doped Titanium Dioxide under Visible Light. *J. Am. Chem. Soc.* **2006**, *128*, 15666–15671, doi:10.1021/ja064164c.
319. Wang, J.; Su, S.; Liu, B.; Cao, M.; Hu, C. One-Pot, Low-Temperature Synthesis of Self-Doped NaTaO3 Nanoclusters for Visible-Light-Driven Photocatalysis. *Chem. Commun.* **2013**, *49*, 7830, doi:10.1039/c3cc42487a.
320. Meyer, T.; Priebe, J.B.; da Silva, R.O.; Peppel, T.; Junge, H.; Beller, M.; Brückner, A.; Wohlrab, S. Advanced Charge Utilization from $NaTaO_3$ Photocatalysts by Multilayer Reduced Graphene Oxide. *Chem. Mater.* **2014**, *26*, 4705–4711, doi:10.1021/cm500949x.
321. Grigoropoulou, G.; Christoforidis, K.C.; Louloudi, M.; Deligiannakis, Y. Structure-Catalytic Function Relationship of SiO 2 -Immobilized Mononuclear Cu Complexes: An EPR Study. *Langmuir* **2007**, *23*, 10407–10418, doi:10.1021/la700815d.
322. Grela, M.A.; Coronel, M.E.J.; Colussi, A.J. Quantitative Spin-Trapping Studies of Weakly Illuminated Titanium Dioxide Sols. Implications for the Mechanism of Photocatalysis. *J. Phys. Chem.* **1996**, *100*, 16940–16946, doi:10.1021/jp953562r.
323. Kanigaridou, Y.; Petala, A.; Frontistis, Z.; Antonopoulou, M.; Solakidou, M.; Konstantinou, I.; Deligiannakis, Y.; Mantzavinos, D.; Kondarides, D.I. Solar Photocatalytic Degradation of Bisphenol A with CuOx /BiVO4 : Insights into the Unexpectedly Favorable Effect of Bicarbonates. *Chemical Engineering Journal* **2017**, *318*, 39–49, doi:10.1016/j.cej.2016.04.145.
324. The Reflection of X-Rays by Crystals. *Proc. R. Soc. Lond. A* **1913**, *88*, 428–438, doi:10.1098/rspa.1913.0040.
325. Doebelin, N.; Kleeberg, R. *Profex* : A Graphical User Interface for the Rietveld Refinement Program *BGMN*. *J Appl Crystallogr* **2015**, *48*, 1573–1580, doi:10.1107/S1600576715014685.
326. Patterson, A.L. The Scherrer Formula for X-Ray Particle Size Determination. *Phys. Rev.* **1939**, *56*, 978–982, doi:10.1103/PhysRev.56.978.
327. Tauc, J.; Grigorovici, R.; Vancu, A. Optical Properties and Electronic Structure of Amorphous Germanium. *physica status solidi (b)* **1966**, *15*, 627–637, doi:10.1002/pssb.19660150224.
328. Beer Bestimmung der Absorption des rothen Lichts in farbigen Flüssigkeiten. *Ann. Phys. Chem.* **1852**, *162*, 78–88, doi:10.1002/andp.18521620505.
329. Brunauer, S.; Emmett, P.H.; Teller, E. Adsorption of Gases in Multimolecular Layers. *J. Am. Chem. Soc.* **1938**, *60*, 309–319, doi:10.1021/ja01269a023.
330. Yaws, C.L. *Chemical Properties Handbook: Physical, Thermodynamic, Environmental, Transport, Safety, and Health Related Properties for Organic and Inorganic Chemicals*; McGraw-Hill handbooks; McGraw-Hill: New York, 1999; ISBN 978-0-07-073401-2.
331. D. Deligiannakis; K. Moularas; P. Psathas; Y. Deligiannakis CFD Modeling of Combustion in Anoxic Flame Spray Pyrolyis. 4 th International Symposium Gas-Phase Synthesis of Functional Nanomaterials: Fundamental Understanding, Modeling and Simulation, Diagnostics, Scale-up and Application, 2020.
332. Aditya, T.; Pal, A.; Pal, T. Nitroarene Reduction: A Trusted Model Reaction to Test Nanoparticle Catalysts. *Chem. Commun.* **2015**, *51*, 9410–9431, doi:10.1039/C5CC01131K.
333. Panigrahi, S.; Basu, S.; Praharaj, S.; Pande, S.; Jana, S.; Pal, A.; Ghosh, S.K.; Pal, T. Synthesis and Size-Selective Catalysis by Supported Gold Nanoparticles: Study on Heterogeneous and Homogeneous Catalytic Process. *J. Phys. Chem. C* **2007**, *111*, 4596–4605, doi:10.1021/jp067554u.
334. Narayanan, K.B.; Sakthivel, N. Synthesis and Characterization of Nano-Gold Composite Using Cylindrocladium Floridanum and Its Heterogeneous Catalysis in the Degradation of 4-Nitrophenol. *Journal of Hazardous Materials* **2011**, *189*, 519–525, doi:10.1016/j.jhazmat.2011.02.069.
335. Travis, A.S. Manufacture and Uses of the Anilines: A Vast Array of Processes and Products. In *The Chemistry of Anilines*; Rappoport, Z., Ed.; John Wiley & Sons, Ltd: Chichester, UK, 2007; pp. 715–782 ISBN 978-0-470-87173-7.
336. Moitra, D.; Ghosh, B.K.; Chandel, M.; Ghosh, N.N. Synthesis of a $BiFeO_3$ Nanowire-Reduced Graphene Oxide Based Magnetically Separable Nanocatalyst and Its Versatile Catalytic Activity towards Multiple Organic Reactions. *RSC Adv.* **2016**, *6*, 97941–97952, doi:10.1039/C6RA22077K.
337. Moularas, C.; Georgiou, Y.; Adamska, K.; Deligiannakis, Y. Thermoplasmonic Heat Generation Efficiency by Nonmonodisperse Core–Shell Ag^0 @SiO_2 Nanoparticle Ensemble. *J. Phys. Chem. C* **2019**, *123*, 22499–22510, doi:10.1021/acs.jpcc.9b06532.
338. Ye, H.; Crooks, R.M. Effect of Elemental Composition of PtPd Bimetallic Nanoparticles Containing an Average of 180 Atoms on the Kinetics of the Electrochemical Oxygen Reduction Reaction. *J. Am. Chem. Soc.* **2007**, *129*, 3627–3633, doi:10.1021/ja068078o.
339. Bletsa, E.; Stathi, P.; Dimos, K.; Louloudi, M.; Deligiannakis, Y. Interfacial Hydrogen Atom Transfer by Nanohybrids Based on Humic Acid Like Polycondensates. *Journal of Colloid and Interface Science* **2015**, *455*, 163–171, doi:10.1016/j.jcis.2015.05.039.
340. Hervés, P.; Pérez-Lorenzo, M.; Liz-Marzán, L.M.; Dzubiella, J.; Lu, Y.; Ballauff, M. Catalysis by Metallic Nanoparticles in Aqueous Solution: Model Reactions. *Chem. Soc. Rev.* **2012**, *41*, 5577, doi:10.1039/c2cs35029g.
341. Mahmoud, M.A.; Saira, F.; El-Sayed, M.A. Experimental Evidence For The Nanocage Effect In Catalysis With Hollow Nanoparticles. *Nano Lett.* **2010**, *10*, 3764–3769, doi:10.1021/nl102497u.
342. Papadas, I.T.; Subrahmanyam, K.S.; Kanatzidis, M.G.; Armatas, G.S. Templated Assembly of $BiFeO_3$ Nanocrystals into 3D Mesoporous Networks for Catalytic Applications. *Nanoscale* **2015**, *7*, 5737–5743, doi:10.1039/C5NR00185D.
343. Moreau, J.M.; Michel, C.; Gerson, R.; James, W.J. Ferroelectric BiFeO3 X-Ray and Neutron Diffraction Study. *Journal of Physics and Chemistry of Solids* **1971**, *32*, 1315–1320, doi:10.1016/S0022-3697(71)80189-0.
344. Shamir, N.; Gurewitz, E.; Shaked, H. The Magnetic Structure of $Bi_2Fe_4O_9$ – Analysis of Neutron Diffraction Measurements. *Acta Crystallographica Section A* **1978**, *34*, 662–666, doi:10.1107/S0567739478001412.
345. Lomanova, N.A.; Gusarov, V.V. INFLUENCE OF SYNTHESIS TEMPERATURE ON BiFeO3 NANOPARTICLES FORMATION. 11.
346. Ru-Shi, L. *Controlled Nanofabrication : Advances and Applications*; Jenny Stanford Publishing, 2012; ISBN 978-0-429-07111-9.
347. Kho, Y.K.; Teoh, W.Y.; Iwase, A.; Mädler, L.; Kudo, A.; Amal, R. Flame Preparation of Visible-Light-Responsive $BiVO_4$ Oxygen Evolution Photocatalysts with Subsequent Activation via Aqueous Route. *ACS Applied Materials & Interfaces* **2011**, *3*, 1997–2004, doi:10.1021/am200247y.
348. Kho, Y.K.; Teoh, W.Y.; Iwase, A.; Mädler, L.; Kudo, A.; Amal, R. Flame Preparation of Visible-Light-Responsive $BiVO_4$ Oxygen Evolution Photocatalysts with Subsequent Activation via Aqueous Route. *ACS Appl. Mater. Interfaces* **2011**, *3*, 1997–2004, doi:10.1021/am200247y.
349. Srivastav, S.K.; S. Gajbhiye, N. Low Temperature Synthesis, Structural, Optical and Magnetic Properties of Bismuth Ferrite Nanoparticles. *Journal of the American Ceramic Society* **2012**, *95*, 3678–3682, doi:10.1111/j.1551-2916.2012.05411.x.

350. Kaczmarek, W.; Graja, A. Lattice Dynamics Study of the Solid Solution (Bi1−xLax) FeO3 by i.r. Spectroscopy. *Solid State Communications* **1975**, *17*, 851–853, doi:10.1016/0038-1098(75)90736-X.
351. Zhao, J.; Liu, T.; Xu, Y.; He, Y.; Chen, W. Synthesis and Characterization of Bi2Fe4O9 Powders. *Materials Chemistry and Physics* **2011**, *128*, 388–391, doi:10.1016/j.matchemphys.2011.03.011.
352. Voll, D.; Beran, A.; Schneider, H. Variation of Infrared Absorption Spectra in the System Bi2Al4−x Fe x O9 (x = 0–4), Structurally Related to Mullite. *Physics and Chemistry of Minerals* **2006**, *33*, 623–628, doi:10.1007/s00269-006-0108-8.
353. *The Infrared Spectra of Minerals*; Farmer, V.C., Ed.; Mineralogical Society monograph; Mineralogical Society: London, 1974; ISBN 978-0-903056-05-2.
354. Arora, M.; Sati, P.C.; Chauhan, S.; Chhoker, S.; Panwar, A.K.; Kumar, M. Structural, Optical and Multiferroic Properties of BiFeO3 Nanoparticles Synthesized by Soft Chemical Route. *Journal of Superconductivity and Novel Magnetism* **2013**, *26*, 443–448, doi:10.1007/s10948-012-1761-4.
355. Yang, Y.; Sun, J.Y.; Zhu, K.; Liu, Y.L.; Chen, J.; Xing, X.R. Raman Study of BiFeO3 with Different Excitation Wavelengths. *Physica B: Condensed Matter* **2009**, *404*, 171–174, doi:10.1016/j.physb.2008.10.029.
356. Bielecki, J.; Svedlindh, P.; Tibebu, D.T.; Cai, S.; Eriksson, S.-G.; Börjesson, L.; Knee, C.S. Structural and Magnetic Properties of Isovalently Substituted Multiferroic BiFeO 3 : Insights from Raman Spectroscopy. *Physical Review B* **2012**, *86*, doi:10.1103/PhysRevB.86.184422.
357. Palai, R.; Schmid, H.; Scott, J.F.; Katiyar, R.S. Raman Spectroscopy of Single-Domain Multiferroic BiFeO 3. *Physical Review B* **2010**, *81*, doi:10.1103/PhysRevB.81.064110.
358. Iliev, M.N.; Litvinchuk, A.P.; Hadjiev, V.G.; Gospodinov, M.M.; Skumryev, V.; Ressouche, E. Phonon and Magnon Scattering of Antiferromagnetic Bi 2 Fe 4 O 9. *Physical Review B* **2010**, *81*, doi:10.1103/PhysRevB.81.024302.
359. Yamashita, T.; Hayes, P. Analysis of XPS Spectra of Fe2+ and Fe3+ Ions in Oxide Materials. *Applied Surface Science* **2008**, *254*, 2441–2449, doi:10.1016/j.apsusc.2007.09.063.
360. Kothari, D.; Reddy, V.R.; Gupta, A.; Phase, D.M.; Lakshmi, N.; Deshpande, S.K.; Awasthi, A.M. Study of the Effect of Mn Doping on the BiFeO3system. *J. Phys.: Condens. Matter* **2007**, *19*, 136202, doi:10.1088/0953-8984/19/13/136202.
361. Grosvenor, A.P.; Kobe, B.A.; Biesinger, M.C.; McIntyre, N.S. Investigation of Multiplet Splitting of Fe 2p XPS Spectra and Bonding in Iron Compounds. *Surface and Interface Analysis* **2004**, *36*, 1564–1574, doi:10.1002/sia.1984.
362. Dharmadhikari, V.S.; Sainkar, S.R.; Badrinarayan, S.; Goswami, A. Characterisation of Thin Films of Bismuth Oxide by X-Ray Photoelectron Spectroscopy. *Journal of Electron Spectroscopy and Related Phenomena* **1982**, *25*, 181–189, doi:10.1016/0368-2048(82)85016-0.
363. Wang, P.W.; Guttag, M.; Tu, C.-S. Surface Modification of Multiferroic BiFeO₃ Ceramic by Argon Sputtering. *JSEMAT* **2014**, *04*, 295–308, doi:10.4236/jsemat.2014.45033.
364. Wu, T.; Liu, L.; Pi, M.; Zhang, D.; Chen, S. Enhanced Magnetic and Photocatalytic Properties of Bi 2 Fe 4 O 9 Semiconductor with Large Exposed (001) Surface. *Applied Surface Science* **2016**, *377*, 253–261, doi:10.1016/j.apsusc.2016.03.140.
365. Singh, A.K.; Mohapatra, S.R.; Khare, P.; Ganguli, N.; Wildes, A.; Siruguri, V.; Kaushik, S.D. Neutron Diffraction and Short Range Ordering Study in Multiferroic Bi $_2$ Fe $_4$ O $_9$. *Materials Research Express* **2019**, *6*, 066107, doi:10.1088/2053-1591/ab0ccc.
366. Baraneedharan, P.; Imran Hussain, S.; Dinesh, V.P.; Siva, C.; Biji, P.; Sivakumar, M. Lattice Doped Zn–SnO2 Nanospheres: A Systematic Exploration of Dopant Ion Effects on Structural, Optical, and Enhanced Gas Sensing Properties. *Applied Surface Science* **2015**, *357*, 1511–1521, doi:10.1016/j.apsusc.2015.09.257.
367. Jun Cho, H.; Onozato, T.; Wei, M.; Sanchela, A.; Ohta, H. Effects of Vacuum Annealing on the Electron Mobility of Epitaxial La-Doped BaSnO 3 Films. *APL Materials* **2019**, *7*, 022507, doi:10.1063/1.5054154.
368. Papadas, I.T.; Kota, S.S.; Kanatzidis, M.G.; Armatas, G.S. Templated Assembly of BiFeO3 Nanocrystals into 3D Mesoporous Networks for Catalytic Applications. **2012**, 8.
369. Moitra, D.; Ghosh, B.K.; Chandel, M.; Ghosh, N.N. Synthesis of BiFeO3 Nanowire- Reduced Graphene Oxide Based Magnetically Separable Nanocatalyst and Its Versatile Catalytic Activity towards Multiple Organic Reactions. 13.
370. Elfiad, A.; Galli, F.; Djadoun, A.; Sennour, M.; Chegrouche, S.; Meddour-Boukhobza, L.; Boffito, D.C. Natural α-Fe 2 O 3 as an Efficient Catalyst for the p-Nitrophenol Reduction. *Materials Science and Engineering: B* **2018**, *229*, 126–134, doi:10.1016/j.mseb.2017.12.009.
371. Li, X.; Wang, X.; Song, S.; Liu, D.; Zhang, H. Selectively Deposited Noble Metal Nanoparticles on Fe $_3$ O $_4$ /Graphene Composites: Stable, Recyclable, and Magnetically Separable Catalysts. *Chemistry - A European Journal* **2012**, *18*, 7601–7607, doi:10.1002/chem.201103726.
372. Larsen, G.K.; Farr, W.; Hunyadi Murph, S.E. Multifunctional Fe $_2$ O $_3$ –Au Nanoparticles with Different Shapes: Enhanced Catalysis, Photothermal Effects, and Magnetic Recyclability. *The Journal of Physical Chemistry C* **2016**, *120*, 15162–15172, doi:10.1021/acs.jpcc.6b03733.
373. Gupta, V.K.; Atar, N.; Yola, M.L.; Üstündağ, Z.; Uzun, L. A Novel Magnetic Fe@Au Core–Shell Nanoparticles Anchored Graphene Oxide Recyclable Nanocatalyst for the Reduction of Nitrophenol Compounds. *Water Research* **2014**, *48*, 210–217, doi:10.1016/j.watres.2013.09.027.
374. Abkowicz-Bieńko, A.J.; Latajka, Z.; Bieńko, D.C.; Michalska, D. Theoretical Infrared Spectrum and Revised Assignment for Para-Nitrophenol. Density Functional Theory Studies. *Chemical Physics* **1999**, *250*, 123–129, doi:10.1016/S0301-0104(99)00296-7.
375. Georgiou, Y.; Perman, J.A.; Bourlinos, A.B.; Deligiannakis, Y. Highly Efficient Arsenite [As(III)] Adsorption by an [MIL-100(Fe)] Metal–Organic Framework: Structural and Mechanistic Insights. *J. Phys. Chem. C* **2018**, *122*, 4859–4869, doi:10.1021/acs.jpcc.7b11247.
376. Pozun, Z.D.; Rodenbusch, S.E.; Keller, E.; Tran, K.; Tang, W.; Stevenson, K.J.; Henkelman, G. A Systematic Investigation of P-Nitrophenol Reduction by Bimetallic Dendrimer Encapsulated Nanoparticles. *J. Phys. Chem. C* **2013**, *117*, 7598–7604, doi:10.1021/jp312588u.
377. Cheng, J.; Hu, P. Utilization of the Three-Dimensional Volcano Surface To Understand the Chemistry of Multiphase Systems in Heterogeneous Catalysis. *J. Am. Chem. Soc.* **2008**, *130*, 10868–10869, doi:10.1021/ja803555g.
378. Palai, R.; Katiyar, R.S.; Schmid, H.; Tissot, P.; Clark, S.J.; Robertson, J.; Redfern, S.A.T.; Catalan, G.; Scott, J.F. β Phase and γ − β Metal-Insulator Transition in Multiferroic Bi Fe O 3. *Physical Review B* **2008**, *77*, doi:10.1103/PhysRevB.77.014110.

379. Moreau, J.M.; Michel, C.; Gerson, R.; James, W.J. Ferroelectric BiFeO3 X-Ray and Neutron Diffraction Study. *Journal of Physics and Chemistry of Solids* **1971**, *32*, 1315–1320, doi:10.1016/S0022-3697(71)80189-0.
380. Shamir, N.; Gurewitz, E.; Shaked, H. The Magnetic Structure of Bi $_2$ Fe $_4$ O $_9$ – Analysis of Neutron Diffraction Measurements. *Acta Crystallographica Section A* **1978**, *34*, 662–666, doi:10.1107/S0567739478001412.
381. Moularas, C.; Georgiou, Y.; Adamska, K.; Deligiannakis, Y. Thermoplasmonic Heat Generation Efficiency by Nonmonodisperse Core–Shell Ag ^{0} @SiO $_2$ Nanoparticle Ensemble. *J. Phys. Chem. C* **2019**, *123*, 22499–22510, doi:10.1021/acs.jpcc.9b06532.
382. Sowmya, N.S.; Srinivas, A.; Suresh, P.; Shukla, A.; Kamat, S.V. Synthesis and Study of Structural, Magnetic and Microwave Absorption Properties in Multiferroic BiFeO3 Electroceramic. *Journal of Materials Science: Materials in Electronics* **2015**, *26*, 5368–5372, doi:10.1007/s10854-015-3081-5.
383. Kho, Y.K.; Teoh, W.Y.; Iwase, A.; Mädler, L.; Kudo, A.; Amal, R. Flame Preparation of Visible-Light-Responsive BiVO $_4$ Oxygen Evolution Photocatalysts with Subsequent Activation via Aqueous Route. *ACS Applied Materials & Interfaces* **2011**, *3*, 1997–2004, doi:10.1021/am200247y.
384. Deligiannakis, Y. Nanomaterials for Environmental Solar Energy Technologies: Applications & Limitations. *KONA* **2018**, *35*, 14–31, doi:10.14356/kona.2018004.
385. Sun, S.; Wang, W.; Zhang, L.; Shang, M. Visible Light-Induced Photocatalytic Oxidation of Phenol and Aqueous Ammonia in Flowerlike Bi $_2$ Fe $_4$ O $_9$ Suspensions. *The Journal of Physical Chemistry C* **2009**, *113*, 12826–12831, doi:10.1021/jp9029826.
386. Srivastav, S.K.; S. Gajbhiye, N. Low Temperature Synthesis, Structural, Optical and Magnetic Properties of Bismuth Ferrite Nanoparticles. *Journal of the American Ceramic Society* **2012**, *95*, 3678–3682, doi:10.1111/j.1551-2916.2012.05411.x.
387. Kaczmarek, W.; Graja, A. Lattice Dynamics Study of the Solid Solution (Bi1−xLax) FeO3 by i.r. Spectroscopy. *Solid State Communications* **1975**, *17*, 851–853, doi:10.1016/0038-1098(75)90736-X.
388. Voll, D.; Beran, A.; Schneider, H. Variation of Infrared Absorption Spectra in the System Bi2Al4−xFexO9 (x = 0–4), Structurally Related to Mullite. *Physics and Chemistry of Minerals* **2006**, *33*, 623–628, doi:10.1007/s00269-006-0108-8.
389. Zhao, J.; Liu, T.; Xu, Y.; He, Y.; Chen, W. Synthesis and Characterization of Bi2Fe4O9 Powders. *Materials Chemistry and Physics* **2011**, *128*, 388–391, doi:10.1016/j.matchemphys.2011.03.011.
390. Fujiwara, K.; Deligiannakis, Y.; Skoutelis, C.G.; Pratsinis, S.E. Visible-Light Active Black TiO2-Ag/TiOx Particles. *Applied Catalysis B: Environmental* **2014**, *154–155*, 9–15, doi:10.1016/j.apcatb.2014.01.060.
391. Arora, M.; Sati, P.C.; Chauhan, S.; Chhoker, S.; Panwar, A.K.; Kumar, M. Structural, Optical and Multiferroic Properties of BiFeO3 Nanoparticles Synthesized by Soft Chemical Route. *Journal of Superconductivity and Novel Magnetism* **2013**, *26*, 443–448, doi:10.1007/s10948-012-1761-4.
392. Yang, Y.; Sun, J.Y.; Zhu, K.; Liu, Y.L.; Chen, J.; Xing, X.R. Raman Study of BiFeO3 with Different Excitation Wavelengths. *Physica B: Condensed Matter* **2009**, *404*, 171–174, doi:10.1016/j.physb.2008.10.029.
393. Iliev, M.N.; Litvinchuk, A.P.; Hadjiev, V.G.; Gospodinov, M.M.; Skumryev, V.; Ressouche, E. Phonon and Magnon Scattering of Antiferromagnetic Bi 2 Fe 4 O 9. *Physical Review B* **2010**, *81*, doi:10.1103/PhysRevB.81.024302.
394. Grosvenor, A.P.; Kobe, B.A.; Biesinger, M.C.; McIntyre, N.S. Investigation of Multiplet Splitting of Fe 2p XPS Spectra and Bonding in Iron Compounds. *Surf. Interface Anal.* **2004**, *36*, 1564–1574, doi:10.1002/sia.1984.
395. Yamashita, T.; Hayes, P. Analysis of XPS Spectra of Fe2+ and Fe3+ Ions in Oxide Materials. *Applied Surface Science* **2008**, *254*, 2441–2449, doi:10.1016/j.apsusc.2007.09.063.
396. Biesinger, M.C.; Payne, B.P.; Grosvenor, A.P.; Lau, L.W.M.; Gerson, A.R.; Smart, R.St.C. Resolving Surface Chemical States in XPS Analysis of First Row Transition Metals, Oxides and Hydroxides: Cr, Mn, Fe, Co and Ni. *Applied Surface Science* **2011**, *257*, 2717–2730, doi:10.1016/j.apsusc.2010.10.051.
397. Dharmadhikari, V.S.; Sainkar, S.R.; Badrinarayan, S.; Goswami, A. Characterisation of Thin Films of Bismuth Oxide by X-Ray Photoelectron Spectroscopy. *Journal of Electron Spectroscopy and Related Phenomena* **1982**, *25*, 181–189, doi:10.1016/0368-2048(82)85016-0.
398. Wang, P.W.; Guttag, M.; Tu, C.-S. Surface Modification of Multiferroic BiFeO3; Ceramic by Argon Sputtering. *JSEMAT* **2014**, *04*, 295–308, doi:10.4236/jsemat.2014.45033.
399. Baraneedharan, P.; Imran Hussain, S.; Dinesh, V.P.; Siva, C.; Biji, P.; Sivakumar, M. Lattice Doped Zn–SnO2 Nanospheres: A Systematic Exploration of Dopant Ion Effects on Structural, Optical, and Enhanced Gas Sensing Properties. *Applied Surface Science* **2015**, *357*, 1511–1521, doi:10.1016/j.apsusc.2015.09.257.
400. Butler, M.A.; Ginley, D.S. Prediction of Flatband Potentials at Semiconductor-Electrolyte Interfaces from Atomic Electronegativities. *J. Electrochem. Soc.* **1978**, *125*, 228–232, doi:10.1149/1.2131419.
401. Li, S.; Zhang, J.; Kibria, M.G.; Mi, Z.; Chaker, M.; Ma, D.; Nechache, R.; Rosei, F. Remarkably Enhanced Photocatalytic Activity of Laser Ablated Au Nanoparticle Decorated BiFeO3 Nanowires under Visible-Light. *Chem. Commun.* **2013**, *49*, 5856, doi:10.1039/c3cc40363g.
402. Primo, A.; Marino, T.; Corma, A.; Molinari, R.; García, H. Efficient Visible-Light Photocatalytic Water Splitting by Minute Amounts of Gold Supported on Nanoparticulate CeO $_2$ Obtained by a Biopolymer Templating Method. *J. Am. Chem. Soc.* **2011**, *133*, 6930–6933, doi:10.1021/ja2011498.
403. Konta, R.; Ishii, T.; Kato, H.; Kudo, A. Photocatalytic Activities of Noble Metal Ion Doped SrTiO $_3$ under Visible Light Irradiation. *J. Phys. Chem. B* **2004**, *108*, 8992–8995, doi:10.1021/jp049556p.
404. Li, R.; Zhang, F.; Wang, D.; Yang, J.; Li, M.; Zhu, J.; Zhou, X.; Han, H.; Li, C. Spatial Separation of Photogenerated Electrons and Holes among {010} and {110} Crystal Facets of BiVO4. *Nat Commun* **2013**, *4*, 1432, doi:10.1038/ncomms2401.
405. Palewicz, A.; Przeniosło, R.; Sosnowska, I.; Hewat, A.W. Atomic Displacements in BiFeO3 as a Function of Temperature: Neutron Diffraction Study. *Acta Crystallographica Section B: Structural Science* **2007**, *63*, 537–544, doi:10.1107/S0108768107023956.
406. Jain, A.; Ong, S.P.; Hautier, G.; Chen, W.; Richards, W.D.; Dacek, S.; Cholia, S.; Gunter, D.; Skinner, D.; Ceder, G.; et al. Commentary: The Materials Project: A Materials Genome Approach to Accelerating Materials Innovation. *APL Materials* **2013**, *1*, doi:10.1063/1.4812323.
407. Giannozzi, P.; Baroni, S.; Bonini, N.; Calandra, M.; Car, R.; Cavazzoni, C.; Ceresoli, D.; Chiarotti, G.L.; Cococcioni, M.; Dabo, I.; et al. QUANTUM ESPRESSO: A Modular and Open-Source Software Project for Quantum Simulations of Materials. *Journal of Physics Condensed Matter* **2009**, *21*, doi:10.1088/0953-8984/21/39/395502.

408. Cococcioni, M.; De Gironcoli, S. Linear Response Approach to the Calculation of the Effective Interaction Parameters in the LDA+U Method. *Physical Review B - Condensed Matter and Materials Physics* **2005**, *71*, 1–16, doi:10.1103/PhysRevB.71.035105.
409. H'Mŏk, H.L.; Martínez Aguilar, E.; Antúnez García, J.; Ribas Ariño, J.; Mestres, L.; Alemany, P.; Galván, D.H.; Siqueiros Beltrones, J.M.; Raymond Herrera, O. Theoretical Justification of Stable Ferromagnetism in Ferroelectric BiFeO 3 by First-Principles. *Computational Materials Science* **2019**, *164*, 66–73, doi:10.1016/j.commatsci.2019.03.040.
410. Clark, S.J.; Robertson, J. Energy Levels of Oxygen Vacancies in BiFeO3by Screened Exchange. *Applied Physics Letters* **2009**, *94*, 1–4, doi:10.1063/1.3070532.
411. Solakidou, M.; Georgiou, Y.; Deligiannakis, Y. Double-Nozzle Flame Spray Pyrolysis as a Potent Technology to Engineer Noble Metal-TiO2 Nanophotocatalysts for Efficient H2 Production. *Energies* **2021**, *14*, 817, doi:10.3390/en14040817.
412. Strobel, R.; Mädler, L.; Piacentini, M.; Maciejewski, M.; Baiker, A.; Pratsinis, S.E. Two-Nozzle Flame Synthesis of Pt/Ba/Al $_2$ O $_3$ for NO $_x$ Storage. *Chem. Mater.* **2006**, *18*, 2532–2537, doi:10.1021/cm0600529.
413. Lovell, E.C.; Großman, H.; Horlyck, J.; Scott, J.; Mädler, L.; Amal, R. Asymmetrical Double Flame Spray Pyrolysis-Designed SiO $_2$ /Ce $_{0.7}$ Zr $_{0.3}$ O $_2$ for the Dry Reforming of Methane. *ACS Appl. Mater. Interfaces* **2019**, *11*, 25766–25777, doi:10.1021/acsami.9b02572.
414. Kumaravel, V.; Imam, M.; Badreldin, A.; Chava, R.; Do, J.; Kang, M.; Abdel-Wahab, A. Photocatalytic Hydrogen Production: Role of Sacrificial Reagents on the Activity of Oxide, Carbon, and Sulfide Catalysts. *Catalysts* **2019**, *9*, 276, doi:10.3390/catal9030276.
415. Khan, M.A.; Nayan, N.; Shadiullah; Ahmad, M.K.; Soon, C.F. Surface Study of CuO Nanopetals by Advanced Nanocharacterization Techniques with Enhanced Optical and Catalytic Properties. *Nanomaterials* **2020**, *10*, 1298, doi:10.3390/nano10071298.
416. Baba-Ahmed, I.; Ghercă, D.; Iordan, A.-R.; Palamaru, M.N.; Mita, C.; Baghdad, R.; Ababei, G.; Lupu, N.; Benamar, M.A.; Abderrahmane, A.; et al. Sequential Synthesis Methodology Yielding Well-Defined Porous 75%SrTiO3/25%NiFe2O4 Nanocomposite. *Nanomaterials* **2021**, *12*, 138, doi:10.3390/nano12010138.
417. López-Suárez, F.E.; Parres-Esclapez, S.; Bueno-López, A.; Illán-Gómez, M.J.; Ura, B.; Trawczynski, J. Role of Surface and Lattice Copper Species in Copper-Containing (Mg/Sr)TiO3 Perovskite Catalysts for Soot Combustion. *Applied Catalysis B: Environmental* **2009**, *93*, 82–89, doi:10.1016/j.apcatb.2009.09.015.
418. van Benthem, K.; Elsässer, C.; French, R.H. Bulk Electronic Structure of SrTiO3: Experiment and Theory. *Journal of Applied Physics* **2001**, *90*, 6156–6164, doi:10.1063/1.1415766.
419. Xia, Y.; He, Z.; Hu, K.; Tang, B.; Su, J.; Liu, Y.; Li, X. Fabrication of N-SrTiO3/p-Cu2O Heterojunction Composites with Enhanced Photocatalytic Performance. *Journal of Alloys and Compounds* **2018**, *753*, 356–363, doi:10.1016/j.jallcom.2018.04.231.
420. Li, W.; Liu, S.; Wang, S.; Guo, Q.; Guo, J. The Roles of Reduced Ti Cations and Oxygen Vacancies in Water Adsorption and Dissociation on SrTiO $_3$ (110). *J. Phys. Chem. C* **2014**, *118*, 2469–2474, doi:10.1021/jp409076y.
421. Ura, B.; Trawczyński, J.; Kotarba, A.; Bieniasz, W.; Illán-Gómez, M.J.; Bueno-López, A.; López-Suárez, F.E. Effect of Potassium Addition on Catalytic Activity of SrTiO3 Catalyst for Diesel Soot Combustion. *Applied Catalysis B: Environmental* **2011**, *101*, 169–175, doi:10.1016/j.apcatb.2010.09.018.
422. Tan, H.; Zhao, Z.; Zhu, W.; Coker, E.N.; Li, B.; Zheng, M.; Yu, W.; Fan, H.; Sun, Z. Oxygen Vacancy Enhanced Photocatalytic Activity of Pervoskite SrTiO $_3$. *ACS Appl. Mater. Interfaces* **2014**, *6*, 19184–19190, doi:10.1021/am5051907.
423. Mai, X.T.; Bui, D.N.; Pham, V.K.; Nguyen, T.H.L.; Nguyen, T.T.L.; Chau, H.D.; Tran, T.K.N. Effect of CuO Loading on the Photocatalytic Activity of SrTiO3 for Hydrogen Evolution. *Inorganics* **2022**, *10*, 130, doi:10.3390/inorganics10090130.
424. Xia, Y.; He, Z.; Hu, K.; Tang, B.; Su, J.; Liu, Y.; Li, X. Fabrication of N-SrTiO3/p-Cu2O Heterojunction Composites with Enhanced Photocatalytic Performance. *Journal of Alloys and Compounds* **2018**, *753*, 356–363, doi:10.1016/j.jallcom.2018.04.231.
425. Ramos-Sanchez, J.E.; Camposeco, R.; Lee, S.-W.; Rodríguez-González, V. Sustainable Synthesis of AgNPs/Strontium-Titanate-Perovskite-like Catalysts for the Photocatalytic Production of Hydrogen. *Catalysis Today* **2020**, *341*, 112–119, doi:10.1016/j.cattod.2019.08.020.
426. Liu, Y.; Xie, L.; Li, Y.; Yang, R.; Qu, J.; Li, Y.; Li, X. Synthesis and High Photocatalytic Hydrogen Production of SrTiO3 Nanoparticles from Water Splitting under UV Irradiation. *Journal of Power Sources* **2008**, *183*, 701–707, doi:10.1016/j.jpowsour.2008.05.057.
427. Macaraig, L.; Chuangchote, S.; Sagawa, T. Electrospun SrTiO $_3$ Nanofibers for Photocatalytic Hydrogen Generation. *J. Mater. Res.* **2014**, *29*, 123–130, doi:10.1557/jmr.2013.259.
428. Qin, Y.; Wang, G.; Wang, Y. Study on the Photocatalytic Property of La-Doped CoO/SrTiO3 for Water Decomposition to Hydrogen. *Catalysis Communications* **2007**, *8*, 926–930, doi:10.1016/j.catcom.2006.11.025.
429. Sakata, Y.; Miyoshi, Y.; Maeda, T.; Ishikiriyama, K.; Yamazaki, Y.; Imamura, H.; Ham, Y.; Hisatomi, T.; Kubota, J.; Yamakata, A.; et al. Photocatalytic Property of Metal Ion Added SrTiO3 to Overall H2O Splitting. *Applied Catalysis A: General* **2016**, *521*, 227–232, doi:10.1016/j.apcata.2015.12.013.
430. Yu, K.; Zhang, C.; Chang, Y.; Feng, Y.; Yang, Z.; Yang, T.; Lou, L.-L.; Liu, S. Novel Three-Dimensionally Ordered Macroporous SrTiO3 Photocatalysts with Remarkably Enhanced Hydrogen Production Performance. *Applied Catalysis B: Environmental* **2017**, *200*, 514–520, doi:10.1016/j.apcatb.2016.07.049.
431. Kumar, A.; Navakoteswara Rao, V.; Kumar, A.; Mushtaq, A.; Sharma, L.; Halder, A.; Pal, S.K.; Shankar, M.V.; Krishnan, V. Three-Dimensional Carbonaceous Aerogels Embedded with Rh-SrTiO $_3$ for Enhanced Hydrogen Evolution Triggered by Efficient Charge Transfer and Light Absorption. *ACS Appl. Energy Mater.* **2020**, *3*, 12134–12147, doi:10.1021/acsaem.0c02229.
432. Lv, S.; Wang, Y.; Zhou, Y.; Liu, Q.; Song, C.; Wang, D. Oxygen Vacancy Stimulated Direct Z-Scheme of Mesoporous Cu2O/TiO2 for Enhanced Photocatalytic Hydrogen Production from Water and Seawater. *Journal of Alloys and Compounds* **2021**, *868*, 159144, doi:10.1016/j.jallcom.2021.159144.
433. Lou, Y.; Zhang, Y.; Cheng, L.; Chen, J.; Zhao, Y. A Stable Plasmonic Cu@Cu $_2$ O/ZnO Heterojunction for Enhanced Photocatalytic Hydrogen Generation. *ChemSusChem* **2018**, *11*, 1505–1511, doi:10.1002/cssc.201800249.
434. Yoo, H.; Kahng, S.; Hyeun Kim, J. Z-Scheme Assisted ZnO/Cu2O-CuO Photocatalysts to Increase Photoactive Electrons in Hydrogen Evolution by Water Splitting. *Solar Energy Materials and Solar Cells* **2020**, *204*, 110211, doi:10.1016/j.solmat.2019.110211.
435. Xiong, Z.; Lei, Z.; Kuang, C.-C.; Chen, X.; Gong, B.; Zhao, Y.; Zhang, J.; Zheng, C.; Wu, J.C.S. Selective Photocatalytic Reduction of CO2 into CH4 over Pt-Cu2O TiO2 Nanocrystals: The Interaction between Pt and Cu2O Cocatalysts. *Applied Catalysis B: Environmental* **2017**, *202*, 695–703, doi:10.1016/j.apcatb.2016.10.001.
436. Chen, B.-R.; Nguyen, V.-H.; Wu, J.C.S.; Martin, R.; Kočí, K. Production of Renewable Fuels by the Photohydrogenation of CO $_2$: Effect of the Cu Species Loaded onto TiO $_2$ Photocatalysts. *Phys. Chem. Chem. Phys.* **2016**, *18*, 4942–4951, doi:10.1039/C5CP06999H.

437. Polliotto, V.; Albanese, E.; Livraghi, S.; Indyka, P.; Sojka, Z.; Pacchioni, G.; Giamello, E. Fifty–Fifty Zr–Ti Solid Solution with a TiO_2-Type Structure: Electronic Structure and Photochemical Properties of Zirconium Titanate $ZrTiO_4$. *J. Phys. Chem. C* **2017**, *121*, 5487–5497, doi:10.1021/acs.jpcc.6b12892.
438. Brailsford, J.R.; Morton, J.R. Paramagnetic Resonance Spectrum of O^- Trapped in KCl, RbCl, and KBr. *The Journal of Chemical Physics* **1969**, *51*, 4794–4798, doi:10.1063/1.1671869.
439. Gionco, C.; Livraghi, S.; Maurelli, S.; Giamello, E.; Tosoni, S.; Di Valentin, C.; Pacchioni, G. Al- and Ga-Doped TiO_2, ZrO_2, and HfO_2: The Nature of O 2p Trapped Holes from a Combined Electron Paramagnetic Resonance (EPR) and Density Functional Theory (DFT) Study. *Chem. Mater.* **2015**, *27*, 3936–3945, doi:10.1021/acs.chemmater.5b00800.
440. Chiesa, M.; Giamello, E.; Livraghi, S.; Paganini, M.C.; Polliotto, V.; Salvadori, E. Electron Magnetic Resonance in Heterogeneous Photocatalysis Research. *J. Phys.: Condens. Matter* **2019**, *31*, 444001, doi:10.1088/1361-648X/ab32c6.
441. Al-Mowali, A.H.; Kuder, W.A.A. An Electron Paramagnetic Resonance Study of Dichlorobis-(π-Cyclopentadienyl)Tantalum(IV), (π-C5H5)2TaCl2. *Journal of Molecular Structure* **1979**, *57*, 141–147, doi:10.1016/0022-2860(79)80239-2.
442. Psathas, P.; Moularas, C.; Smykała, S.; Deligiannakis, Y. Highly Crystalline Nanosized $NaTaO_3$/NiO Heterojunctions Engineered by Double-Nozzle Flame Spray Pyrolysis for Solar-to-H_2 Conversion: Toward Industrial-Scale Synthesis. *ACS Appl. Nano Mater.* **2023**, *6*, 2658–2671, doi:10.1021/acsanm.2c05066.
443. Schulz, H.; Mädler, L.; Pratsinis, S.E.; Burtscher, P.; Moszner, N. Transparent Nanocomposites of Radiopaque, Flame-Made Ta_2O_5/SiO_2 Particles in an Acrylic Matrix. *Adv. Funct. Mater.* **2005**, *15*, 830–837, doi:10.1002/adfm.200400234.
444. Bi, X.; Bai, P.; Yang, T.; Zhang, J.; Li, H.; Chai, Z.; Wang, X. In-Situ Synthesis of Ta2O5@few-Layered rGO Core-Shell Nanosphere with Abundant Oxygen Vacancies for Highly Stable Lithium-Ion Battery. *J Solid State Electrochem* **2020**, *24*, 1567–1575, doi:10.1007/s10008-020-04709-9.
445. Bright, T.J.; Watjen, J.I.; Zhang, Z.M.; Muratore, C.; Voevodin, A.A.; Koukis, D.I.; Tanner, D.B.; Arenas, D.J. Infrared Optical Properties of Amorphous and Nanocrystalline Ta_2O_5 Thin Films. *Journal of Applied Physics* **2013**, *114*, 083515, doi:10.1063/1.4819325.
446. Gonçalves, R.V.; Wojcieszak, R.; Uberman, P.M.; Teixeira, S.R.; Rossi, L.M. Insights into the Active Surface Species Formed on Ta2O5 Nanotubes in the Catalytic Oxidation of CO. *Phys. Chem. Chem. Phys.* **2014**, *16*, 5755, doi:10.1039/c3cp54887b.
447. Grewe, T.; Tüysüz, H. Designing Photocatalysts for Hydrogen Evolution: Are Complex Preparation Strategies Necessary to Produce Active Catalysts? *ChemSusChem* **2015**, *8*, 3084–3091, doi:10.1002/cssc.201500774.
448. Joseph, C.; Bourson, P.; Fontana, M.D. Amorphous to Crystalline Transformation in Ta2O5 Studied by Raman Spectroscopy: Amorphous to Crystalline Transformation in Ta2O5 Studied by Raman Spectroscopy. *J. Raman Spectrosc.* **2012**, *43*, 1146–1150, doi:10.1002/jrs.3142.
449. Dobal, P.S.; Katiyar, R.S.; Jiang, Y.; Guo, R.; Bhalla, A.S. Raman Scattering Study of a Phase Transition in Tantalum Pentoxide. *J. Raman Spectrosc.* **2000**, *31*, 1061–1065, doi:10.1002/1097-4555(200012)31:12<1061::AID-JRS644>3.0.CO;2-G.
450. An, L.; Park, Y.; Sohn, Y.; Onishi, H. Effect of Etching on Electron–Hole Recombination in Sr-Doped $NaTaO_3$ Photocatalysts. *J. Phys. Chem. C* **2015**, *119*, 28440–28447, doi:10.1021/acs.jpcc.5b09638.
451. Teixeira, N.G.; Dias, A.; Moreira, R.L. Raman Scattering Study of the High Temperature Phase Transitions of NaTaO3. *Journal of the European Ceramic Society* **2007**, *27*, 3683–3686, doi:10.1016/j.jeurceramsoc.2007.02.015.
452. Schwan, J.; Ulrich, S.; Batori, V.; Ehrhardt, H.; Silva, S.R.P. Raman Spectroscopy on Amorphous Carbon Films. *Journal of Applied Physics* **1996**, *80*, 440–447, doi:10.1063/1.362745.
453. Cui, E.; Hou, G.; Chen, X.; Zhang, F.; Deng, Y.; Yu, G.; Li, B.; Wu, Y. In-Situ Hydrothermal Fabrication of Sr2FeTaO6/NaTaO3 Heterojunction Photocatalyst Aimed at the Effective Promotion of Electron-Hole Separation and Visible-Light Absorption. *Applied Catalysis B: Environmental* **2019**, *241*, 52–65, doi:10.1016/j.apcatb.2018.09.006.
454. Simpson, R.; White, R.G.; Watts, J.F.; Baker, M.A. XPS Investigation of Monatomic and Cluster Argon Ion Sputtering of Tantalum Pentoxide. *Applied Surface Science* **2017**, *405*, 79–87, doi:10.1016/j.apsusc.2017.02.006.
455. Wenderich, K.; Mul, G. Methods, Mechanism, and Applications of Photodeposition in Photocatalysis: A Review. *Chem. Rev.* **2016**, *116*, 14587–14619, doi:10.1021/acs.chemrev.6b00327.
456. Kudo, A.; Miseki, Y. Heterogeneous Photocatalyst Materials for Water Splitting. *Chem. Soc. Rev.* **2009**, *38*, 253–278, doi:10.1039/B800489G.
457. Husin, H.; Su, W.-N.; Chen, H.-M.; Pan, C.-J.; Chang, S.-H.; Rick, J.; Chuang, W.-T.; Sheu, H.-S.; Hwang, B.-J. Photocatalytic Hydrogen Production on Nickel-Loaded LaxNa1−xTaO3 Prepared by Hydrogen Peroxide-Water Based Process. *Green Chem.* **2011**, *13*, 1745, doi:10.1039/c1gc15070g.
458. Xu, L.; Sun, X.; Tu, H.; Jia, Q.; Gong, H.; Guan, J. Synchronous Etching-Epitaxial Growth Fabrication of Facet-Coupling NaTaO3/Ta2O5 Heterostructured Nanofibers for Enhanced Photocatalytic Hydrogen Production. *Applied Catalysis B: Environmental* **2016**, *184*, 309–319, doi:10.1016/j.apcatb.2015.11.041.
459. Lü, X.; Ding, S.; Lin, T.; Mou, X.; Hong, Z.; Huang, F. Ta_2O_5 Nanowires: A Novel Synthetic Method and Their Solar Energy Utilization. *Dalton Trans.* **2012**, *41*, 622–627, doi:10.1039/C1DT11124H.
460. Zhang, Z.; Yates, J.T. Band Bending in Semiconductors: Chemical and Physical Consequences at Surfaces and Interfaces. *Chem. Rev.* **2012**, *112*, 5520–5551, doi:10.1021/cr3000626.
461. Zhang, Q.; Li, Z.; Wang, S.; Li, R.; Zhang, X.; Liang, Z.; Han, H.; Liao, S.; Li, C. Effect of Redox Cocatalysts Location on Photocatalytic Overall Water Splitting over Cubic $NaTaO_3$ Semiconductor Crystals Exposed with Equivalent Facets. *ACS Catal.* **2016**, *6*, 2182–2191, doi:10.1021/acscatal.5b02503.
462. Low, J.; Yu, J.; Jaroniec, M.; Wageh, S.; Al-Ghamdi, A.A. Heterojunction Photocatalysts. *Adv. Mater.* **2017**, *29*, 1601694, doi:10.1002/adma.201601694.
463. Ziolek, M.; Sobczak, I.; Decyk, P.; Sobańska, K.; Pietrzyk, P.; Sojka, Z. Search for Reactive Intermediates in Catalytic Oxidation with Hydrogen Peroxide over Amorphous Niobium(V) and Tantalum(V) Oxides. *Applied Catalysis B: Environmental* **2015**, *164*, 288–296, doi:10.1016/j.apcatb.2014.09.024.
464. Moularas, C.; Dimitriou, C.; Georgiou, Y.; Evangelakis, G.; Boukos, N.; Deligiannakis, Y. Electron Paramagnetic Resonance Quantifies Hot-Electron Transfer from Plasmonic Ag@SiO_2 to Cr^{6+}/Cr^{5+}/Cr^{3+}. *J. Phys. Chem. C* **2023**, *127*, 2045–2057, doi:10.1021/acs.jpcc.2c07837.

LIST OF PUBLICATIONS RESULTED FROM THIS WORK

(2023) Patent: Hellenic Industrial Property Organisation (O.B.I.), e-filing: 2413-0004728470, «*Method for synthesis of hybrid nanomaterials by low-temperature monomolecular deposition and flame-spray-pyrolysis*» Y. Deligiannakis, M. Solakidou, A. Zindrou, P. Psathas

Publications

(5)	ACS Applied Nano Materials 2023, 6, 4, 2658–267. https://doi.org/10.1021/acsanm.2c05066 «Highly Crystalline Nanosized $NaTaO_3$ /NiO Heterojunctions Engineered by Double-Nozzle Flame Spray Pyrolysis for Solar-to-H_2 Conversion: Toward Industrial-Scale Synthesis» **P. Psathas**, C. Moularas, S. Smykała, and Y. Deligiannakis
(4)	Nanomaterials 2023, 13(3), 482. https://doi.org/10.3390/nano13030482 «In Tandem Control of La-Doping and CuO-Heterojunction on $SrTiO_3$ Perovskite by Double-Nozzle Flame Spray Pyrolysis: Selective H_2 vs. CH_4 Photocatalytic Production from H_2O/CH_3OH» **P. Psathas**, A. Zindrou, C. Papachristodoulou, N. Boukos, Y. Deligiannakis
(3)	Chemical Physics Letters 2021 782:39031. https://doi.org/10.1016/j.cplett.2021.139031 «Electron Paramagnetic Resonance Study of Photo-induced Hole/Electron Pairs in $NaTaO_3$ Nanoparticles» C. Moularas, **P. Psathas**, Y. Deligiannakis
(2)	Energies 2021, 14(17), 5235. https://doi.org/10.3390/en14175235 «Flame Spray Pyrolysis Engineering of Nanosized Mullite-$Bi_2Fe_4O_9$ and Perovskite-$BiFeO_3$ as Highly Efficient Photocatalysts for O_2 Production from H_2O Splitting» **P. Psathas**, M. Solakidou, A. Mantzanis, Y. Deligiannakis
(1)	Powder Technology 2020, 368 268-277. https://doi.org/10.1016/j.powtec.2020.04.059 «Controlled-Phase Synthesis of $Bi_2Fe_4O_9$ & $BiFeO_3$ by Flame Spray Pyrolysis and their evaluation as non-noble metal catalysts for efficient reduction of 4-nitrophenol» **P. Psathas**, Y. Georgiou, C. Moularas, GS. Armatas, Y Deligiannakis

Presentations to National and International Conferences

(6)	16ο Panhellenic symposium of catalysis, 20-22 October 2022, Chania «Synthesis of Perovskites {$NaTaO_3$, $LiTaO_3$}/NiO with Flame Spray Pyrolysis technology for high yield artificial photosynthesis (CO_2/H_2O reduction)» **P. Psathas**, P. Stathi , C. Moularas, Y. Deligiannakis
(5)	XXXV Panhellenic Conference on Solid State Physics & Materials Science, September 2021, Athens. «Development of Tantalum-based Semiconductors with functional NiO/Pt deposition by One-Step Flame Spray Pyrolysis» **P. Psathas**, C. Moularas, Y. Deligiannakis
(4)	1st Online Conference of Young Scientists on "Mineral Resources-Environment-Chemical Engineering", March 2021, Kozani. «Synthesis of $BiFeO_3$ and $Bi_2Fe_4O_9$ by Spray Flame Pyrolysis technology: optimization of photocatalytic O_2 production through control of lattice defects»

	P. Psathas, M**.** Solakidou, A**.** Mantzanis, Y. Deligiannakis
(3)	4th International Symposium Gas-Phase Synthesis of Functional Nanomaterials, 2020 (Duisburg, Germany) «Gas-phase engineering of Tantalum-based nano-ensembles for photocatalytic applications» C. Moularas, **P. Psathas**, Y. Deligiannakis
(2)	Poster: 4th International Symposium Gas-Phase Synthesis of Functional Nanomaterials, 2020 (Duisburg, Germany) «CFD modeling of combustion in anoxic flame spray pyrolysis» D. Deligiannakis, C. Moularas, **P. Psathas**, Y. Deligiannakis
(1)	Poster: 15ο Panhellenic symposium of catalysis, October 2018, Ioannina, Greece. «Controlled-Phase Bismuth-Iron-Oxide Nanophotocatalysts [$BiFeO_3/Bi_2Fe_4O_9$] produced by Flame-Spray-Pyrolysis» **P. Psathas**, E. Mouzourakis, M. Solakidou, and Y. Deligiannakis